Ultrafast Electron Crystallography: Principles and Applications

Thesis by

Ding-Shyue (Jerry) Yang

In Partial Fulfillment of the Requirements
for the Degree of
Doctor of Philosophy

California Institute of Technology
Pasadena, California

2009
(Defended May 5, 2009)

To my parents and my wife Yen-Yu

Acknowledgement

Surely God is my help;
the Lord is the one who sustains me.
Psalms 54:4

Words cannot express my deepest thankfulness to God. I simply could not dismiss His constant guidance through various people as merely a long series of lucky incidences, as I reflect on how I have reached this far into the field of scientific research, all the way beginning from the change of my major from mathematics to chemistry and then the incorporation of physics, to the decision-making process of my coming to Caltech, to my entering Dr. Ahmed Zewail's group and then switching to the current research direction, with the spiritual support for me to hold on this path and, finally, to the result of many previous publications and the formation of this thesis. Special thanks must be given to my teacher Pastor Jeong, who has been teaching me about God and the meaning of life.

I am very grateful to Dr. Zewail, my research advisor, for his providing me with the opportunity to work on the development of ultrafast electron crystallography (UEC), for his unceasing support and encouraging words, and for his enthusiasm about science and his challenge to push me forward. I greatly appreciate his patience with me when I was searching for a breakthrough and managing to meet his high expectation. In addition, if my writing style does make noticeable improvements, his endurance of working on my manuscripts should earn my sincere gratitude.

I thank Drs. Chong-Yu Ruan, Vladimir Lobastov, Franco Vigliotti, and Songye Chen for their construction of the experimental apparatus that enabled all the following studies. Dr. Ruan is particularly appreciated for his leading me into the UEC research, although that period was only 3 months long before his leaving. Dr. Lobastov and Dr. Chen were of great help to me in my further familiarizing with the various aspects of the instrument. Before this research direction switch, I learned the femtosecond techniques and how to be an experimentalist from Dr. Hern Paik, whose great help will be remembered. Mr. I-Ren Lee and Dr. Spencer Baskin are also thanked for the stimulating discussions and collaboration in the gas-phase studies that I initially participated in.

During my 5 years of developing UEC, I was truly fortunate to have the opportunities to work with many talented scientists: chronologically, Dr. Nuh Gedik for the studies of interfacial water assemblies, prototype semiconducting materials and a superconductor thin film; Dr. Peter Baum for the investigation of transient structures during phase transformations; Dr. Jau Tang for theoretical modeling of the interfacial structural dynamics; Dr. Fabrizio Carbone for the studies of graphite and high-temperature superconductors; and Dr. Changshi Lao for the study of semiconducting nanowire materials. The instrumental advance made by Dr. Baum should be specially acknowledged because it is now an essential part of the UEC apparatus, and has enabled many new discoveries that require a femtosecond temporal resolution. In addition to these direct collaborators, I also benefited a great deal from the inspiring conversations and interactions with my colleagues that came from various different training backgrounds in Dr. Zewail's group.

Last but not least, I want to express my thankfulness and love to my parents, who have always been supportive to whatever direction I chose to go, even when it meant a long separation in both space and time between them and their child. My gratefulness and love go to my wife Yen-Yu Shih, for her willingness to set aside her career path and accompany me patiently on the course of my research, even though this pursuit of mine does not intrigue her very much. From our unborn baby, I expect to receive excitement and joy as much as (if not greater than) from my scientific studies in the future.

Abstract

During the last 20 to 30 years, the development and application of time-resolved experimental techniques with a femtosecond temporal resolution have brought to us much knowledge about the fundamental processes in physics, chemistry and biology. Nevertheless, standard spectroscopic methods have their limitation in the determination of the transient structures during ultrafast dynamics at the atomic level, because the spatial resolution is restricted by the wavelength of the probe pulse used. In contract, with the scheme of femtosecond optical initiation and electron probing and through the diffraction phenomenon, ultrafast electron crystallography (UEC) was recently developed as a time-resolved structure-probing technique for condensed-matter studies. The short wavelength and small pulse duration of the highly accelerated electrons used provide the atomic-scale spatiotemporal resolution. In addition, the large electron–matter interaction enables the detection of small transient changes as well as the investigation of surface and interfacial phenomena.

This thesis describes the principles of UEC and its applications to a variety of systems, ranging from nanometer-scale structures to highly correlated materials and to interfacial assemblies. By using a prototype semiconducting material, we elucidated the fundamental processes at work in different parts of the femtosecond-to-nanosecond time range; this investigation led to a conceptual change from the consideration of laser-induced heating to the examination of nonequilibrium structural modifications as a result of the transient dynamical changes in, e.g., carriers, the crystal potential, and phonons. On the basis of such an understanding, we observed and understood the colossal unidirectional expansion induced by the photoexcitation of nanostructures to be a

potential-driven result rather than a thermal one.

For highly correlated materials, we showed the effectiveness of UEC in resolving the transient intermediate structures during phase transformations as well as identifying new phases in the nonequilibrium state. An important breakthrough made by UEC was the confirmation of the anisotropic involvement of lattice in the electron pairing mechanism for high-temperature superconductors. In interfacial assemblies, we also found a nonequilibrium phase transformation in water and the phenomenon of ultrafast annealing for a better order in a self-assembled monolayer. With these successful experiences, we expect more condensed-matter studies by UEC to come.

Contents

Part I. Semiconducting Materials and Nanometer-scale Structures

Part II. Highly Correlated Materials

Part III. Surface Assemblies and Interfacial Phenomena

11. Structures and Dynamics of Self-Assembled Surface Monolayers 325

12. Theoretical Modeling of Structural Dynamics 339

List of Figures

List of Tables

Chapter 1

Introduction[†]

[†] Part of this chapter was presented in the 2008 Everhart Lecture Series on May 1st, 2008; see http://today.caltech.edu/theater/list?subset=science&story_count=end

Being able to see the three-dimensional (3D) structure of a molecule or a condensed matter at the atomic level is crucial to our understanding of the substance and even its further applications. A perfect example would be the celebrated double-helical structure of DNA. Its discovery in 1953 (*1, 2*) had a huge impact on biology and medicine, and marked a new era in our understanding about life. Nowadays, when we talk about the biological activities and functions that occur in a cell, we speak in a way as if the biological macromolecules were visible in front of our eyes. Without clear knowledge of the molecular structures, scientific research endeavors would certainly be limited; the depth of our studies and the insights and applications derived from them could hardly reach their full capacities. For inorganic materials, too, without knowledge of the atomic arrangement in a unit cell, full understanding and even manipulation of the materials properties may not be achieved. In fact, the importance and impact of visualizing 3D structures at the atomic level were many times acknowledged by awarding the discoverers with Nobel prizes. A few examples include the development in solving the structures of inorganic salts, acknowledged in 1914 and 1915, DNA and hemoglobin (*3*) in 1962, borane (*4*) in 1976, photosynthetic reaction center (*5*) in 1988, ATP synthase (*6*) in 1997, and potassium ion channels in cell membranes (*7*) in 2003.

On the basis of the molecular or crystal structure, the research that can be pursued is outlined as follows. Static studies involve knowledge of the physical properties such as mechanical and thermodynamic properties, chemical stability, major forces that exist, etc.; theoretical modeling and calculations are made to further investigate the substance. Dynamics studies often put an emphasis on visualization of dynamical behaviors such as atomic motions, structural changes on different time scales, and reaction pathways. The combination of all these pieces of information allows us to know further the functions of

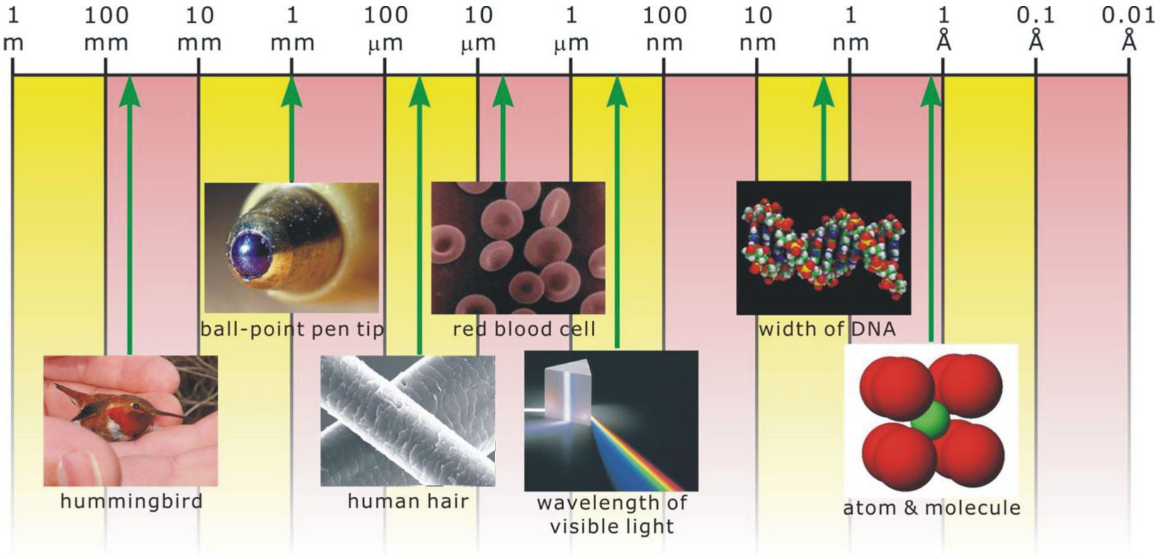

Fig. 1. Several objects and their length scales.

the molecule or material, and to seek the possibilities of modifications and practical applications. Thus, studying structures at the atomic level has been one of the major research directions.

One important issue involved in the structure determination is the length scale (Fig. 1). Objects that can be seen by naked eyes are above tens of micrometers. With the use of an optical microscope, smaller objects with a dimension longer than the wavelength of visible light can be observed. However, below this length scale, visible light does not have the resolution due to the intrinsic diffraction limit. Atoms and molecules are much smaller, on the nanometer-to-angstrom scale. Therefore, one way to resolve this length-scale issue is to use light with a matching wavelength, which is in the range of x-ray, or small particles that also exhibit wave property due to the quantum effect, to detect molecular structures. As an example, for the studies presented in the following chapters, electrons are used and their acceleration by an electric field of 30 kV yields a wavelength of ~0.07 Å, which is much shorter than typical bond lengths and,

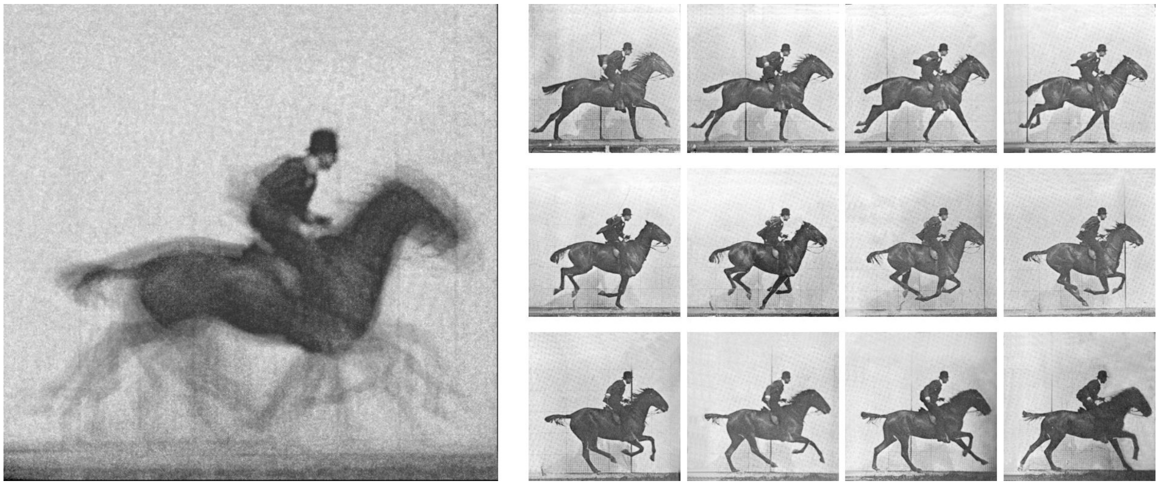

Fig. 2. Sequence of a race horse galloping captured with the use of high-speed photography by Eadweard Muybridge (right). Without a proper temporal resolution, the observation would be similar to the combined image illustrated on the left.

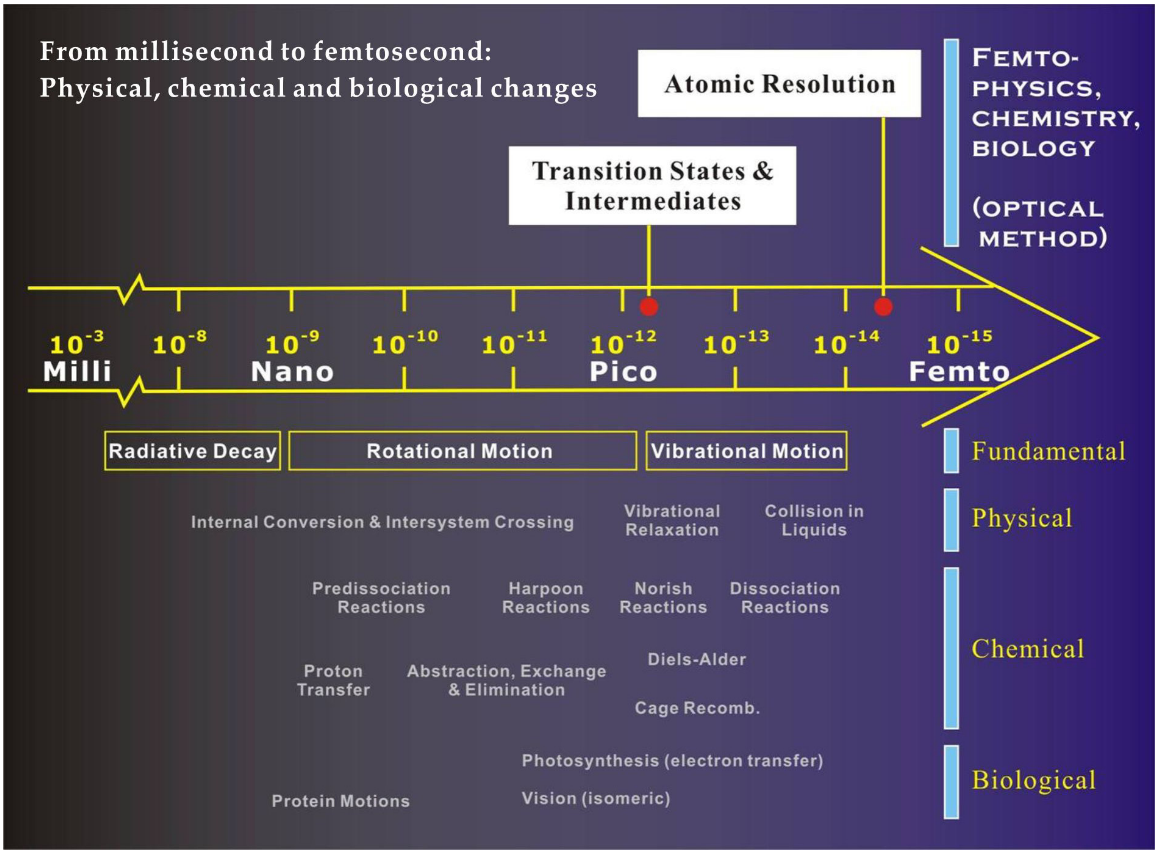

Fig. 3. Examples of physical, chemical and biological processes and their time scales (adapted from Ref. 8). Femtosecond techniques provide the atomic resolution in time.

hence, provides the spatial resolution.

Besides the length-scale issue, traditional experiments suffer from one major problem, which is the poor temporal resolution. Without a proper temporal resolution, only the average atomic positions may be obtained, since atoms are constantly moving due to the zero-point and thermal energies. If important motions are much faster than the resolution of the experimental techniques, the observation cannot provide detailed information about the structure and dynamics involved. In photography, an analogy is shown in the left panel of Fig. 2. The equipment of an ideal temporal resolution [e.g., high-speed photography for capturing the sequence of a race horse galloping (Fig. 2, right)] allows the studies of the structure and dynamics at different moments, which may offer further understanding of the functions and the overall physical picture.

As illustrated in Fig. 3, the fundamental motions at the atomic level, such as electronic changes, vibrational and rotational motions, are in the femtosecond to nanosecond range. The important physical, chemical and biological processes on such a time scale are, for example, collisions, vibrational relaxation, proton transfer and chemical reactions, protein motions and light-induced transformations. To resolve these processes and probe the transient states, experimental techniques that have a suitable temporal resolution are required. For the last 20 to 30 years, such scientific endeavors were in the realm of femtophysics, chemistry and biology (*8, 9*). The observables were typically measured by spectroscopic methods, for example, absorption and luminescence, reflectivity and transmission, mass or photoelectron spectra. While such measurements are giving important dynamics information, the results typically do not reveal the direct snapshots of the structure involved (*10*). In contrast, experimental techniques that can directly provide structural information with an ultrashort (femtosecond to nanosecond) temporal resolution have clear advantages for studies of transient structures.

For the reasons given above, time-resolved x-ray and electron diffraction methods have been under development for more than two decades. A review of their progress until 1997 can be found in Ref. 10. Ultrashort x-ray pulses with a sub-picosecond temporal width were successfully produced in 1996 (*11*); generated by another method, the pulses were used on a real material and diffraction changes were observed in 1997 (*12*). Various groups reported ultrafast x-ray diffraction studies in 1999 and, interestingly, most of them were made on semiconducting materials (*13-15*). Since then, this technique has been applied to the studies of nonthermal melting (*16*), inertial dynamics of thermal disorder (*17*), dynamics of optical (*18*) and acoustic (*19-21*) phonons, the motion of charges (*22*), solid-solid phase transitions (*23*), and transient structural changes (*24*) even in the solution phase (*25, 26*). A brief review that covers the work on transient crystalline structures can be found in Ref. 27.

In our laboratory, the methods of choice have been ultrafast electron diffraction and microscopy (*28*). The advantages of using electrons are many (*29*). First, the large scattering cross section due to the order-of-magnitude stronger electron-matter interaction (compared with the light-matter interaction) provides high sensitivity in detecting small changes and also surface sensitivity for interfacial studies. Second, electrons are less damaging to specimens per useful scattering event. Third, apparatus can be built on the tabletop scale, which allows us to avoid competing for the scarce resource such as a synchrotron x-ray facility. With the use of femtosecond laser pulses, the temporal width of electron pulses generated from a photocathode through the photoelectric effect can be as low as several hundred femtoseconds in the low-flux limit (*30*).

The apparatus of ultrafast electron crystallography (UEC) was the fourth system of the time-resolved electron diffraction technique in our group, specifically dedicated to condensed-matter studies. The earlier three generations were chronologically developed for gas-phase research (*31, 32*). Unlike other groups that also implemented ultrafast electron diffraction for materials studies in transmission geometry at roughly a similar time (*33, 34*), our UEC system (*35*) can be operated in both reflection and transmission geometries for a wider range of applications. Furthermore, research focuses are quite different: for others, the strong emphasis is on irreversible ultrafast melting (*33, 36, 37*) or on coherent film motions and electronic Grüneisen parameters (*38-40*); for us, the experiments are conducted on reversible structural changes, and the research topics include (and are not limited to) nonequilibrium structural dynamics (*41-44*), phase transformations (*45*), highly correlated materials such as high-temperature superconductors (*46, 47*), interfacial thin films (*48-50*), and surface assemblies (*51-53*). Most of these topics will be covered in this thesis.

Chapter 2 describes the fundamental principles related to UEC studies and the dynamics information that may be obtained. Although electron crystallography has been developed into a complex subject, our experience shows that the geometrical consideration and the kinematic (elastic) scattering theory are capable of capturing most of the physical picture from the observed dynamical changes. The UEC methodology, apparatus, and discussion of several experimental concerns are given in Ch. 3.

Chapters 4 and 5 present the studies of nanometer-scale structures of semiconducting materials. In Ch. 4, gallium arsenide is the prototype system and its detailed study forms the foundation for the application of UEC to various other systems (*42*). Following the ultrafast heating made by femtosecond light pulses, we observe a universal behavior of diffraction changes, with amplitudes far exceeding those of thermal heating (in a time of ~10 ps); the lattice change can be monitored with an accuracy of ~0.001 Å. The physical picture for such structural dynamics is described with emphasis on the motion of atoms under the influence of optical and acoustic vibrations, the potential anisotropy of the lattice that results in the weakening of bonding, and the diffusion at much longer times. This work is the result of collaboration with Dr. Nuh Gedik who initiated the idea of working on a quantum-well structure for both reflection and transmission studies.

In Ch. 5, the same picture is applicable to the structural dynamics of zinc oxide nanowires, whose colossal expansion, as a result of the induced antibonding character, is highly anisotropic (quasi-1D) and two orders of magnitude higher than that expected at thermal equilibrium (*44*). This unanticipated ultrafast carrier-driven expansion highlights the optoelectronic consequences of nanometer-scale morphologies. Observation of the electron refraction phenomenon is also discussed. This work is the result of collaboration with Dr. Changshi Lao who contributed the idea of studying nanostructured materials. Prof. Zhong Lin Wang at Georgia Institute of Technology kindly provided the specimens.

Chapters 6 to 8 describe the UEC studies of several highly correlated materials, including vanadium dioxide and high-temperature superconducting cuprates. In Ch. 6, we report the visualization of transitional structures from the initial monoclinic to the final tetragonal phase in crystalline vanadium dioxide (*45*); the change is initiated by near-infrared excitation. By studying the spatiotemporal behavior from all observed Bragg diffractions in 3D, the femtosecond primary vanadium−vanadium bond dilation, the displacements of atoms in picoseconds, and the sound wave shear motion on hundreds of picoseconds are resolved, which elucidates the nature of the structural pathways and the nonconcerted mechanism of the solid-solid phase transformation. This work is made possible because Prof. Liu Hao Tjeng generously gave us some crystals, Prof. George R. Rossman provided the crystal-cutting equipment, and Prof. Nai-Chang Yeh allowed me to use the pulsed laser deposition system for the making of thin films; Dr. Peter Baum is the collaborator of this work. I have to admit that we were fortunate because the plan of cutting and polishing the last crystal did work, and the last product during the many trials of thin-film making gave the correct phase and good crystallinity.

In Ch. 7, an unanticipated nonequilibrium phase transition in lanthanum cuprate is reported, which is recognized through the observation of "structural isosbestic" points in the temporal evolution of diffractions (*46*). Time scales of the structural dynamics of such a transition are examined, and the observed transient behavior also displays a threshold effect for the dependence of *c*-axis expansion on the excitation laser fluence. This threshold for photon doping occurs at ~0.12 photons per copper site, which is intriguingly close to the density (per site) of chemically doped carriers needed to induce superconductivity. The specimens for this work are provided by Drs. Ivan Bozovic and Gennady Logvenov at Brookhaven National Laboratory, and Dr. Nuh Gedik is the collaborator. The finding of structural isosbestic points also assists the understanding of other systems that exhibit similar diffraction changes in time.

In Ch. 8, we provide direct evidence of the role of structural dynamics for electron pairing in high-temperature superconductors; selective atomic motions (buckling of copper–oxygen planes) participate in the anisotropic electron–lattice coupling (*47*). Following carrier excitation by polarized femtosecond heating pulses, the transient structures are examined for different dopings and temperatures. The deformation amplitude reaches 0.5% of the *c*-axis value of 30 Å when the light polarization is in the direction of the copper–oxygen bond, but its decay slows down at 45°. These findings suggest a selective dynamical lattice involvement, with the anisotropic electron–phonon coupling being on a time scale (1 to 3.5 ps depending on the direction) of the same order of magnitude as that of the spin exchange of electron pairing in the high-temperature superconducting phase. The specimens for this work were synthesized and characterized by Dr. Enrico Giannini. Dr. Fabrizio Carbone is the collaborator and an expert in the field of high-temperature superconductors. It was fortunate that during the time of working with him, my suggestion about the polarization-dependent experiments made contribution and helped solidify the conclusions.

Chapters 9 to 11 report the application of UEC to the studies of interfacial water assemblies and self-assembled monolayers on substrates. In Ch. 9, the structure of interfacial water assembly on highly oriented pyrolytic graphite, a hydrophobic surface, is determined to be ordered in the vertical direction, contrary to the expectation that the strong hydrogen bonding of water on hydrophobic surfaces would dominate with suppressed interfacial order (*53*). Because of its terrace morphology, graphite plays the role of a template. Dynamically, following the excitation of graphite by an ultrafast infrared pulse, the interfacial ice structure undergoes nonequilibrium phase transformation, which is identified in the hydrogen-bond network through the observation of a structural isosbestic point.

In Ch. 10, the full account of the structure and dynamics of interfacial water assembly on hydrogen-terminated silicon(111), another hydrophobic surface, is provided. Structurally, due to the lack of guiding forces from the substrate surface and morphology, the ice assembly is polycrystalline with randomly oriented crystallites being of the cubic form, ice *Ic*. Crystallites with {110} preferred orientation are found to be close to the ice-vacuum interface, which may have its origin from the viewpoint of energetics.

Dynamically, upon the ultrafast heating of the substrate, the interfacial ice structure undergoes four stages of changes—ultrafast melting, nonequilibrium phase transformation, annealing, and restructuring—that are closely correlated with the substrate dynamics. Once again, the phase transformation is identified through the observation of structural isosbestic points, and the lattice expansion of ice is found isotropic. We discuss the time scales involved, the nature of energy transfer between the substrate and interfacial ice, and, from the peculiar evolution of structural dynamics observed, its implications and our suggestion for future theoretical investigations. Dr. Nuh Gedik is the collaborator of this work.

In Ch. 11, the first study of self-assembled adsorbates on metal surfaces by UEC is reported (*52*). We investigate single-crystal clean surfaces of Au(111) with and without a monolayer assembly of 2-mercaptoacetic acid as a result of the reaction from 2,2'-dithiodiacetic acid. In addition, a monolayer of iron hemes is studied. Structural dynamics of the substrate (gold) and adsorbate(s) following an ultrafast temperature jump can be observed and isolated. The phenomenon of ultrafast annealing, i.e., an increased order in the originally random assembly observed only on an ultrashort time scale, is recognized, which also has influence on the substrate dynamics. This work is the result of collaboration with Dr. Chong-Yu Ruan.

Lastly, Ch. 12 describes a systematic theoretical study of structural dynamics for a substrate and an adsorbate, and makes comparison with experimental results (*54*). With the use of the harmonic lattice model of a chain of atoms, including anharmonic forces, influences of the impulsive force on the temporal behavior of Bragg diffraction are investigated, and the roles of damping and anharmonicity are also discussed. Extensive simulations are made in order to gain an understanding of the controlling factors of the atomic motions in the substrate, with or without the adsorbate. The results elucidate the importance of coherent wave propagation in the nonequilibrium regime and provide the atomic-scale description of surface and bulk dynamics. The influence of the attenuation length of the impulsive force and the thickness of the substrate (adsorbate) are also considered. For adsorbates, the mismatch of force constants and the coupling with the substrate are examined, thus establishing the conditions for wave-type propagation. Dr. Jau Tang initiated this project of theoretical investigation, and I am grateful that I had the opportunity to participate in it.

References:

1. J. D. Watson, F. H. C. Crick, *Nature* **171**, 737 (1953).
2. J. D. Watson, F. H. C. Crick, *Nature* **171**, 964 (1953).
3. M. F. Perutz *et al.*, *Nature* **185**, 416 (1960).
4. W. N. Lipscomb, Jr., *J. Chem. Phys.* **22**, 985 (1954).
5. J. Deisenhofer, O. Epp, K. Miki, R. Huber, H. Michel, *Nature* **318**, 618 (1985).
6. J. P. Abrahams, A. G. W. Leslie, R. Lutter, J. E. Walker, *Nature* **370**, 621 (1994).
7. D. A. Doyle *et al.*, *Science* **280**, 69 (1998).
8. A. H. Zewail, *J. Phys. Chem.* **100**, 12701 (1996).
9. A. H. Zewail, *Angew. Chem. Int. Ed.* **39**, 2587 (2000).
10. M. Ben-Nun, J. Cao, K. R. Wilson, *J. Phys. Chem. A* **101**, 8743 (1997).
11. R. W. Schoenlein *et al.*, *Science* **274**, 236 (1996).
12. C. Rischel *et al.*, *Nature* **390**, 490 (1997).
13. C. Rose-Petruck *et al.*, *Nature* **398**, 310 (1999).
14. A. Chin *et al.*, *Phys. Rev. Lett.* **83**, 336 (1999).

15. C. W. Siders *et al.*, *Science* **286**, 1340 (1999).

16. A. Rousse *et al.*, *Nature* **410**, 65 (2001).

17. A. M. Lindenberg *et al.*, *Science* **308**, 392 (2005).

18. K. Sokolowski-Tinten *et al.*, *Nature* **422**, 287 (2003).

19. A. M. Lindenberg *et al.*, *Phys. Rev. Lett.* **84**, 111 (2000).

20. A. Cavalleri *et al.*, *Phys. Rev. Lett.* **85**, 586 (2000).

21. M. Bargheer *et al.*, *Science* **306**, 1771 (2004).

22. A. Cavalleri *et al.*, *Nature* **442**, 664 (2006).

23. A. Cavalleri *et al.*, *Phys. Rev. Lett.* **87**, 237401 (2001).

24. S. Techert, F. Schotte, M. Wulff, *Phys. Rev. Lett.* **86**, 2030 (2001).

25. J. Davidsson *et al.*, *Phys. Rev. Lett.* **94**, 245503 (2005).

26. H. Ihee *et al.*, *Science* **309**, 1223 (2005).

27. M. Bargheer, N. Zhavoronkov, M. Woerner, T. Elsaesser, *Chemphyschem* **7**, 783 (2006).

28. A. H. Zewail, *Annu. Rev. Phys. Chem.* **57**, 65 (2006).

29. R. Srinivasan, V. A. Lobastov, C.-Y. Ruan, A. H. Zewail, *Helv. Chim. Acta* **86**, 1763 (2003).

30. V. A. Lobastov *et al.*, in *Ultrafast optics IV,* F. Krausz, G. Korn, P. Corkum, I. A. Walmsley, Eds. (Springer, New York, 2004), pp. 419-435.

31. J. C. Williamson, Ph.D. thesis, California Institute of Technology (1998).

32. R. Srinivasan, Ph.D. thesis, California Institute of Technology (2005).

33. B. J. Siwick, J. R. Dwyer, R. E. Jordan, R. J. D. Miller, *Science* **302**, 1382 (2003).

34. J. Cao *et al.*, *Appl. Phys. Lett.* **83**, 1044 (2003).

35. C.-Y. Ruan, F. Vigliotti, V. A. Lobastov, S. Chen, A. H. Zewail, *Proc. Natl. Acad.*

Sci. USA **101**, 1123 (2004).

36. G. Sciaini *et al.*, *Nature* **458**, 56 (2009).
37. R. Ernstorfer *et al.*, *Science* **323**, 1033 (2009).
38. H. Park, S. Nie, X. Wang, R. Clinite, J. Cao, *J. Phys. Chem. B* **109**, 13854 (2005).
39. S. Nie, X. Wang, H. Park, R. Clinite, J. M. Cao, *Phys. Rev. Lett.* **96**, 025901 (2006).
40. X. Wang *et al.*, *Appl. Phys. Lett.* **92**, 121918 (2008).
41. F. Vigliotti, S. Chen, C.-Y. Ruan, V. A. Lobastov, A. H. Zewail, *Angew. Chem. Int. Ed.* **43**, 2705 (2004).
42. D.-S. Yang, N. Gedik, A. H. Zewail, *J. Phys. Chem. C* **111**, 4889 (2007).
43. F. Carbone, P. Baum, P. Rudolf, A. H. Zewail, *Phys. Rev. Lett.* **100**, 035501 (2008).
44. D.-S. Yang, C. S. Lao, A. H. Zewail, *Science* **321**, 1660 (2008).
45. P. Baum, D.-S. Yang, A. H. Zewail, *Science* **318**, 788 (2007).
46. N. Gedik, D.-S. Yang, G. Logvenov, I. Bozovic, A. H. Zewail, *Science* **316**, 425 (2007).
47. F. Carbone, D.-S. Yang, E. Giannini, A. H. Zewail, *Proc. Natl. Acad. Sci. USA* **105**, 20161 (2008).
48. S. Chen, M. T. Seidel, A. H. Zewail, *Proc. Natl. Acad. Sci. USA* **102**, 8854 (2005).
49. S. Chen, M. T. Seidel, A. H. Zewail, *Angew. Chem. Int. Ed.* **45**, 5154 (2006).
50. M. T. Seidel, S. Y. Chen, A. H. Zewail, *J. Phys. Chem. C* **111**, 4920 (2007).
51. C.-Y. Ruan, V. A. Lobastov, F. Vigliotti, S. Chen, A. H. Zewail, *Science* **304**, 80 (2004).
52. C.-Y. Ruan, D.-S. Yang, A. H. Zewail, *J. Am. Chem. Soc.* **126**, 12797 (2004).
53. D.-S. Yang, A. H. Zewail, *Proc. Natl. Acad. Sci. USA* **106**, 4122 (2009).
54. J. Tang, D.-S. Yang, A. H. Zewail, *J. Phys. Chem. C* **111**, 8957 (2007).

Chapter 2

Ultrafast Electron Crystallography: Principles and Dynamics[†]

[†] Part of this chapter was adapted from D.-S. Yang, N. Gedik, A. H. Zewail, *J. Phys. Chem. C* **111**, 4889 (2007).

Introduction

The geometric nature in the structure analysis of a molecule or a crystal by electron diffraction shares a high degree of similarity with that by x-ray diffraction. The geometrical theory originally developed for x-ray crystallography can, therefore, be used in electron crystallography, and its relevance to our technique is described in this chapter. The major dissimilarities between these two diffraction methods originate from the different radiation–matter interactions. Because x-ray is an electromagnetic wave, its scattering—Thomson scattering if the energy is conserved—is caused by the (polarizable) electron density in the electron shells of the atoms; atomic nuclei are very poorly affected by the electromagnetic field and, hence, invisible to such radiation. Consequently, structure analysis of x-ray diffraction deals with the distribution of electron density that is often concentrated around the nuclei. For electron interaction with matter, however, it is the Coulomb force that governs the scattering because electrons are charged particles, and as a result, the electrostatic potential due to both the positively charged atomic nuclei and their electron clouds should be considered. On the basis of the different interactions involved, the average magnitude of the atomic scattering amplitude of electrons is about 10^3 times that of x-ray, leading to a ratio of 10^6 for the scattered intensities (*1*). Therefore, electrons are strongly scattered by matter, which grants electron diffraction with a higher sensitivity for the probing of nanometer-scale and interfacial structures and in the detection of small structural changes in time.

Before the presentation of the geometrical theory, a quick summary for quantitative description of the intensities of the scattered beams is given here. Derivation of the kinematic (elastic) scattering theory for electron diffraction starts from the time-dependent Schrödinger equation and considers a propagating plane wave for the incident electrons (*1-3*),

$$\Psi_0\left(\vec{r}',t\right) = A\,\exp\left[i\left(\vec{k}_\mathrm{i}\cdot\vec{r}'-\omega t\right)\right] \tag{1}$$

where A denotes the amplitude, $\vec{k}_\mathrm{i}$ the incidence wavevector, and ω the angular frequency. The relativistic effect needs to be taken into account for highly accelerated electrons,

$$eV_0 = \sqrt{\left(m_0^2 c_0^4 + p^2 c_0^2\right)} - m_0 c_0^2 \tag{2}$$

where V_0 is the acceleration voltage (in volt), m_0 the electron's rest mass, p the electron's momentum, and c_0 is the speed of light. According to the de Broglie relation, the electron's wavelength (λ) is equal to h/p and, therefore, can be expressed (in Å) by (*4*)

$$\lambda = h\Big/\sqrt{2m_0 eV_0\left(1+eV_0/2m_0c_0^2\right)} = 12.26\Big/\sqrt{V_0\left(1+0.9785\times10^{-6}V_0\right)}. \tag{3}$$

With the use of the mathematical tool of Green's function, the scattered wave derived in the asymptotic limit for large-L, far-field detection (i.e., Fraunhofer diffraction that is typically the case for crystallographic measurements) and under the first Born approximation is given by (*1-3*)

$$\Psi_\mathrm{S}\left(\vec{L}\right) = -\frac{A\,e^{ikL}}{4\pi L}\int U\left(\vec{r}\right)\exp\left[i\left(\vec{k}_\mathrm{i}-\vec{k}\right)\cdot\vec{r}\right]\mathrm{d}^3\vec{r}\ , \tag{4}$$

where $\vec{k}$ is the outgoing wavevector ($|\,\vec{k}\,| = |\,\vec{k}_\mathrm{i}\,|$) along the direction of $\vec{L}$, $U\left(\vec{r}\right) = \left(2me/\hbar^2\right)V\left(\vec{r}\right)$ is the reduced potential associated with the electrostatic potential of the scattering object, $V\left(\vec{r}\right)$, and the integration runs over the occupied volume.

Therefore, the kinematic theory of electron scattering (Eq. 4) can be deduced with the use of the theory of Fourier integrals, defining the relative scattering amplitude

$$f\left(\vec{s}\right) \equiv \frac{1}{4\pi}\int U\left(\vec{r}\right)\exp\left(-i\,\vec{s}\cdot\vec{r}\right)\mathrm{d}^3\vec{r} \tag{5}$$

with the momentum transfer vector

$$\vec{s} \equiv \vec{k} - \vec{k}_{\mathrm{i}}\,. \tag{6}$$

The observed diffraction intensities, $I(\vec{L}) = \left|\Psi_{\mathrm{S}}(\vec{L})\right|^2$, are therefore in proportion to $\left|f(\vec{s})\right|^2$ (*1, 2*). The detailed structure in the potential of the specimen (thereby the spatial arrangement of atoms) is given by

$$U(\vec{r}) = \frac{1}{8\pi^3}\int 4\pi\, f(\vec{s})\exp(i\,\vec{s}\cdot\vec{r})\,\mathrm{d}^3\vec{s}\,. \tag{7}$$

Thus, these results provide the theoretical basis for the geometrical theory considering the periodic lattice structure in real space and its Fourier transform, the periodic reciprocal lattice, in reciprocal (*k*) space.

If $U(\vec{r})$ is substituted by a sum of reduced atomic potentials, $U_j^{\mathrm{a}}(\vec{r} - \vec{r}_j)$ (displaced according to their central positions in a crystal), where *j* refers to the *j*th atom,

$$U(\vec{r}) = \sum_j U_j^{\mathrm{a}}(\vec{r} - \vec{r}_j), \tag{8}$$

Equation 5 can be rewritten as

$$f(\vec{s}) = \frac{1}{4\pi}\sum_j \exp(-i\,\vec{s}\cdot\vec{r}_j)\int U_j^{\mathrm{a}}(\vec{r} - \vec{r}_j)\exp\left[-i\,\vec{s}\cdot(\vec{r} - \vec{r}_j)\right]\mathrm{d}^3\vec{r} = \sum_j f_j(\vec{s})\exp(-i\,\vec{s}\cdot\vec{r}_j) \tag{9}$$

with the definition of the atomic scattering factor, $f_j(\vec{s})$, being

$$f_j(\vec{s}) \equiv \frac{1}{4\pi}\int U_j^{\mathrm{a}}(\vec{r})\exp(-i\,\vec{s}\cdot\vec{r})\,\mathrm{d}^3\vec{r}\,. \tag{10}$$

The assumption here is that $U_j^{\mathrm{a}}(\vec{r})$ in a crystal is approximately the same as that for an isolated atom (i.e., the valence electrons affect the electron scattering to a very minor extent). Although the absolute values of diffraction intensities may show small deviation from the kinematic theory described above, it will become clear that, from the various studies successfully made, the kinematic approximation is capable of capturing the most important information from the observed diffraction changes in time and, therefore, suitable for the structural dynamics studies using electron diffraction.

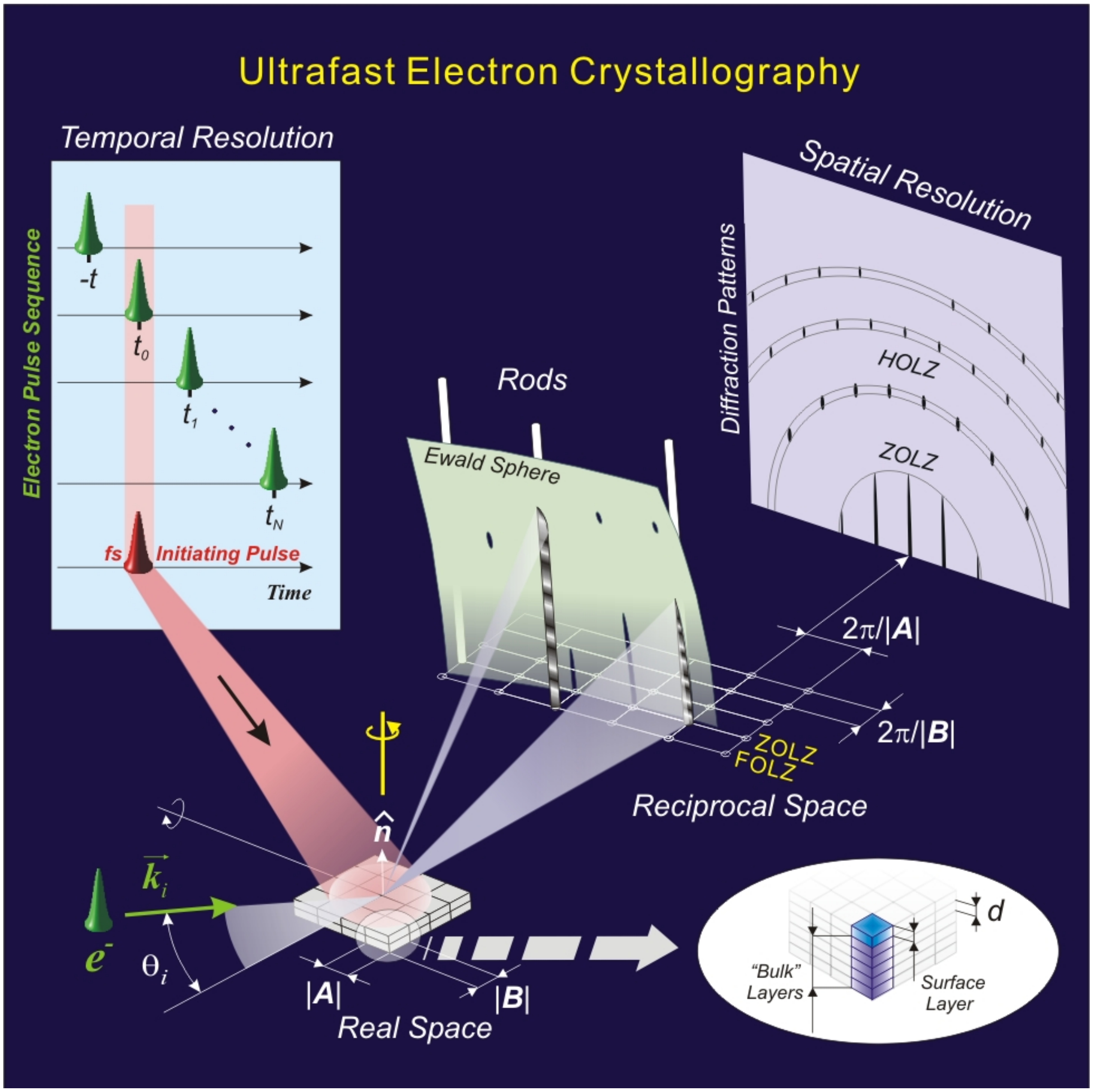

Fig. 1. Schematic of the methodology of UEC in the reflection geometry. The relationship between real and reciprocal lattices and Ewald construction for the formation of diffraction patterns are shown (see Text and Figs. 2 to 4 for details). The temporal and spatial resolutions of UEC are achieved by varying the delay time between the electron probe and initiating heating pulses (upper left), and the recording of the diffraction patterns at different times.

From the discussion below, it is straightforward to see that the geometrical theory for high-energy electron diffraction is much simpler than that for x-ray diffraction because of the very short electron wavelength used. Ultrafast electron crystallography (UEC), a time-resolved electron diffraction technique for condensed-matter studies, can be performed in two modes, reflection or transmission geometry. The implementation in the reflection geometry (Fig. 1) enables us to determine time-resolved nonequilibrium structures of a crystal surface region or adsorbate near the interface, and also their equilibrium structures at steady state. The transmission geometry allows the detection of structures and dynamics of nanometer-scale specimens. In what follows, the theoretical foundation to determine structures, their inhomogeneity, and the corresponding temporal evolution is examined. A typical diffraction image may show a pattern of Bragg spots, streaks, Debye−Scherrer rings, Kikuchi lines or bands, or a combination of these with a scattering background. By monitoring and comparing the changes of different diffraction features, such as position, intensity, width, and shape, we can obtain a more complete picture of structural dynamics. Experimental test cases (gold and silicon) are also provided in this chapter to illustrate the principles invoked.

A. Equilibrium Structures

A.1. Diffraction in Reflection

Spots or rings in an electron diffraction pattern are the result of the constructive interference of scattered waves from different lattice points. In UEC, the electrons have large kinetic energy ($eV_0 = 30\,\text{keV}$) and therefore a small de Broglie wavelength, $\lambda \sim 0.07$ Å from Eq. 3, which is a few percent of a typical atomic spacing (the reason behind the resolution of interatomic distances through diffraction). For elastic scattering, the criterion of constructive interference is described by the Bragg condition:

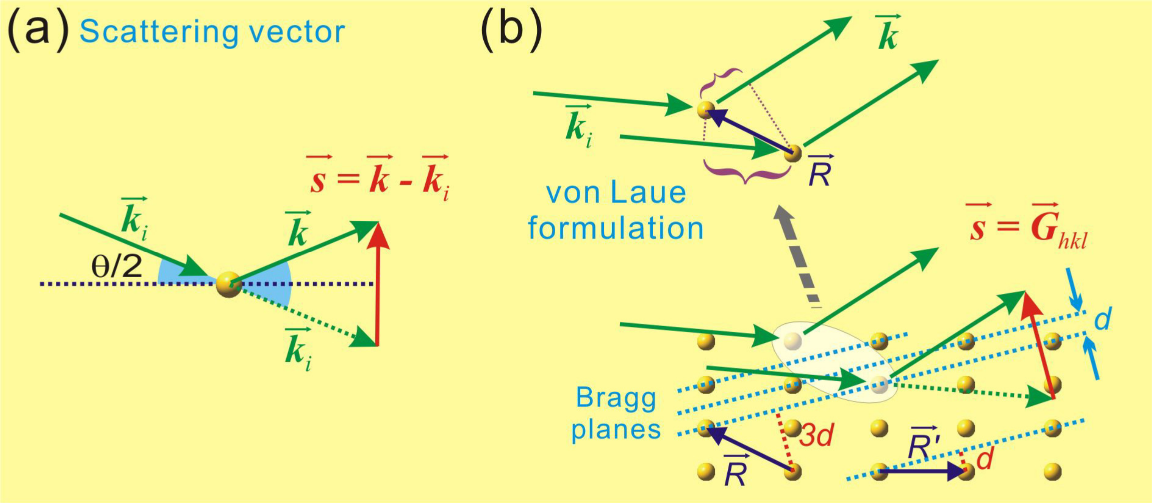

Fig. 2. (a) Vectorial representation for the elastic scattering process. The incidence angle $\theta_i = \theta/2$ and the scattering vector $\vec{s}$ are shown. (b) Upper: The von Laue condition of constructive interference. The phase difference between two outgoing waves scattered by two atoms separated by $\vec{R}$ is indicated by the curly brackets. Lower: Comparison of the von Laue and Bragg formulations for constructive interference conditions. Note that $\vec{s}$ is parallel to the interplanar distance *d* under investigation (i.e., perpendicular to the Bragg planes under probing), and any vector of the real lattice has a projection onto the $\vec{s}$ direction to be an integer multiple of *d*.

$$n\lambda = 2d\sin(\theta/2), \tag{11}$$

which is simply the result of considering crystal planes of reflections; *n* is the order of diffraction, *d* is the distance between adjacent parallel crystal planes, and *θ* is the total angle of deflection from the initial beam. Because *λ* is known, in principle, if *n* is known, the measurement of *θ* gives *d*. In practice, the interplanar distance *d* can be obtained from rocking curves by changing the incidence angle and recording spots of two consecutive orders, *n* and *n* + 1, thus removing the need for assigning the absolute precise magnitudes of *n* and *θ* (see below).

The equivalent picture given by the von Laue formulation considers the geometrical phase shifts of the scatterers themselves. For elastic scattering, because the wavevectors of the incident and scattered electrons ($\vec{k}_{\mathrm{i}}$ and $\vec{k}$) have the same amplitude ($|\vec{k}| = |\vec{k}_{\mathrm{i}}| = 2\pi/\lambda$), the scattering vector (Eq. 6) yields $s = |\vec{s}| = (4\pi/\lambda)\sin(\theta/2)$; see Fig. 2a for the vectorial representation and Appendix A for the convention used. The phase matching of the scattered waves from all scatterers is required for constructive interference (Eq. 9), which means that for all vectors $\vec{R}$ connecting atoms of the Bravais lattice in real space, the Laue condition is satisfied when $\exp\left(i\vec{s}\cdot\vec{R}\right) = 1$, or equivalently, when $\vec{s}\cdot\vec{R} = 2m\pi$ where m is an integer (Fig. 2b, upper). It is noted that the same equation leads to the Bragg condition by substituting the amplitude of $\vec{s}$ and recognizing that the projection of $\vec{R}$ along the $\vec{s}$ direction equals to m times the interplanar distance d (Fig. 2b, lower). Therefore, the Bragg planes under probing are perpendicular to $\vec{s}$, and

$$s\,d = 2n\pi \tag{12}$$

where n is the order of diffraction. Experimentally, since the appearance of a Bragg spot indicates the direction of $\vec{k}$, with the knowledge of $\vec{k}_{\mathrm{i}}$, the crystal planes involved can be deduced since they are always perpendicular to $\vec{s}$ (Fig. 2b, lower).

Incidentally, the reciprocal lattice, which is the Fourier transform of the real lattice spanned by three basis vectors ($\vec{a}$, $\vec{b}$ and $\vec{c}$), can be constructed by three reciprocal basis vectors, $\vec{a}^*$, $\vec{b}^*$ and $\vec{c}^*$, which satisfy the following relationship of inner product:

$$\begin{aligned} &\vec{a}\cdot\vec{a}^* = \vec{b}\cdot\vec{b}^* = \vec{c}\cdot\vec{c}^* = 2\pi \quad \text{and} \\ &\vec{a}\cdot\vec{b}^* = \vec{b}\cdot\vec{c}^* = \vec{c}\cdot\vec{a}^* = \vec{b}\cdot\vec{a}^* = \vec{c}\cdot\vec{b}^* = \vec{a}\cdot\vec{c}^* = 0. \end{aligned} \tag{13}$$

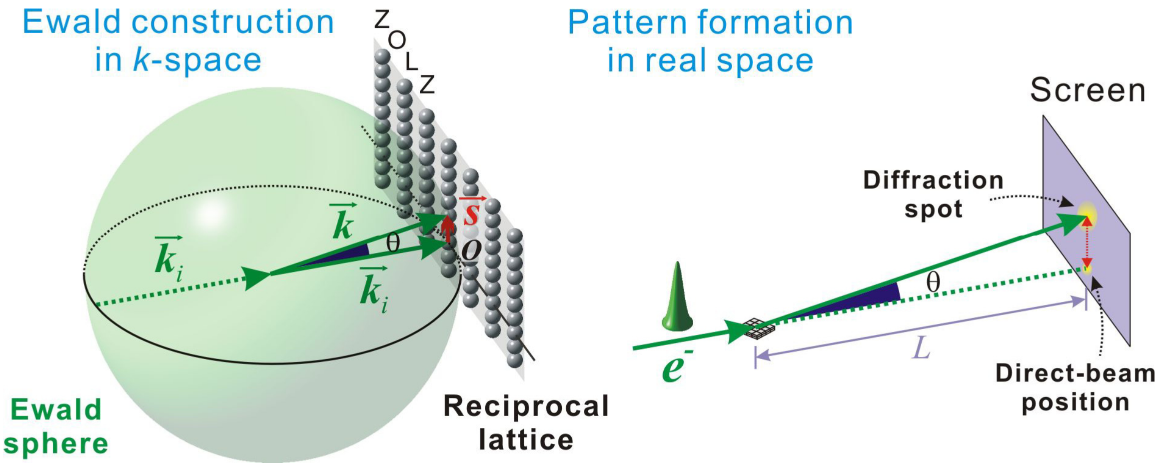

Fig. 3. Left: Ewald construction in *k* space. The Ewald sphere passes through the origin *O* of the reciprocal lattice, and any other intersections between the sphere and reciprocal points (rods) give diffraction spots or streaks. Right: Diffraction pattern formation.

The mathematical formulas for $\vec{a}^*$, $\vec{b}^*$ and $\vec{c}^*$ are written as

$$\vec{a}^* = 2\pi \frac{\vec{b}\times\vec{c}}{\vec{a}\cdot\left(\vec{b}\times\vec{c}\right)}, \quad \vec{b}^* = 2\pi \frac{\vec{c}\times\vec{a}}{\vec{b}\cdot\left(\vec{c}\times\vec{a}\right)}, \quad and \quad \vec{c}^* = 2\pi \frac{\vec{a}\times\vec{b}}{\vec{c}\cdot\left(\vec{a}\times\vec{b}\right)}. \tag{14}$$

Any vector ($\vec{G}$) in the reciprocal lattice can be expressed as their linear sum,

$$\vec{G}_{hkl} = h\vec{a}^* + k\vec{b}^* + l\vec{c}^*, \tag{15}$$

with *h*, *k* and *l* being integer numbers called Miller indices. Consequently, $\exp\left(i\,\vec{G}\cdot\vec{R}\right) = 1$ for all such vectors according to Eq. 13. The Laue condition of constructive interference is hence satisfied if and only if $\vec{s}$ is a unique one of them, i.e., $\vec{s} = \vec{G}_{hkl}$ for certain *h*, *k* and *l* (Fig. 2b).

Therefore, analysis of diffraction patterns is greatly facilitated by using the reciprocal lattice and Ewald construction (*5*), which is based on conservation of energy and momentum of electrons. The Ewald sphere in *k* space is constructed such that the vector from the center of the sphere to the origin of the reciprocal space is $\vec{k}_\mathrm{i}$ (Fig. 3, left); the size of the Ewald sphere is entirely determined by $|\vec{k}_\mathrm{i}|$. According to the Laue

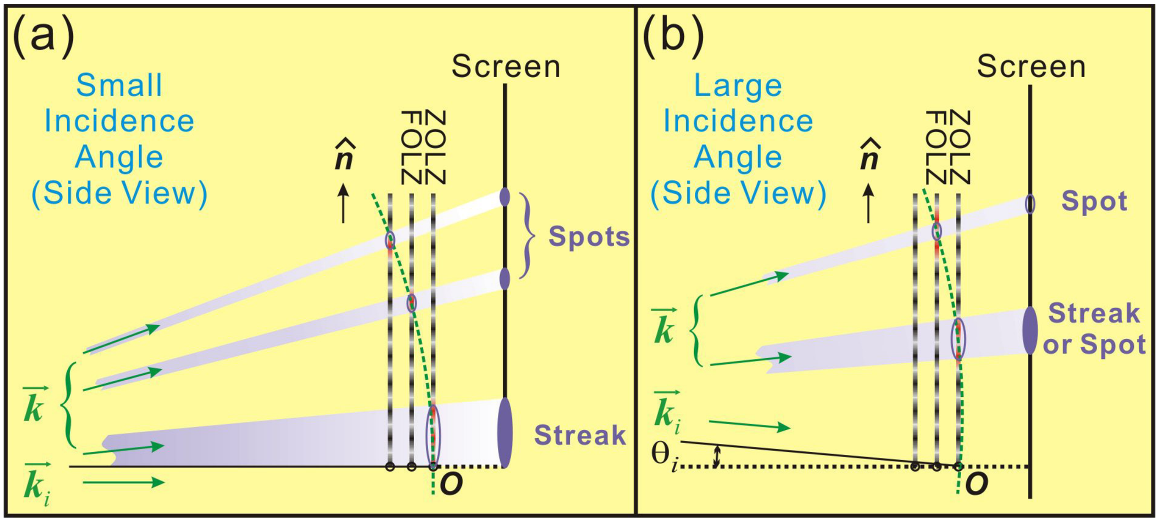

Fig. 4. (a) A side view of Ewald construction at a grazing incidence angle. The intersections between the sphere and ZOLZ (represented as a modulated reciprocal rod here) tend to form streaks, and more spots may appear at higher positions due to the sphere's intersections with HOLZ (FOLZ refers to the first-order Laue zone). (b) A side view of Ewald construction at a larger incidence angle. Diffraction streaks and/or spots will be seen at higher positions on the screen.

condition and conservation of energy and momentum for elastic scattering ($\vec{s} = \vec{k} - \vec{k}_{\mathrm{i}} = \vec{G}_{hkl}$ and $|\vec{k}| = |\vec{k}_{\mathrm{i}}|$), diffraction can occur when both the origin *O* and the reciprocal lattice point (*hkl*) are on the Ewald sphere (Fig. 3, left); in real space, the diffraction can be observed at that geometrical configuration (Fig. 3, right). Thus, Ewald construction provides a geometrical tool for the visualization of satisfaction of the Bragg/Laue condition.

As a note for the reciprocal lattice, reduction of the effective crystal size in real space along the surface normal direction ($\hat{n}$) causes the elongation of the reciprocal lattice points into "rods" along the same direction in reciprocal space, as dictated by Fourier transformation. In other words, as the third dimension of the crystal increases, the rods change to “spots” because they become modulated by the inverse of that spacing (see Fig. 1, middle and lower right). The horizontal width of spots or rods is a measure of the degree of coherence (constructive interference) in the two dimensions of real space. The coherent diffraction is pronounced only when the reciprocal lattice intersects with the sphere (Fig. 1, middle, and Fig. 3, left).

Figure 4 provides a side view of this construction at two different incidence angles. At a grazing incidence, the diffraction pattern may consist of streaks originating from the zeroth-order Laue zone (ZOLZ, a plane in k space both passing through the origin and being perpendicular to $\vec{k}_{\mathrm{i}}$); at higher incidence, many other spots will appear due to higher-order Laue zones (HOLZ, any other k-space planes parallel to ZOLZ but not passing through the origin) (*6*). The appearance of streaks or spots relies on the modulation of the reciprocal rods along the surface normal $\hat{n}$ (a manifestation of the finite depth probed by electrons) and may also be influenced by the surface potential. However, if a zone axis of the surface is aligned perpendicular to $\vec{k}_{\mathrm{i}}$, the horizontal spacings between streaks or spots in a diffraction pattern will correctly provide surface structural information, as shown below.

At this point, it is worth noting that the grazing incidence of electrons ($\theta_{\mathrm{i}} \equiv \theta/2$ in Fig. 2a) at an angle that is only few degrees is the required condition of reflection high-energy electron diffraction (RHEED). The reason can be easily seen from the order-of-magnitude difference between λ and typical d (on the order of an angstrom) and through Eq. 11. Similarly, by inversion, the radius of the Ewald sphere ($2\pi/\lambda$) is found orders of magnitude larger than typical reciprocal vectors (on the order of an inverse angstrom). Its major consequence is that the Ewald sphere may be approximated by a plane in the geometrical theory at the small-angle scattering condition.

So far, we only considered a perfect crystal lattice with atoms at rest (classical, $T = 0$) and a perfect electron source for generating electrons with the same $\vec{k}_\mathrm{i}$. The temperature effect on diffraction (loss of interference by the incoherent movements of atoms) results in loss of intensity, which is described by the Debye–Waller (DW) factors $W(T)$ (*7, 8*),

$$\ln \frac{I}{I_0} \equiv -2W(T) = -\frac{s^2 \langle u^2 \rangle}{3}, \tag{16}$$

where I (I_0) denotes the diffraction intensity from a lattice with (without) thermal vibrations and $\langle u^2 \rangle$ is the mean-square harmonic displacement of the constituent atoms in a unit cell. A fundamental assumption here is the thermal equilibrium among all modes of the lattice at a given well-defined temperature. However, this assumption, as shown later, is not valid when the time scale is ultrashort and/or coherent motions of atoms are involved. In regard to the electron source in reality, the small distribution of momentum of probing electrons ($\hbar \vec{k}_\mathrm{i}$) results in broadening of Bragg spots because such an uncertainty introduces both angular wobbling of the alignment around the average $\vec{k}_\mathrm{i}$ and an additional thickness to the Ewald sphere.

A.2. Experimental Test Cases: Gold and Silicon

In the following discussion, we present experimental test cases [Au(111) and Si(111) surfaces] to demonstrate the extraction of structural information in our UEC studies. The existence of the specimen surface and the geometry of RHEED differentiate the 3 dimensions in space into a two-dimensional (2D) plane parallel to the surface and an axis perpendicular to it (i.e., parallel to the $\hat{n}$). Structural information in the former dimensions can be analyzed through azimuthal (ϕ) rotation of the specimen; the information related to the latter direction can be obtained by changing the incidence angle

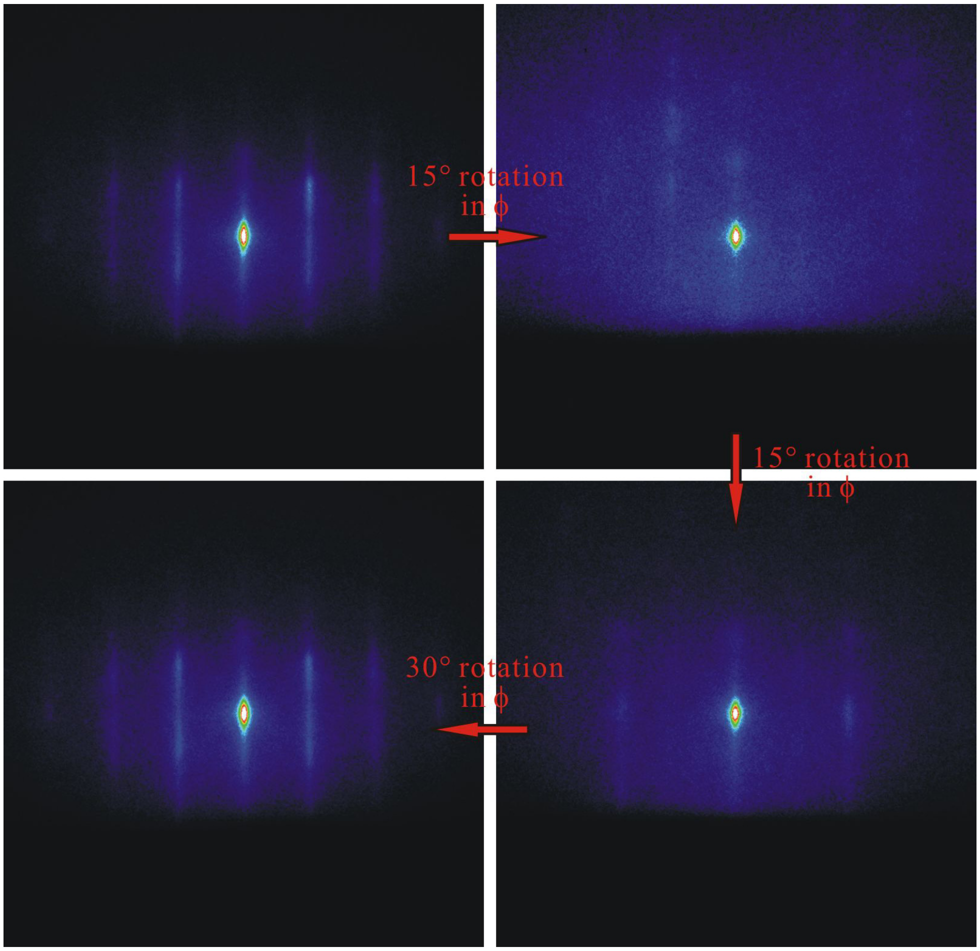

Fig. 5. Diffraction patterns (in false color) of Au(111) recorded at different azimuthal angles (ϕ). Two symmetric patterns with different horizontal spacings are obtained by 30° rotation (upper left and lower right). The same symmetric pattern is seen after a rotation of 60° in total (upper left and lower left).

(θ_i) of electrons, or equivalently, tilting the specimen with respect to the electron beam. We shall illustrate the principles involved with the use of the test cases.

Through azimuthal (ϕ) rotation of the Au(111) specimen, a symmetric diffraction pattern can be observed (Fig. 5, upper left) and its evolution with ϕ is shown in Fig. 5. It can be found that the same pattern appears every 60° azimuthal rotation, which signifies a 6-fold symmetry for the arrangement of the reciprocal lattice (rods) in the 2D plane

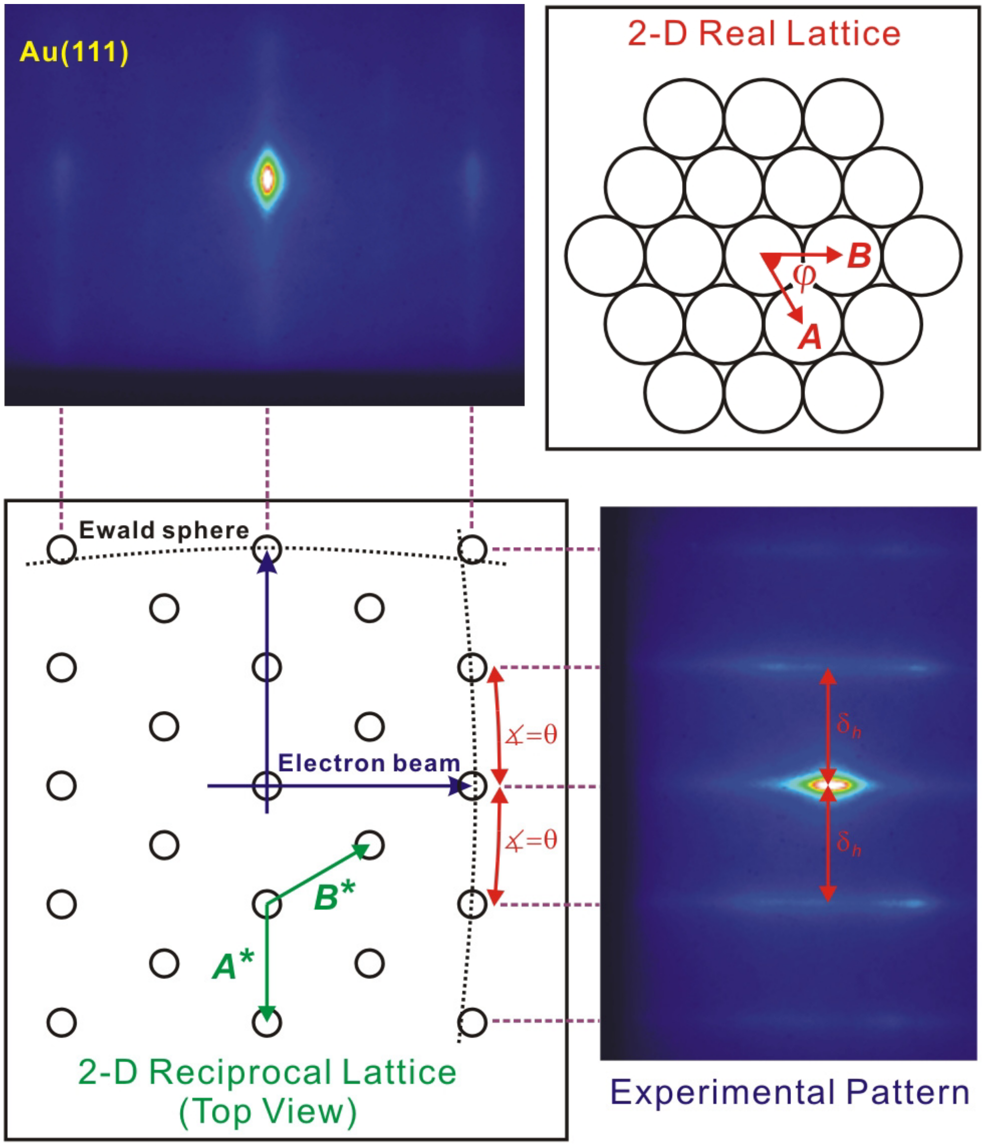

Fig. 6. Experimental and theoretical test case: Au(111) surface. Upper right: A hexagonal 2D lattice. Lower left: The top view of the corresponding reciprocal-lattice rods. The angular relationships between $\boldsymbol{A}$, $\boldsymbol{A}^*$ and $\boldsymbol{B}$, $\boldsymbol{B}^*$ are shown. Symmetric diffraction patterns are formed if the electrons probe the 2D lattice along the zone axes, and two examples are given here. The Ewald sphere intersects with the rods and streaks are formed on the CCD camera; the upper left and lower right panels are the experimental patterns from Au(111) at two azimuthal angles separated by 30°. The minimum spacing between diffraction streaks (δ_h) can be used to derive the 2D structural information.

parallel to the specimen surface. In fact, there are 5 different Bravais lattices in 2D (real space and reciprocal space) and for each, the characteristic ϕ is different; diffraction patterns repeat their appearance every 60° for hexagonal, 90° for square, 180° for rectangular and centered rectangular, and 360° for oblique lattices. Further verification for a certain 2D lattice can be obtained by examining the azimuthal separation between different symmetric patterns (see below). In the case of Au(111), another symmetric pattern can be observed by 30° rotation (Fig. 5, lower right).

Geometrically, two vectors, $\boldsymbol{A}$ and $\boldsymbol{B}$ perpendicular to the $\hat{n}$, form the basis of the 2D lattice in real space [see Fig. 6, upper right panel for Au(111)]. The corresponding reciprocal lattice, given by Fourier transformation, is an array of rods extended along $\hat{n}$ with two basis vectors defined by

$$\boldsymbol{A}^* = 2\pi\,(\boldsymbol{B}\times\hat{n})/|\boldsymbol{A}\times\boldsymbol{B}| \quad \text{and} \quad \boldsymbol{B}^* = 2\pi\,(\hat{n}\times\boldsymbol{A})/|\boldsymbol{A}\times\boldsymbol{B}|. \tag{17}$$

Thus,

$$|\boldsymbol{A}^*| = 2\pi/|\boldsymbol{A}|\sin\varphi \quad \text{and} \quad |\boldsymbol{B}^*| = 2\pi/|\boldsymbol{B}|\sin\varphi, \tag{18}$$

where φ is the angle between $\boldsymbol{A}$ and $\boldsymbol{B}$ (see also Fig. 1, middle). Because of these direct relationships between $\boldsymbol{A}$ and $\boldsymbol{A}^*$ ($\boldsymbol{B}$ and $\boldsymbol{B}^*$), the azimuthal rotation in real space allow us to probe different zone axes of the reciprocal lattice for the observation of symmetric diffraction patterns (Fig. 6, lower left).

For the case of the electron beam propagating along a direction for which the ZOLZ is parallel to $\boldsymbol{A}^*$, the minimum horizontal s will be equal to $|\boldsymbol{A}^*|$ (Laue condition) according to Ewald construction. Therefore, the total angle of deflection

$$\theta = \tan^{-1}(\delta_h/L) = 2\sin^{-1}(s\lambda/4\pi) = 2\sin^{-1}(\lambda\,/\,2|\boldsymbol{A}|\sin\varphi),$$

$$L = \delta_h/\tan[2\sin^{-1}(\lambda\,/\,2|\boldsymbol{A}|\sin\varphi)], \tag{19}$$

where δ_h is the horizontal spacing between spots (rods) and L is the camera length from the scattering position to the camera. By the azimuthal rotation, which yields other symmetric diffraction patterns, the value of φ that depends on the surface crystal structure can be determined. If L is determined independently, the lattice constants $|\boldsymbol{A}|$ and $|\boldsymbol{B}|$ can be obtained with the use of Eq. 19, and the 2D structure is thus determined.

For Au(111), the diffraction patterns taken at two zone axes (Fig. 6, upper left and lower right) correspond well with a hexagonal reciprocal lattice in 2D (Fig. 6, lower left). Therefore, the 2D structure in real space is also a hexagonal lattice with $|\boldsymbol{A}| = |\boldsymbol{B}|$. The smallest horizontal spacing between rods $[(\delta_\mathrm{h})_\mathrm{min}]$ recorded with $L = 17.0$ cm (Fig. 6, lower right) was 106 pixels (1 pixel = 44.94 μm in our system), which gave the experimental value of $|\boldsymbol{A}|$ to be 2.88(5) Å, totally consistent with the literature x-ray value. Through 30° rotation, another zone axis was probed, and the measured spacing between adjacent rods increased and became 1.73 times $(\delta_\mathrm{h})_\mathrm{min}$ (Fig. 6, upper left), which was expected ($\sqrt{3}$ fold) according to the 2D structure.

Conversely, the camera length L can be accurately determined using a crystal lattice whose structure is known, and such an *in situ* measurement is free of any errors due to, e.g., rotation of the crystal. A typical error in L is ~0.2%, which mostly originates from the spatial width and jitter of the electron pulses. However, for a given experimental setting during the time-dependent measurements, it is not the absolute values but the relative changes that are most crucial for deciphering the structural dynamics involved, and the accuracy in the determination of transient changes can be much higher (see, e.g., Chs. 4 and 5).

The third dimension, besides the surface two, of the lattice can be accessed by measurements of the rocking curve that is the change of diffraction spots with the angle of incidence, θ_i ($\equiv \theta/2$). This can be easily understood from the Bragg's formulation for the diffraction condition. For example, the diffraction patterns of Au(111) and Si(111)

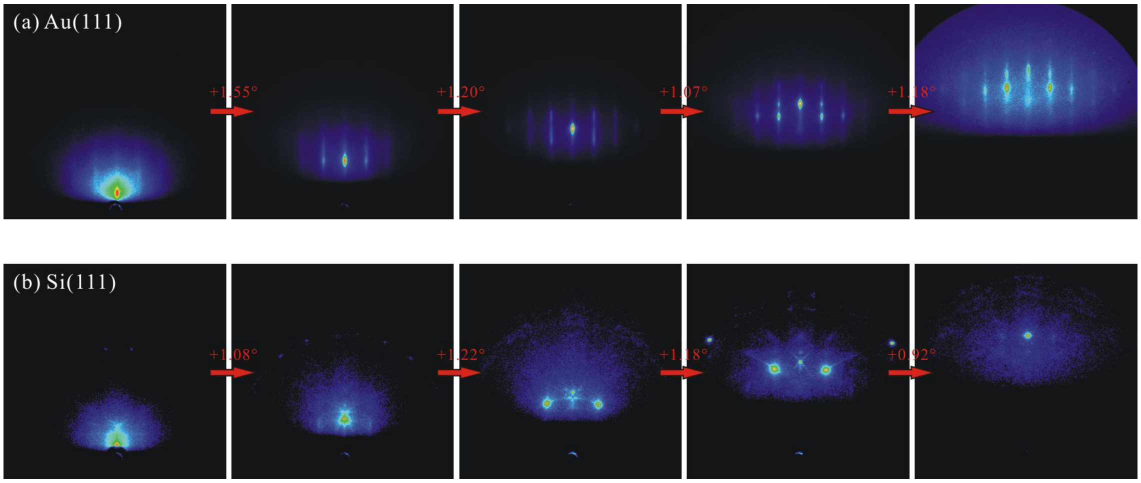

Fig. 7. Diffraction patterns (in false color) of (a) Au(111) and (b) Si(111) recorded at different incidence angles (θ_i). Gold shows rod-like diffraction patterns because it has a large atomic number and electrons can only penetrate top few layers. For silicon, other features such as Kikuchi lines and bands may interfere with rocking-curve construction.

recorded at selected incidence angles are shown in Fig. 7. By determining the angle at which successive orders appear (especially for large n, where there is less interference from 2D, other features and the refraction effect), we can obtain the vertical interplanar distance, the spacing normal to the surface. From Bragg's equation (Eq. 11), the measured change in θ_i for two consecutive orders is given, for small θ_i, by

$$\Delta\theta_i \equiv \Delta(\theta/2) \sim \sin(\theta_i + \Delta\theta_i) - \sin\theta_i = \lambda / 2d. \qquad (20)$$

For consistency, d can also be obtained from the vertical separation between two consecutive spots δ_v ($\equiv \Delta s$) and with the use of the value of L, since

$$\delta_v \approx L\,[\tan(\theta/2 + \Delta\theta) - \tan(\theta/2)] \sim L\,\Delta\theta = 2L\,\Delta(\theta/2) \sim L\lambda / d. \qquad (21)$$

Low-order Bragg spots are not used because they are affected by the refraction effect (see below), by the surface potential, morphology and quality, and of course by the presence of adsorbates. Construction of the rocking curves for the (111) surface of gold and also

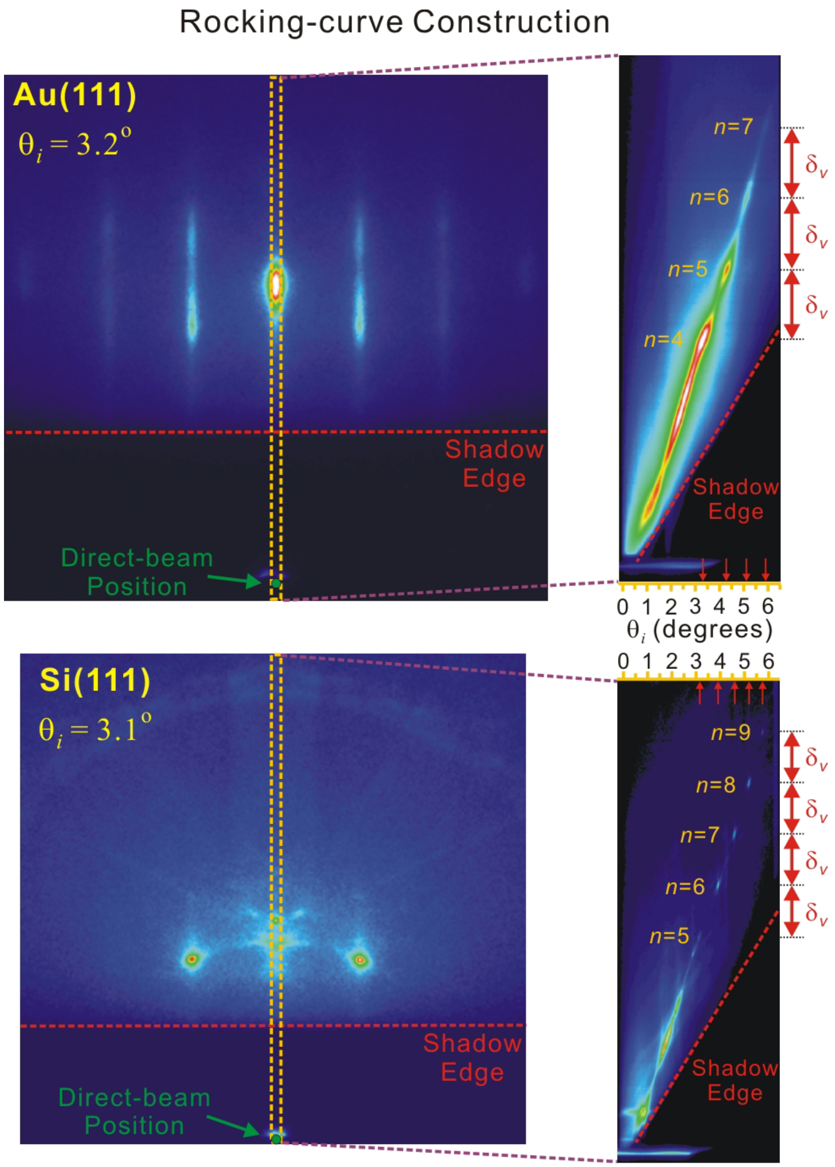

Fig. 8. Observed rocking curves for the (111) surface of gold and silicon. Rocking curves are obtained by recording diffraction patterns at different incidence angles. As the incidence angle is gradually increased, according to Ewald construction, Bragg spots will appear in-phase and out-of-phase alternatively. A narrow vertical strip along a streak is averaged horizontally for each image, resulting in a 1D intensity curve for each incidence angle. These curves are then combined into a 3D figure, i.e., intensity being plotted as a function of the incidence angle and vertical pixel number (a measure of s). At large incidence angles, the Bragg spots appear with regularity and, from both the vertical spacing (δ_v) and the change of incidence angle ($\Delta\theta_i$) between two consecutive diffraction orders, the interplanar distance d can be obtained. The indicated shadow edge is the outgoing electron scattering parallel to the surface.

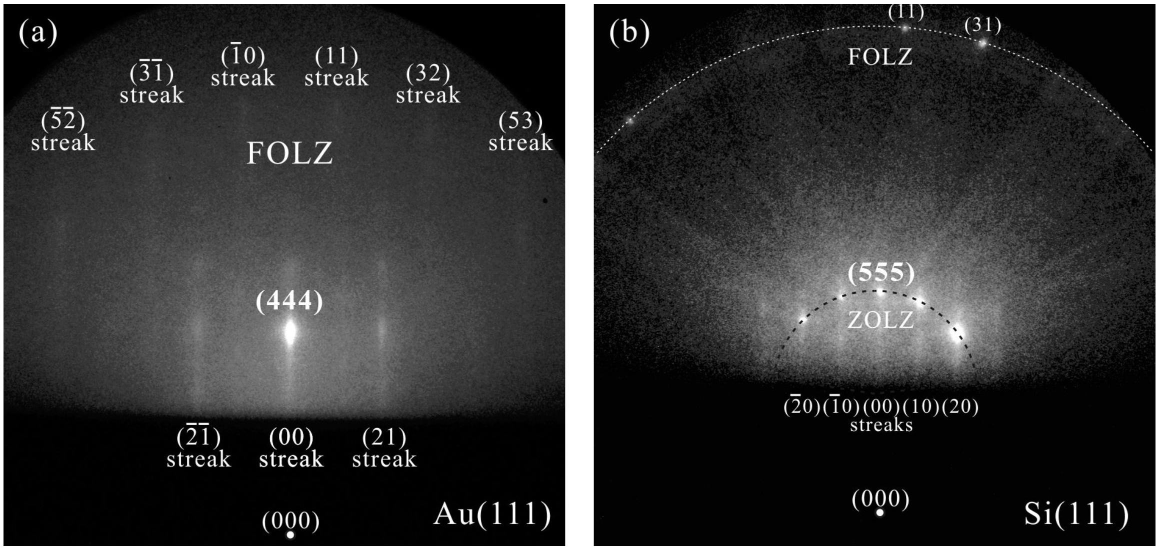

Fig. 9. Indexed diffraction patterns of (a) Au(111) and (b) Si(111). Indices for higher-order Bragg diffractions on the central streak are determined by using the Bragg condition (Eq. 21). Indices for streaks are assigned according to the 2D lattice of the surface plane. Diffractions from the first-order Laue zone (FOLZ) may be out of the camera region if the electron incidence angle is large.

that of silicon is illustrated in Fig. 8. Clearly, high-order Bragg spots appear with regularity, and we obtained $d_{\mathrm{Au(111)}} = 2.36$ Å and $d_{\mathrm{Si(111)}} = 3.15$ Å by using Eq. 21. These values are consistent with the x-ray literature values of the crystals.

Therefore, given the geometry of probing in RHEED, the central streak in the diffraction pattern contains the information about the interplanar distance along the surface normal; the evolution of the horizontal spacing between streaks with the azimuthal angle defines the symmetry of the 2D lattice in the surface plane, and gives the corresponding lattice constants. Although the RHEED technique is not intended for solving unknown crystal structures, it is designed to be used for the structural analysis of exposed crystal surfaces. In Fig. 9, two indexed patterns are shown as examples.

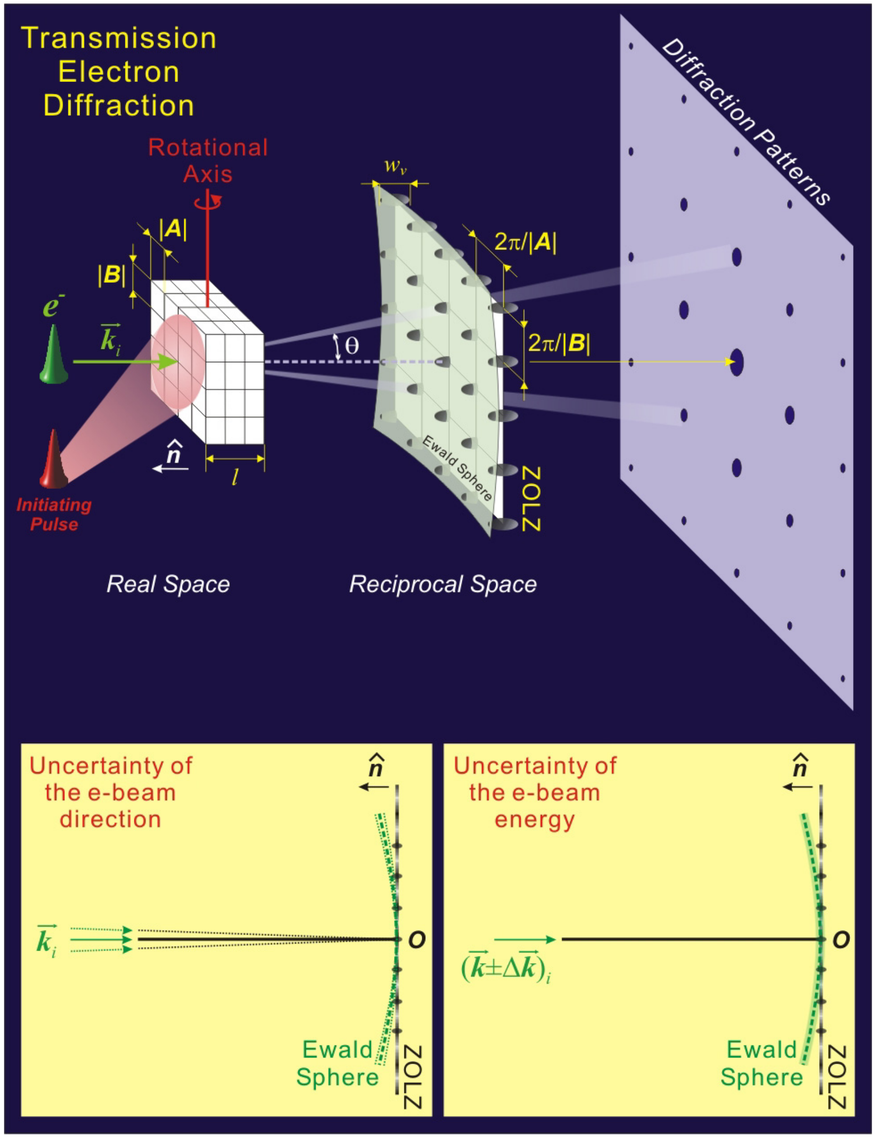

Fig. 10. Diffraction in transmission. Upper: Illustration of UEC methodology in this geometry. The finite thickness of a crystalline film results in the elongation of reciprocal-lattice points into rods along the surface normal $\hat{n}$. Consequently, the Ewald sphere can intersect with many rods and a pattern of Bragg spots of different orders will be formed. Lower left: The effect on Ewald construction due to the uncertainty in the direction of electron-beam propagation. Such directional spread of the electron beam, which causes the Ewald sphere to wobble around the average axis, exists because of the Coulomb repulsion between electrons, i.e., spatial divergence which is reduced using the electron-gun focusing system. Lower right: The effect on Ewald construction due to the uncertainty in the electrons' kinetic energy. The Ewald sphere is given an additional thickness to allow for more intersections with the reciprocal lattice.

For a polycrystalline sample, namely, a sample consisting of many small crystallites randomly oriented in space, a diffraction pattern will show the Debye–Scherrer rings instead of spots. It is because the effective reciprocal lattice becomes a series of concentric spheres centered at the reciprocal space origin (a consequence of the random orientation in real space) and their intersections with the Ewald sphere give rise to rings. From the radial average, a 1D diffraction curve can be obtained; care must be taken and a fitting procedure is often necessary for the determination of the center, because a large part of the rings below the shadow edge is blocked. The peak positions correspond to the values of the reciprocal lattice vectors ($\vec{G}_{hkl}$) for different planes indexed by the Miller indices, (*hkl*). The structure of the crystallites can be obtained by comparing the experimental data with the simulated diffraction curves for different crystal structures, as has been demonstrated in the UEC study of interfacial water (*9*).

A.3. Diffraction in Transmission

In contrast to the reflection mode, the diffraction patterns of crystalline thin films in transmission show many spots of different planes and orders. This is because of several reasons. First, due to the 2D-like thickness of the film in the $\hat{n}$ direction, reciprocal lattice points are elongated into rods along $\hat{n}$, as mentioned previously. Figure 10 illustrates an example in which the electrons are propagating parallel to $\hat{n}$. According to Ewald construction, the origin of the reciprocal space (000) is on the Ewald sphere, and the ZOLZ plane is tangent to the sphere. If the reciprocal lattice consists of points only, no other spots [except the (000)] on the ZOLZ will be in contact with the sphere due to the sphere's curvature. However, because the reciprocal points are elongated (finite 2D thickness), the tips of the rods may intersect with the Ewald sphere so that more Bragg spots appear in the diffraction pattern.

Second, when a macroscopic area is probed, the slight uncertainty of the crystal orientation across the thin film due to its unevenness will introduce a small angular span in the reciprocal lattice so that it has more chance to intersect with the Ewald sphere. Third, the finite spatial convergence/divergence of the electron beam provides an uncertainty of the direction of $\vec{k}_\mathrm{i}$, which results in a solid cone around the average axis. Therefore, Ewald construction indicates that the sphere wobbles around that principal axis and sweeps a larger region in k space, allowing for more intersections (Fig. 10, lower left). Finally, the kinetic energy span of electrons, which causes the uncertainty of $|\vec{k}_\mathrm{i}|$, gives the Ewald sphere an additional thickness to occupy a larger volume in k space. Hence, its intersection with reciprocal rods becomes more likely (Fig. 10, lower right).

Due to the aforementioned reasons, one can see that, in order to record more intense non-center Bragg spots, the crystalline film needs to be slightly rotated away from the original zone axis in order to optimize the overlap between the reciprocal rods and Ewald sphere. However, too much rotation can move the rods entirely away and result in no intersection. The span of rods in reciprocal space can be estimated from the rocking curves acquired through rotation of the crystalline film (along the vertical direction in Fig. 10) to change the incidence angle of the probing electrons, similar to the measurement of rocking curves in reflection experiments. The vertical width of rods (w_v) can be obtained from knowledge of the intensity angular profile of spots ($\Delta\theta_{hkl}$) because

$$w_\mathrm{v} \approx G_\perp \, \Delta\theta_{hkl} \tag{22}$$

where $G_\perp$ is the perpendicular component of G_{hkl} with respect to the rotational axis. We can also estimate the specimen thickness l over which diffraction is effective from the

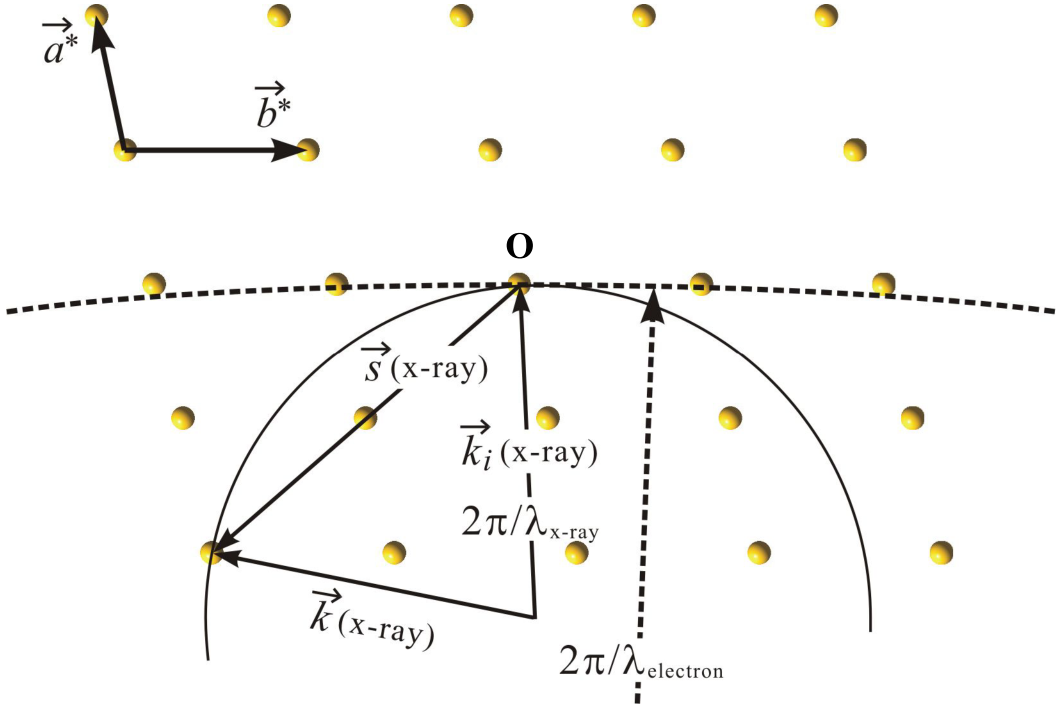

Fig. 11. Ewald construction in *k* space for electron and x-ray diffraction. The typical wavelength of high-energy electrons is much shorter than that of x-ray used for structure analysis, which leads to a much larger Ewald sphere for electrons (dashed arc) than that for x-ray (solid circle). The small-angle approximation can be used in the geometrical theory for electron crystallography and facilitate the visualization of the Laue condition.

Scherrer formula (*7*)

$$l \approx K\lambda/[\Delta\theta_{hkl}\cdot\cos(\theta/2)] = K\cdot 2\pi/w_{\text{v}} \tag{23}$$

where *K* (close to 1) is the shape factor of the average crystallite.

The structure of the 2D crystal is revealed in a single transmission diffraction pattern without rotation. From knowledge of the camera length and by Eq. 19, it is straightforward to obtain the lattice parameters. Of course, if the structure of the crystal under investigation is more complicated than that of a very thin, simple specimen consisting of light elements, one has to consider the issue of intensity, which may additionally involve dynamical scatterings, but generally the determination of the orders of Bragg spots (lattice symmetry) can be obtained. As for a polycrystalline sample, similar procedures, as those discussed in the previous subsection, are used for structural determination.

A.4. Advantages and Selected Topics of Electron Diffraction

Throughout the previous description of the geometrical theory for electron diffraction, the small-angle approximation, $\sin\theta \sim \tan\theta \sim \theta$, was often made. As mentioned earlier, its validity comes from the order-of-magnitude difference between λ and d in Eq. 11. Furthermore, the corresponding Ewald sphere relative to the reciprocal lattice in k space has a large radius and, consequently, may be approximated as a plane. Therefore, visualization of the Laue condition through Ewald construction becomes a simpler task for high-energy electron diffraction, and fast calculations can be carried out to extract the lattice constants from recorded diffraction patterns. This also becomes an advantage for dynamics studies when correlating the observed diffraction changes as a function of time with actual transient modifications in the structures (which will be made clear from the discussion in the next section). In comparison, the typical wavelength of x-ray used for structure analysis is much longer, and the size of the corresponding Ewald sphere is, in fact, comparable to the reciprocal lattice vectors. It is easy to see from Fig. 11 that the Laue condition in Ewald construction for x-ray diffraction is less visual and involves more calculations than those presented above for electron diffraction. Reducing the x-ray wavelength is much more difficult compared to the case of electrons, which is readily attainable by increasing the acceleration voltage.

A.4.1 Surface Morphology and RHEED Pattern

The strong electron–matter interaction offers great opportunities for the studies of

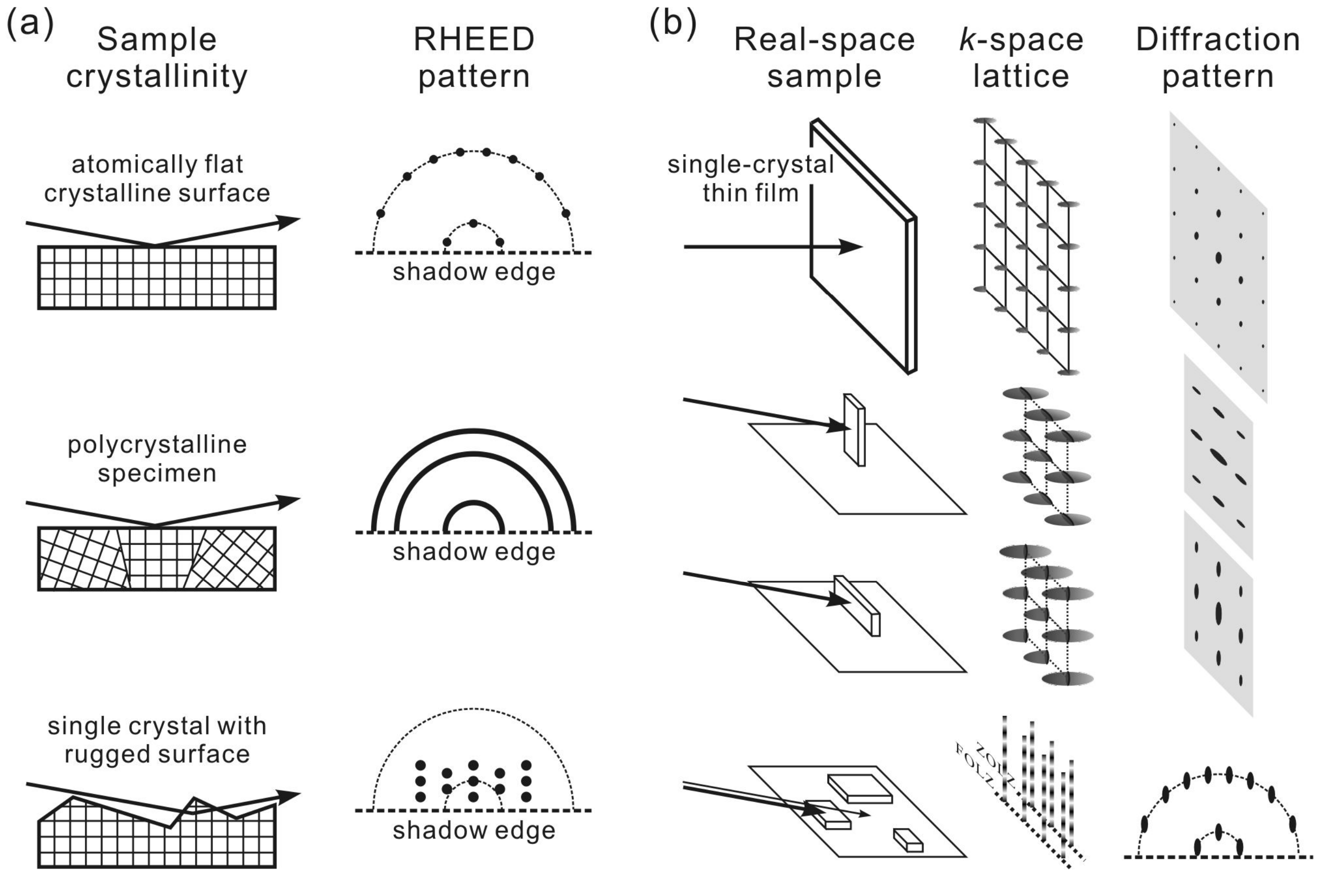

Fig. 12. Schematics for the correlation of (a) sample crystallinity and (b) surface morphology with the observed diffraction pattern. Sample conditions that produce ideal RHEED and transmission patterns are given in the upper panels. Even in reflection geometry, any type of electron penetration results in a transmission-like pattern (panel a, bottom, and panel b, middle). Increase of the spot width is along the direction of the crystallites' reduced dimension, a correlation dictated by the principle of Fourier transformation.

nanometer-scale structures and interfacial phenomena that are less straightforward for x-ray because of its large penetration depth and weak interaction with specimens in general. The same characteristic, however, also makes RHEED sensitive to the surface morphology of the specimen, whose studies in the fields of thin film growth and surface structure determination are actually the main application of this technique (*6, 10, 11*). From the types of diffraction patterns observed, the samples' crystallinity and surface morphology may be deduced, as illustrated in Fig. 12 (*10*). In principle, studies of structural dynamics can be made for all these cases as long as the diffraction spots or rings are distinct and well-defined; in practice, a sample surface that is close to atomically flat (at least within a certain 2D range) is more desirable because rough surface morphology often leads to decrease of diffraction intensity, increase of diffuse scattering background, and broadening of diffraction width that may hinder a proper analysis of temporal changes. Sometimes, well-oriented small crystallites that give a transmission-type pattern may be more beneficial to dynamics studies because of the cross reference obtained from different spots (see Chs. 6 and 7). The stringent requirement of atomically flat surfaces for studies is hence not always necessary.

A.4.2 Electron Mean Free Path and Penetration Depth

It is essential to estimate the electron penetration depth (ζ_e) at a given electron wavelength in a medium. This can be achieved by knowing the mean free path (ℓ_e) for elastic scattering from the total cross section of scattering (σ) and the density of scatterers (N), with the use of the following equations:

$$\ell_\mathrm{e} = \frac{1}{\sigma N} \text{ and the differential cross section } \frac{\mathrm{d}\sigma}{\mathrm{d}\Omega} = \left|f(\vec{s})\right|^2 \qquad (24)$$

where Ω denotes the solid angle. With Eq. 5 and the angular integration of $\mathrm{d}\sigma/\mathrm{d}\Omega$, a screened-potential model that effectively describes the atomic potential for neutral

Table 1: Mean free paths and penetration depths for elastic scattering of electrons.

substance	Z	N (Å^{-3})	ℓ_e (Å) at 30 kV	ζ_e (Å) at 30 kV
graphite	6	$2/(2.46^2 \cdot 6.70 \sin 60°)$	2750	192 at $\theta_i = 4°$
silicon	14	$8/5.43^3$	1010	70 at $\theta_i = 4°$ 35 at $\theta_i = 2°$
interfacial water (cubic form)	8 for O 1 for H	$8/6.358^3$ for O $16/6.358^3$ for H	3050	53 at $\theta_i = 1°$ (transmission-like)
gallium arsenide	31 for Ga 33 for As	$4/5.65^3$ for Ga and As	380	20 at $\theta_i = 3°$
vanadium dioxide (monoclinic)	23 for V 8 for O	4/118 for V 8/118 for O	520	45 at $\theta_i = 5°$
zinc oxide	30 for Zn 8 for O	$2/(3.25^2 \cdot 5.20 \sin 60°)$ for Zn and O	370	20 at $\theta_i = 3°$

elements in relation to the atomic number (Z) and a screening radius gives a good approximation for σ, especially when the scattering angle is not too small (*11*). The final result is

$$\sigma = 0.12\lambda^2 Z^{4/3}. \tag{25}$$

The estimated mean free paths for elastic scattering and the corresponding penetration depths (at typical probing conditions) for several substances are given below in Table 1; their differences should be noted because, without the consideration of refraction,

$$\zeta_e \cong \ell_e \sin\theta_i \quad \text{(for single elastic scattering).} \tag{26}$$

The simple estimation presented above shows that, with the criterion of energy- and momentum-conserved single scattering, electrons probe mostly the surface region of a specimen but do penetrate several unit cells (interplanar distances). The latter property is important in that UEC studies are still capable of resolving bulk-related structural dynamics, with a surface sensitivity. It should be noted that the values of penetration

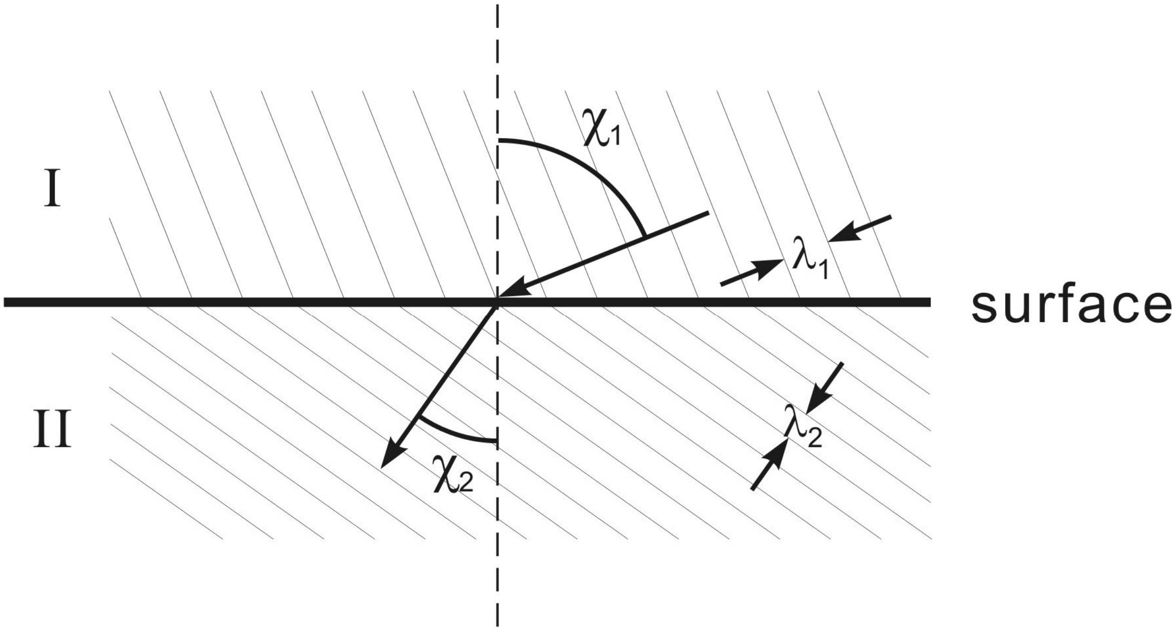

Fig. 13. Tangential continuity at the surface where the wave fronts are refracted. Medium II attracts electrons more than medium I, and the dashed line indicates the surface normal.

depth in Table 1 may be underestimated. If the surface morphology is less perfect than an atomically flat one, or more than one scattering event occurs so to contribute some diffraction intensities, electrons can reach a deeper region into the bulk. When a material contains much heavier elements (e.g., gold), the observed electron diffraction is expected to originate solely from the top layer and form streaks; an example can be seen in Fig. 5.

A.4.3 Inner Potential and Electron Refraction

The phenomenon of electron refraction occurs when the probing particles pass through the interface between vacuum and the specimen or between different materials. This phenomenon exists because electrons experience the difference of the electrostatic potential in different media. Compared to the vacuum environment, the superposition of the atomic potentials in a real material attracts and hence slightly accelerates an electron, which leads to a small change in the wavevector. In an average sense without going into the structural details of atomic arrangement, the mean value of the crystal potential is called the inner potential, V_I (in volts), typically a positive number for attraction. In Fig. 13, medium II has a higher V_I than medium I, causing the traveling electrons to bend toward the surface normal.

Because the discontinuity of V_I appears at the interface along the surface normal, the wavevector change should only occur in that direction. Thus, for a featureless interface, tangential continuity of the wave fronts is required, yielding an analogue of Snell's law in optics (*11*):

$$\frac{\sin\chi_1}{\lambda_1} = \frac{\sin\chi_2}{\lambda_2} \tag{27}$$

where χ_1 (χ_2) is the incident (refractive) angle with respect to the surface normal and λ_1 (λ_2) is the wavelength in medium I (II) (Fig. 13). With the use of Eq. 3, the relative refractivity can be written as

$$n_{12} = \frac{\sin\chi_1}{\sin\chi_2} = \sqrt{\frac{\left(V_0 + V_{\mathrm{I}2}\right)\left[1 + 0.9785\times10^{-6}\left(V_0 + V_{\mathrm{I}2}\right)\right]}{\left(V_0 + V_{\mathrm{I}1}\right)\left[1 + 0.9785\times10^{-6}\left(V_0 + V_{\mathrm{I}1}\right)\right]}} \cong 1 + \frac{V_{\mathrm{I}2} - V_{\mathrm{I}1}}{2V_0}. \tag{28}$$

The approximation is justified because the inner potentials $V_{\mathrm{I}1}$ and $V_{\mathrm{I}2}$ are generally much smaller than the acceleration voltage used. Furthermore, the small-angle approximation valid for typical RHEED experiments gives

$$\theta_\mathrm{i}^2 = \left(\frac{\pi}{2} - \chi_1\right)^2 = \left(\frac{\pi}{2} - \chi_2\right)^2 - \frac{V_{\mathrm{I}2} - V_{\mathrm{I}1}}{V_0}. \tag{29}$$

As an example, for Si(111) with $V_\mathrm{I} \sim 11$ eV, the Bragg angles given by Eq. 11 (without taking into account the structure factor) are $\pi/2 - \chi_2 \approx n\lambda/2d_{\mathrm{Si}(111)} = 11n$ mrad for 30-keV electrons; the corresponding θ_i's for the first 8 orders are nonexistent, 11.4, 27.4, 40.2, 52.3, 64.0, 75.5, and 87.0 mrad, respectively. It is now clear why the regularity of Bragg condition is restored for higher-order spots ($n \geq 5$) in the rocking curve shown in Fig. 8, lower right panel. The reflection of electrons by an atomically flat surface may be the major scattering events at very small incidence angles, which forms the specular spot that has little diffraction contribution for these probing conditions. As a result, UEC studies should be conducted with care with this phenomenon in mind.

A.4.4 Coherence of the Electron Beam

For electromagnetic waves, photons that are generated from a coherent source such as a monochromatic laser can propagate parallel and keep their phase because of their noninteracting nature; the plane-wave description by Eq. 1 is therefore appropriate. Such a model for the wave property of electrons has its limit in reality due to the following reasons. As mentioned earlier, any factor that causes the deviation of $\vec{k}_\mathrm{i}$ will lead to small changes in diffraction condition. Unlike photons, the Coulomb force causes electrons to interact with one another. As a result, collisions and the space-charge effect exist and destroy the coherence of charged particles, especially for a high-density beam. This issue may be reduced by lowering the number of electrons in a spatiotemporal bunch or totally eliminated by using single-electron packets (*12*).

However, real electron sources inevitably have finite sizes and energy spread that result in a finite angular spread ($\Delta\theta$) and the spread of the wavenumber (Δk). The effective coherence length (ξ) is a distance between two points from which the wave packet is scattered with a 180° phase difference (and hence no coherence) (*11*). From Δk and along the electron propagating direction,

$$\xi_{\parallel,\Delta k} = \frac{2\pi}{\Delta k} = \frac{\lambda^2}{\Delta\lambda} \cong \frac{24.52\sqrt{V_0\left(1+0.9785\times10^{-6}V_0\right)}}{\Delta V\left(1+2\times0.9785\times10^{-6}V_0\right)} \text{ (in Å)}, \tag{30}$$

with the use of Eq. 3 and the assumption of the potential spread $\Delta V << V_0$. The value of

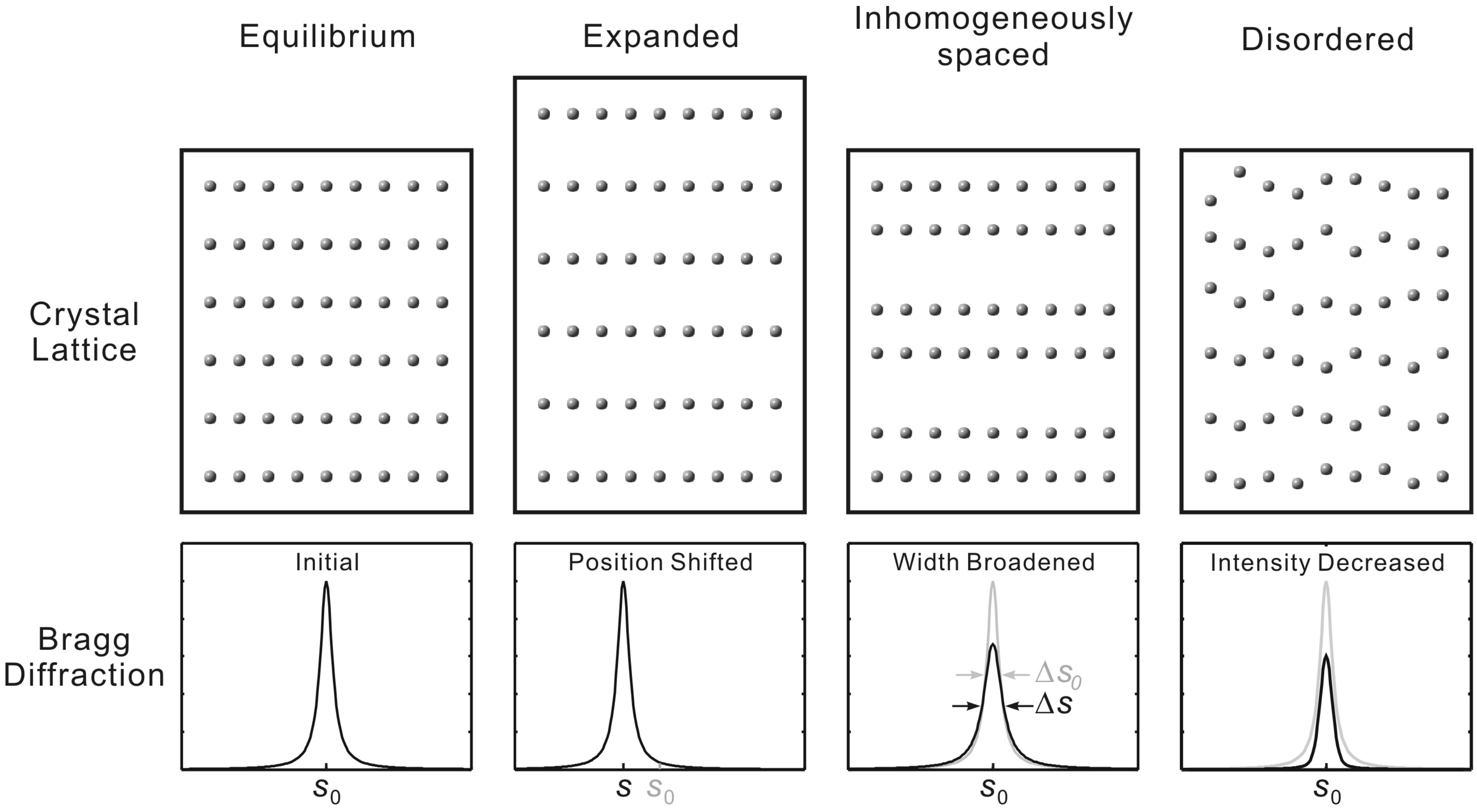

Fig. 14. Structural modifications in the crystal lattice and the corresponding diffraction changes. The diffraction differences observed as a function of time by UEC are therefore indicative of the different atomic motions in the lattice structure.

$\xi_{\|,\Delta k} \sim 41$ nm is obtained for $\Delta V = 10$ V and $V_0 = 30$ kV. From $\Delta\theta$ and perpendicular to the beam direction,

$$\xi_{\perp,\Delta\theta} = 2\pi/\Delta k_{\perp} = 2\pi/(k\Delta\theta) = \lambda/\Delta\theta \tag{31}$$

and has a value of about 7–70 nm for a typical $\Delta\theta$ of 1–0.1 mrad. The angular spread also results in a coherence length along the electron beam direction,

$$\xi_{\|,\Delta\theta} = \frac{2\pi}{\Delta k_{\|}} = \frac{\lambda}{\sin\theta_{\mathrm{i}}\Delta\theta} \tag{32}$$

because $\Delta k_{\|} = \Delta(k\cos\theta_{\mathrm{i}}) = k\sin\theta_{\mathrm{i}}\,\Delta\theta$. For the aforementioned typical $\Delta\theta$ and at $\theta_{\mathrm{i}} = 3°$, $\xi_{\|,\Delta\theta}$ is about 130–1300 nm. The estimation of the coherence length above signifies that electrons generated by a real electron source can only "see" coherently a spatial range of the nanometer to sub-micrometer scale.

B. Nonequilibrium Transient Structures

In time-resolved experiments, the main diffraction features for studies of structural dynamics are the positions, intensities, widths, and the shapes of Bragg spots or Debye–Scherrer rings. Background intensity and Kikuchi patterns may also evolve as a function of time, but in general, their intensities and distributions are weak and diffuse. In the following discussion, we will focus on transient changes of the main diffraction features observed in UEC and make connections with x-ray studies (*13-15*). Summarizing in Fig. 14, in general, the position shift of Bragg spots or rings is directly related to lattice expansion or contraction; the change of the width and shape indicates the emergence of dynamical inhomogeneity; and the intensity change is the result of incoherent thermal motions, coherent lattice vibrations, or phase transitions.

B.1. Shifts of Diffraction Spots and Rings

Following an ultrafast excitation, diffraction spots or rings change their positions vertically and/or horizontally to reflect the changes in interplanar distances. Such changes

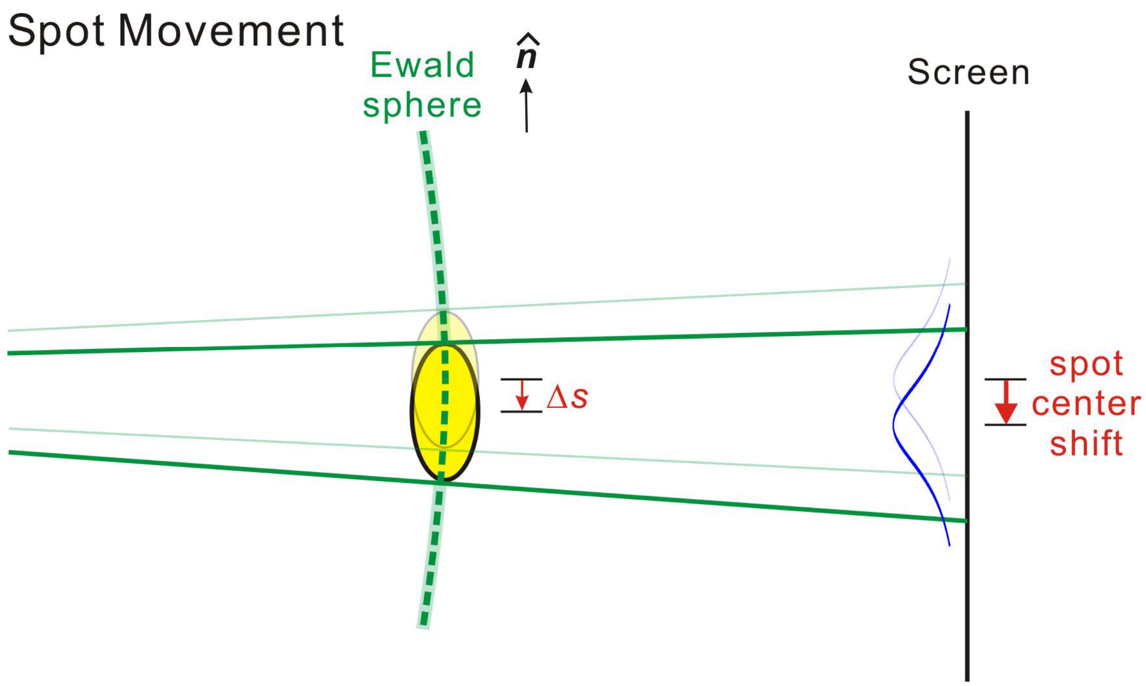

Fig. 15. Temporal changes of diffraction spot position. The faded rods and curves indicate the negative-time equilibrium configuration. As the real lattice expands along $\hat{n}$ at positive times the reciprocal rods move downward, which leads to a downward movement of Bragg spots.

need to be homogeneous (uniformity of distance change) over essentially the entire spatially probed region, a requirement for preserving the Bragg condition. Thus, these shifts provide the unequivocal evidence for the homogeneous lattice expansion or contraction, depending on the direction of the shift.

We first consider the vertical lattice change along $\hat{n}$. According to the Laue condition of Eq. 12, a small vertical shift of the Bragg spot on the center (00) rod, ($0\boldsymbol{A}^* \; 0\boldsymbol{B}^*$), is directly related to the change in the vertical lattice spacing by the following relationship:

$$\Delta s/s = -\Delta d/d = -\Delta(\theta/2)/\tan(\theta/2) \qquad (33)$$

which becomes $-\Delta\theta/\theta$ when θ is small. Consequently, a decrease (increase) in s, i.e., when the Bragg spot shifts toward (away from) the direct beam position in the diffraction pattern, is a measure of the increase (decrease) in d. In reciprocal space, such a lattice change can be visualized as the rods moving parallel to $\hat{n}$ and intersecting with the Ewald sphere but maintaining their size or shape (Fig. 15). The same picture can be applied to the description of movements in the horizontal direction.

On the ultrashort time scale, it is critical to understand the dynamics responsible for a downward shift, which is the observation made in many UEC studies. The first mechanism that comes to mind involves conventional heating, due to the anharmonicity of the lattice. The 1D thermal expansion is usually expressed as $\Delta x = (3g/4b^2)k_B\Delta T$, which is deduced from the anharmonic potential energy $U(x) = bx^2 - \mathrm{g}x^3 - fx^4$ with positive b, g, and f (*16*). However, at room temperature, the (linear) thermal expansion coefficient (α_l) for most of the crystalline solids is on the order of 10^{-5} to 10^{-6} K^{-1}; for example, $\alpha_l \times 10^6 = 2.6$, 5.73 and 14.2 for silicon, gallium arsenide and gold, respectively. Thus, a maximum *thermally driven* change of 1% in lattice spacing requires a lattice temperature jump of about 3850, 1750 and 700 K, which are not reachable at our excitation fluences and in a very short time. To achieve a temperature jump (ΔT_l) at the surface, the fluence for heating required is given by

$$F_{\mathrm{heating}}/\delta = (F_{\mathrm{laser}}/\delta)(1 - R)(E_{\mathrm{excess}}/E_{\mathrm{photon}}) \sim C_l\Delta T_l\,, \tag{34}$$

where δ is the penetration depth (inverse of the absorption coefficient, $1/\alpha$) of the light (photon energy E_{photon}) with fluence F_{laser}; R is the reflectivity, E_{excess} is the above-gap excess energy, and C_l is the heat capacity of the lattice. For gallium arsenide, for example, $C_l = 1.74$ J/cm^{3}K, the band gap $E_{\mathrm{g}} = 1.423$ eV, $R \sim 0.3$ (0.45) and $\delta \sim 710$ (6.4) nm for 800 (266) nm normal-incident light (*17*). A fluence of $F_{\mathrm{laser}} = 10$ (1) mJ/cm^2 at 800 (266) nm gives the value of ΔT_l to be 4.6 K at 800 nm or 340 K at 266 nm.

Experimentally, this is in contradiction with the large observed shift. More importantly, as will be shown in Ch. 4, the spot-shifting behavior for the 800- and 266-nm excitations are contrary to the trend obtained above.

It follows that on the ultrashort time scale, the nonequilibrium state of the lattice must be considered. In this state, only certain types of the atomic motions may be initially launched, and the assumption of thermal equilibrium for all modes is not valid. Furthermore, carrier excitation can affect the lattice potential, resulting in a new state of weaker chemical bonding and hence a different structure. This expansion by a "*potential-driven*," carrier-assisted mechanism does not depend on lattice temperature but on the carrier density. When the number of carriers decreases (through diffusion, for example), the expansion would decrease and the system recovers accordingly. Finally, the expansion in the vertical and horizontal directions may show anisotropy in the temporal behavior with different amplitudes for the change. Manifestation of these features of nonequilibrium behaviors can be seen in the studies made on GaAs (Ch. 4).

B.2. Changes of Widths and Shapes

The widths and shapes of Bragg spots or rings in a diffraction pattern are affected by the crystal size (Eq. 23), inhomogeneity and embedded strain in the sample, by electron refraction due to the shape of the crystallites (Sec. A.4.1), and by the uncertainty of the direction and magnitude of the probing electrons' momentum $\hbar\vec{k}_\mathrm{i}$ (size of the electron beam). However, their transient differences from a static reference can only stem from the structural changes induced by the optical excitation. In the case of polycrystalline samples, the average size of the crystallites may change (e.g., during ultrafast melting or annealing), resulting in the broadening or narrowing of diffraction rings according to the Scherrer formula (Eq. 23). The shape may also develop to a

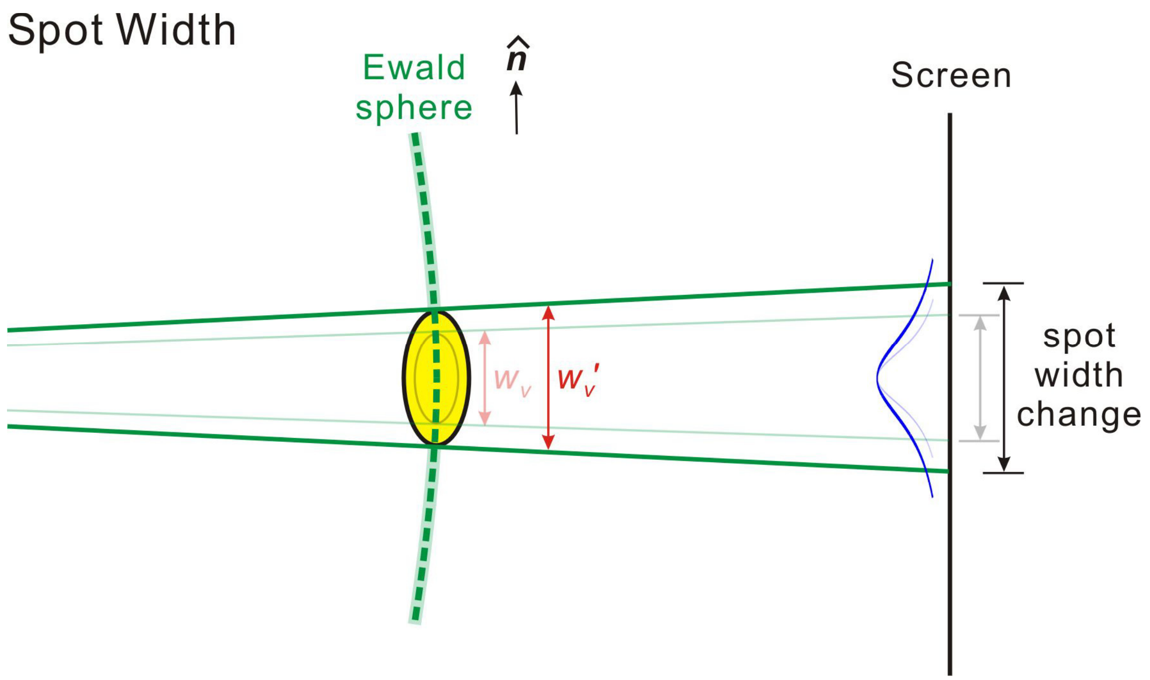

Fig. 16. Temporal changes of diffraction width. The faded rods and curves indicate the negative-time equilibrium configuration. Lattice inhomogeneity (along $\hat{n}$) generated in the crystal makes the reciprocal rods elongated, and their intersections with the Ewald sphere give a diffraction pattern with larger vertical width.

Gaussian-like function, which reflects an increased inhomogeneity. In the case of crystalline samples, however, this spatial size change is not of concern since the crystal essentially preserves its order. Thus, in this case, lattice inhomogeneity is due to a small modification of the average lattice spacing or a strain of propagating acoustic waves following the excitation.

Following the above discussion of the reciprocal-space picture, it is clear that, if the lattice planes evolve to two distributions of distances around *d*, one larger and one smaller, then this strain propagation will result in two side bands (or broadening) in *k* space around the central value (see Fig. 16). Such behavior is commonly caused by an acoustic sound wave of relatively small wavelength. Coherent acoustic motions are typically generated through carrier excitation or from the decay of another type of initially generated lattice vibration, e.g., optical phonons. In an elementary metal, acoustic phonons are directly generated following carrier generation because only one atom exists in the primitive unit cell and there is no optical branch. However, in a semiconductor with more than one atom in the primitive unit cell, optical phonons are present and become the doorway for efficient coupling with the carriers. These optical phonons have a lifetime during which they convert to acoustic ones, and the latter into thermal motions on a time scale determined by the anharmonicity of the lattice.

The inhomogeneity of the lattice generated parallel to the sample surface, i.e., the horizontal broadening of reciprocal-lattice rods, has a more complicated effect: when intersecting with the Ewald sphere, the rod projects not only a larger horizontal width but also an enlarged vertical width in a diffraction pattern. However, the geometry of RHEED allows the contributions to horizontal and vertical widths due to the dynamical inhomogeneity of the lattice along different directions to be distinguished (see Appendix B for the derivation). By monitoring the temporal evolution of spot widths in the directions orthogonal to $\hat{n}$, lattice dynamics along the surface can be followed as a function of time. The difference between the temporal evolution along the vertical and horizontal directions in the diffraction patterns can provide information of such anisotropy. As will be shown in Ch. 4, a key cause of the anisotropy is free movement along the $\hat{n}$ direction (surface vertical vs bulk lateral) and the change in lattice potential.

B.3. Changes of Diffraction Intensities

On the basis of Eq. 9, the diffraction intensity of a Bragg spot (*hkl*) is proportional to the square of the geometrical structure factor *F*(*hkl*), which is given by (*5*)

$$F(hkl) = \sum_j f_j \exp\left(-i\vec{G}_{hkl} \cdot \vec{r}_j\right) = \sum_j f_j \exp\left[-2\pi i\left(h\,x_j + k\,y_j + l\,z_j\right)\right] \qquad (35)$$

where f_j is the atomic scattering factor of the jth atom in a primitive unit cell. Since the determination of $F(hkl)$ involves the positions of atoms, $\vec{r}_j \equiv (x_j, y_j, z_j)$, in a unit cell, any lattice motions that appreciably change their relative positions can cause the diffraction intensity to change. These motions are those of optical phonons (see, e.g., Refs. 13–15 and 18), small-wavelength acoustic phonons, and the thermal motions. In contrast, homogeneous lattice expansion or contraction has no influence on the intensity of the Bragg spots. The contribution of the thermal, incoherent motion (in all directions) in diffraction intensities can be calculated using the DW expression, Eq. 16.

The ability in UEC to resolve the diffraction in time and for different Bragg spots makes possible the separation of contribution by these different processes, especially that horizontal and vertical lattice motions manifest themselves differently. The change of spot intensity on the (00) rod will display vertical motions, whereas those on the side will have contributions from both vertical and horizontal motions. However, incoherent thermal motion affects all of the Bragg spots. For the case of gallium arsenide as an example, this separation is clear. The crystal has a face-centered-cubic lattice with a two-atom basis that has gallium at $\vec{r}_{\text{Ga}} \equiv (0, 0, 0)$ and arsenide at $\vec{r}_{\text{As}} \equiv (1/4, 1/4, 1/4)$ in the unit cell in the equilibrium state. If, say, $\hat{n}$ is [001], the intensity of the Bragg spot $(0\ 0\ 4n)$ on the (00) rod is proportional to

$$|F(0\ 0\ 4n)|^2 = |f_{\text{Ga}}\exp(-8n\pi i z_{\text{Ga}}) + f_{\text{As}}\exp(-8n\pi i z_{\text{As}})|^2. \qquad (36)$$

Thus, those optical phonons that have the Ga and As atoms vibrate against each other along the vertical direction (e.g., longitudinal optical phonons) will affect the structure factor and consequently the diffraction intensity. Horizontal vibrational motions, however, have no influence because their projection on the vertical scattering vector is zero. On the other hand, if thermal motion is responsible for the intensity reduction, Equation 16 provides the theoretical description. By monitoring the extent and time scale of the intensity reduction for different Bragg spots, the lattice motions responsible for the observed changes can be distinguished.

B.4. Transient Changes in Transmission Diffraction

Because of the probing geometry in the transmission mode, transient diffraction patterns of crystalline thin films can directly provide the dynamic information in the 2D structure. Due to the intersection between rods and the Ewald sphere, as shown in Fig. 10, 2D lattice expansion/contraction deduced from decrease/increase of the distances between diffraction spots, or changes of structural homogeneity indicated by the width changes, can be observed experimentally. Transient structural information along the $\hat{n}$ direction could be masked, given the experimental geometry where the electron beam propagation is essentially in the same direction of rods (see Sec. A.3 for discussion). Naturally, if there is substantial lattice expansion along $\hat{n}$ on the picosecond time scale, such change can be observed in the reflection geometry. In transmission, however, this $\hat{n}$-direction lattice motion can lead to intensity changes, as will be shown in Ch. 4.

Transmission electron diffraction has also been applied to studies of polycrystalline metallic thin films by several groups, e.g., those of Miller (*19*), Cao (*20*), and, earlier, Mourou (*21*). The issues of nonthermal solid-to-liquid phase transition and electronically driven lattice changes have been discussed. However, due to the polycrystalline nature of the sample, transient lattice motions in a single crystallite and those between randomly oriented crystallites may be strongly correlated, and this could complicate the interpretation of structural dynamics. The transmission study reported in

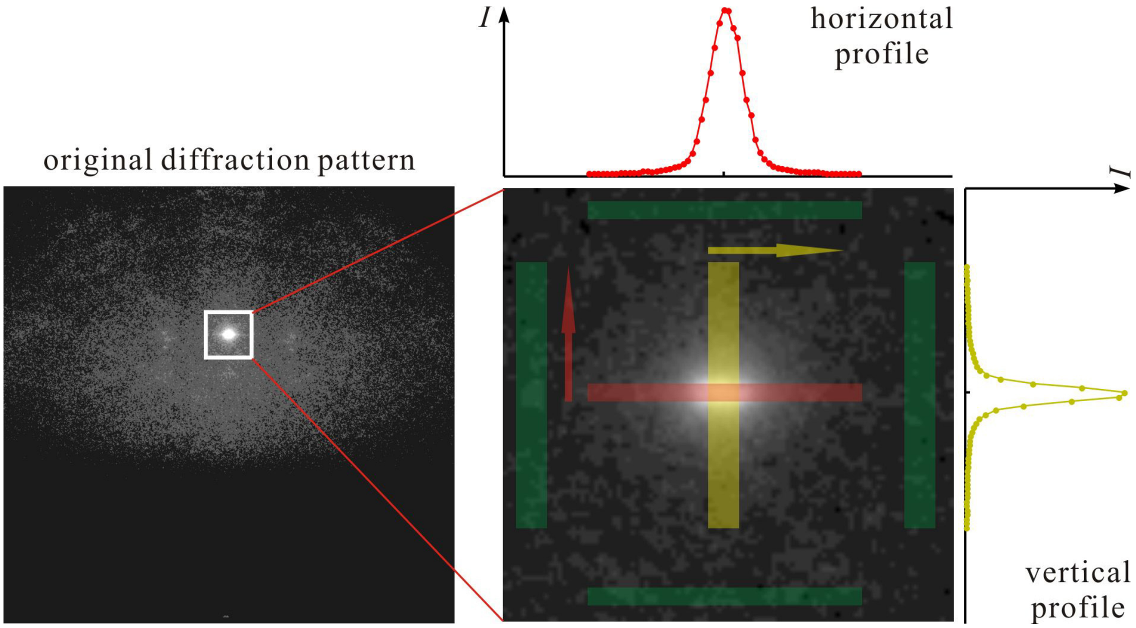

Fig. 17. Extraction of the horizontal and vertical profiles of a Bragg spot. The narrow strips (yellow for the vertical direction and red for the horizontal) are the regions over which intensity averaging is performed. Profiles obtained from the green strips (vicinity of the Bragg spot) may be used for background subtraction when necessary.

Ch. 4 was, to our knowledge, the first study of structural dynamics of a single-crystal semiconductor by electron diffraction, which displays the motion of the entire lattice.

B.5. Extraction of Transient Diffraction Changes

To quantify the aforementioned diffraction changes at transient times, a fitting procedure is invoked to obtain the intensity, position, width and line shape of a Bragg spot or diffraction ring as a function of time. For typical UEC studies, the analysis can be made in 1D by considering the vertical and horizontal directions separately. The first step is to collect the 1D profiles of a certain diffraction feature at different times, by averaging over a narrow strip across the diffraction vertically or horizontally (Fig. 17). The important issue here is to achieve a higher ratio of the signal to the background and noise. The profile obtained from a wider strip may be less noisy but with a lower peak due to

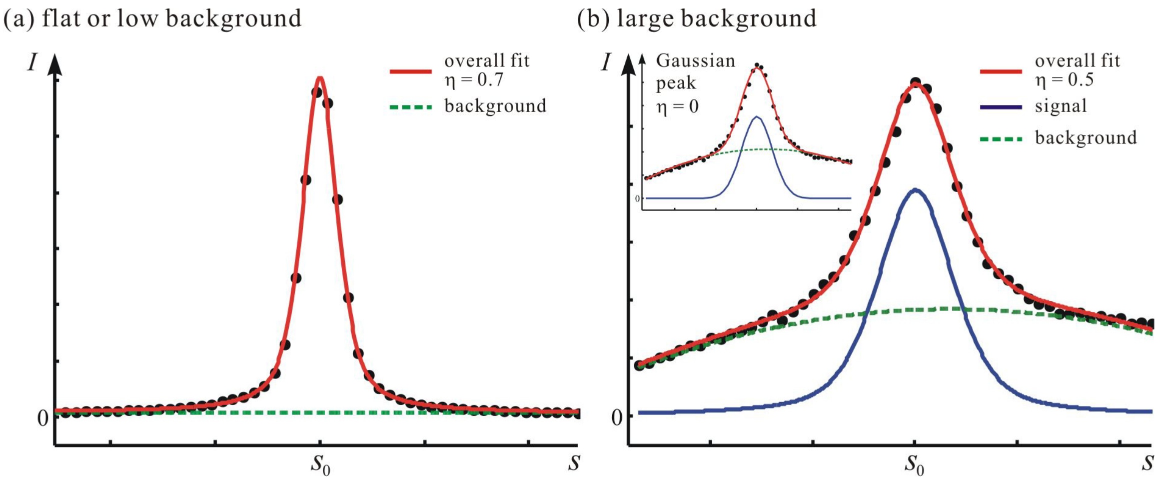

Fig. 18. Results of the fit. (a) A constant offset or linear function is included in the fit of an intensity profile with a flat or low background. (b) A quadratic (or higher-order) function is used for the background. The inset shows the result of the fit that considers a pure Gaussian form for the signal; the small discrepancy is visible.

the background in the less intense part; the profile from a narrower strip contains more contribution from the signal, but can be less smooth. Thus, a balanced choice may be a strip that covers (approximately) the horizontal or vertical full width at half maximum.

For fitting, a pseudo-Voigt shape function, $f_{\mathrm{pV}}(s)$, is used,

$$f_{\mathrm{pV}}(s) = I \cdot \left[\eta \cdot f_{\mathrm{L}}(s) + (1-\eta) \cdot f_{\mathrm{G}}(s)\right], \tag{37}$$

$$f_{\mathrm{L}}(s) = \frac{1}{\pi} \cdot \frac{w/2}{(s-s_0)^2 + (w/2)^2},$$

$$f_{\mathrm{G}}(s) = \frac{2}{w}\sqrt{\frac{2\ln 2}{\pi}}\, \exp\left(\left(\frac{s-s_0}{w}\right)^2 \cdot 4\ln 2\right).$$

The integral of $f_{\mathrm{L}}(s)$ or $f_{\mathrm{G}}(s)$ over s is unity (normalized), and Eq. 37 is a simple sum of the two functions instead of a convolution (Voigt shape). Here, I represents the (1D) integrated intensity, s the scattering vector coordinate, s_0 the peak position, w the (common) full width at half maximum, and η the Lorentzian contribution. Depending on the surface quality and the electron incidence angle, the diffuse background may be low and flat enough such that no subtraction prior to fitting is needed (Figs. 17 and 18a); when the background is not negligible, either a subtraction by the profile obtained from the vicinity of the diffraction feature is made first, or a polynomial (typically quadratic) function is include in the fit (Fig. 18b).

Comparisons between the extracted diffraction features—$I(t)$, $s(t)$, $w(t)$, and $\eta(t)$, where t is the delay time between the electron and optical pulses—are subsequently made to elucidate the structural dynamics and relaxation pathway in the specimen. Based on the previous discussion in Secs. B.1 to B.3, the similarity or difference between these time-dependent features can provide crucial information about the involvement of the candidate (structure-related) physical processes, their synchrony or sequence in time, and the characteristic time constants that govern the structural dynamics.

B.6. Issues of Electron Refraction and Scalability of Diffraction Change

Two issues about the dynamical changes in UEC are addressed. The first one is in regard to the diffraction changes caused by the electron refraction effect. According to the discussion in Sec. A.4.3, the two reasons are the possible slight tilting of the surface normal and the change of the inner potential, both of which result from the optical excitation and may lead to small change in the diffracted beam direction. However, it can be shown from the order-of-magnitude analysis that electron refraction plays a minor role in the diffraction changes discussed above, for typical UEC studies with moderate optical excitation.

The tilting of $\hat{n}$ comes from the different extent of lattice expansion as a result of the gradient of the excitation pulse profile on the specimen. This effect may be much reduced by using a sample size or making the probed area within the region of relatively homogeneous excitation. Furthermore, with the total vertical expansion of the lattice on the order of 1 to 10 Å over the length of the probed region along $\vec{k}_{\mathrm{i}}$ (on the order of 1 mm), electron refraction may cause an angular change of 10^{-4} to 10^{-3} mrad, much less than the uncertainty of $\vec{k}_{\mathrm{i}}$ itself and consequently unimportant. The inner potential of matters is on the order of 10 V, and its change induced by moderate excitation is expected to be on the order of 1 V or less. Thus, from Eq. 29, the induced angular shift would be on the order of $10^{-3.5}$ mrad and hence negligible. For intense excitation, the electron refraction effect due to larger surface or bulk potential change may be observed (*22*); however, care has to be taken in interpreting the relative shifts of diffraction features, which is the next issue discussed below.

On the basis of Eq. 33, diffractions from the same set of crystal planes with different orders (n) are expected to exhibit shifts in proportion to n during the structural dynamics, with the same (normalized) temporal evolution for the movements. In addition, the accompanying changes in their intensities, if exist, should be scalable according to Eq. 16 or Eq. 35, and follow one temporal profile only. The presumption behind is that all of these diffractions originate from spatially the same part of the probed specimen. However, if, for some reason, this is not the case, the scalability of diffraction shifts may not hold; an additional observation that often accompanies with this somewhat counterintuitive phenomenon will be the different time constants for diffractions of different orders.

It should be noted that a pattern of many spots similar to the cases shown in Fig. 12, bottom of panel a and upper three of panel b, comes with a transmission nature. Due to the different electron traveling directions for different diffractions, lower-order spots may originate spatially from the higher part of a crystallite (to avoid the blocking of diffracted electrons by adjacent crystallites or surface structures) and the highest-order one is formed by diffracted electrons that penetrate deeper. The key governing factor here is the mean free path discussed in Sec. A.4.2. Such a phenomenon will be further discussed in Ch. 5 with a real case. Proportionality of diffraction shifts becomes true for solely transmission-type experiments such as studies of polycrystalline samples (electrons penetrating small crystallites and forming the diffractions), and an example can be seen in Ch. 10. For scalability of intensity changes, see Ch. 4 for the transmission case and Ch. 8 for the reflection case.

Appendix A. Conventions

In the diffraction theory, the incoming beam is described by Eq. 1. In this convention, the wavenumber $k = |\vec{k}_\mathrm{i}| = 2\pi/\lambda$, and for electrons, $k = \omega/v$ where $v = \lambda\upsilon$ is the velocity and $\upsilon = \omega/2\pi$ is the frequency; the momentum of the particle $p = \hbar k = mv$, and the de Broglie relation $\lambda = h/p$ which consistently equals to $2\pi/k$. Accordingly, when k is used in this form, a constant factor of 2π appears in diffraction expressions of k, s and others such as the reciprocal basis vectors in 3D (Eqs. 13 and 14), those for a 2D reciprocal lattice (Eq. 16), and the last part of Eq. 23.

Crystallographers use a different convention to define the wavevector, $k = \lambda^{-1}$. As such the factor 2π disappears, and, for example, the important relations $\vec{s} \cdot \vec{R} = 2m\pi$ and $s = (4\pi/\lambda)\sin(\theta/2)$ become simply $\vec{s} \cdot \vec{R} = m$ and $s = (2/\lambda)\sin(\theta/2)$. In such a way, it is straightforward to invert s directly into real-space distances. The crystallography convention is equivalent to rewriting Eq. 1 for $\Psi_0(\vec{r}\,',t)$ with the phase factor being $2\pi\vec{k}_\mathrm{i} \cdot \vec{r}\,' - \omega t$, where the new k_i is $1/\lambda$. The important point is to keep track of the self-consistency regarding the momentum as the conventional $p = \hbar k$, or $p = hk$ with k

being clearly defined. Unfortunately, these definitions, with or without 2π, are used in different areas of diffraction. For example, in gas-phase diffraction, s is defined with 2π included; for most of the following chapters, this convention is used.

Similarly, the definition of the angle of incidence being θ or $\theta/2$ requires a convention. Considering θ to be the total diffraction angle (see Fig. 2a), the incidence angle would be $\theta/2$; if the incidence angle is θ, then the total scattering angle would be 2θ. The definition of s follows.

Appendix B. Reciprocal-space Broadening of Rods

The following simple estimation is made for the effect of horizontal broadening of the rods in reciprocal space on the observed width of diffraction spots. For an ordered structure in 2D, the reciprocal lattice is made of rods, and when modulated by the spacings in the $\hat{n}$ direction, each zone should be considered as a symmetric-top-like shape with $w_\mathrm{h} = w_\mathrm{x}$, w_y being different from $w_\mathrm{v} = w_\mathrm{z}$. Therefore,

$$(2x/w_\mathrm{h})^2 + (2y/w_\mathrm{h})^2 + (2z/w_\mathrm{v})^2 = 1$$

where x and y are the directions (in reciprocal space) orthogonal to $\hat{n}$, z the direction parallel to $\hat{n}$, and w_h (w_v) is the full horizontal (vertical) width. Locally, the Ewald sphere with large radius (large $\hbar k_\mathrm{i}$) will cut through the rods nearly as a tilted plane (Fig. 16) defined by (0, 1, 0) and ($\sin\gamma$, 0, $\cos\gamma$), where γ is the angle between $\hat{n}$ [i.e., (0, 0, 1)] and plane direction. As a result, the elliptical trace where the rod and the plane intersect has a horizontal width w_h but the vertical width becomes $(\tan^2\gamma/w_\mathrm{h}^2 + 1/w_\mathrm{v}^2)^{-1/2}$.

If, due to horizontal inhomogeneity, w_h becomes $w_\mathrm{h} + \Delta w_\mathrm{h}$, the change of the vertical width will be

$$\Delta w_\mathrm{h} \tan^2\gamma/[\tan^2\gamma + (w_\mathrm{h}/w_\mathrm{v})^2]^{3/2},$$

which is much less than or on the same order of Δw_h. This is because in the reflection geometry of UEC, γ is small and w_v and w_h are not significantly different within an order of magnitude. It is noted that w_v and w_h are determined by the inverse of the coherence length (on the order of 10 nm or more) and also affected by the specimen morphology.

References:

1. B. K. Vaĭnshteĭn, *Structure analysis by electron diffraction* (Pergamon Press, Oxford, 1964).
2. H. M. Seip, in *Selected topics in structure chemistry*, P. Andersen, O. Bastiansen, S. Furberg, Eds. (Universitetsforlaget, Oslo, 1967), pp. 25-68.
3. J. C. Williamson, Ph.D. thesis, California Institute of Technology (1998).
4. Z. L. Wang, *Elastic and inelastic scattering in electron diffraction and imaging* (Plenum Press, New York, 1995).
5. N. W. Ashcroft, N. D. Mermin, *Solid state physics* (Saunders College Publishing, Fort Worth, TX, 1976), pp. 101-108.
6. Z. L. Wang, *Reflection electron microscopy and spectroscopy for surface science* (Cambridge Univ. Press, Cambridge, 1996).
7. B. E. Warren, *X-ray diffraction* (Dover, New York, 1990), pp. 38, 253.
8. J. F. Vetelino, S. P. Gaur, S. S. Mitra, *Phys. Rev. B* **5**, 2360 (1972).
9. C.-Y. Ruan, V. A. Lobastov, F. Vigliotti, S. Y. Chen, A. H. Zewail, *Science* **304**, 80 (2004).
10. P. K. Larsen, P. J. Dobson, Eds., *Reflection high-energy electron diffraction and reflection electron imaging of surfaces* (Plenum Press, New York, 1988).
11. A. Ichimiya, P. I. Cohen, *Reflection high-energy electron diffraction* (Cambridge

Univ. Press, Cambridge, 2004).

12. A. Gahlmann, S. T. Park, A. H. Zewail, *Phys. Chem. Chem. Phys.* **10**, 2894 (2008).
13. A. Rousse, C. Rischel, J.-C. Gauthier, *Rev. Mod. Phys.* **73**, 17 (2001).
14. C. Bressler, M. Chergui, *Chem. Rev.* **104**, 1781 (2004).
15. M. Bargheer, N. Zhavoronkov, M. Woerner, T. Elsaesser, *Chemphyschem* **7**, 783 (2006).
16. C. Kittel, *Introduction to solid state physics* (John Wiley & Sons, Inc., New York, 7th ed., 1996), pp. 129-131.
17. S. Adachi, *Optical constants of crystalline and amorphous semiconductors: Numerical data and graphical information* (Kluwer Academic Publishers, Boston, 1999), pp. 221, 225.
18. K. Sokolowski-Tinten *et al.*, *Nature* **422**, 287 (2003).
19. B. J. Siwick, J. R. Dwyer, R. E. Jordan, R. J. D. Miller, *Chem. Phys.* **299**, 285 (2004).
20. S. H. Nie, X. Wang, H. Park, R. Clinite, J. M. Cao, *Phys. Rev. Lett.* **96**, 025901 (2006).
21. S. Williamson, G. Mourou, J. C. M. Li, *Phys. Rev. Lett.* **52**, 2364 (1984).
22. R. K. Raman *et al.*, *Phys. Rev. Lett.* **101**, 077401 (2008).

Chapter 3

Ultrafast Electron Crystallography: Methodology and Apparatus

Introduction

The apparatus of ultrafast electron crystallography (UEC) was built for the studies of condensed matter and surface assemblies (*1, 2*), on the basis of the experiences accumulated through the construction of the first three generations for gas-phase molecular studies in our group (*3, 4*). Conceptually, the UEC technique uses the similar scheme of laser excitation (pump) and electron probing, in which the optical initiation marks the zero of time. With the specimen mounted inside the chamber, its diffraction pattern is digitally recorded. By varying the delay time between the arrival of the optical and electron pulses on the surface of the specimen, diffraction snapshots at different times are obtained; the diffraction patterns contain information about the structural evolution, as a function of time, of the material under study. The analysis of diffraction feature changes provides the temporal profiles for certain physical processes, as described in Ch. 2. Finally, structural dynamics and an overall physical picture are obtained through the correlation between these processes.

The UEC apparatus can be operated in the reflection or transmission detection mode. Their experimental configurations are basically the same, except for a small difference in that for transmission, an additional vertical sample holder is used to support the thin specimens; the electron beam penetrates through a sample instead of being scattered from a surface. This chapter briefly describes the parts that form the apparatus and discusses about several topics in the experimental consideration. Details for the construction of the instrument may be found in Ref. 2. A further development implementing the scheme of pulse front tilting (*5*) was made by Dr. Peter Baum. Its concept for resolving the temporal mismatch between the optical and electron pulses on the specimen (thus improving the temporal resolution of UEC) is also summarized.

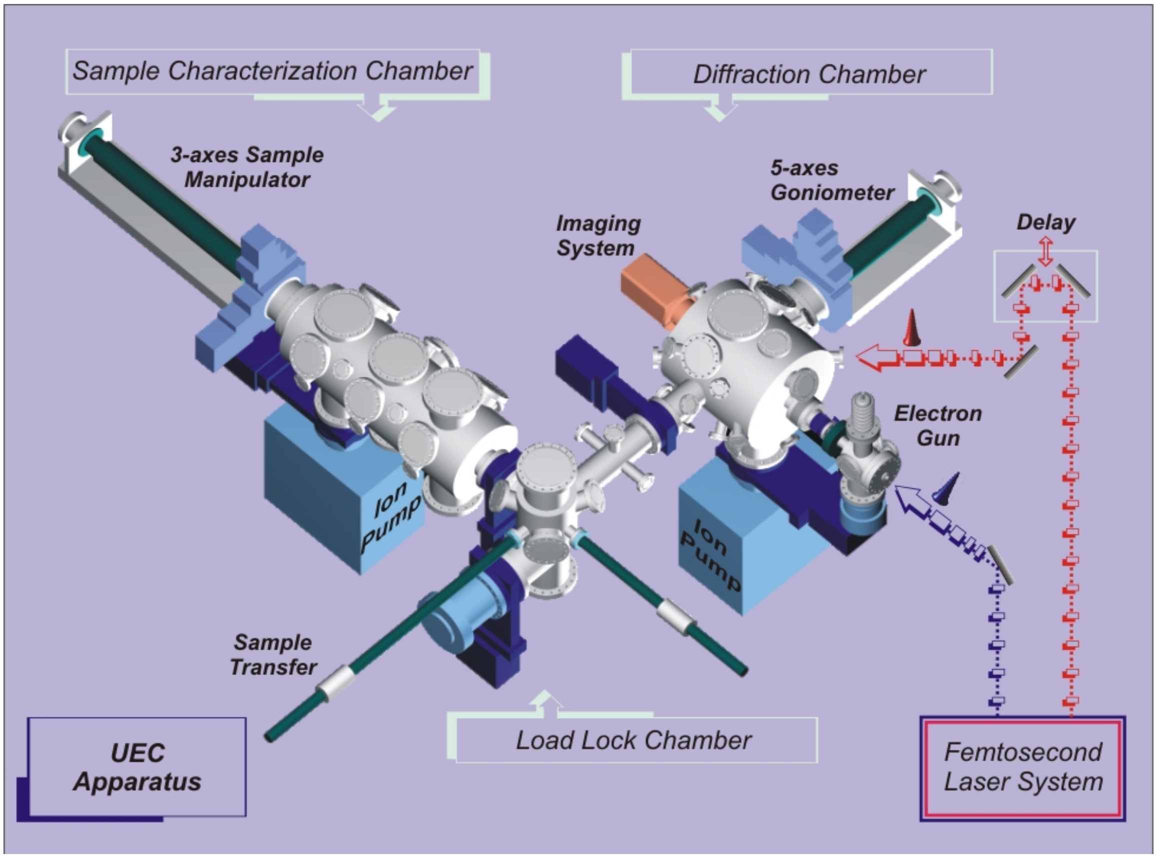

Fig. 1. UEC apparatus. Shown are the three UHV chambers and the two laser beams from the femtosecond laser system for optical excitation and electron generation.

Apparatus of UEC

The UEC apparatus consists of a femtosecond laser system for generation of the electron probe and optical initiating pulses; an assembly of ultrahigh vacuum (UHV) chambers for diffraction, load lock (sample handling) and characterization; an electron gun system in a high vacuum chamber; and a charged-couple device (CCD) camera assembly for pattern recording (Fig. 1). The UHV environment is necessary for the surfaces and interfacial assemblies that are sensitive to pressure as a result of their easy deterioration caused by the bombardment or coverage of gas molecules. Manual and pressurized gate valves (dark blue modules in Fig. 1) were installed for the separation

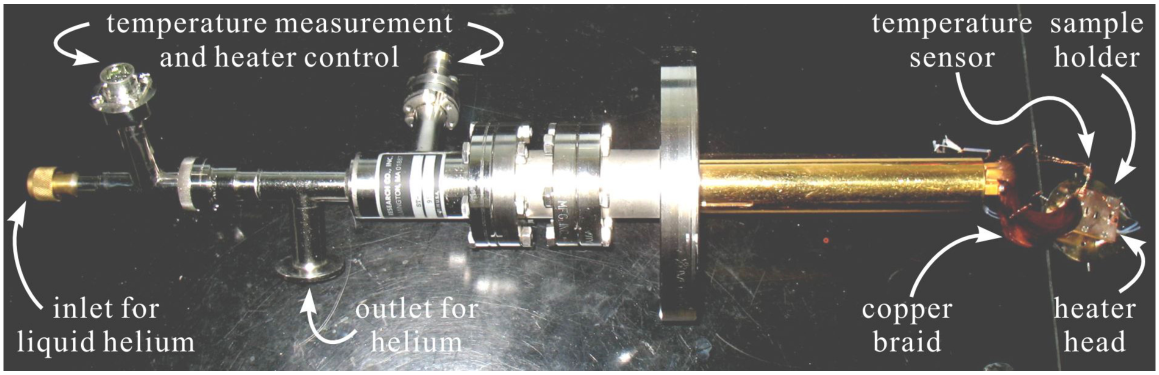

Fig. 2. The cryostat for low-temperature experiments. The copper braid cooled by the flow of liquid helium conducts thermal energy away from the sample holder. A heater is also available for temperature adjustment.

(isolation) of chambers when necessary. The different pressures between the electron gun, diffraction chamber and the CCD camera are maintained through differential pumping.

For position control of the samples, a high precision goniometer (from Transfer Engineering) with 3 degrees of freedom in translation and 2 axes of rotation was installed and housed inside the diffraction chamber. These translations and rotations are manipulated through a computerized interface, allowing for precise alignment of the specimens (supported on a sample holder mounted onto the goniometer), the measurement of rocking curves by changing the incidence angle (θ), and the access of the zone axes at different azimuthal angles (ϕ). The translational precision is 10 μm and the angular precision is 0.005°. Tubes for the flow of liquid nitrogen were connected from the bottom of the goniometer inside the diffraction chamber and intended for low-temperature experiments; the minimum temperature that may be reached by this method is ~100 K. For experiments that require an even lower temperature, the sample holder on the goniometer is coupled to a UHV cryostat (ST-400, Janis Research) that is connected from one side of the diffraction chamber and cooled by liquid helium (Fig. 2).

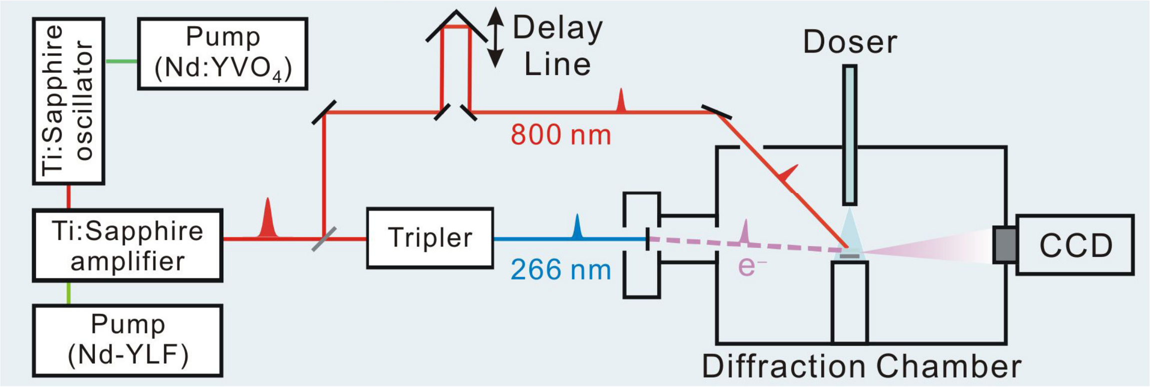

Fig. 3. Schematic of the femtosecond laser system and its integration into the UEC apparatus. The arrangement of the beam paths is specifically for experiments that consider the specimen excitation to be achieved by near-infrared 800-nm light pulses. A capillary doser is connected to the top of the chamber for studies of molecular assembly.

A temperature of ≤20 K is readily achieved without too fast helium consumption. As for experiments that require a temperature higher than the room temperature, the wires installed under the goniometer head can heat the sample holder (up to ~500 K) through the adjustment of the electric current; its influence on the electron beam direction is small and, therefore, does not interfere with the recording of diffraction images.

The femtosecond laser system consists of an oscillator, an amplifier, and two pump lasers (Fig. 3). The mode-locked Ti:sapphire oscillator (Tsunami, Spectra-Physics) is pumped by a continuous-wave, diode-pumped Nd:YVO$_4$ laser (Millennia Vs, Spectra-Physics) with an average power of 5 W at 532 nm. The output of the oscillator is femtosecond laser pulses centered at 800 nm, with a repetition rate of 80 MHz and a pulse energy of 8 nJ. These pulses are amplified by a Ti:sapphire amplifier (Spitfire, Spectra-Physics) pumped by a diode-pumped, Q-switched Nd:YLF laser (Evolution-30, Spectra-Physics) whose repetition rate is 1 kHz and pulse energy is >20 mJ centered at 527 nm. The output of the amplifier is femtosecond pulses centered at 800 nm (1.55 eV),

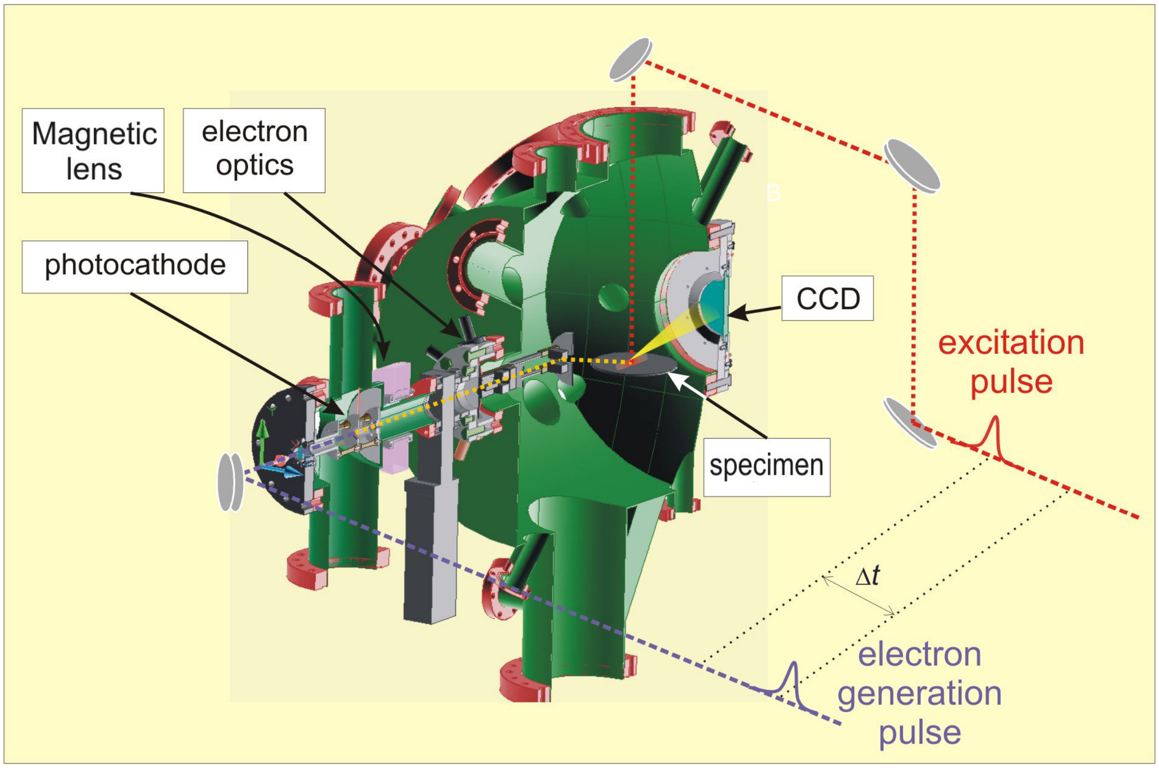

Fig. 4. A cross-sectional view of the electron gun and diffraction chambers, with the paths of the optical excitation and electron generation beams and the CCD camera.

with a full width at half maximum (FWHM) in time equal to ~120 fs and a pulse energy of 2 mJ at 1 kHz.

For experiments that use 800-nm light to excite the specimens, a beam splitter is placed to separate the main beam into two arms (Fig. 3). The path of the stronger beam for excitation contains a movable delay line for the variation of time, which is controlled through a computerized interface; optical pulses are directed and loosely focused at an angle of 60° from the sample's surface normal to initiate the "temperature jump." The energy of the pump pulse can be varied by using neutral density filters. Such a configuration is referred to as the original excitation scheme. The frequency of the weaker beam is tripled via third harmonic generation with the use of a commercial tripler

(TP-1A, U-Oplaz Technologies). This ultraviolet beam at 266 nm (4.65 eV) is used to generate ultrashort electron pulses through the photoelectric effect (see below). In regard to experiments with 266-nm excitation, the beam splitter is placed after the whole 800-nm beam from the amplifier passes through the tripler, in order to separate a stronger arm for initiation and a weaker one for electron generation; the rest of the beam paths remain the same as the original excitation scheme at 800 nm.

Electron pulses are generated by the 266-nm beam back-illuminating the photocathode (Fig. 4), which is made of a thin silver film (~45 nm in thickness) deposited by the vapor deposition method on a sapphire window that is enclosed by a close-fitting groove at the end of the stainless steel cathode set; see Figs. 3-4 and 3-5 in Ref. 4 for illustration of the electron gun assembly. Before deposition of the silver film, the edge of the sapphire window is first glued to the groove rim with the use of conductive silver paint for the window's immobility and good electric contact. The cathode set is connected to a high voltage supply (FC60N2, Glassman High Voltage) through a vacuum feedthrough, and the anode is grounded to the whole chamber system.

In our experiments, the typical pulse energy of the 266-nm beam for the electron generation is on the order of sub-microjoule or below. It is focused on the photocathode, and the number of photoemitted electrons in a pulse is in the range of several hundred to few thousand (adjusted by varying the intensity of the ultraviolet beam with the use of neutral density filters). The purpose of limiting the electron number is to maintain a temporal width of several hundred femtoseconds to few picoseconds that is suitable for the detection of ultrafast structural dynamics (*6*). The photoemitted electrons are accelerated by a voltage of 30 kV in 3 mm, resulting in a de Broglie wavelength of ~0.07 Å. The electron pulses are focused by a magnetic lens and directed onto the specimen after passing through a series of apertures and electrostatic deflection plates. The incidence angle of electrons is typically below 5°. Without hitting any object, the direct beam has a diameter (spatial FWHM) of ~200 μm (about 4 to 5 pixels) on the CCD screen, which becomes a time-independent contribution to the width of diffraction. The resulting average (current) flux of electrons is relatively small, on the order of 0.1–5 pA/mm^2 depending on the probing geometry. Therefore, no electron damage, modification, or charging of the specimens is observed for most experiments.

The CCD assembly (Fig. 2.6 in Ref. 2) has a low noise level and contains an image intensifier (V5181U-06, Hamamatsu), which enables single-electron detection. The camera (Princeton Instruments PI-SCX:1300/W, Roper Scientific) records 16-bit digital images through a computerized interface, with an intensity range from 0 to 65535 ($= 2^{16}-1$). The largest image range has 1340 pixels in the horizontal direction and 1300 pixels in the vertical; the measured pixel size is 44.94±0.25 μm in both directions. With a camera length (from the specimen to the phosphor screen) of ~16.8 cm, each pixel represents a scattering angle of 0.268 mrad, or 0.0240 Å^{-1} in the reciprocal space according to the definition of $s = (4\pi/\lambda)\sin(\theta/2)$. Therefore, with the help of curve fitting, the resolution of our apparatus reaches <0.01 mrad, i.e., few percent of a pixel or equivalent quantities; one example may be seen in Fig. 3b of Ch. 5. To block the undiffracted electrons (the direct beam) from reaching the phosphor screen and saturating the image intensity, a grounded, movable copper tube that serves as the beam trap is used during the recording of diffraction patterns.

The Scheme of Pulse Front Tilting

The most important factor that limits the temporal resolution of UEC, particularly

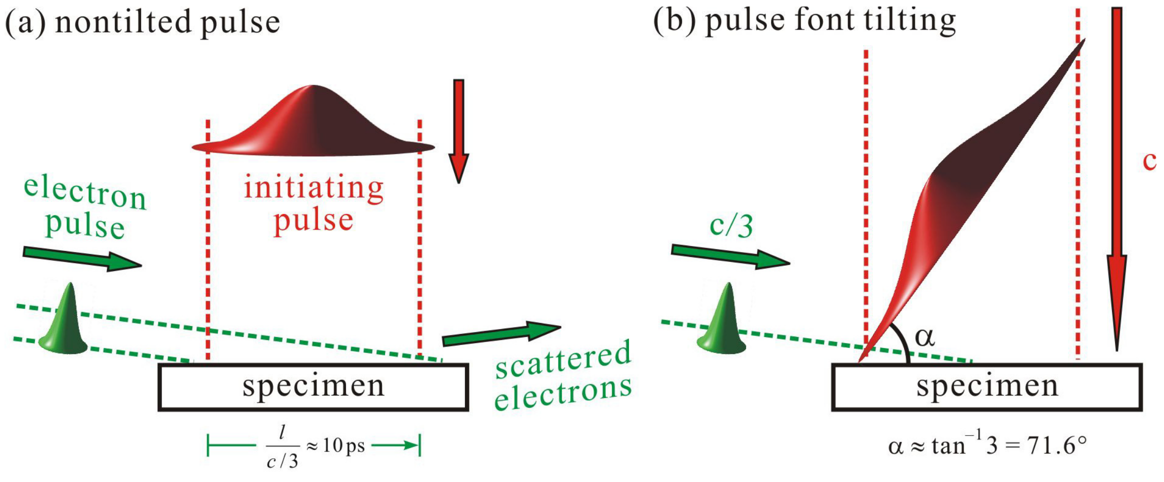

Fig. 5. (a) Mismatch between the arrival times of the nontilted initiating and electron pulses. The resulting temporal resolution is on the order of 10 ps. (b) The scheme of pulse front tilting. The extent of the pulse tilt is solely determined by the ratio of the speed of light to that of electrons.

in reflection experiments, is the mismatch between the optical initiating and electron probe pulses in the interaction region on the specimen. Even if the two pulses have femtosecond temporal widths, given the fact that electrons graze at a small incidence angle and probe the photoexcited region with a longitudinal dimension (*l*) on the order of 1 mm, the mismatch between the arrival times of the optical and electron pulses would be on the order of 10 ps for 30-keV electrons, whose velocity is 1/3 the speed of light (*c*) (Fig. 5a). Improving the temporal resolution in this excitation scheme requires reduction of the interaction region along the electron propagation direction, typically by limiting the useful sample region (see Ch. 4 and Ref. *7*). However, a natural consequence of this method is a substantial decrease of diffraction intensity in a given exposure time; unavoidable prolonged experiments may lead to other undesirable issues such as the long-term instability and sample deterioration.

The scheme of pulse front tilting can be implemented to solve the aforementioned temporal mismatch (*5*). As shown in Fig. 5b, the intensity front of the initiating pulse needs to be tilted by an angle of $\alpha \approx 72°$ to have the synchrony of the two pulses' arrival at every point of the interaction region on the specimen, because the ratio of the traveling speed of light to that of 30-keV electrons is ~3. Experimentally, a grating is used as the diffractive element for 800-nm light to introduce the angular dispersion and, concurrently, the traveling path difference necessary for pulse tilting. In addition, a spherical mirror is placed after the grating to gather the different spectral components originated and then dispersed from the same part of the spatial profile to coincide at the same corresponding point on the specimen; this method is optical imaging and effectively reconstructs the femtosecond optical pulse according to the energy–time uncertainty relation. The resulting reduction in time spread was confirmed to be better than 25 fold (*5*).

In Ch. 6, the application of the pulse tilting scheme proves to be critical to the resolution of ultrafast structural dynamics on the femtosecond time scale. The number of electrons per pulse is reduced to as low as ~500 in that study to minimize the space-charge effect (*6*) and, at the same time, maintain a reasonable duration for the experiments. With such a low flux, the electron pulse width of 322 ± 128 fs has been measured *in situ* at a streaking speed of 140 ± 2 fs/pixel (*8*). Although the overall temporal resolution is determined by convolution of the involved optical and electron pulses with any residual spread from pulse tilting, its improvement to ~400 fs is far better than the 20-ps spread estimated from the sample dimension of ~2 mm probed in the electron propagation direction. The pulse tilting scheme is also applied to the studies reported in Chs. 5, 7 and 8 and in Ref. *9*. Particularly for the latter two cases, the much improved temporal resolution is critical to the new discoveries.

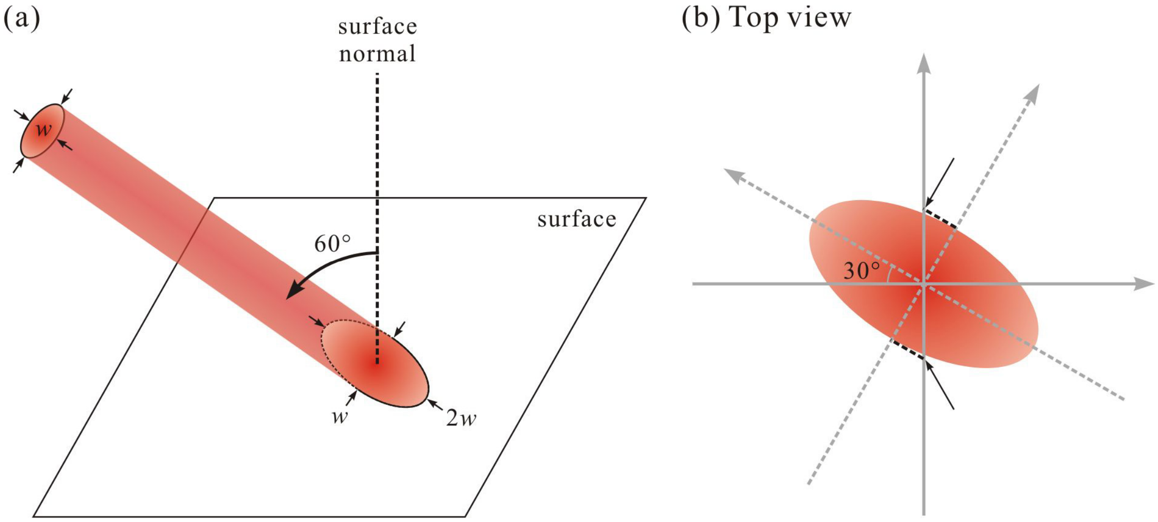

Fig. 6. The original excitation scheme and measurement of the FWHM. (a) The loosely focused optical beam impinges on the specimen at a specific incidence angle. (b) The width measurement determines the distance between the points indicates by the black arrows, which is *w*/cos30° from the trigonometric relationship.

Experimental Consideration in UEC

A. Concerning Initiating Pulses and Optical Excitation

The first important thing to consider about the initiating pulse is the photon energy. Because ultrafast change of a specimen is initiated by photoexcitation in UEC, dynamics studies can only be made for materials that absorb the initiating pulses, whether the absorption is achieved through a one-photon process or through a multi-photon one. Thus, metallic materials and semiconductors with a band gap smaller than 4.65 eV may be investigated using the current laser system; the following chapters give examples for different types of substance. For insulating materials, although energetically possible, simultaneous absorption of two 266-nm photons for photoexcitation would be difficult to achieve due to the weak ultraviolet beam. Two other issues that may also restrict the UEC study of an insulator are the accompanying photoemission (which can affect the electron beam path and probing) and surface charging (as a result of poor electric conduction).

The next important thing is the laser fluence on the specimen. Assuming that the beam profile is of a Gaussian form and its projection on the surface is circular, the peak fluence at the center is $F(r=0) = E_0 \cdot 4 \ln 2/(\pi w^2)$, where E_0 is the integrated pulse energy and w is the spatial FWHM. To define the average fluence (F_{avg}) for such a beam, we consider the illuminated area to be 2 times the FWHM range, which gives $F_{\mathrm{avg}} = 2E_0/(\pi w^2)$ to be smaller than the peak value, $F(r=0)$, but larger than half of it. This estimation is reasonable because the electron probed region (a stripe of 200 μm by few millimeters extending in the electron propagation direction) is intended to be narrower than and coincide with the intense part of the laser footprint in the horizontal direction. Therefore, the task of the estimation of fluence becomes measurement of the FWHM of the laser footprint.

The original excitation scheme produces an elliptical illuminated region on the specimen, as shown in Fig. 6. In the width measurement, the rod part of a needle was used as a blade to block the passing of the laser beam toward a photodiode, by which the intensity was recorded. According to the top view illustrated in Fig. 6b, the edge of the rod moved in the vertical direction, first intercepting with the beam from the bottom (indicated by the lower black arrow) and then totally blocking it (indicated by the upper black arrow); the rod diameter was larger than the FWHM of the beam. Thus, the recorded intensity curve was in the form of an error function, whose derivative was Gaussian with a FWHM equal to $w/\cos 30°$ (Fig. 6b). A typical value for w is 0.726 mm, and hence the corresponding temporal resolution is about 7 ps.

In the scheme of pulse front tilting, the initiating pulses impinge perpendicularly on the specimen, and the horizontal and vertical widths of the stretched elliptical footprint were measured with the help of an auxiliary camera. During the measurement, the laser intensity was attenuated such that the peak fluence on the surface appeared to be just saturated in the screenshot captured by the auxiliary camera. The horizontal and vertical intensity profiles of the footprint were fitted to determine the (scaled) widths. Real FWHM values were obtained by multiplying the widths on the screen with the conversion factor (i.e., the ratio of a length in reality to its appearance in the screenshot), through the help of an object whose size was known. The common FWHM region used is 0.24 mm by 3 mm, which is large enough to make the electron probed region match with the higher fluence part after appropriate alignment (see below).

B. Concerning Electron Pulses and Probing

The important properties of an electron pulse include the number of electrons, its temporal width, and the energy and angular spread. The energy uncertainty is on the order of 10 V, given the output steadiness of the high voltage supply (<0.02% of rated voltage, 60 keV) and the excess energy above the work function of silver (tenths of a volt at most). A crude estimation of the electrons' angular spread in a pulse is given by the ratio of the initial size of photoemitted electrons (restricted by a pinhole of 150 μm) to the distance to reach the magnetic lens (~5 cm), or by the ratio of the pulse diameter on the CCD screen (~200 μm) to the traveling distance of electrons from the magnetic lens (67 cm), which is on the order of 0.1 to 1 mrad. Moreover, the spatial width of the electron beam also contains a small contribution from the little random jitter in the electron propagation direction around the average one. These factors consequently affect the coherence length seen by the electrons (Ch. 2).

Below the saturation level, the total intensity (above the noise level) recorded by the CCD camera is linearly dependent on the number of electrons that reach the phosphor screen, at a given voltage for the image intensifier. Hence, the average electron number per pulse can be obtained by recording many single-pulse images, fitting the profiles to extract their total intensities, widths and positions, and dividing the intensity values by a conversion factor. This factor was previously obtained by counting the total intensity of each single-electron or few-electron event recorded in (at least) hundreds of images without magnetic lens focusing, and fitting the histogram of intensity to the Poisson distribution. The electron-generating 266-nm beam needed to be strongly attenuated such that only several electrons were generated in a pulse, with clear angular separation to make the counting process easier.

The relationship between the electron density in a pulse and its temporal width has been established by performing the streaking experiment (*1, 8*). Typically, for an increment of a thousand electrons per pulse, the width is increased by ≥1 ps. Thus, the major limitation of UEC's temporal resolution is the mismatch between the electron and optical pulses, and its solution by using the scheme of pulse front tilting was described earlier. During the experiments, diffraction patterns without laser excitation are recorded for the characterization of the specimens, and their differences are examined to see if the effect of electron charging, damage or modification exists as a result of constant electron bombardment. Our experiences show that the pulsed electron probing and existence of the bulk part of metallic or semiconducting samples (attached to the holder by conductive copper tape) greatly reduce the chance to encounter these undesirable issues. In contract, the surface morphology that contains sharp tips can be problematic because they may act as photoemitting sources or charge accumulation points, especially with laser excitation.

C. Aligning the Footprints of the Optical and Electron Beams

The major difficulty for the alignment of the interaction region is that the electron

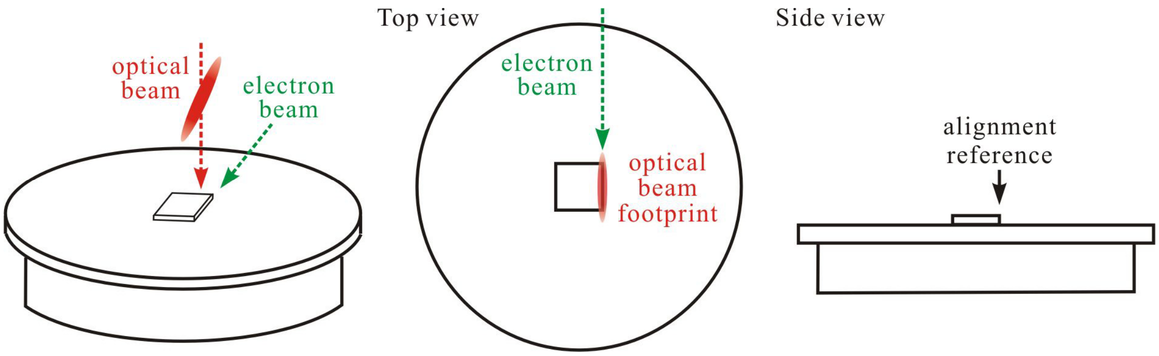

Fig. 7. Schematic for preliminary alignment of the optical and electron pulses. The edge of a substrate (e.g., sapphire) serves as the guideline.

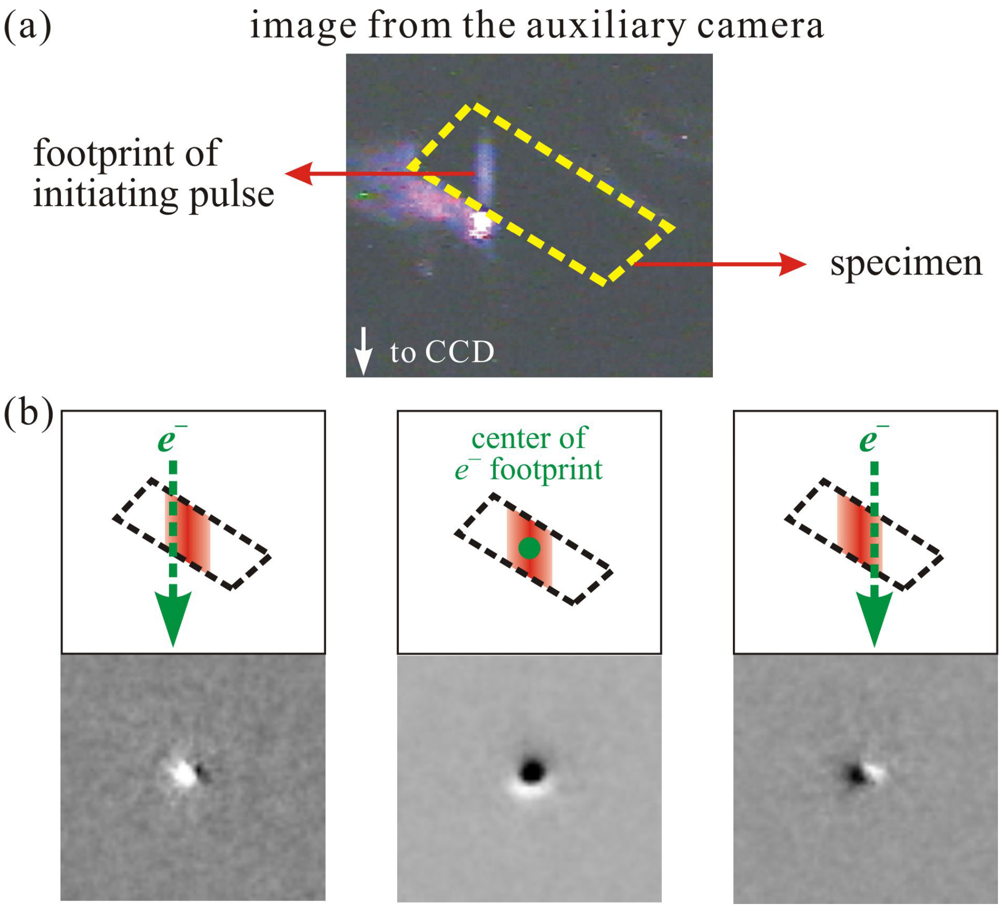

Fig. 8. Fine adjustment for the overlap of the laser and electron footprints. (a) An image taken by the auxiliary camera shows the specimen and the laser footprint. (b) Slight differences in the footprint overlap (upper panels) lead to different results in the diffraction difference images (lower panels).

beam footprint on the specimen is not visible. A method that utilized the tip of a stainless steel needle to intercept with the electron beam path was developed for the original excitation scheme (*2*). However, the alignment can be achieved by another method, with the use of a substrate that has straight and clear edges (e.g., 0.5-mm thick sapphire) and an auxiliary camera to monitor the substrate and the laser footprint (Fig. 7). For preliminary alignment, the substrate is rotated azimuthally such that one of its edges is approximately parallel to the electron path; the height of the goniometer is adjusted so that the electron beam can be blocked by the substrate but not by the sample holder. By moving the goniometer horizontally and monitoring the electron pulses in the CCD images, the edge can serve as a visual guideline for the electron beam path. The laser footprint is directed to match with the edge in the screenshot of the auxiliary camera when the electron beam is half-blocked.

For accurate alignment, the horizontal deflection voltage for electrons is to be adjusted. In the original excitation scheme, a small change of a few volts may be necessary for the observation of largest diffraction difference (referenced to the negative time frame) at positive delay times, which signifies a well-defined interaction region. In the case of the pulse tilting scheme, due to the comparable widths of the laser and electron footprints used, an imperfect alignment on the specimen in the horizontal direction may lead to horizontal asymmetry in the diffraction difference. An example is provided in Fig. 8, which shows the diffraction difference images obtained from a gallium arsenide sample with different overlaps of the footprints. This phenomenon can be related to both the small change in the Bragg condition and electron refraction because of the expanded lattice at positive times and the corresponding tilt of the surface normal for the wing parts of the optical excitation (Fig. 8b, left and right). With regard to the vertical alignment, the height of the specimen is slightly adjusted to obtain the largest diffraction difference. If the sample has a dimension of ~1 to 3 mm, such an adjustment is expected to be achieved easily.

References:

1. C.-Y. Ruan, F. Vigliotti, V. A. Lobastov, S. Chen, A. H. Zewail, *Proc. Natl. Acad. Sci. USA* **101**, 1123 (2004).
2. S. Chen, Ph.D. thesis, California Institute of Technology (2007).
3. J. C. Williamson, Ph.D. thesis, California Institute of Technology (1998).
4. R. Srinivasan, Ph.D. thesis, California Institute of Technology (2005).
5. P. Baum, A. H. Zewail, *Proc. Natl. Acad. Sci. USA* **103**, 16105 (2006).
6. A. Gahlmann, S. T. Park, A. H. Zewail, *Phys. Chem. Chem. Phys.* **10**, 2894 (2008).
7. F. Vigliotti, S. Chen, C.-Y. Ruan, V. A. Lobastov, A. H. Zewail, *Angew. Chem. Int. Ed.* **43**, 2705 (2004).
8. V. A. Lobastov *et al.*, in *Ultrafast optics IV,* F. Krausz, G. Korn, P. Corkum, I. A. Walmsley, Eds., vol. 95 of *Springer series in optical sciences* (Springer, New York, 2004), pp. 419-435.
9. F. Carbone, P. Baum, P. Rudolf, A. H. Zewail, *Phys. Rev. Lett.* **100**, 035501 (2008).

Part I

Semiconducting Materials and Nanometer-scale Structures

Chapter 4

Nonequilibrium Structural Dynamics: Gallium Arsenide as a Prototype System[†]

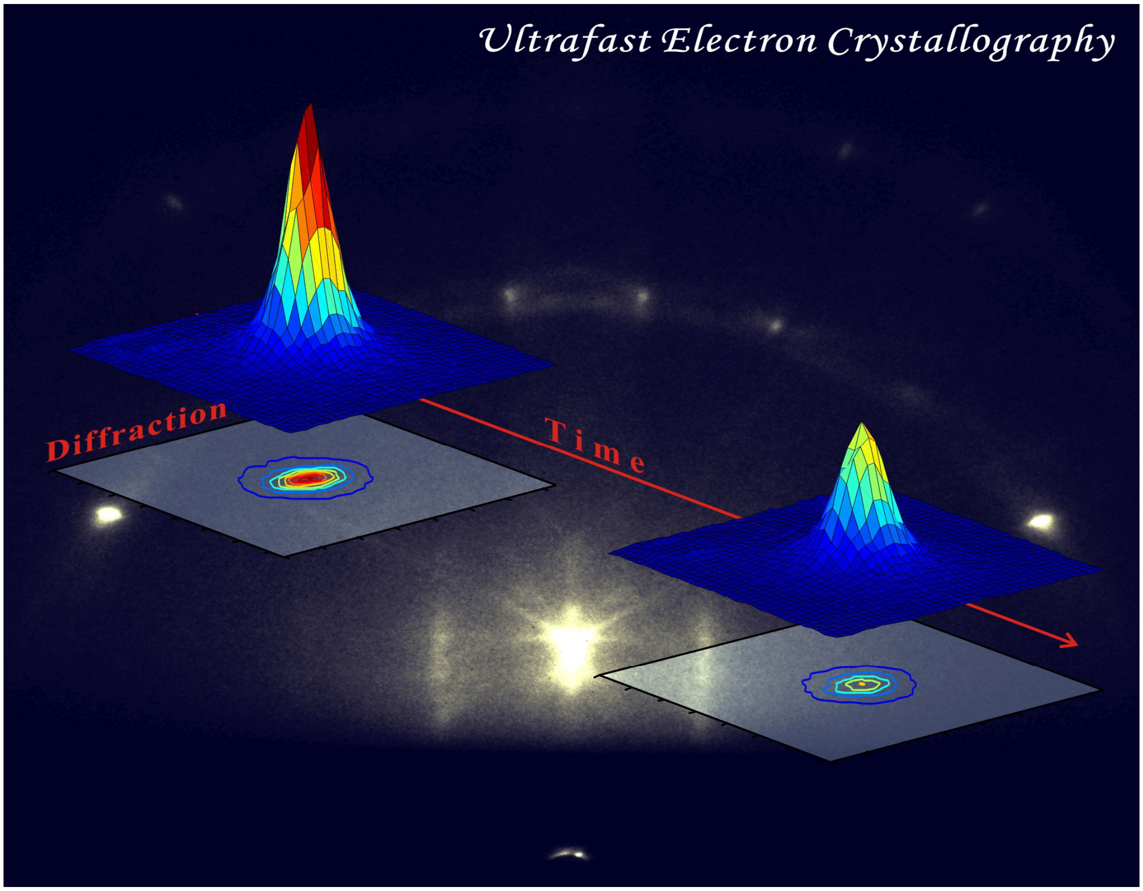

[†] adapted from D.-S. Yang, N. Gedik, A. H. Zewail, *J. Phys. Chem. C* **111**, 4889 (2007).

Introduction

In our laboratory, ultrafast electron diffraction and imaging have been developed to investigate structural dynamics with atomic-scale resolutions (*1, 2*). When it comes to the study of solid-state surfaces and nanometer-scale materials, the advantages of using electrons to probe the transient structures are evident. Because of the much higher electron–matter interaction cross section (small penetration depth) and the high sensitivity to structural changes, electrons are especially suitable for interfacial studies. Ultrafast electron crystallography (UEC) has been the method of choice for studies of such interfacial phenomena in different systems, including surfaces and phase transitions (*3, 4*), interfacial water (*5*) and self-assembled surface monolayers (Ch. 11), and biological model bilayers (*6-8*). For all of these studies, a clear understanding of the dynamics of the underlying crystalline substrate is critical to the characterization of the initial "temperature jump" and subsequent dynamics at interfaces.

Studies of substrates, such as silicon (*3, 6*), gallium arsenide (*4*), and gold (Ch. 11), have shown a universal behavior in that the observed transient, following a femtosecond excitation, displays a downward movement of Bragg diffraction spots (corresponding to increase in lattice interplanar spacings), decrease in total intensity and increase in diffraction width, all of which occur on the ultrashort time scale, from ~10 ps to ~100 ps depending on the system. At longer times, these changes reverse and the diffraction spots ultimately recover the original coordinates, certainly on the time scale between pulses, a millisecond in UEC.

Questions remained as to what causes these universal features and what are the actual nonequilibrium temperatures of the carriers and lattice. In this chapter, I present studies of the direct-gap semiconductor GaAs as a prototype system with a well-defined quantum-well structure of 20 nm thickness and "tuned" band gap energy. Comparisons with the results of the bulk material that has also been studied elucidate mechanisms of structural dynamics. Besides the obvious technological relevance, these semiconductor structures can be made to have atomically flat surfaces, their surface dangling bonds are unique in orienting adsorbates, and extensive studies of their optical responses using ultrafast spectroscopy have been made (*9, 10*). Both direct-gap (GaAs) and indirect-gap (Si) semiconductors are considered in our discussion of the dynamics, but the focus here is on the former. The discussion is extended to include the most significant properties that in general determine the structural dynamics of crystalline semiconductors.

This chapter combines the aforementioned experimental studies to provide a full account of the methodology and its potential in different applications. Sample preparation and the two UEC detection modes, reflection and transmission, are described. Results and analysis are presented for studies made at different excitation wavelengths and detection modes. The Discussion Section covers the key processes involved with carrier excitation, and the lattice motions that cause changes in diffraction features on the short and long time scales. Lastly, a physical picture of structural dynamics is provided to conclude the current investigation.

Materials and Experimental Section

For the transmission experiments, thin GaAs films of 20 nm thickness supported on empty gold grids (Ted Pella, Inc., 300 mesh), or on the grids that have carbon-based support films (Ted Pella, Inc., #01810G-F), were prepared following the procedure reported by Konkar *et al.* (*11*). The lattice-matched heterostructure consisting of a 20-nm GaAs layer above a 50-nm $Al_{0.6}Ga_{0.4}As$ layer was grown on a 450-μm GaAs(001)

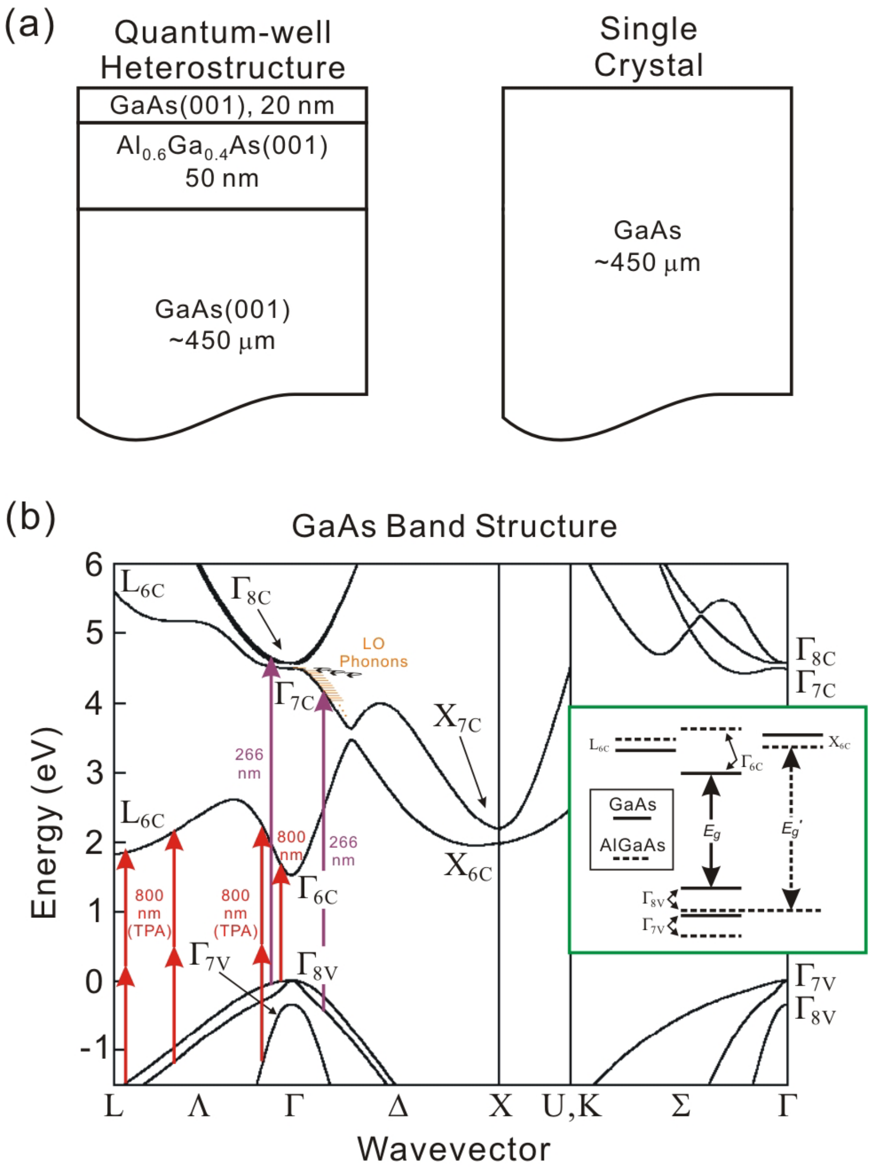

Fig. 1. Crystal and band structure. (a) Comparison of the quantum-well heterostructure studied and the single crystal used in Ref. 4. (b) The electronic band structure of GaAs (*12*) is shown, and the excitations at two different wavelengths (266 and 800 nm) are indicated. Carriers are initially prepared in different regions of the band structure, and their energy relaxation proceeds through optical-phonon emission; the orange short lines indicate different electronic states (Bloch functions) with different crystal wavevectors. The inset shows the band energies at three high-symmetry points (Γ, L and X) for GaAs (solid lines) and $Al_{0.6}Ga_{0.4}As$ (dash lines) (*13*). The direct band gap of GaAs (E_g) and indirect band gap of $Al_{0.6}Ga_{0.4}As$ (E_g') are also indicated.

substrate (Fig. 1a) using the molecular-beam epitaxy (MBE) method (MBE lab at University of California, Santa Barbara). The band structure of GaAs (*12*) and the energetics for the carrier excitation processes are displayed in Fig. 1b; the inset presents a comparison of the band energies at three high-symmetry points for GaAs and $Al_{0.6}Ga_{0.4}As$ (*13*). After the successive mechanical polishing and chemical etching procedures, 20-nm GaAs thin films covered an area of up to ~1 mm^2 on the gold grids. Inside the diffraction chamber, the whole sample area was illuminated by the excitation pump beam, while the electron probe beam was at the central part of the laser-heated region. The $[1\bar{1}0]$ axis of the thin film was oriented vertically (in the laboratory coordinate system) and became the rotational axis. By rotating the GaAs film, we were able to access different crystal planes other than (001). Samples on a grid with or without the carbon-supported film showed the same diffraction patterns.

For the reflection experiments, the heterostructure samples were cleaned by dipping them into a concentrated HCl solution for a few seconds, followed by a fast rinse by deionized water, to remove any native surface oxide. It is known that this cleaning process may increase the amount of elemental arsenic with residual chlorine species on top of the GaAs surface (*14*). From our experiments, no significant effect on structural dynamics from this surface “contamination” was seen. The finite penetration of electrons guaranteed that only the lattice of the GaAs quantum well was probed even if a Bragg spot of relatively higher order (i.e., a relatively large incidence angle) was under investigation to reduce any surface or refraction effect.

The original excitation scheme was used for the current study. The initiating pulses were directed and loosely focused (area of illumination ~ 1.66 mm^2) at an incidence angle of ~60° from the substrate surface normal, to initiate the “temperature

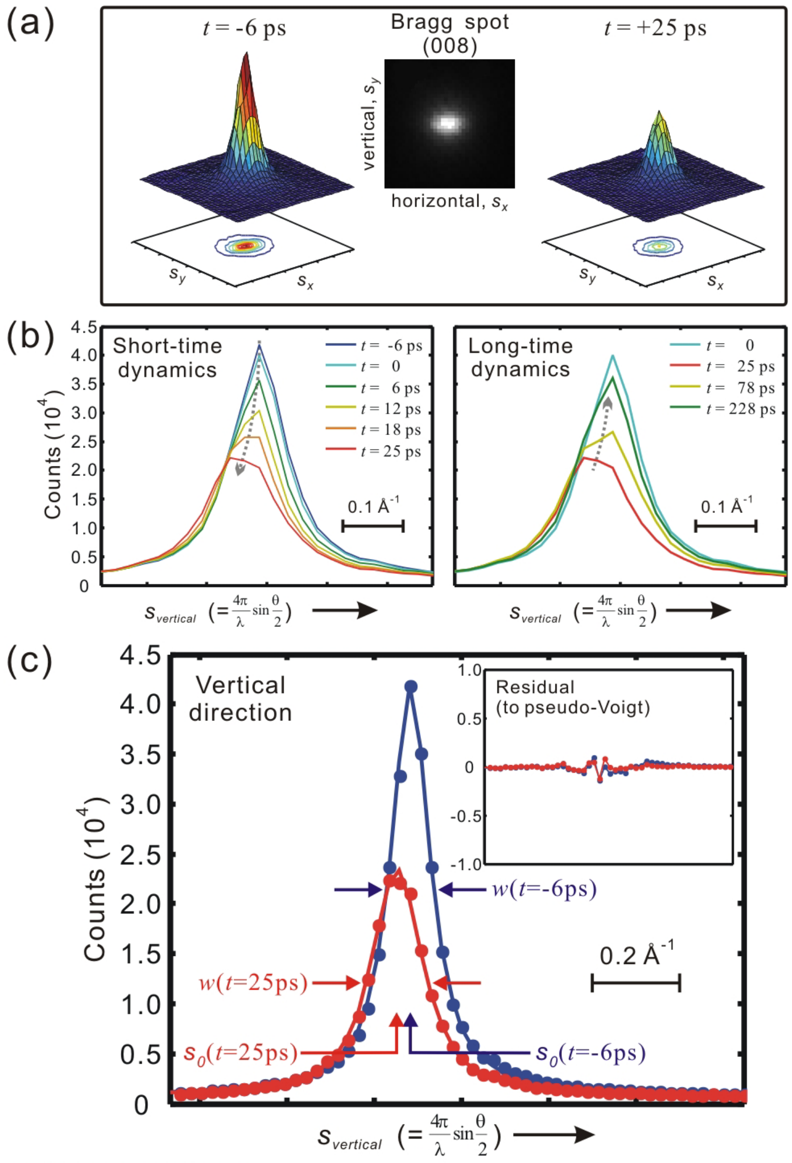

Fig. 2. Bragg spot (008) temporal change. (a) 3D profile and its contour plot of the diffraction at two times, –6 and +25 ps. (b) Left: Short-time dynamics. The initial change is a decrease of the Bragg intensity with little spot movement (0–12 ps), followed by a clear peak shift with more intensity depletion (12–25 ps). Right: Long-time restructuring dynamics. After the minimum spot intensity and maximum position shift are reached, the diffraction profile undergoes a recovery toward the equilibrium state. (c) Fitting of the vertical diffraction profile at $t = -6$ and 25 ps, with the peak position (s_0) and the fwhm (w) indicated for each case. The results of fitting (lines) match very well with the acquired data (dots), and the residuals are shown in the inset. The apparent width gives the minimum coherence length as the total width has a contribution from the instrument function.

jump." In order to minimize the temporal mismatch between the optical and electron pulses and eliminate the interference of diffraction from the unexcited area, a rectangular specimen was oriented so that only a small corner region would be probed. In this way, changes after 1-ps delay could be observed while the number of electrons per pulse was ~2000. The electron beam traveled along the [010] direction (with a grazing incidence angle), and the polarization of the heating pulses was along the $[1\sqrt{3}0]$ direction. From the angular separations between spots on side streaks and the lattice constant of GaAs ($a = 5.653$ Å), a camera length of 16.90±0.03 mm from the scattering position was deduced. The angular difference and scattering-vector change between high-order Bragg spots ($0\ 0\ 4n$) on the central streak also confirmed the correctness of the calculated camera length and the (001) crystal-surface orientation (see Ch. 2). In the reflection experiments, we focused on the dynamics of the (008) Bragg spot (Fig. 2a).

Results and Analysis

The diffraction patterns recorded for the equilibrium structure at room temperature serve as the negative-time frame reference because they represent the system in its thermodynamic equilibrium. At a given delay time, we then obtain the change in diffraction, and with the frame-reference method, the sensitivity is as low as 1% for UED (*2*) and 0.02% for UEC (because of the collective change). In the reflection experiments, the difference images almost always show, around the diffraction spots or rings, an intensity reduction at the original locations and enhancement in the neighboring regions closer to the direct beam position at positive times, which means that the Bragg reflections are shifted toward the smaller s values (Fig. 2b, left panel). This is the signature of lattice expansion following the optical excitation, a direct conclusion from the Laue condition discussed in Ch. 2. If the fluence of the initiating pulses is increased, stronger reduction of the intensities may be seen prior to the emergence of enhancement in the neighboring regions (Fig. 2b, left panel), indicating that certain lattice motions, which cause the Bragg intensities to decrease, occur prior to any appreciable lattice expansion. In this geometry, the observed result was always the change of the diffraction images along $\hat{n}$ without a clear horizontal movement of the Bragg spots (within our experimental temporal range), which is a signature of an anisotropic change in the crystalline structure at short times. Different materials show the maximum reduction of intensities and movement of positions at different delay times, and recovery of those changes (Fig. 2b, right panel) is universal even though their rates may differ.

It should be noted that the observed downward shift of Bragg diffraction reflects the genuine lattice expansion following the optical excitation, and does not result from a downward shift of the direct electron beam trajectory at positive times. To confirm this conclusion, we have simultaneously recorded, by removing the electron beam trap, diffraction patterns together with the direct electron beam projection on the camera. It was observed that, whereas the Bragg spots of the lattice were clearly shifting downward, at early times, the direct beam position made very little of a change and even moved slightly upward. Such an observation, together with the parallel Bragg intensity change at short times, excludes the possibility of an artifact caused by electron-beam shifting due to electronic excitation of the substrate surface.

In the transmission study of a crystalline thin film, by subtracting the negative-time reference frame from the diffraction images, reduction of spot intensities at the spots' original locations can be seen at a positive time after the heating pulse excites the sample, but the recovery is very slow within our temporal window. Another

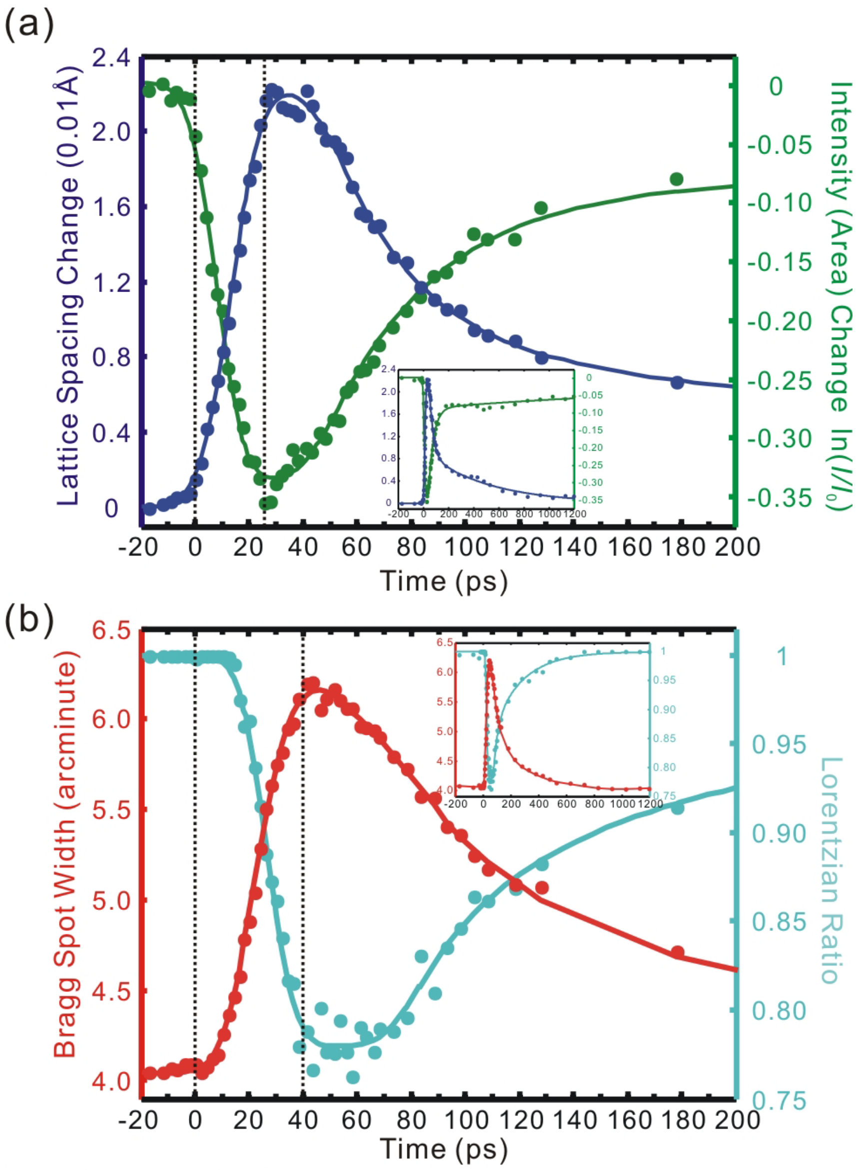

Fig. 3. UEC experimental observations made at 266-nm excitation, fluence 2.2 mJ/cm^2. (a) Early-time behavior of changes in the (008) spot intensity, ln[$I(t)/I_0$] (green dots), and lattice spacing, $\Delta d_{001}(t)$ (blue dots); the solids lines (and also those in the following figures) are made to guide the eyes unless specified. The maximum changes can be observed at $t = 25$ ps as indicated by the dash line. The long-time behavior of temporal changes is shown in the inset. Note the residual changes at $t = 1.2$ ns. (b) Early-time behavior of changes in the (008) spot width, $w(t)$ (red dots), and Lorentzian component, $\eta(t)$ (cyan dots). The maximum changes are seen at a later time, $t = 40$ ps. The long-time behavior is shown in the inset; the two curves return to their negative-time equilibrium values before $t = 800$ ps.

interesting observation is that, unlike the reflection counterpart, the spot positions do not exhibit a substantial movement during the entire temporal range, which leads us to the conclusion that in-plane lattice expansion is negligible. The lack of horizontal shifts for Bragg spots in the reflection detection and in-plane spot movements in the transmission detection points to a consistent physical picture of the vertical (relative to the surface normal) structural changes at short times as being the major contribution to dynamics; see Ch. 2 for the theoretical discussion.

Quantitative analysis of the observed diffraction transient changes was made for the present study of the GaAs(001) heterostructure and thin film, by using the fitting procedure described in Sec. B.5 of Ch. 2. In what follows, I represents the (1D) integrated intensity, s the scattering vector, s_0 the peak position of the Bragg spot, w the full width at half maximum (fwhm), and η the Lorentzian contribution. Because the surface quality was good enough to reduce inelastic and other scattering events, only flat and very low background intensity was seen and no background subtraction prior to fitting was needed; see Fig. 2c for two examples of the fitting results. Comparisons between the extracted diffraction features—$I(t)$, $s(t)$, $w(t)$, and $\eta(t)$, where t is the delay time between the electron and optical pulses—and between the results at different excitation fluences and wavelengths, and in different detection modes, were made to elucidate the structural dynamics and relaxation pathway in GaAs.

A. Reflection Experiments

Figure 3 shows the temporal change of the integrated intensity $I(t)$, lattice constant change $\Delta d_{001}(t)$ along $\hat{n}$ [derived from $s(t)$ using $\Delta d_{001}(t) / a = -\Delta s(t) / s_0(t<0)$], vertical spot fwhm $w(t)$ and the ratio of the Lorentzian component $\eta(t)$ extracted from the vertical fitting of the (008) Bragg spot; all recorded in the reflection experiment with an

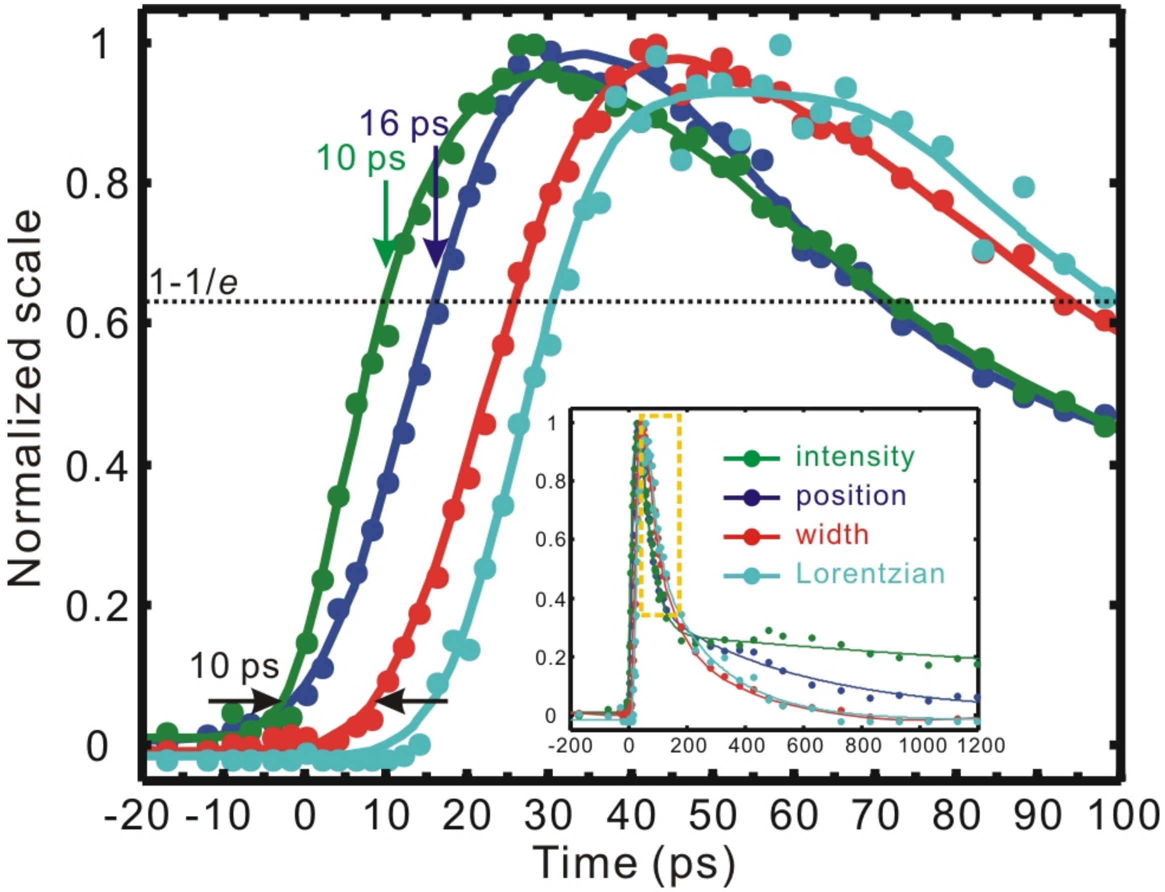

Fig. 4. Ultrafast prompt and delayed diffraction features. Comparison of the early-time behavior of $I(t)$, $\Delta d_{001}(t)$, $w(t)$, and $\eta(t)$ of the (008) Bragg spot is shown on a normalized scale. Clearly, the changes of the width and Lorentzian component are delayed from those of the intensity and lattice spacing by 10 ps (or more). If an exponential rise function is considered, the $1 - 1/e$ value (dash line) in the temporal curves gives the rise times of intensity and lattice spacing change to be 10 and 16 ps, respectively. The inset shows the long-time behavior; $w(t)$ and $\eta(t)$ are similar over the whole temporal range, while a larger residual change is observed in $I(t)$ than in $\Delta d_{001}(t)$ at $t = 1.2$ ns. Within the yellow dashed box, the four profiles are seen to closely resemble each other.

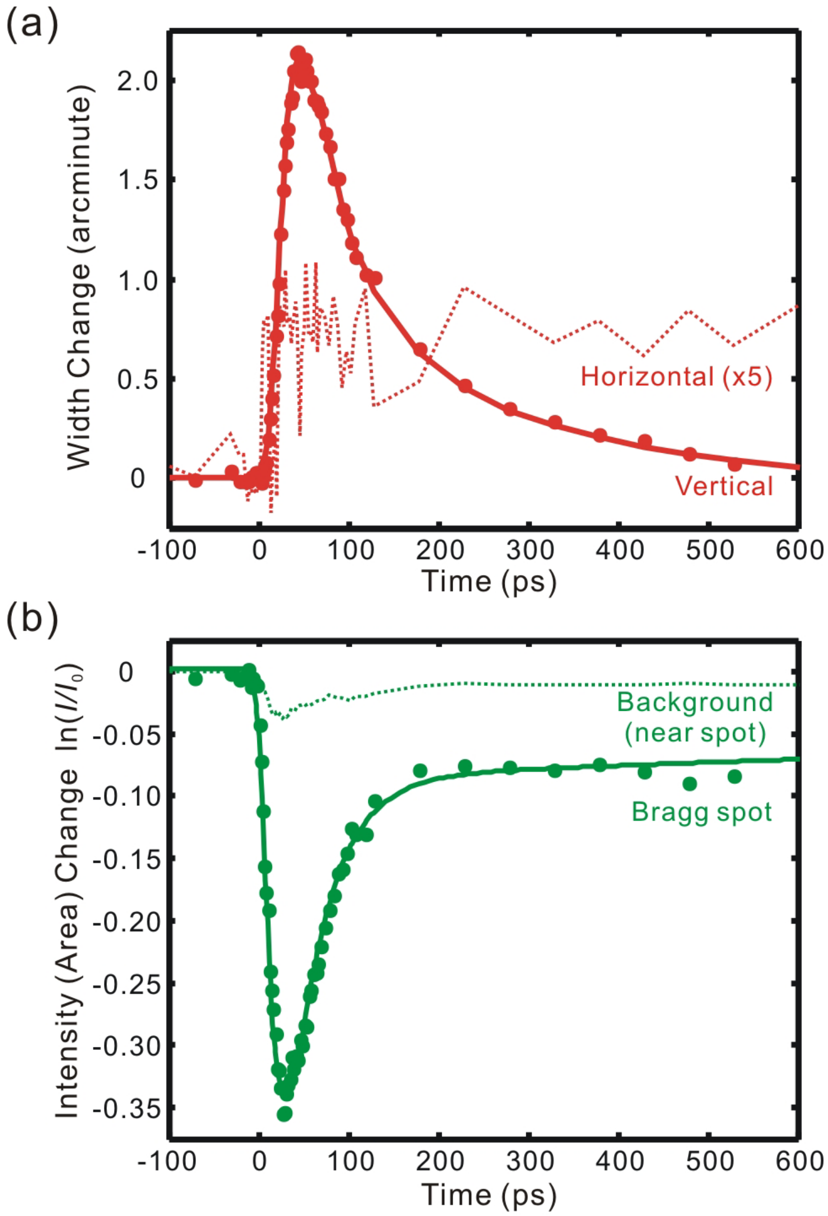

Fig. 5. Diffraction width anisotropy and background scattering. (a) Vertical and horizontal width changes of the (008) Bragg spot as a function of time. Compared to the smooth temporal behavior (rise and decay) of large vertical width change, the horizontal width changes insignificantly and remains for hundreds of picoseconds. (b) Intensity change of the Bragg spot and that of the background in the spot's vicinity. The large amplitude difference shows that the intensity reduction is not due to an overall intensity change of the diffraction pattern.

excitation fluence of 2.2 mJ/cm^2 at 266 nm. At first glance, the four curves seem to exhibit a similar temporal behavior: no change at negative time, rapid change within the first ten(s) of picoseconds immediately after the initiation at the zero of time (t_0), fast recovery on a time scale of tens of picoseconds after the peak change is reached, and finally slower recovery toward the equilibrium structure on a sub-nanosecond to nanosecond (and longer) time scale. However, careful examination brings about several important observations in the temporal behavior of the different diffraction features.

First, the rise part of $\Delta d_{001}(t)$ and $I(t)$ develops and reaches the extremum at $t = 25$ ps with a time constant $\tau \sim 10$ ps (Fig. 3a). This implies that the time scale for the vertical lattice expansion and structural change is ultrafast. Second, the increase in the changes of $w(t)$ and $\eta(t)$ is clearly delayed by ~10 ps behind those of $I(t)$ and $\Delta d_{001}(t)$ (Fig. 4), indicating that dynamical inhomogeneity occurs with a delay or "threshold" in time; the same phenomenon was also confirmed in the dynamics of the (0 0 12) Bragg spot. Third, the change of $I(t)$ grows faster than that of $\Delta d_{001}(t)$, within the first 25 ps, as shown in Fig. 4; the time for $I(t)$ to reach $1 - 1/e$ of its maximum change is apparently smaller than that for $\Delta d_{001}(t)$. Fourth, the horizontal width change as a function of time shows only a positive plateau reached at early time without any noticeable recovery on our time scale, and the amplitude is less than 1/10 of the maximum vertical width increase (Fig. 5a). This difference is a manifestation of the anisotropy in the transient structural change, as discussed above. To further confirm that the background scattering has no effect on the dynamics, we checked the temporal behavior of the background intensity in a rectangular area in the vicinity of the (008) Bragg spot. As shown in Fig. 5b such a contribution, if any, is negligible.

For the other excitation at 800 nm (fluence of 10.9 mJ/cm^2), the temporal change

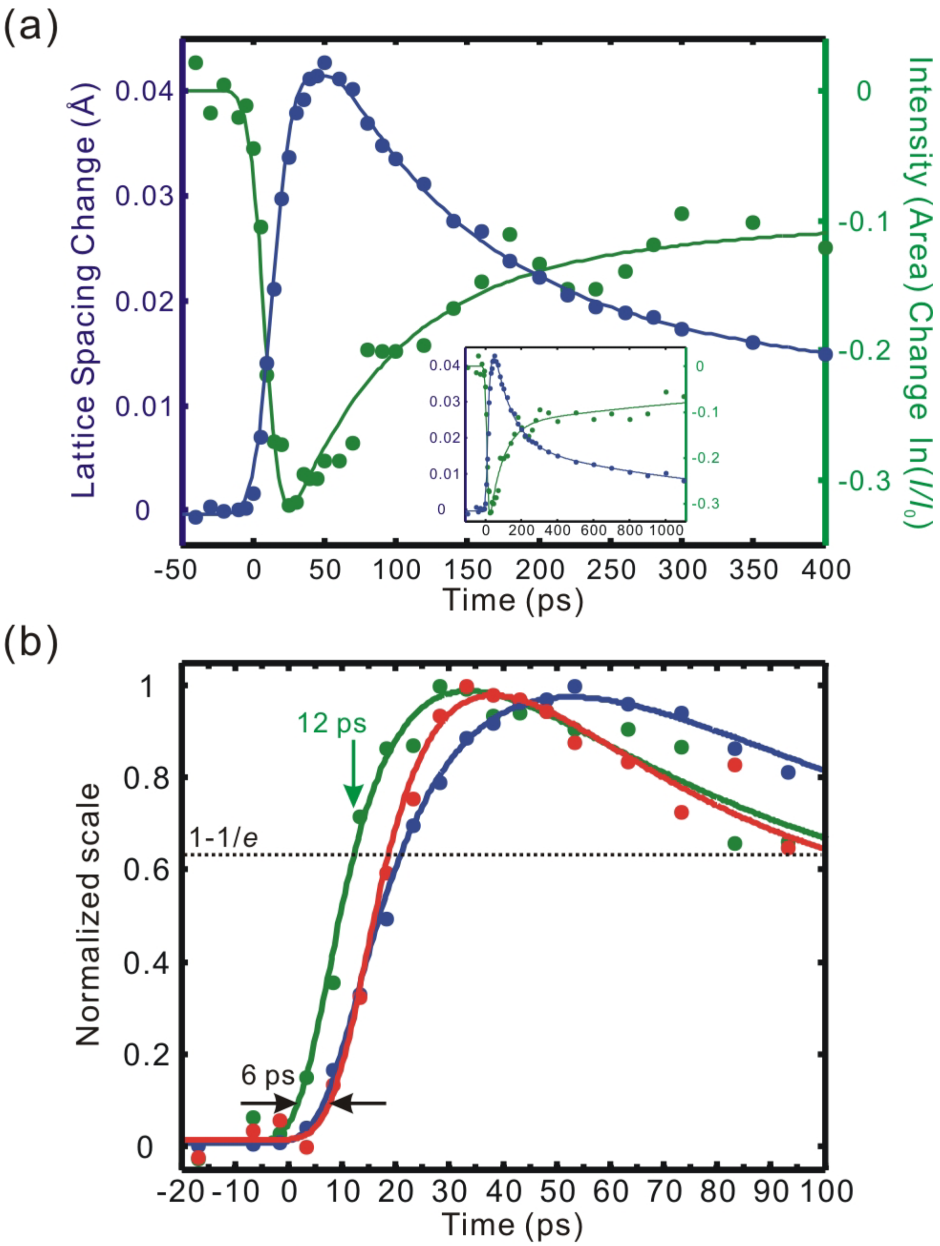

Fig. 6. UEC experimental observations made at 800 nm, fluence 10.9 mJ/cm^2. (a) Early-time behavior of changes of the (008) spot intensity, $\ln[I(t)/I_0]$ (green dots), and lattice spacing, $\Delta d_{001}(t)$ (blue dots). The long-time behavior is shown in the inset. (b) Comparison of the early-time behavior of $I(t)$, $\Delta d_{001}(t)$, and $w(t)$ of the (008) Bragg spot on a normalized scale. Again, $w(t)$ (red dots) is delayed by 6 ps from $I(t)$, but the two curves share a similar rise time of 12 ps. After the maximum changes are reached, the three diffraction features recover with a similar decay rate.

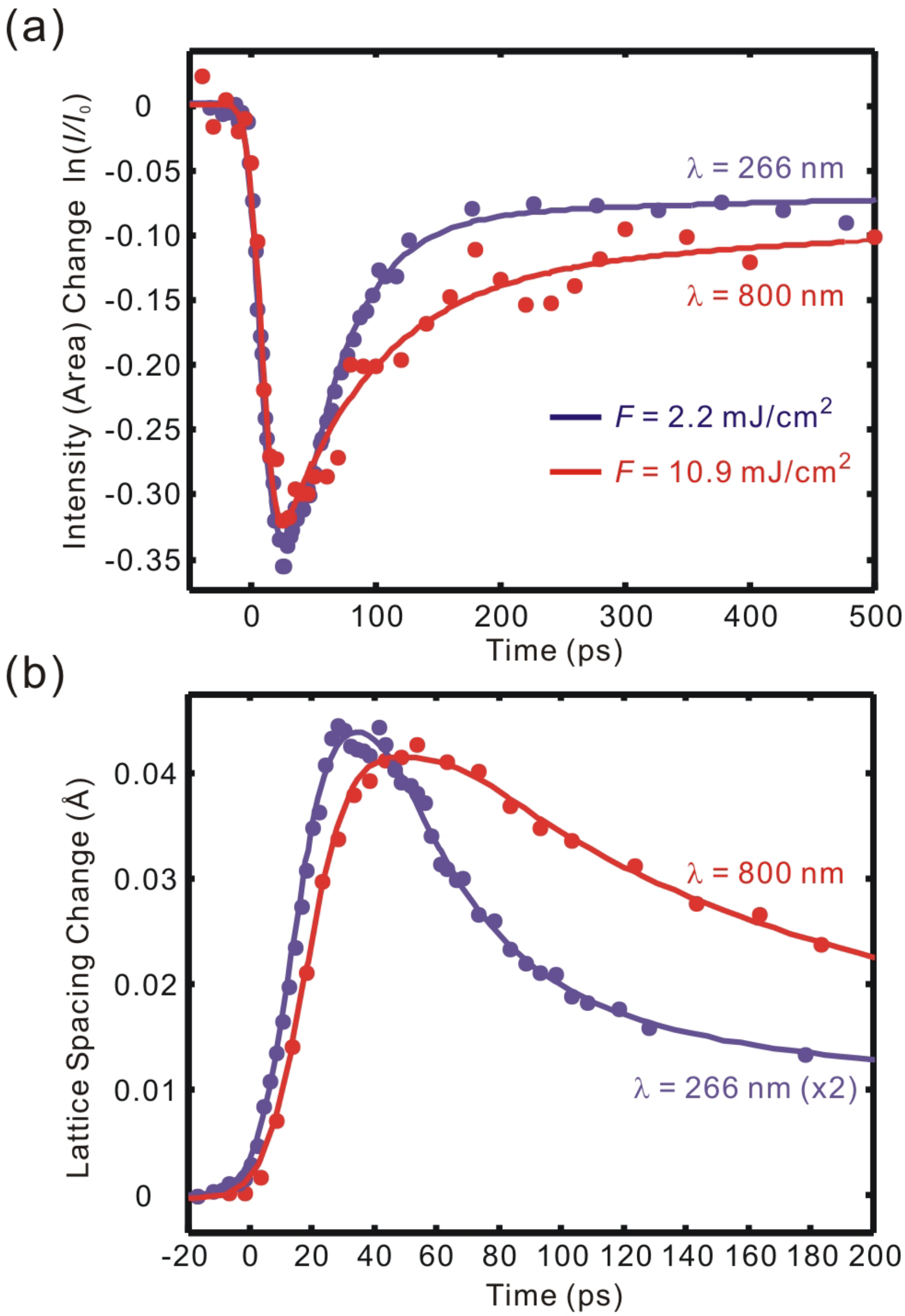

Fig. 7. Effect of fluence and initial excitation. (a) Comparison of (008) spot intensity change; (b) lattice spacing change at the two wavelengths, 266 nm (blue dots) and 800 nm (red dots). Similar profiles for the rise of intensity reduction are observed, with the maximum change occurring at $t = 25$ ps. Lattice expansion at 800 nm is about twice as large as that at 266 nm, although the former one rises more slowly than the latter (see Text for discussions in detail).

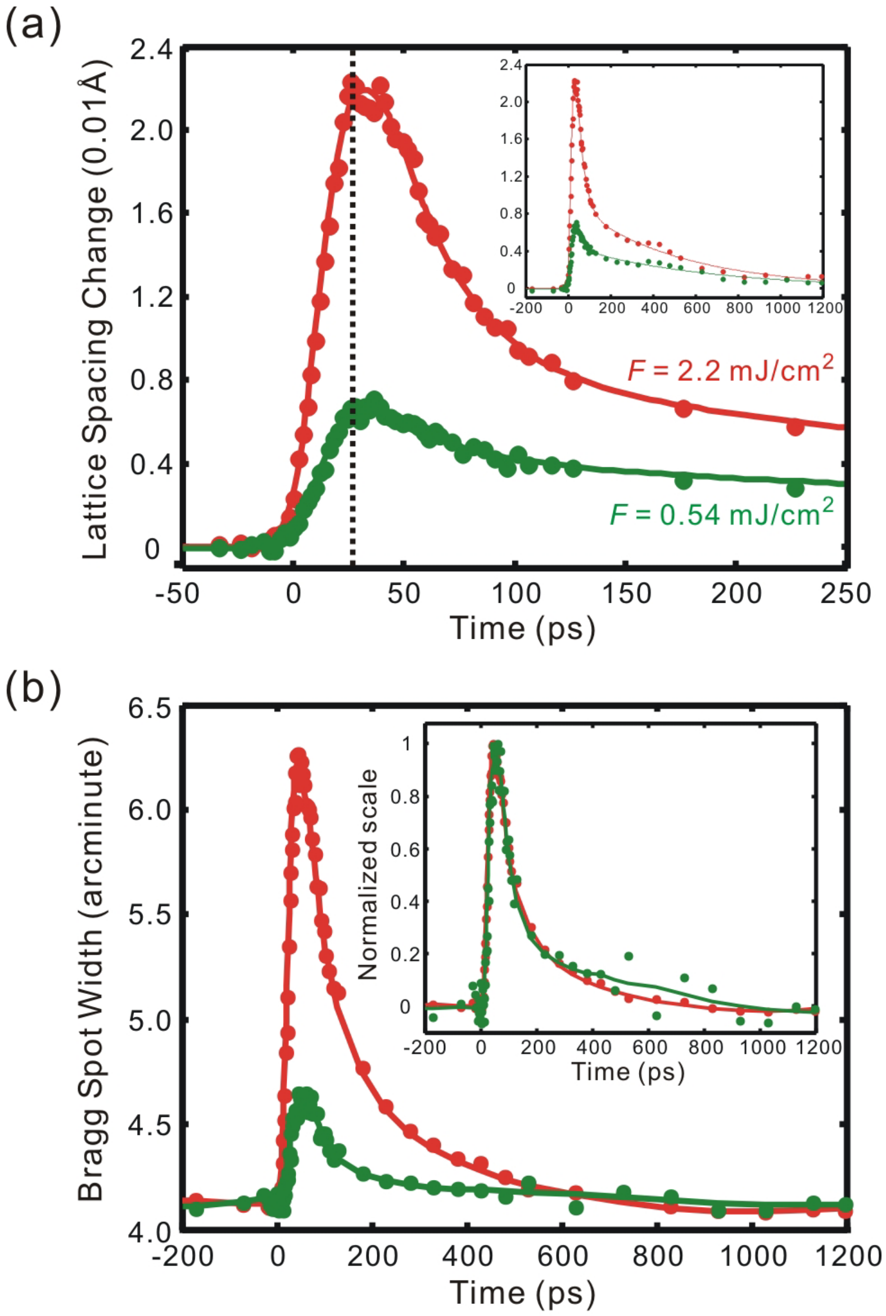

Fig. 8. Fluence dependence at 266 nm. (a) The maximum lattice expansion is observed at $t = 25$ ps regardless of the excitation fluence used, suggesting the same rise time for both cases. The inset shows the long-time behavior and the faster recovery in the high-fluence case. (b) The maximum vertical width change is seen to be linear with the excitation fluence, and the temporal behavior remains essentially unchanged, as shown on a normalized scale in the inset.

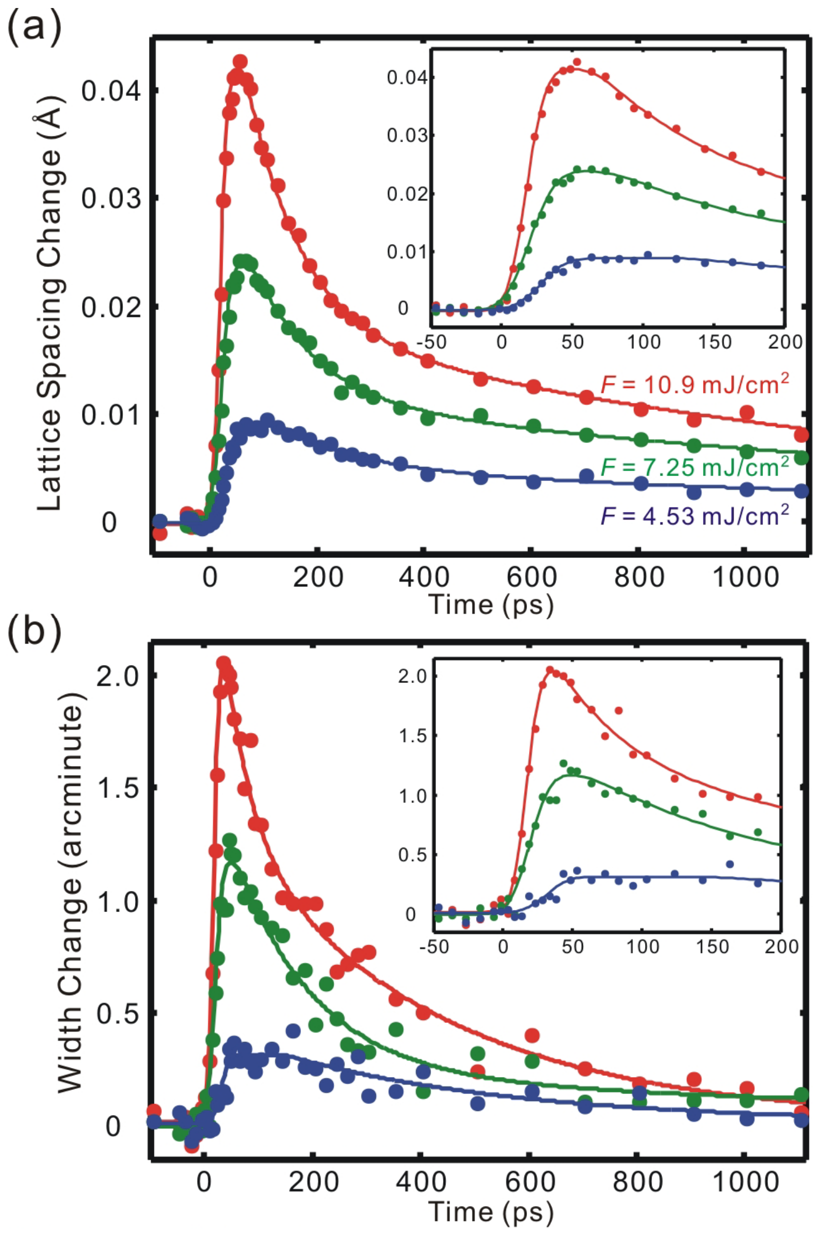

Fig. 9. Fluence dependence at 800 nm. (a) Long-time behavior of the lattice spacing change at three different fluences, with the early time shown in the inset. The maximum expansion is not linear with the fluence due to the two-photon excitation phenomenon. Faster recovery can be observed at high excitation fluences. (b) Similar fluence dependence is seen for the width change: the higher the fluence, the larger the initial fast recovery. In contrast to the results of Fig. 7b, these curves do not resemble each other after normalization.

of the (008) Bragg spot, $I(t)$ and $\Delta d_{001}(t)$, shows similar behavior: a fast rise at early time followed by a seemingly two-component recovery in 1 ns (Fig. 6a). If we plot $I(t)$, $\Delta d_{001}(t)$, and $w(t)$ on a normalized scale, as shown in Fig. 6b, and zoom into the initial changes, it is found that the rise part of $I(t)$ again is not instantaneous but reaches the extremum at $t = 25$ ps; the initial development of the change seems to be very similar at two different excitation wavelengths (Fig. 7a). The increase of the change of $w(t)$ is clearly delayed by ~6 ps behind that of $I(t)$, a phenomenon that is also seen in the previous case of 266-nm excitation. However, the rise part of $\Delta d_{001}(t)$, instead of following closely with that of $I(t)$, is also delayed (Fig. 6b) and has an even slower growth to reach the maximum (Fig. 7b). Such a temporal difference in the behavior of $\Delta d_{001}(t)$ with respect to that of $I(t)$ at two different excitation wavelengths indicates a difference in the dynamics of lattice expansion. It is noticed that the maximum changes of $I(t)$ and $\Delta d_{001}(t)$ are similar or of the same order of magnitude (Fig. 7), suggesting that the lattice receives a similar amount of energy from the photoinjected carriers at early time.

Figures 8 and 9 present the results of the fluence-dependent studies at the two excitation wavelengths. The most noticeable change in the pattern of the dynamics is that, as the excitation fluence at 800 nm is decreased, the prominent peaks of the change of $I(t)$, $\Delta d_{001}(t)$, and $w(t)$ at early times are greatly diminished, and both rise and decay time scales appear to be slower. In contrast, the results from the 266-nm experiments do not show such a pattern change; in fact, after normalization, $w(t)$ is essentially independent of the fluence (Fig. 8b, inset). As will be shown in the Discussion Section, the fluence dependence at 800 nm is the manifestation of a two-photon carrier excitation reaching a different state due to the dispersion of the electronic band structure.

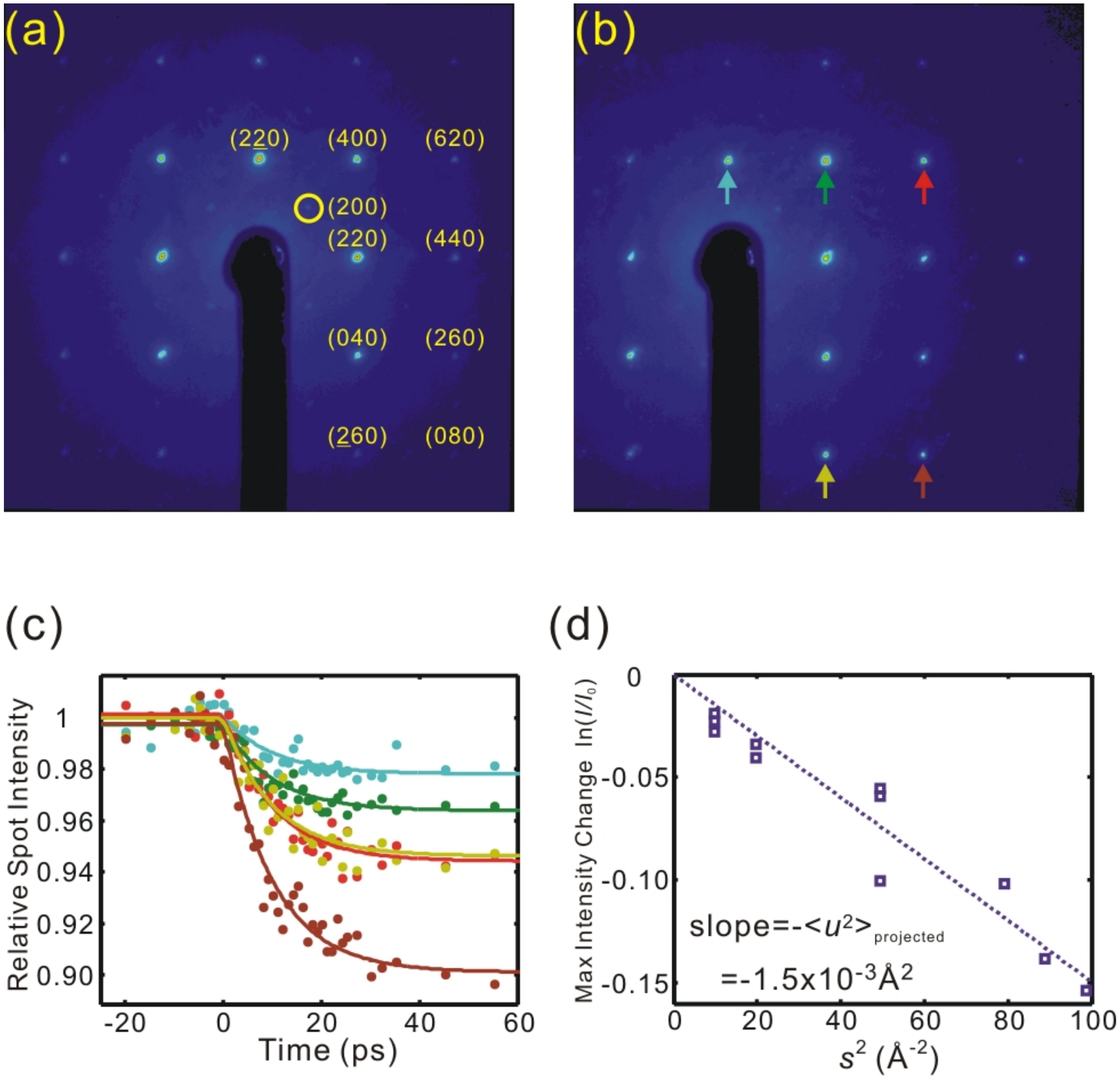

(See next page for the figure caption.)

Fig. 10. (a) Transmission diffraction pattern of GaAs(001). Electrons propagate along the surface normal direction; the black region is the projection of the electron-beam trap on the camera. Miller indices for several Bragg spots are given. (b) Transmission pattern recorded when electrons propagate along a direction 2° away from the normal. The diffraction pattern becomes asymmetric and the Bragg spots on the right-hand side become more intense. Intensities of different spots (some of them are indicated by arrows with different colors) are monitored as a function of time, as shown in (c). Spots with higher Miller indices have larger intensity drops (brown dots), and those spots with the same s [e.g., the two indicated by the red and yellow arrows in (b)] share very similar temporal behavior (red and yellow dots). The intensity reduction curves are fitted by a function of exponential growth, and the same time constant of 10 ps is obtained (solid lines), as in reflection experiments. (d) The maximum intensity changes (on a log scale) is plotted as a function of s^2. A linear relationship is obtained, and the slope is directly related to the vertical atomic motions along $\hat{n}$ (see Text for discussions).

B. Transmission Experiments

A typical diffraction image of the GaAs thin film along the [001] axis is shown in Fig. 10a; the principal axes and Miller indices of some Bragg spots are labeled. By following the intensities of the Bragg spots through the measurement of rocking curves and calculating the corresponding angular spans, we obtained a vertical width of ~0.15 $Å^{-1}$ for the reciprocal rods. With the use of the Scherrer formula (Eq. 23 of Ch. 2), the effective crystalline thickness is estimated to be similar to the known thickness of the GaAs layer, 20 nm.

The GaAs thin film was excited by 266-nm light. No systematic temporal change of the spacing between the spots or in the widths was observed. Figure 10b shows the diffraction image probed along an axis 2^{o} away from the [001] direction, and the intensities of various spots acquired by fitting at different delay times are presented in Fig. 10c. It is found that those Bragg spots with the same amplitude of scattering vectors, for example, (400) and (040) spots, or (620), (260), and $(\bar{2}60)$ spots, have the same behavior (see Fig. 10c for one example). The small intensity change is noticed, as compared to a 30% intensity depletion observed by the reflection method. Different types of gold grids were used to check if the support film on the grid has an effect, but we failed to find major differences in the depletion of spot intensities.

The temporal evolution of all spot intensities can be fitted by a function of exponential growth (convoluted with a proper instrumental response time), and this gives a time constant of ~10 ps. This rise time is reminiscent of what is seen in the reflection experiments at 266 nm. However, instead of recovering from the depleted values, as in the reflection results, the low intensities were sustained for the rest of the temporal range probed. This is expected given the confinement of lattice energy within a thin film and the nature of energy dissipation in a bulk sample; neither does the support film on the gold grid facilitate fast recovery in the GaAs thin film. Finally, we note in Fig. 10c the linear correlation between maximum intensity change for different Bragg spots and the value of s^2 (Fig. 10d), a point that we shall return to in the Discussion Section.

Discussion

The significant observations of the diffraction changes made in these UEC studies can be summarized as follows. First, in reflection experiments, the main diffraction features, $I(t)$, $s(t)$, $w(t)$, and $\eta(t)$, develop their temporal changes on the ultrashort time scale (typically $\tau \sim 10$ ps) and recover toward the equilibrium-state values with multiple time constants, ranging from 30 ps to nanoseconds. In transmission, $I(t)$ also decreases with $\tau = 10$ ps, similar to the reflection case, except that the recovery is not observed within our temporal range. Second, although a seemingly similar behavior (development of change and recovery) is observed for $I(t)$, $s(t)$, $w(t)$, and $\eta(t)$, differences such as delay of the onset of change and rates of development and recovery, can be clearly seen and resolved with our temporal response. Third, the dynamics is strongly dependent on the excitation wavelength and fluence. Fourth, the anisotropy of changes of the spot position and width in the vertical and horizontal directions is evident. In what follows, we address the nature of the nonequilibrium dynamics derived from these UEC observations.

A. Thermal vs Carrier Excitation

A.1. Thermal Heating and the Two-temperature Model

According to the thermal excitation mechanism discussed in Sec. B.1 of Ch. 2, one would have expected, given the highest heating fluences of 266 and 800-nm light used in this study, the maximum lattice expansion at 266 nm to be more than 2 orders of magnitude larger than that at 800 nm. This would be expected because of the huge difference in the temperature rise ΔT_l, which results from the excess energy above the band gap (E_{excess}) and the penetration depth δ (see Eq. 34 of Ch. 2). Also, according to the Debye–Waller factor (Eq. 16 of Ch. 2), this difference in ΔT_l should lead to a pronounced intensity reduction at 266 nm and a negligible change at 800 nm. Furthermore, because of the nature of thermal equilibrium, the widths and shapes of Bragg spots would have to be the same without major temporal changes since the crystal on the average preserves its order (Sec. B.2 of Ch. 2); horizontal lattice expansion due to the temperature rise would have been expected, too. However, as seen from the results (particularly, Fig. 7), the experimental observations contradict the above predictions, and in fact, a reverse trend was observed, as shown in Fig. 7b; the maximum expansion at 800 nm was observed to be twice as large as that at 266 nm. In another experiment with a different incidence angle to record the dynamics of the (206) and $(\bar{2}06)$ Bragg spots on the side rods, no sign of horizontal movement in their positions throughout the entire temporal range was seen, indicating the absence of a horizontal lattice expansion. As a result, the thermal-heating picture fails to account for the structural dynamics on the time scale probed by UEC.

The application of the two-temperature model (*15, 16*) to describe the carrier and lattice dynamics also becomes invalid in the case of semiconductors. In metals, various spectroscopic results have been successfully explained by this model (see, e.g., Refs. 17 and 18 and cited references therein; for a review on the carrier and phonon dynamics in semiconductors, see Ref. 19). Because of the ultrafast equilibration within the electron subsystem on the time scale of a hundred femtoseconds, a temperature is assigned to describe the energy distribution of all electrons. The simplicity of the crystal structure, one atom in the primitive unit cell, indicates that the acoustic phonons are generated while the electrons are releasing their excess energy to the lattice. The equilibration in acoustic modes allows the use of another temperature for the lattice subsystem. However, in semiconductors with more than one atom in the primitive unit cell, optical phonons become the accepting modes and at least three temperatures have to be defined. Carriers more readily interact with optical phonons with a scattering time ($\tau_{\mathrm{e-ph}}$) typically of a few hundred femtoseconds [e.g., ~165 fs in GaAs (*20, 21*) and ~240 fs in Si (*22, 23*)], and the importance of this time scale on the observed nonequilibrium behavior will be addressed below. Finally, in a semiconductor, because of the existence of the band gap and the complex band structure, the highly excited carriers (electrons and holes) may not be able to reach Fermi–Dirac distributions on a femtosecond time scale and therefore, an electron temperature cannot be defined.

A.2. Carrier Excitation

Because lattice dynamics is initiated following the generation of carriers, it is important to examine the carrier processes in semiconductors; an overview of these processes and their optical probing has been provided (*24*). In short, charge carriers are created coherently on the femtosecond time scale with or without the assistance of lattice phonons, when photons of energy higher than the band gap impinge on a semiconductor surface. The coherence among electrons is lost in less than 10 fs at the carrier densities achieved due to the ultrafast carrier–carrier scattering. This results in featureless energy distribution of carriers around the excitation energy. The distribution may be additionally affected by other carrier excitation mechanisms, such as free-carrier absorption and impact ionization. However, the resulting spatial and energy distribution defines the initial condition for the following carrier and lattice dynamics.

The assumption of linear absorption is invalid in the regime of intense-field excitation. The band-filling effect (*25*), a manifestation of the Pauli exclusion principle, prevents an unlimited degree of vertical excitation through single-photon absorption (SPA); a comprehensive review for GaAs has been made (*26*). Carrier excitation through two-photon absorption (TPA), however, not only avoids such a saturation limit but also becomes crucial in influencing the lattice, because these TPA carriers carry higher (above-gap) excess energy. For the fluences used in this study at 800 nm (Fig. 9), we deduced $n_{\mathrm{TPA}}(z{=}0) = 7.1$, 3.2, and $1.2\times10^{19}\ \mathrm{cm}^{-3}$, much higher values than the saturated SPA carrier density ($2.5\times10^{18}\ \mathrm{cm}^{-3}$). Here, $n_{\mathrm{TPA}}(z{=}0)$ is the carrier density near the surface ($z = 0$) calculated with the use of the TPA coefficient and dependence of n_{TPA} on fluence under a similar excitation condition in the literature (*27*).

Carrier excitation by high-energy photons may be further influenced by ambipolar diffusion (*28*) and bleaching of the near-edge valence bands due to density-of-states consideration (*26*). The fast carrier diffusion greatly reduces the density near the surface even before any substantial energy transfer to phonons takes place. We estimate, by using the 1D diffusion equation

$$\frac{\partial n}{\partial t} = D\frac{\partial^2 n}{\partial z^2}$$

$$n(z,t) = \frac{const}{\sqrt{Dt}} \cdot \exp\left(-\frac{z^2}{4Dt}\right) \tag{1}$$

where D is the ambipolar diffusion constant (*29*), an initial density $n(z{=}0)$ of $10^{21}\ \mathrm{cm}^{-3}$ by 266-nm light will drop to $<10^{20}\ \mathrm{cm}^{-3}$ after $t = 200$ fs, which becomes comparable to the value of $n_{\mathrm{TPA}}(z{=}0)$ at 800 nm. In contrast, carriers generated by 800-nm light are much less affected by this diffusion because of the lower initial density (see above) and the large penetration depth (710 nm). Therefore, the similar maximum intensity reduction for the two wavelengths (266 and 800 nm) and the reverse (from thermal) trend of the maximum lattice expansion indicated in Fig. 7 can be rationalized based on the comparable carrier densities near the surface.

Optical studies have shown that intense carrier excitation by photons can strongly affect the electronic state of a semiconductor on the ultrashort time scale (*30*). It is important to point out that the observed equilibration time constant (7 ps) between carriers and the lattice matches well with the rise time for structural changes reported here, even though lattice dynamics was not directly seen in the spectroscopic probing.

A.3. Influence of Band Structures and Lattice Phonons

The dispersion of band structure plays an important role in the final nature of electron distribution. For GaAs, the different excitation wavelengths provide an opportunity to reach different regions and distribution. At 800 nm, the TPA process, which is much more important than the SPA process from Γ_{8v} to Γ_{6c}, occurs not only around the Γ region but also along the Λ direction close to the L_{6c} valley (*31*); thus, accumulation of electrons in the L valley is expected (Fig. 1b). At 266 nm, however, the photon energy matches the critical point E_0' $(+\Delta_0')$ which features the interband transitions through $\Gamma_{8v} \rightarrow (\Gamma_{7c}, \Gamma_{8c})$ and $\Delta_{5v} \rightarrow \Delta_{5c}$ near Γ (*32, 33*), and consequently, a large number of electrons will go to the X valleys after they release some excess energy to the phonons.

The consequence of having the charge carriers in different parts of the band structure is very important. Although essentially no lattice mismatch exists between GaAs and $Al_{0.6}Ga_{0.4}As$, they have different electronic band structures, and the inset of Fig. 1b shows the comparison of the band energies at three high-symmetry points. Thus, according to the heterostructure used in the reflection experiments, electrons at L_{6c} (from TPA at 800 nm) are energetically trapped in the GaAs quantum well, whereas those at X_{6c}

(from SPA at 266 nm) may still be able to diffuse across the $Al_{0.6}Ga_{0.4}As$ layer. As discussed in Sec. B.1 of Ch. 2, more carriers in the electronic excited states may induce significant weakening of the lattice potential and consequently larger lattice expansion as observed in UEC. It is therefore understandable that the large amplitude of expansion at 800 nm (Fig. 7b), compared with that of 266-nm excitation, is a natural result of this carrier trapping.

It is noted that the issue of quantum confinement (continuum vs the discreteness of energy states) arises when one or more of the dimensions of the sample has a size that is close to the bulk exciton electron–hole Bohr radius a_B; for GaAs, it was calculated to be ~12.5 nm (*34*), which is smaller but close to our GaAs layer/film thickness. Therefore, electrons at Γ_{6c} and light holes at Γ_{8v} may experience the confinement effect in the quasi-2D quantum well, since fewer electronic states will be available because of the quantization of allowed energies. However, in structural dynamics, at 266 nm and two photons of 800 nm, it is those high-energy carriers that are most responsible for the observations made here, and these carriers have energy-state structures with no discreteness. Thus, no confinement is expected, and indeed the close resemblance between $I(t)$ and $w(t)$ of reflection experiments at 266 nm (Fig. 3) and those reported in a previous study for bulk GaAs (*4*) confirms this conclusion for our heterostructure and also in transmission experiments. Thus, it is still a good approximation to treat the 20-nm thin layer/film of GaAs as a bulk material as far as the electronic structure is concerned.

Given the initial nonequilibrium state of the material structure, the question of significance is, what is the driving force(s) for the change on the ultrashort time scale. As mentioned earlier, the initially prepared carriers readily interact with optical phonons to transfer their excess energy on the time scale of few hundred femtoseconds. In a polar semiconductor like GaAs, longitudinal optical (LO) phonons are generated through the polar (Fröhlich) interaction with carriers, and this coupling is strongest for the long-wavelength (i.e., small-wavevector) LO phonons since the scattering rate varies as $1/q^2$ ($\boldsymbol{q}$ is the crystal wavevector) (*35*). As a result, more and more LO phonons are accumulated around the Brillouin zone center Γ. Concurrently, the carriers lower their average energy and in the process may occupy other regions of the band structure (e.g., the Γ, L, or X valley). Carrier diffusion can also be occurring in parallel.

Because of the dispersion relation, the LO phonons nearly undergo no propagation, and, thus, can only decay by the generation of other phonons through lattice anharmonicity. The major relaxation channel involves the generation of pairs of longitudinal acoustic (LA) phonons of half of the LO-phonon energy but with opposite $\boldsymbol{q}$, a requirement of the conservation of energy and momentum. The lifetime of a LO phonon, $\tau_{\mathrm{LO}\rightarrow\mathrm{LA}}$, is typically a few picoseconds (*20, 36*), and the generated LA phonons have a large $|\boldsymbol{q}|$ (i.e., a small wavelength), resulting in dynamical inhomogeneity/strain of the lattice because their wavelength is on the length scale of a unit cell. On the ultrashort time scale the distribution in $\boldsymbol{q}$ leads to propagation of a strain packet with the speed of sound, transporting energy away or toward the surface region of the solid. At room temperature, because of the existent thermal phonons ($kT \sim 26$ meV) populated in the acoustic modes, phonon–phonon scattering may take place and randomize the phonon distribution.

B. Nonequilibrium Structural Dynamics

In what follows, GaAs is used as a prototype system to address the nature of nonequilibrium dynamics in semiconductors on the ultrashort time scale. Numerous spectroscopic studies of carrier and lattice dynamics have in the past primarily focused on

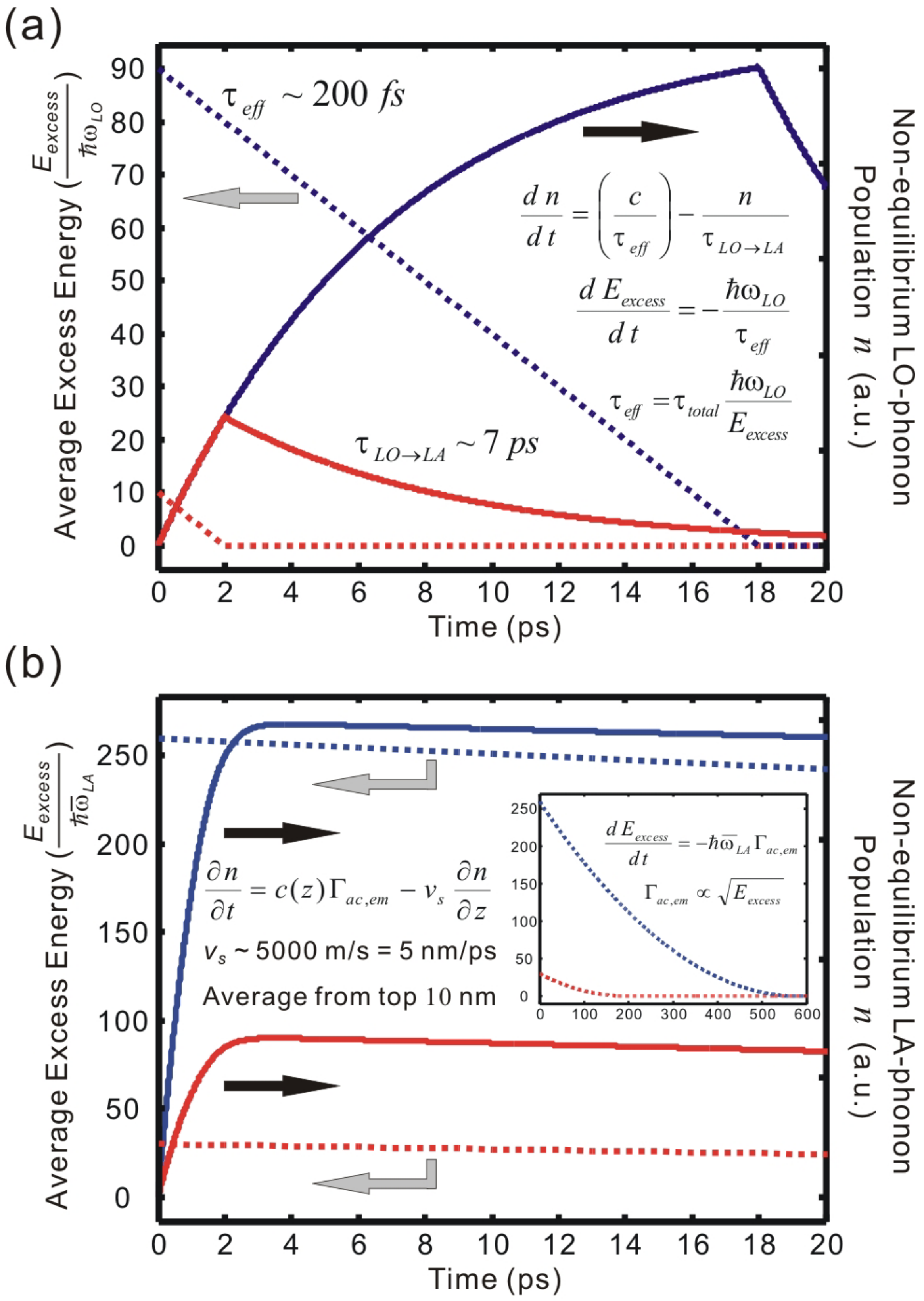

(See next page for the figure caption.)

Fig. 11. Theoretical calculations. (a) LO-phonon population at early times (solid curves). Nonequilibrium phonons are generated during the energy relaxation of carriers (which is governed by the second equation, if a stepwise relaxation mechanism is considered; dash curves). τ_{eff} is an effective LO-phonon generation time including the hot-phonon (phonon-reabsorption) effect. Depending on the initial excess energy (blue: 90 $\hbar\omega_{\mathrm{LO}}$ and red: 10 $\hbar\omega_{\mathrm{LO}}$) the overall time τ_{total} for LO-phonon population is given by the third equation. LO phonons can be converted into LA phonons in a time of ~7 ps, and therefore the LO-phonon population is governed by the sum of a positive generation term and a negative decay term, as shown by the first equation; *c* is a constant which is related to ratio of the carrier density over the number of optical normal modes active in the above-mentioned process. If most of the carriers transfer their excess energy to the lattice, no more source term exists for the generation of LO phonons, giving an exponential decay with the time constant of ~7 ps. (b) LA-phonon population at early times (solid curves) if the direct coupling between carriers and LA phonons is considered. The inset shows the average carrier energy as a function of time. Because the rate of this scattering is slow [on a picosecond time scale, and governed by two equations (*63*) in the inset], energy relaxation of carriers becomes a slow process. The acoustic phonons propagate at the speed of sound, as described by the second term of the equation on the left. Thus, acoustic phonons in the top 10-nm surface region will transit in 2 ps (10 nm divided by the sound velocity in GaAs).

optical and dielectric properties, such as Raman scattering for monitoring the generation and decay of small-q optical phonons (*20, 36*), and surface deflection spectroscopy for probing the generation and motion of LA phonons (*37*). Reflection transient grating (*38*), transient reflectivity, and dielectric function measurements (*30*) have also been introduced to study the lattice temperature and to describe the phonon/electron subsystems. The power of UEC is in its capability to monitor the transient motion and dynamical inhomogeneity of the structure itself.

B.1. Local Atomic Motions: Diffraction Intensity

In physical space, the vibrations of Ga and As atoms (optical phonons) are the first lattice motions generated following the optical carrier excitation, which can alter the structure and change diffraction intensity. As discussed in Sec. B.3 of Ch. 2, it is the vertical Ga–As vibrations along $\hat{n}$ that are responsible for the change, and the more optical phonons are generated, the larger the average amplitude of this vibration and change will be present in the crystal. Indeed, Figures 4 and 6b show that, regardless of the excitation wavelength, reduction of the (008) spot intensity always proceeds ahead and faster than changes of other diffraction features, the spot movement and width change.

The time scale for these local motions is picoseconds. For a range of 0.5 eV of excess energy, the scattering time $\tau_{\text{e–ph}}$ was found to be 165 fs at a low carrier density (*20*), and assuming the same $\tau_{\text{e–ph}}$ for our excess energy (3.23 eV) we can estimate the total time for the intensity loss. Because $\hbar\omega_{\text{LO}}$ = 36 meV, 90 such phonons will be emitted during the process, predicting the rise time to be 90 times 165 fs, which is ~15 ps. However, during such a process, the conversion to acoustic packets may occur and according to optical studies, this conversion takes ~7 ps for GaAs (*20, 30, 36*). Figure 11a

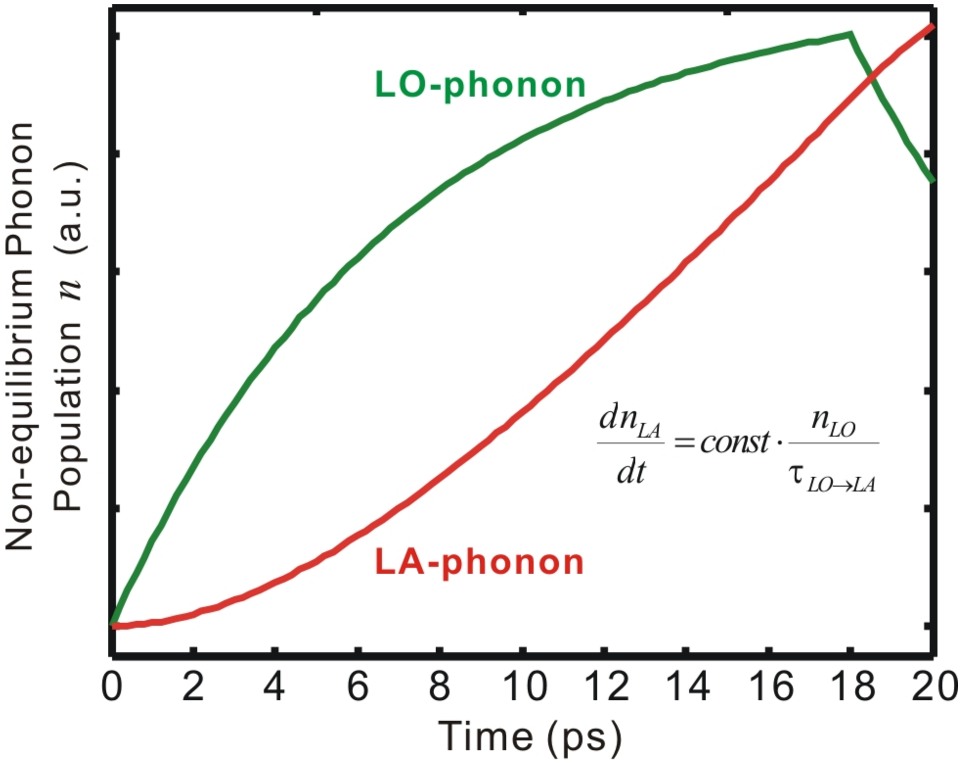

Fig. 12. Comparison of LO and LA-phonon populations at early times. Because of the relatively large LO-phonon lifetime (~7 ps), LA-phonon population rises but with a delay relative to the LO-phonon rise. The direct conversion relationship indicates a similar rise time for both populations.

shows the theoretical results for the generation and conversion of LO phonons which have similar time scales (15 and 7 ps); Figure 11b considers the dominance of acoustic process, and in this case, the rise is simply determined by the speed of sound. Other processes can contribute to the slowing down of the rise, and these include the hot-phonon (phonon-reabsorption) effect (*39*), intervalley scattering (*40, 41*), and screening of the carrier–phonon coupling (*42*). The UEC results provide the experimental evidence for the direct role of lattice motions by optical and acoustic phonons.

As shown in Fig. 4, the intensity drop occurs at an earlier time than the width (and also the Lorentzian component) change, but the slope is nearly the same. This behavior indicates that the observed time lag is a direct measure of the conversion of optical-to-acoustic lattice motions, as the width change must be delayed until dynamical inhomogeneity begins with acoustic/strain propagation; in Fig. 12, the change in population is shown for both LO and LA phonons, and the origin of the time delay is clear. The rise time is observed to be ~10 ps, and this is entirely consistent with the motion responsible for the change being that of optical phonons; it is noted that in Fig. 11b, the rise due to acoustic wave propagation ($v_s \sim 5000$ m/s along $\langle 001 \rangle$ directions) takes place in ~2 ps, shorter than the 10-ps rise.

With the use of the structure factor, $F(008)$, the maximum amplitude of the atomic vibrations along $\hat{n}$ can be estimated from the maximum intensity reduction at $t = 25$ ps (Fig. 7a). Using Eq. 35 of Ch. 2 and a drop of 30% in intensity, ±0.096 Å is obtained for the additional (nonthermal) vertical amplitude for each atom's motion around the equilibrium position (see Appendix A). It is equivalent to a 13.5% change of the vertical Ga–As distance ($a/4 = 1.413$ Å), a percentage close to the Lindemann stability limit (*43*). Experimentally, at a fluence just above the ones we used to conduct our experiments, we observed diffraction changes that did not recover fully, and this long-term deterioration of the material indicates that the damage threshold has been reached. Accordingly, the experimental observations of the intensity change, both the time scale and amplitude, are consistent with theoretical calculations.

For the case of intensity reduction in transmission, the estimation of maximum vibrational amplitude can also be made. It is noticed that the ~10% intensity decrease of the (080) spot in transmission (Fig. 10c) was less than the ~30% of the (008) spot in reflection (Fig. 3a) even though the excitation fluences were somewhat larger in the former case. This difference is due to the fact that the transmission experiments were performed with a small crystal rotation of 2°, and thus, the projection of the vibrational amplitude onto the scattering vector $\boldsymbol{s}$ is relatively small. The linear relation obtained in Fig. 10d between the intensity decrease and s^2 provides a slope that gives $\Delta\langle u^2\rangle_{\mathrm{projected}} = 0.0015\pm0.0002$ Å^2, a measure of the (projected) increase in the mean-square amplitudes $\langle u^2\rangle$ of vertical atomic vibrations. We estimate $\Delta\langle u^2\rangle \sim \Delta\langle u^2\rangle_{\mathrm{projected}}/\sin 2°$ to be 0.043 Å^2, a value which is even larger than $\langle u^2\rangle_{\mathrm{total}}$ of the thermal motion in all directions at room temperature (*44*). Unlike the incoherent, random thermal motion, this additional vertical amplitude is due to the LO phonons generated within the first tens of picoseconds. The resulting increase in the vibrational amplitude for each atom along $\hat{n}$ is ~0.15 Å, which is comparable to the value obtained from the reflection experiments.

B.2. Potential-driven and Anisotropy of Lattice Expansion

The objective here is to understand the time scale, anisotropy, and the amplitude of lattice expansion. First, the optical excitation of GaAs(001) at 266 nm is considered. Initially, the carriers are generated in the excited states near Γ, which means that the electronic wavefunction (Bloch function) has a near-zero crystal wavevector; the positive phase character between neighboring unit cells is preserved, whether or not Ga and As atoms are in the bonding (ground) or antibonding (excited) state, and therefore, lattice expansion at this electronic configuration is not expected. As the carriers transfer their excess energy to optical phonons, they reach different electronic states whose Bloch functions have larger crystal wavevectors, particularly, in this case, along the ⟨001⟩ directions (Fig. 1b). The phase modulation in the wavefunction (with pluses and minuses) along a certain direction indicates that, when carriers occupy these electronic states, unit cells can be modified through the new crystal potential, which leads in this case to a

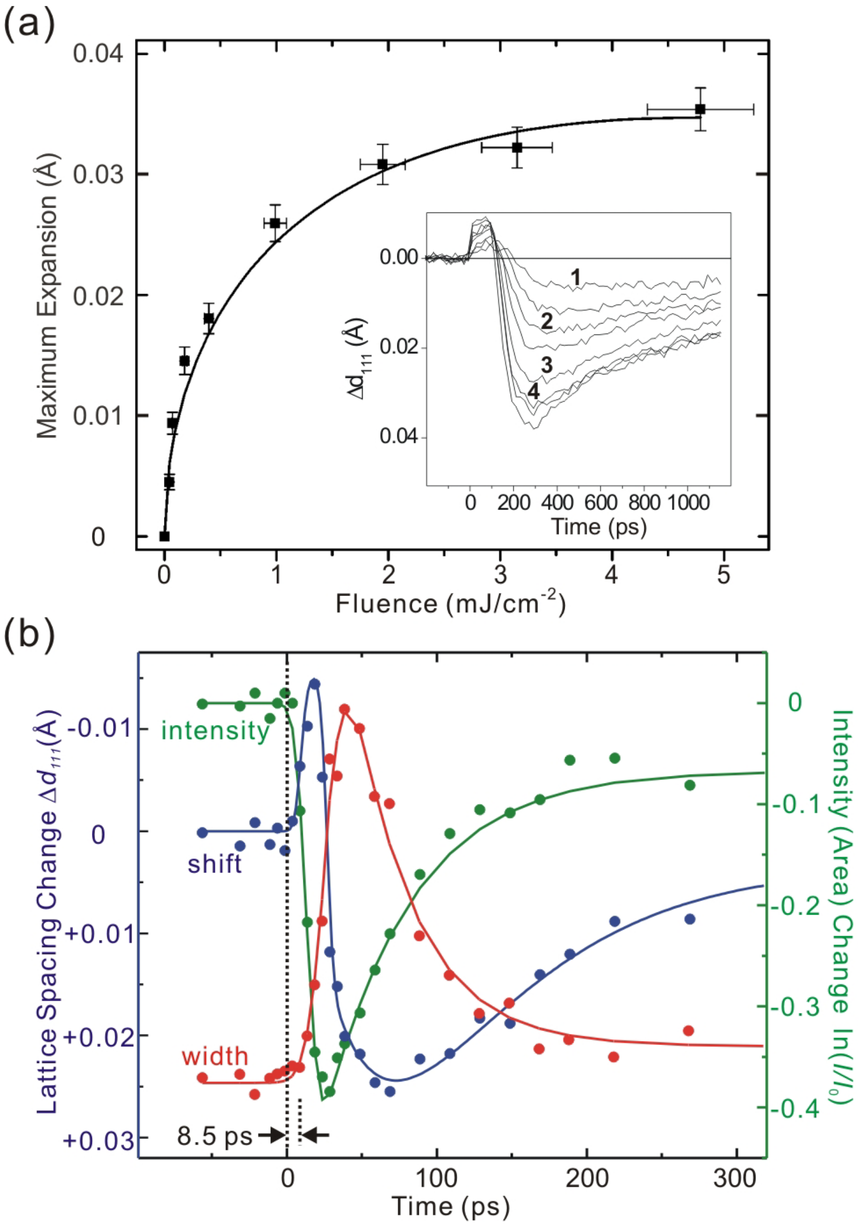

Fig. 13. UEC of single crystals (Ref. 4). (a) Maximum lattice expansion $\Delta d_{111}(t)$ as a function of fluence for 266-nm excitation; the inset shows the overall temporal behavior. Saturation of the maximum expansion at high fluences is evident. (b) Temporal behavior of the (222) spot intensity (green dots) and width (red dots) change, together with that of the "derived" lattice spacing change (blue dots) from the spot position shift. Again, a delay in the width change relative to the intensity drop can be clearly seen. The small amplitude peak in the spot movement at early times is discussed in Text.

weakening of the lattice in the [001] direction. As more and more carriers reach the energy states in the X valley, the larger the potential-driven lattice change will be along the $\hat{n}$ ($\hat{n} = [001] = \mathrm{X}$) direction. The relaxation of such carriers is mediated by optical-phonon emission, and hence, the rate of this process determines the time scale of both phonon generation and lattice expansion.

Indeed, as shown in Fig. 4, the similar rise time for both intensity reduction and lattice expansion confirms this potential-driven picture. Excitation fluence at 266 nm does not change this rise time (Fig. 8a), which is also expected because the time scale for the above-mentioned carrier relaxation does not strongly depend on the carrier density. As for the case of two-photon excitation by 800-nm light, more electrons are generated around the L_{6c} valley (the $\langle 111 \rangle$ directions) and therefore the weakening of the crystal potential along $\hat{n}$ is less effective. The lattice expansion being delayed and slower than the intensity reduction (Fig. 6b) can now be understood as due to the ineffective potential weakening, and/or because of an additional time for intervalley scattering from L to X (see below).

The nonlinear relationship between the excitation fluence at 266 nm and the maximum lattice expansion, as shown in Fig. 13 (adapted from Ref. 4), can also be explained by this potential-driven picture. Due to the rapid increase of the ambipolar diffusion constant as the carrier density becomes very high (*29*), the carriers at a higher fluence will undergo faster diffusion away from the surface region. Therefore, the "efficiency" of making a crystal expand at a high excitation level is greatly reduced; fluence higher than the damage threshold will cause irreversible structural changes. As to the case of 800-nm excitation in this study, because of the heterostructure which hinders diffusion of the carriers in the GaAs layer, the maximum expansion is still in proportion to the fluence used (Fig. 9a). Without the heterostructure, we shall expect a similar fluence dependence of the maximum expansion to be observed at 800 nm as that at 266 nm.

Summarizing, the expansion of the atomic motions along the $\hat{n}$ direction is due to a nonequilibrium state of the lattice influenced by the anisotropy of the potential. From Fig. 7b, a maximum lattice expansion of 0.022–0.042 Å is observed, which corresponds to a 0.4–0.8% change, much larger than the thermal limit; from intensity reduction, we know the structural changes are near the Lindemann limit, as discussed in Sec. B.1 in more detail. The rise of this change occurs in ~10 ps and with the changes in intensity, as discussed above. We note that structural changes by electronic excitation, with nuclear motions, have been studied by optical (*45, 46*), x-ray (*47-50*), and electron diffraction (*51, 52*) methods. However, in the present contribution, we provide the first reported reversible potential-driven structural changes mapped with its anisotropy and lattice-induced changes, using UEC. The effect of radiative recombination and nonradiative Auger processes is considered in Appendix B. The similar rise time (~10 ps) for the development of diffraction changes made at different fluences, wavelengths, and detection geometries confirms the minor role of these two carrier processes which are density-dependent.

In general, the probing of the anisotropy of lattice expansion discussed above is sensitive to the geometry of the experiment. Given the experimental excitation surface area relative to the penetration depth along $\hat{n}$, the horizontal 2D spatial distribution is more uniform (Gaussian-type, bulge on the micrometer or larger scale) compared to the vertical one (excitation penetration depth of nanometer scale). For such a case, the temperature/carrier density gradient in the $\hat{n}$ direction would be expected to lead to more expansion along $\hat{n}$ when compared with lateral expansion. However, as shown above for both the 266 nm (nanometer penetration) and 800 nm (micrometer penetration), the vertical expansions were similar, and in both cases, no lateral expansion was observed. Thus, the important cause of the anisotropy, besides the potential change, is the fact that the surface has no restriction (stress-free) in the vertical direction and is free to expand. The contributions to vertical expansion from different "bulk" stresses integrate at the surface. On the time scale of UEC, we did not observe a horizontal lattice expansion either in the reflection or in the transmission geometry, and these observations are evidence of anisotropic, nonthermal expansion.

B.3. Dynamical inhomogeneity: Width and Shape

When the inhomogeneity is caused by acoustic waves of relatively short wavelength (at $\pm\boldsymbol{q}$), their downward propagation at the speed of sound would decrease their population in the probed surface region; in 2 ps, they can move across a 10-nm length which is on the order of the probed depth. Within the excited (different densities) range, the upward propagation brings the waves generated "inside" the crystal toward the surface, and the net effect is the vertical atomic motions with the surface atoms experiencing the largest change. Ultimately, phonon–phonon scattering will lead to a broadened, randomized distribution in the acoustic modes. Thus, besides the expansion of the lattice, which results in a decrease in the position of diffraction spots (lower s), diffraction broadening due to this dynamical inhomogeneity of lattice spacings is expected.

As shown in Sec. B.2 of Ch. 2, the temporal changes in the spot width and shape are both related to the lattice inhomogeneity, and it is not surprisingly that $w(t)$ and $\eta(t)$ have a similar behavior over the entire temporal range (Fig. 4, inset). Because of the direct relationship in the generation of LO and LA phonons, $w(t)$ is also expected to closely follow $I(t)$, which is confirmed by our observations. At this point, we would like to emphasize that the temporal behavior of $w(t)$ is a consequence of coherent intrinsic structural dynamics, and not simply an artifact due to inhomogeneous sum of contributions from areas of different excitations. We should have observed a very similar temporal behavior for $w(t)$ and $\Delta d_{001}(t)$ if the inhomogeneity were to be static in nature.

It is important to note that the observed dynamical inhomogeneity mostly appears along $\hat{n}$, and not in the 2D plane. As shown in Fig. 5a, the horizontal width change is much smaller and behaves like a step function with time, indicating a relatively very small lattice inhomogeneity along the 2D directions. The anisotropy is evident, and its magnitude is in parallel with a genuine dynamical inhomogeneity, i.e., the larger the change in lattice spacing, the larger the inhomogeneity. This phenomenon is due to the fact that the surface is free of stress compared to the constrained 2D horizontal lattice. Consistent with this picture, Figure 8b shows that the maximum width change is linearly proportional to the fluence at 266 nm, but the temporal behavior remains the same. In the case of 800-nm excitation, due to the nonlinear TPA in GaAs and the heterostructure underneath, a similar linear relationship is not expected. In the following discussion, these differences in temporal behaviors will become clear.

C. Restructuring at Long Times

From all experimental results obtained in the reflection detection mode, it is apparent that there is a temporal recovery of the nonequilibrium structures. This recovery is due to the transfer of excess energy away from the probed region into the bulk, either through carrier diffusion or through lattice relaxation by acoustic energy propagation and/or thermal diffusion. Further examination of the fast recovery of $I(t)$, $\Delta d_{001}(t)$, $w(t)$, and $\eta(t)$ (inset of Fig. 4 and Fig. 6b) shows that they share a similar profile after reaching the maximum. At higher fluence or shorter excitation wavelength, the recovery is even faster in the relatively short-time regime with an apparent time constant as short as 30–40 ps (Fig. 4, inset). The recovery is not observed in transmission experiments because the sample is very thin and there is no dissipation of energy on our time scale.

In order to pinpoint whether the carrier or phonon subsystem is responsible for the observed initial fast decay, it is helpful to first consider the case where there are no carrier and thermal diffusion, a hypothetical situation. For this case, one would expect the crystal structure to recover to its equilibrium state only by the optical-to-acoustic phonon conversion (in ~7 ps) with the acoustic waves propagating into the bulk. As a result, all four diffraction features $I(t)$, $\Delta d_{001}(t)$, $w(t)$, and $\eta(t)$ would return to their corresponding equilibrium values in only ~7 ps, contrary to the experimental results which show fast and slow decays on the picosecond and nanosecond time scales.

Because carriers continue to produce more optical phonons and concurrently undergo ambipolar diffusion, which gradually reduces their density in the surface region, the remaining carriers continue to be the heat source for the lattice. This process influences the dynamics of recovery in the initial phase, and it is reasonable that $I(t)$, $\Delta d_{001}(t)$, $w(t)$ and $\eta(t)$ all recover with the same profile on this time scale. Studies of wavelength and fluence dependence of the profile support this picture. Rapid structural recovery can be seen most prominent in the high-fluence 266-nm data (Fig. 4, inset) because carrier diffusion is significant at this high carrier density which is confined in a narrow spatial distribution of $\delta \sim 6.4$ nm (inverse of the absorption coefficient). Decreasing the fluence at 266 nm does not significantly alter the initial recovery time because carrier diffusion is still dominant for the nanometer-scale excitation; the smaller

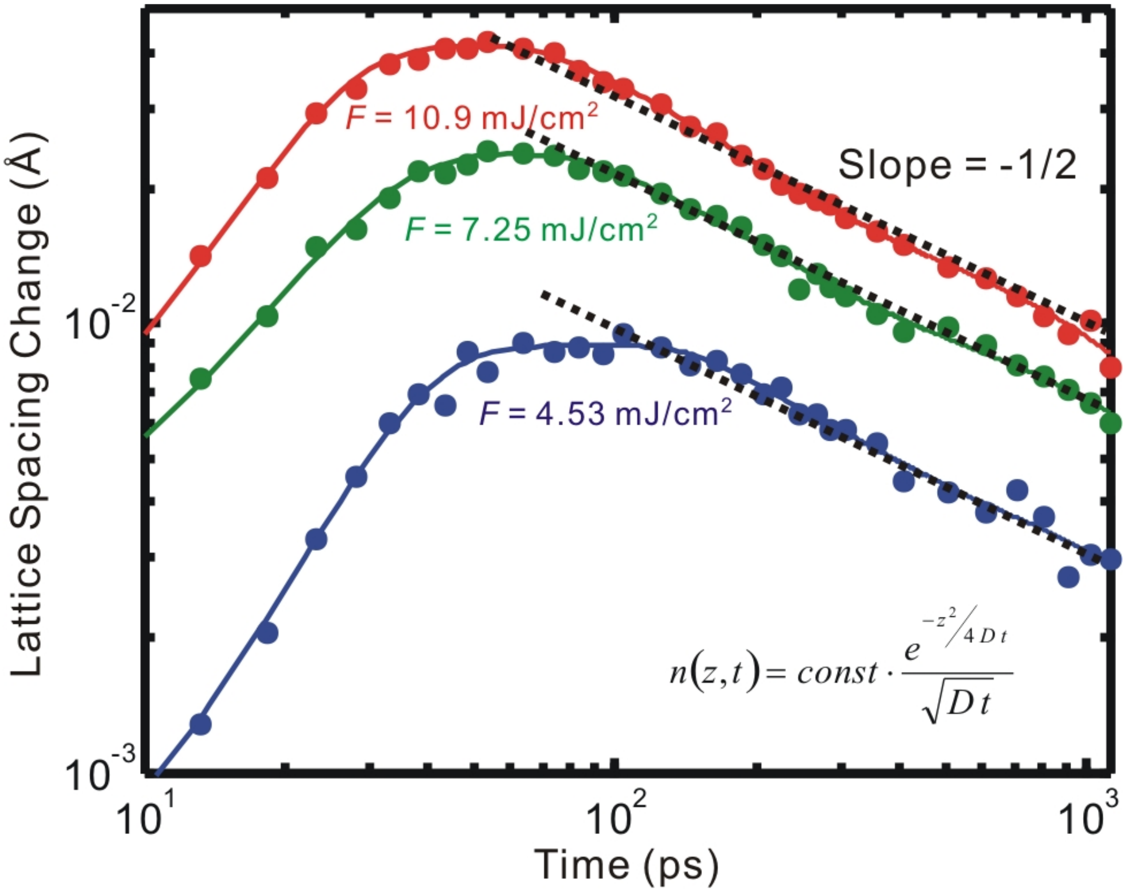

Fig. 14. Lattice spacing change as a function of time and fluence at 800 nm. In Text, the direct connection between the extent of lattice expansion and carrier density at the surface is discussed. The linear decay of lattice expansion with the slope of –1/2 in the log–log plot, together with the fluence dependence, provide strong support of restructuring under the influence of carrier diffusion on the shorter time scale and/or thermal diffusion on the longer time scale.

the excitation thickness, the faster the diffusion (for density effect, see Sec. B.2).

For 800-nm experiments, if the fluence is high, fast recovery of the system is noticeable because of the large TPA carrier density (Fig. 9, red and green curves). It is noted that the spatial distribution of TPA carriers depends on the excitation intensity: the effective absorption coefficient of TPA is $\beta I \sim 1.8\times10^4$ cm^{-1} at the highest fluence used at

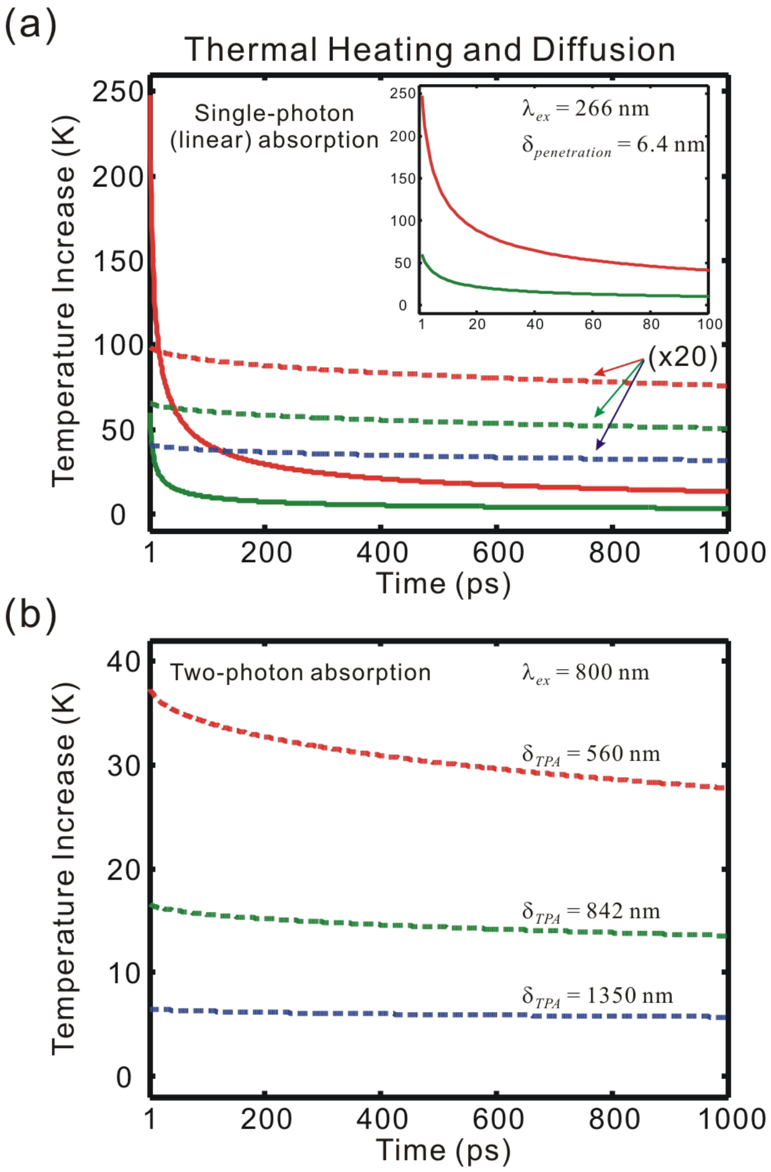

Fig. 15. Heat diffusion. Theoretical lattice temperatures at the surface as a function of time when heat diffusion is considered at the two wavelengths (266 nm, solid lines; 800 nm, dash lines) and the different fluences used. (a) The cases of linear (single-photon) absorption with no band-filling effect; the initial temperature increase is determined by Eq. 34 of Ch. 2. The fast decay is obtained for the 266-nm excitation because of the small penetration depth (the inset shows the early-time behavior). At 800 nm, the surface temperature increase is very small and its decay is very slow, showing a totally different temporal behavior from the 266-nm case, contrary to experimental observations. (b) The cases of TPA at 800 nm; the initial temperature increase is still limited because the excitation region is sub-micrometer to micrometer size. The temperature relaxation is also very slow and totally different from the 266-nm behavior.

800 nm [since $\beta = 210$ cm/GW for our experimental geometry (*27*)] and the penetration depth is estimated to be ~560 nm (SPA carriers are barely affected by diffusion because of saturation within a thickness of tens of micrometers). As the fluence becomes small, however, the number of TPA carriers is greatly reduced, and the excitation spatial distribution becomes essentially flat inside the crystal. Since carrier diffusion is not as important in such cases, fast recovery becomes less distinct or even disappears (Fig. 9, blue curves). Similar results of wavelength and fluence dependence were obtained for silicon using UEC (compare Fig. 4e in Ref. 3 with the red curve in Fig. 5b in Ref. 6), and the above-mentioned physical picture is similarly applicable.

Figure 14 presents an important observation which supports this picture. The slope of the linear decays over time, up to 1 ns, in the log–log plot is –1/2, consistent with the behavior predicted by Eq. 1; near the surface, $\log n(0,t) = (-1/2)\log(t) + \text{constant}$. Because of the heterostructure, diffusion of the TPA carriers at 800 nm can be hindered, but eventually, the system returns to the ground state. On the sub-nanosecond to nanosecond time scale, the relaxation may take place through carrier–carrier scatterings and the (slow) Auger process: some carriers will acquire more energy than others and overcome the energy barrier to diffuse. For 266 nm, in addition to diffusion, the decay has a manifestation of interband conversion, as discussed above.

At longer times, restructuring of the lattice proceeds through thermalization among the vibrational modes. As mentioned earlier, phonon–phonon scatterings of acoustic modes can result in randomization of the phonon distribution and therefore thermalization of the lattice. The relaxation of lattice vibrations may then share some resemblance to the process of heat diffusion. Figure 15 shows results of the theoretical solutions (*53*), using parameters given by our experimental conditions, to the heat diffusion equation:

$$-k\,\frac{\partial^2 T(z,t)}{\partial z^2} = -\,C_l\,\frac{\partial T(z,t)}{\partial t} + \frac{F_{\text{heating}}}{\sqrt{\pi}\,\delta\,t_{\text{p}}}\,e^{-z/\delta}e^{-\left(t/t_{\text{p}}\right)^2} \tag{2}$$

where k is the thermal conductivity (a constant for a cubic lattice) and t_{p} is the laser pulse duration, which is 120 fs divided by $2(\ln 2)^{1/2}$; see Eq. 34 of Ch. 2 for other notations. Equation 2 shows that the higher the heating fluence (F_{heating}), the larger the initial temperature rise; it also shows that the temperature profile into the bulk $T(z)$ and its temporal evolution $T(t)$ are dependent on the penetration depth δ. The purpose of Fig. 15 is to show that, besides the failure of the thermal-heating picture to describe the nonequilibrium dynamics in semiconductors, heat diffusion is a very slow process and only becomes more important on the nanosecond or longer time scale. It is noted that comparison of the results in panels a and b of Fig. 15 for 266 and 800 nm excludes thermal diffusion as a mechanism for restructuring at short times (for the 266-nm excitation). This is because the same process would predict the absence of the fast component at 800 nm, contrary to experimental observations. However, at longer times (e.g., after 200 ps), thermal diffusion cannot be ignored.

When the residual amplitude of the diffraction changes at $t = 1$ ns are examined, one notices that more decay in $w(t)$ and $\eta(t)$ has occurred when compared with that in $I(t)$ and $\Delta d_{001}(t)$. For example, the high-fluence 266-nm data shows that $w(t)$ and $\eta(t)$ have fully returned to their negative-time equilibrium values even before $t = 1$ ns, whereas at $t = 1$ ns, $I(t)$ and $\Delta d_{001}(t)$ are still decaying with 18% and 6% of the corresponding maximum changes (Fig. 3). This $w(t)$ and $\eta(t)$ behavior indicates that dynamical inhomogeneity has vanished on this time scale. The larger residual $I(t)$ (determined by atomic vibrational motions) relative to that of $\Delta d_{001}(t)$ (affected by excited carriers) is consistent with heat conduction being in general a slower process than carrier diffusion. From the 800-nm data, we find that the residual changes in $I(t)$ and $\Delta d_{001}(t)$ at $t = 1$ ns, for each fluence, have very comparable percentage with respect to their maximum values. It is because more photoinjected carriers are confined within the GaAs layer, and hence, the relaxation becomes more difficult such that $\Delta d_{001}(t)$ recovers relatively slowly, even on a sub-nanosecond time scale.

Concluding Remarks: UEC and Structural Dynamics

In the present work, we have demonstrated the capability of UEC to study structural dynamics with combined atomic-scale spatial and ultrafast temporal resolutions. By monitoring changes of the diffraction features (Bragg spots, intensity, width and its homogeneous contribution) at different times, following an "ultrafast heating" of the material, we are able to map out the nature of atomic motions and the time scales of the processes involved: electronic and nuclear at ultrashort times and diffusion at longer times. Structural changes in the nonequilibrium regime and restructuring toward equilibrium are features that were examined in detail. The kinematic description for diffraction, as provided in Ch. 2, is shown to be sufficient for unraveling structural changes in these condensed-matter studies (thin crystals and relatively low atomic numbers). For this and other reasons, important aspects of the theory needed were highlighted in order to obtain structural and dynamical information from diffraction patterns recorded in the reflection and transmission modes of UEC.

One important general finding of this study, which is relevant to others (*3, 4*), is the universality of the structural–temporal behavior. Typically, following the ultrafast heating through carrier excitation of the material, a large change (for cubic GaAs,

$\Delta d_{001}(t)/a = 0.75\%$ at 800 nm) in lattice expansion is observed on the ultrashort time scale, far beyond any thermal expansion: because $\alpha_l = 5.73\times10^{-6}\ \mathrm{K}^{-1}$, this expansion would translate into a temperature rise of ~1300 K. Similar large changes are observed for the intensity drop and width increase. Moreover, the change occurs with a time constant of ~10 ps, and, remarkably, is highly anisotropic; it occurs in the direction normal to the surface. The anisotropy is the result of accumulated surface stress and lattice-potential change as discussed in Sec. B.2 and below.

For the case studied here, the change is prompt for the intensity drop and the Bragg spot movement, but is delayed by ~7 ps for the width and its homogeneous (Lorentzian) contribution. Following the maximum change, these diffraction features reverse the change and take on values in the direction of pre-heating equilibration. We examined in depth this behavior for GaAs as a prototype system and provided a summary of results of numerous experiments made under different conditions: fluence and wavelength of the heating pulse, angle of incidence for the probing electrons (rocking curves), sample thickness and composition, and detection mode (reflection or transmission). In this regard, the study made here on the quantum-well heterostructure (20-nm GaAs on top of 50-nm $Al_{0.6}Ga_{0.4}As$ over 450-μm GaAs) proved essential because of its nanometer-scale structure and the difference in the band structure (Fig. 1b, inset).

The emerging physical picture of structural dynamics defines the following concepts. A general one refers to the nature of the structure following ultrafast heating: a large nonthermal change in a nonequilibrium state. This state cannot be reached by incoherent thermal heating of atoms. It is reached because the excited carriers of the material lower their energy (through the electron–phonon coupling, $\tau_{\mathrm{e-ph}} \sim 165$ fs) by generating well-defined vibrations of atoms in the unit cell (optical phonons) and such deformations produce, by anharmonic couplings, acoustic waves in a few picoseconds (~7 ps for GaAs). Such deformations lead to large-amplitude motions of the lattice, with a distribution of distances (dynamical inhomogeneity, as opposed to distribution of static structural deformations; see Sec. B.2 of Ch. 2). The wavevector of the acoustic packet is relatively large, for energy and momentum conservation, and its short wavelength makes the change on the scale of lattice spacings. This picture for a semiconductor contrasts that of a metal, with one atom in the primitive unit cell, and for which the carriers directly generate these stresses (forces) of acoustic wave propagation.

The consequences of this nonequilibrium behavior are a large change in lattice spacing (Bragg spot movement) and a large decrease in intensity, both without delay since the vertical optical-phonon deformations occur within 165 fs for each phonon. At our excess energy, 90 such phonons results in a total time of ~15 ps for the maximum change. In contrast, the increase in width (dynamic inhomogeneity), although also large, is delayed by ~7 ps, the time scale for conversion to acoustic waves. This behavior is clearly evident in our UEC results (see Figs. 4 and 6b). It is noted that acoustic wave propagation through a 10-nm material takes only ~2 ps since the speed of sound in GaAs is 4731 m/s along the [001] direction.

Another important concept is what we term potential-driven change and anisotropy. Through this unique heating with "three temperatures" of the electrons, lattice-optical, and lattice-acoustic modes, it is important to emphasize the role of carriers in changing the potential and the associated anisotropy. The initial carriers are prepared with a crystal momentum (wavevector) near the zero value (all phases are positive). However, depending on the band structure, carriers can reach other regions with a different crystal momentum, with a phase combination that characterizes a given lattice direction. Now the atoms experience a different potential of weaker bonding and this antibonding character (± phases) facilitates the subsequent nuclear motion in that direction. Thus, such schemes of excitation open the door to studies of "controlled heating" of nonequilibrium structures. This is to be contrasted with heating of metals with a T jump in a lattice through a two-temperature (electron and lattice) scheme; in such cases, the electrons have a much higher temperature than the lattice because of their poor heat capacity, but they equilibrate with the lattice in 1–2 ps. It is important to realize that heating through carriers, although it might have a much smaller occurrence in thermal experiments, cannot be ignored at steady state (infinite time scale); it is certainly of great significance to femtochemistry of catalysis (*18*), and to electronic structural changes with little or no lattice phonon motion (*45, 46*). In general, the anisotropy will result from the free-surface (in contrast to lateral bulk) expansion due to the temperature/carrier density gradient and the potential-driven (antibonding character) change, and both will be prominent at short times.

Toward equilibration, the structure at ultrashort time cools down primarily by diffusion of carriers at early time and also by thermal diffusion on the nanosecond (and longer) time scale. Energy redistribution among modes will not alter the average energy, but if some modes are selectively probed (or excited), then the redistribution will contribute to the decay. The evidence for carrier diffusion, especially at early times, comes from the fact that thermal diffusion at the two wavelengths studied would have entirely different behavior (Fig. 15) at short time (because of difference in penetration length), contrary to the experimental observation. The observed $1/\sqrt{t}$ behavior (Fig. 14) for the restructuring is also consistent with the diffusion of carriers and its fluence dependence. Heat diffusion occurs at longer time (*54*). In the transmission mode, thermal diffusion is extremely slow in the thin samples used, and indeed, we did not observe restructuring on the sub-nanosecond time scale. We also considered depletion of population by other processes, such as Auger and radiative recombination which scale with density (n^3 and n^2, respectively), but they are negligible particularly on the time scale below hundred(s) of picoseconds.

The observed nonequilibrium dynamics of the quantum-well heterostructure is similar to that of chlorine-terminated GaAs(111) (*4*), except for an early-time behavior in the Bragg spot position. Prior to expansion of the lattice there is a relatively small peak that shows the opposite behavior (Fig. 13b). This upward movement in s space may imply a decrease in lattice spacing, opposite to expectations of heating and carriers' weakening of bonding. However, the presence of a chlorine monolayer changes the surface characteristic. After carriers are excited, chlorine atoms will attract the electrons (electronegativity) and therefore a more repulsive surface potential may result in the formation of a diffraction spot at a slightly higher s value. The duration of this initial behavior may provide the time scale of charge separation, and as it diminishes, the normal downward movement of diffraction spot due to lattice expansion is observed. We cannot exclude the role of chlorine electronegativity in inducing polarization and initial contraction of the lattice.

In this comparison with single-crystal dynamics, the following points are noted. First, the width change obtained for single crystals is similar to that for the quantum-well structure; it is delayed from the intensity change. The apparent delay of the spot position (Fig. 13b) is misleading in view of the two, positive and negative, contributions present. Second, in all these studies, the intensity change and spot movement change are similar in profile, and this excludes the notion that spot movement may be due to an artifact caused by change in electron beam trajectory. This is further confirmed by recording changes of the direct electron beam position which was found to be relatively very small and, if any, occurred in opposite direction (see the Results and Analysis Section), indicating the negligible change of crystal (surface) potential in the presence of the heating pulse. Third, unlike the heterostructure with a well-defined nanometer layer and the absence of the chlorine monolayer, bulk material may exhibit the effect of diffraction/refraction in that, given the grazing reflection geometry, an electron beam incident at a spatial position distant from the heated area may be reflected by the underneath crystal planes and pass through (refracted by) the heated region (of different density from the underneath unexcited/less excited region) while exiting the crystal. This indirect interaction could lead to movement of the spot in the opposite direction but still gives rise to the same temporal profile as that of heating one. Care has to be taken to optimize the spatial and temporal overlaps, which had been fully developed for UEC experiments in our laboratories (see Ch. 3). Finally, it is noted that the thickness of the heated "bulge" is on the order of one angstrom, and the movement of spots is indicative of this expansion. Although such a bulge may have a significant consequence on the beam deflection direction in optical reflection experiments, the angstrom displacement causes a negligible effect to the shadow edge in our geometry.

With the same picture, it is straightforward to understand the phenomenon of ultrafast melting. As discussed earlier (Sec. B.1), at high fluences, both the atomic vibrations, with amplitudes near the Lindemann stability limit, and weakening of the crystal potential are induced. The high density of carriers may seriously affect the stability of the crystal structure, and the induced lattice motion may become too large for the surface to maintain its crystallinity. As a result, melting can be observed in the development of Debye–Scherrer rings, instead of Bragg spots; if surface evaporation occurs, the pattern will disappear. Such an ultrafast melting process is again potential-driven and far from being thermal. For polycrystalline silicon, studies of 2D melting were made with UEC (*3*).

Another study of polycrystalline silicon has also been reported with the use of time-resolved electron diffraction in transmission geometry (*55*). In contrast to the study reported here for single crystals (and quantum wells), whose structural dynamics are from a homogeneous lattice, the polycrystalline silicon dynamics must take into account the inhomogeneity of structures and the influence of this sample morphology on the carrier–lattice interaction. Moreover, the photogenerated carrier density in the reported study (*55*) was about one to two orders of magnitude higher than ours (due to the more efficient excitation and the lack of carrier diffusion), resulting in carrier screening and lengthening of the time scale for the electron–phonon coupling. The overall time scale is a few picoseconds, which is still comparable to our observation made in the transmission mode.

In conclusion, the methodology of UEC opens up new opportunities in the studies of materials and interfaces, as can be seen from the following chapters. The far-from-equilibrium structures observed in UEC cannot be appropriately described either by thermal heat diffusion equations (*53*) or by the thermoelastic models (*56*) because they do not take into account the effect of electronic band structure, and in these models, the lattice temperature is only determined by the absorbed fluence and the electron–lattice equilibrium. According to the present study, by changing to a different semiconductor, or even systematically varying the chemical composition, the electronic band structure may be fine-tuned and used to control the state of nonequilibrium dynamics, e.g., faster response of structural changes along a particular crystal direction. Moreover, the use of heterostructures, or the limiting of substrate dimensions, can restrict carrier diffusion, allowing for the use of the substrate as a constant energy source in the studies of interfaces. In future applications, we will greatly benefit from the many investigations of electron crystallography of static structures in materials and biological systems (*57-60*), and from studies of surfaces made on longer time scales (*54*).

Appendix A. Amplitude of Vibrational Motion

The amplitude of the vertical Ga–As vibration (optical phonon) responsible for the intensity reduction of the (008) Bragg spot can be estimated using the structure factor

$$F(008) = f_{\mathrm{Ga}}\exp(-16\pi i z_{\mathrm{Ga}}) + f_{\mathrm{As}}\exp(-16\pi i z_{\mathrm{As}}).$$

Here, two approximations are made to simplify the calculation. First, the mass difference between Ga and As (atomic weight: 69.7 vs 74.9) is neglected, and therefore the two atoms oscillate around the equilibrium positions symmetrically, i.e., $z_{\mathrm{Ga}} = +\delta_z$ and $z_{\mathrm{As}} = 1/4 - \delta_z$ where δ_z is the vertical displacement (relative to the unit-cell length) of the atoms and the 1/4 is the relative position in the unit cell, i.e., (0, 0, 0) for Ga and (1/4, 1/4, 1/4) for As. Second, because of their similar atomic numbers, the atomic scattering factors f_{Ga} and f_{As} will be considered equal. Thus, the (008) spot intensity becomes $|F(008)|^2 = 4|f_{\mathrm{Ga/As}}|^2\cos^2(16\pi\delta_z)$ for different δ_z values; the thermal Debye–Waller damping is not included. The time dependence is in δ_z.

For a harmonic motion, i.e., when $\ddot{\delta}_z = -\omega^2\delta_z$, we have $\delta_z = \delta_z^{\max}\sin(\omega t)$ and it follows that $\mathrm{d}\delta_z = -\omega\,[(\delta_z^{\max})^2 - \delta_z^2]^{1/2}\,\mathrm{d}t$, where $\delta_z^{\max}$ is the maximum value of vibrational amplitude. We now can calculate the average (over half a period, since ω^{-1} is shorter than temporal resolution considered) of $|F(008)|^2$ which is given by

$$<|S(008)|^2> \propto <\cos^2(16\pi\delta_z)> = \int_{-\delta_z^{\max}}^{\delta_z^{\max}} \cos^2(16\pi\delta_z)\frac{dt}{d\delta_z}\,d\delta_z \Big/ \int_{-\delta_z^{\max}}^{\delta_z^{\max}} \frac{dt}{d\delta_z}\,d\delta_z$$

which is equal to $[1 + J(0, 32\pi\delta_z^{\max})]/2$, where J is the Bessel function of the first kind. The experimental diffraction intensity drop, $I(t)/I_0$, is given by the average $\langle\cos^2(16\pi\delta_z)\rangle$. Given that $I(t{=}25\text{ps})/I_0 \sim 70\%$ the amplitude $\delta_z^{\max} = 0.0169$ is obtained, which, when multiplied by the lattice constant ($a = 5.653$ Å), gives the real-space maximum displacement of 0.0955 Å. It is the additional (from thermal; $[\langle u^2\rangle_{\text{thermal}}/3]^{1/2} = 0.0728$ Å) vertical displacement acquired by ultrafast heating. It is interesting that this value is very close to $\Delta d_{001}^{\max}$ measured at 800 nm.

Appendix B. Radiative and Auger Recombination

Radiative recombination of carriers reduces not only the number of carriers but also the total energy in the carrier subsystem because the emitted photons carry energy away. The process is described by the equation $\dot{n} = \dot{p} = -B\,n\,p$, where n (p) is the density of electrons (holes) in the conduction (valence) band, and B is the bimolecular radiative recombination coefficient whose value is typically on the order of 10^{-10} cm^3/s at room temperature (*61, 62*). It follows that the radiative decay rate $1/\tau_{\text{rad}}$ is given by Bn which, for an initial density of 10^{19} cm^{-3} (*53*), is ~10^9 s^{-1}. In 1 ps, the population decay will be negligible ($10^{19} - 10^{16} \sim 10^{19}$ cm^{-3}) Note that using carrier densities of order higher than 10^{19} cm^{-3} to calculate the rate will lead to false estimation because radiative recombination mostly occurs around the Γ valleys due to momentum conservation. In the case of 266-nm excitation, even though larger carrier densities may be created initially, their distribution over a much larger phase space and the band-filling effect exclude the possibility of having a faster radiative recombination rate; relaxation of electrons to Γ_{6c} becomes the rate-determination step but is blocked due to the Pauli exclusion principle by a filled quasi-steady-state valley. For an indirect-gap semiconductor material like Si, the rate will be even slower because the recombination requires the assistance of phonons. Hence, in general, radiative recombination has a negligible effect on the dynamics within the first nanosecond, a temporal range on which UEC focuses.

The nonradiative Auger recombination decreases the carrier density but retains the total energy, and the average energy of the remaining carriers increases. This process can be described by the equation $\dot{n} = -C_p np^2 - C_n n^2 p$, where the coefficients C_p and C_n denote the Auger processes in the valence band and conduction band, respectively. Due to momentum conservation, those recombination events that involve crystal-momentum ranges other than the Γ valley will be less probable (*62*). Thus, through similar simple estimation, the Auger recombination rate is deduced to be $1/\tau_{\text{Auger}} \sim C_{\text{eff}}\, n^2 \sim 10^9\ \text{s}^{-1}$ for an initial density near Γ of $\sim 10^{19}\ \text{cm}^{-3}$ and C_{eff} of $7\times10^{-30}\ \text{cm}^6/\text{s}$ (*62*). This rate may be increased appreciably if the semiconductor materials are subject to very high fluences (*24*). However, for a UEC study in which the recovery of the system is necessary, such regimes are not desirable, so the Auger processes are expected to be on the sub-nanosecond time scale or slower. As discussed in Text, such a carrier relaxation mechanism does not interfere with the structural dynamics at early times.

References:

1. A. H. Zewail, *Annu. Rev. Phys. Chem.* **57**, 65 (2006).

2. R. Srinivasan, V. A. Lobastov, C.-Y. Ruan, A. H. Zewail, *Helv. Chim. Acta* **86**, 1763 (2003).

3. C.-Y. Ruan, F. Vigliotti, V. A. Lobastov, S. Y. Chen, A. H. Zewail, *Proc. Natl. Acad. Sci. USA* **101**, 1123 (2004).

4. F. Vigliotti, S. Y. Chen, C.-Y. Ruan, V. A. Lobastov, A. H. Zewail, *Angew. Chem. Int. Ed.* **43**, 2705 (2004).
5. C.-Y. Ruan, V. A. Lobastov, F. Vigliotti, S. Y. Chen, A. H. Zewail, *Science* **304**, 80 (2004).
6. S. Chen, M. T. Seidel, A. H. Zewail, *Proc. Natl. Acad. Sci. USA* **102**, 8854 (2005).
7. M. T. Seidel, S. Chen, A. H. Zewail, *J. Phys. Chem. C* **111**, 4920 (2007).
8. S. Chen, Ph.D. thesis, California Institute of Technology (2007).
9. D. von der Linde, *Annu. Rev. Mater. Sci.* **18**, 75 (1988).
10. J. Shah, *Ultrafast spectroscopy of semiconductors and semiconductor nanostructures* (Springer, Berlin, 2nd enlarged ed., 1999).
11. A. Konkar, S. Y. Lu, A. Madhukar, *Nano Lett.* **5**, 969 (2005).
12. N. Cavassilas, F. Aniel, K. Boujdaria, G. Fishman, *Phys. Rev. B* **64**, 115207 (2001).
13. M. E. Levinshtein, S. L. Rumyantsev, in *Handbook series on semiconductor parameters,* M. E. Levinshtein, S. L. Rumyantsev, M. Shur, Eds. (World Scientific, Singapore, 1996).
14. M.-G. Kang, S.-H. Sa, H.-H. Park, K.-S. Suh, K.-H. Oh, *Thin Solid Films* **308-309**, 634 (1997).
15. M. I. Kaganov, I. M. Lifshitz, L. V. Tanatarov, *Sov. Phys.-JETP* **4**, 173 (1957).
16. S. I. Anisimov, B. L. Kapeliovich, T. L. Perel'man, *Sov. Phys.-JETP* **39**, 375 (1974).
17. J. Hohlfeld *et al.*, *Chem. Phys.* **251**, 237 (2000).
18. G. Ertl, *Adv. Catal.* **45**, 1 (2000).
19. A. Othonos, *J. Appl. Phys.* **83**, 1789 (1998).
20. J. A. Kash, J. C. Tsang, J. M. Hvam, *Phys. Rev. Lett.* **54**, 2151 (1985).
21. H.-J. Polland, W. W. Rühle, K. Ploog, C. W. Tu, *Phys. Rev. B* **36**, 7722 (1987).

22. T. Sjodin, H. Petek, H.-L. Dai, *Phys. Rev. Lett.* **81**, 5664 (1998).

23. A. J. Sabbah, D. M. Riffe, *Phys. Rev. B* **66**, 165217 (2002).

24. S. K. Sundaram, E. Mazur, *Nat. Mater.* **1**, 217 (2002).

25. Y. H. Lee *et al.*, *Phys. Rev. Lett.* **57**, 2446 (1986).

26. J. S. Blakemore, *J. Appl. Phys.* **53**, R123 (1982).

27. F. Kadlec, H. Němec, P. Kužel, *Phys. Rev. B* **70**, 125205 (2004).

28. E. J. Yoffa, *Appl. Phys. Lett.* **36**, 37 (1980).

29. J. F. Young, H. M. van Driel, *Phys. Rev. B* **26**, 2147 (1982).

30. L. Huang, J. P. Callan, E. N. Glezer, E. Mazur, *Phys. Rev. Lett.* **80**, 185 (1998).

31. A. Dargys, J. Kundrotas, *Handbook on physical properties of Ge, Si, GaAs and InP* (Science and Encyclopedia Publishers, Vilnius, Lithuania, 1994).

32. D. E. Aspnnes, A. A. Studna, *Phys. Rev. B* **7**, 4605 (1973).

33. M. Alouani, L. Brey, N. E. Christensen, *Phys. Rev. B* **37**, 1167 (1988).

34. A. D. Yoffe, *Adv. Phys.* **42**, 173 (1993).

35. J. A. Kash, J. C. Tsang, in *Spectroscopy of nonequilibrium electrons and phonons,* C. V. Shank, B. P. Zakharchenya, Eds. (North-Holland, Amsterdam, 1992).

36. D. von der Linde, J. Kuhl, H. Klingenberg, *Phys. Rev. Lett.* **44**, 1505 (1980).

37. J. J. Baumberg, D. A. Williams, K. Köhler, *Phys. Rev. Lett.* **78**, 3358 (1997).

38. D. M. Pennington, C. B. Harris, *IEEE J. Quantum Electron.* **28**, 2523 (1992).

39. J. Shah, *Hot carriers in semiconductor nanostructures : Physics and applications* (Academic Press, Boston, 1992).

40. J. Shah *et al.*, *Phys. Rev. Lett.* **59**, 2222 (1987).

41. D. Y. Oberli, J. Shah, T. C. Damen, *Phys. Rev. B* **40**, 1323 (1989).

42. E. J. Yoffa, *Phys. Rev. B* **23**, 1909 (1981).

43. F. A. Lindemann, *Phys. Z.* **11**, 609 (1910).

44. J. F. Vetelino, S. P. Gaur, S. S. Mitra, *Phys. Rev. B* **5**, 2360 (1972).

45. P. Saeta, J. K. Wang, Y. Siegal, N. Bloembergen, E. Mazur, *Phys. Rev. Lett.* **67**, 1023 (1991).

46. N. Bloembergen, in *Laser ablation: Mechanisms and applications II,* J. C. Miller, D. B. Geohegan, Eds. (American Institute of Physics Conference Proceedings 288, Woodbury, New York, 1994), pp. 3-10.

47. A. Rousse, C. Rischel, J.-C. Gauthier, *Rev. Mod. Phys.* **73**, 17 (2001).

48. C. Bressler, M. Chergui, *Chem. Rev.* **104**, 1781 (2004).

49. A. M. Lindenberg *et al.*, *Science* **308**, 392 (2005).

50. M. Bargheer, N. Zhavoronkov, M. Woerner, T. Elsaesser, *Chemphyschem* **7**, 783 (2006).

51. B. J. Siwick, J. R. Dwyer, R. E. Jordan, R. J. D. Miller, *Chem. Phys.* **299**, 285 (2004).

52. S. H. Nie, X. Wang, H. Park, R. Clinite, J. M. Cao, *Phys. Rev. Lett.* **96**, 025901 (2006).

53. J. H. Bechtel, *J. Appl. Phys.* **46**, 1585 (1975).

54. H. E. Elsayed-Ali, P. M. Weber, in *Time-resolved diffraction,* J. R. Helliwell, P. M. Rentzepis, Eds. (Oxford Univ. Press, Oxford, 1997), pp. 284.

55. M. Harb *et al.*, *J. Phys. Chem. B* **110**, 25308 (2006).

56. C. Thomsen, H. T. Grahn, H. J. Maris, J. Tauc, *Phys. Rev. B* **34**, 4129 (1986).

57. J. M. Thomas, *Angew. Chem. Int. Ed.* **43**, 2606 (2004).

58. D. L. Dorset, *Z. Kristallogr.* **218**, 237 (2003).

59. D. L. Dorset, *Acta Cryst. B* **52**, 753 (1996).

60. T. E. Weirich, J. L. Lábár, X. Zou, Eds., *Electron crystallography : Novel approaches for structure determination of nanosized materials*, (Springer, Dordrecht, Netherlands, 2006).
61. E. Yablonovitch, T. J. Gmitter, R. Bhat, *Phys. Rev. Lett.* **61**, 2546 (1988).
62. U. Strauss, W. W. Ruhle, K. Kohler, *Appl. Phys. Lett.* **62**, 55 (1993).
63. J. Singh, *Electronic and optoelectronic properties of semiconductor structures* (Cambridge Univ. Press, Cambridge, 2003), pp. 241-243.

Chapter 5

Correlated Unidirectional Behavior in Zinc Oxide Nanowires[†]

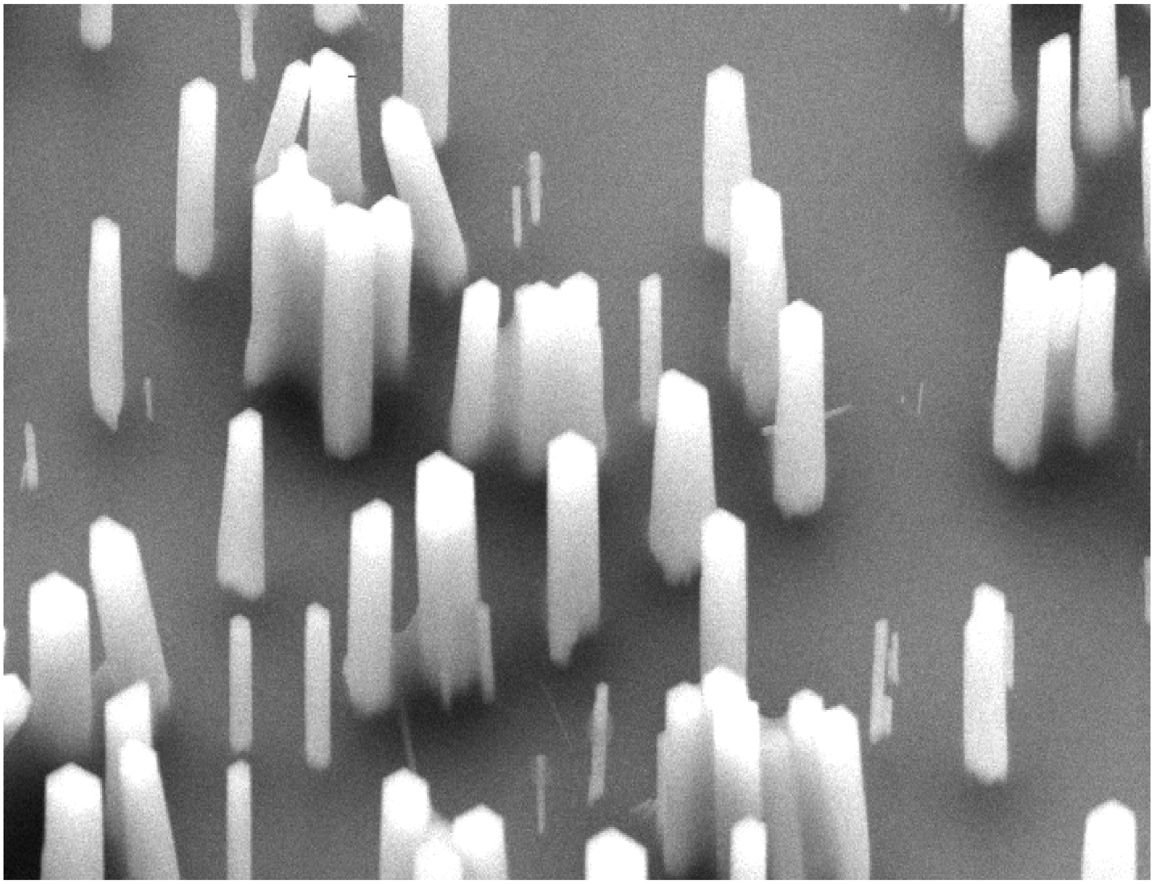

[†] adapted from D.-S. Yang, C. Lao, A. H. Zewail, *Science* **321**, 1660 (2008).

Introduction

Major changes in the physical, chemical or optical properties of a substance can occur as a result of shrinking dimension and changing morphology down to the nanometer scale, primarily because of quantum confinement and surface effects. Quantum dots and nanotubes are examples of such structures, which have the potential for a variety of applications (for reviews, see Refs. 1–7). Among the materials that show promising features for optoelectronics, such as blue-green laser diodes and photonic devices, the wide-gap semiconductor zinc oxide (ZnO) has been one of the most investigated nanowire materials (*8, 9*). At the nanoscale, design of such structures requires fundamental understanding of electronic and nuclear degrees of freedom in the unique nanowire architecture, because they control the effective carrier mobility and properties along the wires. With optical methods (for a review, see Ref. 10), the transient response can be probed, but, because of the wavelengths involved, the atomic-scale structural changes are not determined; electrons of the appropriate wavelength provide the means for the visualization of both.

In this chapter, I present the visualization of the structure and dynamics of vertically aligned ZnO nanowires using ultrafast electron crystallography (UEC). Their unique pancake-type diffraction is the result of the ordered structure together with electron refraction due to the shape of the hexagonal rod-like nanowires. Following electronic excitation of this wide-gap photonic material, the wires were found to exhibit colossal expansions, two orders of magnitude higher than that expected at thermal equilibrium. The expansion is highly anisotropic, a quasi-one-dimensional behavior, and is facilitated by the induced antibonding character. By reducing the density of nanowires, the expansions reach even larger values and occur at shorter times, suggesting a decrease of

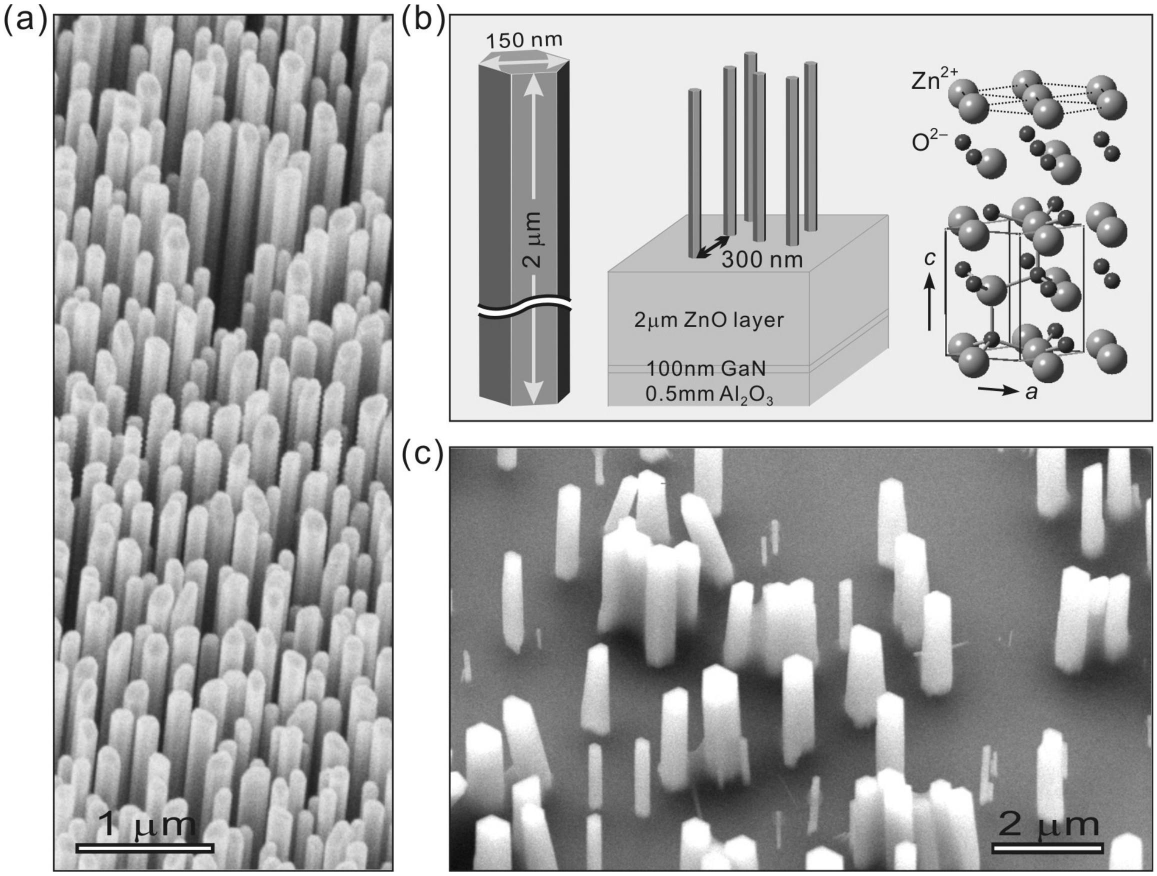

Fig. 1. Scanning electron micrographs and structure of ZnO nanowires. (a) The SEM image of the array fabricated through physical vapor deposition. The high-density wires are vertically aligned. Gold nanoparticles may be present dispersively as a result of the catalyst-assisted synthesis (*11*). (b) The structure (from the known inorganic crystal structure database) together with a schematic showing the average diameter and length of a single wire, the average spacing between wires, and the layer composition below the ZnO array sample. (c) The SEM image of the array fabricated through hydrothermal synthesis. The vertically aligned wires are thicker, on the average, and form an array with a much lower density. No gold nanoparticles are present in the nanowires, since a metallic catalyst is not required for this wet-chemistry synthesis method (*12*).

the structural constraint in transient atomic motions. This unanticipated ultrafast carrier-driven expansion highlights the optoelectronic consequences of nanometer-scale morphologies.

Materials and Experimental Section

The nanowire array was synthesized via a bottom-up process of physical vapor deposition (*11*). A single-crystal sapphire of $(11\bar{2}0)$ surface with a 100-nm GaN layer (grown by metal-organic chemical vapor deposition) was used as the collection substrate. Reaction parameters such as the chamber pressure, temperature and the gas flow rate were varied to obtain the nanowires, which were supported by a ~2-μm layer of ZnO on the substrate, were obtained as a vertically aligned array. As shown in Fig. 1, panels a and b, the wires have an average diameter of ~150 nm, a length of ~2 μm, and an average spacing of ~300 nm. We also studied nanowires prepared by an entirely different method [hydrothermal synthesis (*12*)], and for this case the density of wires is notably lower, as seen in Fig. 1c. Both specimens were characterized by scanning electron microscopy (SEM) (Fig. 1, panels a and c); transmission electron microscopy and X-ray diffraction measurements have also been used to characterize the products of the two aforementioned methods (*11, 12*).

Electron packets at near grazing angles ($\theta_{\text{in}} = 2.7°$) were invoked in our UEC apparatus. A heating pulse preceded in time the electron packet and was used to excite the carriers of the wires. Frames of the far-field diffraction were recorded at different delay times and with the scheme of pulse tilting (for velocity mismatch compensation), which enabled the reported spatiotemporal resolution (*13-16*). Within the experimental repetition period of 1 ms, the sample at room temperature fully recovers to the initial

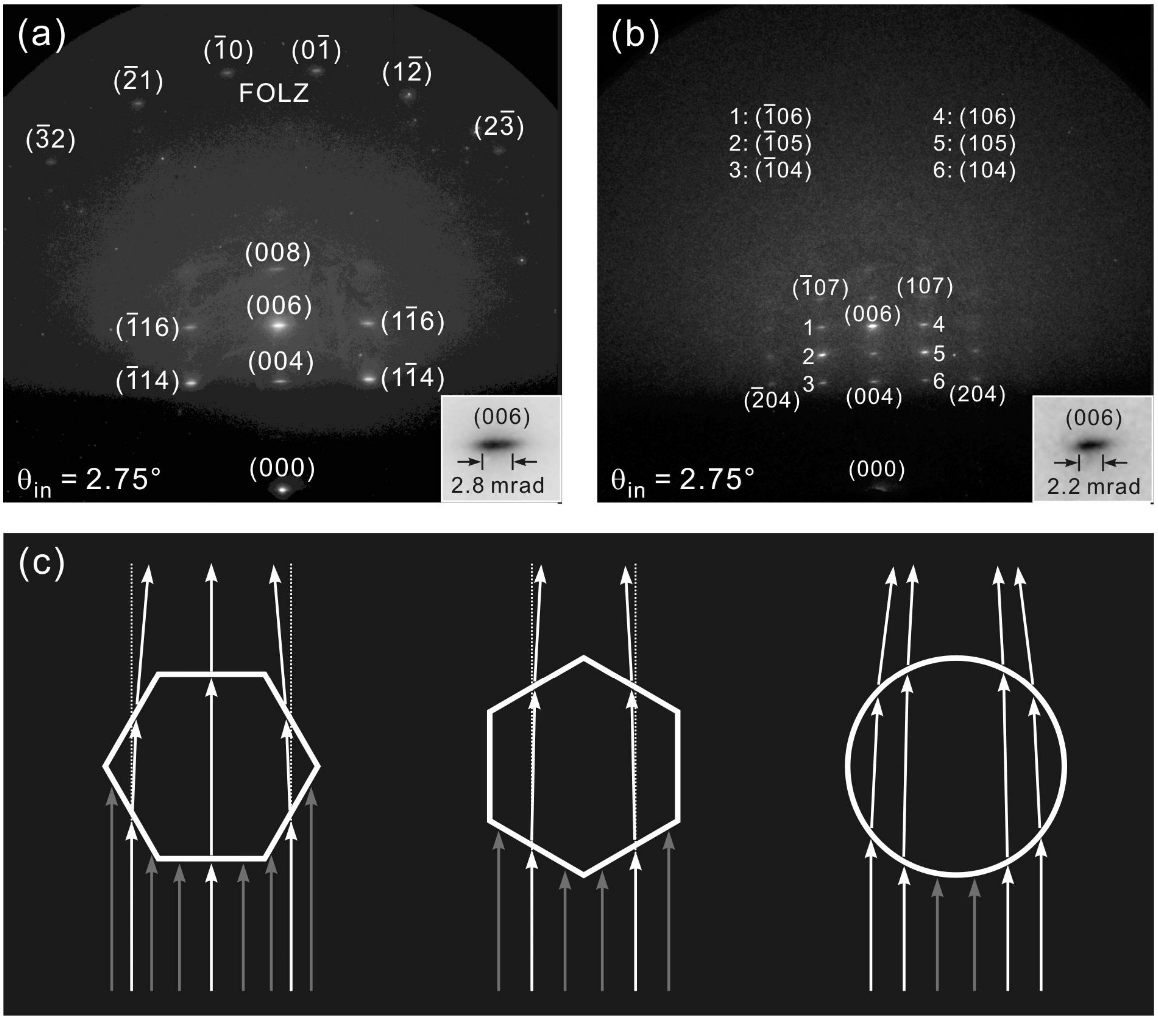

Fig. 2. Pancake-type diffraction and the shape effect of nanowires. The diffraction patterns were obtained at an incidence angle of $\theta_{\text{in}} = 2.75°$, with the electron beam propagating along the [110] direction (a) and the [100] direction (b). From the well-indexed Bragg spots and FOLZ diffractions, the wurtzite ZnO structure is determined; the undiffracted (unblocked) electrons form the (000) spot. The insets show the enlarged horizontal width of the (006) Bragg spot. (c) Refraction of the probing electrons at the vacuum/material interface, and the overall beam deflection caused by the different orientations and geometries of a nanowire (top view).

ground state. This recovery was confirmed by observing no change in the diffraction patterns whether recorded at negative delay time (an effective 1-ms delay) or without the excitation. From the observed intensities, positions, and widths of the Bragg diffractions, we obtained the change of atomic positions with time, the structural factor, and the transient inhomogeneity in the wires. The initial rise of signals was checked by using time delays of 2 ps. The polarization was parallel to the cross section of wires, and in order to ensure uniform excitation of the target region, the electron-probed area on the sample was kept relatively small (~1 mm versus 3 mm for the full-width of the heating-pulse footprint at half maximum). By varying the fluence, the influence of carrier density on structural dynamics was examined, and in this case the wires were directly excited. The maximum optical fluence applied was 22.5 mJ/cm^2. Finally, by using two arrays of nanowires, the effect of their packing density on the substrate was elucidated.

Nanowire Structure and Electron Diffraction

The static structure of the ZnO nanowires without the optical excitation was determined by recording the diffraction patterns at different incidence angles (rocking curves); patterns of two zone axes are given in Fig. 2, panels a and b. With the electron beam propagating along the [110] direction, the patterns consist of both the Bragg spots and the first-order-Laue-zone (FOLZ) diffractions (*17*), and all have horizontally elongated ("pancake") shapes, as seen in Fig. 2a. With a 30° rotation of the specimen, the electron beam becomes directed along the [100] axis, and we only observe the Bragg spots at a larger incidence angle; this is because the FOLZ diffractions are out of the camera region (Fig. 2b). The spacings between the diffraction spots (from the center of the pancakes) translate to the lattice constants of $a = b = 3.25(0)$ Å and $c = 5.20(8)$ Å, entirely consistent with the values for a wurtzite structure of ZnO crystals obtained by x-ray diffraction and calculations (*10, 18*).

The pancake horizontal shape of the Bragg spots (Fig. 2, insets of panels a and b) is distinct from the spots seen in bulk crystal diffraction and mirrors the hexagonal nanostructured wire. Because of the wires' nanometer-scale geometry and the attractive inner potential (V_I) inside the material, the diffracted electron beam is refracted and gives rise to a horizontal spread. Quantitatively, this geometry effect can be described by considering the analogue of Snell's law in optics (*19*), giving:

$$\sin\theta_{\mathrm{vac}} = \left(1 + eV_\mathrm{I}/E_\mathrm{k}\right)^{1/2} \sin\theta_\mathrm{I}\,, \tag{1}$$

where θ_{vac} and θ_I are, respectively, the angles in the vacuum and inside the wires, with respect to the surface normal, and E_k is the kinetic energy of the incident electron, which is 30 keV in our case (see also Sec. A.4.3 of Ch. 2). In general, when the surface layers are parallel and $eV_\mathrm{I} << E_\mathrm{k}$, as in typical UEC experiments (see, e.g., Chs. 4, 6 and 7), this effect is negligible, but for the nanowires the situation is different (see Fig. 2c), and the refraction can be invoked to obtain the geometry of the wires.

Here, we should emphasize that the direct electron beam has a horizontal FWHM of ~1.8 mrad on the camera screen, which is smaller than the observed spreads of 2.8 and 2.2 mrad for the two orientations. Given the relatively large diameter of the nanowires (~150 nm), the Scherrer-type broadening [$D\cdot\Delta s \sim 1$ where D is the particle size and Δs is the scattering spread on the screen (*20*); see also Eq. 23 of Ch. 2] is only <0.05 mrad. Most importantly, the vertical width of Bragg spots is much narrower than the horizontal one for the same electron beam used (Fig. 2).

For a hexagonal wire, with the two orientations of 30° rotation difference (Fig. 2c,

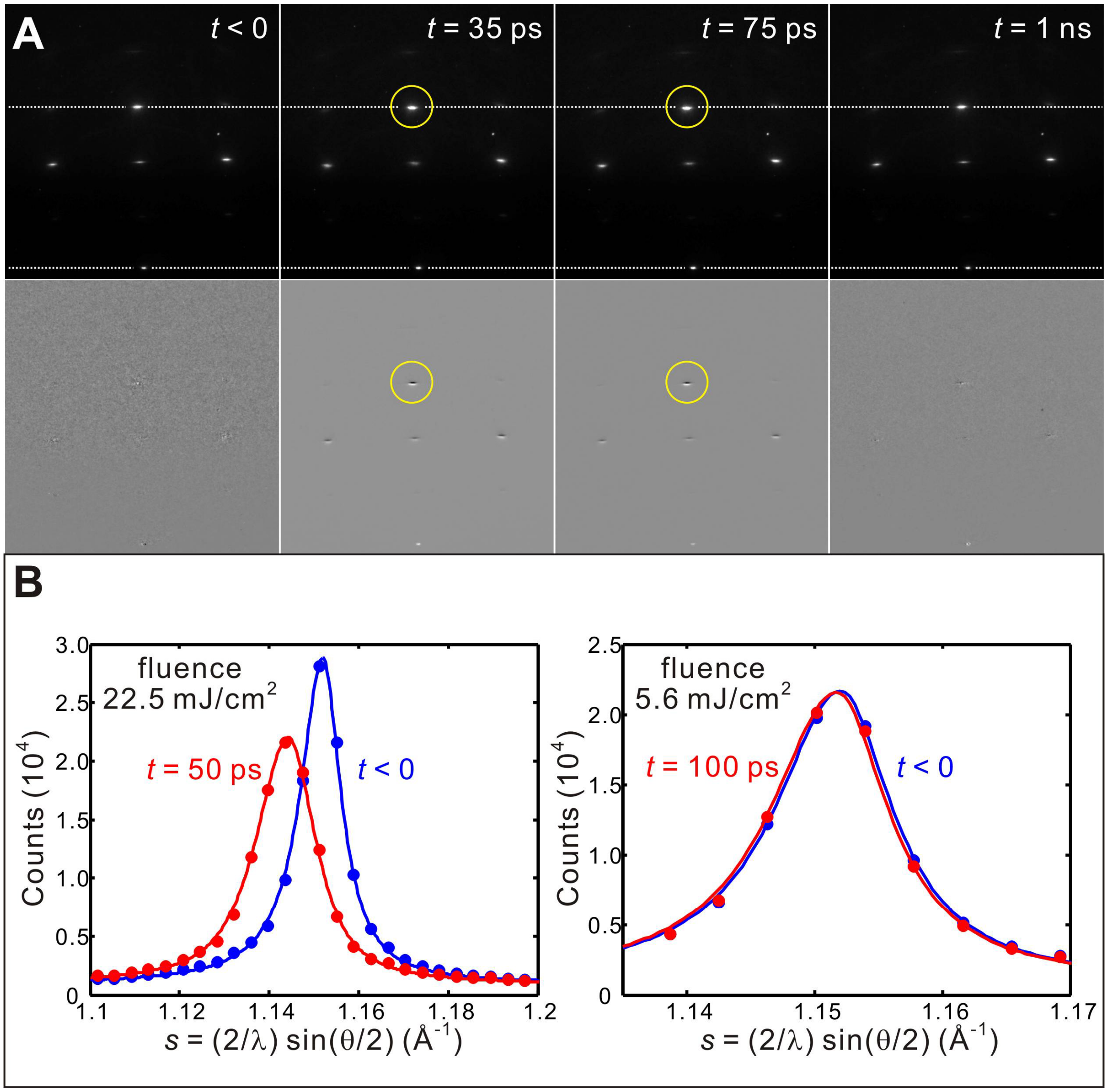

(See next page for the figure caption.)

Fig. 3 (a) Diffraction images (upper panel) and differences (lower panel) at selective delay times. In the original images, the movement of the (006) spot can be seen (yellow circles); the upper dashed line indicates its initial vertical position before excitation. Stationary nature of the (000) direct beam (referenced by the lower dashed line) is evident. The diffraction spots move downward at early times, as indicated by intensity losses (black) at the original positions and gains (white) at lower positions; at longer time the disappearance of diffraction difference signifies the recovery of the excited ZnO nanowires. (b) Vertical cross section of diffraction profiles for the (006) Bragg spot and the fits to pseudo-Voigt functions, at two selective delay times (blue and red), and at the highest (left panel) and lowest (right panel) fluences used. Here, s is the scattering vector and θ is the total deflection angle from the direct beam to the diffraction spot. Temporal evolution of the peak position, intensity and width was obtained from the fits at different delay times. The small shift of the diffraction peak at the lowest fluence well demonstrates the sensitivity of the UEC detection (see Fig. 4b).

left and middle panels), there are two angles of deflection, $\sqrt{3}\,V_{\mathrm{I}}/E_{\mathrm{k}}$ and $V_{\mathrm{I}}/\sqrt{3}E_{\mathrm{k}}$, respectively. Thus, the intensity profile of the pancake is the sum of the contributions from the center and the two sides of the hexagon. For a cylindrical wire (Fig. 2c, right), the intensity profile is determined by the deflections, $\tan\theta_{\mathrm{vac}}(V_{\mathrm{I}}/E_{\mathrm{k}})$, with a width which resembles the case shown on the left of Fig. 2c. The difference between the two geometries is easy to discern: if circular, the rotation of the nanostructure would give no variation in the horizontal spot width, which is inconsistent with the experimental observation. For ZnO, the inner potential V_{I} is 15.9 V (*21*). With the camera being 16.8 cm away from the nanowires, additional diffraction intensities near ±0.92 mrad (Fig. 2c, left) and ±0.31 mrad (Fig 2c, middle) result in the horizontal spread from the spot center. Accordingly, this shape effect properly accounts for the observations made for the two zone axes (Fig. 2, panels a and b). Moreover, from the fact that the probing direction in Fig. 2a is [110] we determine the facets of nanowires to be of {110}, which is again consistent with the preferential growth (*11*). It should be noted that the vertical spot width did not increase, a consequence of the unique elongated geometry.

Laser-induced Dynamics of ZnO Nanowires

Structural dynamics of the wires were obtained from the diffraction frames at different delay times, following the optical excitation. The intensity decrease and vertical spot movement for each Bragg spot were evident in the diffraction. While all of the diffraction spots move downward at early times and recover the original positions at longer times, the unblocked (undiffracted) direct beam did not change, thus eliminating the possibility of surface charging or surface potential change at all fluences used (Fig. 3a; in a later section, we shall address an issue raised with regard to the extent of movement

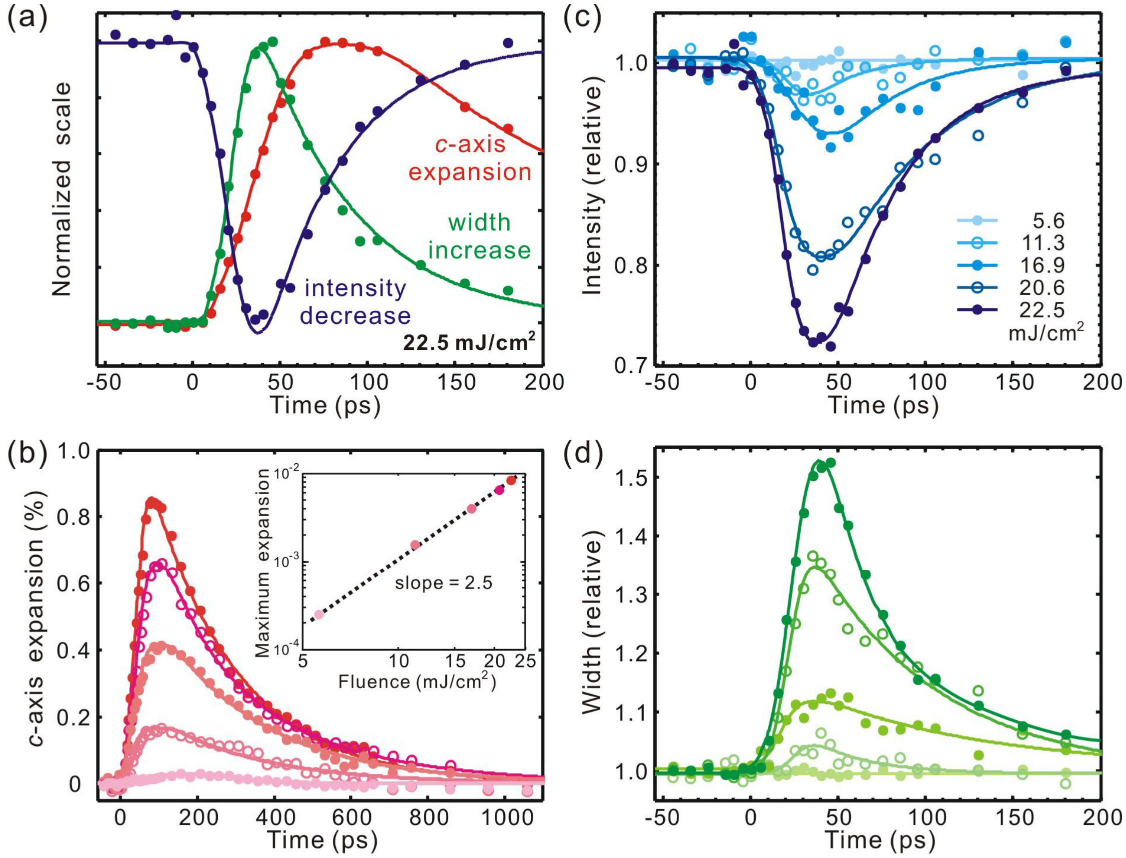

Fig. 4. Structural dynamics. Changes of the *c*-axis expansion, diffraction intensity and width of the (006) Bragg spot with time and at different excitation fluences. All solid lines are fits to the data. (a) The intensity decrease (blue dots) and width increase (green dots) behave similarly, and precede the buildup of structural expansion (red dots). In ~200 ps the former two diffraction features almost recover the original values, whereas the decay of expansion appears on a longer (nanosecond) time scale. (b) A significantly larger *c*-axis expansion was obtained at higher excitation fluences. The fitted slope in the log–log plot (inset) indicates that the maximum expansion is proportional to the fluence to the power of 2.5. At all fluences, however, the expanded nanowires nearly return to their original structure in ~1 ns. (c and d) A more significant intensity decrease and a larger width increase are observed following a stronger excitation. At the lowest fluence used, however, no appreciable diffraction changes are observed.

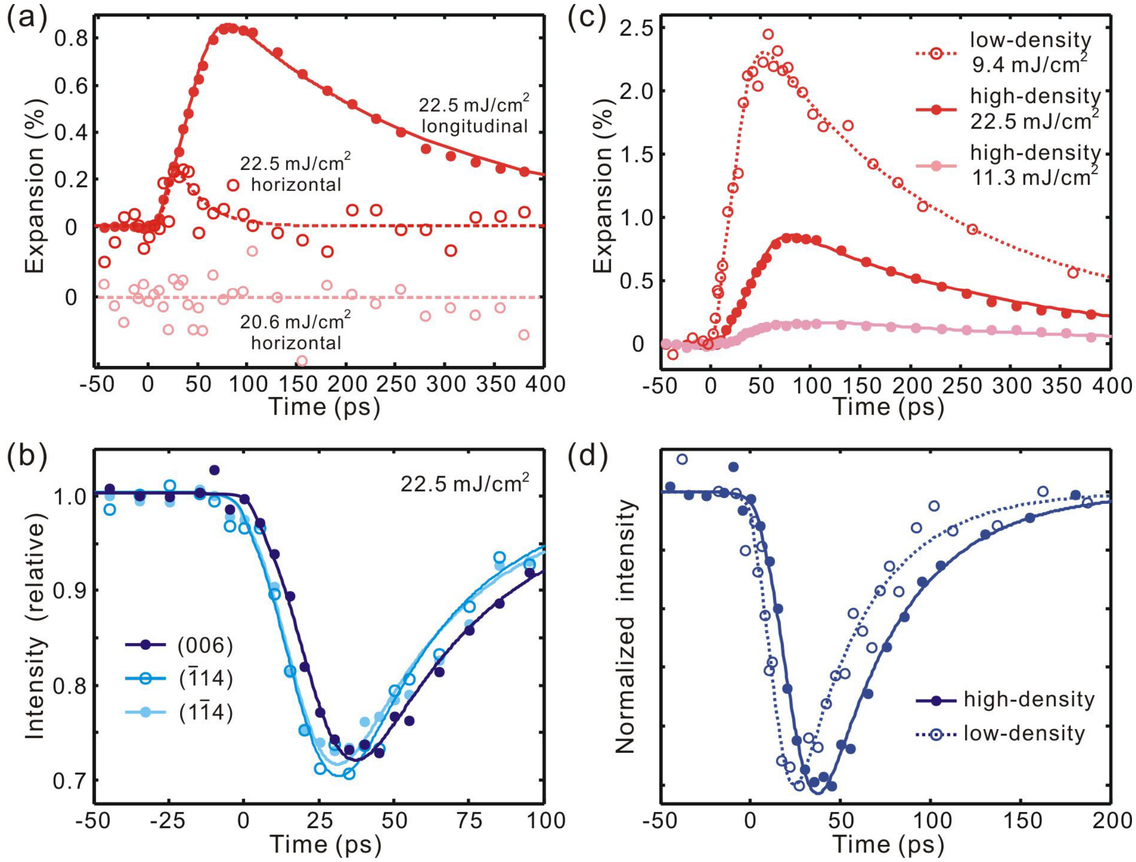

Fig. 5. Anisotropic expansions and density effect. Comparison between the longitudinal and horizontal structural dynamics and between the longitudinal dynamics obtained for the high- and low-density arrays. (a) Horizontal expansion of a wire (open circles) obtained from the horizontal spacing between $(\bar{1}14)$ and $(1\bar{1}4)$ Bragg spots; it is much smaller when compared to the longitudinal expansion (dots), and is only seen at our highest fluence. It also exhibits a faster decay. (b) The intensities of $(\bar{1}14)$ and $(1\bar{1}4)$ spots decrease at earlier time than that of the (006); their temporal behaviors are alike, however. (c and d) Longitudinal expansion and diffraction intensity of the low-density array (open circles) share similar overall temporal evolution with those from the high-density array (dots), but rise on a faster time scale. Even at a smaller excitation fluence, the *c*-axis expansion of the wires in the low-density array is significantly larger than that obtained at higher fluences for the high-density array (c).

for different spots). Quantitative analysis was carried out by fitting the vertical and horizontal intensity profiles of Bragg spots with a pseudo-Voigt function, yielding temporal evolution profiles not only of the spot intensities and positions but also of the widths (Fig. 3b). Because of the high signal-to-noise ratio and the high order of diffraction, the *c*-axis expansion (deduced from the spot vertical position) can be determined with an accuracy of 0.007%; the diffraction intensity and peak width standard deviations are 0.75% and 1.2%, respectively (see the data in Figs. 4 and 5). The sensitivity of our UEC apparatus allows for detection of small diffraction changes as seen in Fig. 4, panels b to d, for the low fluence cases. Typical behavior is shown for the (006) spot: whereas the intensity and vertical width are very similar in behavior and nearly recover (Fig. 4a) in only 200 ps, the rise of expansion along the *c*-axis is delayed in time by ~15 ps and decays on a much longer time scale, reaching completion in about 1 ns.

The fluence dependence of the expansion, intensity and width indicates the role of the (electron-hole) carriers. When the maximum *c*-axis expansion is plotted as a function of fluence in a log–log plot, the dependence follows a linear relationship with a slope value of 2.5 (Fig. 4b, inset). The energy of the excitation photon is less than half of the energy gap of ZnO (3.37 eV) (*10, 18*), and also less than half of the energy gap of wurtzite GaN (3.44 eV) (*11*). Thus, the carriers are generated in the ZnO nanowires by energetically allowed three-photon excitation (3PA) and/or by enhanced two-photon absorption (2PA), both of which are due to the geometry of the nanostructure. We failed to observe diffraction changes when the experiments were repeated on a single-crystal ZnO sample (0.5 mm thick) at the highest fluence, suggesting a significant change in the band gap/carrier density in the wires.

Based on the band structure of ZnO (*18*), the excitation by 2PA generates carriers of somewhat lower energy than the band gap in the Γ region where the momentum is zero; by 3PA, the above-gap excitation becomes possible in the Γ−M(K) regions with momentum along ⟨110⟩ (⟨100⟩). We found consistent studies in the literature. It has been reported that for ZnO crystals, the 2PA is negligible; the 3PA is weak, with a coefficient of ~0.01 $\mathrm{cm}^3/\mathrm{GW}^2$ and saturation intensity of tens of $\mathrm{GW/cm}^2$ at 800 nm (*22, 23*). The vertically aligned ZnO wires exhibit significant enhancement of optical nonlinearities: the 2PA coefficient (α_2) is greater than 10^3 cm/GW (*24, 25*) and the wires show strong 3PA at high excitation intensities (*26*). The increased multiphoton absorption has been attributed to the local-field enhancement due to the surface states and the interaction between the aligned wire facets (*24*). Using the 2PA coefficient of $\alpha_2 \sim 4\times10^3$ cm/GW the effective penetration depth at an intensity of $I = 75\ \mathrm{GW/cm}^2$ is ~33 nm. However, because of saturation, this length can reach micrometers, which results in a more uniform excitation of the wires.

The change of the expansion, intensity and width at different fluences rises after the zero of time and reaches the maximum value nearly at the same time, also consistent with the fact that the wires were directly excited and not heated through a substrate with energy transport through the wire. The temporal evolution profiles of the lattice expansion, intensity and width can be fitted with the following formula, *M*(*t*), convoluted with our instrumental Gaussian response function (*27*),

$$M(t) = A\cdot\left[\exp\left(-\frac{t}{\tau_{decay}}\right)-\exp\left(-\frac{t}{\tau_{rise}}\right)\right]+A(0)\quad \text{for } t>0,$$

$$= \qquad A(0) \qquad \text{for } t<0$$

where A and $A(0)$ are the amplitudes from the induced structural change and at negative times, respectively, and τ_{rise} and τ_{decay} are the time constants for the rise and decay parts

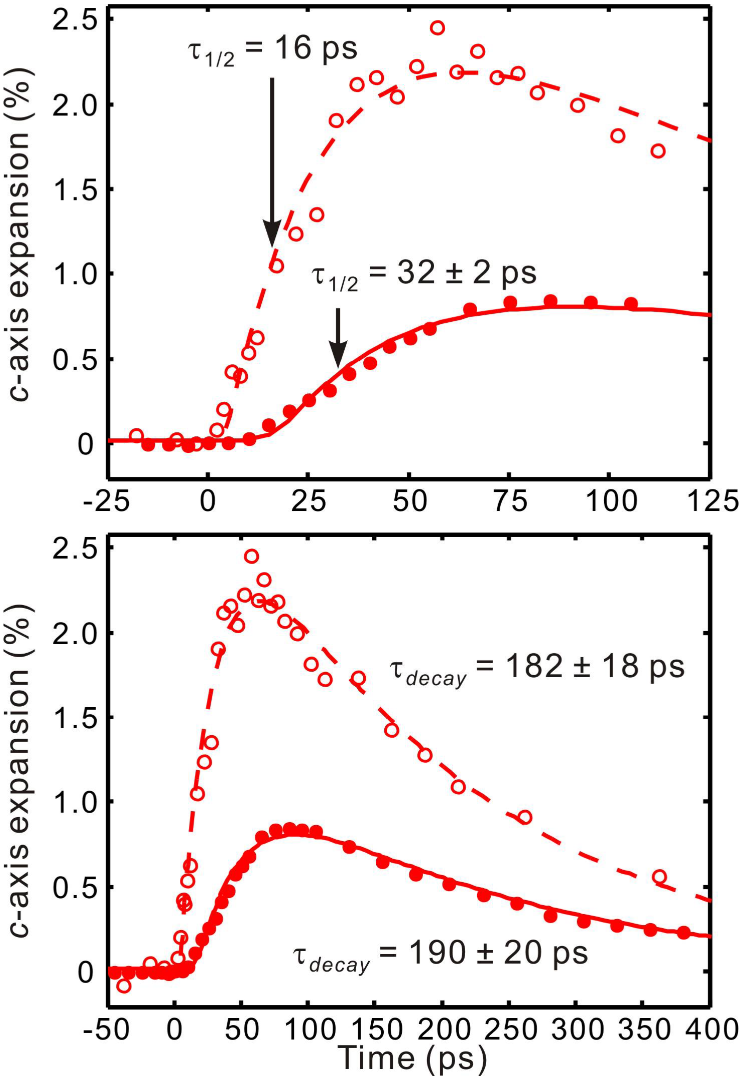

Fig. 6. Temporal evolution of the longitudinal expansion at short-time (upper panel) and long-time (lower panel) scales (Fig. 5c). Both the low-density (open circles and dashed line) and high-density (solid dots and line) nanowire arrays are displayed. The overall dynamics are similar, but the low-density array exhibits a faster rise [τ_{rise} (low density) = 26±3 ps] and larger amplitude in comparison with those of the high-density array [τ_{rise} (high density) = 36±6 ps]. The error bars given in the figure are the step size in the experiments for experimentally determined $\tau_{1/2}$ (upper panel) and standard deviations from the fits (lower panel); because the rises are relatively slow (on the picosecond time scale), there was no need to record the entire profiles with femtosecond steps.

of the change, respectively. For time-resolved electron diffraction of condensed matter, however, the response function accounts for the diffraction *difference* following the optical excitation, since electrons can probe all structures. All solid lines in Fig. 4 and all lines in Fig. 5 were obtained by such fitting (see Fig. 6 for the results of fitting for Fig. 5c as an example). Without losing the physical significance, we shall use the experimentally determined times at half maximum $\tau_{1/2}$ for further discussions.

In Fig. 4a, $\tau_{1/2} = 17$ ps for the intensity and width, and $\tau_{1/2} = 32$ ps for the expansion. The in-plane component of the nanowire, i.e., the horizontal lattice expansion derived from the change in the horizontal spacing between $(\bar{1}14)$ and $(1\bar{1}4)$ spots, is much smaller and only noticeable at the highest fluence, with a significantly faster recovery time (Fig. 5a). The intensity change of $(\bar{1}14)$ and $(1\bar{1}4)$ spots share a similar temporal evolution with that of the (006) spot, but are shifted to earlier time by ~5 ps (Fig. 5b). Lastly, as noted in Fig. 5c, the *c*-axis expansion is higher in amplitude for the low-density array and rises faster than the rate observed for the high-density array.

From the results presented for structure, dynamics and fluence and density dependences, the following picture emerges. The wires display correlated, nonequilibrium behavior in that the behavior is anisotropically driven by the potential of the carriers generated by the excitation, i.e., by the electronic change in bonding. Thermal expansion of the material [using the coefficient $\alpha_c = 2.49\times10^{-6}\ \mathrm{K}^{-1}$ (*18*)] would give $\Delta c/c \sim 2\times10^{-4}$ ($\Delta T \sim 80$ K), which is two orders of magnitude smaller than the observed values. At the highest fluence used, the observed expansion of 1~2% would correspond to a temperature rise of 4000~8000 K, far beyond the decomposition temperature of 1975 K (*18*). In other words, the dynamics are not controlled by a thermal-like, incoherent expansion due to bonding anharmonicity but, instead, by the buildup of amplitudes due to the collective motions of atoms in the wire.

In a one-dimensional model, which considers the influence of a force induced by the excitation field, we can calculate the diffraction resulting from wave-like atomic motions in the wires. The speed of sound along the *c*-axis in ZnO is 6200 m/s and, over the wire length (2 μm), a round-trip wave recurrence of 650 ps would be expected, if the force field is impulsive (see Fig. 2b of Ch. 12), contrary to what was observed. Instead, we observed a buildup of expansion and gradual recovery on a longer time scale (Fig. 4b), a behavior which is obtainable when a sustaining excitation force field is operative (see Fig. 4a of Ch. 12). This sustaining force is the result of carriers' persistence and the potential they generate over the excitation length, on the micrometer scale in this case.

The anisotropic expansion reflects an induced antibonding character along the wire direction. Since the initial carrier generation is near Γ (by 2PA) and in the in-plane $\Gamma-\mathrm{M}$(K) region (by 3PA), carrier-carrier scattering becomes necessary in order to reach the $\Gamma-\mathrm{A}$ region along the wire, *z* direction (the Zn–O bonding). We also note that the promptness of the intensity and width change comes from the direct cascade of optical (and acoustic) phonon generation, which in this case amounts to ~20 for 3PA. As a result, the maximum vertical expansion lags in time the change of both the intensity and width. Besides the temporal behavior discussed, several observations support this conclusion. First, the restructuring for the expansion occurs on a much longer time scale than those of the intensity and width, and it is similar to the decay time of photoluminescence (radiative recombination) of ~1 to 2 ns (*28*). Second, the horizontal expansion is absent at lower fluences, and appears and disappears on a much shorter time scale at our highest fluence (Fig. 5a). This is because the initial excitation induces in-plane movements of atoms, which also signifies that the intensity of $(\bar{1}14)$ and $(1\bar{1}4)$ spots should

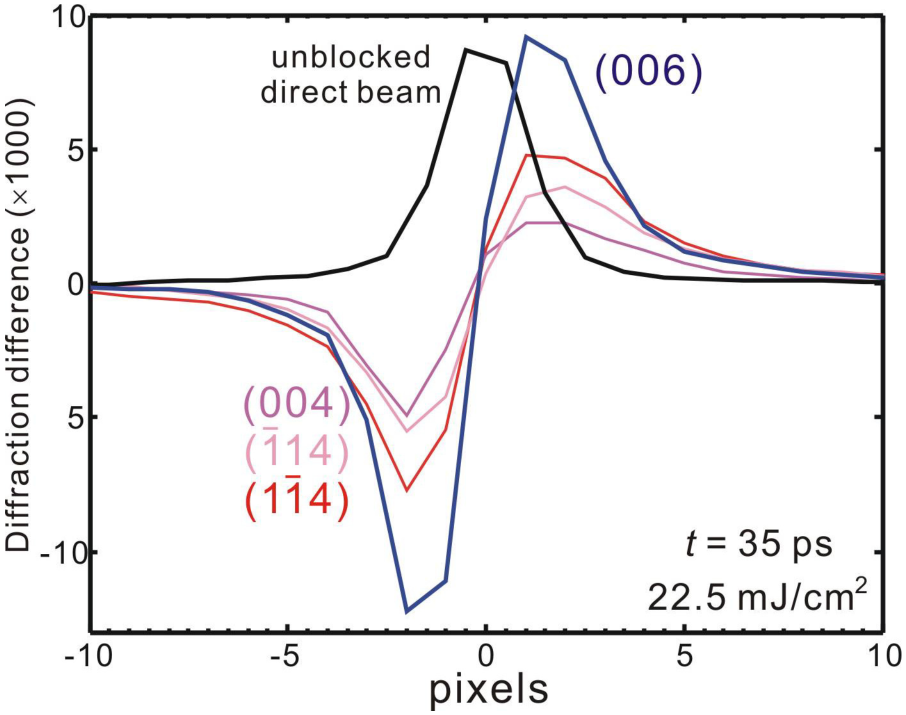

Fig. 7. Diffraction difference for several Bragg spots along the vertical direction (Fig. 3a).

decrease before that of the (006), as observed experimentally. Lastly, as the excitation fluence increases, the density of carriers increases, leading to the observed larger longitudinal expansion.

When these different sets of experiments were repeated on the low-density nanowire array (Fig. 5, panels c and d), we observed similar behavior to that of the high-density array, but with the largest expansion reaching as much as 2% and occurring at earlier times. These observations suggest that in the low-density materials, the nanowires are freer to collectively expand, reaching a nonequilibrium effective “temperature” of 8000 K through the electronic potential change (Zn–O bond weakening) by carriers. Modeling of the electronic–nuclear coupling may quantify this behavior. Although the average separation between wires is 300 nm in the high-density array, the inhomogeneity in distribution (clustering) becomes essential to the extent of expansion.

The Issue of Similar Movement for Different Spots

We have noticed the similar amount of movement for different Bragg spots (Fig. 7), and the allegation of an overall pattern shift due to certain charge effects might seem legitimate. It should be noted that our discovery of a unidirectional behavior in ZnO nanowires, induced by an ultrashort infrared light pulse and probed by electrons, was concluded not only from the movement of few Bragg spots but also from the temporal intensity and width changes in the diffraction. Each of the diffraction features as a function of time has its direct association with certain atomic or lattice motions in the structure, and their response differences in time mirror the processes that occur subsequently in a material. Given the resembling but different temporal dependence for the diffraction features (Fig. 4a), there should be more than one physical process involved in the dynamics of a zinc oxide nanowire. In addition, as mentioned earlier, the lack of a movement over time for the unblocked (undiffracted) direct beam undoubtedly eliminates the explanation of a simple overall pattern shift for our observation.

Photoemission from ZnO wires could not lead to our experimental findings, either. The work function of ZnO is ~5 eV (*29, 30*), larger than the energy provided by three photons of 800-nm light. Besides, such a charge separation would result in a positive potential on the material surface and affect the trajectory of the undiffracted grazing electrons, which is in contradiction to our finding. Furthermore, the diffraction intensity and width changes over time would become inexplicable should the single mechanism of photoemission be responsible. On the contrary, the physical processes mentioned above satisfactorily explained our experimental results; e.g., the fluence dependence of *c*-axis expansion in a log–log plot correctly matches with our proposed model of multiphoton excitation. In fact, the fluence dependence of maximum intensity decrease in a log–log

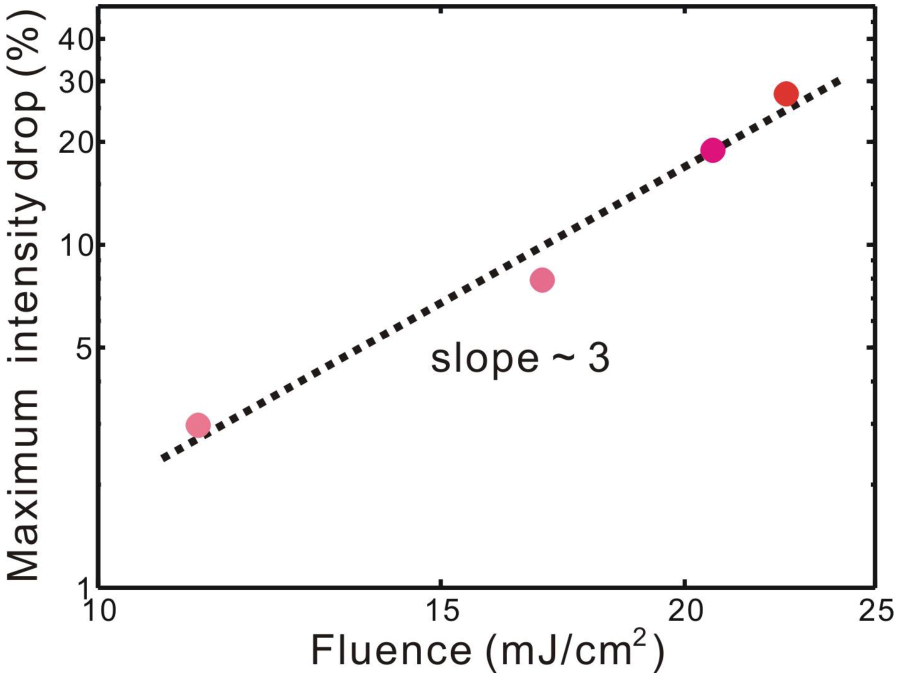

Fig. 8. The fitted slope in the log-log plot indicates that the maximum intensity decrease is proportional to the fluence to the power of 3. (Fig. 4c).

plot has a slope of ~3 (Fig. 8), which is again in a nice agreement with the required 3-photon absorption.

It should also be noted that proportionality of the vertical movement versus the order of the diffraction spot (in accordance with $\Delta c/c = -\Delta s_\perp / s_\perp$) would be valid only if all the spots were from the same structure. Whereas the (006) spot and first-order-Laue-zone diffractions were generated from the reflection nature of our technique, the appearance of other spots, such as (004), $(1\bar{1}4)$ and $(\bar{1}14)$, was due to the transmission-type probing of the current nanostructure. Given the proximity of these spots to the shadow edge, the responsible diffracting structure was only the top of the nanowires where the lattice is free to expand; electron transmission from a lower part could be easily blocked by other adjacent wires. The (006) spot, however, had contribution from both the top and a lower part of tens of nanometers, leading to an averaged, slightly lowered, *c*-axis expansion. A

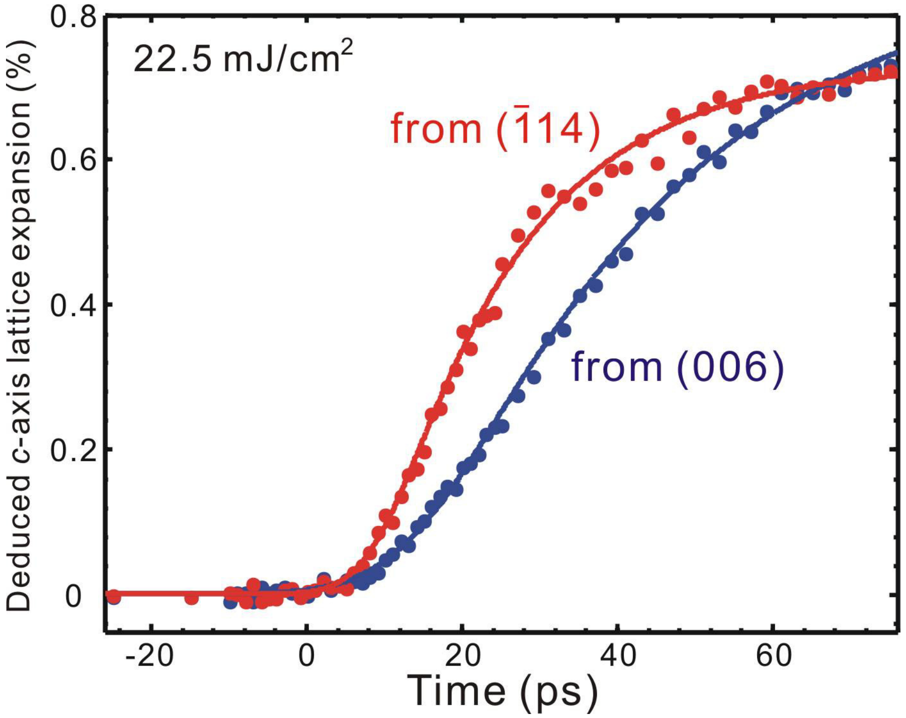

Fig. 9. Longitudinal lattice expansion deduced from the vertical movement of the $(\bar{1}14)$ and (006) spots. The different speed for the rise signifies that the diffractions do not originate from exactly the same part of a nanowire.

natural consequence of this explanation will be an earlier start of spot shift for the (004), $(1\bar{1}4)$ and $(\bar{1}14)$ diffractions, and indeed our analysis supports such a model (Fig. 9).

Conclusion

Visualization of atomic motions during structural change reveals the direct role of electron–nuclear correlations which ultimately control the behavior of macroscopic phenomena, such as the optoelectronic effect in zinc oxide. The unexpected material behavior described above for confined nanostructures is unobservable when the studies are made in the equilibrium state. Only when observed with atomic-scale spatial and femtosecond temporal resolutions can we acquire fundamental understanding of structural perturbations and relaxations for different optical and chemical dopings, and hence the optimization of function at the nanometer scale.

References:

1. M. L. Steigerwald, L. E. Brus, *Acc. Chem. Res.* **23**, 183 (1990).
2. S. Iijima, *Nature* **354**, 56 (1991).
3. G. M. Whitesides, J. P. Mathias, C. T. Seto, *Science* **254**, 1312 (1991).
4. Y. Cui, Q. Wei, H. Park, C. M. Lieber, *Science* **293**, 1289 (2001).
5. A. P. Alivisatos, *Science* **271**, 933 (1996).
6. C. B. Murray, C. R. Kagan, M. G. Bawendi, *Ann. Rev. Mater. Sci.* **30**, 545 (2000).
7. Y. Xia *et al.*, *Adv. Mater.* **15**, 353 (2003).
8. Z. L. Wang, *J. Phys.: Condens. Matter* **16**, R829 (2004).
9. Z. L. Wang, *Mater. Today* **10**, 20 (2007).
10. Ü. Özgur *et al.*, *J. Appl. Phys.* **98**, 041301 (2005).
11. X. Wang *et al.*, *J. Am. Chem. Soc.* **127**, 7920 (2005).
12. L. E. Greene *et al.*, *Nano Lett.* **5**, 1231 (2005).
13. P. Baum, A. H. Zewail, *Proc. Natl. Acad. Sci. USA* **103**, 16105 (2006).
14. N. Gedik, D.-S. Yang, G. Logvenov, I. Bozovic, A. H. Zewail, *Science* **316**, 425 (2007).
15. P. Baum, D.-S. Yang, A. H. Zewail, *Science* **318**, 788 (2007).
16. F. Carbone, P. Baum, P. Rudolf, A. H. Zewail, *Phys. Rev. Lett* **100**, 035501 (2008).
17. Z. L. Wang, *Reflection electron microscopy and spectrsocopy for surface science* (Cambridge Univ. Press, Cambridge, 1996).
18. S. Adachi, Ed., *Handbook on Physical Properties of Semiconductors*, vol. 3 (Kluwer Academic Publishers, Boston, 2004).

19. A. Ichimiya, P. I. Cohen, *Reflection High Energy Electron Diffraction* (Cambridge Univ. Press, Cambridge, 2004), pp. 20-23.
20. B. E. Warren, *X-ray diffraction* (Dover, New York, 1990).
21. E. Müller *et al.*, in *Microscopy of Semiconducting Materials* (Springer, New York, 2006), pp. 303-306.
22. J. He, Y. Qu, H. Li, J. Mi, W. Ji, *Opt. Express* **13**, 9235 (2005).
23. B. Gu, J. He, W. Ji, H.-T. Wang, *J. Appl. Phys.* **103**, 073105 (2008).
24. H. W. Lee *et al.*, *Chem. Phys. Lett.* **447**, 86 (2007).
25. S. Xiao *et al.*, *Chin. Phys. B* **17**, 1291 (2008).
26. C. F. Zhang, Z. W. Dong, G. J. You, S. X. Qian, H. Deng, *Opt. Lett.* **31**, 3345 (2006).
27. S. Pedersen, A. H. Zewail, *Mol. Phys.* **89**, 1455 (1996).
28. M. H. Huang *et al.*, *Science* **292**, 1897 (2001).
29. K. Jacobi, G. Zwicker, A. Gutmann, *Surf. Sci.* **141**, 109 (1984).
30. X. Bai, E. G. Wang, P. Gao, Z. L. Wang, *Nano Lett.* **3**, 1147 (2003).

Part II

Highly Correlated Materials

Chapter 6

Four-dimensional Visualization of Transitional Structures in Phase Transformations[†]

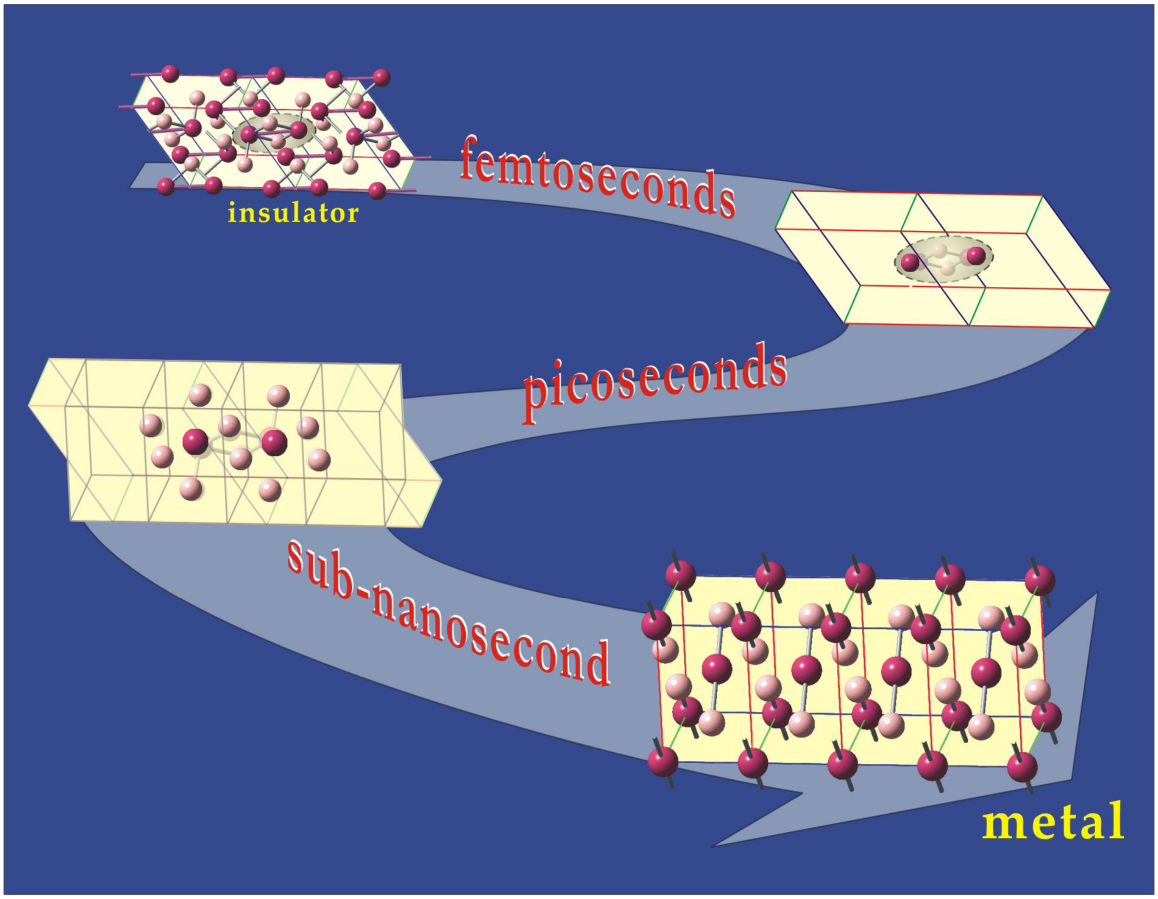

[†] Full account for a previous report by P. Baum, D.-S. Yang, A. H. Zewail *Science* **318**, 788 (2007).

Introduction

A first-order phase transition, which depicts the transformation between two distinct phases of a material at a well-defined temperature, is conventionally achieved through a change in a field variable such as pressure, temperature, magnetic or electric field. The most common examples are those transformations between the solid, liquid and gas states of matter; for such phase transitions, the general macroscopic, thermodynamic description has been established for many decades. However, since a phase transition is not achieved instantaneously, a microscopic understanding of the phenomenon, which demands the knowledge of the transformation mechanisms in advance, is critical to the dynamic description and the kinetics of the transition processes in time. In cases of melting (freezing), vaporization (condensation) and sublimation (deposition), interactions between atoms or molecules, and nucleation and the growth of nuclei accompanying the absorption (release) of thermal energy, are central in the microscopic description (*1*).

As a phase transformation involves collective phenomena, unraveling the relevant microscopic processes at work can be a daunting task. The metal–insulator transition (*2*) is such a transformation with a quantum nature, signifying the abrupt state change between the existence of a massive number of interacting, itinerant electrons and their localization into an ordered, bounded conformation (*3*). One of the best known examples is vanadium dioxide (VO_2), which has been a subject of intensive study for nearly half a century (*4-13*) since the discovery of its first-order metal–insulator transition at a temperature of ~340 K by Morin (*14*). The further complication in its study is the accompanied structural transformation at a very similar, if not exactly the same, temperature between the low-temperature monoclinic (M_1) and high-temperature tetragonal (rutile) crystal structures (*15, 16*). As a result, for the strongly correlated material VO_2, the issue of whether the phase transition at $T = 340\ \mathrm{K}$ is essentially originated from the electron correlation effect [the Mott–Hubbard picture (*7, 17*)] or dominated by the structural vanadium–vanadium (V–V) dimerization/separation [the Peierls picture (*5, 18*)] has long been under debate until even today (*19, 20*). The question of whether or not the temperature of the metal–insulator transition and that of the structural transformation are the same has also been raised and argued (*21*).

To resolve these puzzles satisfactorily, it is more important to look into the dynamics involved in the phase transformation(s), besides understanding the properties of the individual phases. In this regard, the difference in the characteristic time scales for charge carriers and nuclear motions (lattice vibrations) may provide hints to a deeper understanding. It is known that the transformation from the insulating monoclinic phase of VO_2 to the metallic tetragonal phase can also be initiated via photoexcitation of the valence electrons (*22-27*); through the photoreflectivity and phototransmission experiments that are sensitive to the dynamics of the excited carriers, their internal equilibrium is reached in an ultrashort time of ~80 fs (*28*). In contrast, nuclear motions generally occur on a longer time scale, from hundreds of femtoseconds for interatomic vibrations (*29*) to up to tens of picoseconds for lattice expansion over many unit cells (Chs. 4, 5 and 7). Thus, unifying the concomitance of the electronic metal–insulator transition and the structural lattice transformation (from thermodynamic studies) with this temporal disjunction between the electronic and structural equilibriums (in the dynamics) may be the key to settling down the aforementioned debates over many decades.

In fact, we want to point out that the description of only two states (the insulating monoclinic and metallic tetragonal phases) involved during the phase transition process of VO_2 is incompatible with the dynamical behavior observed using time-resolved techniques. The ultrashort time of 80 fs, in which the initial insulating VO_2 appears to already reach a metallic state (*28*), is too short for all the nuclei to arrive at their final positions in the tetragonal structure. With a sound speed of ~4000 m/s in this material (*30*), a distance of ~3 Å would be the upper limit for any nuclear motion in such an ultrashort time; however, the size change of a sub-micrometer crystallite, e.g., the accumulated *b*-axis expansion over 1000 unit cells, is about an order of magnitude larger than the 3-Å limit, let alone the accumulated nuclear movements due to the angular change between the principal axes *a* and *c* (*31*). Therefore, there must be some transitional state(s) during this solid-solid phase transformation, and the identification and even visualization is of the utmost importance.

This concept of the energy landscape and transition and intermediate states has been widely used for reactions and transformations in chemistry and biology; in condensed matter, such use has recently been theoretically addressed for solid-solid transitions involving two thermodynamically stable configurations (*32, 33*). Experimentally, for direct probing of the transitional state(s) during phase transformations, the radiation or particle used must have both a wavelength on the scale of atomic distances and an appropriate temporal resolution, as demonstrated in the studies of melting and lattice dynamics by ultrafast X-ray absorption (*34*) and diffraction (*35-38*), and electron diffraction (*39-41*). In our laboratory, ultrafast electron microscopy and diffraction (*42*) have been the methods of choice for direct observation of the structural dynamics during molecular and phase transitions (*43-45*).

In this chapter, I provide a full account of the structural evolution during the solid–solid phase transformation of VO_2 from the initial monoclinic conformation to the final tetragonal one, using time-resolved electron diffraction with atomic-scale spatial

(a) Real space

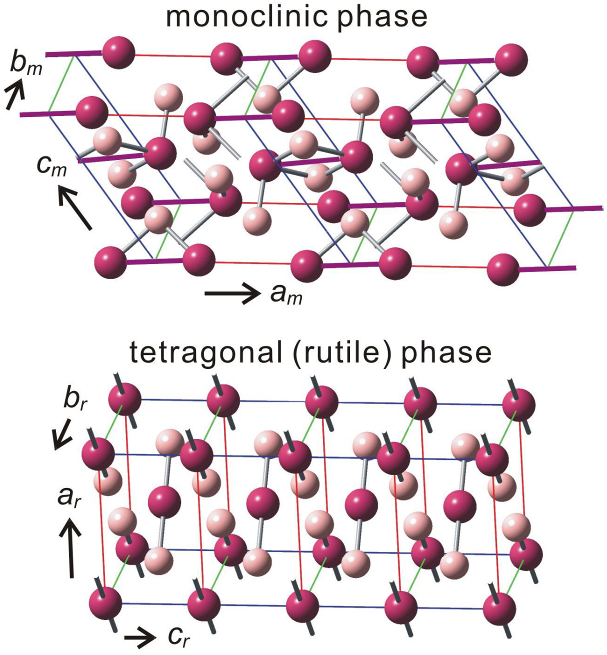

(b) Reciprocal space

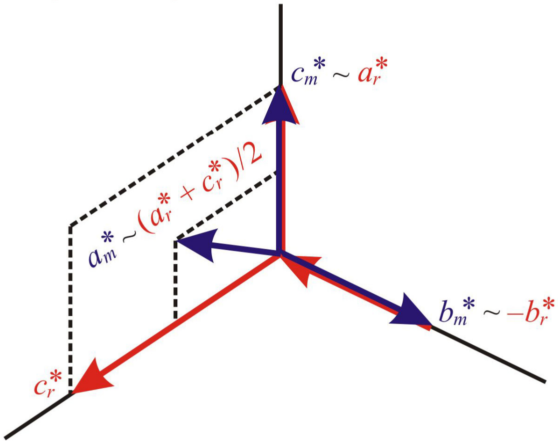

Fig. 1. Real-space crystal structures of VO_2 and the corresponding basis vectors in reciprocal space. (a) Crystal structure of the monoclinic, low-temperature phase (upper panel) and the tetragonal (rutile), high-temperature phase (lower panel). Vanadium atoms are depicted in red and oxygen atoms in pink. The major structural difference is the V–V dimers (indicated by violet lines) in the monoclinic phase and their breakage in the tetragonal phase. Note that the axis definitions change. (b) The relationship between the reciprocal basis vectors for the two phases.

and temporal resolution (*46*). Experiments were performed mainly on VO_2 single crystals, and on a thin-film sample to gather more data for the fluence dependence results. In order to map pathways of nuclear motion, all observed Bragg diffractions of different planes and zone axes were examined on the femtosecond to nanosecond time scale. The match between the observed temporal changes and the calculated structure factor for various indices makes possible the separation of different nuclear motions—the femtosecond primary V−V bond dilation, the displacements of atoms in picoseconds, and the sound-wave shear motion on ~100 ps. Moreover, we found that a minimum fluence of photoexcitation is required to activate the structural transformation at short and long times, and this threshold behavior has a clear dependence on the ambient temperature. The fairly good correspondence between the excitation threshold observed in the photoinduced phase transformation and the thermal energy required by the phase transition thermodynamically at different temperatures convincingly indicates a common transformation mechanism for both scenarios. Thus, with the examination of the thermodynamic studies in recent years (*12, 13, 19*), the present study of structural dynamics offers a unified delineation for this highly correlated material of VO_2.

Experimental Section and Sample Characterization

A. VO_2 Single Crystals

The two thermodynamically stable crystal structures of VO_2 are depicted in Fig. 1a: the vanadium atoms arrange into pairs in the initial monoclinic M_1 phase, whereas all V–V distances are equal in the final tetragonal phase. The crystal axes are assigned differently due to the symmetry change, and the *a* axis of the M_1 phase is conventionally matched with the *c* axis of the tetragonal phase. Therefore, in real space,

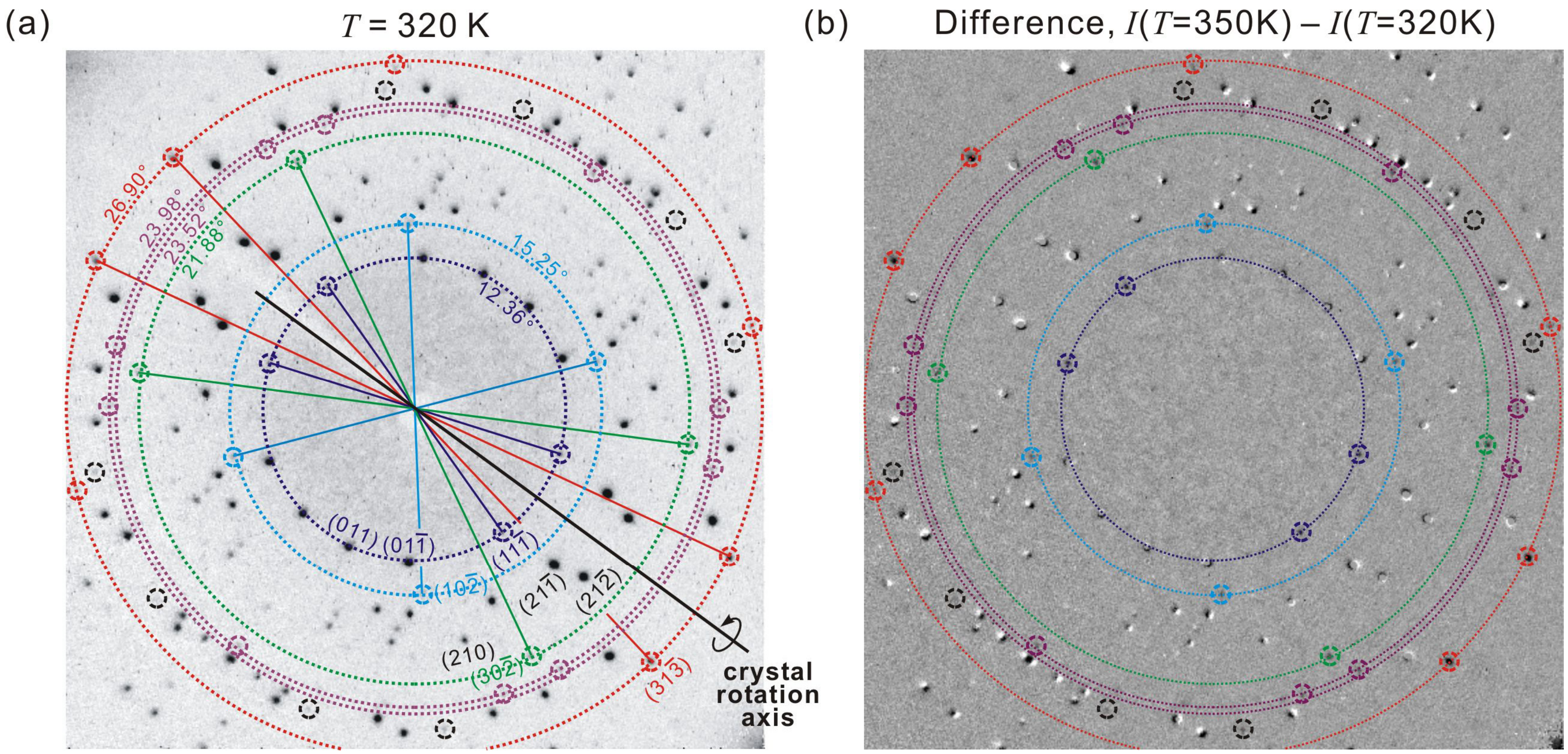

Fig. 2. (a) X-ray diffraction pattern of the low-temperature M_1 phase, obtained by the rotating crystal method. The solid lines connect symmetry-related spots, and indices of a few spots are given. Small dashed circles (on concentric dotted circles with the corresponding scattering angles) indicate those diffractions with an odd h index. (b) Difference of the x-ray patterns from the two phases. Total loss of intensity (appearing as a pure dark spot) is seen for those diffractions encircled by the small dashed circles; other spots show both white and dark parts along the angular direction, signifying a small rotation of the crystal axes between the two phases.

$a_m \sim 2c_r$, $b_m \sim -b_r$ and $c_m \sim a_r - c_r$, where the subscripts m and r refer to the M_1 and rutile (i.e., tetragonal) structures, respectively. The basis vectors in reciprocal space can be deduced, as shown in Fig. 1b. It is clear that any reciprocal lattice point $(hkl)_m$ for the M_1 phase has one-to-one correspondence with one for the tetragonal phase, i.e. $(\frac{h}{2}+l,-k,\frac{h}{2})_r$, except for those with an odd h. Thus, the Bragg diffractions from the M_1 phase with an odd h index become forbidden after the structural transformation into the tetragonal phase; all other diffractions are allowed, with certain changes in their intensities and slight shifts in their positions due to the small modification in the unit-cell parameters (*31*).

In order to minimize or eliminate the effects from the sample inhomogeneity and morphology, stoichiometric deviation, embedded defects, domain sizes, etc., we used single crystals for the current study of structural dynamics in VO_2. Three single crystals of VO_2 with a phase-transition temperature near 340 K have been grown by the vapor transport method (*47*), and were from the same source as those samples in Refs. 12 and 13. Static X-ray diffraction (by a Bruker SMART 1000 CCD diffractometer with graphite monochromated Mo K_α radiation, $\lambda = 0.71073$ Å) was performed for the confirmation of the crystal structures below and above 340 K; the long-range order of the samples was evident from the well-defined diffraction spots shown in Fig. 2. Dotted circles are drawn to indicate those diffractions with an odd h index in the M_1 phase, which are encircled in small dashed circles. Above 340 K, they become forbidden due to the change in the structural symmetry and therefore disappear, showing complete loss of diffraction intensity (appearing as dark spots at the same positions in the difference image, Fig. 2b). All other spots show both bright and dark parts in the difference image, indicating the slight changes in the Bragg spot positions upon the structural transformation. It is noted that most of the shifts contain a clear angular component, which signifies the small

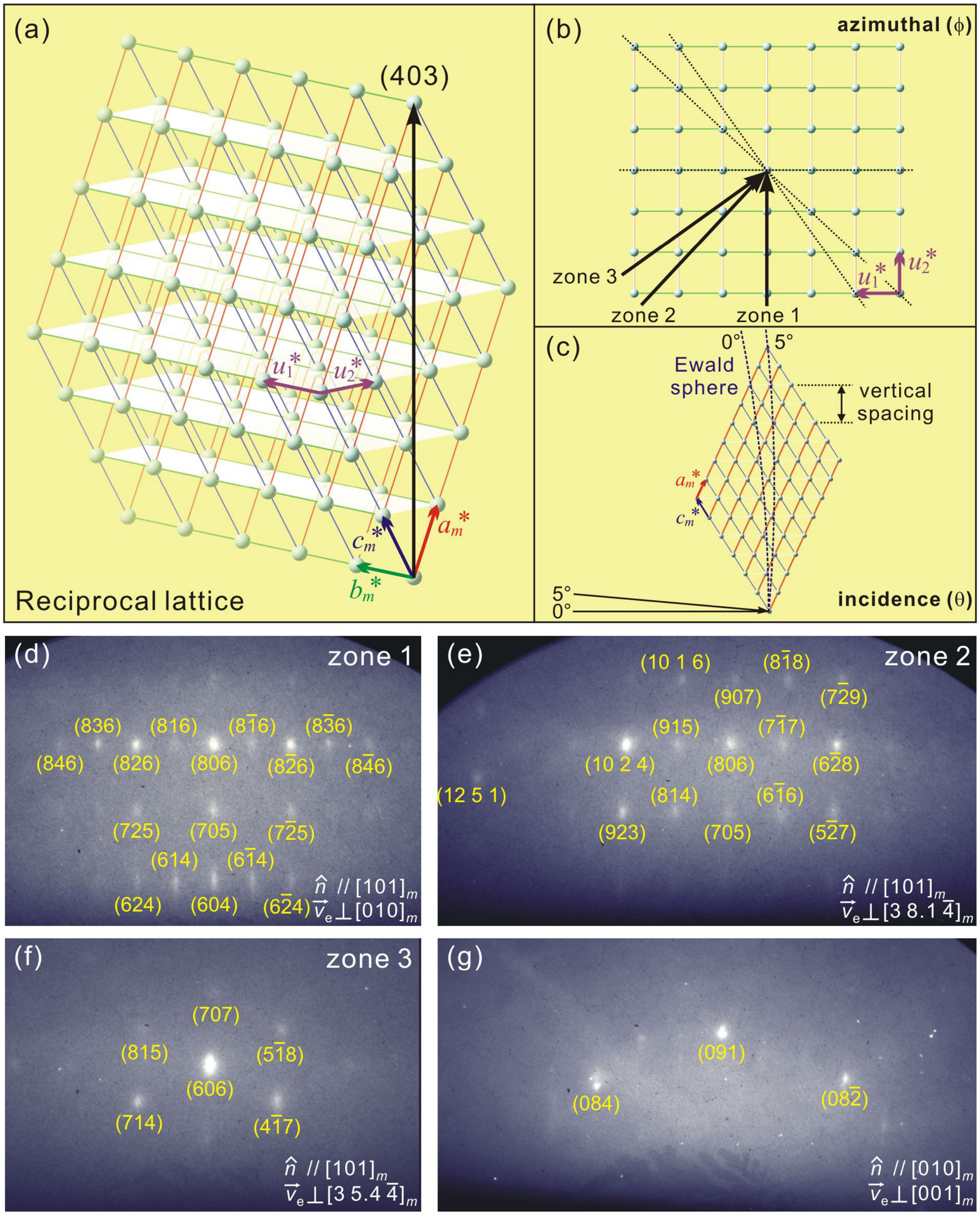

(See next page for the figure caption.)

Fig. 3. Ewald construction in reciprocal space and diffraction patterns observed by UEC. (a) The corresponding reciprocal lattice for the crystal that was mechanically cut and polished; the exposed surface is the $(403)_{\mathrm{m}}$ plane, whose surface normal direction is along the black arrow. Purple arrows are the basis vectors for the plane. (b) Top view of the two-dimensional reciprocal lattice for the $(403)_{\mathrm{m}}$ plane and the three zone axes (indicated by the dashed lines and black arrows) accessed through the azimuthal rotation. (c) Side viewof the Ewald construction (along $\vec{b}_{\mathrm{m}}^{*}$) for satisfaction of the diffraction condition. The vertical separation between the observed Bragg spots is related to the reciprocal vector, $\vec{a}_{\mathrm{m}}^{*} + \vec{c}_{\mathrm{m}}^{*}$, at the electron incidence angle of 5°. (d–g) Typical diffraction patterns observed from different crystal surfaces and different zone axes; $\hat{n}$ is the surface normal direction and $\vec{v}_{\mathrm{e}}$ is the electron propagation direction (zone axis). All Bragg spots can be identified as the monoclinic structure (yellow indices).

angular movements of atoms, or equivalently, a slight rotation of the crystal axes, in accord with a previous study (*31*). Such angular modification causes a shear motion in VO_2 during the phase transition, and it will be shown later that this shear motion plays an important role in the dynamics of the photoinduced phase transition at longer times.

The naturally grown crystal surfaces typically have an area of $\sim 2 \times 2\ \mathrm{mm}^2$. Sometimes even without the process of cleaving or major cleaning, a pattern of well-indexed Bragg spots can be obtained by our facility of reflection electron diffraction. When necessary, the crystal surfaces were polished mechanically and gently wiped clean with acetone. The resulting diffraction patterns become transmission-like due to the electrons probing the sub-micrometer-sized islands of VO_2; however, all spots can be correctly indexed, which shows that VO_2 is hard enough and mechanical polishing of its surfaces is feasible. We observed, by monitoring the intensities of Bragg spots from the top surface of a crystal, a complete phase transformation within 3 K and also the hysteresis phenomenon with a width of 5.6 K, at a rate of heating or cooling of ~0.6 K/min from the bottom of the crystal. Therefore, the numbers reported here for the temperature range and hysteresis width are the upper limits, and the actual values are believed to be smaller (see the inset of Fig. 2 in Ref. 13).

To gather complete crystallographic data for the photoinduced structural dynamics in all three dimensions, one of the crystals was mechanically cut and polished to expose a surface that was not naturally grown and had a nonzero *h* index. Guided by the information from x-ray diffraction, we obtained the $(403)_m$ plane, whose corresponding two-dimensional lattice in reciprocal space is formed by the orthogonal basis vectors of $u_1^* = b_m^*$ and $u_2^* = a_m^* - c_m^*$ (Fig. 3a). Different zone axes of such a crystal surface can be accessed through the azimuthal rotation (ϕ); three such directions are indicated in Fig. 3b and the corresponding static diffraction patterns, obtained at an incidence angle of ~5° at room temperature, are presented in Fig. 3, panels d to f. The small incidence angle of electrons is required for the proper interception of the Ewald sphere with the reciprocal lattice points, as shown in Fig. 3c. For comparison, a diffraction pattern from the unpolished $(010)_m$ surface of another crystal at a similar incidence angle is given in Fig. 3g.

B. VO_2 Thin Films

It is known that VO_2 crystals are prone to fracture after several cycles of the phase transition thermally because of the mechanical tensions caused by the volume change. We also found that they cannot remain intact under the optical excitation above a certain threshold. Hence, for the temperature- and fluence-dependent experiments, we also used thin-film samples to obtain more data points. However, more caution is needed for the study of dynamics on VO_2 thin films. Many issues, such as wrong stoichiometry, the existence of mixed phases, sample inhomogeneity and morphology, small domain sizes and poor connectivity, embedded impurities, additional strain or binding from the underlying substrate, etc., may substantially alter the structural dynamics and consequently lead to different conclusions from those made in the studies of single crystals. Therefore, a close comparison of the thin-film dynamics with the existing data from single crystals is necessary before it is included for further discussions.

Crystalline VO_2 thin films have been successfully fabricated on single-crystal sapphire (Al_2O_3) substrates by using the pulsed laser deposition (PLD) method (*48-51*). With a proper choice of the partial pressure of oxygen and the substrate temperature, the deposited films can be highly oriented and single-phased with the correct stoichiometry and no contamination from the substrate (*50*). Our thin films were prepared with the use

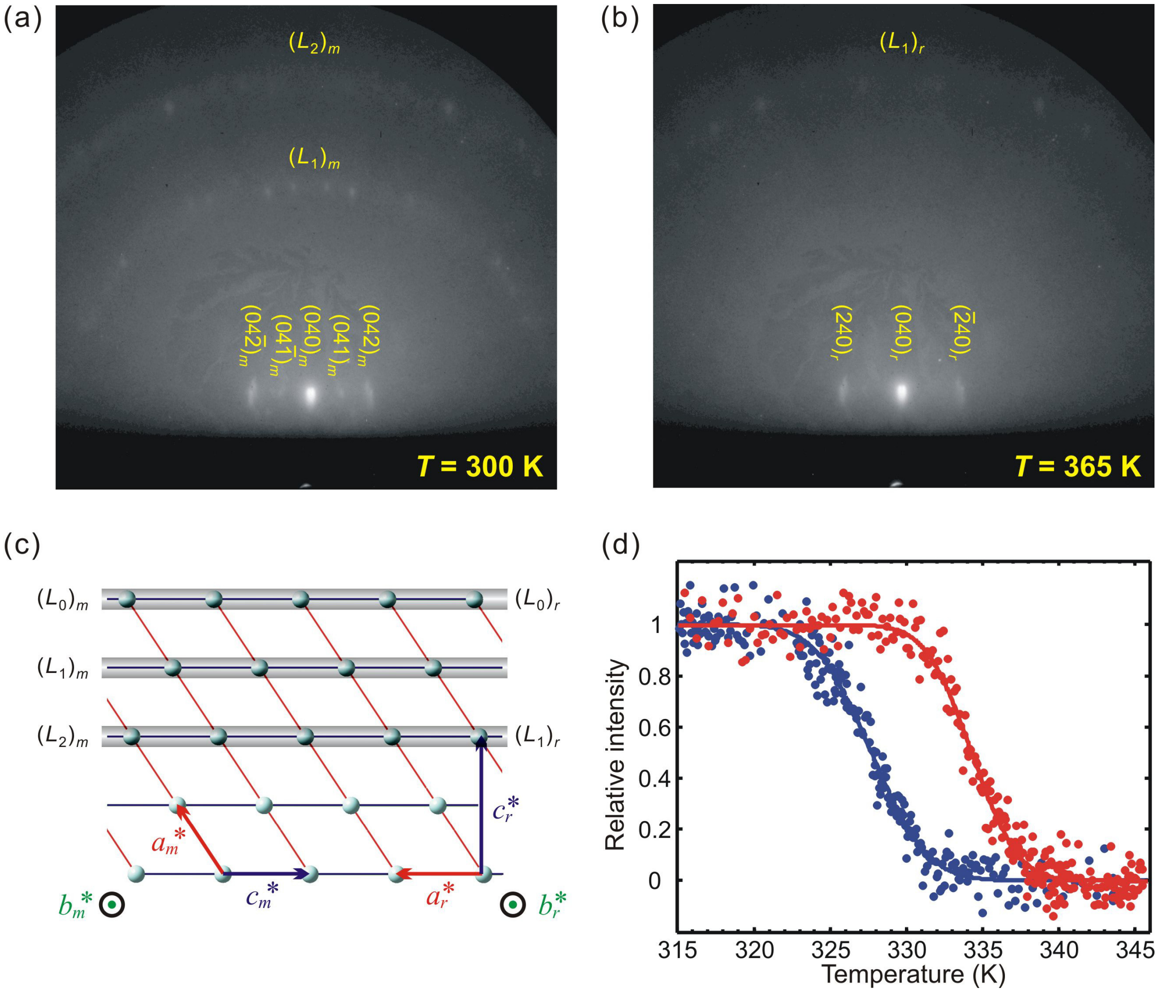

Fig. 4. (a) Reflection diffraction pattern of a VO_2 thin film on $Al_2O_3(10\bar{1}0)$, in the low-temperature M_1 phase. Bragg spots from the zeroth-order Laue zone, $(L_0)_m$, are indexed and the first- and second-order Laue zones [$(L_1)_m$ and $(L_2)_m$, respectively] are indicated. (b) Diffraction pattern of the high-temperature phase. While the Bragg spots from the zeroth-order zone remain clear, only the first-order zone, $(L_1)_r$, can be observed. (c) Relationship between the reciprocal lattices for the two phases. In the high-temperature phase, $(L_1)_m$ is forbidden and therefore $(L_2)_m$ becomes $(L_1)_r$. (d) Diffraction intensity of the four $(L_1)_m$ spots in the center as a function of temperature. The red dots and curve are obtained from the heating procedure and the blue from the cooling procedure.

of a KrF excimer laser [COMPex Pro 102(KrF), Coherent], which has an output of ~300 mJ per 20-ns pulse at a wavelength of 248 nm. Before deposition, the base pressure in the chamber was on the order of 10^{-6} Torr, and a constant flow of the oxygen (10%) and argon (90%) mixture was then introduced, resulting in a total pressure of 28 mTorr. Light pulses at a repetition rate of 20 Hz were focused onto an area of $\sim 11 \times 1.0$ mm^2 on a rotating target of pure vanadium metal (99.9%, ESPI Metals); vanadium atoms were ablated to react with oxygen to form oxide films. The rotating sapphire wafers (EPI-polished, MTI) were held at a temperature of 500°C during the film growth, and the typical target-substrate distance was 9 cm. The thickness of the VO_2 films was ~140 nm (measured by a contact profilometer) after 10^5 laser shots. To enhance the sample homogeneity, domain size and connectivity, the deposited films were annealed for 42 hours in a pure oxygen atmosphere at 10 mTorr.

The insulator–metal phase transition of the thin films was observed by infrared transmission at 2000 nm (0.62 eV) as a function of temperature. The closing of the band gap of ~0.6 eV (*4, 13*) at high temperature leads to a 30–45% decrease in transmittance and a typical width for the hysteresis phenomenon is ~6 K. Among the samples prepared on the Al_2O_3 wafers with different surface planes, we found that $VO_2/Al_2O_3(10\bar{1}0)$ was able to produce a nice reflection pattern from electron diffraction, whereas $VO_2/Al_2O_3(0001)$ and $VO_2/Al_2O_3(1\bar{1}02)$ readily gave transmission-like patterns. All VO_2 films were highly oriented. In Fig. 4, panels a and b, we present the diffraction patterns from $VO_2/Al_2O_3(10\bar{1}0)$ recorded at an incidence angle of 1.75° at two temperatures ($T = 300$ and 365 K, respectively). From the Bragg spots and the noticeable diffractions from the first- and second-order Laue zones, we confirm that the (010) plane of VO_2 is parallel and registers to the wafer plane $(10\bar{1}0)$. The structural transformation can be clearly seen: given the direction of electron probing as in Fig. 4, the first Laue circle, which originates from the reciprocal rods with the index of $h = 1$, disappears as the sample is heated above the transition temperature (Fig. 4c). By gauging the total intensity of the four spots on the middle part of the first Laue circle in Fig. 4a, we observed the phase transformation near 334 K and a hysteresis width of ~6 K (Fig. 4d). These values are satisfactorily consistent with those retrieved from the infrared transmission data.

C. Time-resolved Electron Diffraction

We used near-infrared pulses of 800 nm (1.55 eV) to initiate the phase transformation, whose structural dynamics was followed by diffracting the electron packets after a variable delay time. The maximum optical fluence applied was 25 mJ/cm^2, and a fraction of it was enough to drive the phase transition with a single pulse. The pulse tilting excitation scheme was invoked to resolve the group-velocity mismatch between electrons and light (*46*). At the small angle of incidence, the electron-probed area on the crystal surface is ~2 mm (the sample size) by 0.2 mm (the electron-beam diameter), giving a temporal mismatch as large as 20 ps between the optical excitation and the electron pulses in the original nontilted excitation scheme. By tilting the optical pulse, their temporal synchrony can be achieved on the entire probed crystal surface, reaching a femtosecond temporal resolution convoluted by any residual spread and the involved duration of optical (120 fs) and electron pulses.

Within the experimental repetition period of 1 ms, we observed a full recovery to the initial M_1 phase in all VO_2 samples, which was confirmed by observing no change between the diffraction patterns recorded with the optical excitation at negative delay time (an effective 1-ms delay) and those recorded without the excitation. Thus, the contributions from static heating can be excluded, and the observed diffraction changes reveal the nonequilibrium dynamics following the femtosecond excitation. From the VO_2 single crystals, we observed tens of well-indexed Bragg spots from the three-dimensional reciprocal space (Fig. 3, panels d to g), and 30 of them were intense enough for time-resolved investigations. They were acquired at short (femtosecond to picosecond) and long (sub-nanosecond to 1.3 ns) times at room temperature. For the detection of the femtosecond dynamics, we used a time step of 250 fs and reduced the number of electrons per pulse to as low as ~500, significantly below the space-charge limit (*42*). In such a low flux, the electron pulse width has been measured (322 ± 128 fs) *in situ* at a streaking speed of 140 ± 2 fs/pixel (*52*). After the different stages of the structural transformation of VO_2 were identified, diffraction patterns were recorded with different excitation fluences at two specific delay times, $t = 30$ ps and 1.3 ns. The fluence was adjusted by rotating a polarizer against another fixed one to keep the same polarization. We also performed the same experiment and fluence-dependent study for the structural dynamics at $T \sim 110$ K. From the thin-film sample of $VO_2/Al_2O_3(10\bar{1}0)$, the temporal changes of the (040) Bragg spot at room temperature and at ~100 K were recorded. They can be well compared with the data obtained from the single crystals, thus provide consistent dynamical information. Fluence-dependent experiments were then carried out at various temperatures.

We also checked for possible effects of surface potential change or charge trapping on the diffraction during the transition from the insulator to metal phase; no such effects were found, as evidenced from our observation of a steady position and intensity of the direct, nondiffracted electron beam for scans at all delay times. At 5° incidence, the electrons diffract from a material thickness of about 10 nm; we do not observe rods in the diffraction patterns, but instead well-defined Bragg spots, suggesting that at least ten

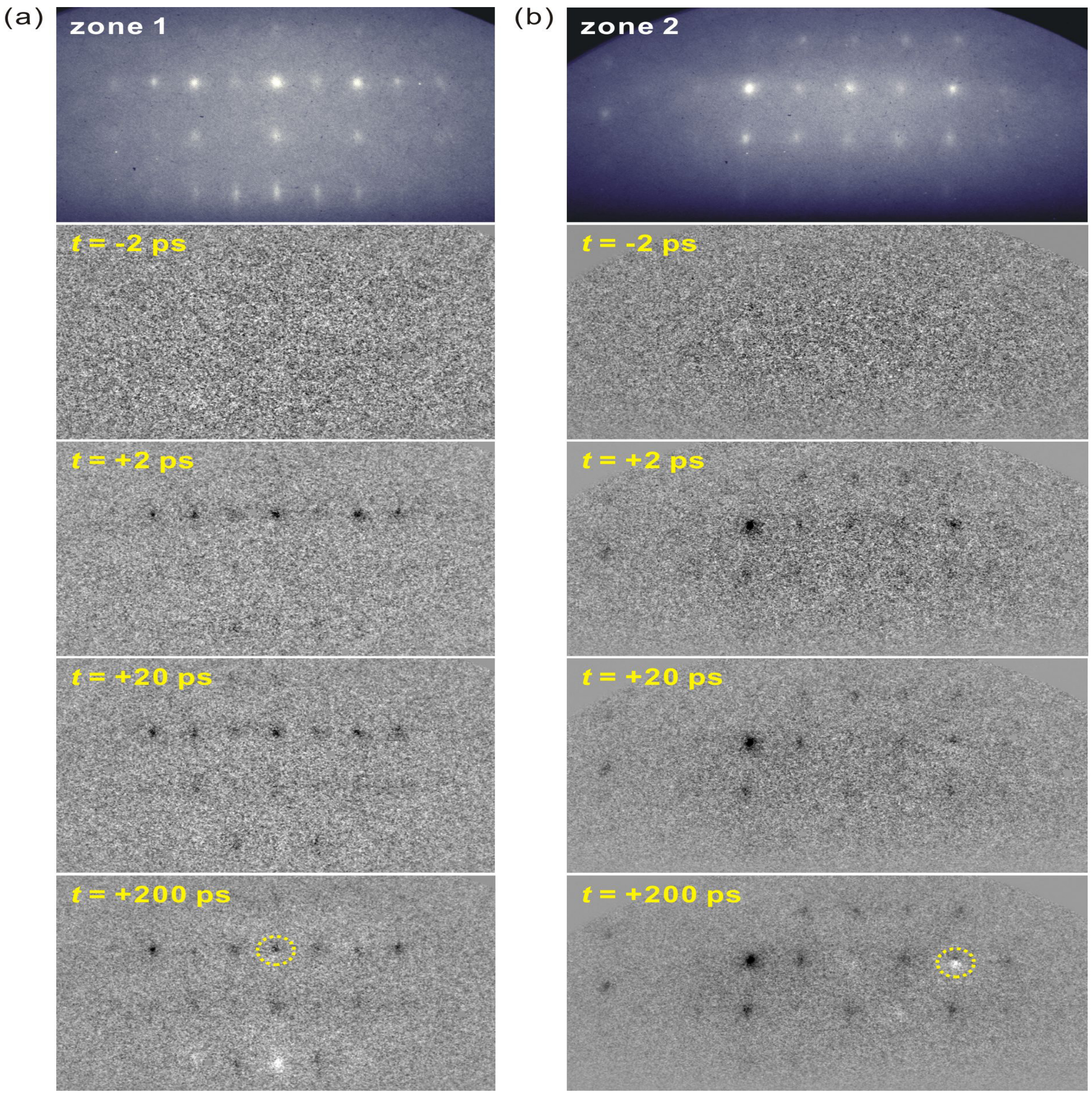

Fig. 5. Diffraction patterns at two zone axes and their time-dependent changes (referenced to the negative time frames), following the femtosecond optical excitation. Before time zero (e.g., *t* = –2 ps), no appreciable diffraction difference is observed. At positive times, dark spots signify intensity depletion and white spots intensity enhancement; the observation of both dark and white parts for the circled spots at *t* = 200 ps signifies a small position shift of the Bragg diffractions at a later time.

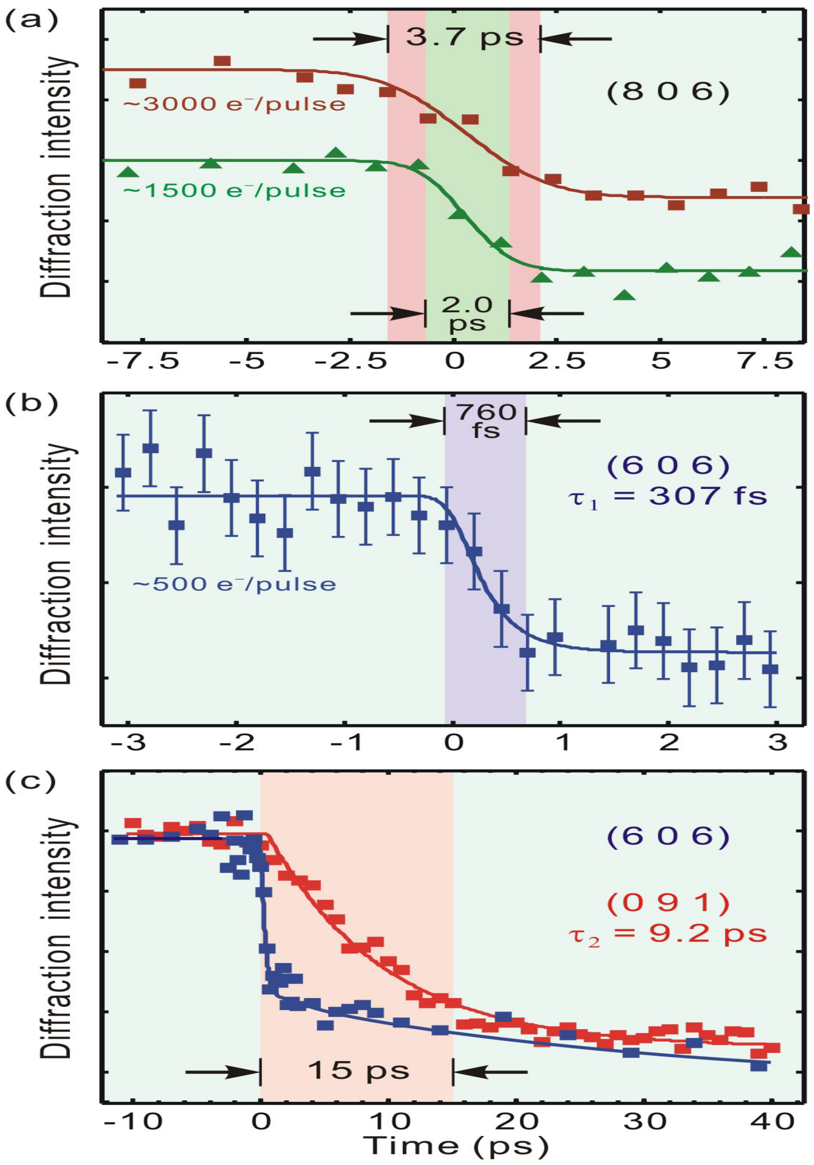

Fig. 6. Ultrafast dynamics of the structural phase transition of VO_2. (a) Intensity change of the (806) Bragg spot with time. The observation was made at a larger number of electrons per pulse. The colored regions indicate the temporal range over which the intensity decrease occurs. The results signify that the ultrafast change is faster than the temporal resolution. (b) Intensity change of the (606) Bragg spot with time. The decay shows an apparent time constant (τ_1) of 307 fs on the total time range of ±3 ps. (c) Intensity changes of the (606) (blue) and (091) (red) spots with time. A femtosecond decay similar to the blue trace was measured for other spots with a nonzero h index; a decay with a time constant (τ_2) of 9.2 ps, similar to the red trace, is measured for spots with $h = 0$ on the total time range of 40 ps. The temporal range values over which the decay is pronounced are 760 fs in (b) and 15 ps in (c). This difference indicates a stepwise mechanism for atomic motions

interatomic layers in the surface-normal direction are contributing to the interferences. We note that a rough estimate of the mean free path of a 30-keV electron gives a penetration depth (~5 nm) that is about 20 times the interplanar separation. By these examinations, we confirm the observed diffraction changes to be from the photoexcited bulk $VO_{2.}$

Results and Analysis

The patterns of diffraction change at four selected delay times, which are referenced to a negative time frame, are shown in Fig. 5 for two zone axes at an excitation fluence above 10 mJ/cm^2. Right before the zero of time, no appreciable difference can be seen, which assures the stability of the data acquisition without a long-term drift. After the zero of time, in only 2 ps, a significant decrease in intensity with no distinct spot movement is observed for some Bragg diffractions; the intensity drop is maintained at a similar level for a period of ~20 ps. Further diffraction changes, such as more intensity decrease or reversed increase, and spot position shift, continue to develop within 200 ps, and the resulting diffraction patterns remain steady for the following 1 ns, which reaches the end of our time range. These different periods signify the time scales involved in the photoinduced structural transformation of VO_2. Hence, to quantify the diffraction differences and characteristic times, we fit the horizontal and vertical profiles of the Bragg spots and retrieve the information of spot intensities, positions and widths as a function of time.

The initial intensity decrease at short times is plotted for three different Bragg spots in Fig. 6. Two types of behaviors are seen: an ultrafast decay that seems to be limited by the electron pulse width and a decay that lacks such fast dynamics but

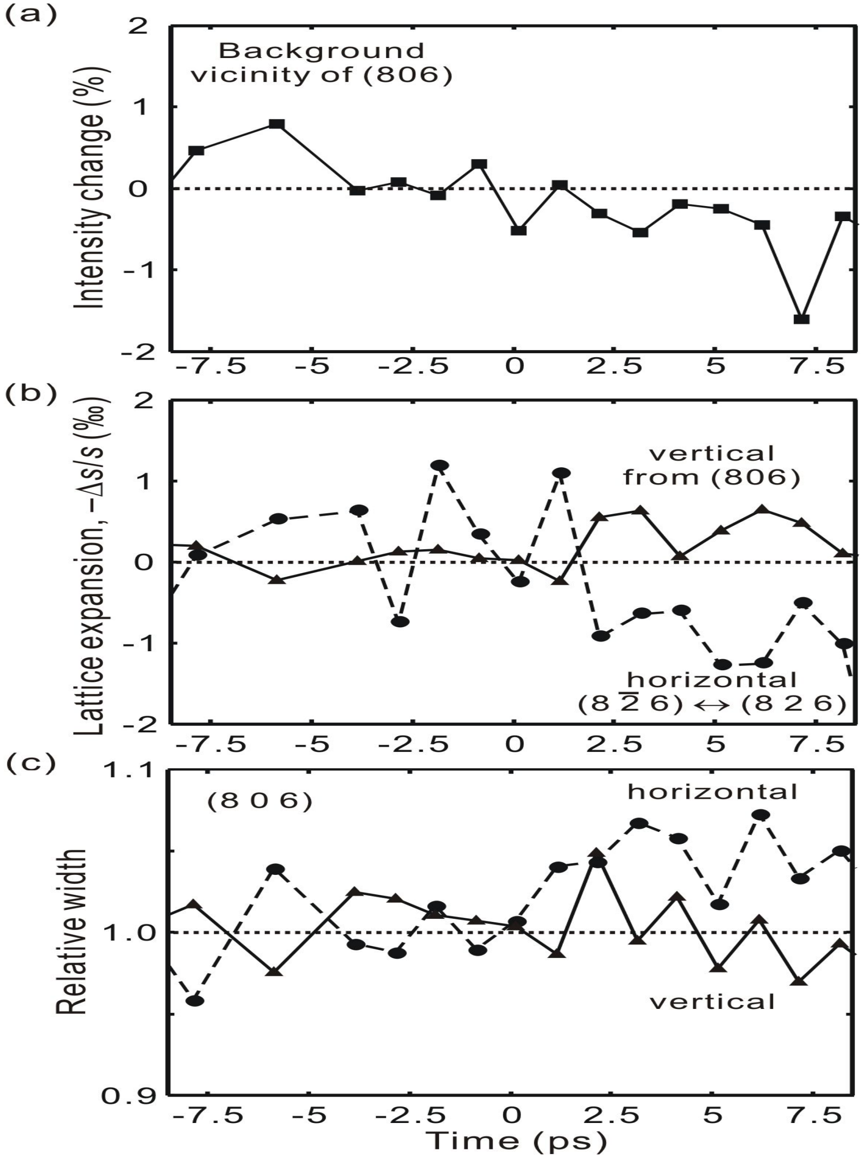

Fig. 7. Other diffraction changes at early delay times. (a) The scattering intensity in the vicinity of the (806) Bragg spot essentially remains at the same level while the diffraction exhibits clear femtosecond intensity decrease. (b) Vertical expansion derived from the position change of the (806) spot and horizontal expansion from the spacing change between the $(8\bar{2}6)$ and (826) spots with time. The Bragg spots keep their original positions at early times, signifying no major unit cell change on this time scale. Note the small scale for the vertical axis. (c) Vertical and horizontal width change of the (806) spot with time. The widths are essentially constant in this time range and their temporal behavior is quite different from those shown in Chs. 4 and 5.

proceeds within a longer period of ~15 ps. By lowering the number of electrons per pulse, the full range for the ultrafast intensity decrease can be reduced from 3.7 ps in Fig. 6a to 760 fs in Fig. 6b. Using the cross correlation between the optical pulse width of 120 fs and the electron pulse width of 322 fs at ~500 electrons per pulse, we deduce a time constant (τ_1) of 307 fs as an upper bound since the unknown residual spread from the setup for the pulse tilting scheme, broadening of the laser pulse in the optical path, and relative large uncertainty in the electron pulse width are not taken into consideration. This femtosecond behavior is manifested in the temporal changes of the following Bragg spots: ($8k6$) shown in Fig. 3d ($k = 0, \pm1, \pm2, \pm3$ or ±4); (10 2 4), (915), (806), $(7\bar{1}7)$, $(6\bar{2}8)$, (10 1 6), (907), $(8\bar{1}8)$, (923), (814), and $(5\bar{2}7)$ in Fig. 3e; (606), (714) and $(4\bar{1}7)$ in Fig. 3f. In contrast, the slower picosecond behavior is not affected by the electron pulse width, and has a time constant (τ_2) of 9.2 ps (Fig. 6c). Such dynamics is observed for the (091), (084) and $(08\bar{2})$ Bragg spots from the single crystal and also for the (040) from the thin-film sample.

We check the temporal changes of the background intensity in the vicinity of the (806) diffraction. Unlike 20% intensity decrease for the spot at 10.2 mJ/cm^2, the intensity of inelastic scattering exhibits essentially no dynamics and maintains a constant level, as shown in Fig. 7a. Therefore, the difference patterns presented in Fig. 5 do not originate from an overall decrease in the number of diffracted electrons that might be caused by the photoinduced insulator–metal transition. They reveal real structural changes during the transformation. The positions and widths of the intensity-decreasing Bragg spots have no significant dynamics at early times, as demonstrated in Fig. 7, panels b and c, respectively. For comparison, a clear Bragg spot movement as large as 2.5% (Ch. 7) and a distinct width broadening of more than 50% (Ch. 4) have been observed in different

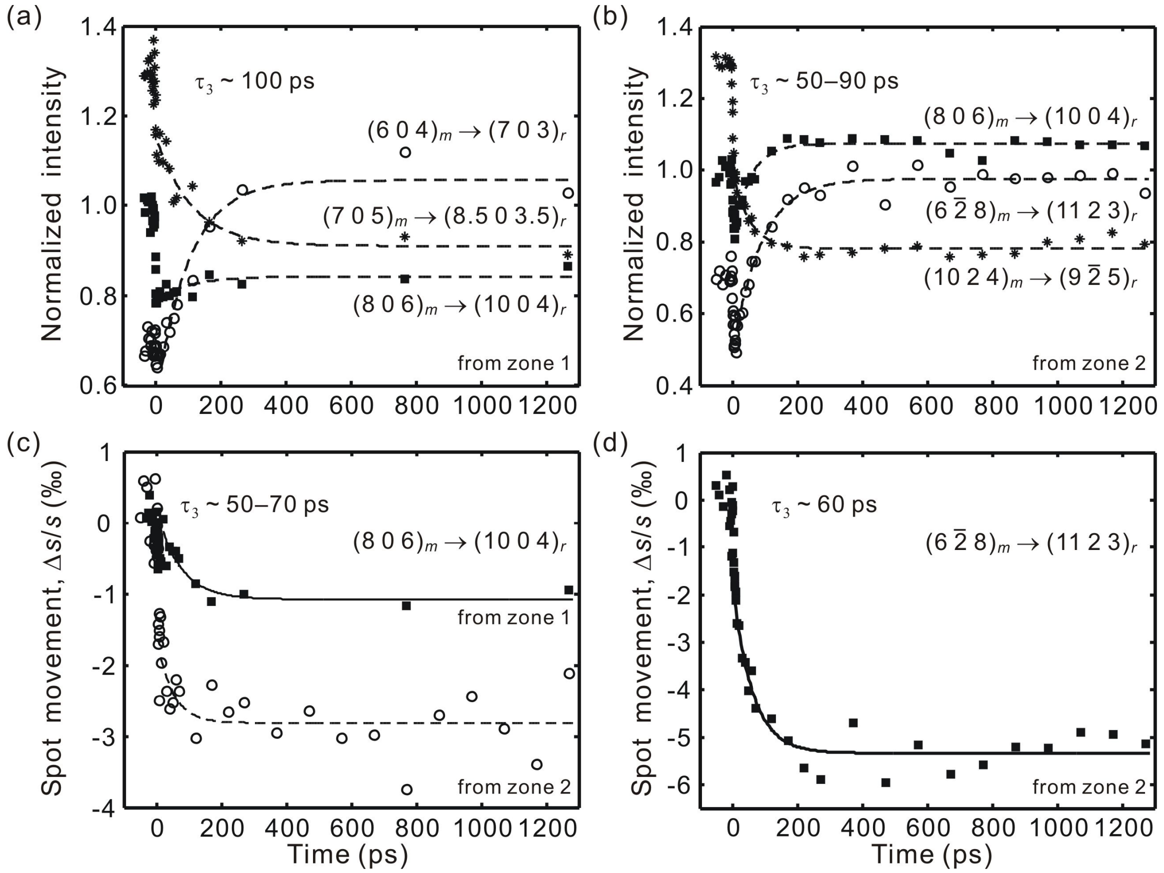

Fig. 8. Long-time change in (a and b) the diffraction intensities (offset vertically by a constant value for clarity) and (c and d) the positions, obtained from the experiments at different zone axes. Indices of the Bragg spots for the M_1 phase and their conversion into the high-temperature ones are provided. The temporal profiles are fitted to a single exponential decay function, and the extracted time constant (τ_3) is given in each panel. These values are similar and, therefore, indicate the time scale for the final lattice conversion from the M_1 phase to the high-temperature one. After the conversion is complete, the diffraction intensities and positions remain for >1 ns.

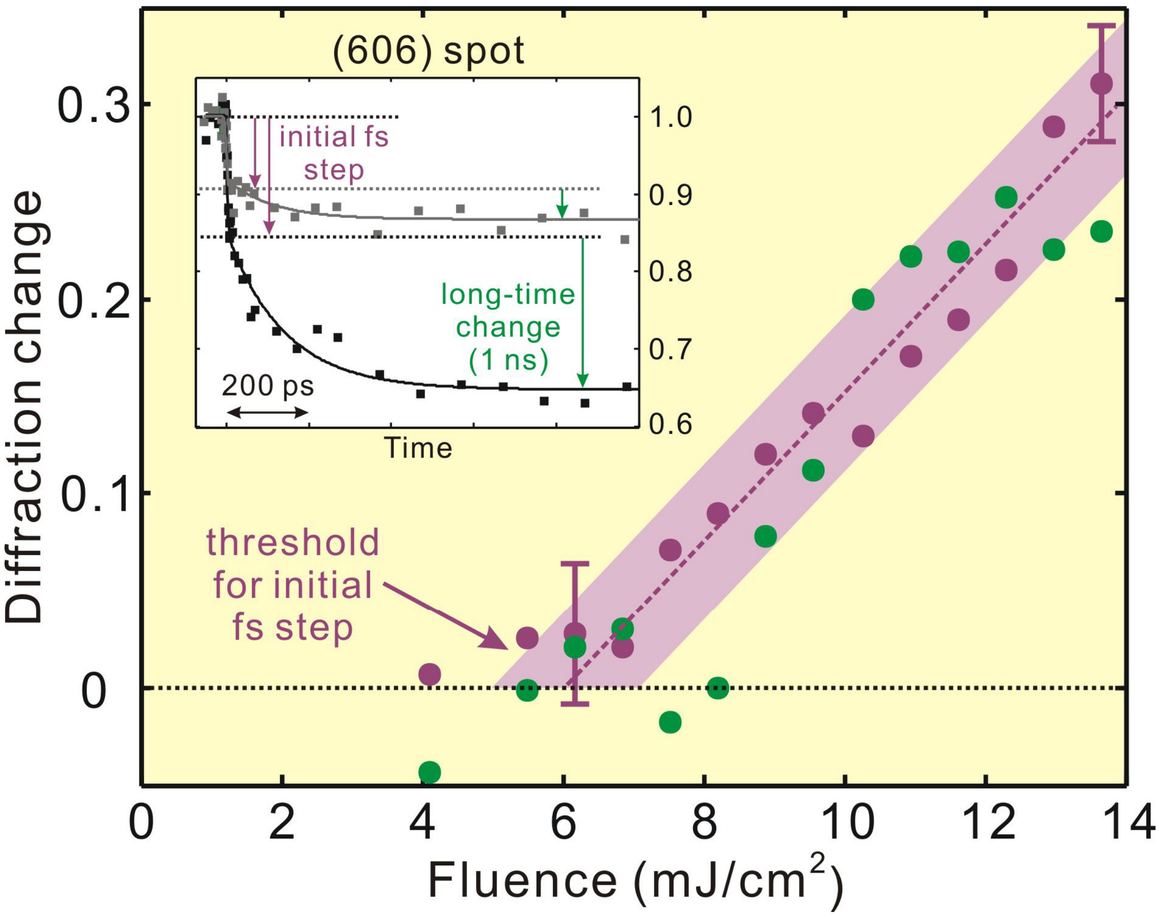

Fig. 9. Dependence of the femtosecond dynamics and the large-scale shear displacement on excitation fluence at room temperature. The magnitude of the initial intensity decrease (violet) and the amplitude of the long-time change (green) are plotted for different excitation fluences. A common threshold region is observed. The inset shows the transients of the (606) Bragg spot for two different excitation fluences. The magnitudes of change were measured at 10 ps and 1 ns.

materials. Thus, the particular manner of the diffraction changes presented here signifies a different transformation mechanism from those reported in other studies.

At a later time, the VO_2 structure has to complete its transition into the tetragonal form. The further changes in the Bragg spot intensities and positions within the experimental time range are shown in Fig. 8. The common feature in these transients is the evolution of diffraction change toward a final value with a time constant (τ_3) of 50~100 ps, followed by its maintenance for 1 ns or longer. Intensity increases and decreases for different spots are observed (Fig. 8, panels a and b), depending on the diffraction indices and also the overlap between the reciprocal lattice points and the Ewald sphere after the structural transformation; more discussion will be given in the next section. For the spot positions, as plotted in Fig. 8, panels c and d, as two examples, we observe ~0.1% (~0.3% in another measurement) and ~0.5% decrease in the reciprocal vectors of the $(806)_m$ and $(6\bar{2}8)_m$ spots, respectively. The calculated changes for these two spots are –0.23~0.33% and –0.19~0.44%, depending on the unit-cell parameters used (*15, 16*); it is noted that these values may need some adjustments due to the slight tilt of the axes (*31*). However, according to the good agreement between our experimental observations and the calculations based on the static structures from x-ray diffraction, we conclude that completion of the transformation to the tetragonal structure occurs on a time scale of ~100 ps after the femtosecond photoexcitation.

After the identification of the short-term and long-term dynamics, fluence dependence of the diffraction intensity was studied at room temperature for two time points, $t = 30$ ps and $t = 1.3$ ns, as shown in Fig. 9 for the (606) Bragg spot as an example. The intensity change displays a nearly linear dependence with a threshold (F_{th}) at 6 ± 1 mJ/cm^2 (*53*). Given the reflectivity (R) of 0.28 and the optical penetration depth

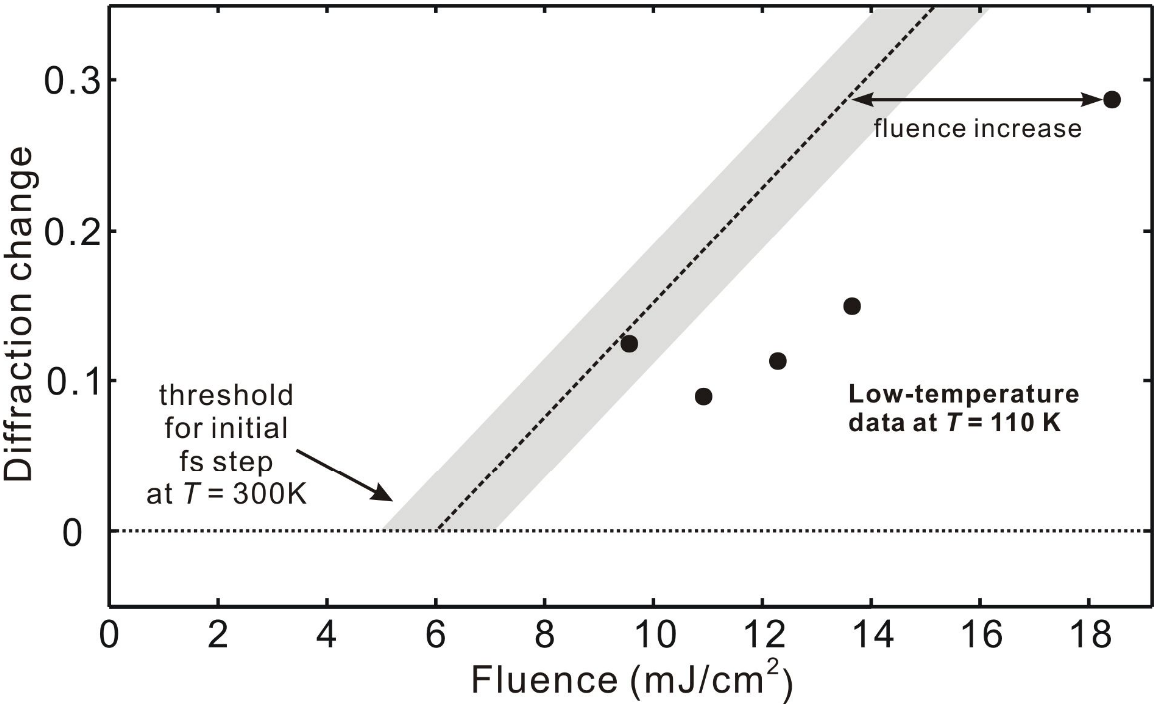

Fig. 10. Comparison of the fluence dependence of the femtosecond dynamics at two temperatures. The dashed line and the shaded region are the same as those in Fig. 9 for room temperature. At $T = 110$ K, an increased fluence (indicated by the horizontal arrow) is required for the observation of the same level of initial intensity decrease at $T = 300$ K.

($1/\alpha$) of ~100 nm at 800 nm (*54*), this threshold fluence corresponds to an optical density of $F_{\mathrm{th}}(1–R)/(1/\alpha) = 430$ mJ/mm^3 absorbed at the surface. With the unit cell volume of 118 Å^3 (*16*), which contains four vanadium ions, such an energy density gives ~0.05 photon per vanadium ion, indicating the minimum fluence required for switching into the new phase in crystalline VO_2. For the spots that exhibit the femtosecond dynamics, the threshold for the sub-nanosecond component is either the same or slightly higher than that for the femtosecond component (Fig. 9), suggesting that the appearance of the long-time dynamics is associated with the initiation of the short-time dynamics.

Prompted by the coincidence between the threshold energy density of

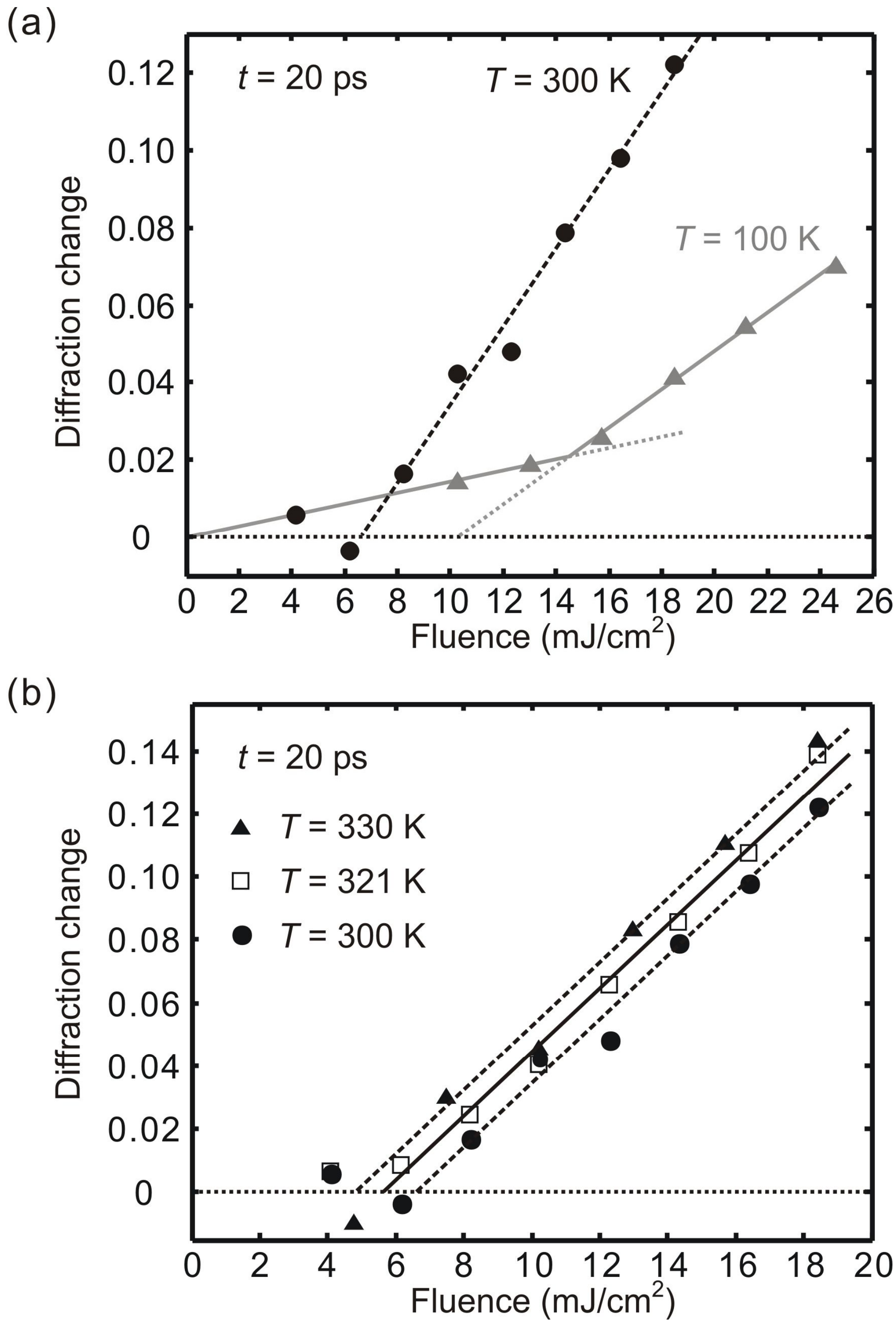

Fig. 11. Fluence dependence of the initial intensity decrease (measured at $t = 20$ ps) for different temperatures. The specimen is a VO_2 film (140 nm in thickness) deposited on $Al_2O_3(10\bar{1}0)$. The thin-film results agree well with those obtained from the VO_2 crystals.

430 ± 72 mJ/mm^3 (i.e., ~1800 ± 300 cal/mole) and the minimum thermal energy necessary for the phase transition from $T = 300$ K [i.e., the required enthalpy increase of ~550 cal/mole plus the latent heat of 1020 cal/mole (*4*)], we set off to investigate the influence of the temperature on F_{th} for the photoinduced transformation. The temporal evolution of diffraction changes at $T = 110$ K is found to be similar to the observation at room temperature. Intriguingly, much larger excitation fluence is required to cause an initial intensity decrease of 30%; the general trend obtained from the low-temperature experiment provides good evidence for an increased threshold (Fig. 10). To verify this observation, we also conducted similar experiments on a thin-film specimen, $VO_2/Al_2O_3(10\bar{1}0)$. The results, presented in Fig. 11a, show a satisfactory agreement: practically the same threshold of F_{th} ~6 mJ/cm^2 is obtained at room temperature and a larger one for the low temperature. Moreover, this threshold fluence becomes lower at temperatures higher than 300 K but below 340 K (Fig. 11b). Such a coincidence between the photoexcitation threshold observed in the current dynamics study and the thermal energy mandated by thermodynamics may be the pivotal connection between the two approaches, dynamical and static, for the study of VO_2. Its importance and implications are discussed in the next section.

Discussion

A. Short-time Dynamics: V–V Bond Dilation and Intracell Adjustment

The absence of a spot shift at early times signifies that no lattice expansion takes place on the ultrashort time scale as a result of the optical excitation (Fig. 7b). In addition, the absence of a clear width change indicates that no significant lattice disorder is introduced (Fig. 7c). Thus, structural modification on a larger scale across many unit cells

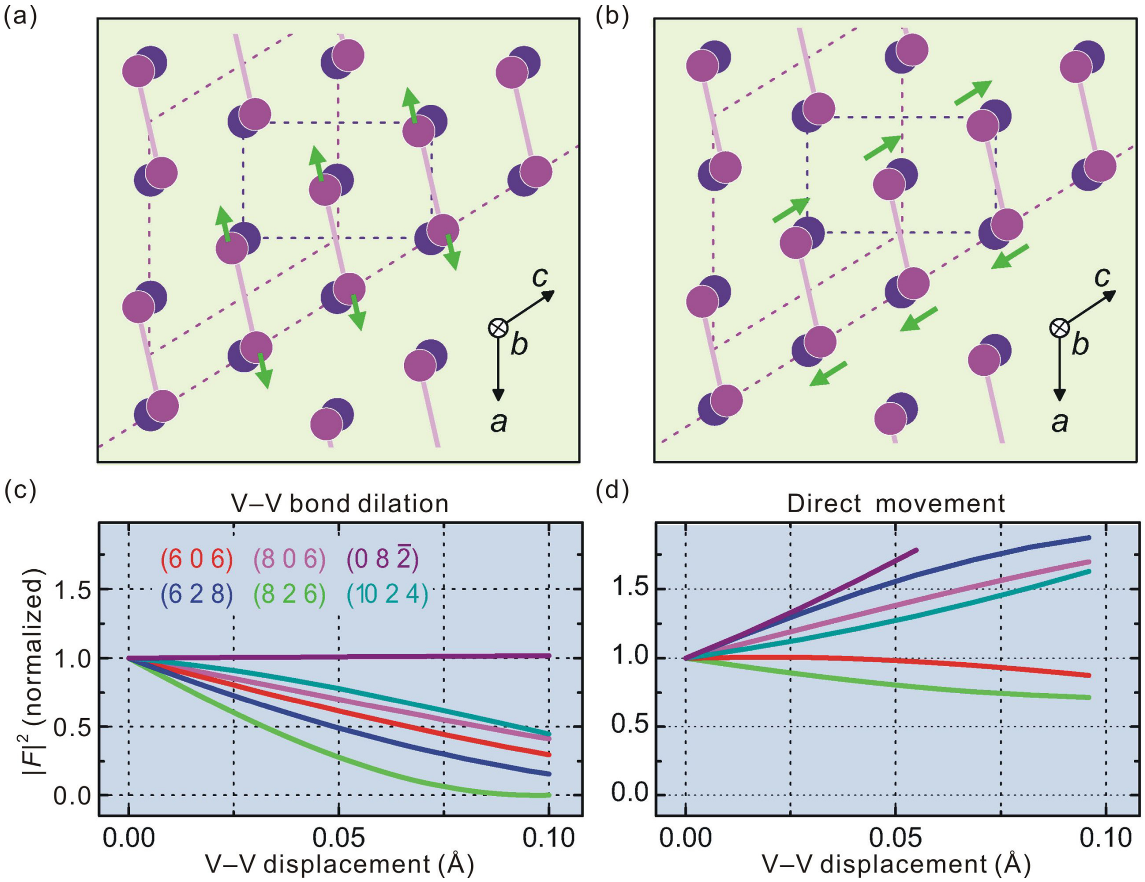

Fig. 12. Atomic movements and the calculated structure factors. (a) Indirect motion of the vanadium ions from the initial (purple) to the final (blue) positions, with the initial step being the displacement of the vanadium ions along the chemical bonds that are mostly along the monoclinic *a* axis. The monoclinic unit cell is depicted as dotted purple lines and the tetragonal unit cell as a blue dotted box. (b) Direct motion of the vanadium ions from the initial (purple) to the final (blue) positions, mostly along the monoclinic *c* axis. The indicated displacements in panels a and b are for delocalized excitation of the lattice. (c) Structure factor and expected intensity change for the listed Bragg spots for the displacement depicted in panel a. (d) Structure factor and intensity change for the displacement depicted in panel b.

is not significant during this time range. These observations also exclude thermal expansion or lattice inhomogeneity (strain) as an important mechanism to consider.

In contrast, the intensities of Bragg spots are influenced by the photoexcitation of valence electrons, signifying that additional atomic motions take place within the unit cell and cause destructive interference to diffraction. Notably, all Bragg spots that show the femtosecond behavior involve nonzero values for the *h*, *k* and *l* indices, whereas those displaying the slower picosecond behavior have a zero *h* index. This distinct difference confirms that the photoexcited material is in a highly nonequilibrium state, and the diffraction intensity decrease cannot be explained by the Debye–Waller factor (Eq. 16 of Ch. 2) derived on the basis of thermal equilibrium. Furthermore, the two behaviors with a clear difference in the time constants signify stepwise atomic motions along different directions. Thus, we should return to the structure factor and consider the possible atomic movements for the observed diffraction changes.

The intensity (*I*) of the Bragg spot (*hkl*) is proportional to the square of the structure factor, *F*(*hkl*), which is determined by the position (*xyz*) of atom *j* within the unit cell,

$$F(hkl) = \sum_j f_j \exp\left[-2\pi i\,(hkl)\cdot(xyz)_j\right];\quad I(hkl) \propto \left|F(hkl)\right|^2, \tag{1}$$

where f_j is the atomic scattering factor. The initial and final vanadium positions in the two phases are depicted in Fig. 12, panels a and b. From the inner product in Eq. 1, it is evident that an atomic movement along a certain direction can only affect those Bragg spots with nonzero components in the Miller indices along that direction. Thus, it is concluded from the experimental results that the initial femtosecond motion is mostly along the *a* axis, which also corresponds to the direction of the V–V bonds in the M_1 structure (Fig. 12a). On the other hand, the picosecond structural transformation projects along the *c* and *b* axes. If the femtosecond motion had significant components along *b* or *c*, it should be manifested in the dynamics of all investigated spots, contrary to the observations. Note that the direct structural evolution from the initial M_1 to the final tetragonal phase is mostly along the *c* axis (Fig. 12b). Therefore, the argument in the Introduction Section is justified: the photoinduced phase transformation of VO_2 involves not only the initial and final states but also transitional structures which appear on the femtosecond and picosecond time scales. The observed stepwise atomic motions indicate that the phase transition proceeds through a nondirect pathway on the multidimensional potential energy surface, and not through a direct structural conversion.

To quantify the short-time structural changes, we calculate for the observed Bragg diffractions the structure factor and intensity changes as a function of the atomic displacement. In Fig. 12c, the results of the V–V bond-weakening (or dilation) motion is displayed. All spots with a nonzero *h* index show a decrease in intensity and for those with $h = 0$, the intensity remains nearly unchanged, as experimentally observed on the femtosecond time scale. In contrast, the direct transformation from the initial to the final structure would cause most spots to show an increase, and some a decrease, in the $|F|^2$ value (Fig. 12d), a behavior which disagrees with the observation within an ultrashort time. It is noted that in the limit of delocalized, uniform excitation across all excited unit cells, even a small-amplitude motion of V–V bond dilation on the order of 10^{-2} Å can cause a substantial decrease in diffraction intensity. This effect is likely to have its origin in the symmetry of the structure: the M_1 phase has a lower symmetry and the structural transformation is a symmetry-raising process.

The initial photoexcitation of the valence electrons in VO_2 may be more localized instead of being uniformly distributed. We also consider this localized scenario by calculating the $|F|^2$ value with four random (instead of all 54) dilated bonds in a 3×3×3 supercell. The results are very similar to those plotted in Fig. 12c, except for a larger V–V separation. For the same amount of intensity decrease, this localized scenario requests ~10 times the V–V displacement obtained from the delocalized scenario, which is on the order of 10^{-1} Å. Such an amount of displacement is a large fraction of the difference between the two V–V bond lengths in the M_1 phase (i.e., 0.588 Å), which can reasonably be the beginning step for the transformation to the equal V–V distances as in the tetragonal phase.

The femtosecond V–V bond dilation can be readily understood from a chemical perspective. The initiating excitation at 1.55 eV is primarily from the $d_{||}$ band that has major contribution from the bonding of vanadium pairs (*5, 19*) to an antibonding state that instantly results in a repulsive force on the atoms. Consequently, they separate along the bond direction in an ultrashort time faster than τ_1 = 307 fs, which is already less than twice the V–V vibrational time of ~170 fs (*28*). In sequence and on a slower time scale, all atoms in the unit cell adjust themselves under the influence of the new electronic state, towards the configuration of the tetragonal phase. These two successive stages of structural evolution constitute the short-time dynamics.

It is worth noting that the dominance of the femtosecond dynamics emerges when the relevant direction of diffraction is monitored; the picosecond component originates from the transversal motion. Therefore, it is expected to see a composite transient behavior in optical reflectivity or diffraction experiments on polycrystalline samples because of the averaging over all orientations. A previous study using time-resolved x-ray diffraction (*24*) reported that the temporal evolution of intensity increase around the (011)-spot region (*55*) from a crystal is dominated by a 12-ps profile, with a relatively

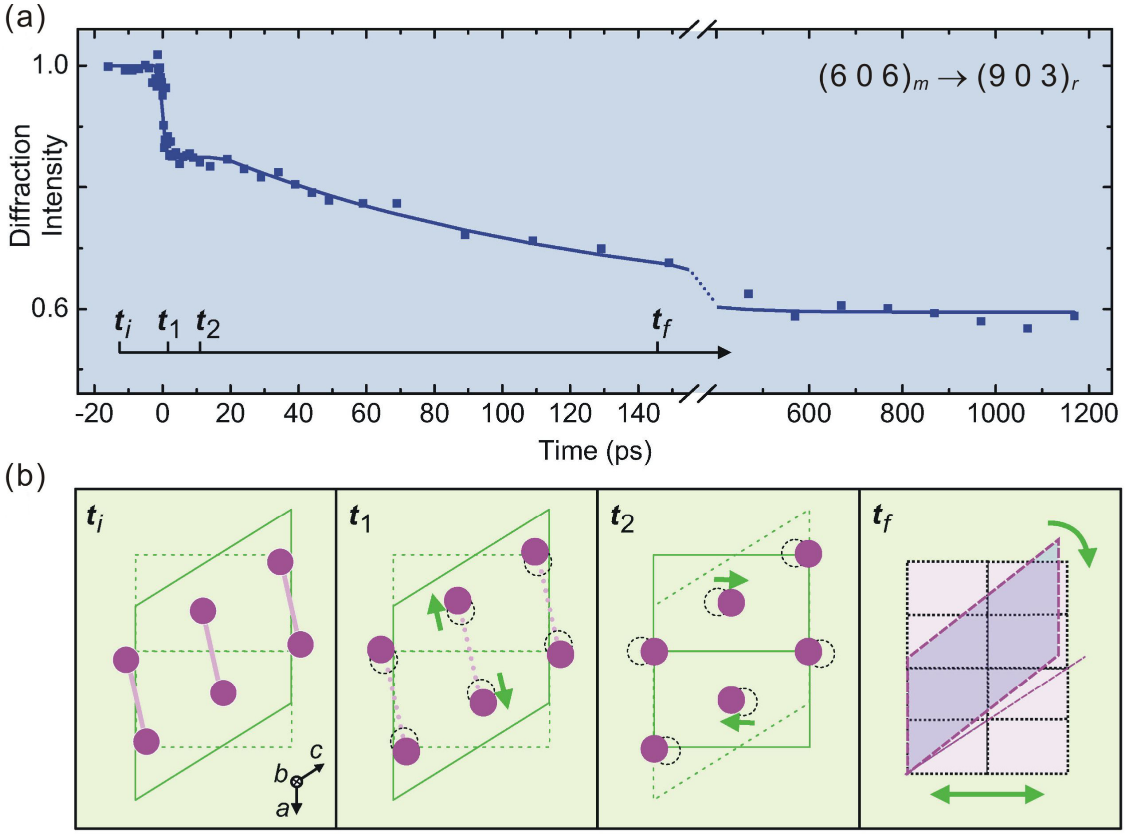

Fig. 13. Transitional structures during the ultrafast phase transformation. (a) The experimental data, here the $(606)_m$-spot (blue), reflects the stepwise atomic motion within the unit cell and, on larger length scales, of shear motion. The important times during the transformation are indicated (t_i: before photoexcitation; t_1: after the femtosecond process; t_2: after the picosecond process; t_f: on a longer time scale). (b) Structural changes at the corresponding times (t_i, t_1, t_2, t_f).

small faster component (≤500 fs). In this work, the transitional structures *en route* to the stable tetragonal configuration are resolved, and distinct coordinates can be defined for the energy landscape of the current photoinduced phase transformation. The overall temporal behavior, up to 1.2 ns, and structural snapshots are presented in Fig. 13 (see below for the long-time dynamics).

Before our recent report on direct probing of the photoinduced structural transformation in VO_2 (*46*), Cavalleri *et al.* reported the ultrafast optical reflectivity changes with a bottleneck time scale believed to be limited by the structure and related to the stretching and tilting of V–V dimers (*28*). Lately, Kübler *et al.* reported coherent structural dynamics of polycrystalline VO_2 within the first picosecond using multi-THz conductivity (*27*). From the spectral region related to the IR-active phonon resonances, they observed oscillations centered at 6 THz and provided a qualitative model with the initial dynamics being the local excitation of molecular V–V dimers into an antibonding state. Here, we want to point out that, while the same initial femtosecond mechanism is reported, this is the first time that the transitional structures are directly resolved and the whole transformation process is mapped up to a nanosecond time. The current study on VO_2 well demonstrates the capability of UEC.

The comparison of $\tau_1 = 307$ fs (an upper bound) with the 80-fs time constant from optical reflectivity (*28*) or with the ≤500-fs one from X-ray diffraction (*24*) is not straightforward, as the former approach is more sensitive to the changes in the electronic configuration of the material whereas the latter integrates the structural changes over the X-ray probing length of micrometers. Future experiments with a ≤100-fs temporal resolution may unravel the time scale of the femtosecond dynamics to be half of the vibrational time (~170 fs) of the equilibrium structure, or one or two vibrational periods due to potential-driven motion (Chs. 4 and 5) in the excited state (*27*). However, it is promising to infer the answer based on the observed threshold behavior (see below).

B. Long-time Dynamics: Carrier Diffusion and Lattice Shear Motion

The transient behavior on the longer, sub-nanosecond time scale reveals another dimension of the structural dynamics. As shown in Fig. 8, after the initial insulator–metal transition, there is a continuous temporal change in the spot intensities and positions which levels off at $t \sim 300$ ps. Specifically, the movements of the $(806)_\mathrm{m}$ and $(6\bar{2}8)_\mathrm{m}$ Bragg spots toward their corresponding positions predicted by the tetragonal structure do not start immediately after the femtosecond optical excitation (Fig. 7b), but proceed after the short-time (femtosecond and picosecond) structural dynamics (Fig. 8, panels c and d). The observation leads us to the conclusion that, within the photoexcited region, the final tetragonal structure is not fully achieved until few hundred picoseconds. The optical reflectivity experiment showed that a metallic state is already reached and maintained after the femtosecond dynamics (*28*). Therefore, the resolved transitional states during the picosecond dynamics (Fig. 13b, t_1 to t_2) and the sub-nanosecond evolution (Fig. 13b, t_2 to t_f) can be assigned as metallic monoclinic and unexpanded metallic tetragonal states, respectively. The existence of a metallic intermediate state with a monoclinic geometry (*21*) is also confirmed, although it is ultrashort-lived in nature (*56*).

With the time scale of ~100 ps in mind, we first examine the possibility of thermal diffusion as the dominant mechanism. The thermal diffusivity coefficient (κ) of VO_2 at $T = 300\mathrm{K}$ is $0.021\ \mathrm{cm^2/s}$, calculated from the relation $\kappa = K/\rho C_l$ where $\rho = 4.67\ \mathrm{g/cm^3}$ is the density, $C_l = 0.67\ \mathrm{J/(g{\cdot}K)}$ is the specific heat and $K = 0.066\ \mathrm{W/(cm{\cdot}K)}$ is the thermal conductivity (*4*). From the optical penetration depth of ~100 nm and the equation of thermal diffusion in one dimension,

$$\frac{\partial T}{\partial t} = \kappa \frac{\partial^2 T}{\partial z^2},$$

we calculate that major heat conduction away from the probed layer must be slower than 1 ns (*57*). In fact, a simple estimation of the characteristic time for the absorbed heat to be well removed from the 100-nm excited region is $(100\ \mathrm{nm})^2/4\kappa \sim 1.2$ ns. Thus, thermal diffusion itself cannot explain the observed ~100-ps dynamics, and is likely a minor factor to consider.

Carrier diffusion within the excited, metallic region, on the other hand, may have a time constant that is on the correct order of magnitude. The carrier diffusion coefficient D_c may be estimated with the use of the Einstein relation, $D_c = \mu \cdot \frac{k_B T}{q}$, where μ is the carrier mobility in the metallic phase, k_B is the Boltzmann constant and q is the charge of a carrier. If q is assumed to be the unit charge and μ is on the order of 1–10 cm^2/(V·s) (*4*), D_c will be on the order of 0.1 cm^2/s, resulting in a diffusion curve resembling to an exponential decay with a time constant of ~100 ps and, therefore, matching with the observation. The relevance of carrier diffusion in the structural dynamics is the following. Excess electrons (carriers), which are not bound by strong correlation with the lattice, may redistribute within the excited metallic region but are impeded by the insulating surrounding. The diffusion of carriers from the surface region of higher carrier density to the less dense bulk means a partial removal of excitation from the electron-probed region, leaving a partial transformation behind. This may explain why the $(705)_m$ spot in Fig. 8a, which is forbidden in the tetragonal structure, does not fully disappear at an intermediate fluence; its intensity does go to zero when a higher fluence is applied (data not shown).

In addition to carrier diffusion, another crucial (maybe even more important) mechanism is the motion of shear and expansion/contraction (Fig. 13b, t_f). The diffusion of electrons into the deeper region may contribute to the generation of this motion, too. As mentioned in the Introduction Section, shear is inevitable for the macroscopic formation of the tetragonal phase. From the static x-ray diffraction measurements, the small angular movements of nearly all Bragg spots upon the phase transition (Fig. 2b) indicate a slight rotation of the crystallographic axes (*31*), which is equivalent to a shear motion. As it travels at the sound speed of ~4000 m/s in VO_2 for a length scale of few hundred nanometers, the time scale is also tens of picoseconds and corresponds well with the observation. This shear motion is further supported by the evolution of Bragg spot intensities. Although the Bragg spots exhibit the same early femtosecond-to-picosecond behavior, they show intensity increase or decrease at the sub-nanosecond scale for different zone axes. Because not all Bragg spots equally well coincide with the Ewald sphere at the same time, shear motion may enhance or suppress the Bragg intensities besides the changes given by the structural transformation. The asymmetric change shown in Fig. 5b is a good example.

We have given a full account of the photoinduced structural dynamics at short and long times, and also distinguished the different stages and the mechanisms involved during the phase transformation. Because of the similar dynamics observed at different fluences, we are able to compare the extent of the diffraction change from a fluence-dependent study at two characteristic times. A different sample temperature does not affect the dynamical behaviors, thus the direct comparison of thresholds retrieved at different temperatures is also feasible.

C. Threshold Behavior: Dynamics vs Thermodynamics

The existence of an excitation threshold for the initiation of the femtosecond V–V bond dilation shows that, from a delocalized energy-band perspective, a minimum density of photodoping is necessary for the change of the band structure into a metallic configuration together with the structural modification. From a chemical perspective, a minimum level of charge excitation (i.e., enough bond weakening) is needed to cause an irrecoverable motion. The requirement of ~0.05 photon per vanadium (equivalent to one electron for every 20 V^{4+} ions) at room temperature is quite low as compared to an electron provided by each V^{4+} ion (its electronic configuration is $3d^1$). This result gives some hints about the easiness of perturbing the VO_2 system. Below this threshold the V–V bond is simply set on a coherent vibrational motion (*27, 28*), although its bond strength is slightly reduced.

Intriguingly, a diffraction intensity decrease due to the induced additional motion of V–V vibration is not clearly discernible when the excitation fluence is below the threshold (Fig. 9). Here is a puzzling inconsistency: according to the scenario of delocalized excitation in Fig. 12c, an intensity decrease would always be present and no threshold behavior would be expected, because the atomic movement for the V–V displacement (on the order of 10^{-2} Å) is comparable to a typical increase in the vibrational amplitude. This puzzle may be resolved by adopting the scenario of localized excitation. At an optical fluence lower than the threshold, because the dispersed excited units cannot form the required connectivity for the macroscopic structural transformation, the strongly correlated material VO_2 only allows an additional vibrational amplitude (on the order of 10^{-2} Å) to be added to the existing V–V thermal motion at room temperature. As mentioned previously, an appreciable decrease in the Bragg spot intensity in this picture needs a V–V displacement (not simply vibration) on the order of 10^{-1} Å. Therefore, it is consistent to observe no appreciable intensity decrease at low fluences. Above the threshold, V–V bond dilation initially occurs at various localized places, with a density higher than one pair per 20 vanadium sites (i.e., per 5 unit cells) to ensure the connectivity through strong correlation; immediately following this initial excitation, the equilibration and intracell adjustment take place in all adjacent unit cells on the picosecond time scale, signifying a collective motion. This mechanism may be regarded

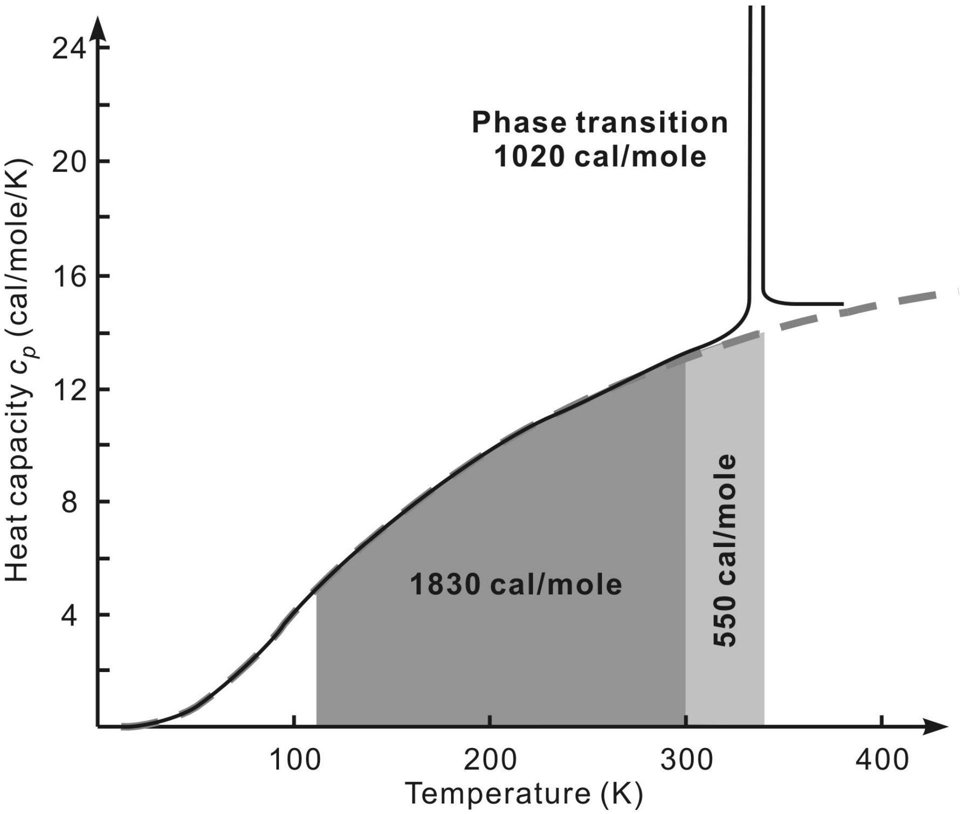

Fig. 14. Heat capacity of VO_2 as a function of temperature (solid lines). The dashed line is the theoretical value for Debye temperature of 750 K (*4*). The values given in the shaded regions are the enthalpy increase required for the corresponding temperature rise. The latent heat for the phase transition equals to 1020 cal/mole.

as the dynamical version of the percolation model considered in temperature-dependent studies (*10, 58*).

The fact that the threshold for the sub-nanosecond component is not below that for the femtosecond component (Fig. 9) indicates the appearance of the long-time dynamics to be associated with the initiation of the short-time dynamics. The major implication is, regardless of the temperature of the material, the necessity of the initial femtosecond V–V bond dilation for the proceeding of the following dynamics, including the intracell adjustment, diffusion of nonbound carriers, lattice expansion/contraction and shear motion. In other words, without the V–V bond dilation, VO_2 maintains the structural intactness in the M_1 phase.

It seems a pure coincidence for the optical density threshold at $T = 300$ K to be close to the minimum thermal energy mandated by the phase transition from the same temperature, if one considers the nature of the femtosecond localized excitation versus the overall macroscopic change in the energy content through thermal means. However, the influence of temperature on the observed threshold strengthens this correlation. If correct, according to Fig. 14, a fluence threshold of 11.3 mJ/cm^2 at $T = 110$ K (or equivalently, an increase of ~6 mJ/cm^2 relative to the room-temperature value, 5.2 mJ/cm^2 derived from the thermodynamic value) is expected; at a temperature just below the transition, a threshold of 3.4 mJ/cm^2 (or a decrease of 1.8 mJ/cm^2) is anticipated. Experimentally, the shift by ~4.5 mJ/cm^2 in Fig. 10 for observing a similar degree of diffraction change at 110 K, and the threshold increase of 4–8 mJ/cm^2 at 100 K in Fig. 11a, give a fairly good agreement with the expected increase of 6 mJ/cm^2. The observed threshold decrease of ~2 mJ/cm^2 at $T = 330$ K in Fig. 11b also makes a good match. Thus, the strong correlation between the optical and thermal energy values at various temperatures encourages a serious comparison between the dynamical behavior of VO_2 and its thermodynamic properties.

In fact, there are other studies reporting a similar fluence threshold at room temperature and some mentioning the trend for the temperature dependence. From a VO_2 film, a threshold of 3 mJ/cm^2 was measured by femtosecond infrared absorption (*26*). From a polycrystalline thin film, the thresholds observed by multi-THz conductivity were 5.3, 4.6 and 3 mJ/cm^2 at $T = 250$, 295 and 325 K, respectively (*27*). From an oriented thin film, the extrapolated threshold from the photoinduced conductivity measurements

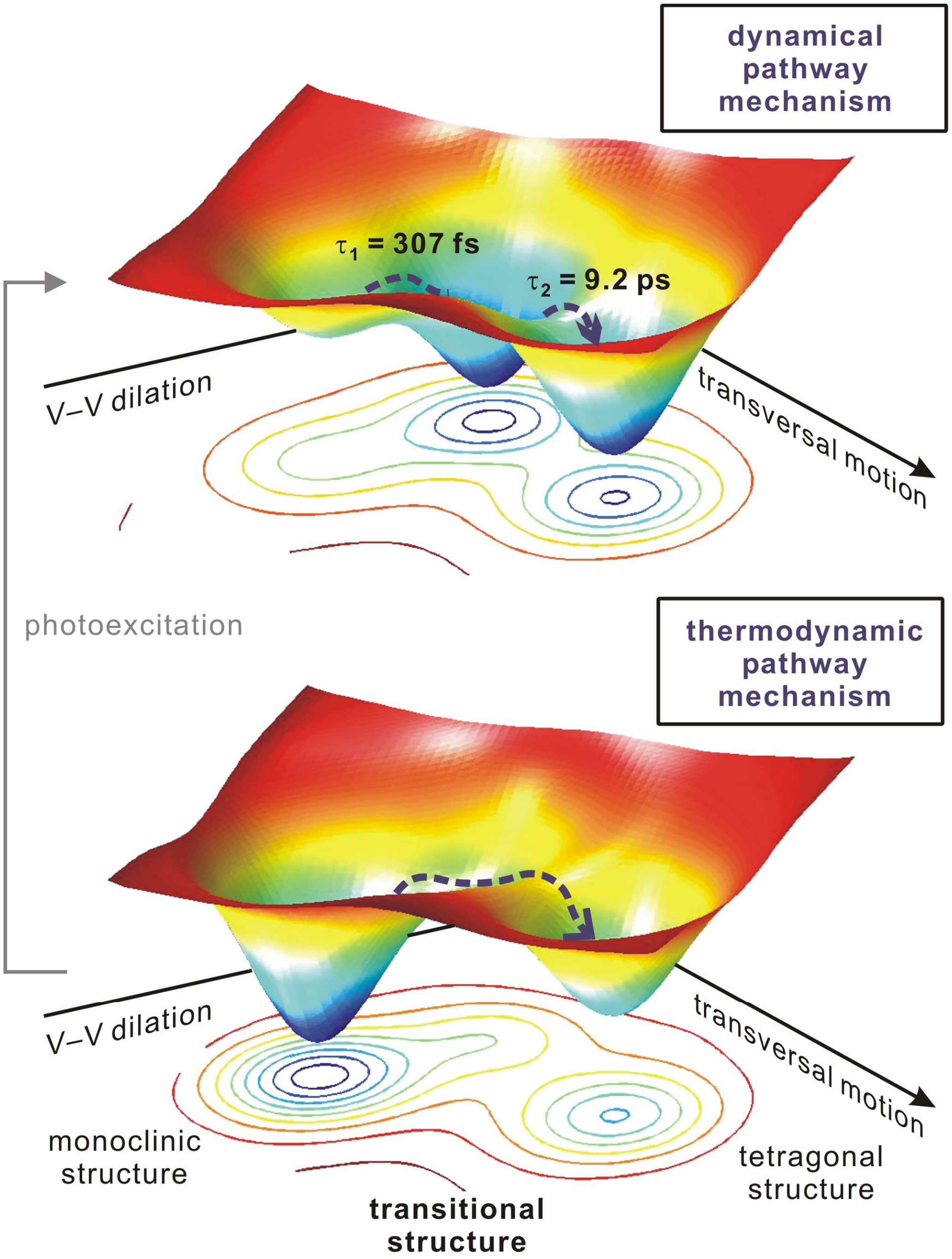

Fig. 15. The stepwise mechanism for the insulator–metal, monoclinic–tetragonal phase transition of VO_2, through the photoexcitation (upper panel) or the thermal means (lower panel). Structural intermediates are involved in the transformation process, and the initial step is the dilation of V–V dimers in the M_1 phase. A change in temperature leads to the change in the relative energies of all three (initial, intermediate and final) states.

decreased from 7 mJ/cm^2 at $T = 300$ K to 2 mJ/cm^2 at 330 K (*58*). The general agreement for the threshold value from various groups and different samples, and its temperature dependence following a similar trend, further support the aforementioned correlation.

The common theme shared by the VO_2 structural dynamics and several recent studies on the static electronic structure (*12, 13, 19*) is the crucial role of the V–V dimer unit. On the basis of this understanding and the correlation between the optical and thermal energy thresholds, we propose a common transformation mechanism: the phase transition from the insulator (M_1) to metal (tetragonal) state is initiated by the dilation of the correlated/connected V–V bonds, whether it is induced optically or thermally. An illustration is given in Fig. 15: the relative energies of the initial, transitional intermediate and final states will be affected by temperature which may facilitate or hinder the transformation. In a static picture, the band gap of ~0.6 eV for the M_1 phase (*4, 13*), which is more than 20 times the thermal energy of 29.3 meV at 340 K, cannot be theoretically reproduced without a simultaneous consideration of the structural aspect and correlation within singlet V–V pairs (*19*). The molecular, correlated nature of V–V dimers in the M_1 phase cannot be fully described either by the Mott-Hubbard (electron correlation) model or by the Peierls dimerization (*12*). Treating a V–V pair as one molecular unit, which is also supported by the current results of structural dynamics, becomes the key to understanding the thermodynamic and dynamical properties of VO_2.

Since the structural and electron correlation effects are intertwined, the allegation of different temperatures for the insulator–metal and structural phase transitions may become poorly supported (*21, 56*). However, transitional intermediates do exist on an ultrashort time scale, as shown in this work. In regard to the femtosecond V–V bond dilation, considering the molecular and correlated nature of the dimers, one may expect the time constant, τ_1, to be roughly half of the vibrational time of 170 fs if an inertial separation is operative, which matches with the optical reflectivity results (*28*); or about one vibrational cycle if excitation is equilibrated and shared by several dimers, leaving the bond stretching motion to be in charge (*27*). According to our previous discussion about the scenario of localized excitation, we predict that the former mechanism is likely to occur with a much higher excitation fluence, whereas the latter is more probable for a fluence that does not exceed the threshold too much.

Conclusion

The advantage of using UEC to unravel the atomic motions during a structural phase transition is demonstrated by the results reported here for VO_2. The elementary steps follow a nonconcerted mechanism involving a sequence of transitional structures, first intracell atomic displacements on the femtosecond and picosecond time scales, followed by carrier diffusion and long-range shear motion within a sub-nanosecond time and at the speed of sound. The V–V bond dilation is the initial step of the insulator–metal transition and structural transformation, providing a dynamical molecular picture. The correlation between the thermal and photoinduced transition thresholds at different temperatures suggests the common pathway mechanism for the transition and connects the dynamics and thermodynamics research approaches into a unified description for this material. With four-dimensional atomic-scale spatial and temporal resolution, we expect, by using this table-top approach, many future extensions in the studies of strongly correlated materials and phase transformations, designed nanometer-scale materials and biological systems.

References and Footnotes:

1. P. Papon, J. Leblond, P. H. E. Meijer, *The physics of phase transitions: Concepts and applications* (Springer, New York, 2nd ed., 2006).
2. M. Imada, A. Fujimori, Y. Tokura, *Rev. Mod. Phys.* **70**, 1039 (1998).
3. P. P. Edwards, R. L. Johnston, C. N. R. Rao, D. P. Tunstall, F. Hensel, *Phil. Trans. R. Soc. A* **356**, 5 (1998).
4. C. N. Berglund, H. J. Guggenheim, *Phys. Rev.* **185**, 1022 (1969).
5. J. B. Goodenough, *J. Solid State Chem.* **3**, 490 (1971).
6. M. Marezio, B. McWhan, P. D. Dernier, J. P. Remeika, *Phys. Rev. B* **5**, 2541 (1972).
7. A. Zylbersztejn, N. F. Mott, *Phys. Rev. B* **11**, 4383 (1975).
8. D. Paquet, P. Leroux-Hugon, *Phys. Rev. B* **22**, 5284 (1980).
9. S. Shin *et al.*, *Phys. Rev. B* **41**, 4993 (1990).
10. H. S. Choi, J. S. Ahn, J. H. Jung, T. W. Noh, D. H. Kim, *Phys. Rev. B* **54**, 4621 (1996).
11. K. Okazaki *et al.*, *Phys. Rev. B* **69**, 165104 (2004).
12. M. W. Haverkort *et al.*, *Phys. Rev. Lett.* **95**, 196404 (2005).
13. T. C. Koethe *et al.*, *Phys. Rev. Lett.* **97**, 116402 (2006).
14. F. J. Morin, *Phys. Rev. Lett.* **3**, 34 (1959).
15. G. Andersson, *Acta Chem. Scand.* **10**, 623 (1956).
16. K. D. Rogers, *Powder Diffr.* **8**, 240 (1993).
17. T. M. Rice, H. Launois, J. P. Pouget, *Phys. Rev. Lett.* **73**, 3042 (1994).
18. R. M. Wentzcovitch, W. W. Schulz, P. B. Allen, *Phys. Rev. Lett.* **72**, 3389 (1994).

19. S. Biermann, A. Poteryaev, A. I. Lichtenstein, A. Georges, *Phys. Rev. Lett.* **94**, 026404 (2005).
20. M. M. Qazilbash *et al.*, *Science* **318**, 1750 (2007).
21. H.-T. Kim *et al.*, *Phys. Rev. Lett.* **97**, 266401 (2006).
22. M. F. Becker *et al.*, *Appl. Phys. Lett.* **65**, 1507 (1994).
23. M. F. Becker *et al.*, *J. Appl. Phys.* **79**, 2404 (1996).
24. A. Cavalleri *et al.*, *Phys. Rev. Lett.* **87**, 237401 (2001).
25. G. I. Petrov, V. V. Yakovlev, J. A. Squier, *Opt. Lett.* **27**, 655 (2002).
26. A. Cavalleri *et al.*, *Phys. Rev. Lett.* **95**, 067405 (2005).
27. C. Kübler *et al.*, *Phys. Rev. Lett.* **99**, 116401 (2007).
28. A. Cavalleri, T. Dekorsy, H. H. W. Chong, J. C. Kieffer, R. W. Schoenlein, *Phys. Rev. B* **70**, 161102(R) (2004).
29. K. Sokolowski-Tinten *et al.*, *Nature* **422**, 287 (2003).
30. D. Maurer, A. Leue, R. Heichele, V. Müller, *Phys. Rev. B* **60**, 13249 (1999).
31. D. Kucharczyk, T. Niklewski, *J. Appl. Cryst.* **12**, 370 (1979).
32. K. J. Caspersen, E. A. Carter, *Proc. Natl. Acad. Sci. USA* **102**, 6738 (2005).
33. D. R. Trinkle *et al.*, *Phys. Rev. Lett.* **91**, 025701 (2003).
34. C. Bressler, M. Chergui, *Chem. Rev.* **104**, 1781 (2004).
35. A. Rousse, C. Rischel, J. C. Gauthier, *Rev. Mod. Phys.* **73**, 17 (2001).
36. K. Sokolowski-Tinten, D. von der Linde, *J. Phys.: Condens. Matter* **16**, R1517 (2004).
37. M. Bargheer, N. Zhavoronkov, M. Woerner, T. Elsaesser, *Chemphyschem* **7**, 783 (2006).
38. K. J. Gaffney, H. N. Chapman, *Science* **316**, 1444 (2007).

39. H. E. Elsayed-Ali, G. A. Mourou, *Appl. Phys. Lett.* **52**, 103 (1988).
40. B. J. Siwick, J. R. Dwyer, R. E. Jordan, R. J. D. Miller, *Science* **302**, 1382 (2003).
41. H. Park, S. Nie, X. Wang, R. Clinite, J. Cao, *J. Phys. Chem. B* **109**, 13854 (2005).
42. A. H. Zewail, *Annu. Rev. Phys. Chem.* **57**, 65 (2006).
43. N. Gedik, D.-S. Yang, G. Logvenov, I. Bozovic, A. H. Zewail, *Science* **316**, 425 (2007).
44. M. S. Grinolds, V. A. Lobastov, J. Weissenrieder, A. H. Zewail, *Proc. Natl. Acad. Sci. USA* **103**, 18427 (2006).
45. V. A. Lobastov, J. Weissenrieder, J. Tang, A. H. Zewail, *Nano Lett.* **7**, 2552 (2007).
46. P. Baum, D. S. Yang, A. H. Zewail, *Science* **318**, 788 (2007).
47. W. Bruckner *et al.*, *Vanadiumoxide* (Akademie-Verlag, Berlin, 1983).
48. M. Borek, F. Qian, V. Nagabushnam, R. K. Singh, *Appl. Phys. Lett.* **63**, 3288 (1993).
49. D. H. Kim, H. S. Kwok, *Appl. Phys. Lett.* **65**, 3188 (1994).
50. Z. P. Wu *et al.*, *J. Phys.: Condens. Matter* **10**, L765 (1998).
51. S. Lysenko, V. Vikhnin, F. Fernandez, A. Rua, H. Liu, *Phys. Rev. B* **75**, 075109 (2007).
52. V. A. Lobastov *et al.*, in *Ultrafast Optics IV,* F. Krausz, G. Korn, P. Corkum, I. A. Walmsley, Eds. (Springer, New York, 2004), vol. 95, pp. 419-435.
53. The error bar is derived from the uncertainties in the experimentally observed intensity decreases, which were obtained by fitting the spot profiles. Depending on the approximation used for estimation of the fluence, e.g., whether an average value across a larger region or the peak value at center is calculated, an overestimation of ~2 mJ/cm^2 may be present.

54. H. W. Verleur, A. S. Barker Jr., C. N. Berglund, *Phys. Rev.* **172**, 788 (1968).

55. Given the X-ray wavelength (1.54 Å) and diffraction angle (13.9°) reported (*24*), the Bragg peak should be indexed as (011) of the M_1 phase but was assigned as (110) of the M_1 phase (*24*). Upon transformation the peak becomes (110) of the tetragonal phase.

56. According to the reported X-ray diffraction patterns (*21*), the VO_2 phase involved was likely the M_2 phase (*59*) or a mixture of several structures, because the diffraction peaks that show temperature-dependent change do not correspond to the M_1 structure but can be related to the M_2 structure.

57. J. H. Bechtel, *J. Appl. Phys.* **46**, 1585 (1975).

58. D. J. Hilton *et al.*, *Phys. Rev. Lett.* **99**, 226401 (2007).

59. M. Marezio, B. McWhan, P. D. Dernier, J. P. Remeika, *Phys. Rev. B* **5**, 2541 (1972).

Chapter 7

Nonequilibrium Phase Transformations in Cuprates[†]

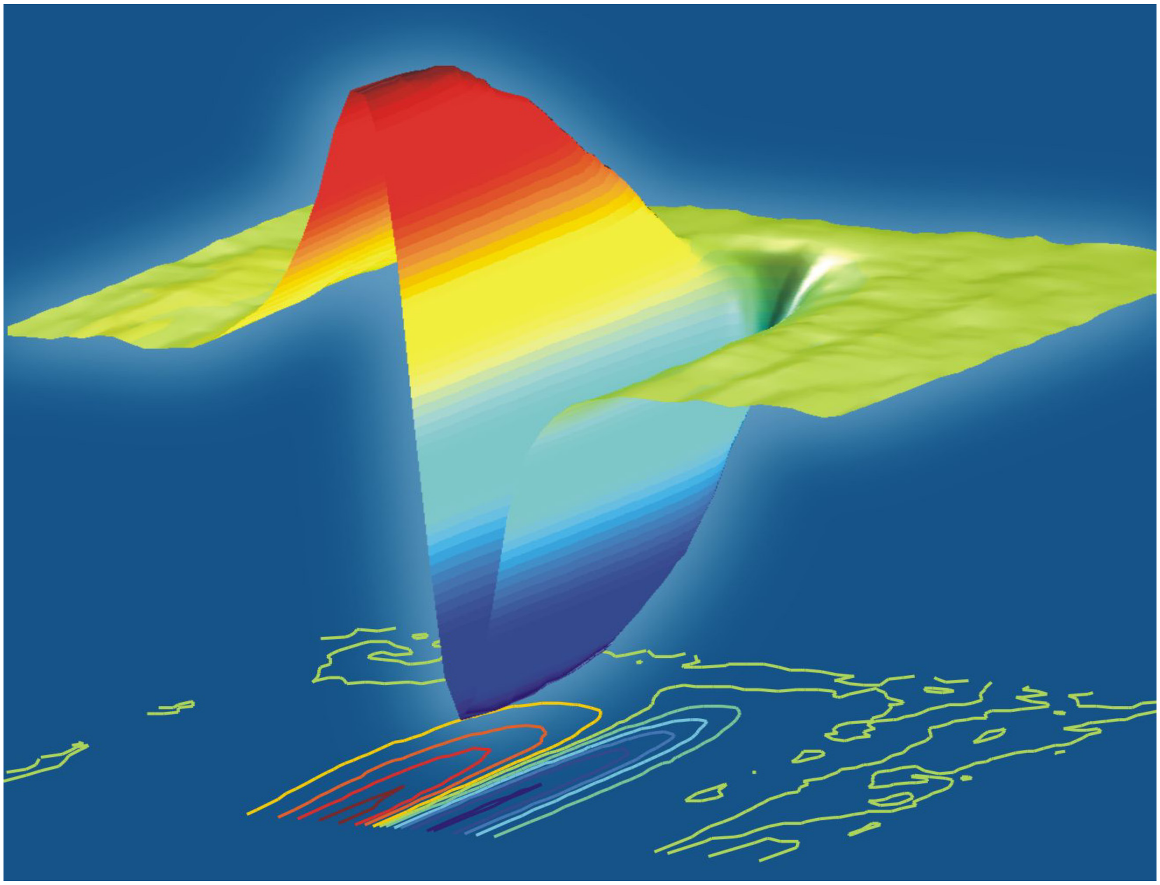

[†] adapted from N. Gedik, D.-S. Yang, G. Logvenov, I. Bozovic, A. H. Zewail, *Science* **316**, 425 (2007).

Introduction

The physical and chemical properties of materials can be altered as a result of the generation of metastable structures (*1*), electronic and/or structural modifications (*2, 3*), and phase transitions (*4*). For the latter, much of the work has been done on solids at equilibrium, namely when temperature or pressure becomes the variable of change. In contrast, transient structures of nonequilibrium phases, which are formed by collective interactions, are elusive and less studied because they are inaccessible to conventional studies of the equilibrium state. Initiated by photons, the structural changes underlying such transitions involve charge redistribution and lattice relaxation culminating in a process termed a photoinduced phase transition (*5-7*). In order to understand the nature of these optically dark phases, it is important to observe the structural changes with the use of time-resolved methods, especially ultrafast electron microscopy (*8-10*), electron diffraction (*10-12*), and x-ray absorption and diffraction (*13-17*). In this chapter, the direct observation of the nonequilibrium structural phase transition in superconducting cuprates is reported.

Materials and Experimental Section

The material that we chose to study is oxygen-doped $La_2CuO_{4+\delta}$ (LCO); although the undoped material is an antiferromagnetic Mott insulator, doping confers superconductivity below the critical temperature (T_c) and metallic properties at room temperature. Thin films were grown on a $LaSrAlO_4$ substrate by means of an atomic-layer molecular beam epitaxy (MBE) system (*18*). The films under study were characterized during growth by reflection high-energy electron diffraction and *ex situ* by atomic force microscopy (AFM), x-ray diffraction, and measurements of resistivity and

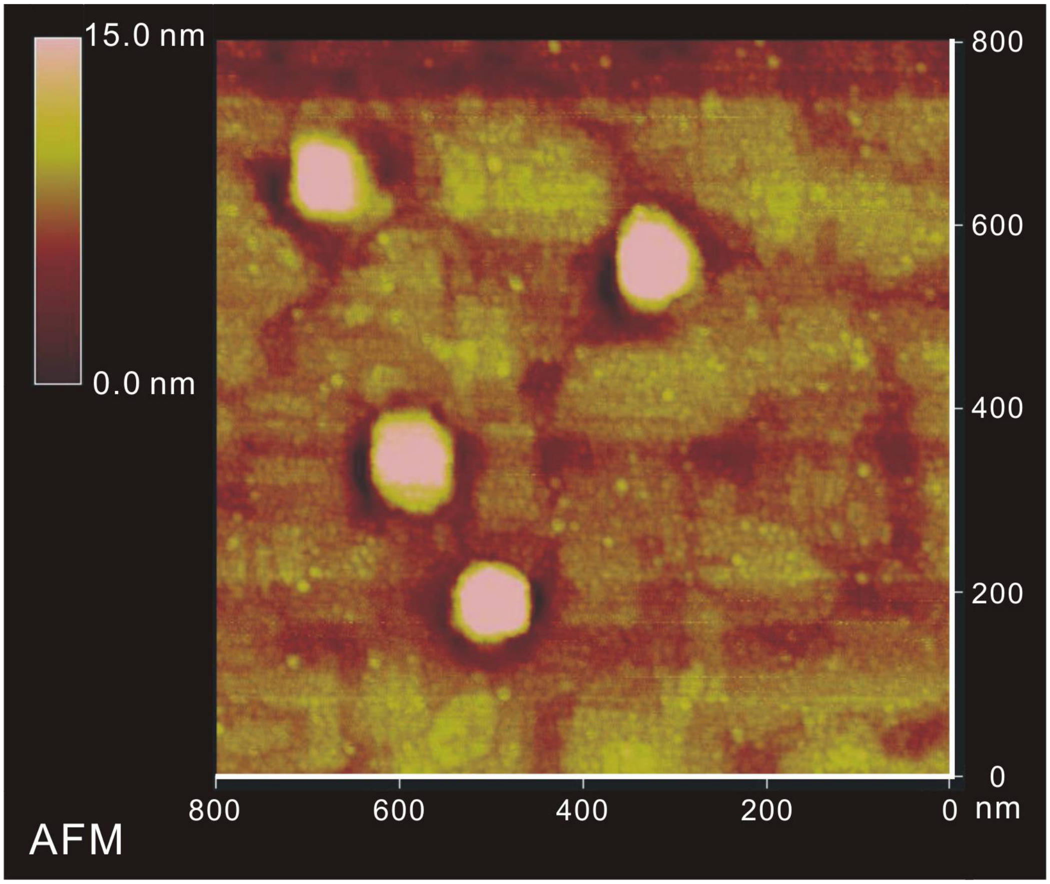

Fig. 1. AFM image of the topography of the LCO surface. The scan range is 800 nm by 800 nm. The surface of the film is atomically flat except for a few three-dimensional islands seen as circular white regions in the image. They are cylindrically shaped with a base diameter of ~50 nm and a typical height of ~20 nm. These structures are small LCO islands epitaxially aligned with the underlying cuprate film.

magnetic susceptibility as a function of temperature. The products are single-crystal films, and AFM shows atomically smooth surfaces (root-mean-square roughness in the 0.3- to 0.6-nm range). In few films, we observed some surface roughness, in the form of some islands with a typical width of 50 to 200 nm and a height of ~20 nm, small enough for transmission electron diffraction to be observed (Fig. 1). The islands were verified to have the same crystal structure and conductivity as those of the single crystal, as

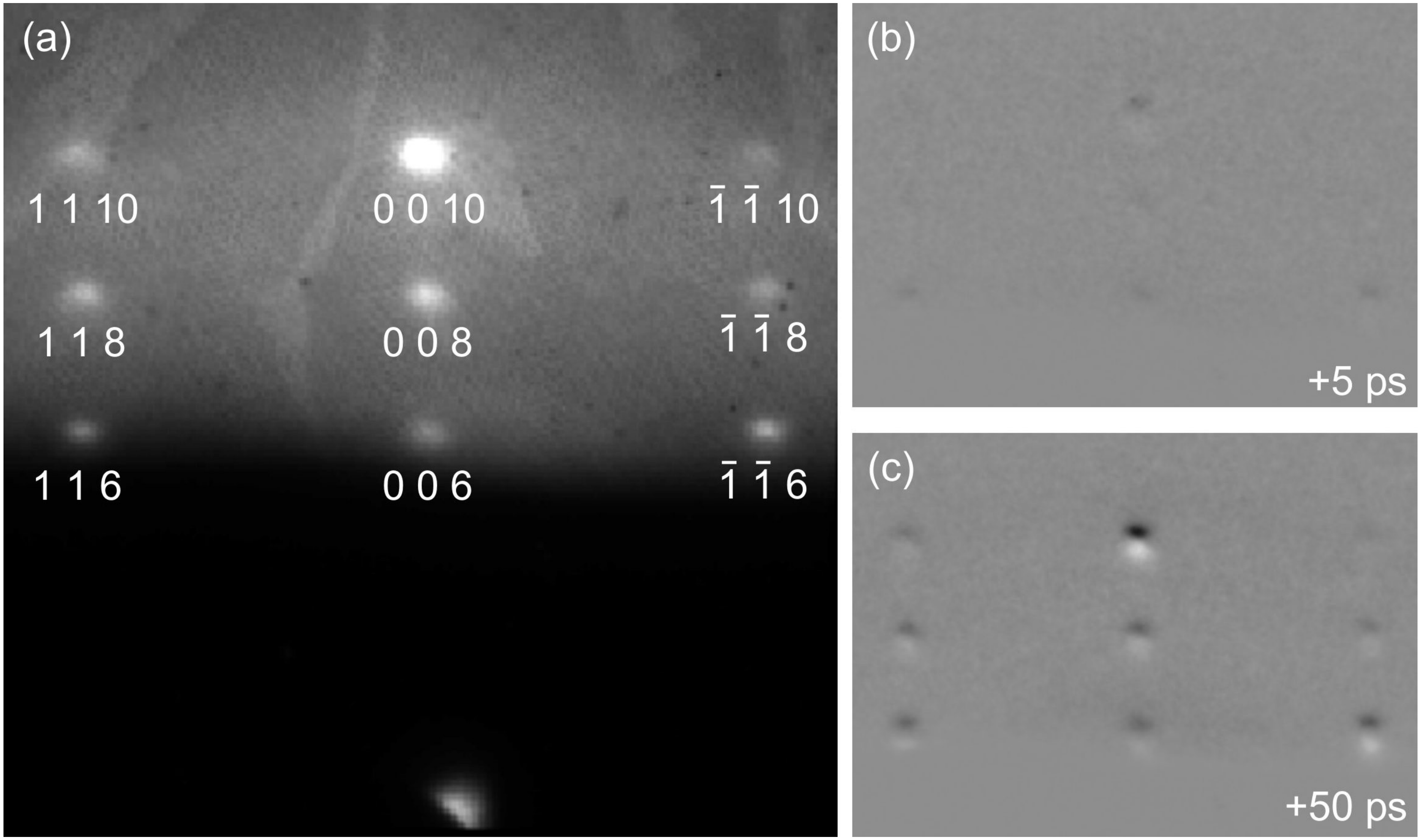

Fig. 2. (a) Diffraction pattern of $La_2CuO_{4+\delta}$ obtained at equilibrium. The pattern is transmission-like, and the spots are indexed with the use of the tetragonal unit cell. (b and c) Diffraction difference images (referenced to panel a) at +5 ps and +50 ps, respectively.

evidenced by measurements of the lattice constants and by electric force microscopy, respectively. One such film, with a thickness of 52 nm and a critical temperature $T_c \sim 32$ K, was chosen for the present study.

Ultrafast electron crystallography (UEC) has been established as a method for studying surfaces and nanometer-scale materials with atomic-scale resolutions. The sample was photoexcited by 800-nm light pulses (with a temporal width of 120 fs) and probed by electron packets generated via the photoelectric effect. In order to observe lower-order Bragg diffractions from the material, the incidence angle of electrons ($\theta/2$) is set typically between ~1° and 2°. The scheme of pulse front tilting (*19*) was used for all experiments reported here to achieve the necessary time resolution and sensitivity. To tune the temperature and incidence angle (for rocking curve measurements), we mounted the sample on a metallic holder coupled to a cryostat that was capable of reaching 10 K, which in turn was placed on a goniometer with an angular precision of 0.005°.

Results and Analysis

In Fig. 2a, the static diffraction pattern obtained at room temperature is shown with no excitation. From the observed Bragg spots in s space, where $s = (4\pi/\lambda)\sin(\theta/2)$, we indexed the pattern using the tetragonal unit cell of the cuprate $La_2CuO_{4+\delta}$. Analysis of the diffraction patterns for different zone axes gives lattice constants of $a = b = 3.76$ Å and $c = 13.1 \pm 0.1$ Å, which are in agreement with the x-ray diffraction measurements made on the same film ($a = b = 3.755$ Å and $c = 13.20$ Å). The error range in the determination of the absolute values of the lattice constants comes from the uncertainty in determining the sample-to-camera distance. However, relative changes can be measured with much better accuracy, reaching below 0.01 Å (or 0.001 Å through fitting).

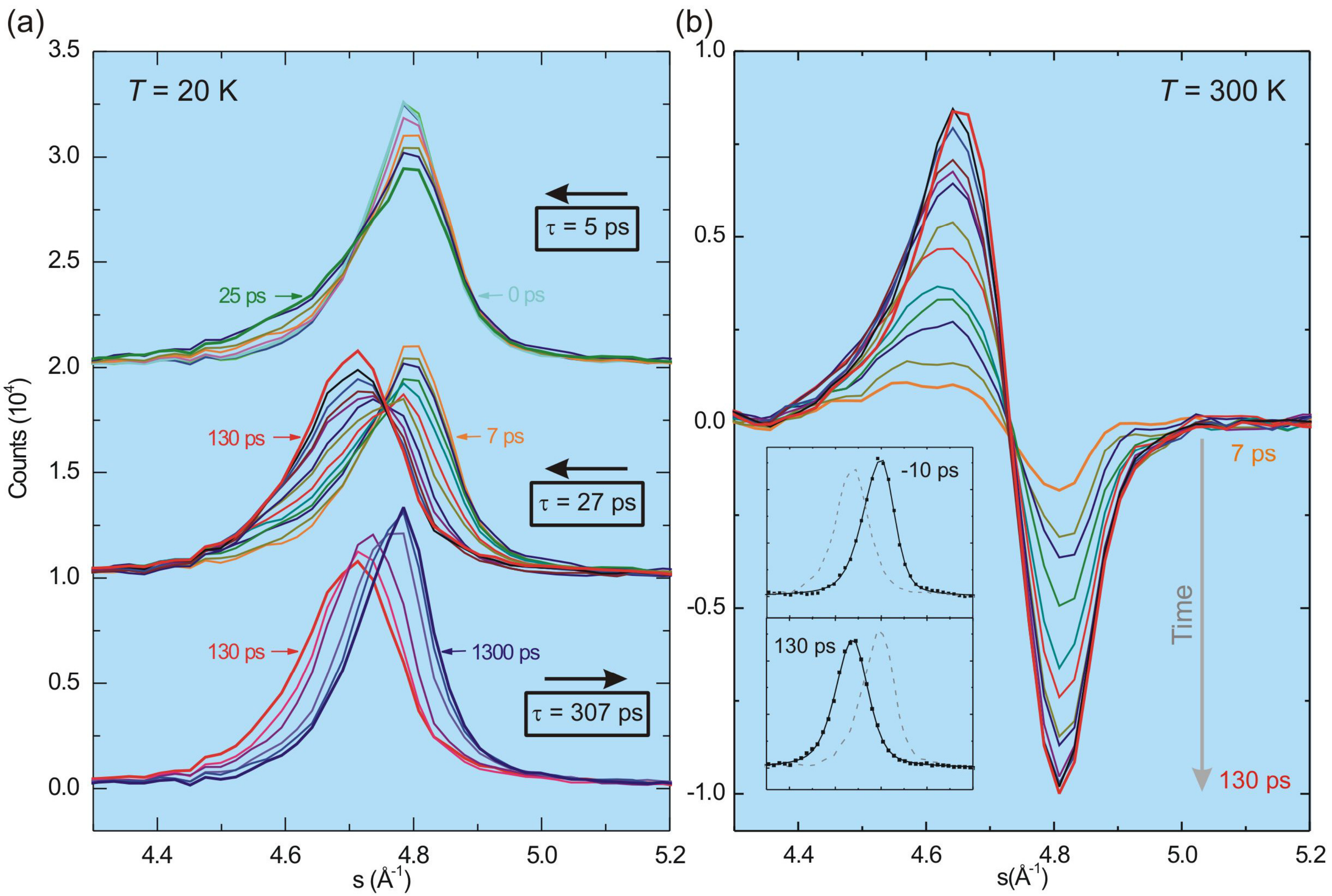

(See next page for the figure caption.)

Fig. 3. Diffraction evolution with time. (a) Profiles of the (0 0 10) Bragg spot along the *c*-axis direction at different times. The fluence is 20.6 mJ/cm^2 and temperature is 20 K. A small background (determined experimentally from a nearby diffuse region on the CCD) was subtracted. Similar diffraction results were obtained at room temperature and at $T = 100$ K. Three distinct behaviors are shown: between 0 and 25 ps [top; time (t) = –34, –11, 0, 1, 7, 13, 19 and 25 ps]; between 7 and 130 ps (middle; $t = 7$, 13, 19, 25, 34, 43, 52, 61, 70, 79, 88, 101, 130 ps), there is a prominent structural isosbestic point at $s = 4.76$ Å^{-1}; and on a much longer time scale (bottom; $t = 130$, 191, 266, 516, 816, 1300 ps), the restructuring back to the ground state is observed. For the recovery, the curves continuously shift to higher s values (shorter c) without crossing. The black arrows indicate the direction of temporal evolution for the formation and restructuring of the transient phase. (b) Difference profiles of the (0 0 10) Bragg spot along the *c*-axis direction at different times, referenced to the negative time frame. The fluence is 20.6 mJ/cm^2 and temperature is 300 K. The structural isosbestic point is clearly seen near zero intensity, and the depletion of the initial structure and the growth of the transient structure are apparent. The inset shows the Voigt-type function fit for the diffraction intensity profiles at two different times: –10 and +130 ps.

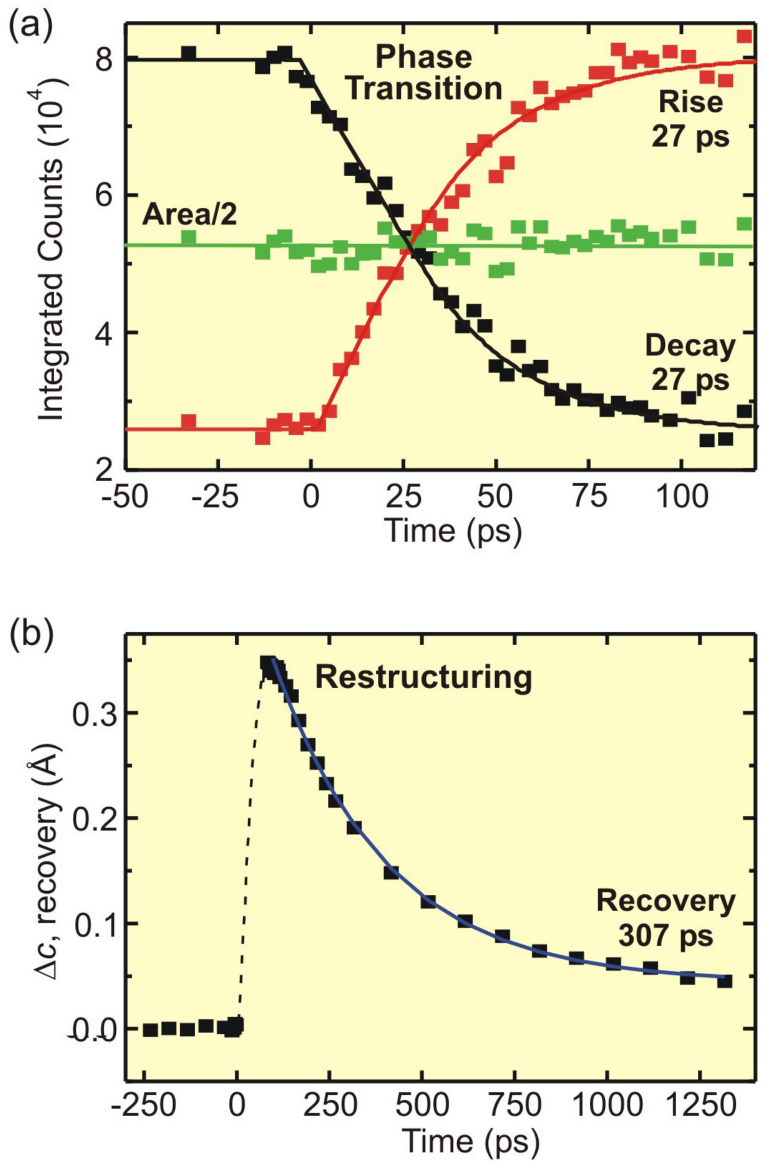

Fig. 4. Time scales of structural changes. (a) Integrated intensity decay (black squares) and rise (red squares) of the structural isosbestic behavior shown in Fig. 3b. The green squares show, at given times, the total integrated intensity divided by two. The average of the black and red squares yields the green squares. The lines are guide to the eye. The intensity decay and rise give a time constant of 27 ps; the initial 5-ps range is not included. (b) Recovery of the *c*-axis lattice constant change (black squares). Dashed line indicates an average *c*-axis lattice spacing in the phase-transition region where more than one state is involved. The blue curve is a fit to an exponential decay with a time constant of 307 ps and a constant offset of 0.04 Å.

Structural dynamics of the material were obtained by recording the diffraction frames at different times, before and after the arrival of the optical excitation pulse. In Fig. 2, panels b and c, two representative diffraction difference patterns are shown. These difference patterns display the changes induced by the initiation pulse; they are frames obtained at the specified times and referenced, by subtraction, to a frame at negative time (i.e., before optical excitation). At 1.55 eV, the femtosecond pulse only excites the material because the substrate is transparent to the 800-nm light; the penetration depth of the laser pulse in the material is 143 nm (*20*), which far exceeds that of the probing electron pulse (~10 nm). Therefore, the observed structural dynamics can only originate from the cuprate film.

After the femtosecond initial excitation, the observed Bragg spots shift downward (along the c direction), indicating an increase in the c-axis lattice constant. For other Bragg spots, the shift scales correctly with the order of diffraction. For example, the shift (Δs in s space) of the (008) spot is 80% of that of the (0 0 10) spot, in accord with the relationship $\Delta c/c = -\Delta s/s$. (We measured no change in the position of the direct electron beam on the CCD camera.) The observed changes are on three different time scales, characterized by time constants of 5 ps and 27 ps for the formation of the transient phase and 307 ps for structural recovery (see Figs. 3 and 4).

The change with time is striking. In Fig. 3a, we plot the vertical profiles of the (0 0 10) Bragg spot along the c direction at different times. At negative times, the Bragg peak is centered at an s value corresponding to the equilibrium c value of the lattice: $s = 10\,|\boldsymbol{c}^*| = 4.80$ Å^{-1}, where $|\boldsymbol{c}^*| = 2\pi/c = 0.480$ Å^{-1}. The structure at positive times evolves first in a few picoseconds and then changes drastically in tens of picoseconds; for example, at 120 ps after the excitation, the peak becomes centered at a lower value

($s = 4.70$ Å^{-1}) corresponding to a huge increase (~2.5%) in the *c*-axis lattice constant. We studied the material behavior at three different temperatures, 20, 100 and 300 K.

The unexpected feature of Fig. 3 is that, before restructuring, all of the curves obtained at different times cross at a single point, $s = 4.76$ Å^{-1}, at the fluence of 20.6 mJ/cm^2. What was expected, as observed in semiconducting materials (Chs. 4 and 5), was that the peak would shift continuously while the intensity decreased with time. Neither behavior is observed here at the high signal-to-noise level achieved (Figs. 3 and 4). Thus, this intensity sharing with a common crossing point, as shown below, indicates a structural transition from the initial phase to a new one. Such a crossing behavior in spectroscopy would be termed an isosbestic point, corresponding to the spectral position where two interconverting species have equal absorbance; regardless of the populations of the two states, the total absorption at the isosbestic point does not change.

For the structural dynamics studied, we observe the interconversion between two structures with different *c*-axis lattice constants and, for this reason, we term this point the structural isosbestic point. At this particular *s* value, the two structures involved are diffracting equally, and their coexistence is evidenced in the temporal changes. The influence of the time-independent instrumental response function (from the electron beam size) has been taken into consideration. For the case of two interconverting structures with Gaussian intensity profiles, it can be shown mathematically that instrumental broadening only modifies the widths, but structural isosbestic points remain robust. The behavior of interconversion is clearly illustrated in Fig. 3b, where we display, as a function of time, the depletion of the initial structure and the growth of the transient-phase structure. The data, which was acquired over the same time delays as those of Fig. 3a (middle), were obtained by referencing all frames to the diffraction profile of the equilibrium structure at negative time. In the inset of Fig. 3b, the actual diffraction profile of the (0 0 10) Bragg spot is shown at two different times, –10 and +130 ps, with each profile fitted to a Voigt-type function.

The decay of the initial structure and the formation of the new structure are quantified by integrating the intensity underneath the (0 0 10) diffraction curves. For the diffraction data obtained in Fig. 3b, the green line in Fig. 4a is the total integrated intensity divided by two. The fact that it is not changing with time rules out the involvement of intensity-depletion processes, such as those described by the Debye–Waller mechanism (Eq. 16 of Ch. 2); in that case, the mean vibrational displacement of the atoms would have increased and caused a decrease in diffraction intensity, contrary to what is observed. Moreover, because the linear expansion coefficient is $\alpha_l \leq 1.0\times10^{-5}\ \mathrm{K}^{-1}$ (*21*), a 2.5% increase in the lattice constant would correspond to an unphysical rise of 2500 K in the lattice temperature. The black and red curves are the total integrated intensity to the right and left of the crossing point in Fig. 3b, respectively. They reflect the population change of the initial structure and that of the new one. The population of the initial structure (black curve in Fig. 4a) decays with a time constant of 27 ps, describing the growth of the transient phase.

The restructuring at longer times is depicted by Δc as a function of time in Fig. 4b. The dashed line near time zero represents an average value of c for the structures that are present. With no crossing, the value of Δc decreases and reaches an asymptote at ~1 ns. This restructuring after the phase transition can be described by an exponential decay with a time constant of 307 ps with an offset of about 0.04 Å. Accordingly, even after 1 ns, the restructuring is incomplete and, for complete equilibration, a much longer time scale is required. Some contribution from a temperature rise induced by the laser pulse

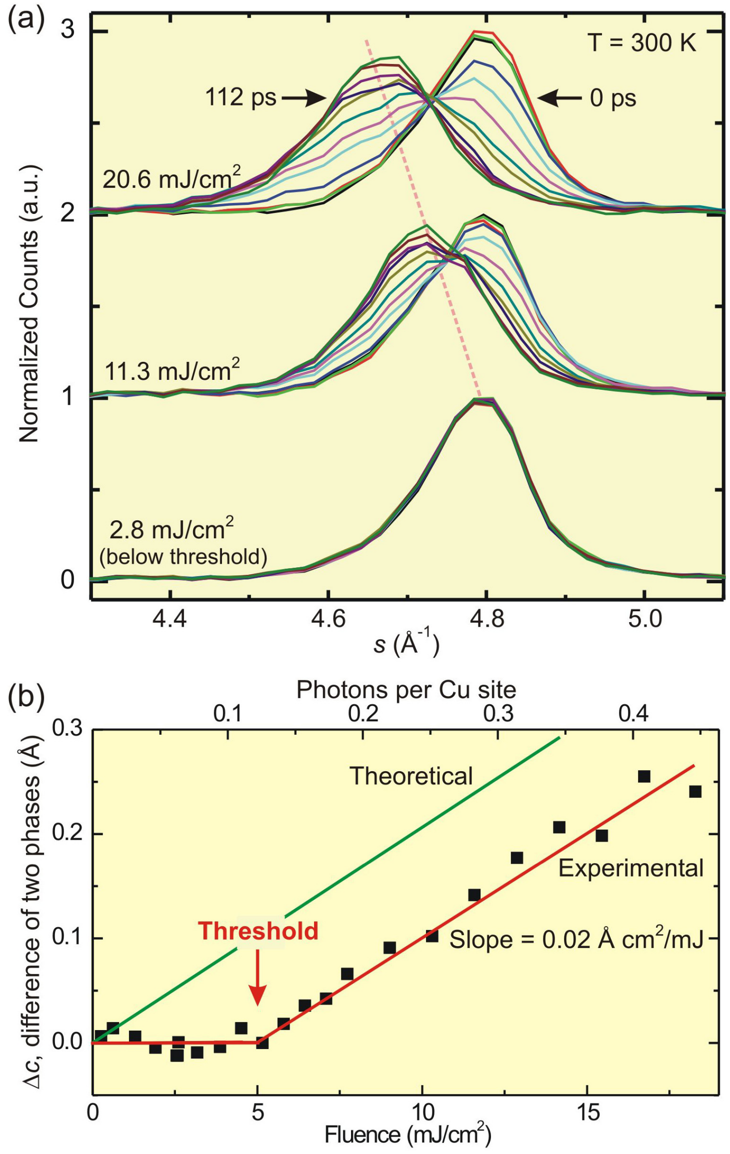

Fig. 5. Threshold behavior and fluence dependence. (a) Typical diffraction profiles at three fluences, 2.8 (below threshold), 11.3 and 20.6 mJ/cm^2 (above threshold). The profile for the equilibrium phase remains at the same *s* value, whereas that for the transient phase (indicated by the dashed line) shifts toward a lower *s* value as the fluence increases. The structural isosbestic point is robust. All peaks are normalized to the $t = 0$ peak maximum at each fluence; the displacement for different fluence is in arbitrary units (a.u.). (b) The difference of the *c*-axis lattice constant between the two phases, $\Delta c_{\max} = c(130\text{ ps}) - c(-85\text{ ps})$, as a function of fluence. The horizontal axis on the top shows the number of photons absorbed per copper site as calculated with the use of the linear absorption coefficient. There is a clear threshold at 5 mJ/cm^2. Above the threshold, Δc increases linearly with fluence with a slope of 0.02 Å/(mJ/cm^2) (red line). The theoretical calculations (green line) yield a slope that is in good agreement with that obtained from the experimental data.

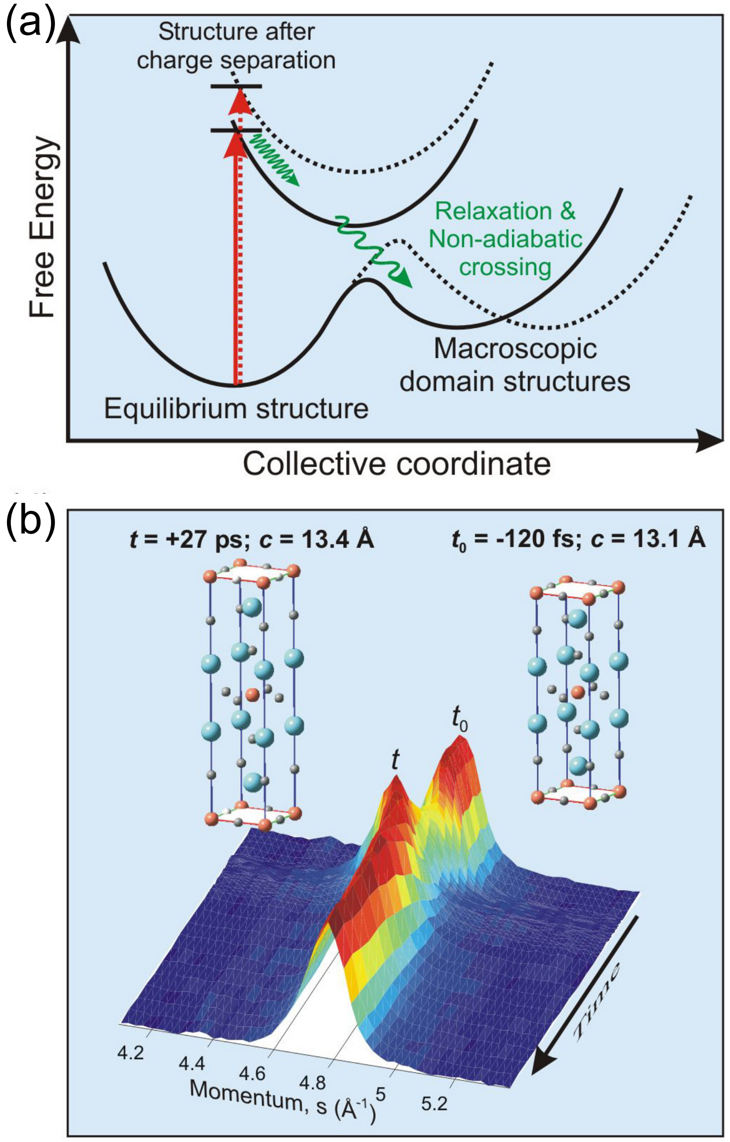

Fig. 6. Trajectories of structural changes. (a) Free-energy curves. The initial charge-transfer excitation leads, after lattice relaxation and nonadiabatic crossing (*5-7*), to the new structure, in this case with the charge being transferred from oxygen to copper. Further increase in the energy of the charge-transfer subsystem results in displacement of the curves (dotted curves) (*24*). Red arrows indicate excitation, and green arrows indicate the relaxation and nonadiabatic processes. (b) The temporal evolution of the (0 0 10) Bragg diffraction in the *s*–*t* space is shown as a three-dimensional plot (bottom). The initial structure of $La_2CuO_{4+\delta}$ before time zero (t_0) is shown on the upper right corner [copper (red spheres), oxygen (grey spheres) and lanthanum (blue spheres)]. After the phase transition, the new structure is indicated with a higher *c*-axis lattice constant (upper left corner). The change is exaggerated for illustration purposes. As restructuring takes place, the positions of the Bragg diffraction spots move continuously toward the equilibrium *s* values on a slower time scale.

may be present; the 1-ms delay between pulses is sufficient for the cooling of the sample.

Another notable feature of this structural phase transition is its dependence on the fluence of the initiating pulse. The maximum lattice constant change, $\Delta c_{\max} = c(130\ \text{ps}) - c(-85\ \text{ps})$, is shown in Fig. 5, panels a (for the profiles at three typical fluences) and b (for all the fluences studied). A threshold at 5 mJ/cm^2 is observed, below which no structural change can be detected. Above this fluence value, the basic picture described above—a crossing point at initial times and continuous restructuring at long times—is robust (see Fig. 5a). The time scales do not change either. However, the lattice constant (c) of the transient-phase structure changes with the laser fluence (F) [i.e., $\Delta c_{\max} = p\ (F - F_{\text{th}})$, where the slope $p = 0.02$ Å/(mJ/cm^2) and F_{th} is the threshold fluence].

Discussion: The Physical Picture

From the results of structures and dynamics observed in the cuprate superconductor, the following simple model is suggested. At 1.55 eV, the excitation pulse induces a charge transfer (Fig. 6a) from oxygen (O^{2-}) to copper (Cu^{2+}) in the *a*–*b* copper–oxygen planes (*22*). With the lattice relaxation being involved, the excitation is shared microscopically (exciton-type), and finally a transition to a transient phase is made (macroscopic domain). This transient phase requires a three-dimensional lattice ordering. The net charge distribution in the transient phase results in the weakening of interplanar Coulomb attractions, leading to expansion along the c axis. The behavior is nonlinear in that when the number of transformed sites is below a critical value, the macroscopic transition is not sustainable. The threshold, which has also been observed in organic crystals (*7*), reflects this need for cooperativity at the macroscopic scale. The crystal domain is at least 20 nm^2 (from the apparent peak width, Δs_{w}, which gives the minimum coherence length); the maximum is determined by the 800-nm wavelength used. Symmetry breaking is not evident because charge transfer is in a plane perpendicular to the *c*-axis expansion, whereas, in Ref. 7, charge separation is along the axis of expansion.

At any fluence above the threshold, the interconversion is between two phases (isosbestic point). In order to account for the large magnitude of the expansion and its dependence on the fluence, a uniform charge distribution was considered, after the in-plane charge transfer from oxygen to copper. In the domains of the transient phase, the charges on copper and oxygen become $Q(\mathrm{Cu}) = 2 - \delta_\mathrm{p}$ and $Q(\mathrm{O}) = -2 + \delta_\mathrm{p}/2$, respectively, where δ_p is the transferred fractional charge determined by the number of photons absorbed per copper site; the changes refer to the copper–oxygen planes with the valence of all the other atoms remaining the same. The ionic cohesion energy $U(\boldsymbol{r}_1, ..., \boldsymbol{r}_N, \delta_\mathrm{p})$, where $\boldsymbol{r}_i$ ($i = 1, ..., N$) are the coordinates of the atoms in the unit cell, was then calculated as the sum of the Madelung energy and the core repulsion energy; the latter was modeled as the sum of binary repulsion terms in the standard Born–Meier form of $A_j\exp(-r_j/d_\mathrm{BM})$, where the index j enumerates the relevant nearest-neighbor pairs (O–O, Cu–O, and La–O), and A_j and d_BM are the pair-wise atomic constants (*23*). For the equilibrium structure ($\delta_\mathrm{p} = 0$), the parameters were optimized to match the experimentally determined equilibrium distances and the known lattice elastic constants. For a given fluence (equivalent to δ_p), the cohesive energy $U(\boldsymbol{r}_1, ..., \boldsymbol{r}_N, \delta_\mathrm{p})$ was then calculated to determine the new crystal configuration by minimizing the potential energy. The calculations give the observed magnitude for the change along the *c* axis and the linear dependence on fluence, as shown by the green line in Fig. 5b. The agreement of the slope confirms the role of the charge distribution in the formation of the transient phase. A full dynamical theory must consider such a distribution as the system evolves in time. Electron transfer theory predicts that an increase in free energy will lead to a shift of the potential (*24*) and to a further increase of the expansion (Fig. 6a).

The dynamical nature of the energy landscape is determined by these changes in the electronic distribution and by the nuclear motions. For other materials exhibiting neutral-to-charged domain transitions, Nasu (*5*) has elucidated the origin of local and global minima, which are reminiscent of macromolecular structures (*25-27*), on the ground-state potential surface. More than one local minimum state may exist as a result of nonadiabatic "covalent–ionic" interactions (*28*) between the two potentials involved (*5, 6*). The multidimensional nature of the landscape requires consideration of dynamical trajectories and the possible bifurcation (*29*), in this case with the *c*-axis changes defining a unique coordinate. In our results, the disparity in yield for the 5-ps and 27-ps time regimes may suggest that the dynamics involve bifurcation with two types of trajectories, those that are direct and lead to a large *c*-axis structural change (low yield), and those that concurrently involve expansion and lattice relaxation (high yield) (*29*).

Figure 6b depicts the observed trajectories in momentum–time space and the two structures, only with *c*-axis expansions. The anisotropy of expansion is due to the fact that the sample is free to expand along the surface normal direction, whereas in *a–b* planes, the laser-excited region is constrained by the surrounding unexcited region. Moreover, for in-plane charge transfer, the Coulomb repulsion is mainly interplanar, which results in a substantial expansion along the *c* axis with essentially no lattice change in the *a–b* planes.

Unlike the phase formation dynamics, the recovery is a continuous process of shrinking the *c*-axis value without crossing. In other words, after the femtosecond initial excitation and charge separation, the photoinduced phase transition can only recover toward the equilibrium structure by charge recombination and lattice relaxation (Fig. 6a and Refs. 5–7). For electron transfer processes (*24*), the recombination occurs on a much longer time scale than that of the charge transfer. For the cuprate, the time scale is more than an order of magnitude longer than the formation time of the transient phase. Optical phonons may be involved, but when the temperature was lowered from $T = 300$ to 100 or 20 K, we observed essentially the same recovery time. These observations suggest the involvement of lattice (acoustic) phonons, because the Debye temperature for this material is 163 K (*30*). The observed decay time of 307 ps is very close to the lifetime (300 ps) of coherent acoustic waves observed in the same material (*31*).

Finally, the meaning of the threshold value for the cuprate is addressed. What was not expected was the absolute value of the threshold in relation to charge distribution. Knowing the value of the threshold (5 mJ/cm^2) and the absorption coefficient at 800 nm ($\alpha = 7\times10^4$ cm^{-1}) (*20*), we obtained a value close to 0.12 photon per copper site. For the doped material used, the fractional charge on a copper site is 0.16 at the optimal doping level for superconductivity. The implication of this similarity is that chemical and light-induced carrier doping may be related. If general, this implication is important for the prospect of light-mediated control. When cuprates are doped chemically, the optical conductivity shows that the spectral weight of the charge-transfer gap is transferred into the intragap region (Mott transition); the photoinduced optical reflectivity and absorption display a similar behavior (*22, 32*).

Conclusion

The combined atomic-scale spatial and ultrafast temporal resolutions of UEC enabled the direct observation of structural nonequilibrium phase transitions in nanometer-scale materials. The macroscopic transient structures are undetectable by optical probes with wavelengths longer than lattice spacings; the time scales of optical response and structural changes are also very different. For the cuprate studied, the observed phase transition is the result of electronic charge redistribution and lattice collective interactions that form domains. The similarity of the apparent threshold for photon doping and the chemical doping required for superconductivity may have its origin in the nature of the photoinduced inverse Mott transition (*33*). With UEC, it is now possible to explore these phenomena for different chemical and photon dopings and in materials of varying structures (see Ch. 8).

References:

1. S. Ramdas *et al.*, *Nature* **284**, 153 (1980).
2. J. M. Thomas, *Phil. Trans. R. Soc. London Ser. A* **277**, 251 (1974).
3. N. Bloembergen, in *Laser ablation: Mechanisms and applications II,* J. C. Miller, D. B. Geohegan, Eds. (American Institute of Physics Conference Proceedings 288, Woodbury, New York, 1994), pp. 3-10.
4. R. W. Cahn, P. Haasen, E. J. Kramer, Eds., *Materials science and technology: A comprehensive treatment Vol. 5*, (VCH, New York, 1991).
5. K. Nasu, Ed., *Photoinduced phase transition* (World Scientific, Hackensack, NJ, 2004) and cited references therein.
6. M. Kuwata-Gonokami, S. Koshihara, Eds., *J. Phys. Soc. Jpn.* **75**, 011001~011008 (2006).
7. E. Collet *et al.*, *Science* **300**, 612 (2003).
8. M. S. Grinolds, V. A. Lobastov, J. Weissenrieder, A. H. Zewail, *Proc. Natl. Acad.*

Sci. USA **103**, 18427 (2006).

9. J. M. Thomas, *Angew. Chem. Int. Ed.* **44**, 5563 (2005).
10. A. H. Zewail, *Annu. Rev. Phys. Chem.* **57**, 65 (2006).
11. X. Zou, in *Electron crystallography: Novel approaches for structure determination of nanosized materials,* T. E. Weirich, J. L. Lábár, X. Zou, Eds. (Springer, Dordrecht, Netherlands, 2006).
12. B. J. Siwick, J. R. Dwyer, R. E. Jordan, R. J. D. Miller, *Science* **302**, 1382 (2003).
13. C. Bressler, M. Chergui, *Chem. Rev.* **104**, 1781 (2004).
14. A. Rousse, C. Rischel, J.-C. Gauthier, *Rev. Mod. Phys.* **73**, 17 (2001).
15. D. von der Linde, K. Sokolowski-Tinten, J. Bialkowski, *Appl. Surf. Sci.* **109-110**, 1 (1997).
16. M. Bargheer, N. Zhavoronkov, M. Woerner, T. Elsaesser, *Chemphyschem* **7**, 783 (2006).
17. A. Cavalleri, M. Rini, R. W. Schoenlein, *J. Phys. Soc. Jpn.* **75**, 011004 (2006).
18. I. Bozovic, *IEEE Trans. Appl. Supercond.* **11**, 2686 (2001).
19. P. Baum, A. H. Zewail, *Proc. Natl. Acad. Sci. USA* **103**, 16105 (2006).
20. M. Suzuki, *Phys. Rev. B* **39**, 2312 (1989).
21. J. D. Yu, Y. Inaguma, M. Itoh, M. Oguni, T. Kyômen, *Phys. Rev. B* **54**, 7455 (1996).
22. D. N. Basov, T. Timusk, *Rev. Mod. Phys.* **77**, 721 (2005).
23. B. Piveteau, C. Noguera, *Phys. Rev. B* **43**, 493 (1991).
24. R. A. Marcus, *Angew. Chem. Int. Ed.* **32**, 1111 (1993).
25. P. F. McMillan, D. C. Clary, *Phil. Trans. R. Soc. London Ser. A* **363**, 311 (2005).
26. P. G. Wolynes, J. N. Onuchic, D. Thirumalai, *Science* **267**, 1619 (1995).

27. C. M. Dobson, *Nature* **426**, 884 (2003).

28. A. Mokhtari, P. Cong, J. L. Herek, A. H. Zewail, *Nature* **348**, 225 (1990).

29. K. B. Møller, A. H. Zewail, *Chem. Phys. Lett.* **295**, 1 (1998).

30. K. Kumagai *et al.*, *Phys. Rev. Lett.* **60**, 724 (1988).

31. I. Bozovic *et al.*, *Phys. Rev. B* **69**, 132503 (2004).

32. J. D. Perkins, R. J. Birgeneau, J. M. Graybeal, M. A. Kastner, D. S. Kleinberg, *Phys. Rev. B* **58**, 9390 (1998).

33. A. Pergament, A. Morak, *J. Phys. A Math. Gen.* **39**, 4619 (2006).

Chapter 8

Direct Role of Structural Dynamics in Electron–Lattice Coupling of Superconducting Cuprates[†]

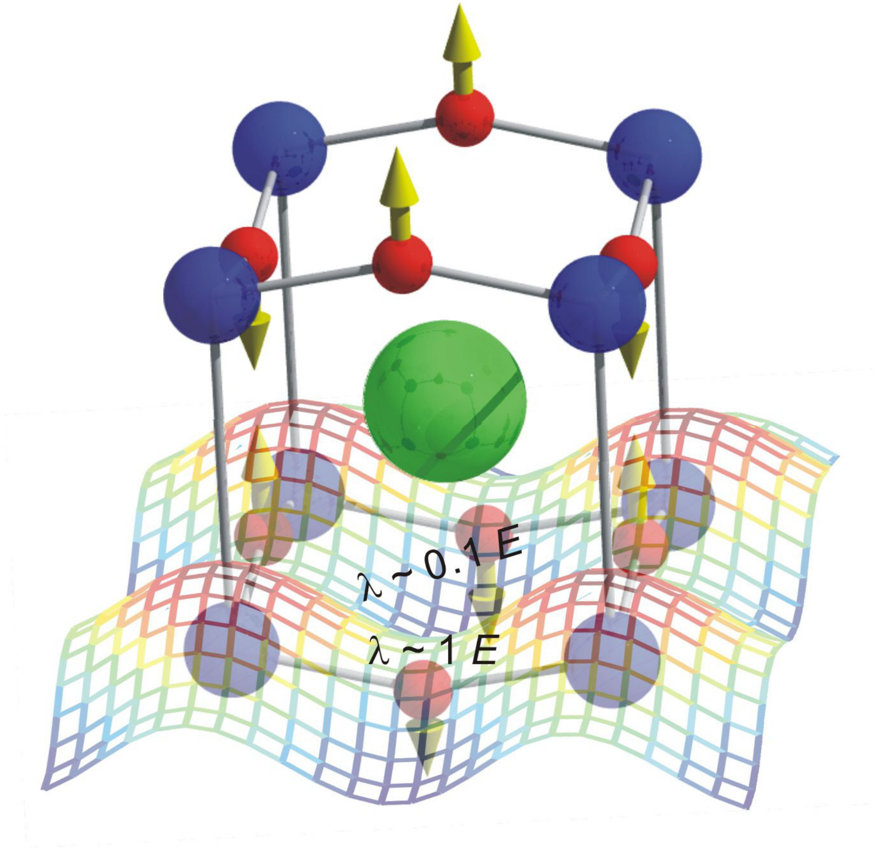

[†] adapted from F. Carbone, D.-S. Yang, E. Giannini, A. H. Zewail, *Proc. Natl. Acad. Sci. USA* **105**, 20161 (2008).

Introduction

The pairing of electrons is now accepted as being essential in the formation of the superconducting condensate in high-temperature superconductors. What is debatable is the nature of forces ('glue') holding the pairs (*1*). The mechanism is different from that of conventional superconductors; for them, loss of the electric resistance is due to phonon-mediated electron pairing (Bardeen–Cooper–Schrieffer, BCS) (*2*). Ceramic cuprates become superconductors when extra holes or electrons are doped into their magnetically ordered charge-transfer insulator (ground) state (*3, 4*); the highest transition temperature (T_c) occurs at a doping of 0.15 extra hole per copper ion and it increases with the number (n) of Cu–O planes per unit cell, reaching a maximum at $n = 3$ (*5*). Because of the *d*-wave symmetry of the superconducting gap (*6*), the relatively small isotope effect (*7, 8*), and the magnitude of electron repulsion (U) and exchange (J) (appropriate for the antiferromagnetic phase), magnetic interactions have been considered as the source of binding (*1, 9*). The role of phonons in pair formation has also been discussed, from both experimental and theoretical perspectives (*10, 11*).

Angle-resolved photoemission spectroscopy (ARPES) experiments revealed the presence of kinks in the band dispersion at energies corresponding to specific (optical) phonon modes (*7, 11-13*). In some samples, inelastic neutron scattering data at similar energies supported a magnetic resonance mode below the transition temperature (*14*). The issue was raised over whether the low-energy features observed in the ARPES spectra are induced by magnetic or structural bosonic coupling. Based on energetics, the out-of-plane motion of the oxygen ions in the Cu–O plane, referred to as the out-of-plane buckling mode, has been assigned as responsible for the kink in the band dispersion observed along the direction of Cu–O bonds (*11, 12*). However, the electron–phonon coupling strength obtained by means of angle-integrated probes is not particularly large (*15*). This finding, together with the *d*-wave symmetry of the superconducting-phase order parameter (*6*), has been among the main arguments against a lattice-mediated pairing mechanism, because the BCS theory of electron–phonon coupling favors an *s*-wave order parameter (*16*).

Theoretical calculations have suggested that selective optical-phonon excitation could lead to an anisotropic electron–phonon coupling (*11*). In cuprate superconductors, it has been demonstrated, by using time-resolved photoemission (*15*) and time-resolved optical reflectivity (*17*), that the excited charge carriers preferentially couple to a phonon subset before decaying through anharmonic coupling to all other vibrations of the lattice. Moreover, the anomalous superconductivity-induced transfer of optical spectral weight and its doping dependence (*17-19*), usually considered as a hallmark of a non-BCS pairing mechanism, can be accounted for within a BCS model combined with a *d*-wave order parameter, for certain band structures (*20*). It is now known that the strength of the pairing potential (estimated from Nernst effect experiments) decreases as extra oxygen is doped into the unit cell, whereas the coherence length of the Cooper pairs increases with doping (*21*). The net effect is that for the condensate, a subtle compromise between pairing interaction and coherence needs to be achieved in order for high-temperature superconductivity to occur. To date, there has not been a direct observation of the actual structural change or anisotropy of electron–phonon coupling in the superconducting state.

This chapter describes, by using time-resolved electron diffraction, the temporal evolution of the structure following polarized carrier excitation by a femtosecond pulse, for different temperatures (for the metallic and superconducting states) and doping levels (from underdoped to optimally doped specimens). Specifically, different compositions were investigated by varying the doping level and number of Cu–O planes per unit cell in the Bi, Sr, Ca, Cu, and O (BSCCO) family; 7 different crystals for a total of 30 cleavages were studied. The initial femtosecond excitation transfers the system from the superconducting to the metallic state (*15*), breaking pairs (*17*). With the electron and lattice temperatures being vastly different (see below), energy of carriers is lowered through electron–phonon coupling that can be defined not only for the metallic but also for the superconducting-state phase (*22*).

By varying the polarization of carrier excitation, we observed major differences in the decay of the (00) diffraction rod that is correlated with the *c*-axis structural dynamics. The deduced structural changes on the time scale reported provide information on the mode(s) of atomic motions and the associated electron–phonon interactions. The striking polarization effect on the *c*-axis motion is consistent with a highly anisotropic electron–phonon coupling to the B_{1g} out-of-plane buckling mode (50 meV), with the maximum amplitude of atomic motions being ~0.15 Å. The anisotropy follows the symmetry of the *d*-wave superconducting gap, with the largest coupling along the Cu–O bond where the gap has its maximum value. Along this direction, the electron–phonon coupling parameter is obtained to be $\lambda = 0.55$ in the optimally doped two-layered sample, whereas at 45° it is $\lambda = 0.08$. The previously reported value of 0.26 (*15*), within the framework of the Eliashberg formalism (*23*), thus represents an average over the different directions.

Materials and Experimental Section

The investigated specimens were the following: optimally doped and underdoped two-layered $Bi_2Sr_2CaCu_2O_{8+\delta}$ (Bi2212), and optimally doped three-layered $Bi_2Sr_2Ca_2Cu_3O_{10+\delta}$ (Bi2223). The optimally doped samples of Bi2212 and Bi2223 were

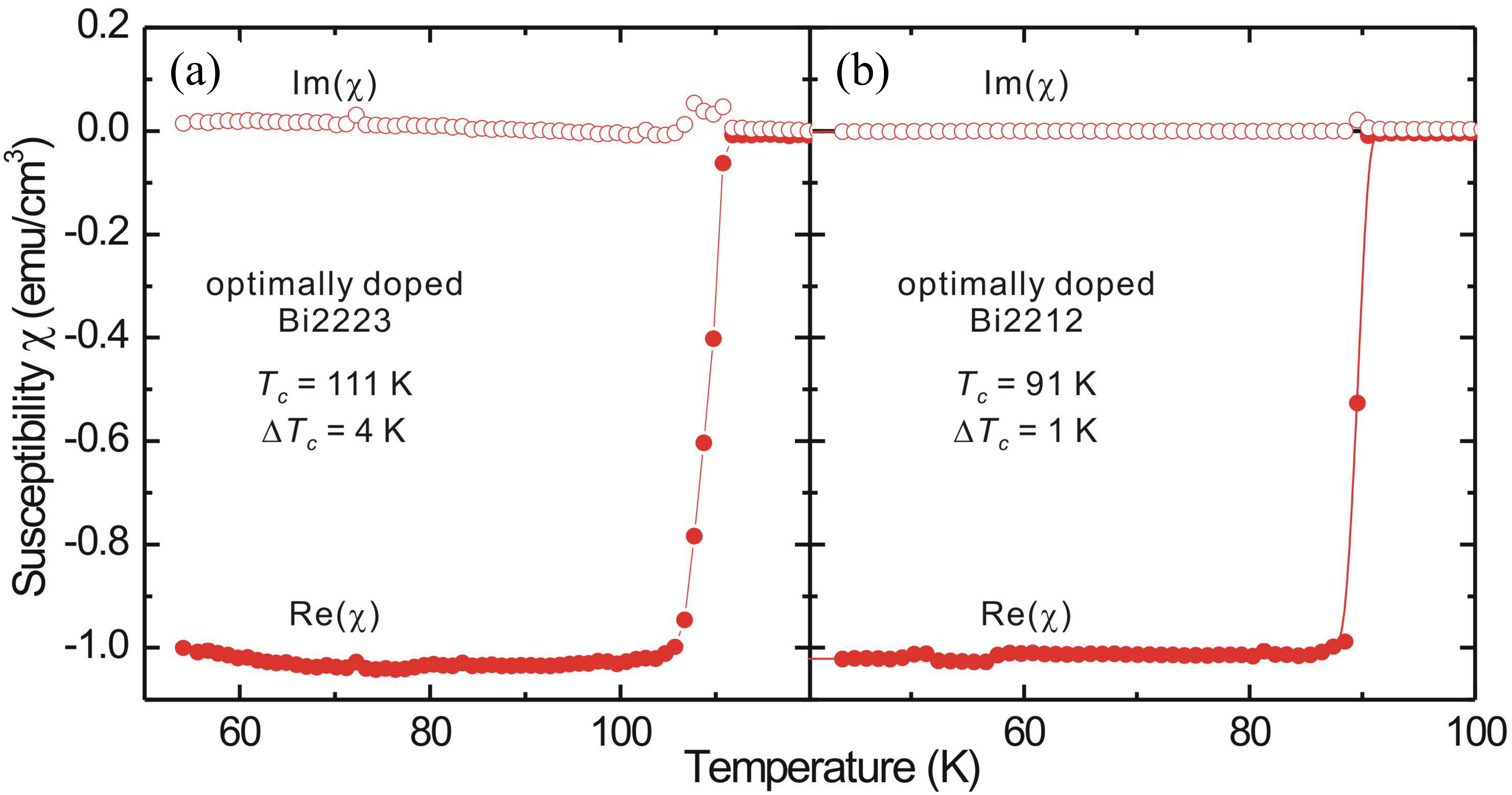

Fig. 1. Sample characterization. (a) Temperature dependence of the magnetic susceptibility of an optimally doped Bi2223 specimen. (b) Temperature dependence of the magnetic susceptibility of a representative optimally doped Bi2212 specimen investigated. The sharp transition attests the crystallinity and composition homogeneity of our samples.

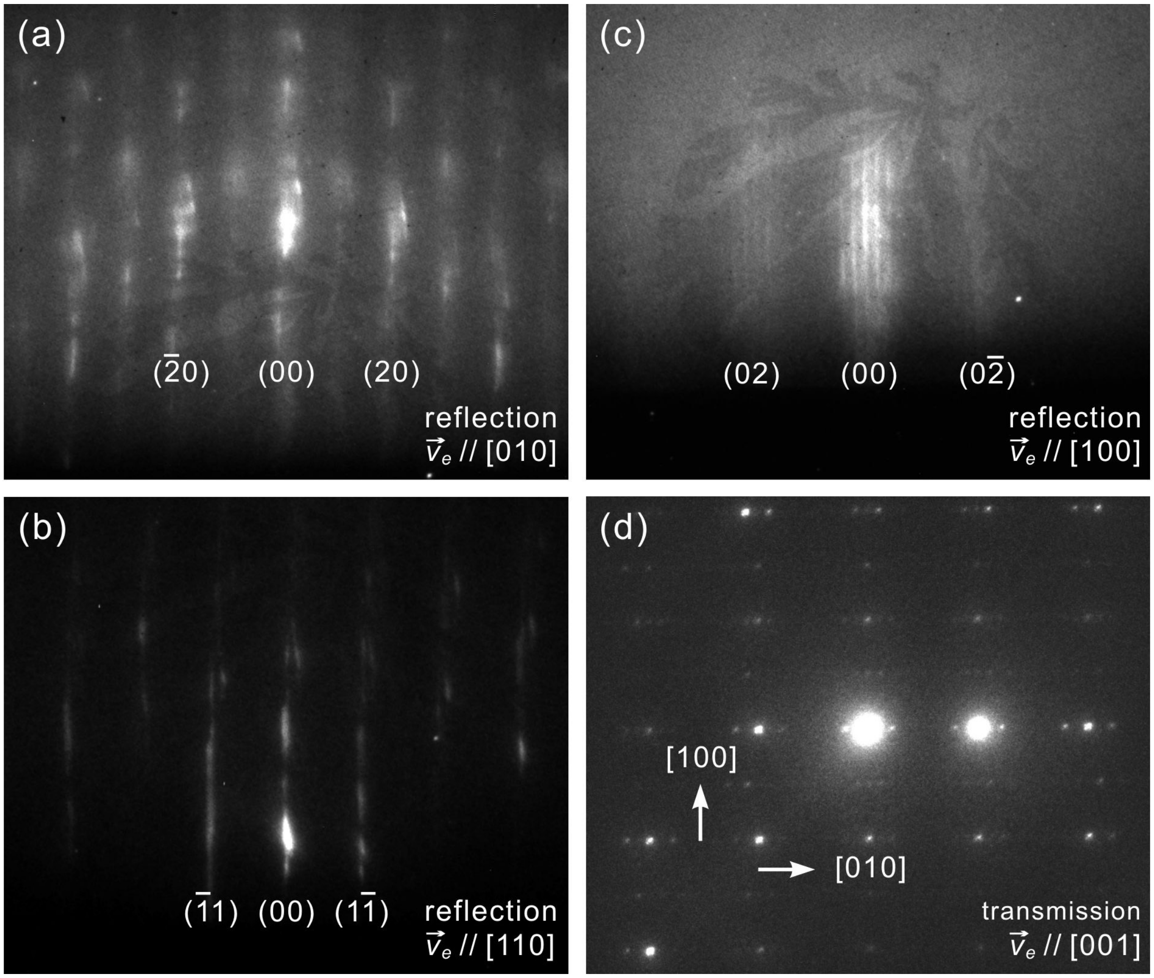

Fig. 2. Static diffraction patterns of optimally doped Bi2212. (a–c) Reflection patterns obtained at three different electron probing directions $\vec{v}_e$ (by rotating the crystalline sample), as indicated in the lower right corner. The large lattice constant along *c* and the nanometer depth of electron probing give rise to the rod-like patterns; from panel a, the intensity modulation along the diffraction rods gives the out-of-plane lattice parameter of *c* =30 Å. The indices for different diffraction rods are given. Note that the satellites of the main diffraction rods in panel c manifest the 27-Å modulation along the *b* axis of Bi2212. (d) Transmission diffraction pattern obtained by our electron microscope. The square in-plane structure is evident, with the presence of the *b*-axis modulation that is seen in panel c also.

grown by the travel solvent floating zone technique (*24*). The superconducting transition temperature was found to be $T_c = 91$ K in Bi2212 ($\Delta T_c = 1$ K), and $T_c = 111$ K in Bi2223 ($\Delta T_c = 4$ K). The underdoped Bi2212 sample was grown by the self-flux method (*25*), annealed in an oxygen-deficient atmosphere, and its transition temperature was $T_c = 56$ K ($\Delta T_c < 6$ K). The magnetic susceptibility curves for two representative specimens are displayed in Fig. 1.

All samples were cleaved in situ at low temperature, under a pressure on the order of 10^{-10} mbar to obtain a clean surface. An ultrashort (120 fs) infrared (800 nm) laser pulse was used to induce a temperature jump in the specimen, and the far-field diffraction of electron pulses was used to monitor the structural dynamics. The delay time between the pulses of carrier excitation and electron probing was varied while monitoring the change of Bragg diffraction intensities. The polarization of the excitation pulse was rotated with a half-wave plate and made parallel to the *a*–*b* plane of the material. In all these experiments, the fluence ranged from a few mJ/cm^2 and up to 20 mJ/cm^2.

Results from Optimally Doped $Bi_2Sr_2CaCu_2O_{8+\delta}$

We begin by discussing the results obtained for Bi2212. In Fig. 2, the static diffraction patterns of a single crystal of optimally doped Bi2212 are displayed. The patterns were recorded in the reflection geometry with the electron beam directed along three different axes, namely, the [010], [110], and [100] directions, as displayed in panels a to c. The diffraction rods, which display the two-dimensional nature of probing (Fig. 2, caption), were indexed for the tetragonal structure, giving the in-plane lattice parameters of $a = b = 5.40$ Å that are consistent with the x-ray values. The lattice modulation is resolved along the *b* axis with a period of 27 Å, again in agreement with the x-ray data

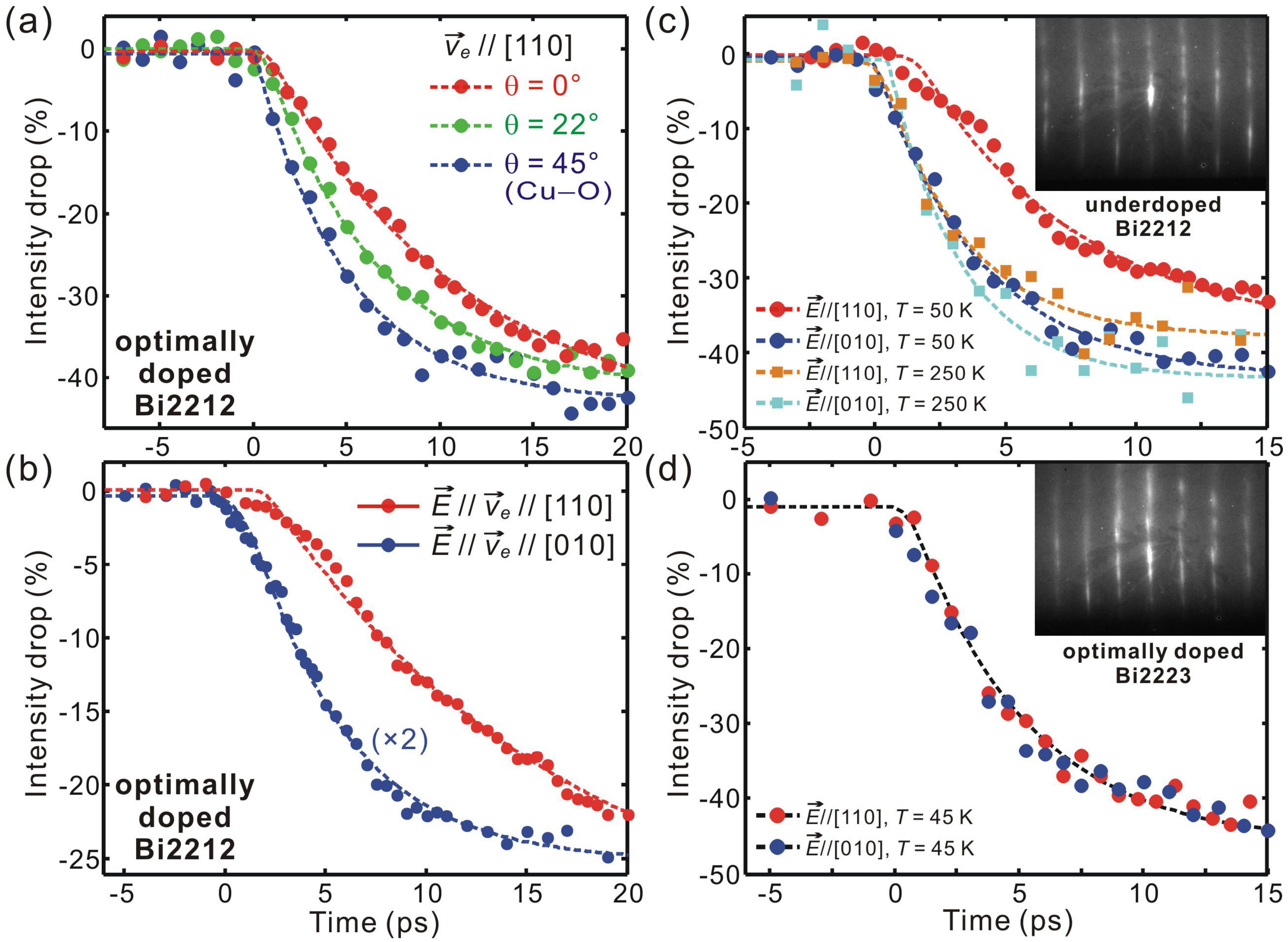

(See next page for the figure caption.)

Fig. 3. Time-resolved diffraction. (a) Diffraction intensity change of the (00) rod at different polarizations in optimally doped Bi2212. The laser fluence was 20 mJ/cm^2 and the temperature was 50 K. The electron probing was kept along [110] (Fig. 2b), and θ is the angle of polarization away from the probing direction (adjusted by rotation of a half-wave plate). The dotted lines (and also those in panels b to d) show the fits to an apparent exponential decay. (b) Diffraction intensity change of the (00) rod, from the same specimen, obtained with the optical polarization being parallel to the electron probing. By rotating the crystal, the time-dependent change was measured for the two zone axes (Fig. 2, panels a and b). (c) Diffraction intensity change of the (00) rod for an underdoped Bi2212 sample ($T_c = 56$ K), at two temperatures and two polarizations. The inset shows the diffraction pattern obtained from the specimen, revealing the good quality of the crystal. (d) Diffraction intensity change obtained from a three-layered, optimally doped Bi2223 specimen at 45 K for two polarizations. The diffraction pattern is displayed as an inset.

(*24*). The in-plane lattice constants, as well as the modulation, were confirmed for the specimens studied using our electron microscope, and one micrograph is given in Fig. 2d.

The temporal evolution of diffraction frames (with polarized excitation) is sensitive to motions of atoms during the structural change. In Fig. 3a, the intensity decay of the (00) rod [due to motions of the ions (Debye–Waller effect)] is plotted for three different polarizations ($\vec{E}$) of the excitation pulse: $\vec{E}$//[010], the direction of Cu–O bonds; $\vec{E}$//[110], the direction at 45°; and the one at 22°. The data were taken at $T = 50$ K. At longer times, up to 1 ns, these transients recover very slowly; because of the poor *c*-axis conductivity and metallic *ab*-plane, heat transport is mainly lateral, but is complete on the time scale of our pulse repetition time (1 ms). In Fig. 3b, another set of data was obtained by rotating the sample while keeping the polarization parallel to the electron beam direction. The temporal evolution of the (00) diffraction intensity obtained from the two different orientations (electron beam parallel to the Cu–O bond; see diffraction pattern in Fig. 2a, and at 45°, Fig. 2b) shows the same anisotropic behavior as that obtained by rotating the polarization, ruling out possible experimental artifacts.

The intensity decay for different polarizations was found to have distinct time constants (see below): the decay is faster when the polarization is along the Cu–O bond and slows down when polarization is along the [110] direction (45° from the Cu–O bond). When charge carriers are excited impulsively through light in a crystal, the electron and lattice temperatures are driven out of equilibrium, but they equilibrate through electron–phonon coupling. Excitation of phonons causes the diffraction intensity to change with time, and this decrease mirrors an increase of the mean atomic displacement in the corresponding direction, with a temperature assigned to the displacement through a time-dependent Debye–Waller factor (Eq. 16 of Ch. 2):

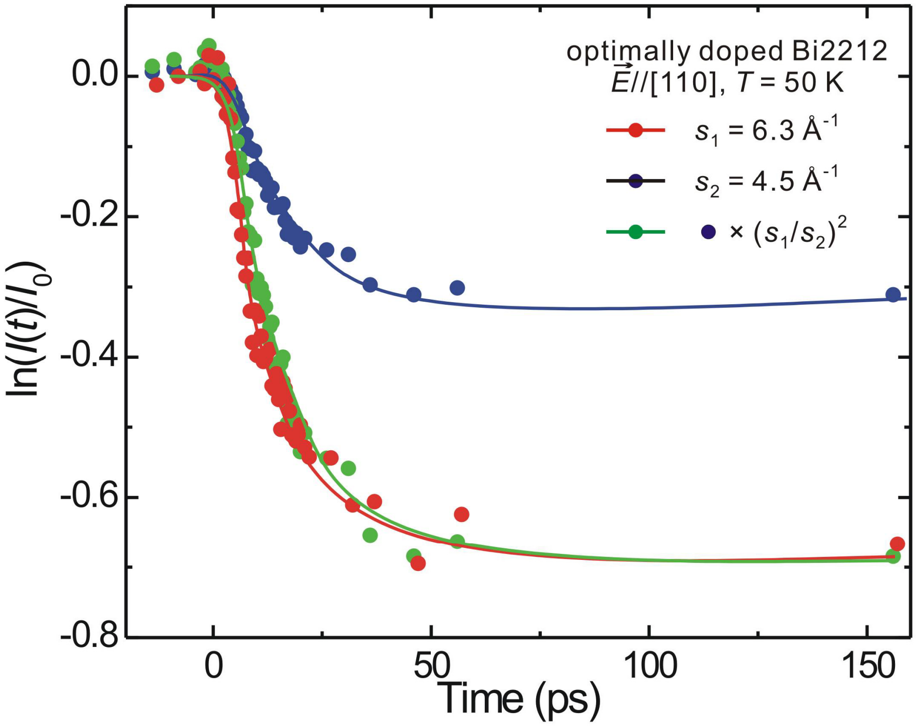

Fig. 4 Intensity scaling between two diffractions. Shown are the decay of two distinct Bragg peaks, observed at $s_1 = 6.3$ Å^{-1} (red) and $s_2 = 4.5$ Å^{-1} (blue). The green curve is obtained by multiplying the data at $s = s_2$ by the factor of $(s_1/s_2)^2$, according to Eq. 2, and its match with the data at $s = s_1$ confirms the structurally induced diffraction changes following the carrier excitation.

$$\ln[I(t)/I_0] = -2W(t) = -s^2\langle \delta u^2(t)\rangle / 3, \tag{1}$$

where $I(t)$ is the intensity of rod diffraction at a given time t after excitation, I_0 is the intensity before excitation, s is the scattering vector, and $\langle \delta u^2(t)\rangle$ is the mean square atomic displacement. It is noted that at a given time, two distinct Bragg diffraction features appearing at $s = s_1$ and s_2 along the same direction should obey the following scaling relation on the basis of Eq. 1:

$$\frac{\ln(I_{S_1}/I_0)}{\ln(I_{S_2}/I_0)} = (\frac{s_1}{s_2})^2 . \tag{2}$$

In Fig 4, we display the intensity changes for two different Bragg spots on the (00) rod, recorded in the same pattern. The correct scaling relationship confirms that the observed intensity changes indeed originate from structural motions.

From the results reported here for $[I(t)/I_0]_{\min}$, the maximum root-mean-square value for the amplitude of the motion, $\sqrt{\langle \delta u^2(t)\rangle}_{\max}$, is obtained to be ~0.15 Å at the fluence of 20 mJ/cm^2. Given the *c*-axis distance of 30 Å, this represents a change of 0.5%; or, with respect to the separation of Cu–O planes (3.2 Å), such a motion signifies a much larger change of 4.7%. In regard to the temporal evolution of $\sqrt{\langle \delta u^2(t)\rangle}$ deduced from $I(t)$ according to Eq. 1, different mechanisms may be considered for the fitting. One possible model considers nonequilibrium phase transition in ultrafast melting, in which the inertial dynamics (*26*) can be invoked with $\sqrt{\langle \delta u^2(t)\rangle}$ being related to the velocity of the motion, resulting in a Gaussian dependence on time. However, this mechanism can be ruled out because it gives a velocity to be 0.025 Å/ps, far less than the root-mean-square velocity of 1.45 Å/ps at 50 K. The appropriate description for the nonequilibrium dynamics here should take into account the energy transfer from the photoexcited carriers to the optical phonons, as mentioned previously (see Chs. 4 and 5).

Analysis and Discussion: The Three–temperature Model

The observed anisotropy of decay with polarization indicates the distinct *c*-axis distortion and the difference in electron–phonon coupling. In order to obtain the magnitude of the couplings, we shall invoke the well-known model of electron and lattice temperatures, dividing the lattice modes into those that are strongly coupled to the electrons and the rest that are not. The results from simulation may be compared with the experimentally extracted temperature using Eq. 1, and the expression of the atomic displacement for a Debye solid is given by

$$\left\langle \delta u^2(t) \right\rangle = \frac{9\hbar^2 \Delta T(t)}{M k_B \Theta_D^2}, \tag{3}$$

where M is the average mass in the unit cell, k_B is Boltzmann constant, $\hbar$ is the reduced Planck constant, and Θ_D is the Debye temperature of the material (*27*).

Conventionally, the two-temperature model (*23*) is used to describe laser-induced heating of the electron and phonon subsystems in an elementary metal. Its success is the result of the isotropic electron–phonon coupling in a simple lattice structure, i.e., one atom per primitive unit cell. In complex, strongly correlated materials like high-T_c superconductors, however, such a model becomes inappropriate because photoexcited carriers may anisotropically and preferentially couple to certain optical phonon modes, resulting in the failure of assignment of a single temperature to the whole lattice structure. In the three-temperature model described in Ref. 15, in addition to the electron temperature T_e, two temperatures are defined for the lattice part: the hot-phonon temperature, T_p, for the subset of phonon modes to which the laser-excited conduction-band carriers transfer their excess energy, and the lattice temperature, T_l, for the rest of the phonon modes that are thermalized through anharmonic coupling. As an approximation, the spectrum of the hot phonons $F(\Omega)$ is assumed to follow an Einstein model, $F(\Omega) = \delta(\Omega - \Omega_0)$, where δ denotes the Dirac delta function, Ω the energy, and Ω_0 the energy of a hot phonon. Effectiveness of the energy transfer between the carriers and hot phonons is described by the dimensionless parameter λ, $\lambda = 2\int \Omega^{-1}\alpha^2 F d\Omega$, where $\alpha^2 F$ is the Eliashberg coupling function (*23*). The rate equations describing the temporal evolution of the three temperatures are given by

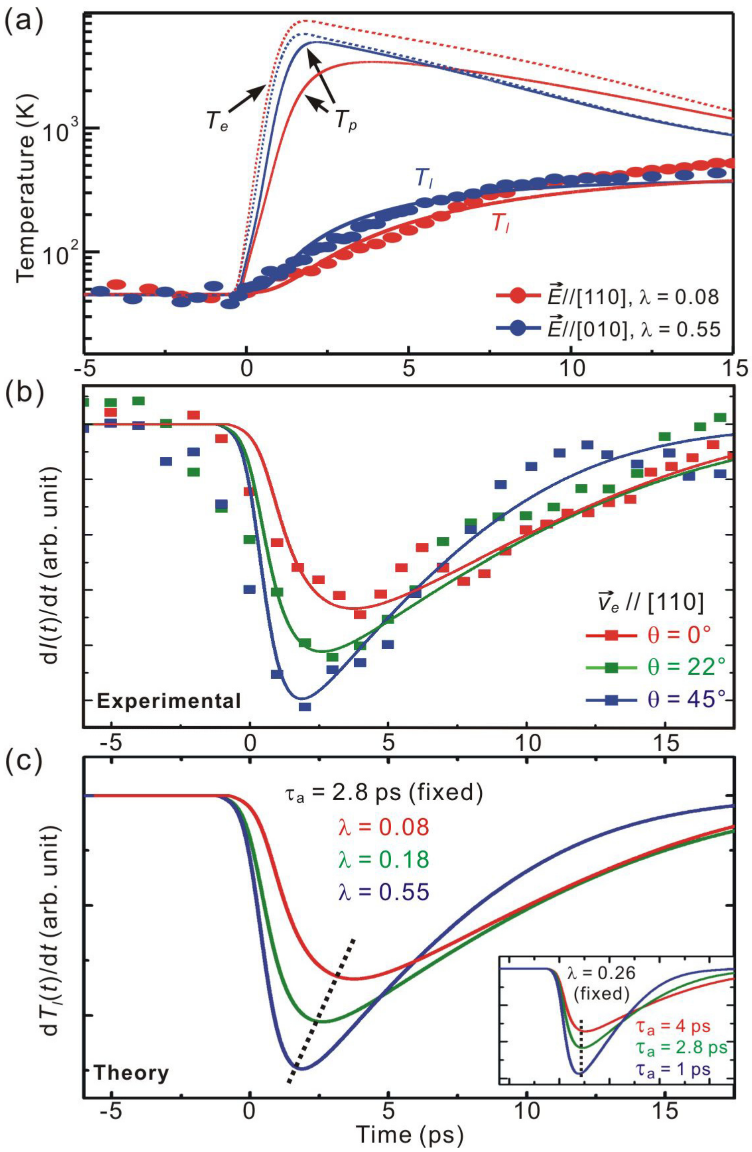

Fig. 5. Experimental and theoretical intensity transients. (a) Lattice temperature derived from diffraction using Eqs. 1 and 3, for different polarizations, along [010] (blue dots) and [110] (red dots), in optimally doped Bi2212. From the three-temperature model described, we obtain $\lambda = 0.08$ for $\vec{E}$ //[110] (T_l, red solid line) and $\lambda = 0.55$ for $\vec{E}$ //[010] (T_l, blue solid line). The electronic (T_e, dashed lines) and hot-phonon (T_p, solid lines) temperatures are also displayed. (b) Derivatives of the (00) diffraction intensity derived from Fig. 3a for different polarizations. (c) Derivatives of the simulated lattice temperature within the three-temperature model, for different λ with a fixed anharmonic coupling time $\tau_a = 2.8$ ps (also shown in panel b) and for different τ_a with a fixed $\lambda = 0.26$ (inset). The clear shift of the minimum position is only observed when λ is varied (black dotted lines).

$$\frac{dT_{\mathrm{e}}}{dt} = -\frac{3\lambda\Omega_0^3}{\hbar\pi k_{\mathrm{B}}^2}\frac{n_{\mathrm{e}}-n_{\mathrm{p}}}{T_{\mathrm{e}}} + \frac{P}{C_{\mathrm{e}}}, \tag{4}$$

$$\frac{dT_{\mathrm{p}}}{dt} = \frac{C_{\mathrm{e}}}{C_{\mathrm{p}}}\frac{3\lambda\Omega_0^3}{\hbar\pi k_{\mathrm{B}}^2}\frac{n_{\mathrm{e}}-n_{\mathrm{p}}}{T_{\mathrm{e}}} - \frac{T_{\mathrm{p}}-T_l}{\tau_{\mathrm{a}}}, \tag{5}$$

$$\frac{dT_l}{dt} = \frac{C_{\mathrm{p}}}{C_l}\frac{T_{\mathrm{p}}-T_l}{\tau_{\mathrm{a}}}, \tag{6}$$

where $\tau_{\mathrm{a}} = 2.8$ ps is the characteristic time for the anharmonic coupling of the hot phonons to the lattice, n_{e} and n_{p} are the electron and hot-phonon distributions given by $n_{\mathrm{e,p}} = (e^{\Omega_0/k_{\mathrm{B}}T_{\mathrm{e,p}}}-1)^{-1}$, and P is the laser fluence function; a ratio of 10^3 between the electronic specific heat C_{e} and the lattice specific heat (C_{p} and C_l) is known (*15*).

In Fig. 5a, we plot the equivalent temperature associated with the *c*-axis displacement of the optimally doped Bi2212 specimen, for different polarizations, together with theoretical predictions given by the three-temperature model. In our calculations, the values of the parameters were chosen to be the same as in Ref. 15, except for the excitation source that has a fluence of 20 mJ/cm^2 and duration of 120 fs in our case. The initial heating of the charge carriers by the excitation pulse is on the femtosecond time scale, during which an electronic temperature, T_{e}, is established. The coupling of carriers to a subset of phonon modes defines an equivalent temperature, T_{p}, for that phonon subset and, subsequently, the relaxation to all other modes establishes the lattice temperature, T_l. It follows that the stronger the electron–phonon coupling, the faster the decay of the diffraction intensity. From the results in Fig. 5a, we obtained $\lambda = 0.08$ for $\vec{E}$//[110] and 0.55 for $\vec{E}$//[010] in optimally doped Bi2212. The average value at optimal doping is in good agreement with the results ($\lambda = 0.26$) of Ref. 15, which angularly integrates the photoemission among different crystallographic directions, and also in agreement with "frozen-phonon" calculations (*28*).

The rate of diffraction change provides the time scales of selective electron–phonon coupling and the decay of initial modes involved. In Fig. 5b, the derivatives of the diffraction intensity as a function of time, $\mathrm{d}I(t)/\mathrm{d}t$, are displayed for different polarizations (Fig. 3a). The presence of a clear inversion point reflects the two processes involved, the one associated with the coupling between excited carriers and optical phonons, and the second that corresponds to the decay of optical modes, by anharmonicity into all other vibrations. The minimum in the derivative, signaling the crossover between these two processes, shifts toward an earlier time when the polarization becomes along the Cu–O bond. In Fig. 5c, the derivative of the simulated lattice temperature within the three-temperature model, $\mathrm{d}T_l(t)/\mathrm{d}t$, shows a similar two-process behavior. The clear shift of the minimum to an earlier time can be reproduced by varying the electron–phonon coupling parameter, λ; in contrast, a change in the anharmonic coupling constant, τ_a, does not affect the early process and the corresponding time of the derivative minimum has little shift (Fig. 5c, inset). Thus, consistent with the results of Fig. 5a, this analysis indicates that the anisotropic behavior of the diffraction intensity is indeed due to a directional electron–phonon coupling.

The derivative minima occur at times of ~1.0, 2.0 and 3.5 ps for, respectively, the polarization at 0°, 22° and 45° with respect to the Cu–O bond direction (Fig. 5b). Theoretically, the initial rate of the electron–phonon scattering can be obtained through the equation (*23*)

$$\frac{1}{\tau_{\mathrm{el-ph}}} = \frac{3\hbar\lambda\langle\omega^2\rangle}{\pi k_\mathrm{B} T_\mathrm{e}}\left(1 - \frac{\hbar^2\langle\omega^4\rangle}{12\langle\omega^2\rangle(k_\mathrm{B}T_\mathrm{e})(k_\mathrm{B}T_l)} + \cdots\right) \approx \frac{3\hbar\lambda\langle\omega^2\rangle}{\pi k_\mathrm{B} T_\mathrm{e}}, \tag{7}$$

where $\tau_{\text{el-ph}}$ is the characteristic coupling time constant and ω is the angular frequency of the coupled modes. Given the values of λ (0.55, 0.18 and 0.08 in Fig. 5c), we obtained

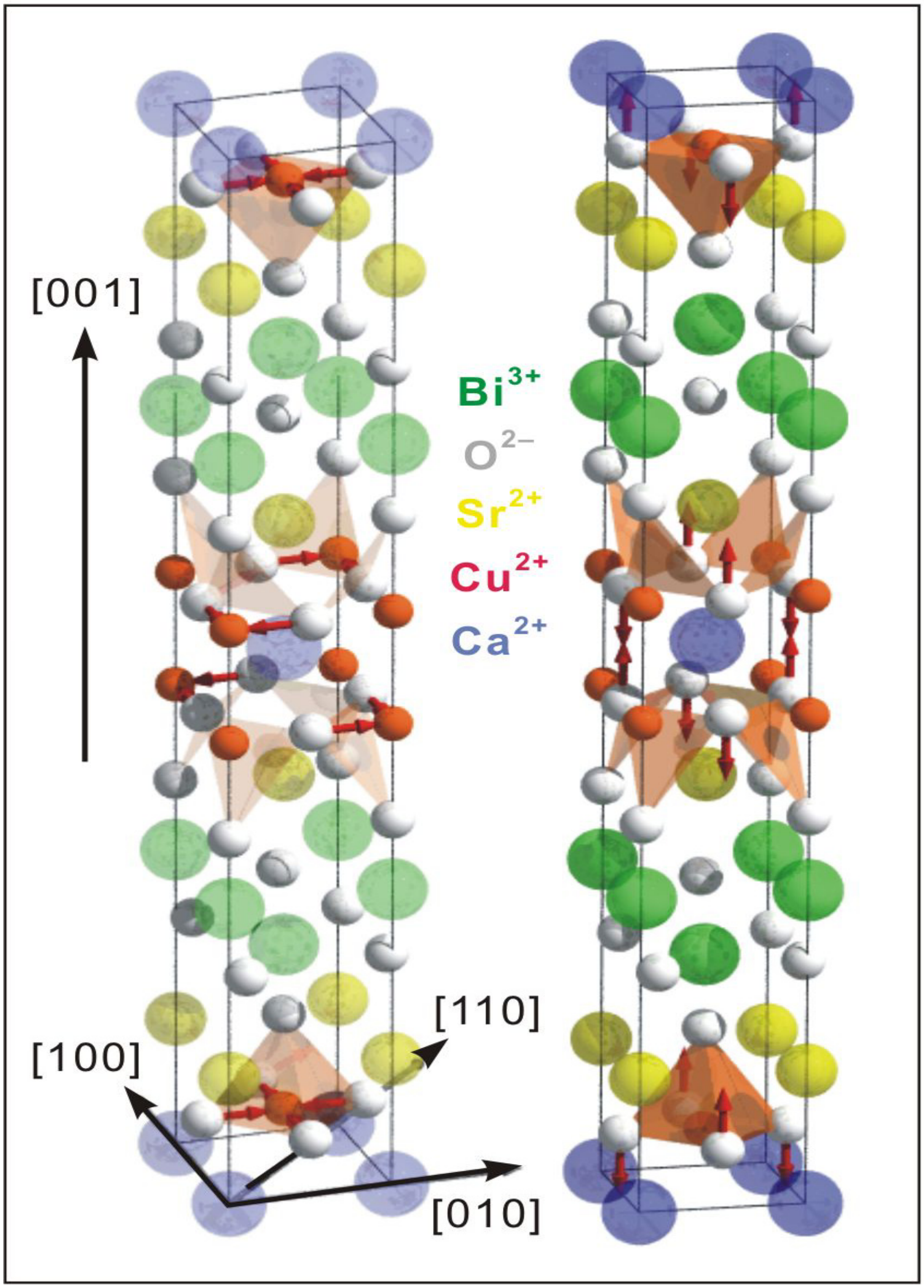

Fig. 6. Three-dimensional structure of Bi2212 (*24*), indicating the main crystallographic directions. Relevant to our work are the red arrows which show the atomic movements in the in-plane breathing mode (left panel) and those in the out-of-plane buckling mode (right panel).

$\tau_{\text{el-ph}}$ to be 290 fs, 900 fs and 2.0 ps with an initial $T_e = 6000$ K and $T_l = 50$ K. In Ref. 15, $\tau_{\text{el-ph}}$ was reported to be 110 fs for $T_e \sim 600$ K. Given the difference in fluence, hence T_e, the values of $\tau_{\text{el-ph}}$ obtained here (using Eq. 7) are in reasonable agreement with the average value obtained in Ref. 15. It should be emphasized that, within such time scale for the electron–phonon coupling, the lattice temperature T_l remains below T_c; in Fig. 5a, the temperature crossover ($T_l > T_c$) occurs at 2~3 ps.

The influence of polarization on the (00) diffraction rod (which gives the structural dynamics along the *c* axis) reveals the unique interplay between the in-plane electronic properties and the out-of-plane distortion. Among the high-energy optical phonons that are efficiently coupled at early times, the in-plane breathing and out-of-plane buckling modes are favored (Fig. 6) (*7, 12*) because of their high energy and involvement with carrier excitation at 1.55 eV. Our observation of a faster *c*-axis dynamics when the polarization is along the Cu–O bond implies a selective coupling between the excitation of charge carriers and specific high-momentum phonons. A plausible scheme is the stronger coupling between the antinodal ([010]) charge carriers and the out-of-plane buckling vibration of the oxygen ions in the Cu–O planes (*29*).

Results and Analysis from Samples with Different Compositions

Further information was obtained by studying different compositions (dopings and number of layers) and temperatures. In Fig. 3c we display the results obtained for an underdoped Bi2212 ($T_c = 56$ K), also at two temperatures. The anisotropy is evident at low temperature, giving the values of $\lambda = 0.12$ for $\vec{E}$//[110] and 1.0 for $\vec{E}$//[010] (Fig. 7a). However, at higher temperature, the decay of both polarizations is similar and reaches the fastest profile recorded. This behavior is understood in view of the two types

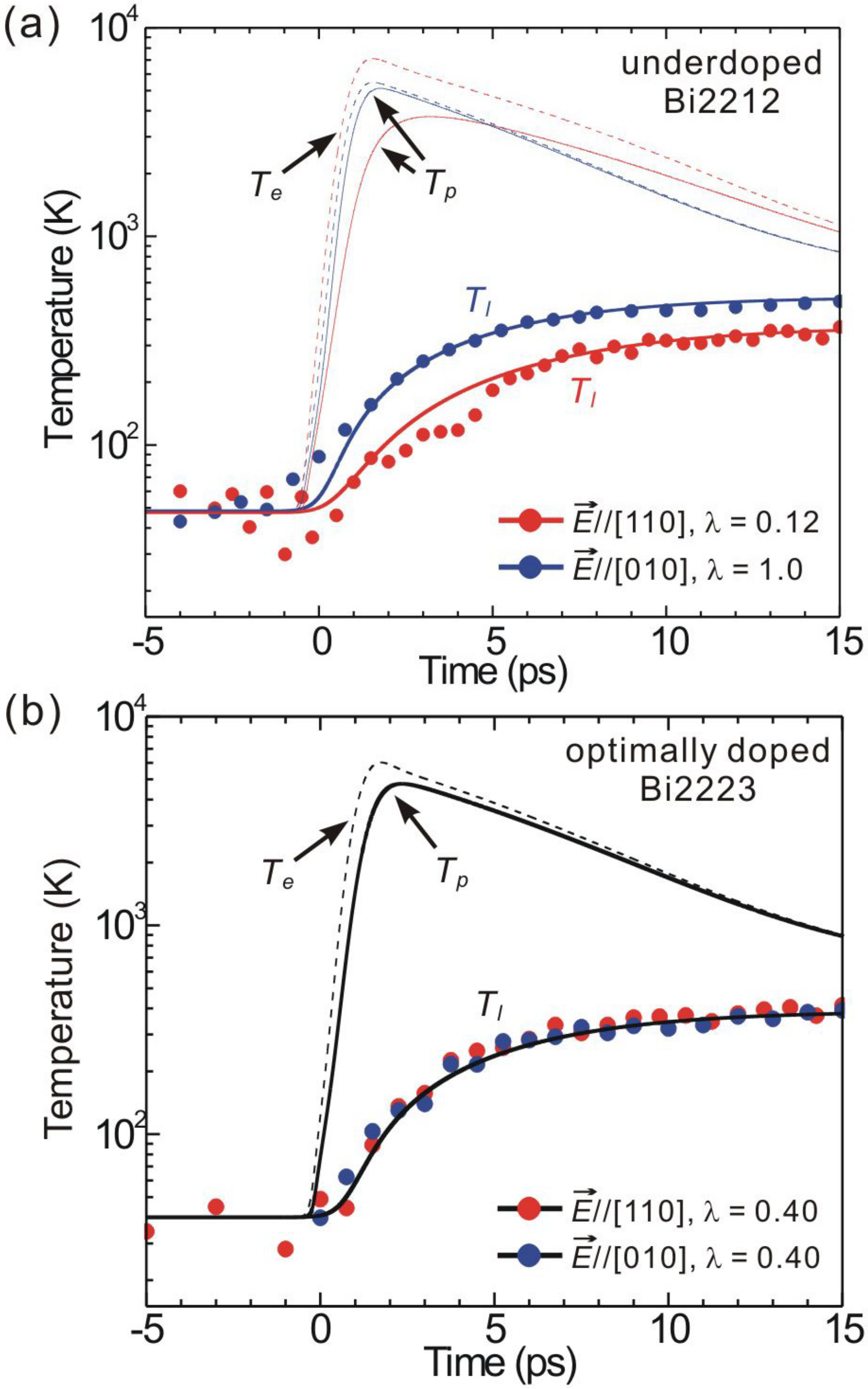

Fig. 7. Lattice temperatures derived from the diffraction intensity data by using Eqs. 1 and 3 for different polarizations, along [010] (blue dots) and [110] (red dots), in (a) the underdoped Bi2212 and in (b) the optimally doped Bi2223. Dashed and solid lines show the calculated temporal evolution of the three temperatures, T_e, T_p and T_l.

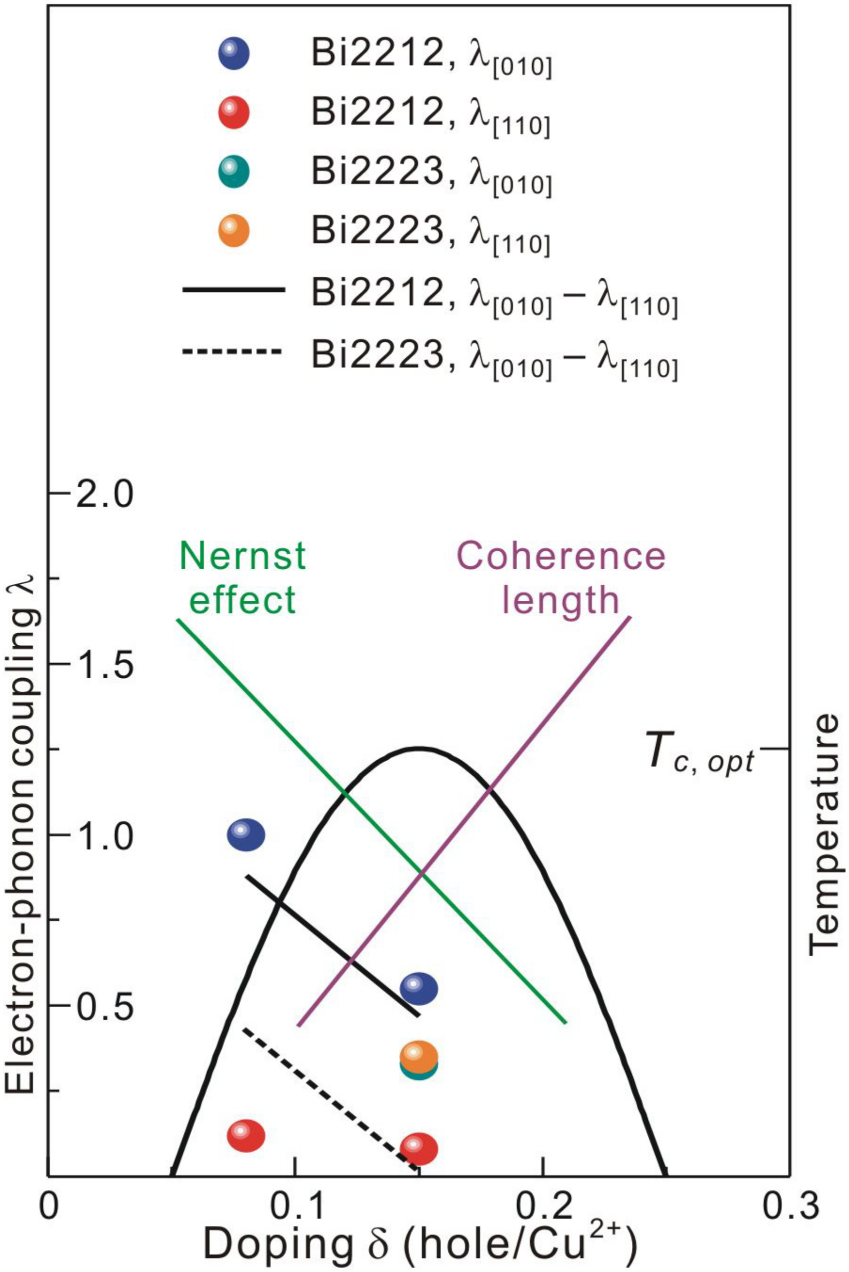

Fig. 8. The doping dependence of the coupling constant (λ) along the [010] and [110] directions in Bi2212 (blue and red dots, respectively) and its anisotropy ($\Delta\lambda$ between the two directions; black solid line), as well as λ along the [010] and [110] directions in Bi2223 (green and orange dots, respectively) and the extrapolated anisotropy (black dashed line). A qualitative sketch of the upper critical field (green line), Cooper-pair coherence length (violet line) and T_c (black curve) is also shown (*21*).

of phonons present at high temperature, those created through carrier–phonon coupling (low-temperature) and the ones by thermal excitation. This behavior with temperature is consistent with the optical reflection studies made by Gedik *et al.* (*30*).

On the other hand, for optimally doped Bi2223, we observed no significant anisotropy even in the low temperature regime (Fig. 3d). In fact, the intensity decay of the (00) rod for light polarized along [110] becomes essentially that of the [010] direction (see Fig. 3, panels b and d). The electron–phonon coupling in Bi2223 is thus similar for both directions ($\lambda = 0.40$; see Fig. 7b), signifying that the out-of-plane buckling motions are coupled more isotropically to the initial carrier excitation, likely due to the somewhat modified band structure (e.g., larger plasma frequency; see Ref. 31) from that of Bi2212. This observation is consistent with the more isotropic superconducting properties of Bi2223 (*32*). The screening effect for the inner Cu–O layer by the outer ones in Bi2223 (*33*), and the less structural anisotropy between the in-plane and out-of-plane Cu–O distances (*32*), might also play a role in the disappearance of the anisotropic electron–phonon coupling.

In Fig. 8, the doping dependence of λ and the anisotropy observed for different polarizations, $\Delta\lambda = \lambda_{[010]} - \lambda_{[110]}$ (obtained from repeated experiments on different samples and cleavages), are displayed, together with the qualitative trend of the upper critical field (Nernst effect) and coherence length (*21*). The similarity in trend with the upper critical field behavior, which can be related to the pair correlation strength, is suggestive of the lattice involvement especially in this distinct phase region where the spin binding is decreasing. In view of an alternative explanation for the doping dependence of the critical field (*34*), our observation of an anisotropic coupling between the lattice and different light polarization may also be consistent with the idea of a dichotomy between nodal and antinodal carriers, with the latter forming a charge density wave competing with superconductivity (*35*). Future experiments will be performed to complete the trends up to the overdoping regime for different superconductor transitions (*36*).

Conclusion

The observation of atomic motions and the directional electron–phonon coupling suggests that structural dynamics is an integral part of the description of the mechanism of high-temperature superconductivity. The anisotropic carrier–phonon coupling, reaching its maximum along the Cu–O bond, and the distortion of the Cu–O planes, suggest a direct role for structural dynamics and considerations (*37, 38*) beyond simple two-dimensional models. Recent theoretical work has incorporated lattice phonons in the *t-J* model to account for the observed optical conductivity (*39*), whereas new band structure calculations suggested that large and directional electron–phonon coupling can favor spin ordering (*40*). It is worth noting that the reported time scale of electron–phonon coupling (at the photon/chemical doping level used) is of the same order of magnitude as that of spin exchange (40 fs) in the undoped phase. This implies that both the magnetic interactions and lattice structural changes should be taken into account for the microscopic description of the pair formation. Because it is now possible to examine the influence of these structural effects in the superconducting phase, by means of ultrafast electron crystallography, it is hoped that the reported results here can stimulate the development of theoretical models that explicitly incorporate the role of atomic motions in the mechanism of high-temperature superconductivity.

References and Footnote:

1. P. W. Anderson, *Science* **316**, 1705 (2007).
2. J. Bardeen, L. N. Cooper, J. R. Schrieffer, *Phys. Rev.* **106**, 162 (1957).
3. W. E. Pickett, *Rev. Mod. Phys.* **61**, 433 (1989).
4. P. Horsch, W. Stephan, in *Electronic properties of high-temperature superconductors,* H. Kuzmany, M. Mehring, J. Fink, Eds. (Springer, Berlin, 1993).
5. B. A. Scott, E. Y. Suard, C. C. Tsuei, D. B. Mitzi, T. R. McGuire, *Physica C* **230**, 239 (1994).
6. D. J. van Harlingen, *Rev. Mod. Phys.* **67**, 515 (1995).
7. G. H. Gweon *et al.*, *Nature* **430**, 187 (2004).
8. D. Zech *et al.*, *Nature* **371**, 681 (1994).
9. P. W. Anderson, *Science* **235**, 1196 (1987).
10. J. A. Slezak *et al.*, *Proc. Natl. Acad. Sci. USA* **105**, 3203 (2008).
11. T. P. Devereaux, T. Cuk, Z. X. Shen, N. Nagaosa, *Phys. Rev. Lett.* **93**, 117004 (2004).
12. T. Cuk *et al.*, *Phys. Rev. Lett.* **93**, 117003 (2004).
13. W. Meevasana *et al.*, *Phys. Rev. Lett.* **96**, 157003 (2006).
14. S. M. Hayden, H. A. Mook, P. Dai, T. G. Perring, F. Dohan, *Nature* **429**, 531 (2004).
15. L. Perfetti *et al.*, *Phys. Rev. Lett.* **99**, 197001 (2007).
16. J. Annett, N. Goldenfeld, S. R. Renn, *Phys. Rev. B* **43**, 2778 (1991).
17. N. Gedik *et al.*, *Phys. Rev. Lett.* **95**, 117005 (2005).
18. H. J. A. Molegraaf, C. Presura, D. van der Marel, P. H. Kes, M. Li, *Science* **295**, 2239 (2002).

19. F. Carbone *et al.*, *Phys. Rev. B* **74**, 064510 (2006).
20. F. Marsiglio, F. Carbone, A. B. Kuzmenko, D. van der Marel, *Phys. Rev. B* **74**, 174516 (2006).
21. Y. Wang *et al.*, *Science* **299**, 86 (2003).
22. D. J. Scalapino, J. R. Schrieffer, J. W. Wilkins, *Phys. Rev.* **148**, 263 (1966).
23. P. B. Allen, *Phys. Rev. Lett.* **59**, 1460 (1987).
24. E. Giannini, V. Garnier, R. Gladyshevskii, R. Flukiger, *Supercond. Sci. Technol.* **17**, 220 (2004).
25. N. Nakamura, M. Shimotomai, *Physica C* **185**, 439 (1991).
26. A. M. Lindenberg *et al.*, *Science* **308**, 392 (2005).
27. P. Stampfli, K. H. Bennemann, *Phys. Rev. B* **46**, 10686 (1992).
28. S. Y. Savrasov, O. K. Andersen, *Phys. Rev. Lett.* **77**, 4430 (1996).
29. Unlike semiconductors where selectivity of *k*-vector in transient optical absorption is defined, in conventional metals the intraband transition (Drude region) involves near isotropic phonon-assisted transitions. In cuprates, nonconventional intraband transitions, even within the Drude region, may exist (*41, 42*). Moreover, on the ultrashort time scale, phonons are selectively coupled. However, at 1.55 eV, cuprates has a more complex structure of bands, and a contribution from the interband charge transfer will define a Cu–O polarization anisotropy. Given this complexity we cannot with certainty assign such a direction.
30. N. Gedik *et al.*, *Phys. Rev. B* **70**, 014504 (2004).
31. F. Carbone *et al.*, *Phys. Rev. B* **74**, 024502 (2006).
32. E. Giannini *et al.*, *Curr. Appl. Phys.* **8**, 115 (2008).
33. H. Kotegawa *et al.*, *Phys. Rev. B* **64**, 064515 (2001).

34. A. D. Beyer, C.-T. Chen, M. S. Grinolds, M. L. Teague, N.-C. Yeh, *Physica C* **468**, 471 (2008).
35. C.-T. Chen, A. D. Beyer, N.-C. Yeh, *Solid State Commun.* **143**, 447 (2007).
36. P. P. Edwards, N. F. Mott, A. S. Alexandrov, *J. Supercond.* **11**, 151 (1998).
37. J. C. Phillips, *Proc. Natl. Acad. Sci. USA* **105**, 9917 (2008).
38. J. Tahir-Kheli, W. A. Goddard III, *Phys. Rev. B* **76**, 014514 (2007).
39. A. S. Mishchenko *et al.*, *Phys. Rev. Lett.* **100**, 166401 (2008).
40. T. Jarlborg, *Phys. Rev. B* **68**, 172501 (2003).
41. W. Stephan, P. Horsch, *Phys. Rev. B* **42**, 8736 (1990).
42. P. Kuiper *et al.*, *Phys. Rev. Lett.* **80**, 5204 (1998) and cited references therein.

Part III

Surface Assemblies and Interfacial Phenomena

Chapter 9

Ordered Water Structure and Its Dynamics at Hydrophobic Graphite Interfaces[†]

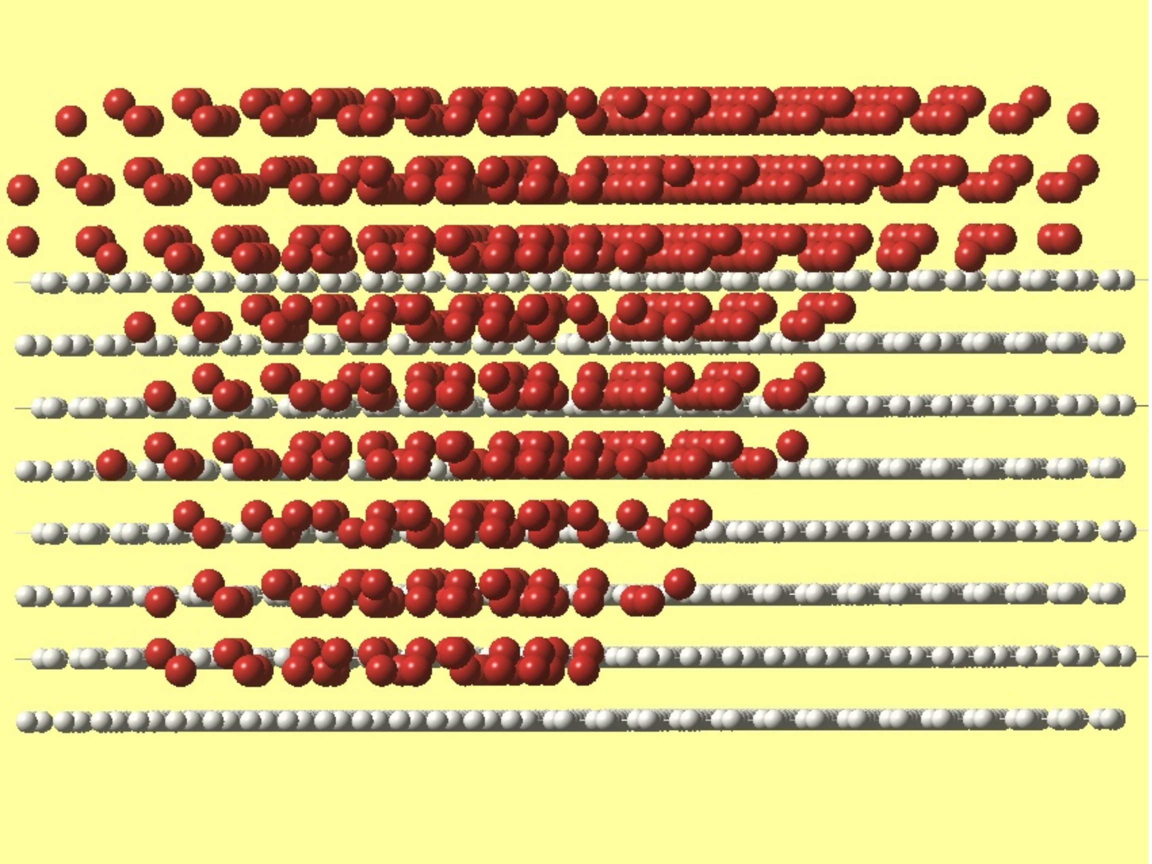

[†] adapted from D.-S. Yang, A. H. Zewail, *Proc. Natl. Acad. Sci. USA* **106**, XXXX (2009).

Introduction

Water at interfaces is fundamental to the understanding of various phenomena, such as wetting, molecular recognition and macromolecular folding. When compared with bulk phases (*1, 2*), the nanometer-scale interface is believed to have a unique function in nanotribology (*3, 4*), chemical reactivity (*4-6*) and biological structure and dynamics (*7-10*). From the structural point of view, considering the energetics, the determining factor at interfaces is the delicate balance of hydrogen bonding among water molecules and the comparable interactions with a substance, defining the two extremes of hydrophobic and hydrophilic behavior. However, the time scales of structural dynamics are important for defining the microscopic mechanisms of relaxations and the role of substrate structure and morphology (*11*). For water ice on a hydrophilic substrate, the ordered layers are evidenced by their diffraction (Bragg spots), and this long-range order is lost when the ice assembly becomes at a distance from the substrate (*12*). On hydrophobic surfaces, the expected picture is that randomly oriented crystallites form with no interfacial long-range order, because of the stronger intermolecular interactions when compared with those of water–substrate.

In this chapter, I describe the determination of the structure and dynamical behavior of a water assembly on highly oriented pyrolytic graphite (HOPG), a hydrophobic substrate. Through diffraction, ultrafast electron crystallography (UEC) provides the position of atomic planes and the temporal change of the structure. Electron crystallography (*13*), because of the large electron scattering cross section, is ideal for these surface and interface probings. Here, it is shown that the layered structure of HOPG serves as a substrate and promotes the crystalline order in the ice thin film along the surface normal direction. Upon heating the substrate by an infrared femtosecond pulse, the interfacial ice assembly goes through nonequilibrium phase transformation, into a highly expanded lattice, a dynamical behavior evidenced by the appearance of a "structural isosbestic point" in the diffraction profiles. The ice "melting" time is 10 ps and the new phase grows in 20 ps, whereas the restructuring time is significantly longer, being 75 and 390 ps. From the intense Bragg (spot) diffraction, it is concluded that ice on hydrophobic graphite has a high degree of order on the nanometer scale (and also in the expanded state) similar to that reported on a hydrophilic substrate (*12*). This finding suggests the important role of surface morphology.

Materials and Experimental Section

The HOPG substrate, which was obtained from Structure Probe, Inc. (grade 1), was cleaved and immediately mounted on the goniometer inside the diffraction chamber; an ultrahigh vacuum of $\sim 10^{-10}$ torr at low temperature was maintained during the experiment. To prepare the interfacial water assembly, the goniometer was first cooled down to $T = 100$ K by a constant flow of liquid nitrogen, and the flow rate was decreased to achieve a higher temperature when necessary. At 3 cm above the substrate, molecules of water (NANOpure, resistivity > 18.0 MΩ·cm) were effused through a micrometer-sized pinhole of a doser system containing only saturated water vapor (~20 Torr) at room temperature (*12*). The extent of water layer deposition was controlled by the dose time. The amorphous solid water initially deposited on HOPG at $T = 100$ K begins to transform into a polycrystalline assembly of the cubic-ice structure at $T \sim 135$ K, with a preference of vertical stacking of (111) bilayers but no horizontal orientation order.

The time-resolved experiments were carried out after the deposited interfacial water was thermally crystallized (annealed) and then maintained at $T = 100$ K. We used

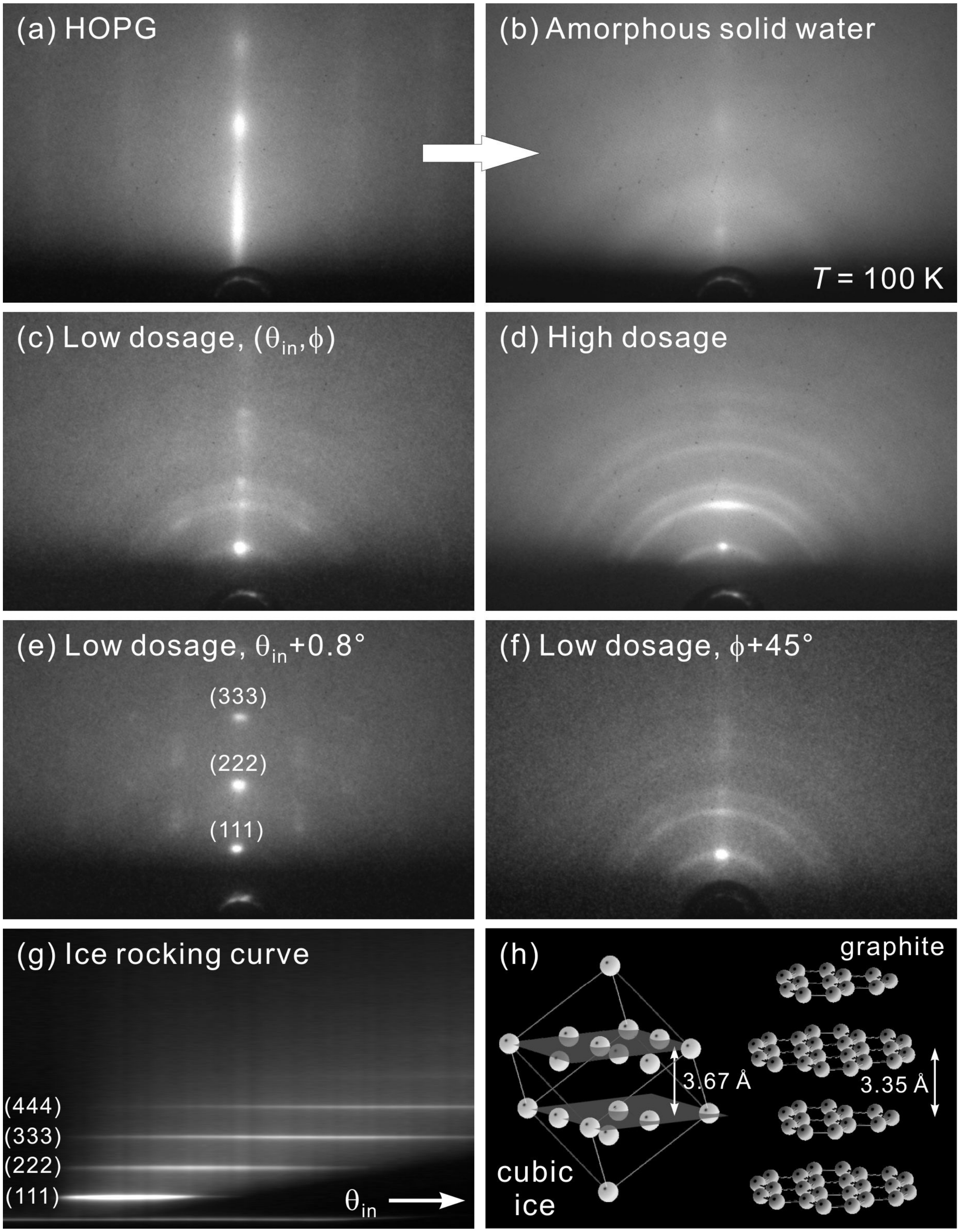

(See next page for the figure caption.)

Fig. 1. Diffraction patterns of ice on hydrophobic graphite at various conditions. (a) Diffraction pattern of a freshly cleaved HOPG surface. The grazing incidence and nanometer depth of electron probing give rise to the rod-like pattern. (b) Diffraction pattern at the same probing condition as panel a after the deposition of water molecules at a surface temperature of $T = 100$ K. The diffuse scattering without distinct diffraction features indicates that the water assembly is in an amorphous state. (c) Diffraction pattern from a thin interfacial water layer after its crystallization into an ice assembly through thermal annealing. The most distinct diffraction feature is the intense Bragg spot at the center, signifying an ordered structure along the surface normal direction. (d) The pattern from a thicker ice assembly at the same probing condition as panel c. While the central Bragg spot is still apparent, a Debye–Scherrer ring pattern becomes clearly evident, indicating that the ice crystallites away from the substrate surface are randomly oriented. (e) The pattern from a thin ice assembly at a larger incidence angle (θ_{in}+0.8°). Higher orders of the original (111) Bragg spot are now apparent. (f) The pattern from a thin ice assembly at a different azimuthal angle (ϕ+45°) by rotating the substrate. From such an azimuthal search, the lack of other spots except for the original central one reflects the lack of a horizontal orientation order in the ice structure. (g) Rocking curve for a thin ice assembly obtained by collecting the central rod area of diffraction patterns as a function of θ_{in}. The equally spaced streaks are indicative of ordered vertical stacking of ice bilayers. (h) Structures of cubic ice (hydrogen atoms are omitted) and graphite.

120-fs near-infrared pulses (800 nm) to induce the substrate temperature (*T*) jump; at this wavelength and adsorbate thickness there is no absorption in the ice layers. The electron diffraction patterns were recorded for different delay times between the optical and electron pulses, with a grazing electron incidence angle of $\theta_{in} \sim 0.6°$. The optical excitation fluence used was up to 39 mJ/cm^2 at the peak. The scheme of pulse front tilting (*14-17*), which enables femtosecond resolution, was not employed because, in the case discussed here, the doser system for water deposition was connected on top of the chamber and the temporal resolution (capable of detecting 2-ps change; 7 ps in total) was sufficient for the dynamics. The ice–substrate composite was fully recovered in less than 1 ms without noticeable water sublimation, as evidenced by the reproducibility of the diffraction pattern at negative times and for our experimental repetition rate of 1 kHz.

Results and Discussion

In Fig. 1, the diffraction patterns obtained in the absence of the *T*-jump are displayed. The bare substrate shows an intense, intensity-modulated diffraction rod in the center and faint ones on the sides, indicating the regular vertical stacking of graphite sheets and the lack of long-range (micrometer-scale) horizontal orientation (Fig. 1a). With water molecules immobilized on the surface at $T = 100$ K, the graphite pattern becomes weaker and is replaced by diffuse scattering from the initially formed amorphous phase (Fig. 1b); its thickness, depending on dose time, is on the order of 10 nm, which was estimated from the electron penetration depth at 30 keV. Crystallization of the amorphous film begins at ~135 K, which is close to the reported transition temperature (*1, 2*). Completion of crystallization occurs at about 145–150 K, and total sublimation at near 150–160 K, both depending on the film thickness.

The crystallized ice layers show intriguing diffraction patterns. For smaller thickness layers, an intense Bragg spot appears at the middle of the first Debye–Scherrer ring, together with a weak ring pattern that indicates the existence of some randomly oriented ice crystallites (Fig. 1c). Higher orders of this intense Bragg spot can be seen in the rocking curve at larger incidence angles, θ_{in} (Fig. 1, panels e and g). No other spots can be found during the azimuthal rotation (ϕ) of the substrate (Fig. 1f), which reflects the lack of a horizontal orientation order in the ice assembly (Ch. 2). For a thicker layer structure, the diffraction ring pattern intensifies and the aforementioned Bragg spot on the first ring, although less intense, is still apparent (Fig. 1d). These results are in sharp contrast with the many-spot pattern observed from the ordered crystalline ice on a hydrophilic surface (*12*), and with the pure ring pattern observed from the randomly oriented polycrystalline ice on other hydrophobic surfaces, such as hydrogen-terminated silicon (Ch. 10), or when water is away from the surface (*12*).

In order to determine the structure of ice, radial averaging of the diffraction rings was made. The one-dimensional diffraction intensity profile, with its distinct peaks, matches well with the theoretically derived profile of the cubic-ice structure *Ic*, giving a lattice constant of $a = 6.36$ Å; the hexagonal structure *Ih* was excluded because of its different pattern (*12*). The enhancement of rings in diffraction from a thicker adsorbate indicates that the randomly oriented ice *Ic* crystallites are in the upper part of the ice assembly, away from the influence of the substrate. However, near the graphite surface water molecules form an ordered structure. A Bragg spot in the center on the (111) ring was observed without other spots on other rings. This uniquely intense spot signifies that the (111) planes of ice are stacked with order in parallel with the substrate planes (001), but without an azimuthal long-range order. In this configuration, for the (111) planes of

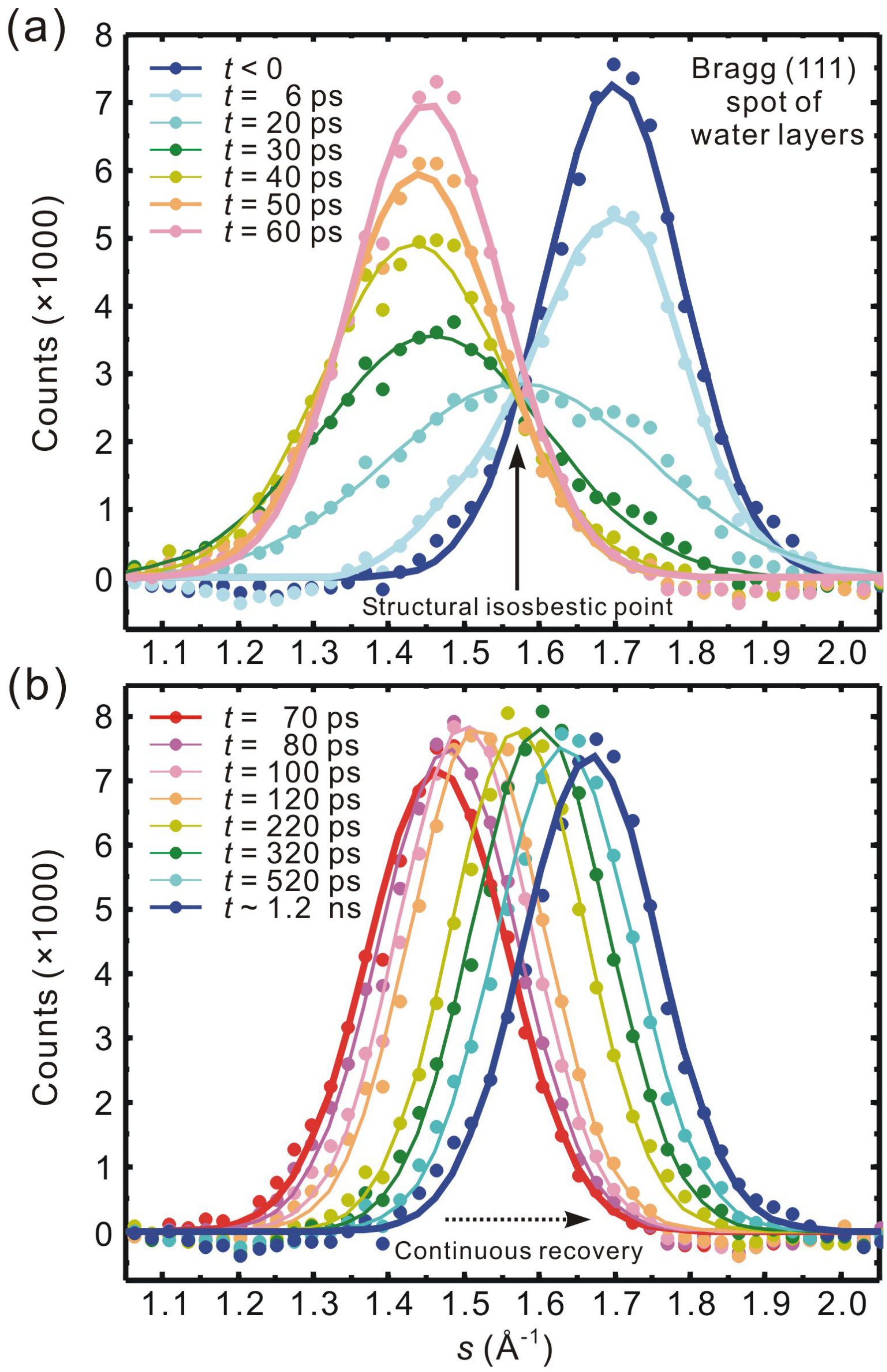

Fig. 2. Diffraction vertical profiles at different times. Shown are the family of curves for the (111) Bragg spot of interfacial ice on graphite, at (a) early times and (b) longer times. The initial peak fluence for graphite *T*-jump is 24 mJ/cm^2. It is noted that the early-time dynamics displays a structural isosbestic point, whereas the longer-time behavior depicts a continuous profile shift toward the initial, ground-state structure.

cubic ice, the out-of-plane O–H bonds are perpendicular to the planes (see below).

Such an ordered conformation is possible because of the structural morphology of graphite. Layered HOPG is known to have a stepped structure and terraces (*18*). Also, the interplanar distance ($a/\sqrt{3}$ = 3.67 Å) between (111) planes of cubic ice and that between the sheets of HOPG (3.35 Å) are comparable within 10% (Fig. 1h). Molecular dynamics simulations have suggested that, even at a higher temperature, water molecules in contact with graphite tend to project some hydrogen atoms toward the surface (*19, 20*), a preference that is compatible with the stacking of (111) planes of ice *Ic*. Therefore, the HOPG substrate becomes a confinement template for structural ordering of the interfacial assembly, even though water–graphite interactions are somewhat weaker than those of water–water in the network. Random orientation of ice crystallites resumes when such influence is attenuated at a distance away from the substrate.

For studies of ice dynamics, we focus on the (111) Bragg spot under the condition given in Fig. 1c, at low dosage and small θ_{in} of 0.6°; under such conditions, the (111) specular diffraction is the most prominent. It was found that the spot exhibits a large vertical-only movement with unique intensity change as a function of time. In Fig. 2, vertical profiles of the diffraction spot at different delay times t are displayed. Initially, the diffraction spot is located at $s = 1.71$ Å^{-1}, where the momentum transfer value $s = (4\pi/\lambda)\sin(\theta/2)$, the de Broglie wavelength $\lambda = 0.07$ Å at 30 keV, and θ is the total scattering angle. Immediately after the substrate is heated, the (111) Bragg spot intensity decreases, followed by a profile transformation to a new position at $s = 1.45$ Å^{-1}. This change in s corresponds to an 18% increase in the (111) water bilayer separation. The huge change was unexpected, but equally surprising was the crossing of all curves at the same point (a structural isosbestic point) in the middle with $s = 1.57$ Å^{-1} (Fig. 2a,

$t = 6$ to 50 ps). After the transformation, the diffraction intensity recovers and the peak position continuously shifts (not through the isosbestic point) toward the original equilibrium value (Fig. 2b). The clear difference in the evolution of the diffraction curves at early and later times is easy to discern.

The appearance of a structural isosbestic point at early times signifies that the initial conversion involves two distinct states, the untransformed ground-state ice structure and a transformed, expanded one. In spectroscopic studies, the appearance of an isosbestic point in the spectra as evidence for interconverting chemical or structural species has been called into question (*21, 22*). However, the main problem there is the presence of inhomogeneous broadenings. In diffraction, the well-defined Bragg spots can only originate from a long-range ordered (homogeneous) structure. Moreover, the clear shift of the diffraction peak during the early-time dynamics, with the existence of only one isosbestic point and no overlap in the wings, is in sharp contrast with the results given in Ref. 21. In fact, the well-separated peaks before time zero and after 50 ps demarcate the two distinct structures involved, each with a well-defined diffraction peak width. Moreover, as suggested in Ref. 21, the confirmation of a true chemical or structural conversion must come from time-dependent measurements, as reported here using diffraction.

Therefore, it was legitimate to fit the early-time diffraction profile to two Gaussian peaks centered at $s = 1.71$ Å^{-1} and 1.45 Å^{-1}, with variable intensities but having a width similar to the ground-state value of ~0.20 Å^{-1}. The width of a diffraction peak is determined by the size of the electron beam (a constant value), the broadening effect described by the Scherrer formula due to the finite size of ordered structure (Eq. 23 of Ch. 2), and electron refraction due to the shape of the crystallites (see Chs. 2 and 5).

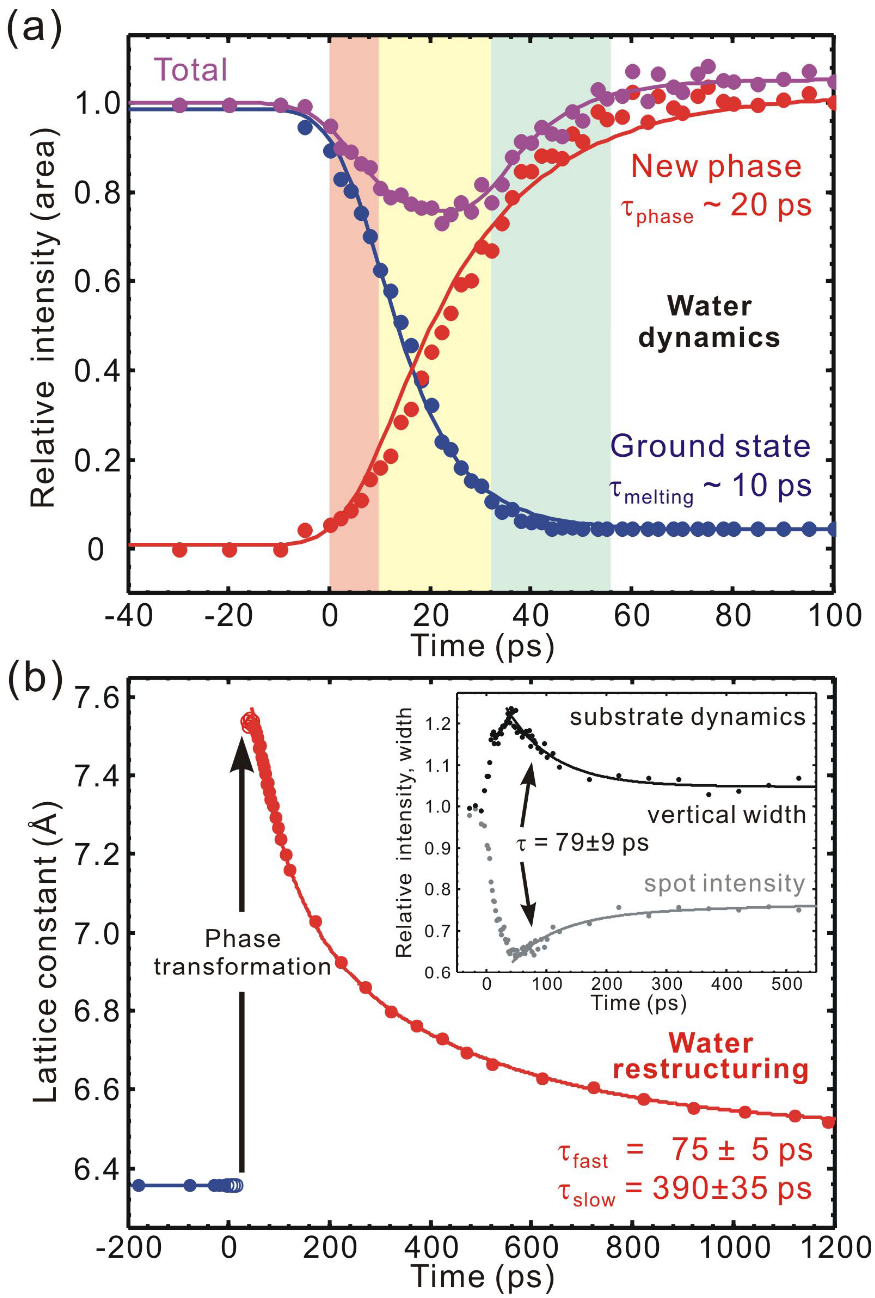

Fig. 3. Evolution of the collective phase and its restructuring to the ground state. (a) Depletion of the ground-state ice structure and growth of the new phase, together with the sum of their proportions. Three sequential stages are noted for the dynamics, from left to right in different colors: ultrafast melting, nonequilibrium phase transformation, and structural annealing. (b) Restructuring of the expanded lattice at longer times. Inset: Temporal evolution of the intensity and width of the (004) spot of graphite.

During a nonequilibrium phase transformation, the latter two factors, in principle, do not change significantly, leading the width for each Gaussian profile to remain similar to that of the ground-state. The temporal evolution of the intensity of each component and their sum, relative to the unperturbed value at negative times, is shown in Fig. 3a. It follows from the plot that the ground-state structure disappears with a time constant of $\tau_{\text{melting}} \sim 10$ ps, and the new phase grows with a time constant of $\tau_{\text{phase}} \sim 20$ ps. The total intensity, as described earlier, shows a relatively small decrease following time zero, but maintains a constant value, which is supportive evidence for structural phase transformation; the initial and final states of the conversion have the same electron diffraction cross section as both contain oxygen and hydrogen.

Unlike the structural phase transition observed in charge-induced correlated solids (Ch. 7), the behavior in the present case of the ice–graphite composite is the result of collective structural expansion and across-interface energy transfer. The lattice of graphite has been shown to undergo an interlayer contraction followed by a large expansion with a time constant of ~7 ps (*15*). The "old-structure" disappearance time τ_{melting} for ice given here matches well with the convolution of the 7-ps time for graphite with the instrumental response, indicating that the breakage of the original assembly conformation is due to the vibrational coupling of ice with underlying graphite. It is noted that, after time zero, the energy deposited induces large-amplitude motion which results in diffraction intensity to decrease by ~20% (Fig. 3a, purple). We estimate a vertical vibrational amplitude of $\langle \delta u_z^2 \rangle^{1/2} \sim 0.28$ Å for oxygen atoms, using the Debye–Waller factor (Eq. 16 of Ch. 2).

In order to accommodate such a large structural perturbation and the undulating substrate, the stack of (111) water bilayers expands collectively, similar to a phase

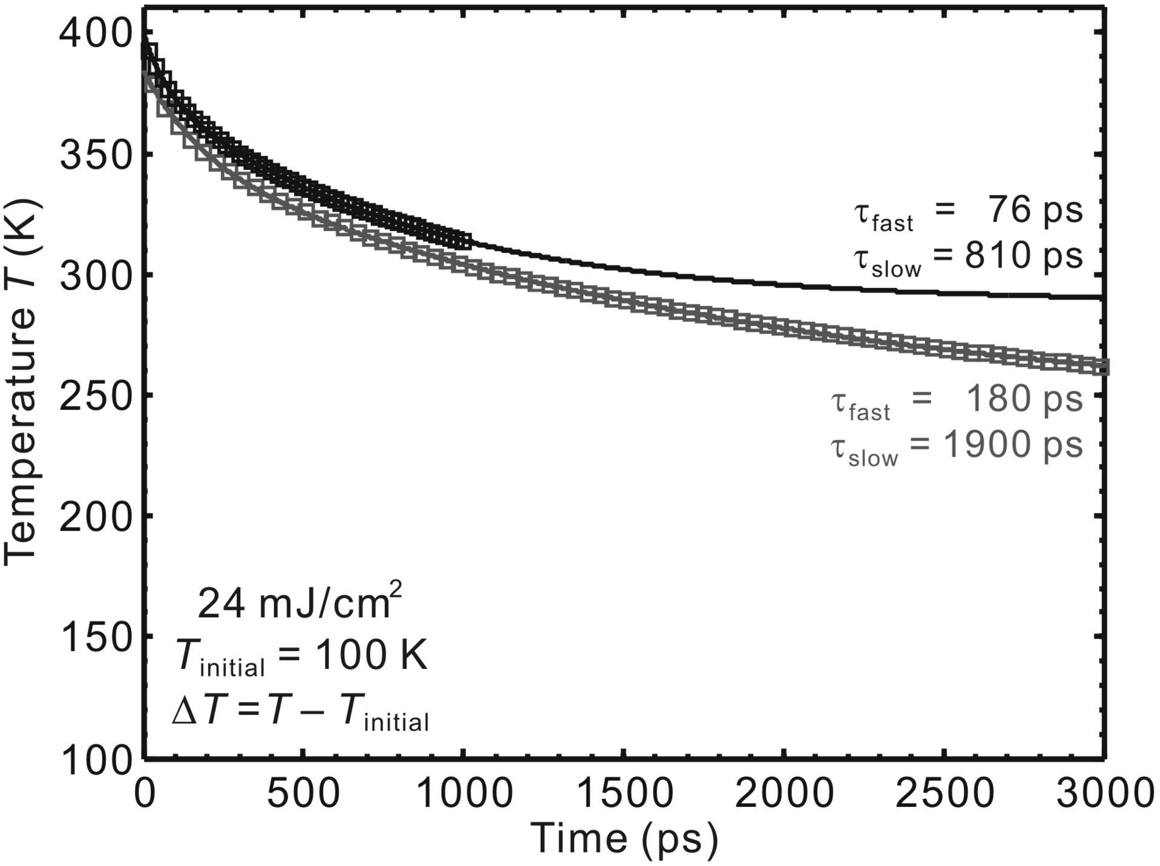

Fig. 4. One-dimensional heat diffusion in the substrate (graphite). Shown is the temperature change as a function of time considering two temporal ranges, up to 1 ns and 3 ns. The following values were used in the simulation: the full fluence of 24 mJ/cm^2, reflectivity of ~30%, heat capacity of 1.33 J g^{-1} K^{-1} at the substrate initial temperature of 100 K (*37*), density of 2.266 g/cm^3, thermal conductivity of 0.157 W cm^{-1} K^{-1} at 100 K (*37*), and penetration depth of 187 nm at the excitation wavelength of 800 nm (*38*). We note that the derived time constants are affected by the time range but the profiles are robust; see Text for discussion of the asymptotic value. The top trace is shifted by 10 K for clarity.

transformation, with a rise time τ_{phase}. It is noted that connectivity in the network of hydrogen bonds prevents the sublimation of ice, even though the large expansion motion (*23*) seems to exceed the equilibrium Lindemann limit for thermal melting, i.e., when the root-mean-square amplitude of thermal vibration exceeds ~10% of the nearest-neighbor distance. With time, the amplitude buildup of the substrate atomic motions comes to an end, and this is reached when a plateau in the intensity and vertical width is experimentally realized (Fig. 3b, inset; see also Ch. 2).

When this state of mature phase formation is reached, the transformed ice structure behaves collectively and begins its recovery as a unit. At these time scales, the diffraction curves can be fitted to a single Gaussian profile. From the observed shifts at different times, we obtained the lattice constants given in Fig. 3b. The expanded ice lattice is seen to restructure continually to the ground-state structure with two apparent time constants, $\tau_{\text{fast}} = 75\pm5$ ps and $\tau_{\text{slow}} = 390\pm35$ ps. In Fig. 4, we present calculations of the temperature versus time using the one-dimensional heat diffusion equation (Eq. 2 of Ch. 4), considering the fluence of the laser pulse and the initial temperature of graphite (100 K). The temporal behavior exhibits apparent biexponential decay, but the time constants extracted depend on the range of time delay during which the data are obtained; our time range is 1.2 ns and from the simulation, τ_{fast} and τ_{slow} become 76 and 810 ps, respectively. It is interesting to note that such a simple diffusion model reproduces the featured two exponentials, and that the fast component observed in ice matches that of graphite ($\tau_{\text{fast}} = 79\pm9$ ps in Fig. 3b, inset). Also, the asymptotic temperature at long times in Fig. 4 mirrors the behavior in graphite (Fig. 3b, inset) but for ice, the restructuring is close to 85% complete in 1.2 ns (Fig. 3b). These findings suggest that restructuring of ice is determined by heat dissipation in the substrate and that the exchange of energy

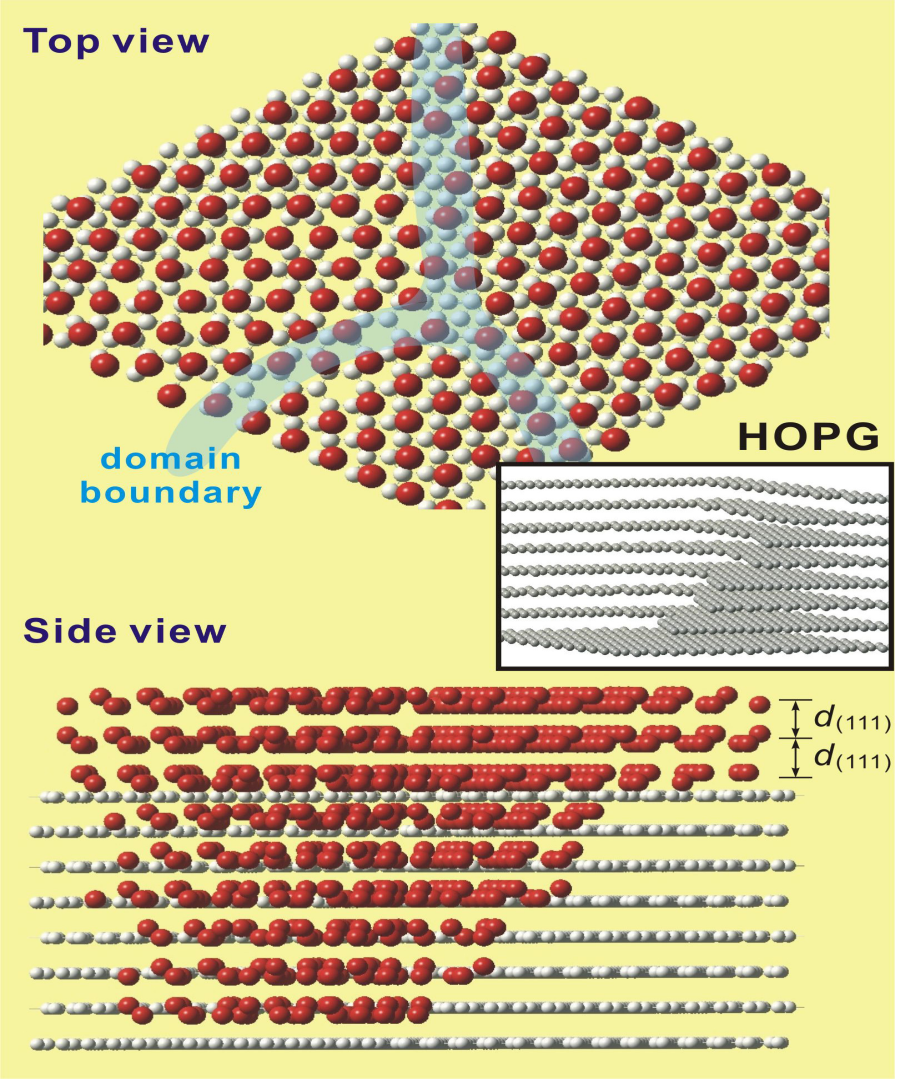

Fig. 5. Schematic representation of the structure for the water layers on hydrophobic graphite (HOPG). Oxygen atoms are in red, carbon in light grey, and hydrogen atoms are omitted for clarity. (Upper) Top view revealing the hexagonal arrangement of oxygen atoms in the (111) planes of cubic ice. Domains with different azimuthal orientations are depicted. (Lower) Side view showing the water bilayers stacked along the surface normal direction. The steps and terrace of HOPG, and the similarity in distance between water bilayers and graphite layers, lead to the observed vertical order. (Inset) Schematic of layered HOPG with an emphasis on its stepped structure. The many steps depicted in a small region are not drawn to scale.

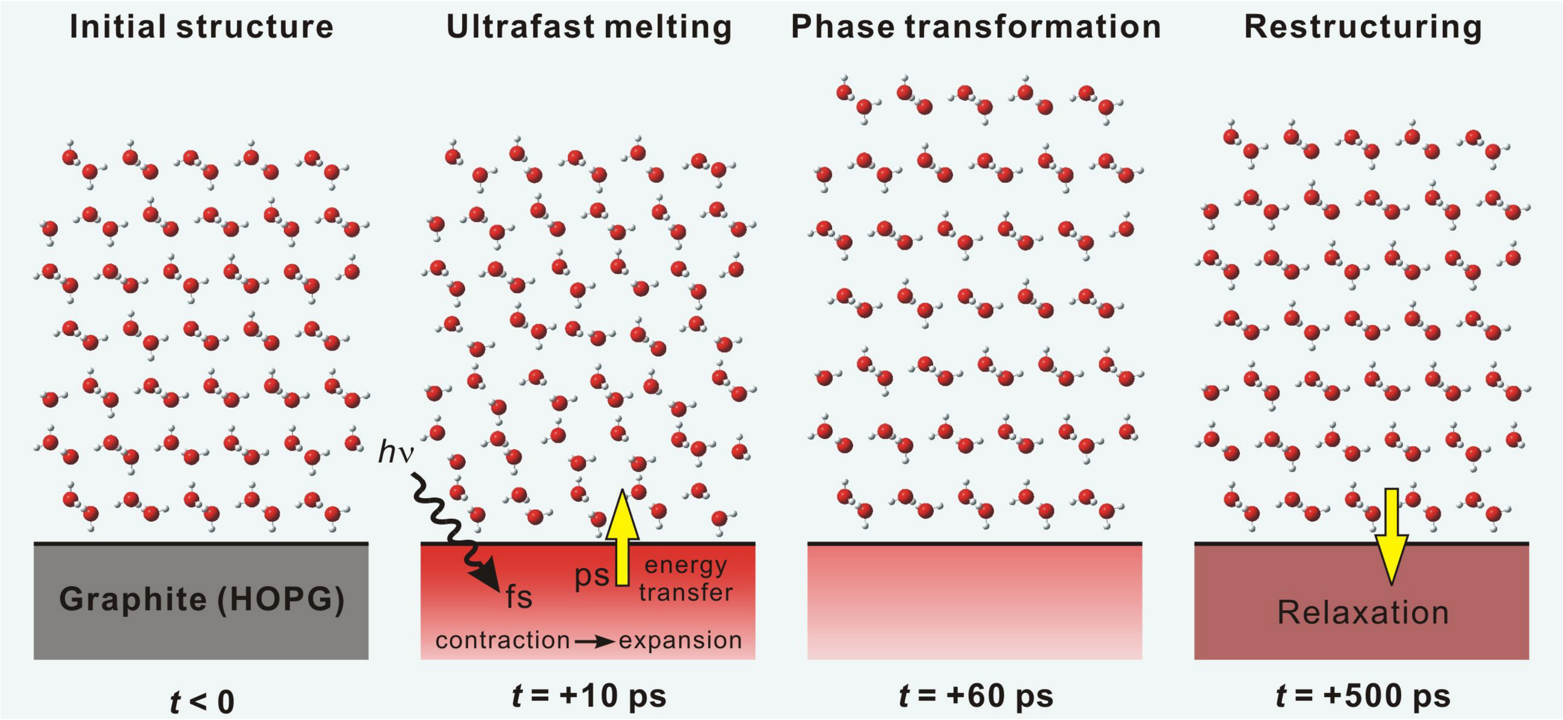

Fig. 6. Schematic representation of the dynamics for the ice layers on graphite. (Middle left) After the ultrafast heating initiated by an infrared light pulse, the substrate undergoes lattice contraction followed by expansion (*15*). The transfer of vibrational energy to the interfacial ice assembly leads to (partial) structural randomization in the first 10 ps. (Middle right) A collective structural motion in ice then takes place, which results in a nonequilibrium phase transformation into an expanded ice structure. (Right) On a longer time, energy transfer from ice to the substrate together with the relaxation of graphite itself establishes equilibration of the composite system; the ice structure subsequently returns to its original state.

between ice and the substrate is ultrafast both ways, i.e., there is no bottleneck in the adsorbate–substrate heating and cooling.

Conclusion

The observations by UEC unravel the unique nature of structure and dynamics of an interfacial water assembly on graphite, a hydrophobic substrate. In comparing the ordered behavior on graphite with the nonordered (long range) behavior on another hydrophobic surface, hydrogen-terminated silicon(111) (Ch. 10), it is concluded that surface morphology plays a direct role in stabilizing the ordered network on graphite, as schematically shown in Fig. 5. For ice on Pt(111), both the surface steps and screw dislocations are critical in the formation of metastable cubic structure (and not the hexagonal one) and in the growth (*24*).

Spectroscopic investigation of interfacial D_2O ice, using sum-frequency generation with longer time resolution, suggested the presence of melted regions, but neither the structure nor the order was possible to observe with atomic-scale resolutions (*25*). Unlike in conventional heating, the lack of sublimation of ice on the time scale reported here is due to ultrafast melting (or softening) in $\tau_{\text{melting}} \sim 10$ ps and restructuring in $\tau_{\text{fast}} = 75$ ps and $\tau_{\text{slow}} = 390$ ps (see Fig. 6), with the cooling being determined by substrate heat diffusion characteristic. These time scales are significantly different from those deduced in figure 3(b) of Ref. 25 for ice on CO/Pt(111) but the picture is valid.

The structural (nonequilibrium) expansion reported here may correlate with the large thermal expansion of confined water when compared with the bulk property reflected in an increased density at the interface (*26*). However, significant hindrance of hydrogen-bond mobility has serious consequences on relaxation in bulk (*27, 28*) and especially at interfaces (*12, 29*). Clearly, studies of hydrophobic/hydrophilic properties at interfaces (*30-32*), and the contrast with bulk properties (*33*), are of interest in many fields, and diffraction methods provide the means for elucidating structures and dynamics at the nanometer scale during phase transformations (*34-36*).

References and Footnote:

1. P. G. Debenedetti, H. E. Stanley, *Phys. Today* **56**, 40 (2003).
2. C. A. Angell, *Science* **319**, 582 (2008).
3. M. Binggeli, C. M. Mate, *Appl. Phys. Lett.* **65**, 415 (1994).
4. M. A. Henderson, *Surf. Sci. Rep.* **46**, 5 (2002).
5. G. E. Brown *et al.*, *Chem. Rev.* **99**, 77 (1999).
6. G. E. Brown, *Science* **294**, 67 (2001).
7. K. Gawrisch *et al.*, *Biophys. J.* **61**, 1213 (1992).
8. G. M. Whitesides, P. W. Snyder, D. T. Moustakas, K. A. Mirica, in *Physical biology: From atoms to medicine,* A. H. Zewail, Ed. (Imperial College Press, London, 2008), pp. 189-215.
9. S. K. Pal, A. H. Zewail, *Chem. Rev.* **104**, 2099 (2004).
10. L. Y. Zhang *et al.*, *Proc. Natl. Acad. Sci. USA* **104**, 18461 (2007).
11. A. H. Zewail, *Annu. Rev. Phys. Chem.* **57**, 65 (2006).
12. C.-Y. Ruan, V. A. Lobastov, F. Vigliotti, S. Chen, A. H. Zewail, *Science* **304**, 80 (2004).
13. X. Zou, S. Hovmöller, *Acta Cryst. A* **64**, 149 (2008).
14. N. Gedik, D.-S. Yang, G. Logvenov, I. Bozovic, A. H. Zewail, *Science* **316**, 425 (2007).

15. F. Carbone, P. Baum, P. Rudolf, A. H. Zewail, *Phys. Rev. Lett.* **100**, 035501 (2008).
16. P. Baum, A. H. Zewail, *Proc. Natl. Acad. Sci. USA* **103**, 16105 (2006).
17. P. Baum, D. S. Yang, A. H. Zewail, *Science* **318**, 788 (2007).
18. G. M. Francis, L. Kuipers, J. R. A. Cleaver, R. E. Palmer, *J. Appl. Phys.* **79**, 2942 (1996).
19. M. C. Gordillo, J. Martí, *J. Chem. Phys.* **117**, 3425 (2002).
20. D. Argyris, N. R. Tummala, A. Striolo, D. R. Cole, *J. Phys. Chem. C* **112**, 13587 (2008).
21. P. L. Geissler, *J. Am. Chem. Soc.* **127**, 14930 (2005).
22. J. D. Smith *et al.*, *Proc. Natl. Acad. Sci. USA* **102**, 14171 (2005).
23. We also measured the ice dynamics at different graphite excitation fluences (11, 24 and 39 mJ/cm^2), and the corresponding lattice expansions of the transient phase are 8.45%, 18.5% and 22.7%, respectively. The absence of a threshold, with a near linear dependence for ice mirrors the linearity found for the graphite substrate (*39*). However, at very high fluences, saturation of vibrational motions in highly excited HOPG would have to be considered (*39*).
24. K. Thürmer, N. C. Bartelt, *Phys. Rev. B* **77**, 195425 (2008).
25. J. Kubota, A. Wada, S. S. Kano, K. Domen, *Chem. Phys. Lett.* **377**, 217 (2003).
26. S. H. Garofalini, T. S. Mahadevan, S. Xu, G. W. Scherer, *Chemphyschem* **9**, 1997 (2008).
27. R. Rey, K. B. Møller, J. T. Hynes, *Chem. Rev.* **104**, 1915 (2004).
28. E. T. J. Nibbering, T. Elsaesser, *Chem. Rev.* **104**, 1887 (2004).
29. M. Schmeisser, H. Iglev, A. Laubereau, *J. Phys. Chem. B* **111**, 11271 (2007).
30. A. P. Willard, D. Chandler, *J. Phys. Chem. B* **112**, 6187 (2008).

31. B. J. Gertner, J. T. Hynes, *Science* **271**, 1563 (1996).
32. P. Ball, *Chem. Rev.* **108**, 74 (2008).
33. A. D. Buckingham, J. E. Del Bene, S. A. C. McDowell, *Chem. Phys. Lett.* **463**, 1 (2008).
34. P. Jenniskens, D. F. Blake, *Science* **265**, 753 (1994).
35. P. Jenniskens, D. F. Blake, *Astrophys. J.* **473**, 1104 (1996).
36. L. Delzeit, D. F. Blake, *J. Geophys. Res.* **106**, 33371 (2001).
37. J. Steinbeck, G. Braunstein, M. S. Dresselhaus, T. Venkatesan, D. C. Jacobson, *J. Appl. Phys.* **58**, 4374 (1985).
38. A. B. Kuzmenko, E. van Heumen, F. Carbone, D. van der Marel, *Phys. Rev. Lett.* **100**, 117401 (2008).
39. R. K. Raman *et al.*, *Phys. Rev. Lett.* **101**, 077401 (2008).

Chapter 10

Structures and Dynamics of Interfacial Water Assembly on a Hydrophobic Silicon Surface

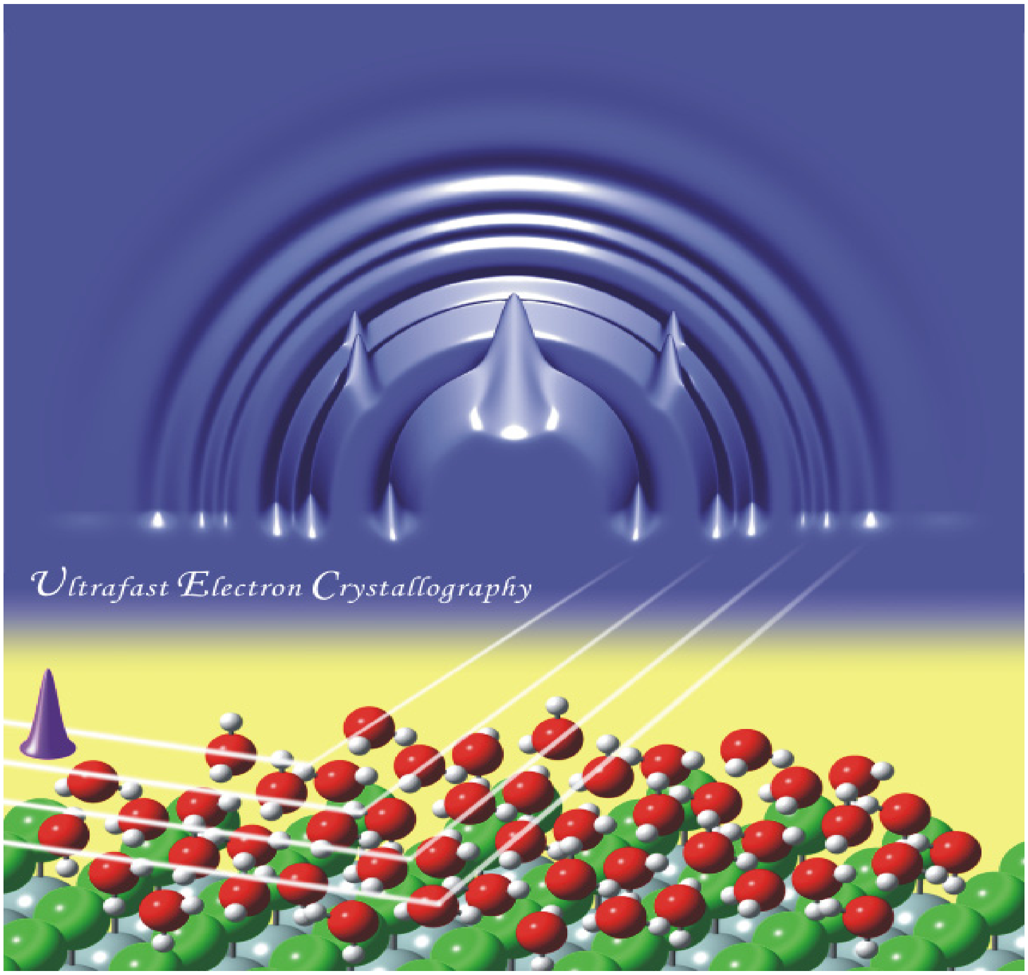

Introduction

The study of water at interfaces on the nanometer scale is of fundamental significance, principally as a result of the ubiquitous nature of hydrophobic and hydrophilic interactions throughout the physical, chemical and biological sciences (*1-3*). The understanding of various important phenomena—such as wetting (*4-6*) and hydration (*7-9*), chemical reactivity (*5, 10, 11*), molecular recognition (*12, 13*), and macromolecular folding (*14*)—eminently relies on the elucidation of the structure and dynamics of interfacial water. However, because of the polar nature of a water molecule, the directional nature of hydrogen bonding, and comparable water–substance interactions, even a further understanding of the structure of interfacial water assemblies presents several challenges (*15*). Moreover, besides the energetics, the time scales of atomic motions and structural dynamics, whether locally or collectively over a long range, are important for defining the microscopic mechanisms of relaxations, the stability and phase transformations between various water structures, and the role of substrate structure and morphology (see Ch. 9).

Structurally, interfacial water may adopt a number of different structures, ranging from amorphous solid water with only a short-range molecular order (*16*), to crystalline polymorphs which exhibit ordering of a longer range with or without the assistance from the neighboring substance. Spectroscopic techniques, such as internal reflection (*17*) and second-harmonic and sum-frequency generation (SFG) spectroscopy (*2, 18, 19*), are capable of capturing signatures of structural and surface molecular changes. For example, static SFG measurements showed the decay length of polar ordering of ice films on a Pt(111) surface to be ~30 monolayers (*20*); transient SFG response from D_2O ice on CO/Pt(111) has indicated the presence of melting and recrystallization without desorption

(*21*). However, these studies provide only indirect information about the overall structure and order of an interfacial water assembly, let alone the resolution of the motions and dynamics at atomic scale.

A recent real-space study of the formation of ice films as many as 30 molecular layers thick under the influence of the Pt(111) surface morphology was performed using scanning tunneling microscopy (*22*). In our laboratory, direct structural determination of interfacial water is achieved through reciprocal-space diffraction of electrons. When exploited in reflection geometry, electron crystallography (*23*) is ideal for surface and interface probings because of the large electron scattering cross section. With the equipment of an ultrashort temporal resolution, the technique of ultrafast electron crystallography (UEC) can provide direct knowledge of both static and transient structures of an interfacial water assembly from the diffraction images recorded, with atomic-scale spatial resolution. As demonstrated in a previous report for water on a hydrophilic substrate (*24*), the structure and dynamics of ordered water layers were found to be different from those of the bulk.

In this chapter, I focus on the properties of interfacial water deposited onto a hydrophobic substrate—the hydrogen-terminated silicon (111) surface—under the ultrahigh vacuum (UHV) condition. Structurally, without a substantial interaction with the underlying substrate (*24*) or the assistance from a morphology template (Ch. 9), the immobilized water molecules are shown to rearrange into randomly oriented crystallites of the cubic ice (*Ic*) form; a detailed structural analysis will be presented. Dynamically, after the ultrafast heating of the silicon substrate by an infrared femtosecond pulse, the interfacial ice crystallites goes through nonequilibrium phase transformation into a highly expanded lattice. This dynamical behavior is evidenced by the appearance of a “structural isosbestic point” in the diffraction profiles, which was also observed in interfacial water assemblies on graphite (Ch. 9). From the time scales involved and fluence dependence of the structural dynamics, a physical picture is reached for the dynamics and interaction between interfacial water and the underlying silicon substrate.

Materials and Experimental Section

The silicon substrate with an atomically flat hydrogen-terminated (111) surface [H/Si(111)] was prepared from a crystalline wafer (*p*-type B-doped, 0.5 mm in thickness, $\rho = 1\text{–}30\ \Omega\cdot\text{cm}$), by first cleaning and oxidizing in a standard RCA–1 solution (*25*) followed by etching in a 40 wt% NH_4F solution for 3 minutes and rinsing in deionized water for a few seconds (*26, 27*). After the surface preparation, the substrate was immediately mounted onto a goniometer in the diffraction chamber for an ultrahigh vacuum environment. In order to achieve the best thermal contact, a sheet of indium was placed underneath the sample and mechanical clips were used to secure it to the sample holder. A calibrated K-type thermocouple was directly attached to the substrate surface, using copper tape and a mechanical clip, for measurement of the sample temperature with an accuracy of ±0.5 K. The entire sample holder was readily cooled and maintained at low temperature by a controlled flow of liquid nitrogen.

At the base temperature of $T \sim 100$ K the H/Si(111) surface was dosed by water (NANOpure, resistivity > 18.0 MΩ·cm), using a capillary doser (connected on top of the diffraction chamber) containing only saturated water vapor of ~20 Torr at room temperature after repeated freeze–pump–thaw cycles; molecules of water were then effused through a micrometer-sized pinhole that was 3 cm above the substrate inside the chamber (*24*). The pressure in the diffraction chamber was in the 10^{-9}-torr range while dosing and at ~10^{-10} torr during the diffraction experiments. By controlling the dose time, different amounts of water were deposited on the substrate surface. Without the initiating T-jump laser pulse, the UEC apparatus can be used to record static (time-averaged) diffraction patterns in the reflection geometry, allowing characterization of the structure of the interfacial water assembly. Such patterns contain diffraction features that correspond to the intersections of the Ewald sphere and the reciprocal lattice defined by the sample (Ch. 2), and are characterized by the momentum transfer coordinate $s = (4\pi/\lambda)\sin(\theta/2)$ where θ is the total angle of scattering.

The time-resolved experiments were carried out after the deposited interfacial water was thermally crystallized (annealed) and then maintained at $T = 100$ K. At the excitation wavelength of 800 nm for substrate temperature jump and at the present adsorbate thickness, there is no absorption in the water layers. The electron beam had a cross section diameter of ~300 μm on the screen, and was directed onto the sample at a grazing incidence angle of typically <1° to probe nanometer-scale interfacial assemblies. No surface charging or deterioration was resulted from the electron bombardment, as evidenced by the steadiness of the unblocked (undiffracted) electron beam and the diffraction pattern that are repeatedly recorded over many hours. The electron diffraction patterns were recorded for different delay times between the optical and electron pulses. The optical excitation fluence used was up to 90 mJ/cm^2 at the peak. Because of the capillary doser above the chamber, the scheme of pulse front tilting that enables femtosecond resolution (*28*) was not employed, but the temporal resolution (capable of detecting 2-ps change; 7 ps in total) was sufficient for the dynamics. The ice–substrate composite was fully recovered in less than 1 ms without noticeable water sublimation, as evidenced by the reproducibility of the diffraction pattern at negative times and for our

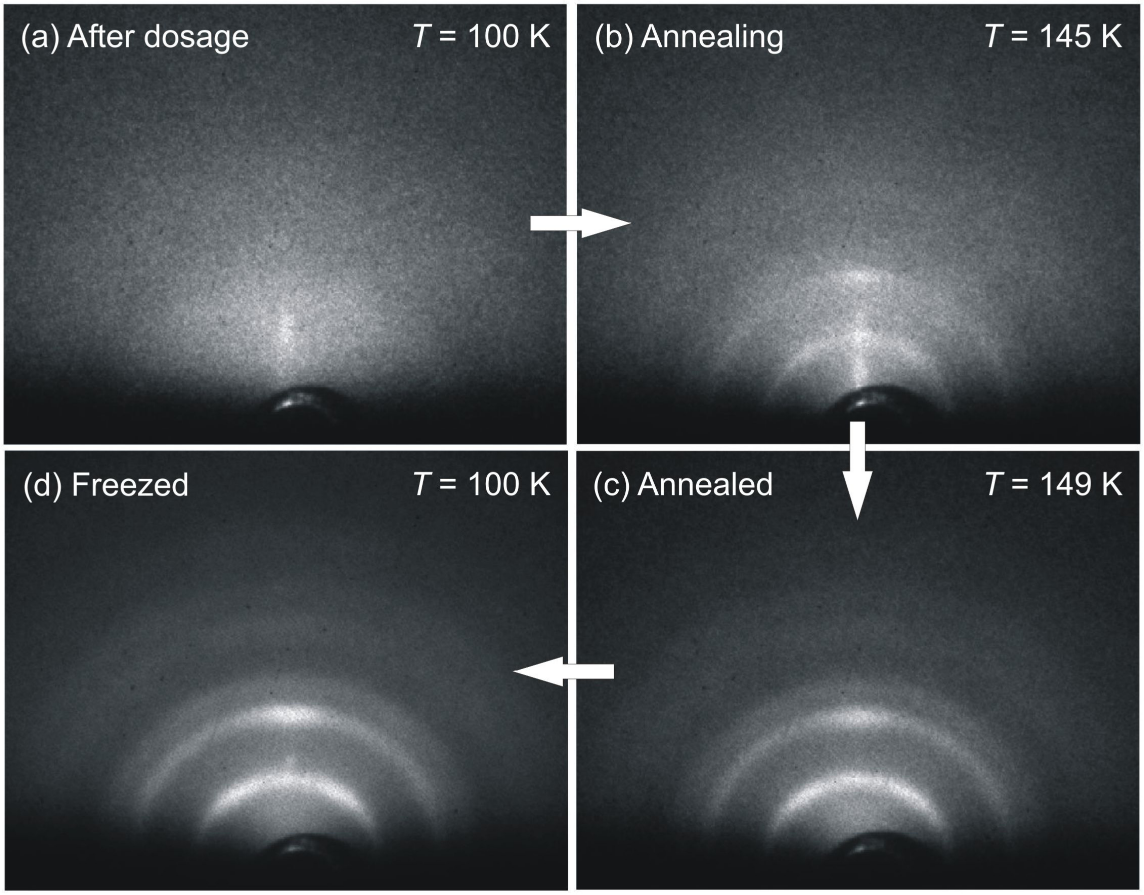

Fig. 1. Diffraction patterns of vapor-deposited water on H/Si(111) at various conditions. (a) Diffraction pattern after the deposition of water molecules at a surface temperature of $T = 100$ K. The diffuse scattering without distinct diffraction features indicates that the water assembly is in an amorphous state. The faint rod-like feature in the center is from the underlying silicon substrate. (b) Diffraction pattern at $T = 145$ K during the process of thermal annealing. Features of Debye–Scherrer diffraction rings appear, indicating the formation of randomly oriented crystallites in the assembly. The rod-like feature in the center is again from silicon. (c) Diffraction pattern at $T = 149$ K after full crystallization of the water assembly into polycrystalline ice. The better diffraction of ice crystallites fully obscures that of the substrate. (d) The pattern of the thermally annealed ice assembly maintained at $T = 100$ K.

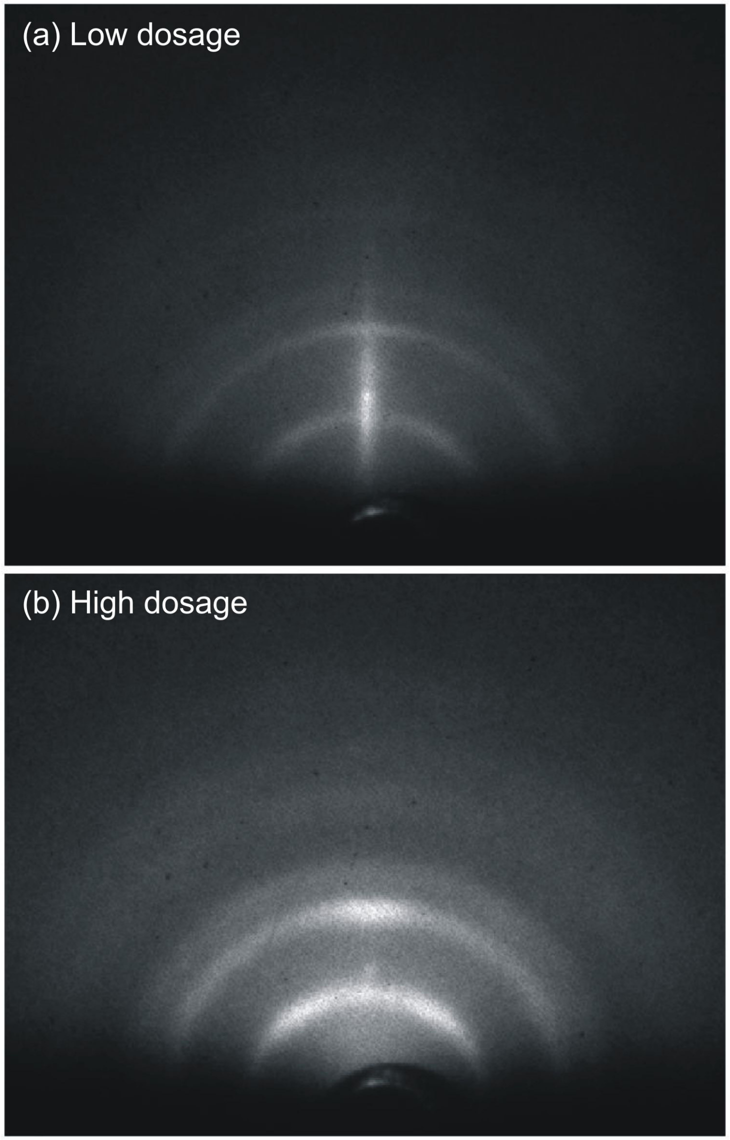

Fig. 2. Diffraction of ice assemblies with different film thickness. (a) The pattern from a thin interfacial ice layer (lower water dosage with a dose time of 10 minutes). The ring intensities are relatively weak, and the thickness of the ice assembly is not enough to block the electron probing of the silicon substrate, which gives the rod-like diffraction feature at a small incidence angle. (b) The pattern from a thick ice layer (higher water dosage with a dose time of 45 minutes). The film thickness is now larger than the penetration depth of 30-keV electrons at this incidence angle, and therefore diffraction of silicon is almost obscured. The increasing prominence of arcs on the first two rings arises from the crystallites with {110} preferred orientation, suggesting their locations above the polycrystalline component (see Text and Figs. 4 and 5).

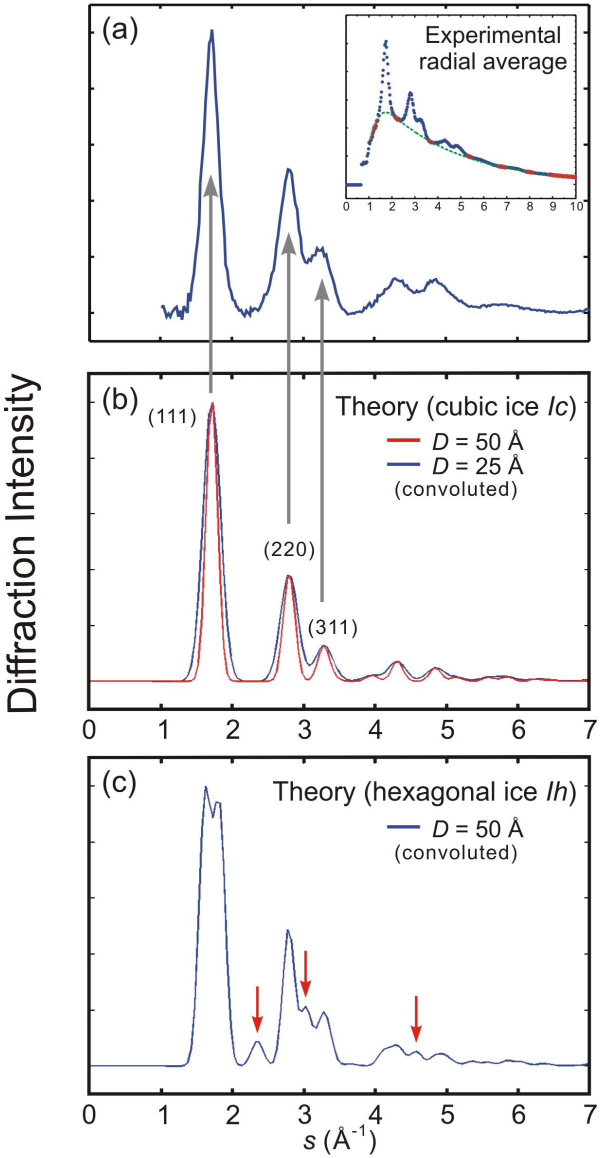

Fig. 3. Radially averaged diffraction profile and calculated patterns for two polycrystalline polymorphs of ice. (a) Shown in the inset is the original radial average of the diffraction pattern obtained (blue dots), which contains a diffuse background that was fitted considering the regions with no peaks (red dots) and subsequently removed (green dashed line). The final result emphasizes the Bragg diffractions arising from the ordered structure of ice. (b) Calculated polycrystalline diffraction patterns for the cubic-ice polymorph, ice *Ic*, with average crystallite sizes of 25 Å (blue) and 50 Å (red); the width contains convolution of the instrumental electron spread. The three most intense diffractions are labeled with the corresponding Miller indices. (c) Calculated polycrystalline diffraction pattern for the hexagonal-ice polymorph, ice *Ih* ($a = 4.506$ Å, $c = 7.346$ Å), with an average crystallite size of 50 Å. Red arrows indicate the diffraction peaks that are missing in the observed pattern illustrated in panel a.

experimental repetition rate of 1 kHz.

Structure of Interfacial Water

A. Diffraction and Structural Determination

After vapor deposition of water onto H/Si(111) at $T \sim 100$ K, the diffraction pattern from the silicon substrate is replaced by diffuse scattering, indicating the absence of structural order in the initially formed amorphous phase of water (Fig. 1a). As T increases at a ramp rate of ~7.5 K/min, new features in the diffraction pattern vaguely appear at $T > 135$ K; at around 145 K, the formation of Debye–Scherrer diffraction rings is observed (Fig. 1b), which become more distinct at $T = 149$ K (Fig. 1c). After lowering the substrate temperature back to 100 K the ring pattern remains prominent (Fig. 1d). Such a pattern change after the annealing process is a clear indication of a phase transition in the interfacial water layers from an amorphous structure, with only short-range order, to a crystalline phase of ice exhibiting longer-range ordering of water molecules. This transformation at low temperature has also been observed previously (*29-31*). It is noted that the ice film thickness, depending on dose time, is on the order of 10 nm estimated from the electron penetration depth at 30 keV (see Fig. 2).

The appearance of Debye–Scherrer rings is characteristic of diffraction from a polycrystalline sample comprising a large number of randomly oriented small crystallites (*32*). Here, the diffraction intensity distribution depends solely on the magnitude of the momentum transfer coordinate s, and therefore we may represent this distribution as a function of s by radially averaging the pattern. A typical intensity curve is plotted in the inset of Fig. 3a, featuring several diffraction peaks superimposed on a decaying diffuse background. This background contains contributions from inelastic scattering and thermal diffuse scattering (*33*), as well as any remaining amorphous water (*29, 34*); toward low *s* values, it also exhibits a sharp decrease that corresponds to the shadow of the sample in the direction of the electron beam propagation (i.e., the shadow edge; see also Fig. 1). In order to subtract the background and hence focus on the diffraction peaks, we select the regions with no Debye–Scherrer ring feature and fit them with the function of an exponential rise (for the shadow edge) times an exponential decay (for the gradual decreasing part) (*35*). The final pattern that emphasizes the elastic scattering contribution from Bragg diffractions of the interfacial ice is shown in Fig. 3a.

It is known that two ice polymorphs are possible at our experimental conditions: ice of the cubic form *Ic* (space group $\mathrm{Fd\overline{3}m}$) (*36*) and that of the common hexagonal form *Ih* (space group $\mathrm{P6_3/mmc}$) (*37, 38*). In Fig. 3, panels b and c, we present the radially averaged diffraction intensity curves calculated for the two polycrystalline polymorphs *Ic* and *Ih*, respectively (*39*). It is evident that the peak positions in our diffraction data are in excellent agreement with those of ice *Ic*, thus confirm the assignment of ice *Ic* to the structure of interfacial ice crystallites formed on H/Si(111) in vacuum; the possibility of formation of ice *Ih* can be confidently excluded by the absence of the characteristic ice *Ih* Bragg reflections at $s = 2.3$, 3.0 and 4.6 Å^{-1} (Fig. 3c). No clear evidence is seen for the formation of hexagonal-like stacking faults, as was observed in other studies of ice *Ic* crystallization (*31, 36*), although we acknowledge that the (111) diffraction peak width may obscure such features.

In a previous study of interfacial water by this laboratory on a *hydrophilic* surface, chlorine-terminated Si(111), the appearance of distinct diffraction spots superimposed upon diffraction rings indicated the formation of an ordered, crystalline ice *Ic* structure as well as a randomly oriented polycrystalline component (*24*). In the present study on a *hydrophobic* substrate, however, no Bragg spots but Debye–Scherrer diffraction rings are observed, signifying that the ice *Ic* crystallites do not adopt a well-defined orientation with respect to the silicon substrate. The lack of orientational order among the ice crystallites originates from two reasons: (i) from the energetics point of view, stronger intermolecular hydrogen bonds and weak water–substrate interfacial interaction make longer-range ordering of crystalline ice unfavorable, and (ii) the atomically flat H/Si(111) surface provides no template structure for guided growth of ice along a certain direction (Ch. 9). As a result of no guiding force, clusters of water molecules form small ice crystallites during the annealing process without extensive crystalline growth.

Given the diffraction peak width of ~0.25 $Å^{-1}$ and the instrumental electron spread of ~0.16 $Å^{-1}$, the diameter of ice crystallites is estimated to be ~30 Å by both diffraction simulation (Fig. 3b) and Scherrer formula (Eq. 23 of Ch. 2). However, this diameter can be as large as 50 Å or more if the amorphous component in the ice assembly (*29*), which effectively increases our diffraction peak widths and consequently leads to an underestimated crystallite diameter, is taken into account. The difference in crystallite size among previous studies and our result is noted (*29, 30, 34, 36, 40, 41*), which stems most likely from the different crystallization conditions employed and also provides a reasonable explanation for the stacking fault features often observed in larger crystallites of ice *Ic* (*34, 36, 42*).

B. Ice Crystallites with Preferred Orientation

A closer look into the intensity distribution along the first two diffraction rings shows that some regions are relatively more intense (Fig. 2b). The broad arcs of additional intensity superimposed upon the circular rings are indicative of certain preferred crystallite orientation, or texture, within the polycrystalline sample (*32*),

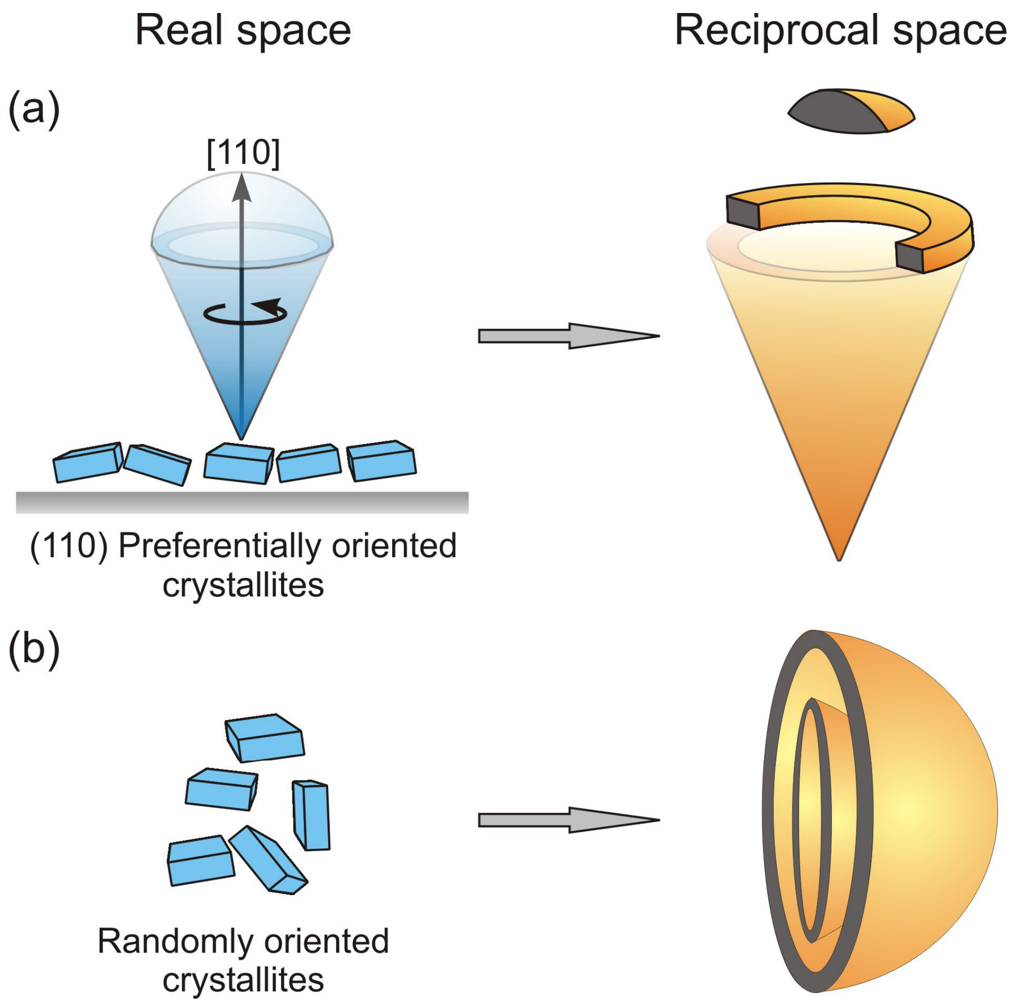

Fig. 4. Illustration of the correlation between crystallite orientation in real space and diffraction in reciprocal space. (a) For crystallites with (110) preferred orientation, their [110] vectors lie roughly perpendicular to the substrate surface with angular deviations that are contained in a spherical cone (left). The angular span of this cone is reflected in reciprocal space, showing a cylindrical symmetry in the resulting intensity distribution (right). The dark gray regions indicate the intersections with the Ewald sphere that give rise to the broad arc features in the diffraction pattern. (b) All orientations are populated for randomly oriented crystallites, assuming that a sufficient number of crystallites are probed (left). The corresponding reciprocal space contains a set of concentric spherical shells (right), giving rise to the Debye–Scherrer rings in diffraction (dark gray regions).

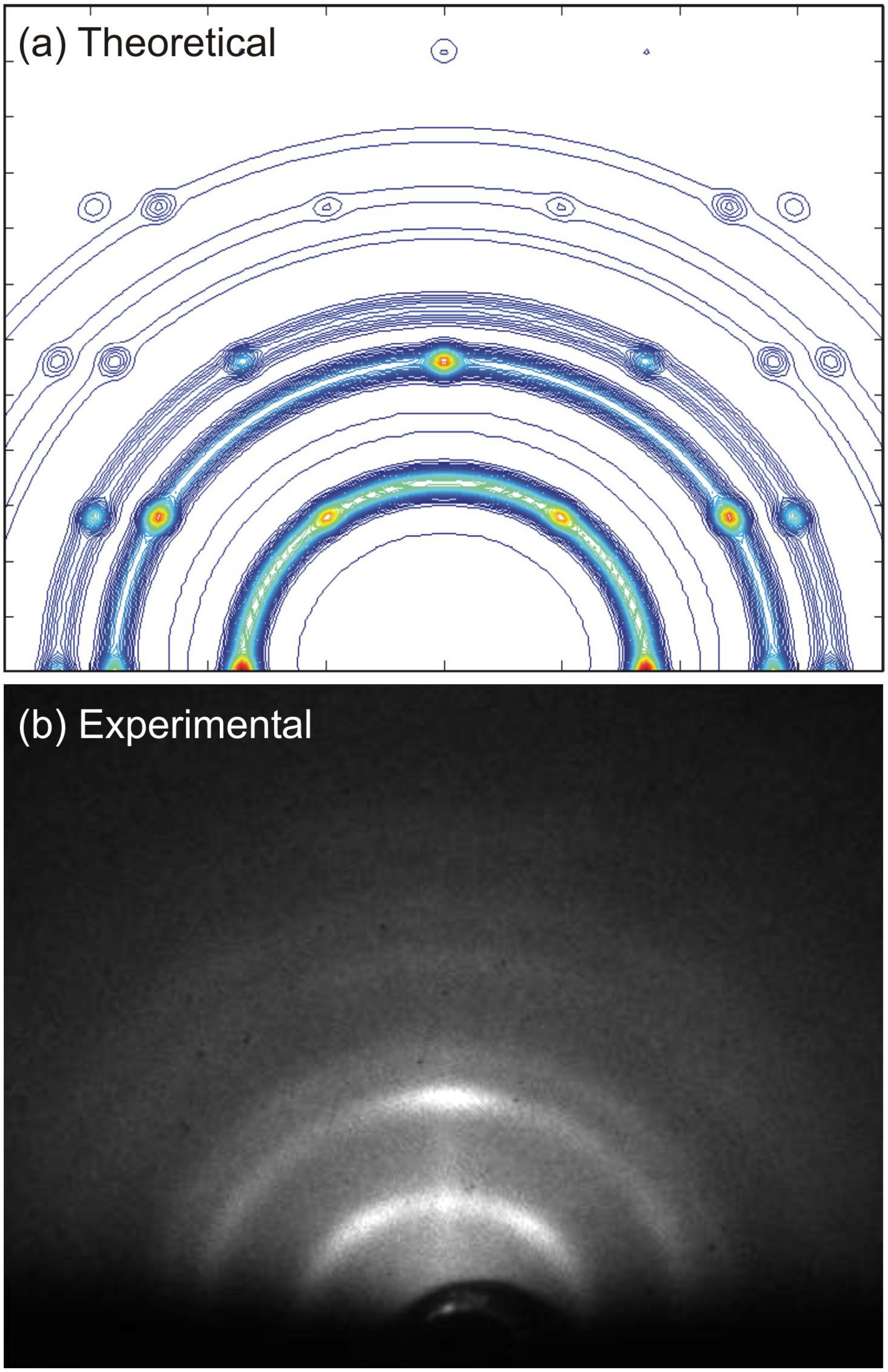

Fig. 5. Comparison of (a) theoretical simulation and (b) experimental observation of diffraction from an interfacial ice assembly containing both randomly and preferentially oriented crystallites of ice *Ic*.

namely, a significant number of ice *Ic* crystallites more or less oriented with a specific lattice plane parallel to the substrate surface but with random rotation around an azimuthal axis approximately perpendicular to the substrate. Figure 4 illustrates the correlation between the real-space morphology and the reciprocal-space intersection with the Ewald sphere (diffraction pattern), showing that crystallites with preferred orientation remove the spherical symmetry of the reciprocal space for a randomly oriented polycrystalline sample and result in localized intensity distribution.

From the observation of an apparent intensity increase in the middle region of the (220) ring (Fig. 2b) and simple geometrical argument, it is straightforward to conclude that the preferred orientation is the {110} planes [(110) and five other equivalent sets of planes in the cubic structure] being approximately parallel to the substrate surface. This assignment is further supported by the appearance of two arcs of increased intensity on the (111) ring: the angle between the vectors from the direct beam origin to the center of an arc on the (111) ring and to the middle of the (220) ring is approximately 35°, coinciding with the angles between the (111) [$(11\bar{1})$] and (110) planes in the cubic structure. In Fig. 5a, the simulated pattern for coexisting randomly and preferentially oriented crystallites of ice *Ic* is presented, and the various regions that show an intensity increase match reasonably with the experimental data (Fig. 5b). The fairly extended arc (with a span of ~30°) observed in the middle of the (220) ring indicate that the angular distribution of the preferred [110] axis is within a ~15° cone around the substrate surface normal (Fig. 4a).

Furthermore, it is found that the {110} preferred orientation is more favored by those crystallites near the ice–vacuum interface. It is noted from the experiments that the diffraction feature of intensified arcs is particularly pronounced from a thick ice assembly

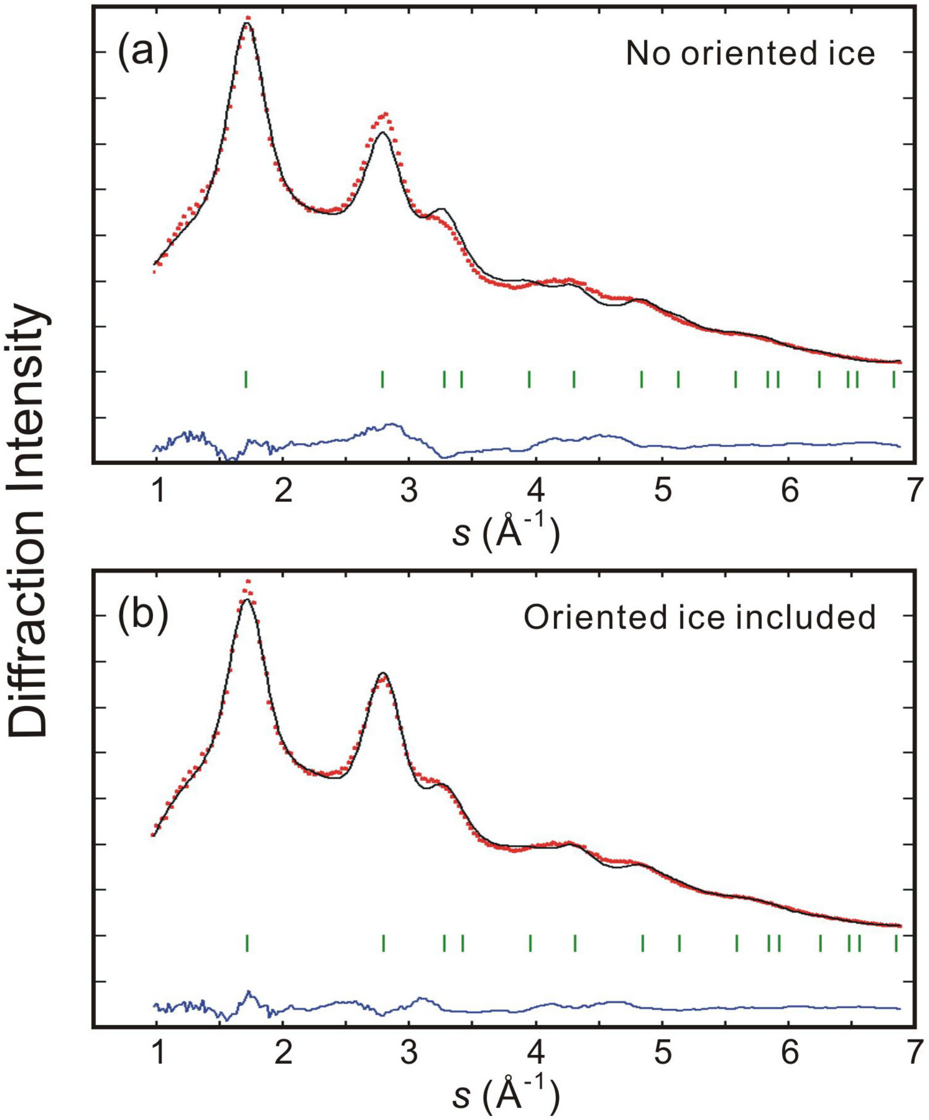

Fig. 6. Comparison of simulated diffraction curve (black line) and radially averaged diffraction profile obtained experimentally (red dots). (a) For an assembly containing only crystallites of random orientation; the refined factor for overall isotropic atomic displacement was $B = 1.24$ Å^2. (b) The Rietveld preferred orientation function is included in the simulation of diffraction pattern. The refined factor for overall isotropic atomic displacement was $B = 1.55$ Å^2, which matches well with the reported value for oxygen (*36*). The blue curve in each panel is the residual difference between the simulation and experiment.

(Fig. 2b), compared with that from a thinner one (Fig. 2a). Such an observation signifies the probing, and hence the presence, of the preferred oriented crystallites from above; they are not located only next to the hydrophobic surface because, with the randomly oriented component covering above, more homogeneous intensity along the diffraction rings would be expected for a thicker ice assembly, given the finite penetration depth of electrons. From the viewpoint of energetics, among all low-indexed crystal planes, the {110} preferred oriented ice is able to have many in-plane hydrogen bonds and leave the fewest dangling O–H bonds pointing directly into vacuum, thus it becomes a more stable structure near the ice–vacuum interface.

The extent of preferred orientation and refined lattice constant are obtained by least-squares analysis, or Rietveld refinement (*43*), of the radially averaged diffraction pattern (*44, 45*). Here, for the consideration of purely random orientation of crystallites, the relative Bragg peak intensities were fixed, being calculated from the known structure of ice *Ic*. However, parameters defining the background, Bragg peak positions and shapes were simultaneously refined to optimize an agreement between the experimental and simulated radial curves (*46*). The result is shown in Fig. 6a, with the weighted-profile *R*-value being $R_{\mathrm{wp}} = 3.6$ % (the Bragg *R*-value being $R_{\mathrm{Bragg}} = 8.2$ %) (*47*); the difference curve indicates rather clear discrepancies between the two patterns, particularly in the intensities of the first two Bragg peaks.

With preferred oriented ice included in the analysis, the experimentally observed pattern can be better modeled using the method of Rietveld (*43*). The Bragg peak intensities $I(hkl)$ are subsequently multiplied by the factor $\kappa + (1-\kappa)\cdot\exp(r\alpha^2)$, where κ is the fraction of polycrystalline component in the sample, r an optimizable quantity related to the diffraction strength of preferred oriented ice, and α the acute angle between the

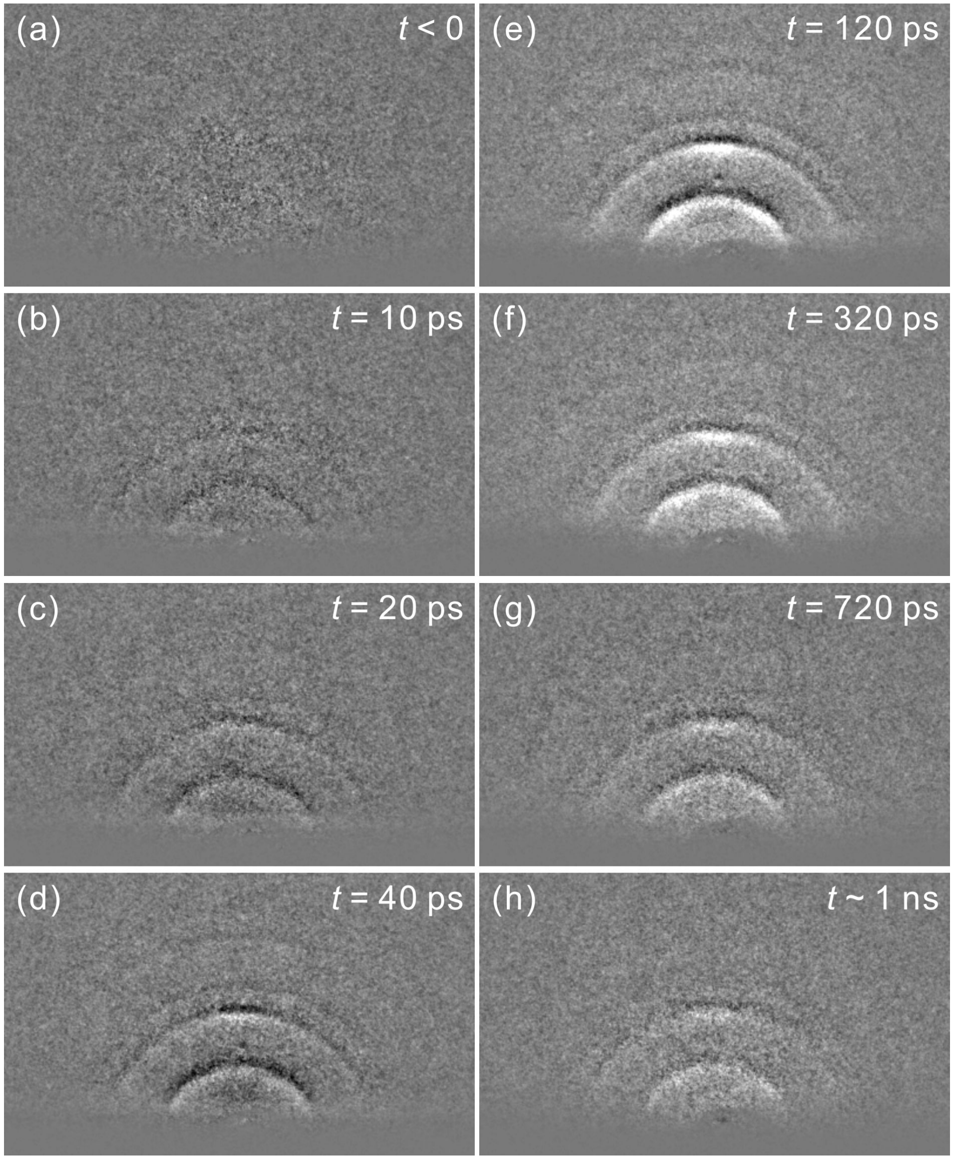

Fig. 7. Diffraction difference images at various delay times. The reference time frame is at $t = -380$ ps. (a) No diffraction difference is detected at negative times. (b–c) Depletion of the intensities of Debye–Scherrer rings is noticed after the substrate T-jump induced by a femtosecond infrared pulse. (d–e) Enhancement of the ring intensities underneath the depletion indicates shifts of the original ring positions toward smaller s values. At $t \sim 100$ ps the diffraction difference reaches its maximum. (f–h) Decay of the diffraction difference means the recovery of diffraction patterns toward the original one, which signifies that the polycrystalline ice assembly is restructuring to the original ground state.

plane (*hkl*) and the plane of preferred orientation. The effect of this procedure is to increase the simulated intensities of those Bragg reflections arising from planes more parallel to the preferred orientation [the (110) plane in the present case] and decrease those arising from planes at a large angle to the plane of preferred orientation. The result in given in Fig. 6b, showing a clear improvement in the level of agreement between the calculated and experimental patterns, with R_{wp} decreasing to 2.1 % (R_{Bragg} to 2.7 %). The refined value of $\kappa = 0.44$ signifies that a slightly greater fraction (56 %) of the ice assembly probed by electrons is roughly {110}-oriented. The value of $r = -2.53$ is consistent with the presence of plate-like crystallites lying parallel to the surface. Lastly, the unit cell parameter determined after least-squares fitting agrees well with the value reported previously [a = 6.35(3) Å versus a = 6.358 Å (*36, 40*)].

Dynamics of Interfacial Water: Results and Analysis

The dynamics of interfacial ice on H/Si(111) was monitored as a function of time following the substrate *T*-jump induced by the infrared laser pulse. The diffraction difference images, obtained by subtracting a reference frame at negative time from patterns at selective delay times, are shown in Fig. 7. The zero of time was consistently determined in two independent experiments to be the onset of intensity change of the specular spot from the silicon substrate. The fact that no diffraction difference was observed at negative times (Fig. 7a), as expected, signifies full recovery of the ice assembly in less than one millisecond given by the repetition rate (1 kHz) of our system. Also, from scan to scan the diffraction images did not exhibit substantial changes, indicating the lack of a major sublimation loss of interfacial water on the time scale of our experiment. Therefore, the long-term stability over many pulses and scans was

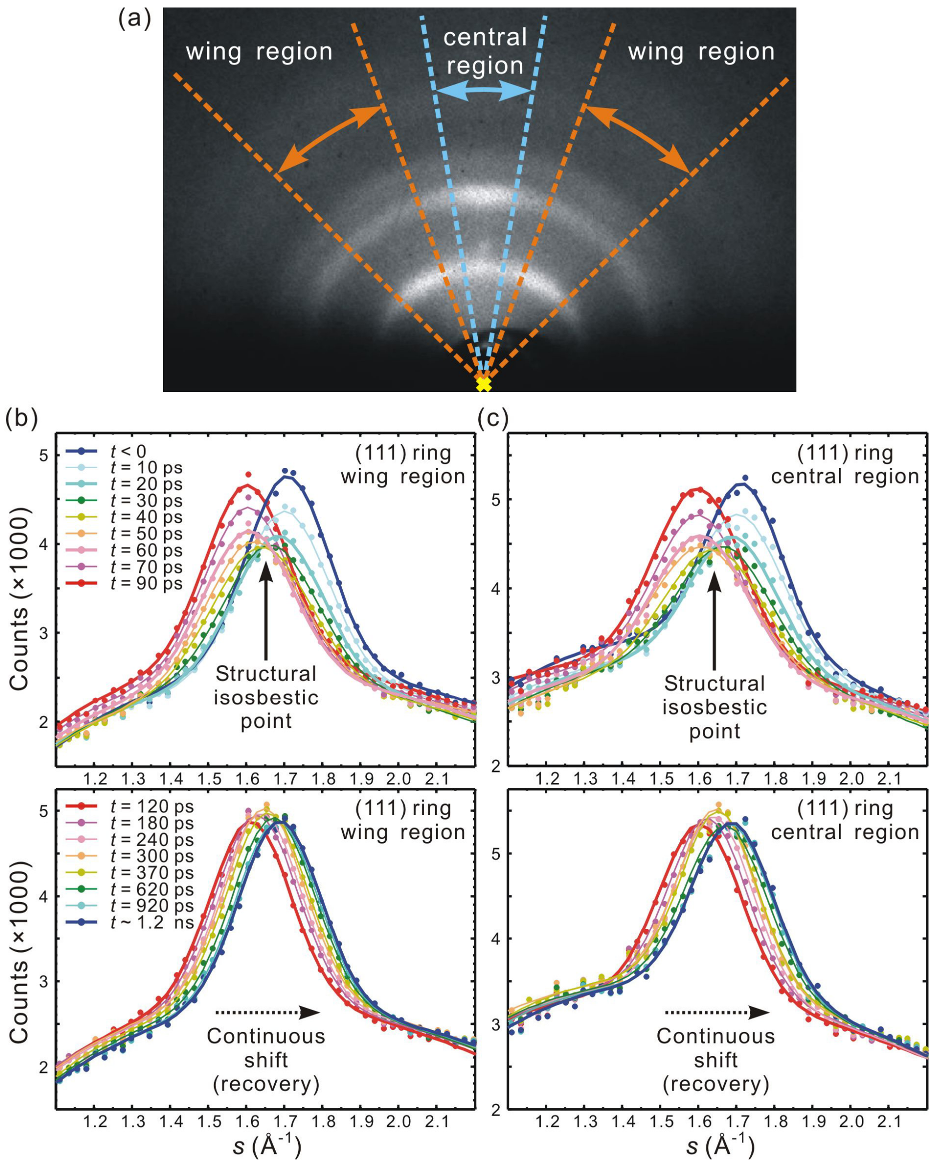

Fig. 8. Analysis of diffraction at different delay times and for different regions. (a) Diffraction pattern with indication of two types of regions considered for radial averaging (with respect to the central axis, ±20° to ±45° for the red regions and –10° to 10° for the blue). The yellow cross marks the origin of Debye–Scherrer rings. (b) The family of curves for the (111) diffraction ring at early times (upper) and longer times (lower), which are obtained by radially averaging the wing regions without any background removal. (c) The family of curves from the central region for early times (upper) and longer times (lower). The same behavior shown in panels b and c indicates the negligible role of crystallite orientation in the dynamics of ice (see Text for the four stages of diffraction change observed). The initial peak fluence for silicon *T*-jump is 77 mJ/cm^2.

maintained even in this volatile system.

Immediately after the heating pulse impinges on the substrate (i.e., the time zero), depletion of the diffraction ring intensities was observed (Fig. 7, panels b and c), indicating that partial depletion of the original structure, whether by larger atomic motions or through ultrafast melting, takes place at this stage. Later, as presented in Fig. 7, panels d and e, the difference patterns show shifts of the original rings toward slightly smaller s values; the diffraction difference is most distinct at $t \sim 100$ ps. Such diffraction ring shifts are clear indication of an expanded structure in ice on this time scale. After the maximum change is reached, the ice assembly restructures, recovering toward the initial structure, as evidenced by less and less diffraction difference at longer times (Fig. 7, panels f to h). After $t = 1$ ns, only a residual amount of change remains (Fig. 7h), which means that the full recovery of the system is likely on the nanosecond time scale.

In order to investigate the dynamics quantitatively, radial averages of the diffraction pattern at each delay time were performed over two different angular ranges (Fig. 8a), to first examine any difference in the structural dynamics between randomly oriented and preferentially oriented ice *Ic* crystallites (*48*). From the comparison between Fig. 8, panels b and c for the (111) ring at an excitation fluence of $F_{max} = 77$ mJ/cm^2 at the peak, it is shown that all ice *Ic* crystallites, with or without the preferred orientation, exhibit the same type of structural evolution with no phenomenological difference in behavior (thus the crystallite orientation effect can be neglected in the following analysis and discussion): (i) for the first 20 ps (Stage I), a decrease in diffraction intensity without a significant profile movement, (ii) from $t = 20$ ps to $t = 60$ ps (Stage II) the observation of a clear profile shift, with all curves crossing at the same point (a “structural isosbestic” point), (iii) from $t = 60$ ps to $t = 120$ ps (Stage III), an increase in diffraction intensity at

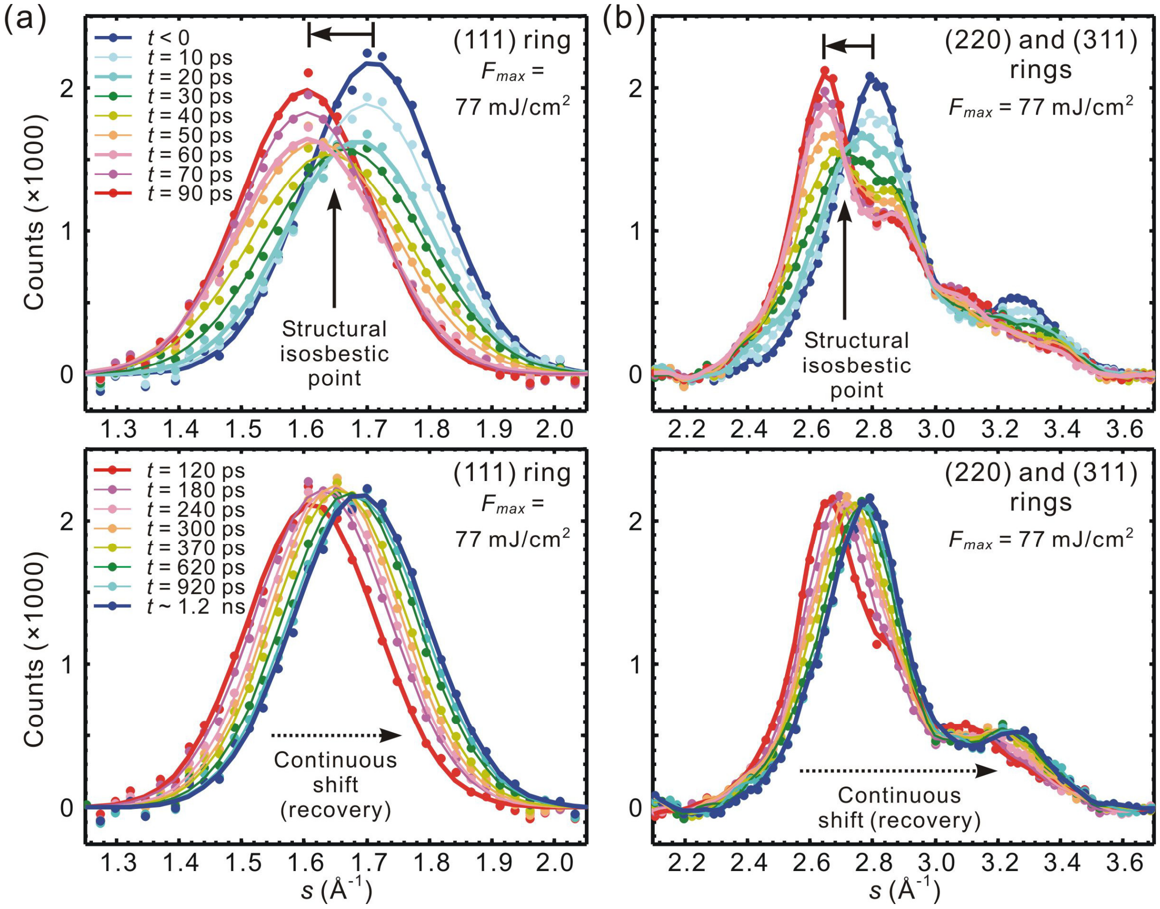

Fig. 9. Diffraction profiles at different times after removal of the diffuse background. Shown are the family of curves for (a) the (111) ring from the wing regions and (b) the (220) and (311) rings from the central region, as indicated in Fig. 8a. At early times, diffraction profiles go through stages of intensity decrease, curve crossing at the same point termed a structural isosbestic point, and intensity recovery (upper panels). At longer times, diffraction profiles move toward their original positions continuously, with their intensities maintained at the same level (lower panels). The initial peak fluence for silicon *T*-jump is 77 mJ/cm^2.

the new peak position, and (iv) at longer times (Stage IV) the continuous shift of the diffraction profile, not through the isosbestic point, toward the original, equilibrium position (see the upper panels in Fig. 8, panels b and c for the first three stages, and the lower panels for the last stage). It should be noted that the distinct difference in the evolution of the diffraction curves at early and later times is easy to discern, even without removal of the diffuse background. Similar discoveries in interfacial ice on another hydrophobic substrate were also observed (Ch. 9). I shall discuss in detail about the observation of a structural isosbestic point in diffraction and its implication of a nonequilibrium phase transformation at transient times in the next section.

Figure 9 shows the curves for the first three diffraction rings at early and later times for $F_{max} = 77$ mJ/cm^2, after removal of the background. (Except for the studies of fluence dependence, the following results and analysis are from the experiment of a thicker assembly at the excitation fluence of $F_{max} = 77$ mJ/cm^2 at the peak.) The structural isosbestic points manifested from $t = 20$ ps to $t = 60$ ps from the (111) and (220) rings and continuous recovery of their peak positions at later times cause immediate attention. In addition, the aforementioned stages of diffraction change for the evolution of the (111) ring are also valid for that of the (220) ring. Such consistency further confirms that our observations result from the structural dynamics of ice *Ic* crystallites. Also, the phenomena reported here are robust for both thinner and thicker interfacial ice films, as observed in repeated experiments.

Furthermore, the extents of the profile shifts reveal that the structural expansion in ice *Ic* crystallites in the present study is isotropic. An isotropic lattice expansion of the cubic structure requires the position change of the (*hkl*) diffraction ring, $\Delta s(hkl) = s_0(hkl) - s(hkl)$, to be scaled with $\sqrt{h^2 + k^2 + l^2}$, because the initial interplanar distance

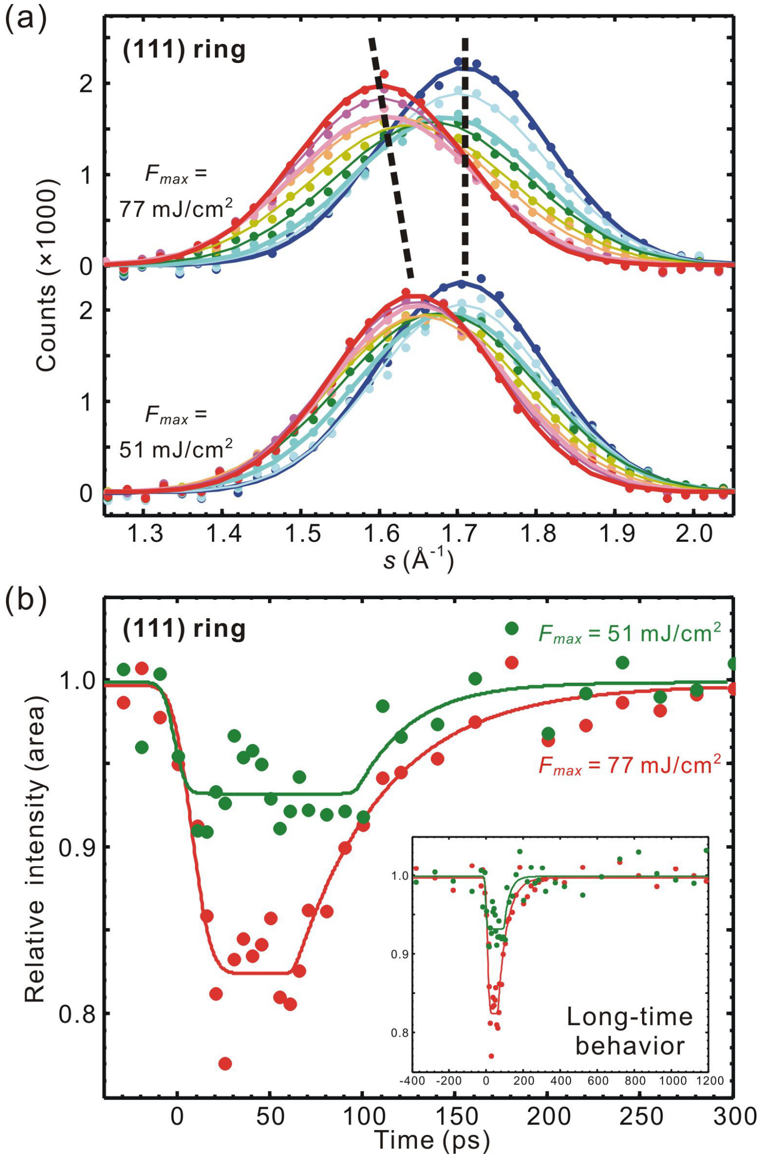

Fig. 10. Early-time evolution of the (111) diffraction at two fluences. (a) Fluence dependence of the curve crossing behavior at a structural isosbestic point. The two dashed lines indicate the original and transformed profile positions. (b) Total intensity under the (111) profile as a function of time. The initial decrease depends on the fluence used, but a common observation is the intensity being at a constant value within a short duration, followed by recovery to the original level and its maintenance at long times (see inset for the long-time behavior).

$d_0(hkl)$ between the (hkl) planes and the lattice constant a_0 satisfy the following relationship, $d_0(hkl) = a_0 / \sqrt{h^2 + k^2 + l^2}$ (the subscript denotes the original value), and the diffraction criterion asks that $s_0(hkl) \cdot d_0(hkl) = s(hkl) \cdot d(hkl) = 2\pi$. That is,

$$\frac{\Delta s(hkl)}{s_0(hkl)} = \frac{d(hkl) - d_0(hkl)}{d(hkl)} = \frac{a - a_0}{a} \tag{1}$$

for a cubic isotropic expansion from a_0 to a. In Fig. 9, upper panels, the (111) and (220) rings are initially located at $s_0(111) = 1.71$ Å^{-1} and $s_0(220) = 2.80$ Å^{-1}, and subsequently transform to the apparent positions of $s(111) = 1.61$ Å^{-1} and $s(220) = 2.64$ Å^{-1}, respectively, at $t = 60$ ps. The fact that the diffraction patterns show the satisfaction of Eq. 1 thus supports our claim.

We also performed the study at different excitation fluences on the substrate surface. As shown in Fig. 10a, the early-time dynamics exhibits the isosbestic point behavior, and the profile shift of the (111) diffraction ring is in proportion to the laser fluence applied. Integration of the intensity under the diffraction profile shows, respectively, an initial total intensity loss, the duration of constant intensity, recovery to the original value and its maintenance for the four stages of change mentioned above, regardless of the different fluences used (Fig. 10b). As discussed in the next section, the intensity depletion signifies the partial destruction or melting at the crystallites' grain boundaries and the later intensity recovery the growth or annealing of crystallites near their boundaries at later times. Moreover, the temporal match of the constant intensity and the isosbestic point behavior gives further evidence for the nonequilibrium phase transformation of ice crystallites induced by the energy transfer from the substrate.

More precise quantification and temporal evolution of the lattice expansion at different fluences require fitting of the diffraction profile. The appearance of a structural

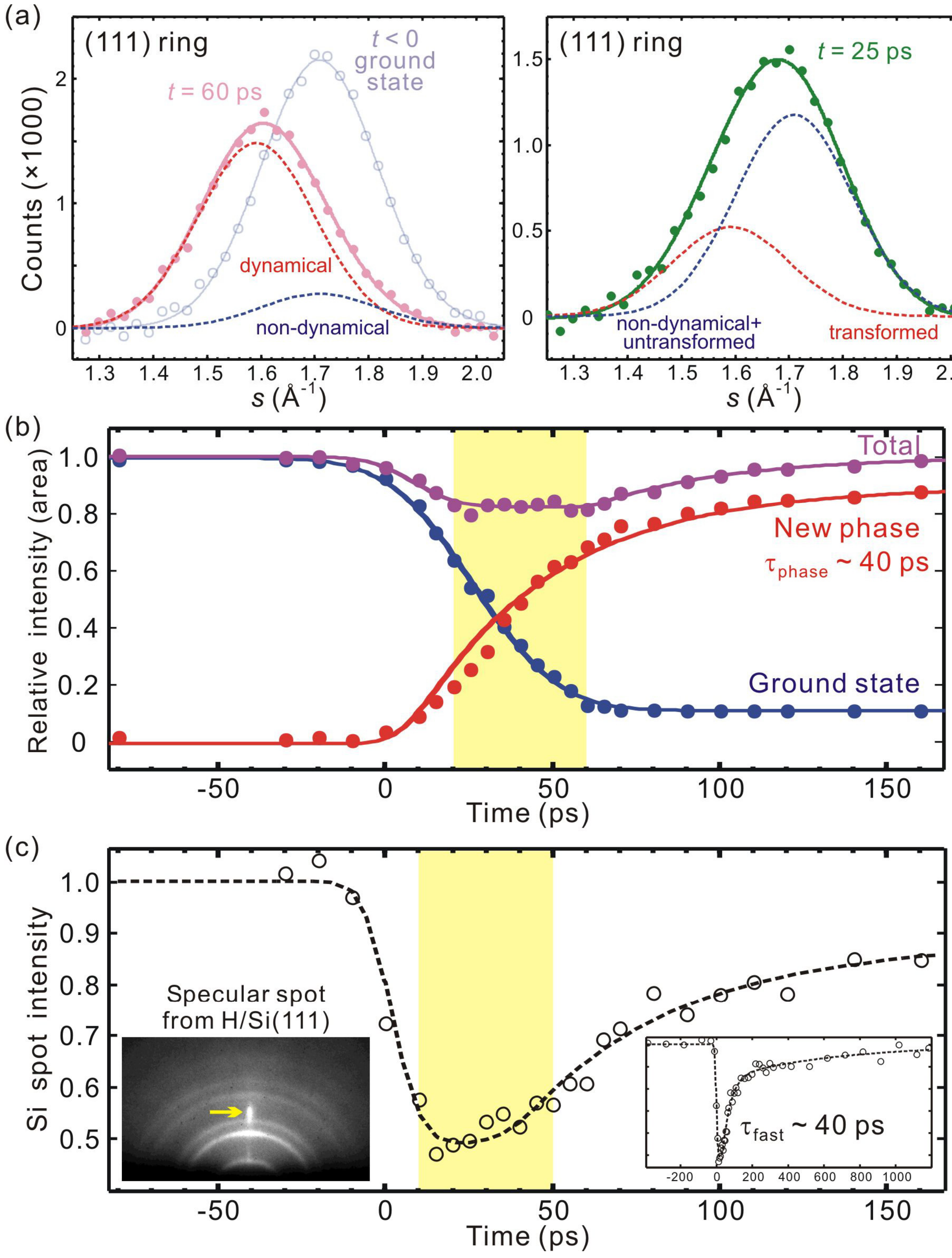

(See next page for the figure caption.)

Fig. 11. Quantitative analysis of the diffractions of interfacial ice and silicon. (a) Fitting of the (111) diffraction profile considering that only two states, the ground state and transformed one, are involved. (Left panel) The light blue circles and pink dots are the data at negative time and at $t = 60$ ps, respectively. A Gaussian profile is fitted to the negative-time data and served as a reference (light blue solid curve). Two Gaussian peaks are used to fit the data at $t = 60$ ps (which is also the end of Stage II), with one being of the same width at the original position but with a variable intensity (blue dashed curve), and the other being of a similar width but having its position and intensity as variables (red dashed curve). The former peak represents the nondynamical portion in the diffraction and the latter the dynamical portion (see Text for details). The final result of the two-Gaussian fit is shown as the pink solid curve. (Right panel) Two-Gaussian fit to the data at $t = 25$ ps (green dots), as an example showing the fitting procedure for all profiles at early times. The blue dashed curve has the same width and position as those of the negative-time profile (light blue solid curve in the right panel) but with a variable intensity, representing the sum of the nondynamical and untransformed portions in the diffraction. The red dashed curve has the same width and position as those of the transformed peak (red dashed curve in the right panel), with its intensity as a variable. The final result is shown as the green solid curve, which nicely accounts for the small asymmetry that appeared in the experimental data at $t = 25$ ps. The agreement between the data and the fit at each delay time has also been checked. (b) Depletion of the ground state of ice structure (blue) and growth of the new phase (red), together with the sum of their proportions (purple). The yellow region indicates the duration of Stage II when the curve crossing behavior at a structural isosbestic point manifests itself. Note that the total intensity also remains constant during this time range. The transformation into the new phase follows approximately a function of exponential rise and has a time constant of $\tau_{\text{phase}} \sim 40$ ps. The slight delayed start in the growth with respect to the depletion of the ground state signifies the structural dynamics of ultrafast melting in the first stage (see Text for details). The small constant level of the ground state after Stage II is due to the nondynamical portion in the diffraction (Fig. 10a, blue dashed curve in the left panel). (c) Intensity evolution of the specular spot from the silicon substrate (pointed by a yellow arrow in the left inset). The yellow region indicates the time range when the specular intensity is at its minimum level. The right inset shows the long-time behavior.

isosbestic point at early times signifies the conversion involving two distinct states, the untransformed ground-state structure and a transformed, expanded one, thus making it legitimate to fit the early-time (111) diffraction profile by two Gaussian peaks at fixed positions, with variable intensities representing the interconverting populations between the two. The ground-state peak is centered at $s_0(111) = 1.71$ Å^{-1} (the negative-time value) and the transformed-state one at a position determined from the two-Gaussian fit using the diffraction profile at $t = 60$ ps, i.e., the end of Stage II (Fig. 11a, left). During Stage I and II, the width for the ground-state peak remains the original value of ~0.25 Å^{-1} determined previously. Also, the transformed-state peak has a width similar to or marginally larger than the ground-state value, because the proper description for the dynamical transformation in this study asks the average size of the expanded ice crystallites to be about that of the original; the width of a diffraction profile is contributed by the size of the electron beam (a constant value), the broadening effect described by the Scherrer formula due to the finite size of ordered structure (presumably a nearly constant effect), and electron refraction due to the shape of the crystallites (a small and nearly constant effect; see Chs. 2 and 5).

Figure 11a shows the results of profile fitting at two different times as examples, and Fig. 11b the relative populations for the ground-state and transformed structures, together with their sum. We find that the peak for the transformed structure is centered at $s = 1.59$ Å^{-1} for $F_{max} = 77$ mJ/cm^2, which corresponds to a 7.6% increase in the lattice constant of ice crystallites, to $a = 6.84$ Å. The existence of a constant, nondynamical portion for all times results from the electron probing of unexcited regions due to the overlap difference between the laser-excited area and the electron beam footprint, thus is subsequently removed from the diffraction profiles in Stage III and IV to eliminate its

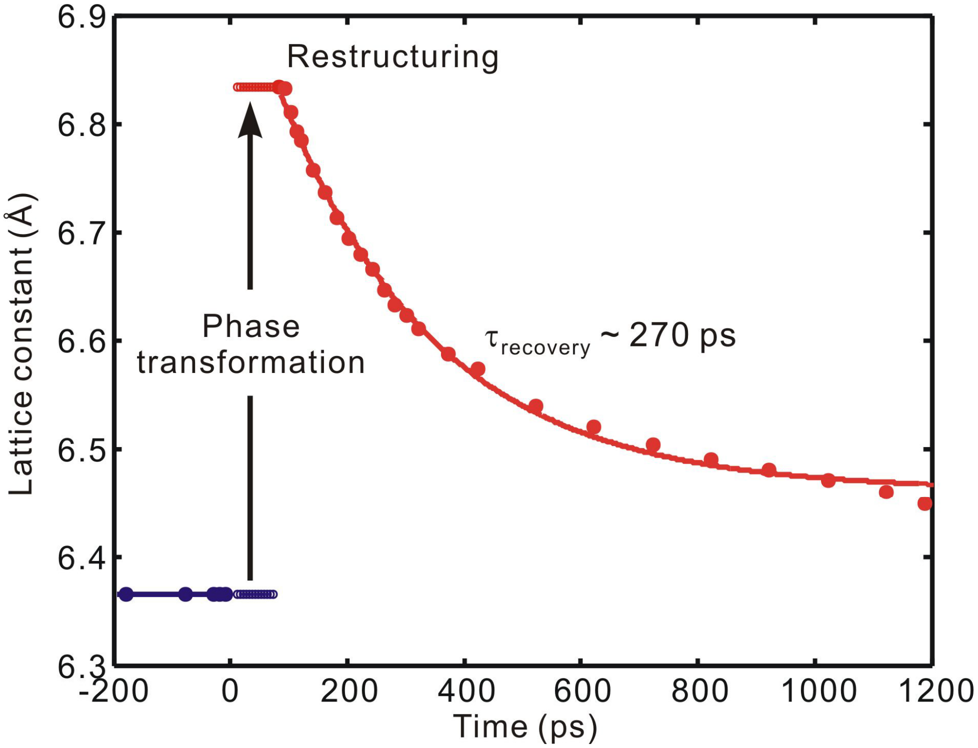

Fig. 12. Restructuring of the expanded lattice at longer times. The continuous recovery of the lattice constant (red dots) to the equilibrium value (blue dots) exhibits an apparent form of single exponential decay, with a time constant of $\tau_{\text{recovery}} \sim 270$ ps. The remaining 20% change at $t = 1.2$ ns takes longer time to diminish.

interference with the recovery of the transformed phase (see the constant residual level of the blue curve after $t = 60$ ps in Fig. 11b). The original structure is found to disappear with a time constant of $\tau_{\text{melting}} \sim 20$ ps, and the new phase grows with a time constant of $\tau_{\text{phase}} \sim 40$ ps. The sum of the two phases reproduces the total intensity evolution show in Fig. 10b. For comparison and later discussion about the energy transfer across the interface that induces the dynamics in ice, intensity of the specular spot from the substrate (seen in an experiment with coverage of interfacial ice, at a larger electron incidence angle) is plotted as a function of time in Fig. 11c.

After the mature structural transformation is reached, the transformed ice

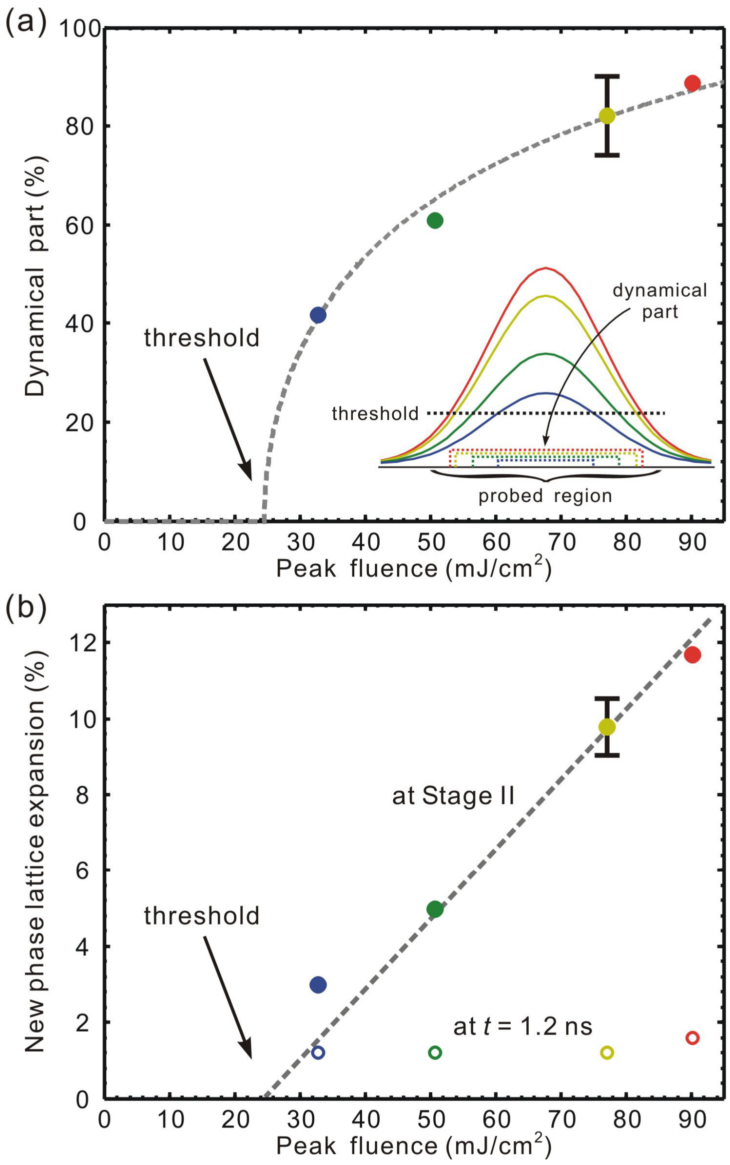

Fig. 13. Fluence dependence of (a) the dynamical portion in the diffraction of ice and (b) the corresponding lattice expansion of the new phase (solid dots); the error bar is also given for each panel. The nonlinearity is noted from the missing of the origin in the trend. By considering an effective threshold for significant two-photon absorption that is able to initiate dynamics of the interfacial ice above (panel a, inset), we can fit the fluence dependence of the dynamical portion with the gray dashed line, where the threshold value is about 25 mJ/cm^2 (see Text for details). A similar threshold is also found in (b). At t = 1.2 ns, the remaining lattice expansion of the transformed part is nearly fluence independent (open circles).

structure behaves collectively and starts its recovery as a unit. Therefore, the diffraction curves in Stage III and IV (after removal of the nondynamical portion mentioned above) can be fitted by a single Gaussian profile. From the observed peak shifts at different times we obtained the lattice constants as given in Fig. 12. The expanded ice *Ic* crystallites are seen to restructure continually to the ground-state structure, with an apparent time constant of $\tau_{\text{recovery}} \sim 270$ ps. This time constant is found to exhibit a slight dependence on the thickness of the ice assembly, varying from the given number for a thicker film to ~200 ps for a thinner one. The restructuring of ice is close to 80% complete in 1.2 ns, and the remaining lattice expansion (~1.5% of the lattice constant) is likely to diminish on the nanosecond scale.

More complete fluence-dependent studies were carried out on another ice assembly to investigate the extent of lattice expansion in the transformed phase. Interestingly, from fitting of the diffraction profile at $t = 60$ ps, it is found that the nondynamical portion varies with the excitation fluence on the substrate, in a nonlinear fashion (Fig. 13a); particularly, for a fluence below 30 mJ/cm^2 at the peak, the nondynamical portion reaches 100% because nearly no diffraction shift was measured. Consistently, a threshold behavior seems to also appear in the fluence dependence of the obtained lattice expansion (Fig. 13b, solid dots). At the highest fluence used, however, the isotropic structural expansion reaches ~12% of the lattice constant, whose atomic movements seem to exceed the equilibrium Lindemann limit for thermal melting, i.e., when the root-mean-square amplitude of thermal vibration exceeds ~10% of the nearest-neighbor distance (*49, 50*). In contrast, the remaining structural expansion of about 1.3~1.7% at $t = 1.2$ ns shows almost no dependence on excitation fluence. As discussed below, these observations reveal crucial information about dynamics of the silicon substrate and the adsorbate of interfacial ice assembly, and the energy transfer between the two.

Discussion

Understanding the dynamics of interfacial ice requires knowledge of that of the underlying substrate because water molecules have no absorption at 800 nm, and dynamical changes are initiated in the substrate. I shall first address the fluence-dependent responses of H/Si(111) upon illumination of an infrared pulse, followed by discussion about the meaning and implication of observing a structural isosbestic point. A complete picture for the dynamics of interfacial water–substrate composite, together with the time scales involved, will be presented afterward.

A. Dynamics of Hydrogen-terminated Silicon

Silicon is a semiconductor with an indirect band gap of $E_g = 1.165$ eV at $T = 100$ K (*51*). Energetically, excitation by one-photon absorption (1PA) at 800 nm ($E = 1.55$ eV) can be achieved in silicon; however, conservation of momentum requires simultaneous generation of phonon(s) in the lattice. As a result, the phonon-assisted, indirect absorption has a very low probability (i.e., a small absorption coefficient, or equivalently, a large penetration depth on the order of tens of μm) when compared with a direct absorption. In contrast, two-photon absorption (2PA) offers an excitation energy ($E = 3.10$ eV) that is close to the direct gap near the Brillouin zone center Γ ($E_0^{'} \sim 3.35$ eV) and along Λ line ($E_1 \sim 3.45$ eV) (*52*). Photoexcitation by 2PA is therefore expected to become more important as the fluence of 800-nm light increases above a certain threshold (*53*).

Previously, the structural dynamics of gallium arsenide, a direct-gap semiconductor, was discussed in a detailed study from this laboratory using UEC (Ch. 4). The important dynamical processes involved include (i) the antibonding character caused by electrons photoexcited into the conduction bands, which leads to the anisotropic lattice expansion, (ii) the cascade of transfer of the above-gap excess energy from photoexcited carriers to optical phonons, which results in the lattice motion and consequently a diffraction intensity decrease, (iii) the subsequent optical-to-acoustic phonon decay, which induces the inhomogeneity in the lattice structure and therefore diffraction width broadening, and (iv) on a longer time, carrier and energy diffusion into the bulk and other processes such as radiative and Auger recombination, which contributes the sub-nanosecond to nanosecond dynamics. These processes can also be used to describe the dynamics of the silicon substrate in this study.

With the optical-phonon energy of 64 meV at Γ (*51*) and the time constant of 240 fs for carrier–phonon scattering in silicon (*53, 54*), each photoexcited electron–hole pair by 1PA can produce up to 6 optical phonons in the lattice in less than 2 ps; each pair by 2PA, however, has much more excess energy and is able to generate up to 30 phonons in about 7 ps, as long as the effect of band filling due to Pauli exclusion principle is not severe. Therefore, once the excitation fluence is large enough, one should expect a major role of the 2PA carriers in the structural dynamics of silicon probed by UEC; after convolution with the instrumental response of 7 ps, a diffraction intensity decrease due to phonon motions is anticipated to be on a 10-ps time. This has been observed experimentally (for excitation by 266-nm light, considering its direct absorption and large excess energy to release from the carriers), as shown in the inset of Fig. 3c and early-time depletion of Fig. 4c in Ref. 55.

In this study, intensity of the specular spot from the substrate is also seen to decrease on a 10-ps time. It signifies, on such a time scale, an increase in the atomic motions near the surface that destroys the surface homogeneity (coherence) required for stronger specular reflection (Fig. 11c). Such an observation also infers the importance of 2PA in silicon to dynamics of the substrate and consequently that of the interfacial ice assembly, in the fluence range used here. From $t = 10$ ps to $t = 50$ ps, the lattice motions remain at a substantial level because of the continuing optical-phonon generation by carriers that is delayed due to the hot-phonon effect and intervalley carrier–carrier scattering (Ch. 4). Later, the decay of atomic motions is found to exhibit a fast component with a time constant of $\tau_{\mathrm{fast}} \sim 40$ ps and a slow one on the sub-nanosecond scale.

The vital role of 2PA in silicon at early times is further evidenced by the fluence dependence of dynamical responses in the interfacial ice assembly (Fig. 13). According to Ref. 53, the highest fluence used produces mainly energetic 2PA carriers that can supply a substantial amount of energy, leading to the current observation of the large lattice expansion in ice *Ic* crystallites. At one third of this fluence or below (i.e., at ≤ 30 mJ/cm^2), however, nearly no dynamical change in ice was measurable. Based on this nonlinear response, together with the fluence-dependent dynamical portion in the diffraction profile (Fig. 13a) and the argument concerning carriers' excess energy available to structural dynamics, we reach the conclusion that the 2PA mechanism predominantly defines the dynamics of interfacial ice at early times. With such an understanding the result of Fig. 13a can therefore be explained, through a simple calculation using Gaussian profiles of the same width to represent different optical fluences on the substrate, and a cut-off threshold for the effective 2PA region within the electron-probed range (Fig. 13a, inset). The threshold is estimated to be ~25 mJ/cm^2, in a good agreement with the experimental finding and with the trend shown in Fig. 13b.

At longer times, relaxation of the silicon substrate is achieved through mechanisms such as carrier diffusion into the bulk (*56*), Auger recombination (*57*), radiative recombination, and heat diffusion (*58*). Auger recombination effectively reduces the number of carriers and releases additional energy to the lattice, which becomes the energy source at longer times. Other mechanisms effectively remove energy from the surface region and hence affect the energy content in the overlaying ice assembly. As for the Si–H vibration at the interface, previous studies showed its lifetime to be ~0.8 ns (*59*). Although such a time scale seems relevant, however, these vibrators are less important to our observations because the energy that causes structural motions is from the photocarriers and phonons that are subsequently generated; Si–H vibration plays at most the role of energy-transfer intermediate at the interface.

B. Structural Isosbestic Point

In spectroscopy, the curve crossing behavior at a common point in the spectra—known as an isosbestic point—is regarded, when relevant, as a signature of a chemical reaction or structural interconversion in progress between two species whose total concentration remains constant. In diffraction (capable of direct structure probing), however, such a behavior—naturally termed a "structural isosbestic" point—was rarely reported even in equilibrium studies (*60*) and was recently found in time-resolved experiments from this laboratory (Chs. 7 and 9). Similar to the argument in the spectroscopic counterpart, the appearance of such points in diffraction curves at transient times indicates a distinct structural conversion from the unexcited ground state to excited one(s), as these states are causally related due to the nature of the UEC technique. In fact, this conversion further signifies the phenomenon of nonequilibrium phase transformation, given the distinct difference between the two states involved and their separation by a free-energy barrier (overcome through excitation) in phase space.

Typical and expected diffraction changes in UEC are continuous profile shifts with intensity decrease and recovery, as observed in many previous studies (see, e.g., Chs. 4 and 5). In highly correlated materials, photoexcited carriers forming transient macroscopic domains lead to the two-state transformation behavior (Ch. 7). The current observation of structural isosbestic points in the dynamics of interfacial ice, similar to the result in Ch. 9, hence reflects the unusual properties of a hydrogen bond network upon an external input of vibrational energy. The observed nonequilibrium phase transformation in ice *Ic* crystallites is further confirmed by the fact that curve crossing is clearly seen for all intense diffraction rings from ice, and the conclusion of isotropic expansion based on the ring shifts is compatible with principally random orientation of ice crystallites.

Additional evidence for the existence of structural isosbestic points and the inferred phase transformation comes from the constant total intensity during curve crossing, an observation that is equivalent to the total concentration of the two species being constant during a chemical reaction or conversion in the spectroscopic counterpart. It is because the initial and final states of the conversion have the same electron diffraction cross section as both contain the same number and types of atoms. In the current study, the result of Fig. 10b therefore strengthens our picture.

It is noted that, in spectroscopic studies, the appearance of an isosbestic point in the spectra as evidence for interconverting chemical or structural species has been called into question (*61, 62*). However, the main problem there is the presence of inhomogeneous broadening. In diffraction, the well-defined Bragg spots or rings can only originate from a long-range ordered (homogeneous) structure, rather than from an ensemble or inhomogeneous distribution of distances. Moreover, the clear shifts of diffraction peaks during the early-time dynamics, with the existence of only one isosbestic point for one ring and no overlap in the wings, are in sharp contrast with the results given in Ref. 61. It is worth noting that the curve crossing behavior in the upper panels of Fig. 9 cannot be simply reproduced by adding a series of small profiles with the same width and located at different *s* values, thus the notion of continuous structural change is invalidated. In fact, the well-separated peaks before the time zero and after 60 ps demarcate the two distinct structures involved, each with a well-defined diffraction peak width. Furthermore, as suggested in Ref. 61, the confirmation of a true chemical or structural conversion must come from time-dependent measurements, as reported here using UEC.

C. Dynamics of Interfacial Polycrystalline Ice

Dynamics of polycrystalline ice heavily depends on that of the underlying substrate (Ch. 9). From the estimate ice film thickness, approximately 10^{14} water molecules were accumulated above the surface in the region of laser heating and electron probing. Compared with the carrier density [on the order of 10^{20} cm^{-3} (*53*)] created near the interface and the subsequent generation of phonons, the number of water molecules and their heat capacity are limited. Thus, dynamics of the silicon substrate is not much altered by the existence of interfacial ice, but dynamics of the latter follows closely that of the former.

Ice can receive energy from the underlying substrate through vibrational coupling (phonon generation) in the lattice. Cubic ice exhibits four different vibrational bands in the infrared spectrum: intramolecular O–H stretching, intramolecular H–O–H bending, librational and translational modes in decreasing order of the corresponding frequency (*63*). An efficient energy transfer is therefore expected when frequencies of the phonons

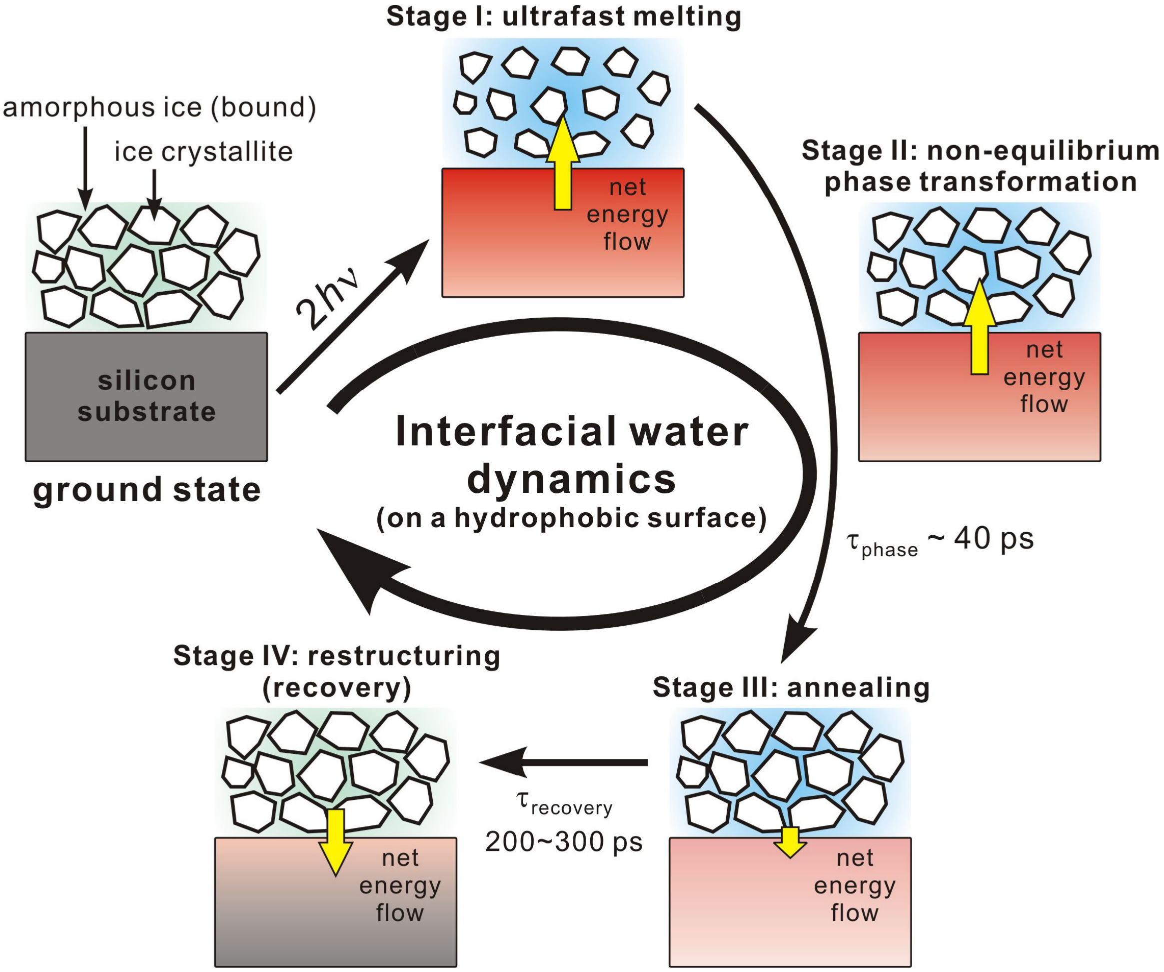

Fig. 14. Schematic representation of dynamics of the ice assembly on H/Si(111). For the substrate, the gray color and the red of different color levels represent the unexcited status and regions with different photoexcitation levels, respectively. The yellow arrows indicate the direction of the net energy flow in different stages. For interfacial ice, the different sizes of ice crystallites (not drawn to scale) are depicted to illustrate the structural dynamics at work in different stages. The sky blue (pale green) color is used to indicate water molecules that have a larger (low) mobility in the amorphous part of the ice assembly.

in silicon and in ice are matched. Optical phonons in silicon have a frequency of ~500 cm^{-1}, and acoustic ones are of even lower frequencies (*51*). Thus, excitation in the intramolecular bands of ice is unlikely because of their high frequencies, but the lower bound of the librational band and, more importantly, the entire translational vibrational band are in the frequency range of silicon phonons (*64, 65*). It is therefore not merely a coincidence to find translational movement of water molecules into an expanded structure as energy transfers from silicon to the translational vibrational band of ice. It is noted that across-interface carrier transfer (*66, 67*) from silicon to the polycrystalline ice, as an energy transfer pathway, is of little concern because of the semiconducting (nonmetallic) nature of silicon, insufficient carrier energy, and the less relevant sub-picosecond time scale involved. Such carrier transfer for the induction of a permanent structural change (*68*) can also be eliminated, since no diffraction change was accumulated in the repeated experimental cycles at 1 kHz.

With the understanding of energy transfer across the interface, the following picture emerges for the four stages of structural dynamics (Fig. 14).

C.1. Stage I—Ultrafast Melting

In the initial 20 ps after the laser heating, carriers photoexcited in silicon through 2PA start to release their excess energy preferably by generating optical phonons, which anharmonically decay [on a time scale of ~4 ps (*69*)] into acoustic phonons of lower frequencies that are able to couple with the translational vibrational band of ice *Ic* and hence transfer energy. The necessary time for this process was experimentally discernible from the small time difference between the onset of ice diffraction intensity decrease (purple in Fig. 11b) and that of silicon specular intensity drop (Fig. 11c). Upon receipt of energy into its structure, atoms in the ice *Ic* crystallites undergo enlarged vibrational motions; those near the grain boundaries may even exhibit significant translational deviation from their original positions, a transient phenomenon that can be termed ultrafast melting. This is evidenced by the initial decrease of diffraction intensity before the profile shift (Fig. 9, upper panels).

From the initial 7% and 17% intensity decrease (Fig. 10b), the induced vibrational amplitude, $\langle \delta u^2 \rangle^{1/2}$, is estimated to be about 0.27 Å and 0.44 Å, respectively, for oxygen atoms using the Debye–Waller factor (Eq. 16 of Ch. 2). These numbers are much greater than the root-mean-square displacement of at most a few hundredth of an angstrom at $T = 100$ K, and also larger than the zero-point amplitude of the oxygen atoms (*64*). Moreover, the induced motions reach about 10% and 16% of the nearest-neighbor O–O distance of 2.75 Å, which is close to or exceed the equilibrium Lindemann limit for thermal melting. However, the observed structural dynamics is not induced through thermal means, and it seems that the ice assembly withstands the vibrational motions and resists the loss of water molecules on this ultrashort time scale, suggesting connectivity and the cooperative nature of a hydrogen bond network.

Large atomic motions in the amorphous part of the ice assembly and near the crystallite boundaries are crucial and necessary for the later dynamics. Given the indefinite structure of amorphous ice and the principally random orientation of crystallites, because of orientational mismatch of vibrational modes, energy transferring across the interface will be “trapped” and retain in the assembly, instead of wavelike acoustic propagation that has been noted in the crystalline ice structure (*24*). If those atoms remained in a somewhat rigid network, ice *Ic* crystallites would encounter restraint during the later expansion because of the limited space, which hinders the accommodation of energy input in the assembly. Therefore, an increased mobility (and consequently structural flexibility) for those water molecules can be inferred.

C.2. Stage II—Nonequilibrium Phase Transformation

In this stage, generation of a significant number of phonons persists in the substrate (indicated by the sustaining reduced specular intensity shown in Fig. 10c, $t = 10$ ps to $t = 50$ ps), and energy continues to couple into the ice assembly with a small time delay (Fig. 10b, $t = 20$ ps to $t = 60$ ps). It was to our surprise to discover that ice *Ic* crystallites, supported by this "phonon bath," undergo a two-state-only structural phase transformation rather than a continuous change. We want to emphasize that this observation is not due to the resolution limit in time or in space. As shown in Fig. 11b, the new phase develops with a time constant of $\tau_{\text{phase}} \sim 40$ ps that is similar to the duration of Stage II, signifying a causal relation between the substrate dynamics and the structural transformation of interfacial ice.

The observed large expansion of ice lattice is also quite special among the laser-induced ultrafast structural dynamics. Most of the time-resolved diffraction studies [including x-ray's (*70*)] reported on the lattice change of materials that are initially photoexcited by photons directly. For interfacial ice, however, it is the *phonon* field indirectly generated underneath (from carriers) that leads to the expansion. Also, ice *Ic* crystallites were found to expand isotropically, unlike the unidirectional motion observed in a supported model membrane (*71*). The difference can be attributed to the randomness in crystallites' orientation such that the spatial asymmetry (i.e., the special role of the surface normal direction) manifested in almost all other UEC studies (see, e.g., Chs. 4, 5 and 7 and Ref. 71) no longer exists here.

It is also intriguing to find that, under a similar excitation condition, the lattice expansion of ice is much larger than that of covalently bonded systems (*71*) without sublimation, a phenomenon that may be directly associated with the relatively small strength of an individual hydrogen bond but the flexible and cooperative nature of a network (*72, 73*). The dynamical change is nonthermal in that an unreasonable temperature rise of thousands of Kelvin would be derived using the thermal expansion coefficient of ice (*74*). The fluence dependence of expansion of the new phase appears to be linear with a threshold (Fig. 13b, solid dots); however, since the dynamical portion is also dependent on fluence (Fig. 13a), it is more sensible to compare the total volume increase, which is, effectively, the product of the numbers in panels a and b of Fig. 13 at each fluence. We found from this analysis a quadratic dependence with a similar threshold, consistent with the generation of 2PA carriers being quadratically dependent on fluence, and the aforementioned dominant role of these carriers as the ultimate energy source for ice expansion.

This new dynamical property of polycrystalline ice under a strong external perturbation may be important to deeper understanding of the collective and dynamic nature of a hydrogen bond network, on a scale beyond the size of small water clusters (*75*). The different dynamics for polycrystalline and crystalline (*24*) structures are also quite intriguing, and will be detailed in another work.

C.3. Stage III—Annealing

Following the phase transformation, the diffraction intensity recovery at the transformed profile position (Fig. 9, upper panels after curve crossing) is indicative of the first step toward structural relaxation. It means a structural change in the ice assembly opposite to that during Stage I. That is, vibrational motion of atoms in the ice *Ic* crystallites becomes reduced, and those water molecules near the grain boundaries may even adopt positions that fit the adjacent crystalline order, a transient phenomenon that can be termed annealing. Consequently, the new phase becomes fully mature in this stage, and the diffraction intensity finally reaches the same value as that of the original phase (Fig. 11b, after the yellow region).

The governing factor for this structural annealing is that the energy input from the substrate starts to drop significantly in Stage III, as evidenced by the fast recovery with $\tau_{\text{fast}} \sim 40$ ps shown in the inset of Fig. 11c. Now, the direction of the net energy flow is going to reverse; it was upward from the substrate to the assembly in Stages I and II (Fig. 14). Therefore, it can be reasonably concluded that, toward the end of Stage III, a dynamical equilibrium between the ice assembly and the silicon substrate is established, leading to the recovery of ice–substrate composite in the next stage.

C.4. Stage IV—Restructuring

On the sub-nanosecond to nanosecond time scale, ice *Ic* crystallites restructure by recovering continuously toward the original lattice constant (Fig. 12), along with the slow relaxation of the underlying silicon substrate. The weak dependence of the recovery time constant, τ_{recovery}, on the ice film thickness indicates that the energy dissipation in silicon into the bulk is the most important determining factor for relaxation of interfacial ice. Again, the reason is that the heat capacity of those interfacial water molecules is relatively insignificant when compared with that of the substrate, and no major bottleneck in the adsorbate–substrate heating and cooling.

It is interesting to find that the remaining lattice expansion of ice at $t = 1.2$ ns is almost fluence independent (Fig. 13b, open circles), implying a larger apparent rate for restructuring in the case with a higher fluence. These results become understandable when the status of the silicon substrate is examined. At higher fluences, the effective penetration depth for 2PA is smaller (i.e., gradient of the carrier density profile along the surface normal is larger), which leads to faster carrier and heat diffusion into the bulk. The large number of carriers by 2PA makes Auger recombination occur in a faster rate, resulting in a faster substrate relaxation. The combined effect is that the residual change at $t = 1.2$ ns in the substrate becomes less fluence dependent, and so does that of the interfacial ice.

Another intriguing observation is that the diffraction intensity remains a constant value as the original in this stage (Fig. 10b, inset), while the profile is shifting continuously (Fig. 9, lower panels). It signifies that the average atomic motion has been quenched to a level similar to that before the zero of time, although all the intermolecular distances are appreciably larger than the equilibrium values. As a result, the validity of using a Lennard–Jones type of anharmonic potential with fixed parameters to describe the fast structural dynamics of a water assembly becomes questionable, because such a model would anticipate larger intermolecular vibrations in an expanded lattice. Further theoretical endeavors are therefore encouraged to investigate whether the electrostatic term included in many water models (*76, 77*) can resolve this issue and satisfactorily explain the experimental observation here, or some modification for the intermolecular interaction term (*78, 79*) or the overall pair-wise potential (*80*) can be made. In addition, through modeling, the coupling between polarization (partial charges) of a water molecule and translational molecular movements in the network (*81*) may be revealed for transient structures that can only be accessed dynamically.

Concluding Remarks: Interfacial Ice on H/Si(111) and on Graphite

From UEC studies of an assembly on different hydrophobic surfaces (Ch. 9), we are able to gain further insights on the structural and dynamical properties of interfacial ice. Statically, due to their weak interaction with the substrate, water molecules do not adopt the symmetry of the substrate surface and the azimuthal orientations of ice crystallites are therefore random. However, the terraced surface morphology of highly oriented pyrolytic graphite provides an additional guiding force to assist the order of water layers along the surface normal direction. In the present study, the lack of such a template structure on H/Si(111) makes the intermolecular water–water interaction the most dominant factor for crystallites' orientation, resulting in a diffraction pattern of rings instead of observation of well-defined Bragg spots.

From analysis of the diffraction patterns the structure of polycrystalline ice was confirmed to be of the cubic form, ice *Ic*. Further away from the substrate, because of the energetics at the ice–vacuum interface, ice *Ic* crystallites prefer the exposure of {110} planes to minimize the number of dangling O–H bonds, leading to the observation of {110} preferred orientation for ice crystallites near the vacuum in a thick assembly. Structural optimization with consideration of this preferred orientation gave a lattice constant that agrees well with the literature value.

For the dynamics of interfacial ice, we found the determining factor to be the dynamics of the substrate following an ultrafast "*T*-jump" by a femtosecond infrared pulse. Carriers photogenerated in silicon by two-photon absorption were the most crucial source of energy because of their larger above-gap excess energy available to the lattice. The across-interface energy transfer from the substrate couples with the translational vibrational band of ice and causes initial large atomic motions, or a melting-like phenomenon, in the ice assembly, as manifested by an initial diffraction intensity decrease on an ultrashort time scale. Subsequently, nonequilibrium phase transformation of ice *Ic* crystallites into an isotropically expanded lattice follows, which is evidenced by the appearance of structural isosbestic points, a curve crossing behavior, in the temporal evolution of diffraction profiles.

As soon as the substrate experiences a significant reduction in its lattice energy, the ice assembly starts its path to restructuring, first by greatly quenching the atomic motions or by structural annealing, which is inferred from the quick recovery of diffraction intensity to the original level. At longer times, the substrate undergoes a slow relaxation, and the expanded ice crystallites exhibit a continuous decrease in their lattice constant, toward the equilibrium value. Based on the peculiar evolution of the observed diffraction changes, theoretical investigations are suggested in order to acquire better understanding about the correlation between molecular polarization and intermolecular interaction at transient times.

It was shown that, although the aforementioned picture for the four stages of ice structural dynamics remains robust, the dynamical behaviors of interfacial ice at different stages and their corresponding time constants are closely related to the characteristics of substrate dynamics. Graphite was found to exhibit ultrafast structural contraction and expansion (*82*), and it is therefore understandable to see that the interfacial ice on graphite goes through the first three stages of structural dynamics more quickly than that on silicon does (Ch. 9). Also, graphite is a semimetal that has no band gap and adsorbs 800-nm light better, which makes the photocarriers more concentrated and their energy entirely available to the lattice dynamics. The much larger expansion of the ice assembly on graphite is thus expected. However, regardless of what the substrate is, the large atomic motions and significant expansion of ice at transient times do not lead to a total melting or sublimation of the assembly. This picture was consistently suggested by a previous spectroscopic study of interfacial D_2O ice, using sum-frequency generation with longer time resolution, although neither the structure nor the order can be directly observed with atomic resolutions (*21*).

The observations made by ultrafast electron crystallography unravel the unique nature of structure and dynamics of interfacial water assembly on hydrophobic substrates. It may be interesting to find some similarity in time constants reported in a study of the structural dynamics of liquid water following direct electronic excitation, using time-resolved x-ray diffraction with a poor temporal resolution (*83*). With these recent developments of ultrafast diffraction methods, we are now equipped with direct means for elucidating structures and dynamics at nanometer scale, such as those during phase transformations (*29, 30, 84*) or concerning hydrophobic/hydrophilic properties at interfaces (*85-87*) and their contrast with bulk ones (*88*).

References and Footnotes:

1. G. M. Whitesides, B. Grzybowski, *Science* **295**, 2418 (2002).
2. K. B. Eisenthal, *Chem. Rev.* **96**, 1343 (1996).
3. G. A. Jeffrey, *An introduction to hydrogen bonding* (Oxford Univ. Press, New York, 1997).
4. M. Binggeli, C. M. Mate, *Appl. Phys. Lett.* **65**, 415 (1994).
5. M. A. Henderson, *Surf. Sci. Rep.* **46**, 5 (2002).
6. A. Verdaguer, G. M. Sacha, H. Bluhm, M. Salmeron, *Chem. Rev.* **106**, 1478 (2006).
7. K. Gawrisch *et al.*, *Biophys. J.* **61**, 1213 (1992).
8. W. Zhao, D. E. Moilanen, E. E. Fenn, M. D. Fayer, *J. Am. Chem. Soc.* **130**, 13927 (2008).
9. L. Y. Zhang *et al.*, *Proc. Natl. Acad. Sci. USA* **104**, 18461 (2007).

10. G. E. Brown *et al.*, *Chem. Rev.* **99**, 77 (1999).
11. G. E. Brown, *Science* **294**, 67 (2001).
12. S. K. Pal, A. H. Zewail, *Chem. Rev.* **104**, 2099 (2004).
13. G. M. Whitesides, P. W. Snyder, D. T. Moustakas, K. A. Mirica, in *Physical biology: from atoms to medicine,* A. H. Zewail, Ed. (Imperial College Press, London, 2008), pp. 189-215.
14. Y. Levy, J. N. Onuchic, *Annu. Rev. Biophys. Biomol. Struct.* **35**, 389 (2006).
15. G. W. Robinson, S.-B. Zhu, S. Singh, M. W. Evans, *Water in biology, chemistry and physics: Experimental overviews and computational methodologies* (World Scientific, New Jersey, 1996).
16. C. A. Angell, *Annu. Rev. Phys. Chem.* **55**, 559 (2004).
17. M. R. Yalamanchili, A. A. Atia, J. D. Miller, *Langmuir* **12**, 4176 (1996).
18. Y. R. Shen, *Nature* **337**, 519 (1989).
19. Y. R. Shen, V. Ostroverkhov, *Chem. Rev.* **106**, 1140 (2006).
20. X. C. Su, L. Lianos, Y. R. Shen, G. A. Somorjai, *Phys. Rev. Lett.* **80**, 1533 (1998).
21. J. Kubota, A. Wada, S. S. Kano, K. Domen, *Chem. Phys. Lett.* **377**, 217 (2003).
22. K. Thürmer, N. C. Bartelt, *Phys. Rev. B* **77**, 195425 (2008).
23. X. Zou, S. Hovmöller, *Acta Crystallogr. Sect. A* **64**, 149 (2008).
24. C.-Y. Ruan, V. A. Lobastov, F. Vigliotti, S. Chen, A. H. Zewail, *Science* **304**, 80 (2004).
25. W. Kern, *Handbook of semiconductor wafer cleaning technology : science, technology, and applications* (Noyes Publications, Park Ridge, N.J., 1993).
26. G. S. Higashi, Y. J. Chabal, G. W. Trucks, K. Raghavachari, *Appl. Phys. Lett.* **56**, 656 (1990).

27. P. Dumas, Y. J. Chabal, P. Jakob, *Surf. Sci.* **269**, 867 (1992).

28. P. Baum, A. H. Zewail, *Proc. Natl. Acad. Sci. USA* **103**, 16105 (2006).

29. P. Jenniskens, D. F. Blake, *Science* **265**, 753 (1994).

30. P. Jenniskens, D. F. Blake, *Astrophys. J.* **473**, 1104 (1996).

31. B. J. Murray, D. A. Knopf, A. K. Bertram, *Nature* **434**, 202 (2005).

32. B. K. Vaĭnshteĭn, *Structure analysis by electron diffraction* (Pergamon Press, Oxford, 1964).

33. Z. L. Wang, *Elastic and inelastic scattering in electron diffraction and imaging* (Plenum Press, New York, 1995).

34. I. Kohl, E. Mayer, A. Hallbrucker, *Phys. Chem. Chem. Phys.* **2**, 1579 (2000).

35. We found that it is equally effective to use a Lorentzian or polynomial function for the decay part, and the result is practically the same.

36. W. F. Kuhs, D. V. Bliss, J. L. Finney, *J. Phys. Colloq. C1* **48**, 631 (1987).

37. W. H. Barnes, *Proc. R. Soc. London Ser. A* **125**, 670 (1929).

38. W. F. Kuhs, M. S. Lehmann, *J. Phys. Chem.* **87**, 4312 (1983).

39. Diffraction profiles were calculated using kinematic scattering theory. The estimated size of ice *Ic* crystallites that were vapor-deposited on a hydrophobic surface was on the order of <100 Å. According to Ref. 32, dynamic effects would become important only when the scattering domain size is approximately 450 Å. The use of kinematic, rather than dynamic, scattering theory is therefore justified in the present work.

40. L. G. Dowell, A. P. Rinfret, *Nature* **188**, 1144 (1960).

41. L. S. Bartell, J. F. Huang, *J. Phys. Chem.* **98**, 7455 (1994).

42. G. P. Johari, *J. Chem. Phys.* **122**, 194504 (2005).

43. H. M. Rietveld, *J. Appl. Cryst.* **2**, 65 (1969).

44. T. Roisnel, J. Rodríguez-Carvajal, in *Materials Science Forum, Proceedings of the Seventh European Powder Diffraction Conference (EPDIC 7),* R. Delhez, E. J. Mittenmeijer, Eds. (2000), pp. 118-123.

45. J. Rodríguez-Carvajal, in *IUCr Commission on Powder Diffraction Newsletter*. (2001), vol. 26, pp. 12-19.

46. Least-squares refinement was performed using the program FullProf (*44, 45*). Relative atomic positions in a unit cell were of the cubic structure, and the isotropic atomic displacement factors [$B_O = 1.56$ Å^2 and $B_H = 2.02$ Å^2 (*38*)] were fixed. The diffraction peaks were described by pseudo-Voigt functions, whereas the background was modeled by a polynomial function. The cubic unit-cell parameter that determines the positions of diffraction peaks was refined during the process.

47. R. A. Young, Ed., *The rietveld method* (Oxford Univ. Press, Oxford, 1995).

48. From the aforementioned structural analysis and Figure 5, the wing regions of the (111) ring have diffraction contributions from both randomly oriented and preferentially oriented ice crystallites, whereas the central region is from the former type only.

49. J. N. Shapiro, *Phys. Rev. B* **1**, 3982 (1970).

50. J. M. Ziman, *Principles of the theory of solids* (Cambridge Univ. Press, Cambridge, 2nd ed., 1972).

51. A. Dargys, J. Kundrotas, *Handbook on physical properties of Ge, Si, GaAs and InP* (Science and Encyclopedia Publishers, Vilnius, 1994).

52. P. Lautenschlager, M. Garriga, L. Viña, M. Cardona, *Phys. Rev. B* **36**, 4821 (1987).

53. T. Sjodin, H. Petek, H.-L. Dai, *Phys. Rev. Lett.* **81**, 5664 (1998).

54. A. J. Sabbah, D. M. Riffe, *Phys. Rev. B* **66**, 165217 (2002).

55. C.-Y. Ruan, F. Vigliotti, V. A. Lobastov, S. Chen, A. H. Zewail, *Proc. Natl. Acad. Sci. USA* **101**, 1123 (2004).

56. C. V. Shank, R. Yen, C. Hirlimann, *Phys. Rev. Lett.* **50**, 454 (1983).

57. M. C. Downer, C. V. Shank, *Phys. Rev. Lett.* **56**, 761 (1986).

58. J. H. Bechtel, *J. Appl. Phys.* **46**, 1585 (1975).

59. P. Guyot-Sionnest, P. Dumas, Y. J. Chabal, G. S. Higashi, *Phys. Rev. Lett.* **64**, 2156 (1990).

60. G. W. Robinson, C. H. Cho, J. Urquidi, *J. Chem. Phys.* **111**, 698 (1999).

61. P. L. Geissler, *J. Am. Chem. Soc.* **127**, 14930 (2005).

62. J. D. Smith *et al.*, *Proc. Natl. Acad. Sci. USA* **102**, 14171 (2005).

63. C. Y. Lee, D. Vanderbilt, K. Laasonen, R. Car, M. Parrinello, *Phys. Rev. B* **47**, 4863 (1993).

64. J. E. Bertie, E. Whalley, *J. Chem. Phys.* **46**, 1271 (1967).

65. D. D. Klug, E. Whalley, E. C. Svensson, J. H. Root, V. F. Sears, *Phys. Rev. B* **44**, 841 (1991).

66. C. Gahl, U. Bovensiepen, C. Frischkorn, M. Wolf, *Phys. Rev. Lett.* **89**, 107402 (2002).

67. J. Stähler, C. Gahl, U. Bovensiepen, M. Wolf, *J. Phys. Chem. B* **110**, 9637 (2006).

68. D. Chakarov, B. Kasemo, *Phys. Rev. Lett.* **81**, 5181 (1998).

69. J. Menéndez, M. Cardona, *Phys. Rev. B* **29**, 2051 (1984).

70. M. Bargheer, N. Zhavoronkov, M. Woerner, T. Elsaesser, *ChemPhysChem* **7**, 783 (2006).

71. M. T. Seidel, S. Y. Chen, A. H. Zewail, *J. Phys. Chem. C* **111**, 4920 (2007).

72. M. I. Heggie, C. D. Latham, S. C. P. Maynard, R. Jones, *Chem. Phys. Lett.* **249**, 485 (1996).

73. P. L. Silvestrelli, M. Parrinello, *J. Chem. Phys.* **111**, 3572 (1999).

74. H. Tanaka, *J. Chem. Phys.* **108**, 4887 (1998).

75. F. N. Keutsch, R. J. Saykally, *Proc. Natl. Acad. Soc. USA* **98**, 10533 (2001).

76. W. L. Jorgensen, J. Chandrasekhar, J. D. Madura, R. W. Impey, M. L. Klein, *J. Chem. Phys.* **79**, 926 (1983).

77. H. J. C. Berendsen, J. R. Grigera, T. P. Straatsma, *J. Phys. Chem.* **91**, 6269 (1987).

78. O. Mishima, H. E. Stanley, *Nature* **396**, 329 (1998).

79. R. Kumar, J. L. Skinner, *J. Phys. Chem. B* **112**, 8311 (2008).

80. B. Guillot, Y. Guissani, *J. Chem. Phys.* **114**, 6720 (2001).

81. B. Chen, J. H. Xing, J. I. Siepmann, *J. Phys. Chem B.* **104**, 2391 (2000).

82. F. Carbone, P. Baum, P. Rudolf, A. H. Zewail, *Phys. Rev. Lett.* **100**, 035501 (2008).

83. A. M. Lindenberg *et al.*, *J. Chem. Phys.* **122**, 204507 (2005).

84. L. Delzeit, D. F. Blake, *J. Geophys. Res.* **106**, 33371 (2001).

85. B. J. Gertner, J. T. Hynes, *Science* **271**, 1563 (1996).

86. A. P. Willard, D. Chandler, *J. Phys. Chem. B* **112**, 6187 (2008).

87. P. Ball, *Chem. Rev.* **108**, 74 (2008).

88. A. D. Buckingham, J. E. Del Bene, S. A. C. McDowell, *Chem. Phys. Lett.* **463**, 1 (2008).

Chapter 11

Structures and Dynamics of Self-Assembled Surface Monolayers[†]

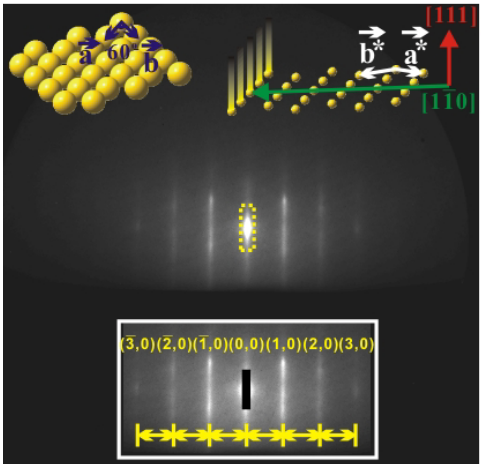

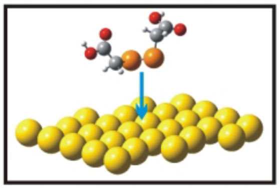

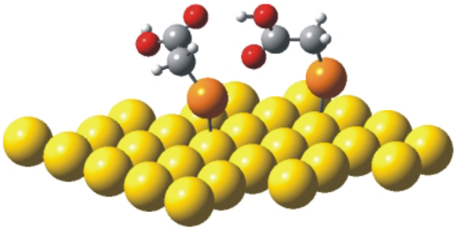

[†] adapted from C.-Y. Ruan, D.-S. Yang, A. H. Zewail, *J. Am. Chem. Soc.* **126**, 12797 (2004).

Introduction

When a beam of ultrashort electron pulses impinges on a crystal surface, diffraction patterns can be resolved in time (femtosecond to picosecond) and in space (picometer). Because of the large cross section for electron interaction with matter, the sensitivity is sub-monolayer. The methodology of ultrafast electron crystallography (UEC) makes possible the study of surface atoms and adsorbates of nanometer length scale. In this chapter, I briefly describe our initial study of self-assembled (*1*) adsorbates on metal surfaces. Specifically, we studied single-crystal clean surfaces of Au(111) with and without a monolayer of reaction involving the assembly of 2-mercaptoacetic acid from 2,2′-dithiodiacetic acid (*2*). Monolayers of iron hemes were also studied. The current investigation is different from the studies of Languir–Blodgett films of fatty acids and phospholipids made in our group (*3, 4*) in terms of the nature of the surface assemblies and the interaction involved at the interface. With UEC, we are able to observe and isolate structural dynamics of the substrate (gold) and adsorbate(s) following an ultrafast temperature jump.

The single-crystal substrate has a long-range order, which results in well-defined Bragg diffraction spots and streaks in the Laue zones. In the presence of adsorbates, new diffraction features appear depending on the degree of order—Bragg spots if perfectly ordered and Debye–Scherrer rings if ordered (within small domains) but randomly oriented. Using the method of diffraction frame referencing (*5*), gating of the distinct coherent diffraction features (Bragg spots, streaks or Debye–Scherrer rings) or the incoherent features (diffuse background or Kikuchi scattering) as a function of time allows for independent isolation of dynamics originated from different structures. This isolation is aided by the ability to obtain the diffraction at small and large angles in real

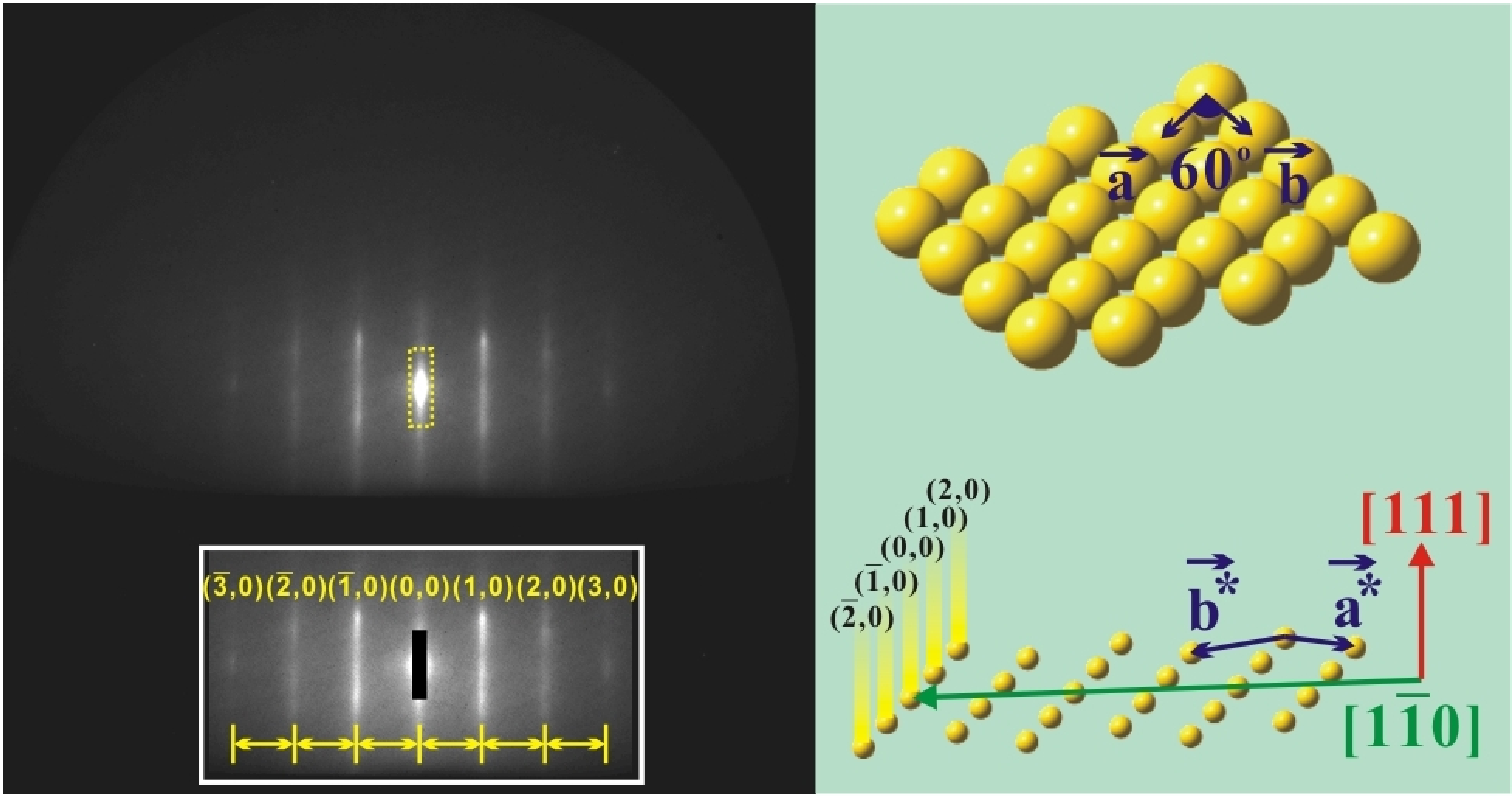

Fig. 1. (Left) Diffraction images of single-crystal Au(111). The inset shows the streaks at higher contrast, indexed according to the Miller indices (*h*, *k*), where *k* represents the order of Laue zones. (Right) Real-space representation of Au(111) (top) together with reciprocal lattice rods corresponding to the two-dimensional Au(111) surface (bottom).

time. UEC is thus uniquely suited for examining structural dynamics at the interface with atomic-scale spatial and temporal resolutions.

Materials and Experimental Section

Gold(111) films of 150 nm thickness on mica substrates were purchased from Molecular Imaging; the single-crystal domain from STM images is more than 200×200 nm. The thiolated surface was prepared following procedures of Ref. 2, which were also used for the preparation of thiolated alkanes and heme assembly. In solution, the disulfide bond of 2,2′-dithiodiacetic acid breaks to form the more stable sulfur–gold interfacial bonds (*2, 6*). The samples were then rinsed copiously with ethanol, dried in nitrogen ambient, and immediately mounted onto the goniometer of our UEC diffraction chamber (at a pressure of $\sim 5\times10^{-10}$ Torr). To initiate the change, we used near-IR 800-nm femtosecond pulses, and to probe, we generated ultrashort electron pulses (30 keV). The pulses can be as short as 300–600 fs but here a pulse width of ~2 ps was used at the number of electrons per pulse applied. The electron pulses were timed to arrive either before or after the initiating pulse, and diffraction patterns were recorded on a CCD camera assembly. All experiments were performed at room temperature except for studies of diffuse scattering at small angles when the substrate temperature was reduced to 120 K to suppress thermal background.

Results and Analysis

For the clean unmodified gold substrate, the diffraction patterns consist of well-resolved Bragg spots and streak features (Fig. 1). The positions of these spots and streaks, together with the geometrically established specular reflection and shadow edges

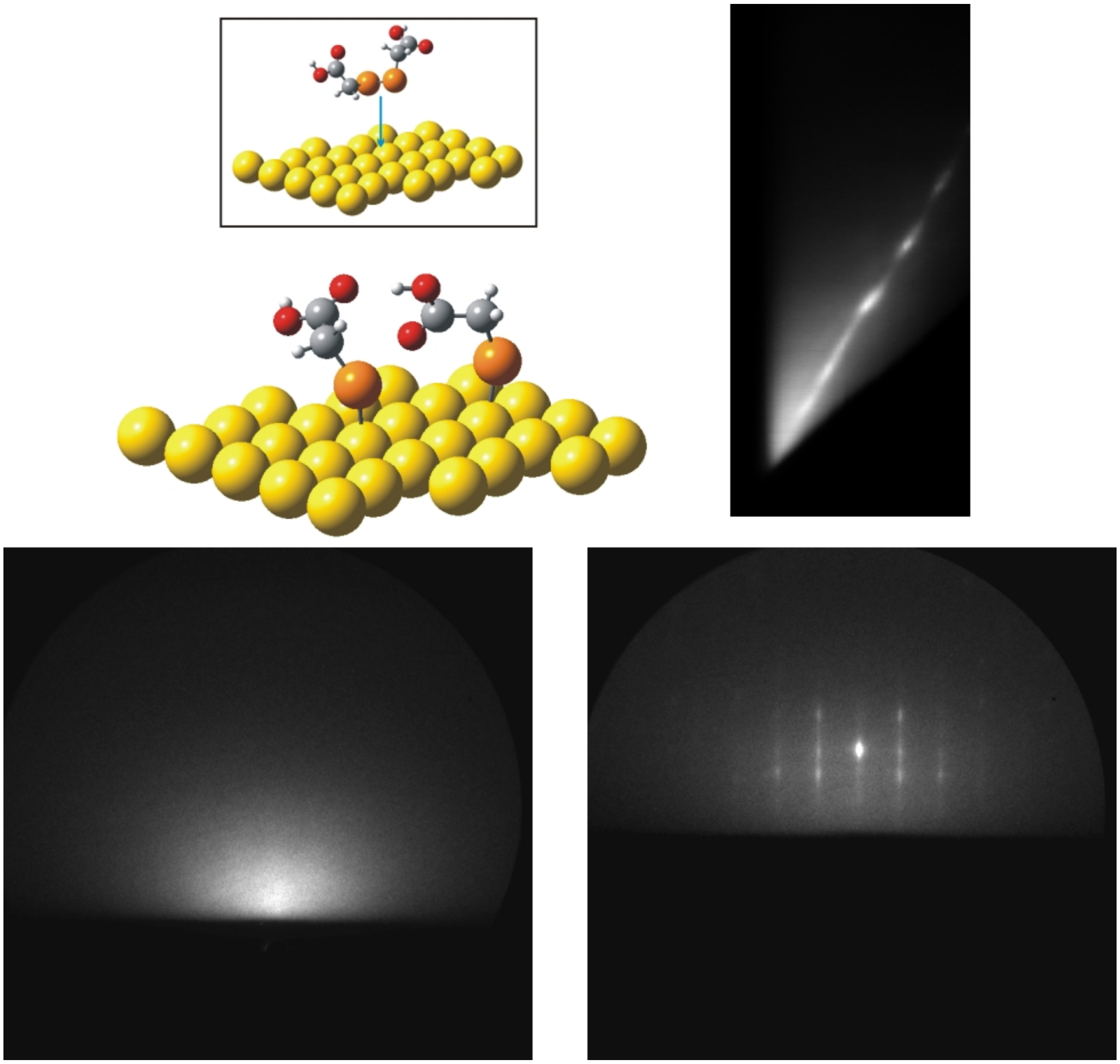

Fig. 2. (Top left) Representation of the structures involved in the reaction of 2,2′-dithiodiacetic acid and a clean gold surface. (Top right) The experimentally observed rocking curve *s* (vertical) vs θ_{in} (horizontal), where *s* is the scattering vector and θ_{in} is the incidence angle. Note the different orders observed as a function of θ_{in}, which were detected by gating the (0,0) streak. (Bottom left) Static diffuse scattering obtained without temporal resolution at a small incidence angle of ~1°. (Bottom right) Gold-type streaks (see Fig. 1) obtained for the thiolated surface when the incidence angle is relatively large (~4.2°). Note that the shadow edge is different for small- and large-angle diffractions, reflecting the geometry of electron incidence on the surface.

for calibration, directly provide the structure of the two-dimensional reciprocal lattice of the (111) planes of the face-centered-cubic crystal. As noted in Fig. 1, we observed the streaks in the zeroth-order Laue zone, indexed by (h, 0), where the integer h is a Miller index. The rods of the two-dimensional reciprocal lattice are modulated because of the few surface layers in the c^* direction of the reciprocal space. From their horizontal separation in the diffraction pattern, the lattice spacing of the Au(111) plane was obtained, which is consistent with that of the literature x-ray value ($d_{\mathrm{Au-Au}} = 2.884$ Å). We also obtained the rocking curves and observed the different orders satisfying the Bragg/Laue conditions: $s \cdot d_{(111)} = 2\pi n$, where n is the order of diffraction and s is the scattering vector, $s = (4\pi/\lambda_e)\sin(\theta/2)$, with θ being the acute deflection angle between the incident and outgoing wave vectors and λ_e the wavelength of the electron (at 30 keV, $\lambda_e \cong 0.07$ Å). From the rocking curves, the (c^*) interplanar Bragg reflections for clean and thiolated gold surfaces were identified at incidence angles of 3.4 and 4.2°, and these Bragg spots were gated to give lattice dynamics of the (111) planes at $d_{(111)} = 2.355$ Å.

The self-assembled monolayer (SAM) on gold results in a much different diffraction pattern, depending on the angle of incidence (Fig. 2). At low incidence angles (~1°), diffuse scattering was observed (Fig. 2, bottom left), while at relatively higher incidence angles (~4.2°), the gold-type behavior of Fig. 1 was basically recovered (Fig. 2, bottom right). Accordingly, the SAM reaction shown in Fig. 2 for 2-mercaptoacetic acid on gold resulted in surface diffraction of what appears to be a randomly oriented adsorbate; however, when the electron was allowed (at the larger incidence angles) to penetrate the bulk surface layers, gold diffraction was seen even with the thiolated surface layer being present. To check for the order of diffraction we compared rocking curves with and without thiolation (Fig. 2, top right). This *static* picture was completely

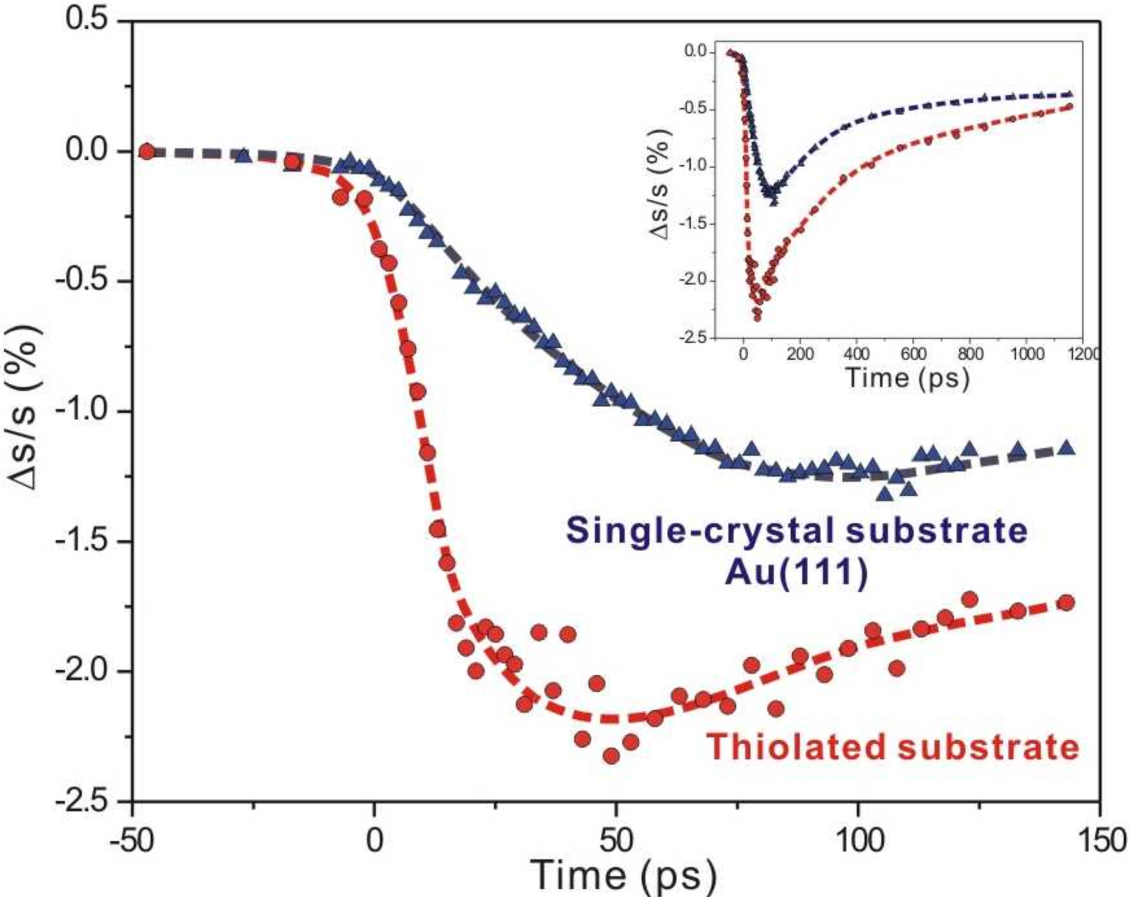

Fig. 3. Relative changes of the scattering vector *s* vs time for the Bragg spot monitored. The inset shows the restructuring on a longer time scale. The dashed lines are guides to the eye.

altered when the dynamics was obtained using ultrafast initiation by a heating pulse.

Following the ultrafast temperature jump, the structural evolution from Bragg spots was monitored: peak position (lattice expansion), width (homogeneity of the long-range order), and intensity (atomic motions). Clean and thiolated surfaces show striking differences in structural dynamics (Fig. 3). As manifested in the shift of the Bragg spot position in the diffraction pattern, the thiolated surface needs only ~20 ps to reach 80% of its maximum change. This change corresponds to a lattice expansion of 2.2%, or 52 mÅ increase in the (111) interplanar distance. For the clean gold surface,

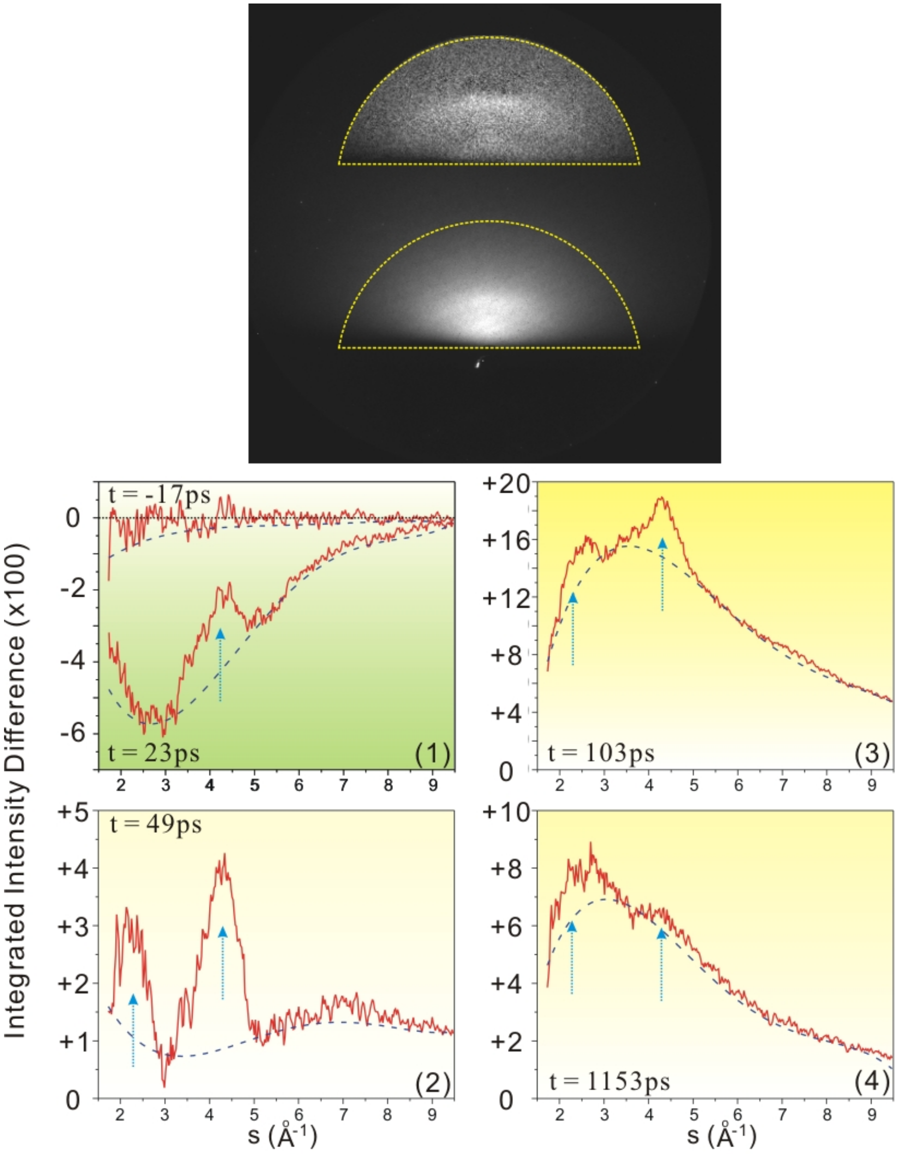

Fig. 4. (Top) Diffraction image difference following ultrafast heating of the thiolated substrates: *t* = 88 ps; reference *t* = –47 ps (upper). The lower diffraction pattern is a frame at *t* = –47 ps. (Bottom) Integrated difference of the radial average versus *s* at different delay times (t_{ref} = –47 ps). Frames 1–4 describe the following: (1) reference to negative time (–47 ps) frame at –17 ps and depletion of diffuse scattering at *t* = 23 ps; (2) coherent diffraction; (3) increase of diffuse scattering; and (4) recovery of diffuse scattering. Dashed lines represent simulated (polynomial) incoherent scattering and upward arrows indicate the positions of coherent peaks. Note the positive and negative change in the difference and the different scales used on the vertical axes.

however, it requires at least ~55 ps to reach 80%, depending on cleanliness, of its maximum change (1.3%). The determined surface movement on the order of 0.1 Å is the precursor impulse for adsorbate and bulk lattice heating.

It has been found that the degree of cleanliness and/or surface reconstruction changes the time response; e.g., freshly prepared gold samples give an even slower response. However, the distinct difference between unthiolated and thiolated surfaces is reproducible. It should be noted that the substrate–adsorbate composite fully recovers within 1 ms according to our instrumental repetition rate, as the surface is observed to restructure back to the same ground state (Fig. 3, inset); there is no influence of the probing electrons on the surface, as no irreversible loss of structure (deterioration of the diffraction pattern) was seen. Temporal evolution of the vertical width of the Bragg spot, which reflects the long-range order of the stacked (111) planes, is also noticeable: the thiolated surface shows initial broadening (loss of order) followed by narrowing of the peak (enhancement of order), while the clean gold surface shows a slower response. The decrease in peak intensity reflects change in the atomic motion and temperature, and again for the thiolated surface, the behavior is different from that of clean gold. It is noted that for a clean gold film, the temporal profiles for the position, vertical width and intensity of the Bragg spot are similar.

At an incidence angle of ~1°, i.e., gating the molecular diffraction region, we observed the emergence of Debye–Scherrer rings and the dramatic change in the diffraction background, but only after the IR laser heating (Fig. 4). In the radially averaged one-dimensional diffraction intensity curves, these changes in structural dynamics of the adsorbates were followed by monitoring the evolution of diffraction peaks and background. The near maximum formation of the long-range order is reached at 49 ps, as observed in the prominence of the coherent diffraction peaks (Fig. 4, bottom). For the incoherent scattering background, an ultrafast increase of intensity (~5 ps) just after the laser heating is noted and followed by a depletion of intensity for ~30 ps; at longer times the background continues to increase (Fig. 4, bottom). Remarkably, these difference frames are showing the *depletion* (negative difference) at early times and simultaneously the appearance of a coherent ring structure, while at longer times the diffuse signal is positively *increasing* at the expense of the coherent signal. The restructuring is not complete even at $t > 1$ ns. As noted in the inset of Fig. 3, at $t \sim 1$ ns there still remains expansion of the lattice, and similarly here the adsorbate has not fully relaxed and mostly disordered. Ultimately, the frame difference of −17 ps would be recovered, as evidenced from the decrease in scattering amplitude between the frames at long times; see, e.g., $t = 103$ and 1153 ps (Fig. 4).

Discussion

These observations are rich for deciphering structural dynamics of the substrate and adsorbate. First, the observed lattice dynamics of clean gold substrate is unexpected. Although electron–phonon coupling is known in metallic gold to occur within ~1 ps (*7, 8*), the observed increase in lattice expansion in nearly 50 ps (instead of a decrease after ~1 ps) elucidates the existence of a nonequilibrium state among the modes responsible for surface and lattice expansion. Since our electron probing region is within the optically heated depth [~13 nm; the skin depth equals to $\lambda/4\pi k$, with the imaginary part of refractive index k being ~5 at $\lambda = 800$ nm (*9*)], complete equilibration would not lead to the observation of further expansion after 1 ps.

Consistent observations have been made by Mazney *et al.* using the time-resolved probe-beam deflection technique (*10*): They found similar slow surface expansion of supported gold films on the order of 100 ps and dependent on the film thickness, and these results showed that the long surface expansion rise time is due to the fast nonequilibrium electron diffusion into the bulk and the slow, accumulated expansion at the surface with the longitudinal sound velocity of 3240 m/s (*10*). It is noted that our observed dynamics may also have contribution from the slower coupling between high-frequency (local) modes excited at an early time and the lattice acoustic (coherent and long-range) modes that lead to the expansion; at longer times the system equilibrates and the lattice restructures, as shown in Fig. 3. Because of the mismatch between mode frequencies, this behavior is reminiscent of energy redistribution in molecules (*11*), and the time constant is not significantly different from those of semiconductors (see Chs. 4 and 5).

The change in expansion dynamics from the unmodified gold surface to the thiolated surface is thus consistent with the adsorbate having many modes. The surface assembly provides another direction for the energy flow instead of the unidirectional diffusion into the bulk. In addition, excess energy can couple more effectively to the vibrational modes of the adsorbate molecules than to the mismatched low-frequency acoustic modes of bulk lattice, which practically retains more energy near the surface region (leading to a larger surface expansion) and reduces the expansion rise time, as shown in Fig. 3.

The diffraction pattern at small angle and negative time, i.e., when the electron pulse diffracts before the arrival of the heating pulse, appears to be diffuse. However, as shown in Fig. 4, the coherent scattering (Debye–Scherrer rings) becomes dominant at a positive time of $t = 49$ ps. Thus, the timing of the electron pulse is critical for structural isolation and determination. Because the *s* value below the shadow edge is ≤1.5 Å^{-1} at our incidence angle, the coherent peak positions are of n = 2 and 3. From the corresponding *s* values we obtained a lattice constant of 5±0.6 Å for the molecular assembly. This distance is reasonable given that typical S–S distance on a gold(111) surface is ~√3 times the Au–Au distance (2.884 Å), i.e., ~5 Å (*12*).

Dynamically speaking, this temporally isolated coherent diffraction from the assembly reaches its maximum but then is lost to the incoherent background at longer times, indicating that the orientational order of the assembly is dynamically controlled, and we can establish the time scale for this "ultrafast annealing." The evolution of background scattering also reflects the change in the long-range surface order and homogeneity. The initial temperature jump introduces dramatic depletion of the background within the first ~30 ps, and then a swift inversion of the trend appears, during which the molecular coherent peak sharpens and the background scattering begins to increase significantly. The initial depletion reflects the transient temperature-induced homogeneity, while after 30 ps the identity of inhomogeneous surface distributions leads to the increase of the background intensity (Fig. 4). Clearly, the time resolution is essential for isolating coherent structural dynamics of the self-assembled layers, which statistically are not ordered at long times.

Concluding Remarks

This study has demonstrated that the structure and dynamics of self-assembled monolayer and metal substrate can be isolated and studied with atomic-scale spatial and temporal resolutions and with monolayer sensitivity. This is made possible using UEC and its ability to isolate diffraction at different angles of real-time frames with atomic-scale resolution. Moreover, it is shown that for complex molecular structures, the resolution in time is crucial for observing the coherent diffraction (ordered structure), otherwise buried in diffuse scattering (disordered structure), and at long times disorder of assembly is evident. With this in mind, we also studied monolayers of alkanethiols and thio-derivatized hemes on Au(111) surfaces, and were able to record the diffractions and their changes with time although the patterns are diffuse. Intriguingly, horizontal (asymmetric) intensity redistribution in the diffuse scattering was seen from heme samples at positive times, which, on the basis of the annealing phenomenon described previously, can be attributed to the transient reorganization of the sulfur–gold bonds at the interface and rotation of the heme groups, causing changes in the efficiency of electron scattering in the horizontal direction. In the future, the applications of UEC to SAMs of other biological networks may reveal other structural and dynamical information of interest.

References:

1. C. D. Bain, G. M. Whitesides, *Science* **240**, 62 (1988) and cited references therein.
2. M. Shimizu *et al.*, *Biochem. Biophys. Res. Commun.* **310**, 606 (2003) and cited references therein.
3. M. T. Seidel, S. Chen, A. H. Zewail, *J. Phys. Chem. C* **111**, 4920 (2007).
4. S. Chen, Ph.D. thesis, California Institute of Technology (2007).
5. R. Srinivasan, V. A. Lobastov, C. Y. Ruan, A. H. Zewail, *Helv. Chim. Acta* **86**, 1763 (2003).
6. R. G. Nuzzo, D. L. Allara, *J. Am. Chem. Soc.* **105**, 4481 (1983).
7. C. K. Sun, F. Vallée, L. H. Acioli, E. P. Ippen, J. G. Fujimoto, *Phys. Rev. B* **50**,

15337 (1994) and cited references therein.

8. C. Suárez, W. E. Bron, T. Juhasz, *Phys. Rev. Lett.* **75**, 4536 (1995) and cited references therein.
9. P. B. Johnson, R. W. Christy, *Phys. Rev. B* **6**, 4370 (1972).
10. A. A. Maznev, J. Hohlfeld, J. Güdde, *J. Appl. Phys.* **82**, 5082 (1997) and cited references therein.
11. P. M. Felker, A. H. Zewail, *Phys. Rev. Lett.* **53**, 501 (1984).
12. A. Ulman, *Chem. Rev.* **96**, 1533 (1996).

Chapter 12

Theoretical Modeling of Structural Dynamics[†]

[†] adapted from J. Tang, D.-S. Yang, A. H. Zewail, *J. Phys. Chem. C* **111**, 8957 (2007).

Introduction

The developments in ultrafast electron crystallography (UEC) have provided the means to study structural dynamics following femtosecond optical excitations. Some of the systems investigated are metallic (Ch. 11) and semiconducting (Ch. 4) materials and oriented molecules on a substrate (*1*). In these studies, a general behavior was found; namely, a large-amplitude expansion of the lattice structure on the ultrashort time scale and restructuring at longer times. Such structural dynamics were directly derived from the temporal change of the position of Bragg spots (or diffraction rings), which are often accompanied by similar temporal profiles for the diffraction intensities and widths.

The pertinent questions are several: What causes the large structural change at short times? What is the atomic-scale description of the phenomena? What determines the time scales for reaching the maximum change and for restructuring? In previous chapters, the transient lattice expansion in semiconductors was shown to be potential-driven with a critical role for phonon-induced coherent motion (Chs. 4 and 5). The time scales of hot carriers and their interactions with phonons, and the relaxation through subsequent phonon–phonon couplings, were also shown to be important in the description of the dynamics. However, a theory at the microscopic level is necessary for further investigation of the forces controlling the atomic-scale motions. Such a model may also be important for elucidation of laser-induced melting and ablation (*2-4*) and acoustic wave generation (*5-14*), and for studies involving transient optical reflectivity (*15-17*), time-resolved x-ray diffraction (*18-24*), and transmission electron diffraction of metals (*25-27*).

In this chapter, a theoretical study is presented for the investigation of the atomic forces responsible for the structural changes of substrates and adsorbates following an optical excitation. For the simplest case, the substrate–adsorbate system can be modeled as atoms connected by harmonic oscillators in linear chains, taking into account frictional damping and the external driving force. The impulse-induced structural dynamics of this array of atoms was simulated for forces with different functional forms. The time dependence of the position of Bragg diffraction spots was systematically analyzed in order to determine the relevant controlling factors. Comparison with the experimental results was then made.

In what follows, it will be shown that, following an ultrashort impulse, a thin film (~30 nm) may exhibit cycles of oscillatory expansion and contraction that disappear in a thick substrate. Unlike the ordinary linear expansion in static, thermal equilibrium, which is incoherent and has its origin in the (local) anharmonicity of the crystal potential, the large-amplitude expansion is driven by the impulsive force, which results in a coherent, nonlocal sound wave effect. Such expansion is followed by a slow decay, cycles of periodic expansion and contraction, or both. For adsorbates, this far-from-equilibrium expansion, with some contraction at short times, is also observed. The maximum shift of a Bragg spot and the corresponding delay time are found to be dependent on the chain length of the adsorbate and on the nature of the coupling between the substrate and adsorbate.

This chapter is organized as follows: All of the relevant terms used in this work are summarized in Table 1. In the Theory Section, the model Hamiltonian and the equations of motion for the substrate and adsorbate atoms are described, together with the needed diffraction expressions of UEC. Afterward, the methodology and results of numerical simulations are presented. Discussions of the importance of different parameters and their association with real systems are provided before the conclusion.

Table 1: Nomenclature for Symbols

N (N_{A})	no. of substrate (adsorbate) atoms in the 1D array
z_n (Z_n)	displacement of the nth atom in the substrate (adsorbate)
m (m_{A})	mass of a substrate (adsorbate) atom
ω (ω_{A})	angular frequency of the spring in the substrate (adsorbate)
ℓ (ℓ_A)	interatomic distance between substrate (adsorbate) atoms at equilibrium; lattice spacing
γ	friction coefficient; frictional damping factor for the spring oscillations
F_n (G_n)	external impulsive force on the nth atom in the substrate (adsorbate)
L	thickness of the substrate; $L \equiv (N-1)\,\ell$
Λ_{F}	attenuation length of the impulsive force
τ_{rise} and τ_{decay}	rise and decay time constants of the impulsive force
v_{s}	sound velocity in the substrate; $v_{\mathrm{s}} = \ell\,\omega$
s	wavevector change (in the crystallographer's convention) of the elastically scattered electrons along the surface normal direction
$\langle \Delta s(t) \rangle$	shift of the peak position of the first-order Bragg spot
ζ_{e}	penetration depth of the probing electrons
τ_{S}, τ_{A}, τ_{SA}	effective time constants for heat transfer between adjacent atoms in the substrate, in the adsorbate, and across the adsorbate–substrate interface, respectively

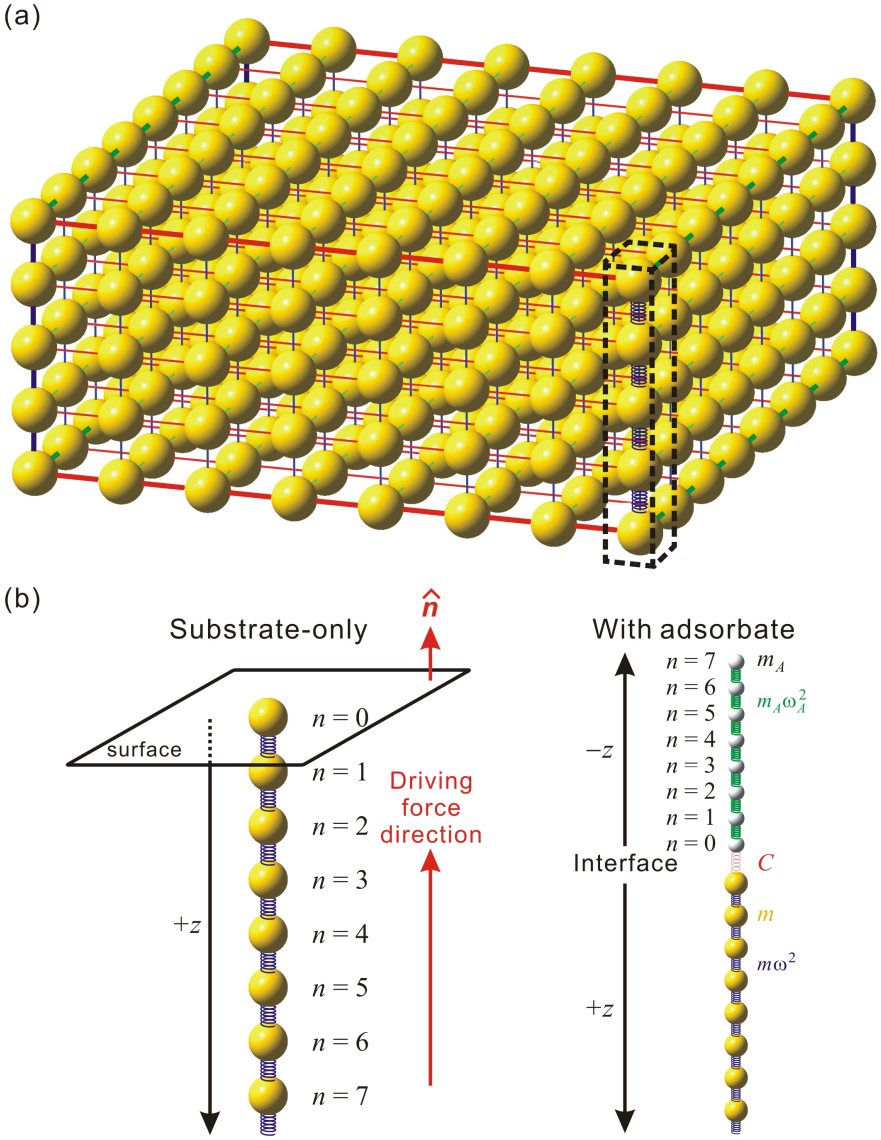

Fig. 1. Atomic picture of the substrate/adsorbate composite system. (a) A 3D simple lattice. Each lattice site is an atom that is connected to the neighboring ones by springs. The 3D lattice is further simplified as a 1D array of atoms along the surface normal direction (black dashed box) (b) The 1D atomic arrays considered in our microscopic model for only the substrate (left) and for the substrate/adsorbate composite system (right). The surface normal and driving-force directions are indicated, and the indices of atoms are shown. Masses of the substrate and adsorbate atoms and the force constants for different bondings are labeled with the corresponding colors.

Theory: Microscopic Models and Structural Dynamics

Here, a simple lattice consisting of arrays of atoms connected by springs is considered (Fig. 1). Due to the stress constraints of the surface and the geometry of the laser-excited region, lattice expansion occurs mainly along the surface normal direction. In the expansion-restricted, two-dimensional (2D) horizontal directions on the surface, hundreds of micrometers to a few millimeters (relatively uniform with a low excitation gradient) are covered, whereas the lattice under the excitation of only nanometer-to-micrometer penetration into the bulk (high excitation gradient) is free to expand along the surface normal direction (Ch. 4). Thus, the 3D lattice (Fig. 1a) can be further simplified as spring-connected atoms in a 1D chain, and such simplification should not be of major consequence in the description of dynamical phenomena on the time scale of interest. The same consideration can also be applied to the modeling of adsorbates on a substrate (Fig. 1b). In the following section, we first consider this microscopic model for the substrate and derive the analytical solutions for the atomic motions under the influence of impulsive force; manifestations of such dynamics in the UEC patterns will be deduced. The microscopic model for adsorbate molecules on the substrate will then be provided.

A. Substrates

The substrate atoms, each with a mass, m, are coupled to their nearest neighbors through harmonic springs with a force constant $m\omega^2$, where ω is the angular frequency. Due to the aforementioned excitation geometry, the external force, induced by a femtosecond laser pulse, is taken to be parallel to the z axis (the chain axis), and it causes atomic motions along this direction. Therefore, the Hamiltonian for a chain of N atoms is given by

$H_S = \sum_{n=0}^{N-1} \frac{p_n^2}{2m} + \frac{m\omega^2}{2} \sum_{n=0}^{N-2} (z_n - z_{n+1})^2$; the atoms are indexed from $n = 0$ to N–1, and p and z are the momentum and displacement, respectively. [See Appendix A for the application of the more general Fermi–Pasta–Ulam model (*28*), which contains an anharmonic cubic term in the Hamiltonian.]

If the vibrational motion is damped by a frictional force and the nth atom is subject to an external impulsive force, $F_n(t)$, the equations of motion for such a system are given by

$$\begin{aligned}
&\frac{d^2}{dt^2} z_0 + \gamma \frac{d}{dt} z_0 + \omega^2 (z_0 - z_1) = \frac{F_0(t)}{m}, \\
&\frac{d^2}{dt^2} z_n + \gamma \frac{d}{dt} z_n + \omega^2 (2z_n - z_{n-1} - z_{n+1}) = \frac{F_n(t)}{m}, \quad (n = 1, 2, \cdots, N-2) \qquad (1) \\
&\frac{d^2}{dt^2} z_{N-1} + \gamma \frac{d}{dt} z_{N-1} + \omega^2 (-z_{N-2} + z_{N-1}) = \frac{F_{N-1}(t)}{m},
\end{aligned}$$

where γ is a friction parameter; here, we loosely term a friction coefficient. With the initial condition at time zero for the nth atom (defining $\dot{z}_n(0)$ and $z_n(0)$ as the velocity and displacement at time $t = 0$), Eq. 1 can be solved analytically (see Appendix B for details). The closed-form solution is

$$\begin{aligned}
z_n(t) = {} & \frac{1}{N} \sum_{j=0}^{N-1} \left[z_j(0) + \dot{z}_j(0) \frac{1 - e^{-\gamma t}}{\gamma} + \frac{1}{M} \int_0^t d\tau\, F_j(\tau) \frac{1 - e^{-\gamma(t-\tau)}}{\gamma} \right] \\
& + \frac{2}{N} \sum_{k=1}^{N-1} \sum_{j=0}^{N-1} \cos\left(\frac{\pi k}{N} \left(n + \frac{1}{2} \right) \right) \cos\left(\frac{\pi k}{N} \left(j + \frac{1}{2} \right) \right) \times \qquad (2) \\
& \left[\begin{array}{l} z_j(0) e^{-\frac{\gamma t}{2}} \left(\cos(\Lambda_k t) + \dfrac{\gamma \sin(\Lambda_k t)}{2\Lambda_k} \right) + \dot{z}_j(0) e^{-\frac{\gamma t}{2}} \dfrac{\sin(\Lambda_k t)}{\Lambda_k} \\ + \dfrac{1}{m} \displaystyle\int_0^t d\tau\, F_j(\tau) e^{-\frac{\gamma(t-\tau)}{2}} \dfrac{\sin(\Lambda_k (t-\tau))}{\Lambda_k} \end{array} \right],
\end{aligned}$$

where $M \equiv Nm$, $\Lambda_k = \Omega_k\sqrt{1-\left(\gamma^2/4\Omega_k^2\right)}$ for the kth normal mode, and $\Omega_k = 2\omega \sin(\pi k/2N)$, which is the angular frequency if friction is absent. The first sum in Eq. 2 describes the motion for the center of mass of the chain. It can be omitted if the concern is only for the relative motions between atoms. The remaining part in Eq. 2 describes the motion of each atom and, therefore, is relevant to the observations made by diffraction methods; the intensity and position of a Bragg diffraction spot depend on the relative atomic distances but not on the absolute position of the center of mass.

The index k (from 1 to N–1) enumerates the normal modes in the atomic chain. Accordingly, two eigenvalues, λ_{1k} and $\lambda_{2k} = -\gamma/2 \pm i\Lambda_k$, are found for each vibrational mode; their appearance in the exponents determines the type of atomic motions that may be seen. If the friction coefficient, γ, is small (the underdamped regime), $i\Lambda_k$ is a pure imaginary number which leads to an oscillatory motion, $\exp(i\Lambda_k)$. Because of the dependence of Ω_k on the wavevector (defined as $\pi k/N\ell$, where ℓ is the lattice spacing), this dispersion relation indicates that wave propagation may be expected, and the slope near zero wavevector gives the speed of sound. In contrast, if γ is much greater than $\Omega_k/2$ (the overdamped regime), $i\Lambda_k$ becomes a real number, and nonoscillatory damped motions are to be expected in the array of atoms.

The regimes of underdamped (coherent) and overdamped (diffusive) atomic motions can be seen in the form of Eq. 1 in the continuum limit. The present harmonic model for a discrete lattice array can be simplified in the limit of a small ℓ, relative to the spatial profile of the impulsive force. The discrete rate equation for each site can then be approximated by a differential equation involving a continuous position variable, z. With the definitions of total elastic modulus, $K \equiv m\omega^2/(N-1)$, and total length $L \equiv (N-1)\ell$, Eq. 1 reduces in the continuum limit to

$$\frac{\partial^2}{\partial t^2}q(z,t)+\gamma\frac{\partial}{\partial t}q(z,t)-\frac{KL^2}{M}\frac{\partial^2}{\partial z^2}q(z,t)=\frac{F(z,t)}{M}, \tag{3}$$

where $q(z, t)$ is the vibrational amplitude at position z and time t, and $F(z, t)/M$ is the force per unit mass. In the absence of friction, that is, when $\gamma = 0$, Eq. 3 becomes

$$\frac{\partial^2}{\partial t^2}q(z,t)-\frac{KL^2}{M}\frac{\partial^2}{\partial z^2}q(z,t)=\frac{F(z,t)}{M}, \tag{4}$$

which resembles the inhomogeneous 1D wave equation with a propagation speed (sound velocity) $v_{\mathrm{S}} \equiv L\sqrt{K/M} = \ell\,\omega$. Note that this value is exactly the slope of the aforementioned dispersion relation (Ω_k vs $\pi k/N\ell$) near zero wavevector: $[\mathrm{d}\Omega_k/\mathrm{d}(\pi k/N\ell)]_{k\to 0} = \ell\,\omega$.

On the other hand, in the overdamped regime with $\gamma \gg \omega$, and for $t \gg \gamma/\omega^2$, Eq. 3 can be approximated by

$$\frac{\partial}{\partial t}q(z,t)-\frac{KL^2}{M\gamma}\frac{\partial^2}{\partial z^2}q(z,t)=\frac{F(z,t)}{M\gamma}, \tag{5}$$

which is in the form of a 1D diffusion equation with a diffusion constant $D \equiv KL^2/M\gamma = \omega^2\ell^2/\gamma = \ell^2/\tau_{\mathrm{D}}$, where τ_{D}, or γ/ω^2, is the diffusion correlation time. Thus, the more general Eq. 3 bridges two extremes, the wave equation of Eq. 4 and the diffusion equation of Eq. 5, with each regime representing one type of atomic motion.

B. Observables in UEC

On the basis of the aforementioned model, the position of the nth atom along the chain direction (which is opposite to the surface normal) is $n\ell + z_n(t)$, where $z_n(t)$ is its time-dependent displacement from the equilibrium position. Given such a geometry at time t, the amplitude $A(\vec{s},t)$ of the elastically scattered electrons, with the momentum transfer $\hbar\cdot 2\pi\vec{s}$ being parallel to the surface normal, is the Fourier transform (*29*) of the potential U_n of the nuclei and electrons in the s domain,

$$\begin{aligned} A(\vec{s},t) &= \sum_{n=0}^{N-1} \int d^3 r_n\, U_n(\vec{r}_n)\, e^{i2\pi\vec{s}\cdot\vec{r}_n}\, e^{i2\pi|\vec{s}|(n\ell+z_n(t))} \\ &= \sum_{n=0}^{N-1} e^{i2\pi|\vec{s}|(n\ell+z_n(t))}\, \overline{U}_n(\vec{s}), \end{aligned} \tag{6}$$

where $\overline{U}_n(\vec{s}) \equiv \int d^3 r_n\, U_n(\vec{r}_n)\, e^{i2\pi\vec{s}\cdot\vec{r}_n}$; the wavevector, $\vec{s}$, is defined here using the crystallographer's convention. The atomic scattering factor, $\overline{U}_n(\vec{s})$, for electron diffraction for the *n*th atom may be approximated by a Gaussian function of the wavevector $s \equiv |\,\vec{s}\,|$, expressed as $\exp(-\pi^2 s^2 / 2\sigma_{\mathrm{S},n}^2)$, with the Debye–Waller factor included. The subscript S stands for substrate. For an array of N identical atoms, $\overline{U}_n(\vec{s})$ is independent of the site index n, and the normalized diffraction intensity, $I_\mathrm{S}(s, t)/I_0$ (relative to the direct beam intensity I_0), for a given s becomes

$$\frac{I_S(s,t)}{I_0} = \left|\frac{A(\vec{s},t)}{N}\right|^2 = \left|\frac{1}{N}\sum_{n=0}^{N-1} \exp\!\left[-\pi^2 s^2/2\sigma_\mathrm{S}^2 + i\,2\pi s\left(n\,\ell + z_n(t)\right)\right]\right|^2 . \tag{7}$$

For all simulations presented in this study, $\sigma_\mathrm{S}\ell = 5$ is used so that higher-order Bragg spots are attenuated when compared with the first-order one.

Because of the periodicity of the lattice, $I_\mathrm{S}(s, t)$ exhibits a sinc-function dependence on s whenever $s\,\ell$ is close to an integer. If there are no atomic displacements, that is, $z_n(t) = 0$ for all lattice sites, the jth Bragg spot will peak at $s = j/\ell$. If all N atoms are assumed to contribute to the Bragg diffraction, the first moment of $I_\mathrm{S}(s, t)$ (i.e., the peak shift of the Bragg diffraction, $\langle \Delta s(t)\rangle_\mathrm{S}$) for the first Bragg spot at $s \sim 1/\ell$ can be calculated using

$$\left\langle \Delta s(t)\right\rangle_S \equiv \frac{\int_{s_1}^{s_2} ds\; s\, I_S(s,t)}{\int_{s_1}^{s_2} ds\; I_S(s,t)} - \frac{1}{\ell}, \tag{8}$$

where $s_1 = (1 - 1/N)/\ell$ and $s_2 = (1 + 1/N)/\ell$ correspond to the edges of the central Bragg peak near $1/\ell$; the width of the central dominant lobe of $I_S(s, t)$ is inversely proportional to $N\ell$. It follows that information about lattice dynamics can be obtained by monitoring $\langle \Delta s(t) \rangle_S$, the deviation of the average peak position at time t.

Due to the large kinetic energy of the probing electrons used in UEC, low-order Bragg diffraction can only be observed at a grazing incidence angle. In such a reflection geometry, because of the large electron–material scattering cross section and the small penetration depth of the incident electrons, a smaller number of (fewer layers of) atoms N_B near the surface contribute to the Bragg diffraction substantially. Therefore, N in Eqs. 7 and 8 needs to be replaced by N_B in order to take this attenuation effect into account; or more precisely, if ζ_e ($\zeta_e/N\ell \ll 1$) is the penetration depth of the electron beam, Eq. 7 can be replaced by

$$\frac{I_S(s,t)}{I_0} = \left| \frac{1}{N} \sum_{n=0}^{N-1} \exp\left[-\pi^2 s^2 / 2\sigma_S^2 + i 2\pi s \left(n\ell + z_n(t) \right) - n\ell / \zeta_e \right] \right|^2 . \tag{9}$$

The lower and upper bounds for the integration in Eq. 8 accordingly change to $s_1 = 1/\ell - 1/\zeta_e$ and $s_2 = 1/\ell + 1/\zeta_e$.

C. Adsorbates

So far, only the substrate has been considered. The above harmonic model for a substrate slab can be further extended to include chainlike molecules oriented on the substrate surface. We shall consider two connected chains along a 1D line, with the bottom region representing the substrate and the top the adsorbate, as illustrated in Fig. 1b. The total Hamiltonian H is then given by

$$\begin{aligned}
&H = H_{\mathrm{S}} + H_{\mathrm{A}} + H_{\mathrm{AS}}\,,\\
&H_{\mathrm{S}} = \sum_{n=0}^{N-1} \frac{p_n^2}{2m} + \frac{m\omega^2}{2} \sum_{n=0}^{N-2} \left(z_n - z_{n+1}\right)^2,\\
&H_{\mathrm{A}} = \sum_{n=0}^{N_{\mathrm{A}}-1} \frac{P_n^2}{2m_{\mathrm{A}}} + \frac{m_{\mathrm{A}}\,\omega_{\mathrm{A}}^2}{2} \sum_{n=0}^{N_A-2} \left(Z_n - Z_{n+1}\right)^2,\\
&H_{\mathrm{SA}} = \frac{C}{2}\left(z_0 - Z_0\right)^2,
\end{aligned} \tag{10}$$

where H_{S} is the Hamiltonian for the substrate, H_{A} describes a monolayer of chainlike adsorbates with N_{A} atoms (each has a mass m_{A}, and the spring constant is $m_{\mathrm{A}}\omega_{\mathrm{A}}^{2}$), and H_{SA} describes the coupling; the subscript A stands for adsorbate. The lower-case letters p and z denote the momentum and displacement for a substrate atom, and the capital letters P and Z, for an atom of the adsorbate molecule. The equations of motion according to such a Hamiltonian, with additional frictional force and external impulsive force $F_n(t)$ on the nth substrate atom and $G_n(t)$ on the nth adsorbate atom, can be written as

$$\begin{aligned}
&\frac{d}{dt} z_n = \frac{p_n}{m} \quad (n = 0, \ldots, N-1)\\
&\frac{d}{dt} Z_n = \frac{P_n}{m_{\mathrm{A}}} \quad (n = 0, \ldots, N_{\mathrm{A}}-1)
\end{aligned} \tag{11}$$

and

$$\begin{aligned}
&\frac{d}{dt} p_0 = F_0(t) - \gamma\, p_0 - m\omega^2 (z_0 - z_1) - C(z_0 - Z_0)\\
&\frac{d}{dt} p_n = F_n(t) - \gamma\, p_n - m\omega^2 (2z_n - z_{n-1} - z_{n+1}) \quad (n = 1, \ldots, N-2)\\
&\frac{d}{dt} p_{N-1} = F_{N-1}(t) - \gamma\, p_{N-1} - m\omega^2 (z_{N-1} - z_{N-2})\\
&\frac{d}{dt} P_0 = G_0(t) - \gamma_A\, P_0 - m_A\omega_A^2 (Z_0 - Z_1) - C(Z_0 - z_0)\\
&\frac{d}{dt} P_n = G_n(t) - \gamma_A\, P_n - m_A\omega_A^2 (2Z_n - Z_{n-1} - Z_{n+1}) \quad (n = 1, \ldots, N_A - 2)\\
&\frac{d}{dt} P_{N_A-1} = G_{N_A-1}(t) - \gamma_A\, P_{N_A-1} - m_A\omega_A^2 (Z_{N_A-1} - Z_{N_A-2})\,.
\end{aligned} \tag{12}$$

Similar to the structural dynamics of the adsorbate, the normalized diffraction intensity $I_A(s, t)$ for an N_A-unit chainlike molecule is given by

$$\frac{I_A(s,t)}{I_0} = \left| \frac{1}{N_A} \sum_{n=0}^{N_A - 1} \exp\left[-\pi^2 s^2 / 2\sigma_A^2 + i 2\pi s \left(-n \ell_A + Z_n(t) \right) \right] \right|^2 , \tag{13}$$

where the negative sign for the phase $2\pi s(-n \ell_A)$ from the nth atom is due to our convention of indexing adsorbate atoms on the $-z$ axis and substrate ones on the $+z$. For the first-order Bragg spot, $\langle \Delta s(t) \rangle_A$ is given by

$$\left\langle \Delta s(t) \right\rangle_A \equiv \frac{\int_{s_1}^{s_2} ds \, s \, I_A(s,t)}{\int_{s_1}^{s_2} ds \, I_A(s,t)} - \frac{1}{\ell_A}, \tag{14}$$

where $s_1 = (1 - 1/N_A)/\ell_A$ and $s_2 = (1 + 1/N_A)/\ell_A$.

Numerical Simulations and Results

A. Methodology: The Substrate

To understand the manifestations of dynamical changes of the substrate lattice structure in diffraction, we shall calculate $z_n(t)$ using the analytical solution of Eq. 2 or the numerical solution of Eq. A2, followed by the computation of $\langle \Delta s(t) \rangle_S$ using Eq. 8. It is therefore necessary to specify the temporal and spatial profiles of the driving force, $F_n(t)$, in order to proceed with the calculations. For simplicity, this impulsive force is assumed to extend spatially into the substrate slab with an exponential attenuation, that is, $F_n(t) = F_0(t) \cdot \exp(-n \ell / \Lambda_F)$, where Λ_F is the attenuation length.

The temporal profile of the stress impulse $F_0(t)$ can take a pulse shape such as a Gaussian or a stretched exponential function. For the former case, $F_0(t) = -|F_0| \cdot \exp(-(t-\tau_0)^2/2\tau_p^2)$, where τ_0 is the delay time and τ_p is the duration of the impulse;

the negative sign of F_0 is due to the convention of placing the lattice sites on the $+z$ axis and therefore the laser-induced expansion impulse being along the $-z$ direction. For the latter case, we consider the stretched exponential function in the form of $f(t/\tau) \equiv \exp(-\sqrt{t/\tau})$, and the temporal stress profile to be $F_0(t) = -|F_0|\cdot[-f(t/\tau_{\text{rise}})+f(t/\tau_{\text{decay}})]/[-f(\tau_{\text{max}}/\tau_{\text{rise}})+f(\tau_{\text{max}}/\tau_{\text{decay}})]$; such a profile with a decay time τ_{decay} longer than the rise time τ_{rise} (i.e., $0 < \tau_{\text{rise}} < \tau_{\text{decay}}$) reaches its maximum amplitude at $t = \tau_{\text{max}}$, where $\sqrt{\tau_{\text{max}}} = \ln\sqrt{\tau_{\text{decay}}/\tau_{\text{rise}}} \Big/ \left(\sqrt{\tau_{\text{rise}}^{-1}} - \sqrt{\tau_{\text{decay}}^{-1}}\right)$. Compared to the Gaussian profile, the stretched exponential form has a longer trailing tail, which may represent better the actual stress caused by the change of crystal potential, lattice temperature in the substrate, or both; that is, the impulse represents an "induced force" or "temperature jump" rather than the ultrashort laser pulse itself. The physical meanings of the rise and decay time constants will be addressed in the Discussion Section.

Another type of temporal profile for the impulsive force may originate from a diffusion-controlled mechanism such as carrier diffusion, heat conduction, or both. In this case, the long-time decay of the impulse follows a temporal dependence of $1/\sqrt{t}$. To take into account the rise of the impulse and the diffusion-type decay at longer times, we can have the temporal impulse profile expressed as

$$F_0(t) = -|F_0|\cdot[(1-\exp(-t/\tau_{\text{rise}}))(1+\tau_{\text{max}}/\tau_{\text{decay}})^{1/2}]/[(1-\exp(-\tau_{\text{max}}/\tau_{\text{rise}}))(1+t/\tau_{\text{decay}})^{1/2}]$$

with $0 < \tau_{\text{rise}} < \tau_{\text{decay}}$, where $\tau_{\text{max}} \equiv \tau_{\text{rise}}\cdot\ln(3 + 2\tau_{\text{decay}}/\tau_{\text{rise}})$ is the time for $|F_0(t)|$ to reach its maximum. Following such an impulse profile, it will be shown that the temporal evolution of $\langle\Delta s(t)\rangle_{\text{S}}$, when displayed on a logarithmic scale in time, reflects the simple dependence of $1/\sqrt{t}$ at longer times, which has been observed experimentally (Ch. 4).

The parameters deduced from the properties of gold are used for the following

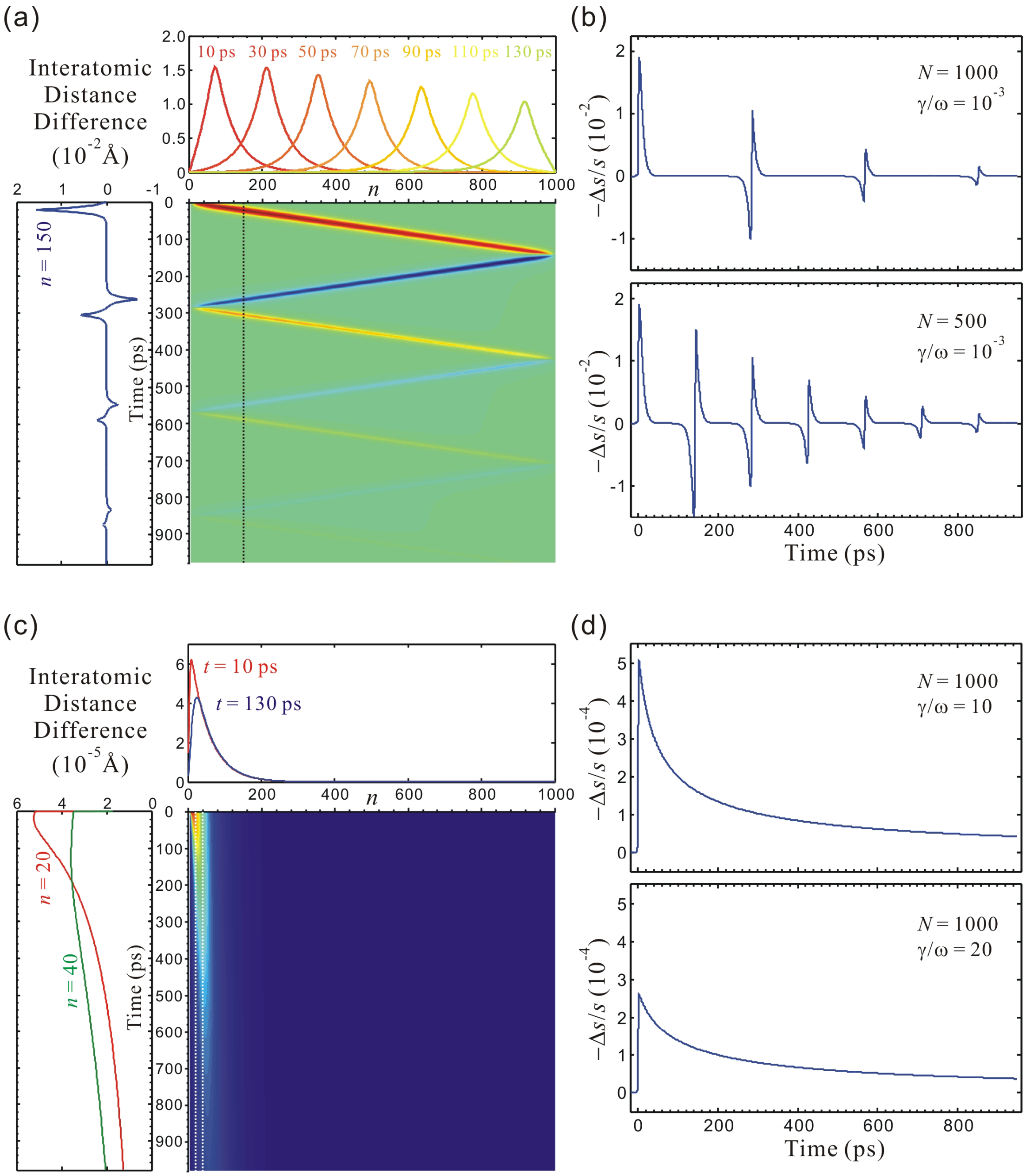

(See next page for the figure caption.)

Fig. 2. Substrate structural dynamics. Both the underdamped and overdamped regimes are considered in the time domain and diffraction space. The external force has a temporal profile of the stretched exponential functional form with $\tau_{\text{rise}} = \tau_{\text{decay}} = 1$ ps, an attenuation length $\Lambda_{\text{F}} = 50\,\ell$, and a maximum value $|F_0| = 10^{-11}$ N; $N = 1000$. (a) The underdamped regime with $\gamma/\omega = 10^{-3}$. The temporal and spatial dependence of the interatomic distance change, $z_n(t) - z_{n-1}(t)$, is shown in a 2D plot. The zigzag pattern clearly shows the nature of wave propagation for lattice deformation in the slab; the upper panel shows the lattice deformation at selected times and illustrates the wave propagation phenomenon. The waveform travels at the speed of sound (2030 m/s), which is evident from the time (~280 ps) when the wave returns to the surface (i.e., the round-trip traveling time). The left panel shows the temporal dependence of the interatomic distance change at a given site $n = 150$. (b) Temporal dependence of the relative change in the peak position of the first-order Bragg spot, $-\Delta s/s$; the electron probing depth $\zeta_{\text{e}} = 10\,\ell$ covers the lattice changes near the surface only. A positive (negative) diffraction change refers to expansion (contraction) of the lattice in the surface region. Manifestation of the propagation of the lattice deformation waveform can be found from the recurrence of diffraction changes (upper); the recurrence period is reduced by half if the slab thickness is halved (lower). The decay of the signal is due to the frictional damping. (c) The overdamped regime with $\gamma/\omega = 10$. Compared to the 2D plot in panel a, the fast wave propagation (the zigzag pattern) disappears and is replaced by much slower temporal evolution of lattice changes. Note that the change of interatomic distances is more than 2 orders of magnitude smaller than those in panel a. In addition, due to the strong frictional damping, the changes are rather limited within the top of the slab (upper panel), and their slow time scale can be seen more clearly in the left panel. (d) $-\Delta s/s$ vs time. The diffraction change is much smaller than that in panel b, and its temporal evolution is slow (upper). With a larger friction coefficient, the diffraction change becomes even smaller and is on an even longer time scale (lower).

numerical simulations. First, the propagation velocity v_s (= $\ell\,\omega$ in the continuum and friction-free limit) is presumed to be equal to the experimentally measured sound velocity of 2030 m/s for the extensional mode (*30*). With ℓ being equal to the smallest spacing between atoms in crystalline gold (2.88 Å), we obtain $\omega = 7.05\times10^{12}$ rad/s, or $\nu = \omega/2\pi = 37\ \text{cm}^{-1}$. Each gold atom has a mass of $m = 3.27\times10^{-25}$ kg, which therefore leads to a force constant of $m\omega^2 = 16.3$ N/m. As for the consideration of a moderate driving force, $|F_0|$ is chosen to be 10^{-11} N. We use $\zeta_e/\ell = 10$ to take into account the finite penetration depth of the probing electrons in the substrate. For the structural dynamics probed by UEC, the substrate is at its thermal equilibrium prior to the laser excitation; thus, for simplicity, the initial velocities and atomic displacements from the equilibrium positions are all taken to be 0 at negative times.

B. Substrate Structural Dynamics

To illustrate the different atomic motions in the underdamped and overdamped regimes, we plot in Fig. 2 the results of numerical simulations for $z_n(t)$ and the corresponding diffraction spot shift $\langle\Delta s(t)\rangle_S$ using the same parameters and external force (stretched exponential function for the temporal profile), except for the value of γ. It is clear that in the underdamped regime, wave propagation inside the slab and reflection at the boundaries are the dominant features of the atomic motions (the zigzag pattern in Fig. 2a); the value of the friction coefficient determines the rate of the waveform damping at longer times. For a slab of $N = 1000$, the traveling time required for a round trip is ~280 ps, and it is reduced by half if the slab thickness is halved (Fig. 2b). Upon the return of the waveform to the surface, a contraction is seen first and closely followed by the expansion; this lattice contraction exists because the returning expansion waveform compresses the surface lattice from underneath before it is reflected at the free boundary

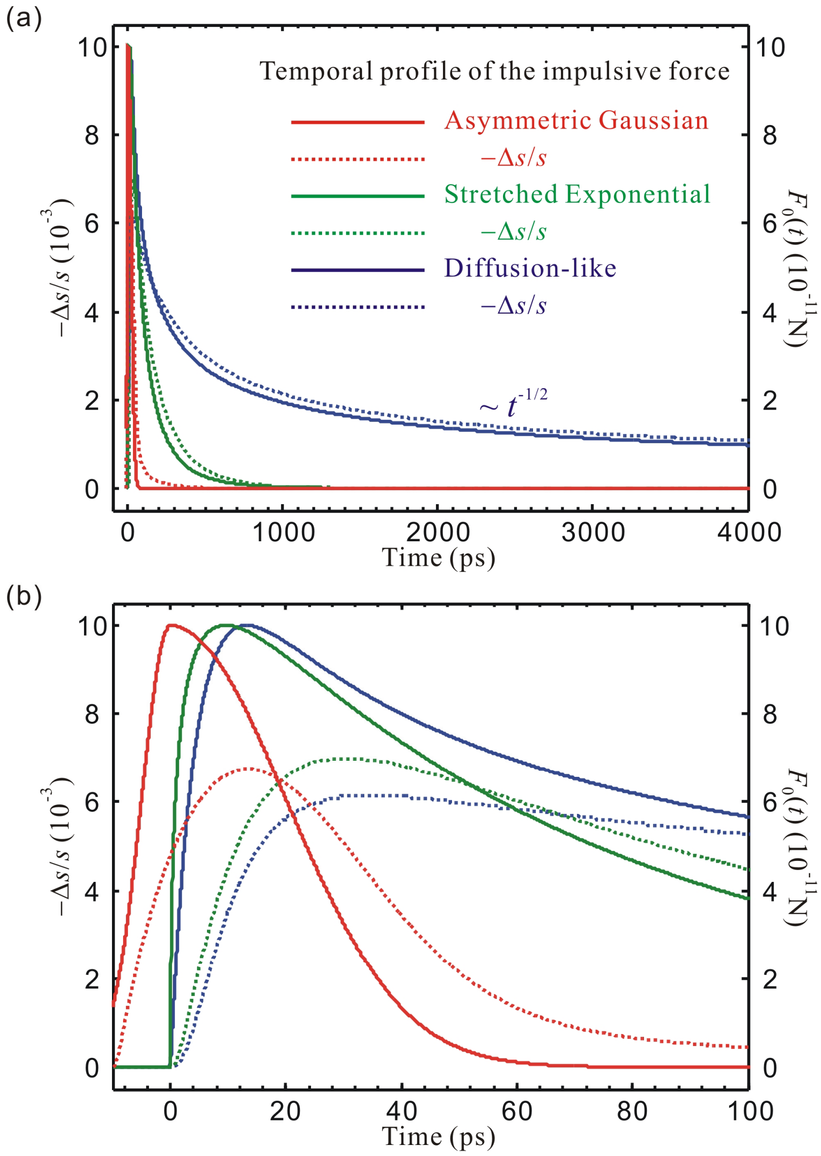

Fig. 3. Effect of force profile on diffraction change with time. Different temporal force profiles $F_0(t)$ and the corresponding diffraction changes, $-\Delta s/s$, are shown on (a) longer and (b) shorter time scales. The common parameters are $N = 1000$, $\gamma/\omega = 10^{-2}$, $|F_0| = 10^{-11}$ N, $\Lambda_F = 500\,\ell$, $\tau_{\mathrm{rise}} = 5$ ps, $\tau_{\mathrm{decay}} = 20$ ps, and $\zeta_e = 10\,\ell$. (a) On a longer time scale, $-\Delta s/s$ resembles $F_0(t)$; for the external force with a diffusion-like temporal dependence ($\sim t^{-1/2}$), the corresponding diffraction change also exhibits a similar behavior. (b) For a given $|F_0|$, the maximum change in $-\Delta s/s$ is similar, and its appearance time follows the peak of the impulse profile.

and leads to the surface expansion. It is noted that broadening of the traveling lattice deformation is minor due to the long-wave propagation (a width of ~50 ℓ) considered here.

In contrast, the diffusive nature of the atomic motions is seen in the overdamped regimes (Fig. 2c); not many features can be observed from the structural dynamics, except for the diffusion-type slow decay after an initial rise (Fig. 2d). A larger γ leads to a smaller diffraction spot shift initially. At a first glance, the temporal behavior of the decay seems to resemble the experimentally observed dynamics, but the very small magnitude of spot shift (at least an order of magnitude less than that in the underdamped regime) does not match with our experimental observations of large lattice expansions. In addition, the physical properties of crystalline materials negate the large-friction scenario: the phenomenon of sound wave propagation always exists in ordered solids. It is noted that, according to Eq. 5 with a given D, the diffusion time scale for a distance of electron probing ($\zeta_e = 10\ \ell$), which governs the decay of the $\langle \Delta s(t) \rangle_S$ signal, becomes $(\zeta_e / \ell)^2\ \tau_D = (\zeta_e / \ell)^2 (\gamma / \omega^2) = 14.2\ (\gamma / \omega)$ ps (Fig. 2d, on the order of hundreds of picoseconds). A large γ might probably occur in a system that is extremely highly excited (large electronic and lattice interaction), or is not ordered, with numerous low-frequency local degrees of freedom that define the friction. However, neither of these scenarios is within the consideration of our model. Thus, the overdamped regime as a proper description of the structural dynamics can be ruled out. In what follows, we shall only consider the underdamped regime; typically, $\gamma / \omega = 10^{-2}$.

Figure 3 presents the influence of the functional form of the temporal force profile $F_0(t)$ on the diffraction change $\langle \Delta s(t) \rangle_S$; the calculations were performed using the same parameters except for the different forms described in the previous subsection. It is

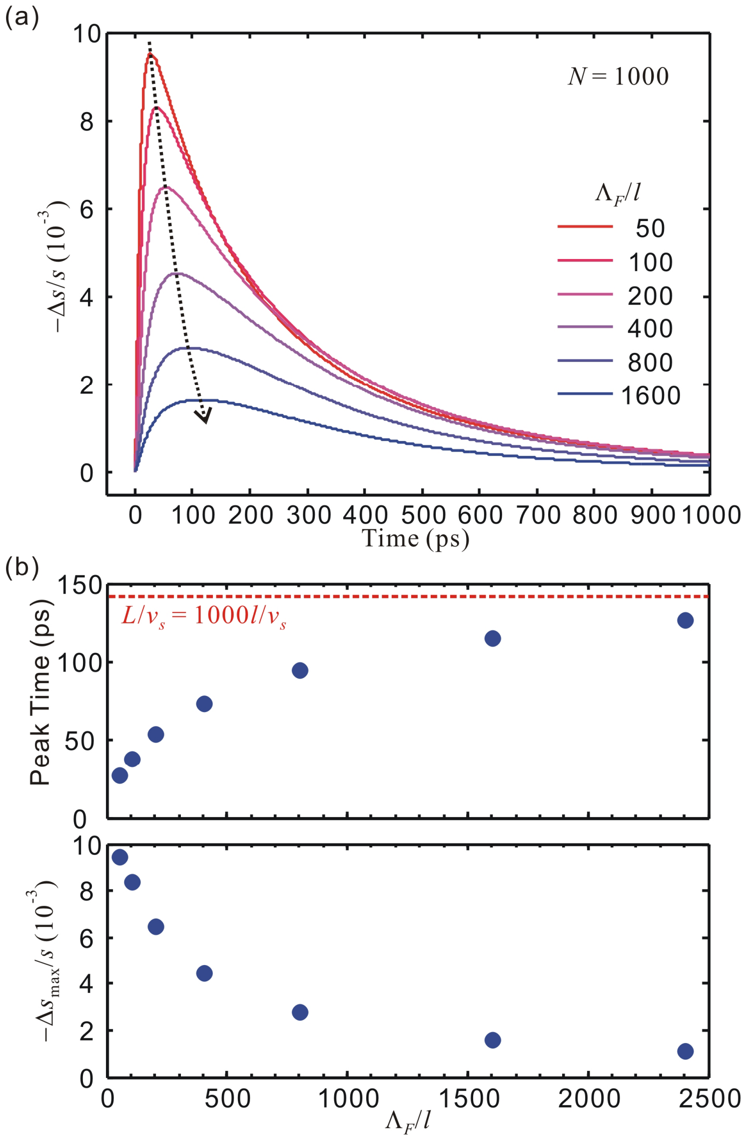

Fig. 4. Effect of the spatial attenuation length of the impulse force on diffraction changes. (a) The driving force has a temporal profile of the stretched exponential functional form with $\tau_{\text{rise}} = 5$ ps and $\tau_{\text{decay}} = 50$ ps; $|F_0| = 10^{-11}$ N, $N = 1000$ and $\gamma/\omega = 10^{-2}$. As the impulsive force extends deeper into the bulk (larger Λ_{F}), the maximum of $-\Delta s/s$ decreases and appears at a later time. The decay of $-\Delta s/s$ in the cases of small Λ_{F} is more apparent. (b) The dependence of the peak delay time (upper panel) and maximum diffraction change (lower panel) on Λ_{F}. The asymptotic value L/v_{s} in the upper panel has its origin in the propagation's being wavelike in nature.

noticeable that the features of wave propagation/reflection and recurring contraction/expansion disappear, which will be further examined later. The purpose of this figure is to show that the external driving force determines the overall shape of the diffraction transient; the faster the force decays, the sooner the diffraction change disappears. In other words, from the experimentally observed diffraction changes, the knowledge about the impulsive force in an optically excited material can be obtained. Another interesting observation is that for a given value of $|F_0|$ (10^{-11} N here), the maximum change in $\langle \Delta s(t) \rangle_\mathrm{S}$ seems to be less affected by the temporal difference in $F_0(t)$, although its appearance time closely follows the impulse profile.

In order to elucidate the effect of the penetration of the impulsive force, we use the same temporal profile of the stretched exponential function and the same parameters (N, γ, etc.) but vary the attenuation length, Λ_F, of the force in the simulations. Figure 4a shows that as Λ_F becomes larger, the maximum diffraction spot shift diminishes and appears at a later time; the decay of the transient change is much apparent in the cases of small Λ_F. The latter observation may be connected with the experimentally observed fast decays. Figure 4b shows the dependence of the peak time and maximum spot shift on Λ_F. The trends may be understood according to the following arguments. A larger attenuation length means less difference between the driving forces on neighboring atoms, which results in a smaller lattice expansion and, consequently, a smaller diffraction spot shift (Fig. 4b, lower panel). Moreover, as Λ_F becomes comparable to the slab thickness, substantial driving force exists not only at the surface but also within the slab, even at the other end. As a result, the lattice deformation originated from the bulk will propagate toward the surface at the speed of sound, and the interference between different contributions shifts the peak time of $\langle \Delta s(t) \rangle_\mathrm{S}$. The asymptotic value L/v_s clearly indicates

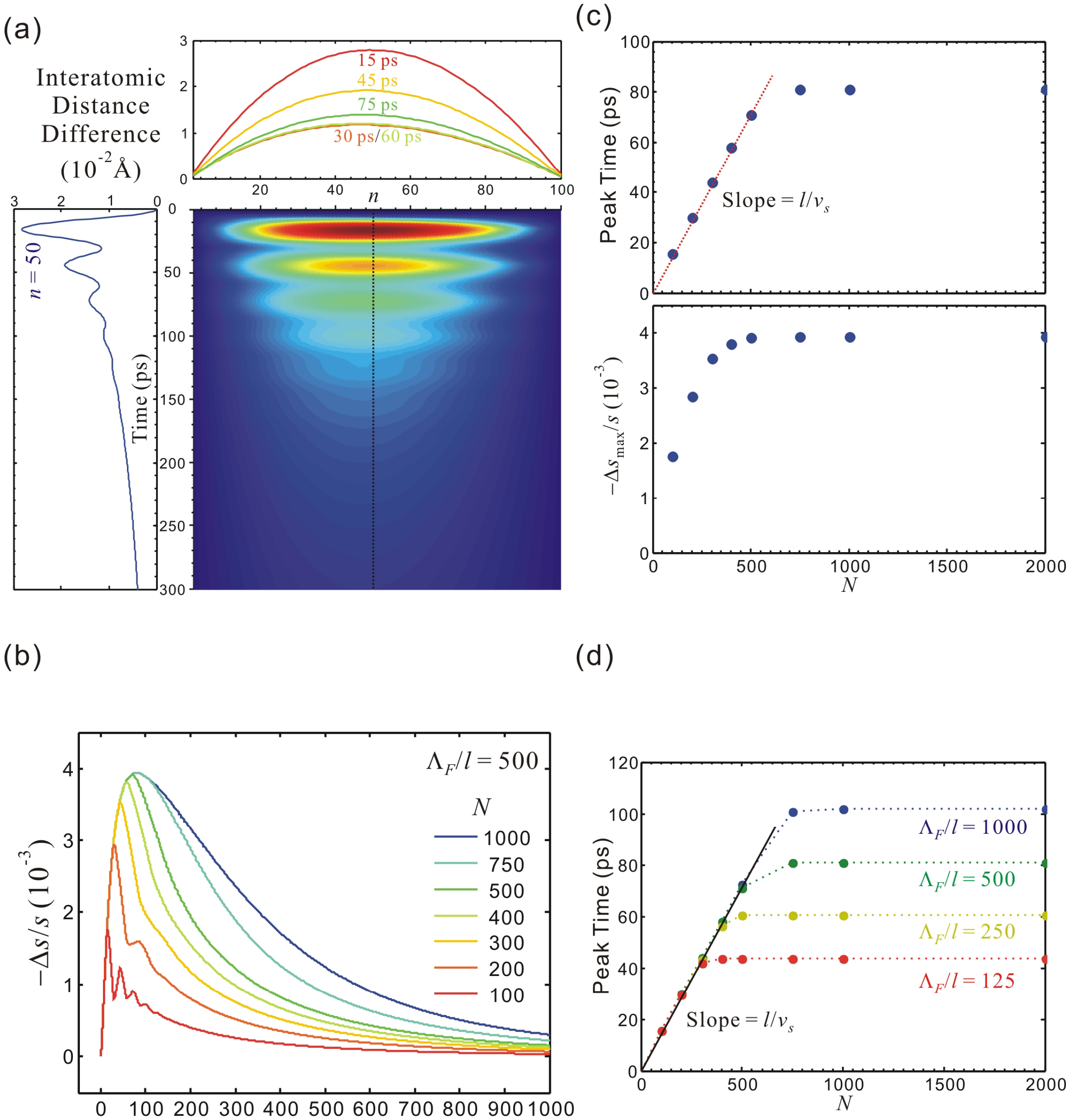

(See next page for the figure caption.)

Fig. 5. Effect of the slab thickness on structural dynamics and diffraction changes. The driving force has the same temporal profile and maximum value as in Fig. 4, and $\gamma/\omega = 10^{-2}$. (a) Temporal and spatial dependence of the interatomic distance changes in a 2D plot; $N = 100$ and $\Lambda_F = 100\,\ell$. In such a thin slab, the whole substrate exhibits a coherent breathing motion (a standing wave, as evident in the upper panel), and the oscillation period is the same as the round-trip traveling time (28.4 ps) for wave propagation. The slab center has the largest lattice deformation, whose temporal evolution is shown in the left panel. (b) Temporal evolution of $-\Delta s/s$ with different N; $\Lambda_F = 500\,\ell$ is kept the same. It is clear that the coherent breathing motion is only apparent in a thin substrate; as the slab thickness increases (for $N < \Lambda_F/\ell$), such a breathing motion disappears, but both the maximum diffraction change and its appearance delay time increase. However, further increase in N, beyond Λ_F/ℓ, does not affect the increase in the diffraction change at early times. These phenomena are the combined results of the wave propagation and the frictional damping in the lattice in the underdamped regime. (c) Dependence of the peak delay time (upper panel) and maximum diffraction change (lower panel) on N from the results in panel b. The linear increase in the peak delay time is the evidence of the wavelike propagation in the system; the peak delay time is equal to $N\ell/v_s = L/v_s$ (half of the round-trip traveling time). (d) The N-dependence shown in the upper plot of panel c is general, even for different values of Λ_F.

the nature of wave propagation in the lattice (Fig. 4b, upper panel).

Through the comparison between Figures 2b and 4a, the reason for the disappearance of the apparent oscillatory behavior in $\langle \Delta s(t) \rangle_S$ becomes clear. In a thick substrate slab, the larger friction constantly diminishes the lattice deformation and makes its return to the surface insignificant. In addition, as the rise and decay time constants of the driving force become larger, the $\langle \Delta s(t) \rangle_S$ signal follows and may cover the recurring components. However, the phenomenon of wave propagation still exists in these cases, since it is intrinsic in the underdamped regime.

Figure 5 presents, with Λ_F and other parameters being fixed, the dependence of the structural dynamics and diffraction change on the slab thickness. Interestingly, in a thinner slab of $N = 100$ ($L = 28.8$ nm), a coherent breathing motion (a standing wave) for the whole substrate is found, and the oscillation period is the same as the round-trip traveling time (28.4 ps) for wave propagation (Fig. 5a). The coherent motion is the result of the interference between the lattice deformation components generated at different parts of the substrate. In fact, Fig. 5a is not very different from Fig. 2a: the decrease of the substrate thickness reduces the round-trip traveling time, and the increase in the time constants of the impulse spatially broadens the width of lattice deformation (the horizontal axis in the figures) and temporally induces an average effect of the deformation amplitude (the vertical axis in the figures). It is noted that in such a system, the surface expands the least, and the atoms near the middle of the slab actually experience the largest increase in interatomic spacings. At longer times, the frictional force and the decay of the impulsive force dictate the decrease of the lattice expansion.

The aforementioned coherent motion disappears as the substrate thickness increases (Fig. 5b). This result is therefore expected because of the increase in the wave traveling time (which means less temporal average effect; the vertical axis in Fig. 5a) and the weaker interference by the lattice deformation from the deeper part of the substrate (the dissipation of structural changes due to the frictional force). Thus, for a given Λ_F, the maximum diffraction spot shift increases and occurs at a later time as N becomes greater (but still remains smaller than Λ_F/ℓ). When the dependence on N is plotted (Fig. 5c), the linear increase in the peak time (upper panel, $N < \Lambda_F/\ell$) indicates once again the nature of wave propagation in the underdamped regime; the saturation phenomenon can also be understood because a further increase in N beyond Λ_F/ℓ only brings in limited additional contribution of the lattice changes and hence will not affect the structural dynamics near the surface. By changing Λ_F, such a relationship of the substrate thickness still remains valid, as demonstrated in Fig. 5d.

C. Methodology: The Adsorbate

As shown in Subsection C of the Theory Section, the adsorbate assembly is treated similar to that of the substrate slab, provided that they are separately considered. However, because of the coupling between the two (H_{SA} of Eq. 10), further considerations of how to determine the temporal and spatial profiles of the impulsive forces over both the substrate and adsorbate are required. Here, instead of assuming different force profiles of $F_n(t)$ and $G_n(t)$ for the substrate and adsorbate separately, we consider the following model. Initially, the excitation laser pulse is only absorbed by the substrate and causes a temperature jump. Because of the spatial temperature gradient and energy transfer, the adsorbate acquires a temperature increase from the heated substrate. By considering the energy transport in the substrate/adsorbate composite system, the induced lattice strains (driving forces) can be formulated, and we can simulate the structural responses (z_n and Z_n) and, consequently, the diffraction changes ($\langle \Delta s \rangle_S$ and

$\langle \Delta s \rangle_{\mathrm{A}}$), which correspond to structural dynamics of the substrate and adsorbate over time.

With the substrate temperature, T_n, at the nth lattice site and the adsorbate temperature, Y_n, at the nth atom, temperature changes can be expressed in the following equations describing the energy flow in terms of temperature gradients:

$$\begin{aligned}
&\frac{d}{dt}T_0 = S_0(t) - \frac{1}{\tau_{\mathrm{S}}}\left(T_0 - T_1\right) - \frac{1}{\tau_{\mathrm{SA}}}\left(T_0 - Y_0\right),\\
&\frac{d}{dt}T_n = S_n(t) - \frac{1}{\tau_{\mathrm{S}}}\left(2T_n - T_{n-1} - T_{n+1}\right) \qquad (n=1,\ldots,N-2),\\
&\frac{d}{dt}T_{N-1} = S_{N-1}(t) - \frac{1}{\tau_{\mathrm{S}}}\left(T_{N-1} - T_{N-2}\right),\\
&\frac{d}{dt}Y_0 = -\frac{1}{\tau_{\mathrm{A}}}\left(Y_0 - Y_1\right) - \frac{1}{\tau_{\mathrm{SA}}}\left(Y_0 - T_0\right),\\
&\frac{d}{dt}Y_n = -\frac{1}{\tau_{\mathrm{A}}}\left(2Y_n - Y_{n-1} - Y_{n+1}\right) \qquad (n=1,\ldots,N_{\mathrm{A}}-2),\\
&\frac{d}{dt}Y_{N_{\mathrm{A}}-1} = -\frac{1}{\tau_{\mathrm{A}}}\left(Y_{N_A-1} - Y_{N_A-2}\right).
\end{aligned} \tag{15}$$

The second and fifth equations in the group indicate that these temperatures at different sites are governed by a heat transfer process. Since the energy content at a certain site is equal to the temperature within a constant factor, the left-hand side of Eq. 15, which is proportional to the time derivative of the energy content, is proportional (without an external heat source) to the net difference between the incoming and outgoing energy fluxes which are linearly associated with the energy (temperature) gradients. This difference in temperature gradients gives the right-hand side of Eq. 15 a second-order, spatial, finite difference of temperatures for the nonboundary atomic sites in the case of a discrete lattice.

In Eq. 15, τ_{S}, τ_{A} and τ_{SA} are the effective time constants of energy transfer between adjacent atoms in the substrate, in the adsorbate, and at the interface, respectively; they originate from the combination of lattice spacings, thermal conductivities, and heat capacities for the substrate and adsorbate. These time constants are treated as parameters and may not necessarily correspond to the actual values in the thermally equilibrated diffusion regime. The external source $S_n(t)$ represents the absorbed heat which in this case is the laser heating pulse; it has the following temporal and spatial dependences invoked:

$$S_n(t) = S_0(t)\, e^{-\frac{n\,\ell}{\zeta_{\mathrm{laser}}}} = \sqrt{\frac{4\ln 2}{\pi}}\,\frac{S_0}{\tau_{\mathrm{p}}}\, e^{-4\ln 2\left(\frac{t-\tau_0}{\tau_{\mathrm{p}}}\right)^2}\, e^{-\frac{n\,\ell}{\zeta_{\mathrm{laser}}}}\,, \qquad (16)$$

where ζ_{laser} is the penetration depth of the laser in the substrate. We use $\zeta_{\mathrm{laser}} = 16.3$ nm for the gold substrate and the full-width-at-half-maximum (fwhm) of the laser pulse to be 200 fs.

The impulsive force is assumed to linearly depend on the temperature change; that is, $F_n(t) = const\times T_n(t)$ and $G_n(t) = const\times Y_n(t)$ where *const* is a proportionality constant related to the Grüneisen parameter γ_{lat} of the material. This linear relationship originates from the following equations: the longitudinal stress impulse $\delta\sigma_{33} = -\gamma_{\mathrm{lat}}C_{\mathrm{lat}}\delta T$ where C_{lat} is the specific heat per unit volume (*5, 8*), and the total force impulse (over an area of square unit cell length) $F = \ell^2\,\delta\sigma_{33}$. Therefore, with $\gamma_{\mathrm{lat}} \sim 3$ and $C_{\mathrm{lat}} = 2.5\times10^6$ J/(m^3·K) for gold (*8*), *const* is about 6.2×10^{-13} N/K. In the present study, *const* is assumed to be 10^{-12} N/K for both the substrate and adsorbate for simplicity. Therefore, after the temperatures, $T_n(t)$ and $Y_n(t)$ with both the spatial and temporal evolution, are obtained by solving Eq. 15, we obtain $F_n(t)$ and $G_n(t)$, which can then be substituted into Eqs. 11 and 12 for the calculation of $z_n(t)$ and $Z_n(t)$.

For the UEC investigation of the substrate/adsorbate composite system, we need to consider the underdamped regime, and for this purpose, we consider the damping factor $\gamma/\omega = 0.01$ for the substrate and $\gamma_{\mathrm{A}}/\omega_{\mathrm{A}} = 0.1$ for the adsorbate. A larger adsorbate friction coefficient is used because the assembly of chainlike molecules often has a less

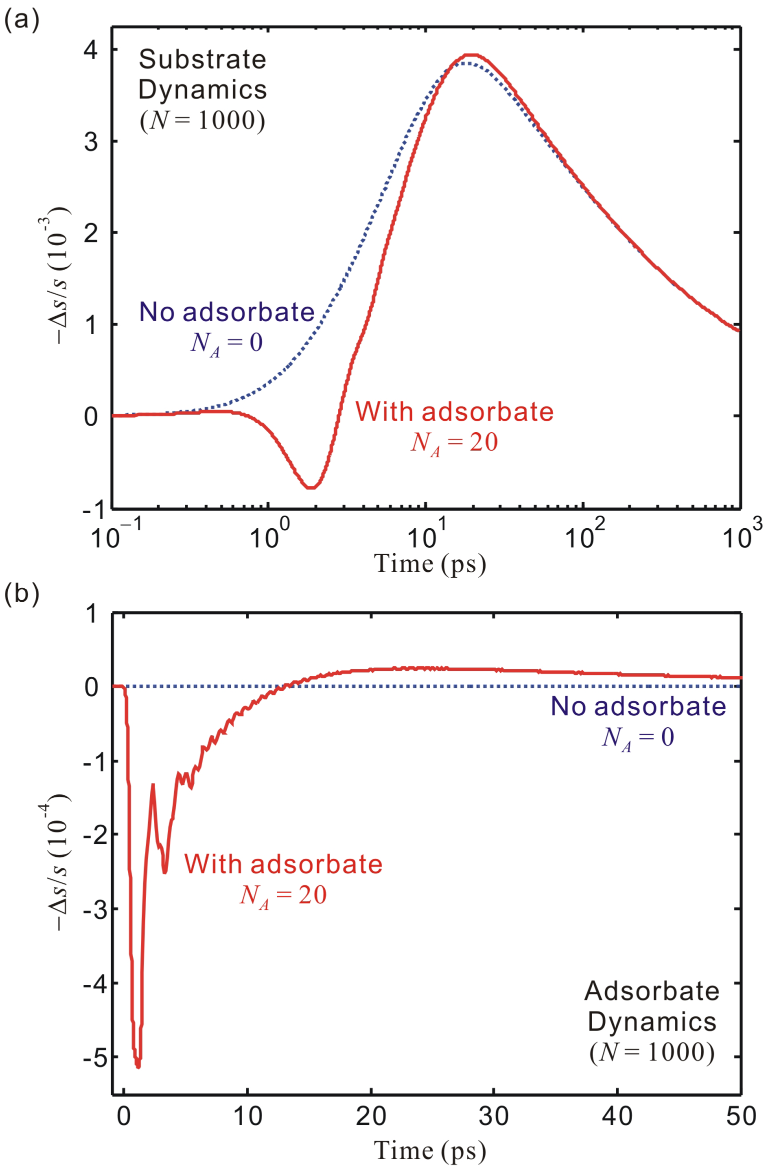

Fig. 6. Substrate and adsorbate dynamics, in the absence of coupling. Diffraction changes from (a) the substrate and (b) the adsorbate without direct energy transfer across the interface are shown. (a) The substrate dynamics in the presence of the adsorbate (red solid line) and with no adsorbate (blue dashed line). Although the long-time dynamics is less affected, the existence of the adsorbate causes a small contraction in the surface region of the substrate at early time, followed by a lattice expansion on a time scale of ~10 ps. Note that the time axis is a logarithmic scale. (b) The adsorbate dynamics (red solid line). Due to the expansion movement of the substrate, the adsorbate mostly shows contraction; the many oscillations are the results of wave propagation and frictional damping in the adsorbate and the interference between the substrate and adsorbate motions.

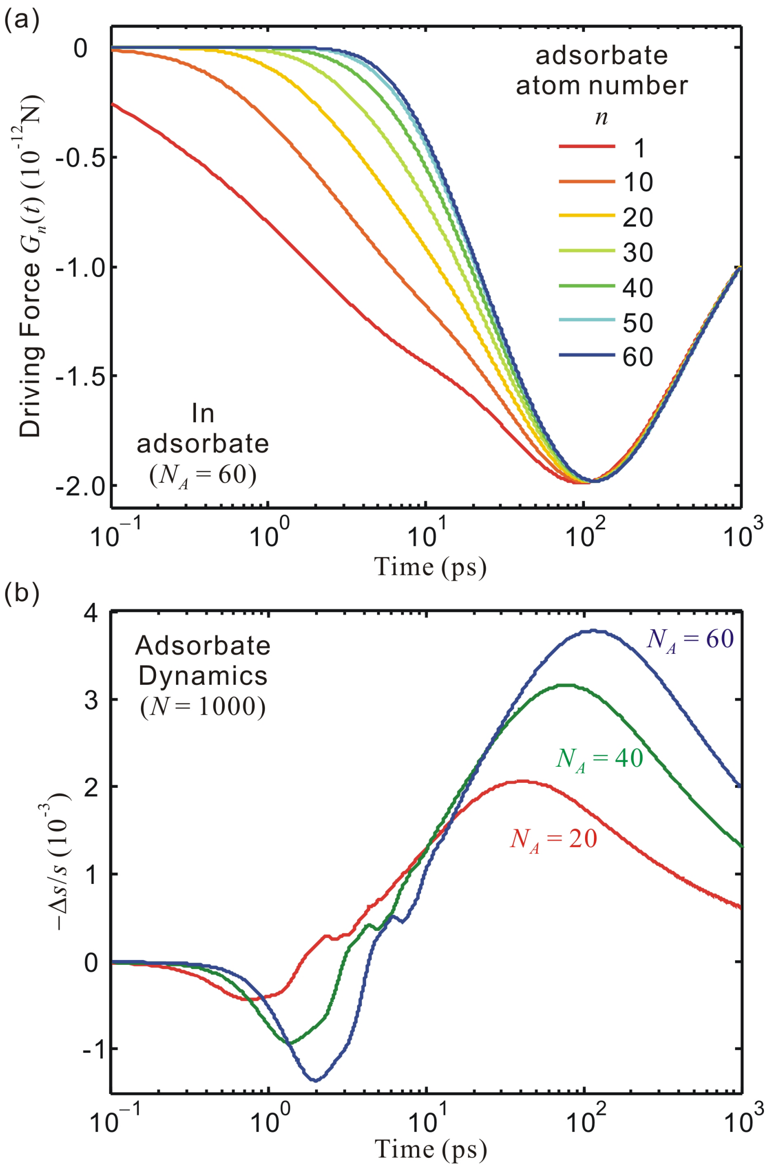

Fig. 7. Substrate and adsorbate structural dynamics in the presence of coupling. Adsorbate atom driving force and the effect of adsorbate length, $N_A \ell_A$, on dynamics are shown. Here, for the simulation of heat transfer in the substrate/adsorbate composite system, $\tau_S = \tau_A = 0.01$ ps and $\tau_{SA} = 1$ ps are used (see text for details about other parameters). (a) The delay in the onset of change in the external driving force reflects the speed of heat transfer across the interface. In tens of picoseconds, the entire adsorbate of the molecular system acquires the new temperature. (b) The adsorbate dynamics shows a small contraction in the molecular structure at a very early time, followed by expansion in tens of picoseconds and restructuring on an even longer time scale. As N_A increases, a clearer contraction and larger expansion are obtained; the maximum expansion/contraction also appears at a later time.

ordered structure, and frictional motions are, in general, more frequent. The force constants used for the substrate, adsorbate, and the interfacial spring are 16.3, 50, and 5 N/m, respectively. The relative magnitudes of these force constant values are to reflect the strength of different bondings in the composite system. The time constant, τ_S, is assumed to be 0.01 ps to reflect the fast energy conduction (through ballistic carrier transport) in gold, and τ_A and τ_{SA} for the adsorbate and the interfacial junction are variables.

D. Adsorbate Structural Dynamics

Let us first consider the structural dynamics of both the substrate and the adsorbate under the condition of no substantial energy transport across the interface. In this case, the external impulsive force is exclusively applied to only the substrate atoms, and the adsorbate atoms, with one end connected to the substrate, are governed by the (underdamped) oscillators. In Fig. 6, the calculated $\langle \Delta s(t) \rangle_S$ and $\langle \Delta s(t) \rangle_A$ show that, because of the existence of an unexcited adsorbate molecule above the substrate, the initial expansion of the underlying substrate atoms in the adsorbate direction leads to a transient contraction near the substrate surface at very short time; the long-time behavior is relatively unaffected (Fig. 6a). In contrast, the adsorbate mostly shows contraction due to the expansion movement of the substrate (Fig. 6b). It follows from the simulations that, without energy coupling across the interface, the adsorbate will show only contraction in the interatomic spacings, contrary to the lattice expansion observed experimentally.

If the energy transfer across the interface is switched on, a different temporal behavior in the adsorbate dynamics arises. We first examine the temporal and spatial evolution of the temperature (which is also the impulsive force by a constant factor) in the adsorbate (Fig. 7a). The rate of the amplitude increases at the interface ($n = 0$) is

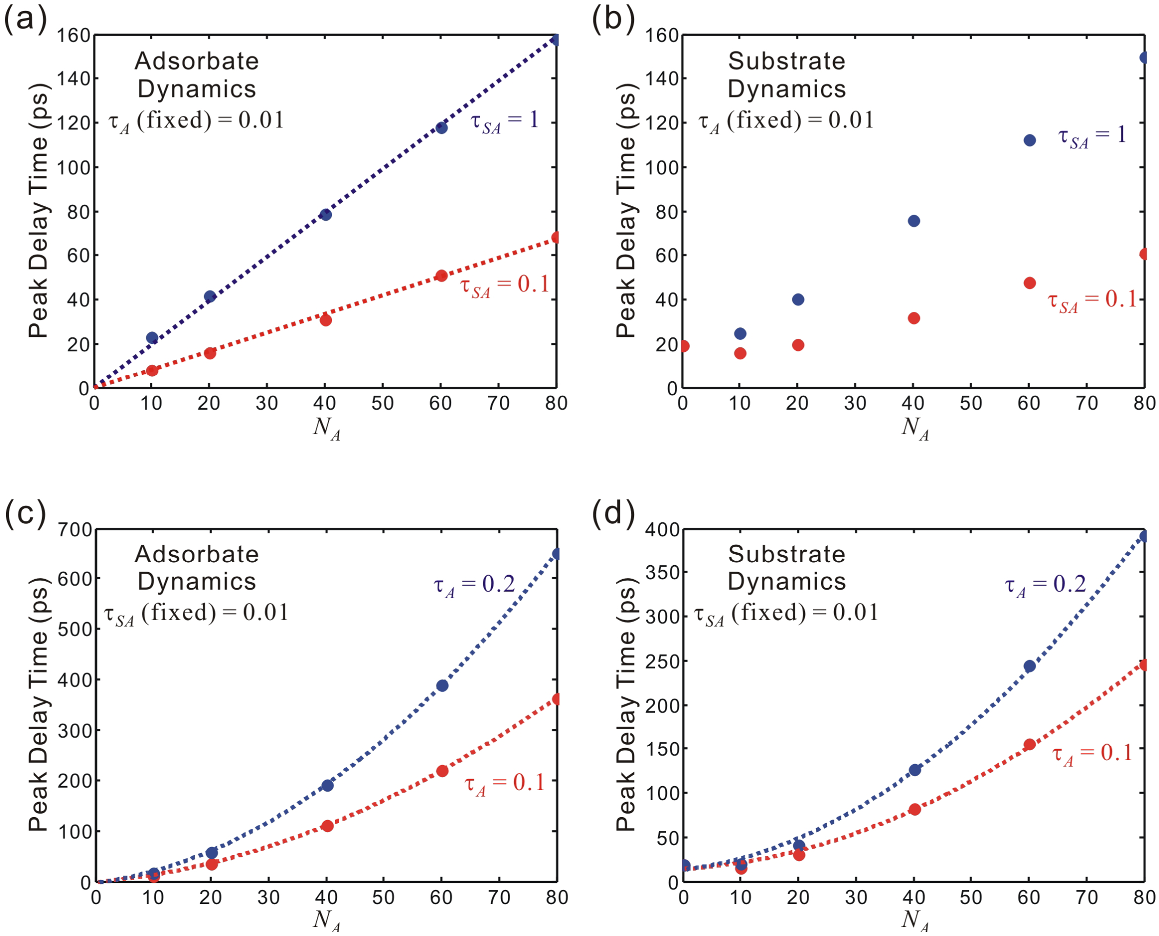

Fig. 8. Adsorbate dynamics dependence on transfer time. Dependence of the peak delay times of diffraction changes $-\langle\Delta s(t)\rangle_A/s$ and $-\langle\Delta s(t)\rangle_S/s$ on N_A with selected values of τ_{SA} and τ_A is shown. (a) When τ_{SA} is much larger than τ_A, the peak delay time of the adsorbate dynamics appears to be linearly dependent on N_A. (b) The peak delay time of the substrate dynamics also becomes larger as the adsorbate molecule becomes longer; in the cases of short adsorbate molecules, interference between the adsorbate and substrate motions may shift the peak delay time of the substrate dynamics to a smaller value. (c and d) When τ_{SA} is fixed and much smaller than τ_A, the peak delay times of the adsorbate and substrate dynamics appear to be quadratic with N_A. This dependence is a consequence of 1D heat diffusion along the adsorbate chain; τ_A becomes the dominant controlling factor for the heat transfer.

naturally controlled by τ_{SA}, and the delay time in the onset of change for atoms farther away from the interface is governed by τ_{A}. After equilibration of the adsorbate molecule is reached, the impulse at different atoms decays homogeneously at a rate determined again by τ_{SA}.

Figure 7b presents the temporal evolution of the diffraction change for different lengths of the adsorbate molecule. Because of the energy transfer to the adsorbate, the contraction-only dynamics in Fig. 6b is modified with the inclusion of structural expansion and recovery over a longer time scale. The maximum change in $\langle \Delta s(t) \rangle_{\mathrm{A}}$ and its corresponding time increase with adsorbate length; this is reminiscent of a similar trend observed in Fig. 5b. Hence, the previous arguments about lattice deformation propagation and the interference between structural changes generated at different atoms can be applied here for the understanding of Fig. 7b.

The adsorbate/substrate (A/S) dynamics can be further categorized into the (A/S) coupling-controlled and (A) heat-transfer-controlled regimes. If τ_{SA} is appreciably longer than τ_{S} and τ_{A}, one can expect the thermal coupling at the interface to be the bottleneck of the energy transfer: a longer τ_{SA} leads to further delay in the peak of $\langle \Delta s(t) \rangle_{\mathrm{A/S}}$ (Fig. 8, panels a and b). It is reasonable to see that, for a given τ_{SA}, the peak time is in a linear relationship with N_{A}, because the deterministic step occurs at the interface and an additional adsorbate length only linearly shifts the time at which maximum structural changes are reached. This is the coupling-controlled regime. In contrast, if τ_{A} is larger or comparable to τ_{SA}, the diffusion process in the adsorbate becomes the dominant factor for the structural dynamics. As a result, the peak time of $\langle \Delta s(t) \rangle_{\mathrm{A/S}}$ shows a quadratic dependence on N_{A} ($\sim(N_{\mathrm{A}}\,\ell_A)^2/D_{\mathrm{eff}}$ where $D_{\mathrm{eff}} = \ell_A^2/\tau_{\mathrm{A}}$), a consequence of 1D heat diffusion along the adsorbate chain (Fig. 8, panels c and d). This is the heat-transfer-controlled scenario. It is natural that for the same N_A, a larger τ_A makes the peak time appear at a later time.

It is noted that the peak time of $\langle \Delta s(t) \rangle_A$ is unaffected if the adsorbate force constant, $m_A \omega_A^2$, or the coupling force constant, C, in Eq. 12 is doubled. Thus, the rise of a diffraction spot shift is, indeed, determined by the induced thermal impulse, which is solely controlled by those heat-transfer correlation time constants. It is interesting to see that the size of the adsorbate molecules can influence the magnitude and peak time of $\langle \Delta s(t) \rangle_S$. Such an effect is mainly contributed by the adsorbate structural dynamics on the substrate surface layers where the diffraction is measured.

Discussion and Conclusion

As presented in the numerical results and figures, the important variables in the present microscopic model can be categorized into the following four: (1) the underdamped vs overdamped regime, which is determined by the relative magnitudes of the friction coefficient γ and the vibrational angular frequency ω; (2) the functional form for the temporal profile of the impulsive force, $F_0(t)$; (3) the substrate thickness, $N\ell$, and the attenuation length, Λ_F, for the impulse spatial profile F_n; and (4) the adsorbate effect, that is, the dependence of structural dynamics on the adsorbate chain length $N_A\ell$ and on the time scales of energy transport within the adsorbate and across the interface. We have concluded that the underdamped regime is appropriate for the UEC observations studied. This conclusion directly supports the wave-propagating structural changes of the lattice, which plays a key role in the phenomena of coherent lattice motions and interferences in structural deformation.

Structural dynamics closely follows the temporal evolution of $F_0(t)$. With a moderate driving force, the lattice may have up to a few percent changes in the interatomic spacings, resulting in a clear diffraction spot shift. This observation is fundamentally significant in that the observed lattice expansion deduced from the Bragg spot movement is not necessarily linked to conventional thermal expansions due to a temperature rise. In fact, it has been experimentally shown that the picture of thermal equilibrium cannot account for ultrafast structural dynamics (Ch. 4). However, using the simple microscopic model with an external driving force, we are able to obtain the calculated temporal behavior of the diffraction spot shift, which is similar to the experimental observations. Such a model is useful in relating UEC experimental results to motions of individual atoms and to the forces exerted.

The three different types of functional forms for $F_0(t)$ may each correspond to a certain condition in a specific type of materials. First, a Gaussian impulse profile with a full width at half maximum close to the excitation pulse width may be suitable for the discussion of the structural dynamics of metals following low-energy and low-fluence optical excitation. It is generally known that in such a condition, the electrons and lattice of a metal may reach an equilibrium on a sub-picosecond to picosecond time scale (*31*), which implies the legitimacy of translating the electronic excitation impulse into an impulsive force in the lattice. In contrast, if the carriers and lattice do not equilibrate on a sub-picosecond time scale, which is common in a semiconductor because of the involvement of optical phonons (Ch. 4) and possibly in a highly excited metal, a stretched exponential function may be better suited for describing the rise and decay of the impulsive force. For such a case, τ_{rise} and τ_{decay} are important parameters and their values may provide additional information about the electronic and lattice dynamics in the excited material. The third type of impulse, governed by a diffusive-type process, may also seem appropriate for many systems in which carrier or heat diffusion is involved. If an experiment shows that the spot shift follows the $1/\sqrt{t}$ relation at longer times, it may be a good indication that a diffusion-controlled impulse is at play.

By changing the two length variables, the substrate thickness $N\ell$ (i.e., the number of substrate atoms N) and the impulse attenuation length, Λ_F, different structural dynamics in the lattice can be seen, as shown in Figs. 4 and 5. A coherent lattice motion was obtained when both N and Λ_F are small (on the order of a few to tens of nanometers) and comparable. Here, the characteristic of wave propagation in the lattice system is the key. The coherent motion becomes less distinct due to a larger substrate thickness and the existence of the friction. From Fig. 5, panels b and c, it is also understood that an experimentally observed slow spot shift may not be interpreted as the result of a slow growth in the driving force; the delay in the peak time may very likely originate from the collective motion of the thicker substrate lattice.

These N- and Λ_F-dependence investigations suggest experimental thickness-dependent studies on different materials, such as crystalline metals and semiconductors, using UEC. According to the present study, we expect to observe the dependence of the time and amplitude for the maximum diffraction spot shift with metal thickness, whereas such dependence may be absent in the case of semiconductors for the following reasons. Laser excitation of metals first induces hot electrons near the surface, which permeate the whole substrate slab quickly due to their high mobility. Therefore, the induced impulsive force is likely to have an attenuation length greater than the slab thickness, and the results in Fig. 5 can be tested. In the case of semiconductors, they typically have smaller thermal conductivity and lower carrier mobility, and the generation and decay of different types of phonons may not be described well by the present model; the deterministic factors for the peak time of $\langle \Delta s(t) \rangle_S$ have been identified experimentally (Ch. 4).

For the adsorbate effect, the simplest case of energy transfer was considered to simulate the impulsive force, although other types of force forms may be developed. However, the calculations well demonstrated the corresponding structural dynamics in the adsorbate under the variation of three important control parameters: the number of adsorbate atoms N_A, and the effective heat-transfer time constants τ_{SA} and τ_A. In short, a larger maximum diffraction spot shift will be found at a later delay time if the adsorbate molecule is longer. The coupling-controlled and heat-transfer-controlled regimes for the structural dynamics were observed, and they are governed by the relative magnitude of τ_{SA} and τ_A.

Finally, it is important to point out one of the major differences between the current impulsive force approach and the conventional heating picture. According to the latter model, as we increase the length of adsorbate molecules, oriented on the same substrate with the same interaction strength at the interface, and for the same substrate excitation fluence, the total temperature jump will decrease in the adsorbate. This is expected because of the increase in total heat capacity. Hence, as the chains becomes longer, smaller expansion of the interatomic spacings is expected. The experimental observations (*1*) are in contrast with such a prediction, and instead, they agree with the results of the present study, which indicate an increase in expansion as the chain length increases. Therefore, the nonthermal nature of ultrafast structural dynamics requires consideration of atomic motions and the forces involved. The theoretical treatment presented here can be further extended to semiconductors and other materials and for different types of forces and structures depending on the experiments of concern in UEC and related studies.

Appendix A. The Fermi–Pasta–Ulam Model

The Fermi–Pasta–Ulam Hamiltonian (*28*) with an anharmonic cubic term is

$$H=\sum_{n=0}^{N-1}\frac{p_n^2}{2m}+\frac{m\omega^2}{2}\sum_{n=0}^{N-2}\left(z_n-z_{n+1}\right)^2+\frac{\alpha\, m\omega^2}{3}\sum_{n=0}^{N-2}\left(z_n-z_{n+1}\right)^3, \tag{A1}$$

where α is the anharmonicity factor (*32*) that is associated with the static linear thermal expansion coefficient β by $\beta = \alpha\, k_B\, (m\omega^2\, \ell\,)^{-1}$. For gold, with the spring force constant $m\omega^2 = 16.3$ N/m, $\ell = 2.88$ Å and $\beta \sim 1.4\times10^{-5}\ \mathrm{K}^{-1}$, α is $\sim 4.8\times10^{9}\ \mathrm{m}^{-1}$. Such a value makes the anharmonic term insignificant if compared with the harmonic term: for the structural changes on the order of a few percent or less, namely, $z_n - z_{n-1}$ of about a few picometers, $\alpha\ (z_n - z_{n-1}) \ll 1$. Thus, in general, one can neglect the factor α in the simulation of lattice dynamics. For the application of a very large laser fluence such that $|\Delta s/s| \sim 0.1$ but below the damage threshold (and therefore, $z_n - z_{n-1}$ is on the order of a few tenths of an angstrom), the consideration of the anharmonic cubic term leads to the following equations of motion:

$$\begin{aligned}
&\frac{d}{dt}z_n=\frac{p_n}{m}\quad (n=1,\ldots,N)\\
&\frac{d}{dt}p_0=F_0(t)-\gamma\, p_0-m\omega^2\left(z_0-z_1\right)\left[1+\alpha\left(z_0-z_1\right)\right]\\
&\frac{d}{dt}p_n=F_n(t)-\gamma\, p_n-m\omega^2\left(2z_n-z_{n-1}-z_{n+1}\right)\left[1+\alpha\left(z_{n-1}-z_{n+1}\right)\right]\quad (n=1,\ldots,N-2)\\
&\frac{d}{dt}p_{N-1}=F_{N-1}(t)-\gamma\, p_{N-1}-m\omega^2\left(z_{N-1}-z_{N-2}\right)\left[1+\alpha\left(z_{N-2}-z_{N-1}\right)\right].
\end{aligned} \tag{A2}$$

The sixth-order Runge–Kutta method can be used to obtain a numerical solution to the above equations, provided that $F_n(t)$'s are calculated from the two-temperature model or specified using a simple functional form.

Appendix B. Derivation of Equation 2

Equation 1 can be expressed in a matrix form as

$$\frac{d^2}{dt^2}\boldsymbol{z}+\gamma\frac{d}{dt}\boldsymbol{z}+\omega^2\boldsymbol{A}\boldsymbol{z}=\frac{\boldsymbol{F}(t)}{m}, \tag{B1}$$

where $\boldsymbol{z}$ is a column vector of the atomic displacements (z_0, z_1, z_2, …, z_{N-1}) and $\boldsymbol{F}$ is that of the impulsive force components (F_0, F_1, F_2, …, F_{N-1}). The matrix elements of the N-by-N matrix $\boldsymbol{A}$ are given by $\boldsymbol{A}_{ij} = 2\delta_{i,j} - \delta_{i,j+1} - \delta_{i+1,j}$ for $1 \le i, j \le N-2$ and by $\boldsymbol{A}_{0j} = \delta_{0,j} - \delta_{1,j}$ and $\boldsymbol{A}_{i,N-1} = \delta_{i,N-1} - \delta_{i+1,N-1}$; $\delta_{i,j}$ is the Kronecker delta function. With the use of the Laplace transform, Eq. B1 is turned into

$$\begin{aligned}\bar{\boldsymbol{z}}(s) &= \frac{1}{s^2+\gamma s+\omega^2\boldsymbol{A}}\cdot\frac{\overline{\boldsymbol{F}}(s)}{m}\\ &\quad+\frac{s+\gamma}{s^2+\gamma s+\omega^2\boldsymbol{A}}\cdot\boldsymbol{z}(0)+\frac{1}{s^2+\gamma s+\omega^2\boldsymbol{A}}\cdot\dot{\boldsymbol{z}}(0),\end{aligned} \tag{B2}$$

where $\bar{\boldsymbol{z}}(s)$ and $\overline{\boldsymbol{F}}(s)$ are the Laplace transformation of $\boldsymbol{z}(t)$ and $\boldsymbol{F}(t)$, respectively.

With the definitions of the column vectors $\bar{\boldsymbol{y}}(s)=\boldsymbol{U}\,\bar{\boldsymbol{z}}(s)$ and $\overline{\boldsymbol{H}}(s)=\boldsymbol{U}\,\overline{\boldsymbol{F}}(s)$ where $\boldsymbol{U}$ is a unitary transformation that diagonalizes $\boldsymbol{A}$, Eq. B2 becomes a set of indexed equations,

$$\begin{aligned}\bar{y}_k(s) &= \frac{1}{s^2+\gamma s+\Omega_k^2}\cdot\frac{\overline{H}_k(s)}{m}\\ &\quad+\frac{s+\gamma}{s^2+\gamma s+\Omega_k^2}\cdot y_k(0)+\frac{1}{s^2+\gamma s+\Omega_k^2}\cdot\dot{y}_k(0),\end{aligned} \tag{B3}$$

where $\boldsymbol{y}(0)=\boldsymbol{U}\,\boldsymbol{z}(0)$ and $\dot{\boldsymbol{y}}(0)=\boldsymbol{U}\,\dot{\boldsymbol{z}}(0)$, k is the row index, and $\Omega_k = 2\omega\sin(\pi k/2N)$ is the kth element of the diagonalized matrix $\boldsymbol{U}^{\mathrm{T}}\boldsymbol{A}\boldsymbol{U}$. The two roots to the characteristic quadratic equation $\lambda^2 + \gamma\ \ \lambda + \Omega_k^2 = 0$ are λ_{1k}, $\lambda_{2k} = -\gamma\ \ /2 \pm i\Lambda_k$, where $\Lambda_k = \Omega_k\sqrt{1-\left(\gamma^2/4\Omega_k^2\right)}$.

Consequently, Eq. B3 can be converted into the time domain by the inverse Laplace transform as follows:

$$\begin{aligned} y_k(t) &= \frac{1}{m}\int_0^t d\tau\, H_{\boldsymbol{k}}(\tau)\left[e^{\lambda_{1k}(t-\tau)} - e^{\lambda_{2k}(t-\tau)}\right]\Big/\left(\lambda_{1k}-\lambda_{2k}\right) \\ &\quad + y_k(0)\left[\left(\lambda_{1k}+\gamma\right)e^{\lambda_{1k}t} - \left(\lambda_{2k}+\gamma\right)e^{\lambda_{2k}t}\right]\Big/\left(\lambda_{1k}-\lambda_{2k}\right) \\ &\quad + \dot{y}_k(0)\left(e^{\lambda_{1k}t} - e^{\lambda_{2k}t}\right)\Big/\left(\lambda_{1k}-\lambda_{2k}\right). \end{aligned} \tag{B4}$$

One can show that the unitary matrix $\boldsymbol{U}$ is simply a cosine Fourier transform (*33*). Hence,

$$\begin{aligned} z_n(t) &= \sum_{k=0}^{N-1} y_k(t)\cos\left(\frac{k\pi}{N}\left(n+\frac{1}{2}\right)\right), \\ \dot{z}_n(t) &= \sum_{k=0}^{N-1} \dot{y}_k(t)\cos\left(\frac{k\pi}{N}\left(n+\frac{1}{2}\right)\right), \\ F_n(t) &= \sum_{k=0}^{N-1} H_k(t)\cos\left(\frac{k\pi}{N}\left(n+\frac{1}{2}\right)\right), \end{aligned} \tag{B5}$$

and reversely,

$$\begin{aligned} y_0(0) &= \frac{1}{N}\sum_{j=0}^{N-1} z_j(0), \quad y_k(0) = \frac{2}{N}\sum_{j=0}^{N-1} z_j(0)\cos\left(\frac{k\pi}{N}\left(j+\frac{1}{2}\right)\right), \\ \dot{y}_0(0) &= \frac{1}{N}\sum_{j=0}^{N-1} \dot{z}_j(0), \quad \dot{y}_k(0) = \frac{2}{N}\sum_{j=0}^{N-1} \dot{z}_j(0)\cos\left(\frac{k\pi}{N}\left(j+\frac{1}{2}\right)\right), \\ H_0(0) &= \frac{1}{N}\sum_{j=0}^{N-1} F_j(0), \quad H_k(0) = \frac{2}{N}\sum_{j=0}^{N-1} F_j(0)\cos\left(\frac{k\pi}{N}\left(j+\frac{1}{2}\right)\right). \end{aligned} \tag{B6}$$

Therefore, by substituting Eq. B6 into Eq. B4 and then Eq. B5, with the values of λ_{1k} and λ_{2k}, Eq. 2 is readily obtained.

References:

1. M. T. Seidel, S. Chen, A. H. Zewail, *J. Phys. Chem. C* **111**, 4920 (2007).
2. J. H. Bechtel, *J. Appl. Phys.* **46**, 1585 (1975).
3. L. Jiang, H.-L. Tsai, *J. Heat Transfer* **127**, 1167 (2005).
4. S.-S. Wellershoff, J. Hohlfeld, J. Güdde, E. Matthias, *Appl. Phys. A* **69**, S99 (1999).
5. C. Thomsen, H. T. Grahn, H. J. Maris, J. Tauc, *Phys. Rev. B* **34**, 4129 (1986).

6. G. L. Eesley, B. M. Clemens, C. A. Paddock, *Appl. Phys. Lett.* **50**, 717 (1987).
7. O. B. Wright, K. Kawashima, *Phys. Rev. Lett.* **69**, 1668 (1992).
8. O. B. Wright, *Phys. Rev. B* **49**, 9985 (1994).
9. J. H. Hodak, A. Henglein, G. V. Hartland, *J. Phys. Chem. B* **104**, 9954 (2000).
10. M. Hase, K. Ishioka, J. Demsar, K. Ushida, M. Kitajima, *Phys. Rev. B* **71**, 184301 (2005).
11. C. Rossignol, J. M. Rampnoux, M. Perton, B. Audoin, S. Dilhaire, *Phys. Rev. Lett.* **94**, 166106 (2005).
12. G. V. Hartland, *Phys. Chem. Chem. Phys.* **6**, 5263 (2004).
13. G. V. Hartland, *J. Chem. Phys.* **116**, 8048 (2002).
14. G. V. Hartland, M. Hu, O. Wilson, P. Mulvaney, J. E. Sader, *J. Phys. Chem. B* **106**, 743 (2002).
15. S. D. Brorson, J. G. Fujimoto, E. P. Ippen, *Phys. Rev. Lett.* **59**, 1962 (1987).
16. C. K. Sun, F. Vallée, L. Acioli, E. P. Ippen, J. G. Fujimoto, *Phys. Rev. B* **48**, 12365 (1993).
17. J. Hohlfeld, J. G. Muller, S. S. Wellershoff, E. Matthias, *Appl. Phys. B* **64**, 387 (1997).
18. J. Chen, I. V. Tomov, H. E. Elsayed-Ali, P. M. Rentzepis, *Chem. Phys. Lett.* **419**, 374 (2006).
19. I. V. Tomov, P. Chen, P. M. Rentzepis, *J. Appl. Cryst.* **28**, 358 (1995).
20. C. Rose-Petruck *et al.*, *Nature* **398**, 310 (1999).
21. A. Cavalleri *et al.*, *Phys. Rev. Lett.* **85**, 586 (2000).
22. A. Plech *et al.*, *Europhys. Lett.* **61**, 762 (2003).
23. M. F. DeCamp *et al.*, *J. Synchrotron Radiat.* **12**, 177 (2005).

24. A. M. Lindenberg *et al.*, *Phys. Rev. Lett.* **84**, 111 (2000).
25. J. R. Dwyer *et al.*, *Philos. Trans. R. Soc. Ser. A* **364**, 741 (2006).
26. H. Park, X. Wang, S. Nie, R. Clinite, J. Cao, *Phys. Rev. B* **72**, 100301(R) (2005).
27. S. Nie, X. Wang, H. Park, R. Clinite, J. Cao, *Phys. Rev. Lett.* **96**, 025901 (2006).
28. E. Fermi, J. Pasta, S. Ulam, *LA*–1940 (1955).
29. J. M. Cowley, *Diffraction physics* (Elsevier, Amsterdam, 3rd ed., 1995).
30. *CRC handbook of chemistry and physics* (CRC Press, Boca Ration, FL, 1995), pp. E-43.
31. J. Hohlfeld *et al.*, *Chem. Phys.* **251**, 237 (2000).
32. C. Kittel, *Introduction to solid state physics* (Wiley, New York, 7th ed., 1996).
33. J. Tang, S. N. Dikshit, J. R. Norris, *J. Chem. Phys.* **103**, 2873 (1995).